

PROGRAMME AND ABSTRACTS

# Intermetallics 2021



## International Conference

04–08 October 2021



Educational Center Kloster Banz, Germany

[www.intermetallics-conference.de](http://www.intermetallics-conference.de)

Monday, 04 October School on advanced characterisation methods for intermetallics*	Tuesday, 05 October	Wednesday, 06 October	Thursday, 07 October	Friday, 08 October
Seminar room 1	Seminar room 1	Seminar room 1	Seminar room 1	Seminar room 1
09:00–10:30	09:00–10:30	09:00–10:30	09:00–10:30	09:00–10:30
Introduction to Synchrotron generated photons and neutrons p. 8	Titanium aluminides I p. 9	TCP phases p. 12	Intermetallics p. 13	Additive manufacturing of intermetallics p. 16
Coffee break	Coffee break	Coffee break	Coffee break	Coffee break
11:00–12:30	11:00–12:30	11:00–12:30	11:00–12:30	11:00–12:30
Synchrotron imaging for materials science and engineering p. 8	Silicides p. 9	High entropy alloys p. 12	Iron aluminides p. 13	Titanium aluminides III p. 16
Lunch	Lunch	Lunch	Lunch	Lunch
13:30–15:00	14:00–15:30	13:30–21:00	14:00–15:30	
Transmission electron microscopy of intermetallic phases p. 8	Physical properties p. 10	Excursion and conference dinner p. 7	Titanium aluminides II p. 14	
Coffee break	Coffee break		Coffee break	
15:30–17:00	15:50–17:05		15:50–17:05	
A primer to atom probe tomography and its application to intermetallics p. 8	Modelling p. 10		Nickel aluminides and nickel base alloys p. 14	
	Coffee break		Coffee break	
Foyer	17:25–18:40		17:25–18:40	
18:30–20:00	Corrosion p. 11		Functional intermetallics p. 15	
Welcome reception p. 7				
Seminar room 1	19:00–21:00			
20:00–21:00	Poster session p. 17			
Conference opening p. 8				

\* The school is especially intended for students and young scientists, the possible number of participants is limited. A registration is necessary.



Welcome note .....	4
Organisation and imprint .....	5
General information .....	6
General hints for authors and presenters .....	7
Social and cultural programme .....	7
Scientific programme	
Monday, 04 October .....	8
Tuesday, 05 October .....	9
Wednesday, 06 October .....	12
Thursday, 07 October .....	13
Friday, 08 October .....	16
Poster session • Tuesday, 05 October .....	17
Abstracts .....	19
Index of presenting authors, invited speakers and chairs .....	202

Dear Colleagues and Friends,

It is meanwhile a pleasant tradition to welcome you at our upcoming Intermetallics 2021 conference. In this successfully established series of conferences we already organize the fifth meeting, which is scheduled from 4<sup>th</sup> till 8<sup>th</sup> October 2021.

Following our tradition the conference focuses on materials based on intermetallic phases (intermetallics) to be envisaged for structural as well as functional applications. With a beneficial combination of high strength, low density and good corrosion resistance, they are specifically suited for applications at high temperatures and in severe environments. As some intermetallic phases show unique physical properties, they are also of interest for various functional applications. In addition, their possible appearance, thermodynamic stability, and role as strengthening phases in multi-component Compositionally Complex Alloys (CCAs) or High Entropy Alloys (HEAs) are recent scientific issues, which are also in the focus of this conference.

The choice of local organisers and members of the international advisory board will provide not only representation of all relevant topics but also a good balance between fundamental research and application-related issues. Following the successful scheme of the latest conference, the Intermetallics 2021 will be held as a single-session conference. A high-profile poster session will be an additional highlight. We will precede the conference with the 'School on Advanced Characterization Methods for Intermetallics', which is specifically devoted to young researchers up to the PhD level.

Even though the worldwide situation of the current pandemic was accompanied with many uncertainties in terms of the organization of the Intermetallics, we are very grateful that the large majority of the participants will be able to attend the conference in person. Traditionally, the conference takes place at the Educational Center Kloster Banz near Bamberg, Germany. The cloister is situated in a remote place above the valley of the river Main. As a well-known educational centre, it is an ideal place for conferences with its relaxing atmosphere. In addition, being situated in the central part of Germany, it is easily accessible from Nuremberg, Munich and Frankfurt airports.

We are looking forward to welcoming you at Kloster Banz,

Your Intermetallics 2021 Congress Team



**Venue**

Educational Center Kloster Banz  
Hanns-Seidel-Stiftung e. V.  
96231 Bad Staffelstein, Germany

---

**Date**

04–08 October 2021

---

**Scientific organiser**

Manja Krüger, Otto-von-Guericke Universität Magdeburg, Magdeburg, Germany

---

**Scientific co-organisers and programme committee**

Volker Güther, GfE Metalle und Materialien GmbH, Nuremberg, Germany  
Martin Heilmaier, Karlsruhe Institute of Technology, Karlsruhe, Germany  
Svea Mayer, Montanuniversität Leoben, Leoben, Austria  
Martin Palm, MPI für Eisenforschung GmbH, Düsseldorf, Germany  
Florian Pyczak, Helmholtz-Zentrum Hereon, Geesthacht, Germany  
Frank Stein, MPI für Eisenforschung GmbH, Düsseldorf, Germany

---

**International advisory board**

Bernard Bewlay, GE Global Research, Niskayuna, NY/USA  
Gabriele Cacciamani, University of Genoa, Genoa, Italy  
Helmut Clemens, Montanuniversität Leoben, Leoben, Austria  
Nathalie Dupin, Calcul Thermodynamique, Orcet, France  
Martin Friák, Institute of Physics of Materials, Brno, Czech Republic  
Easo George, Oak Ridge National Laboratory, Oak Ridge, TN/USA  
Juri Grin, MPI for Chemical Physics of Solids, Dresden, Germany  
Cláudio Schön, University São Paulo, São Paulo, Brazil  
Masao Takeyama, Tokyo Institute of Technology, Tokyo, Japan  
Michel Vilasi, University of Lorraine, Nancy, France

---

**Conference organisation**

Conventus Congressmanagement & Marketing GmbH  
Anja Kreuzmann/Julian Unger  
Carl-Pulfrich-Straße 1  
07745 Jena, Germany  
Phone +49 3641 31 16-357/-330  
Fax +49 3641 31 16-243  
intermetallics@conventus.de  
www.conventus.de

---


**Design/Layout**


Setting krea.tif-art UG (limited liability)  
Print 13 September 2021  
Circulation 100  
Editorial Deadline 10 September 2021

	<b>Registration fees</b>	<b>In person</b>	<b>Digital</b>
	Regular	700 EUR	350 EUR
	Student	350 EUR	200 EUR
	Accompanying person*	150 EUR	
	School on advanced characterisation methods for intermetallic**	included	

	<b>Social programme***</b>	
	Welcome reception, 04 October	included
	Excursion with conference dinner, 06 October	included

\* Welcome reception and conference dinner is included.  
 \*\* Number of participants limited and only for in person students.  
 \*\*\* Registration for the social programme is required.


	<b>Opening hours check-in</b>			
	Monday, 04 October	08:30 a.m.–12:00 p.m.	and	05:00 p.m.–08:00 p.m.
	Tuesday, 05 October	08:30 a.m.–12:00 p.m.	and	03:00 p.m.–06:00 p.m.
	Wednesday, 06 October	09:00 a.m.–12:30 p.m.		
	Thursday, 07 October	09:00 a.m.–12:00 p.m.	and	03:00 p.m.–06:00 p.m.
	Friday, 08 October	09:00 a.m.–12:30 p.m.		


 **Internet**  
 Wireless-Lan is available for free. You do not need to enter a password/code.

 **Certificate of attendance**  
 Certificates of attendance will first be made available on the last day of the conference at the check-in desk.


 **Poster prizes**  
 The three best posters will be awarded with 300 EUR each, sponsored by our partner GfE Metalle und Materialien GmbH



 **Poster session**  
 Posters will be rated on Tuesday, 05 October, 07:00 p.m. Authors are requested to be present at their posters during the poster session in the Kutschenhalle. Drinks and finger food will be served during the poster session. Pinboards will be numbered. The pinboards are only to be used with the designated pins. You will find your poster number in the programme book on page 24. Please note that all posters should be hanging on Tuesday, 05 October, by 01:00 p.m. and be removed after the poster session! Posters that have not been removed by that time will be available at the check-in desk until the end of the conference.

 **Catering**  
 Foods and drinks during the breaks will be provided.  
 For your information: the closest city with alternative restaurants is Bad Staffelstein, which is 5.5 km away (approximately 1 hour by foot, 7 minutes by car).

 **Smoking**  
 Smoking is prohibited inside the entire conference area.

 **Taxi | Taxi Dütsch | Phone +49 9573 52 06/+49 9571 52 06**  
 Price from Bad Staffelstein to Kloster Banz about 13 EUR\*  
 Price from Lichtenfels to Kloster Banz about 16 EUR\*

\* Prices are subject to change.



### Submitting your presentation/technical information

Please prepare your presentation as PDF or MS Office Power-Point for Windows in 16:9 aspect ratio.

A presentation notebook with a PDF reader and MS Office Power-Point will be provided. Notebook, presenter and laser pointer will be available at the speaker's podium in the lecture hall. The use of personal notebooks is possible upon agreement. However, it may interrupt the flow of the programme in the lecture hall. You will be assisted by a technical supervisor.

To guarantee a smooth running programme please upload your presentation on time – at least 2 hours before your presentation starts. For submission, please use a USB flash drive that is not protected by any software. Professional staff and equipment will be available for you to arrange and preview your presentation.

Please note: certain encodings for video and audio files could lead to technical problems.

### Time Allotment

Please prepare your presentation for the allotted amount of time. Chairs and moderators may interrupt should you overrun your time limit.

Allotted time is assigned as follows (speaking + discussion time):

Invited talks            25 + 5 minutes discussion

Abstract talks           12 + 3 minutes discussion

## SOCIAL AND CULTURAL PROGRAMME



### Welcome reception\* | Monday, 04 October

Come together for drinks and snacks. Enjoy the evening and allow yourself interesting conversations with colleagues, old friends and new acquaintances.

06:30 p.m.            Welcome reception

08:00 p.m.            Opening remarks  
Manja Krüger (Magdeburg/DE)

08:15 p.m.            Industrialization of titanium aluminides – challenges and surprises  
Volker Güther (Nuremberg/DE)

### Excursion and conference dinner\* | Wednesday, 06 October

Restricted by the current pandemic, we offer all participants two options for the afternoon. There are 40 places available per option.

**Option 1:** Join our bus tour to Bamberg. During an extended tour you will experience how unique Bamberg is. In the historic city ensemble with churches and monasteries, with bridges, narrow streets and squares, with half-timbered houses and baroque facades, you can still feel the magic of the past. Afterwards, you have free time to explore the old town on your own before returning by bus to Banz Monastery.

**Option 2:** stay with us in the immediate vicinity of the monastery. Together with the Baroque pilgrimage church of Vierzehnheiligen and the striking Staffelberg, on which there was once a Celtic oppidum, Banz forms the Franconian triumvirate. Hike in two groups to these two sights and enjoy time on site with a cool beer after strenuous metres of altitude have been covered. If one or the other's legs get heavy, a minibus can take you safely to your destination and also back to the monastery. We look forward to many enthusiastic hikers and hope for good weather.

For the conference dinner, all participants will meet again at the monastery to round off the evening in a cosy atmosphere. There will also be an evening lecture and the poster award ceremony.

07:00 p.m.            Alloy design for oxidation resistance in the Mo-Si-B system  
John Perepezko (Madison, WI/US)

\* A registration is necessary.

09:00 a.m.–03:30 p.m. School on advanced characterisation methods for intermetallics

09:00 a.m. Introduction to Synchrotron generated photons and neutrons and their use for diffraction studies of intermetallics  
Florian Pyczak (Geesthacht/DE)

Diffraction as well as Imaging can be done with photons and neutrons. Photons share many properties with X-rays known from lab sources but are in the examples covered in the school generated at a Synchrotron. So certain peculiarities of this type of radiation are discussed. Neutrons differ in many ways from photons how they interact with matter and how they can be produced. So not only neutron generation but also where it is advantageous to use them for materials characterisation is covered. Diffraction experiments can give information about present phases, texture, internal stresses, grain sizes and many other properties of intermetallic alloys. It will be shown how such information can be retrieved from the diffraction patterns. If diffraction measurements are performed using in situ specimen environments it is possible to mimic the situation a material experiences during service or processing. For example elevated temperatures or external stresses can be applied on the specimens. On selected examples the contribution shows how such experiments are performed on intermetallic alloys, how the data is evaluated and which information can be gained from the measured data.

10:30 a.m.–11:00 a.m. *Coffee break*

11:00 a.m. Synchrotron imaging for materials science and engineering  
Guillermo Requena (Köln/DE)

Three dimensional microstructure characterization at different scales plays the key role for understanding the quantitative relationship between processing, microstructure and properties. Synchrotron sources can provide spatial resolution down to sub- $\mu\text{m}$  range, high time resolution critical for in situ experiments and multimodal experimental data by simultaneous combination with other synchrotron techniques, e. g. diffraction. All these characteristics will be introduced in the frame of basic theoretical concepts and practical examples. A strong focus will be given to application cases for which synchrotron imaging techniques have been decisive to develop new materials as well as to understand the thermo-mechanical behaviour of structural materials such as Al-, Ti-alloys and composites.

12:30 p.m.–02:00 p.m. *Lunch*

02:00 p.m. Transmission electron microscopy of intermetallic phases: from basics to atomic resolution characterization  
Christian Liebscher (Düsseldorf/DE)

The transmission electron microscope (TEM) is a versatile tool to study the microstructure, crystallography, chemical composition and local bonding behavior of materials. This lecture will introduce the basics of conventional TEM imaging and electron diffraction of intermetallic phases, highlight techniques to measure the chemical composition and site preference of alloying elements in intermetallic compounds and conclude with techniques to determine the atomic structure of complex intermetallics. The aim of the lecture is to provide insights into the fundamental aspects of the various TEM techniques and to showcase their application for uncovering the structure of a broad variety of intermetallic phases relevant in advanced engineering materials.

03:00 p.m. *Coffee break*

03:30 p.m.–05:00 p.m. A primer to atom probe tomography and its application to intermetallics  
Stoichko Antonov (Düsseldorf/DE)

Atom probe tomography (APT) provides three-dimensional compositional information at the sub-nanometre resolution. Additionally, it is sensitivity in the range of parts per million for all elements, including light elements such as hydrogen, carbon or boron, making it uniquely capable of revealing insight on compositional features in the microstructure and their effect on the properties of various material systems. This lecture will be divided into two parts. It will start by providing background on basics of atom probe tomography, such as field evaporation and data acquisition and reconstruction, followed by common approaches to sample preparation. The second half will focus on data analysis by using a few case studies that pertain to intermetallics research that show the possibilities and limitations of the technique, and how it would ideally be used in correlation to other techniques, e. g. electron microscopy, to extract additional information from the sample.

06:30 p.m.–08:00 p.m. Welcome reception

08:00 p.m.–09:00 p.m. Conference opening

08:00 p.m. Opening remarks  
Manja Krüger (Magdeburg/DE)

08:15 p.m. Opening talk: Industrialization of titanium aluminides – challenges and surprises  
O–IT–01 Volker Güther (Nuremberg/DE)

09:00 a.m.–10:30 a.m. Titanium aluminides I  
Chair Volker Güther (Nuremberg/DE)

09:00 a.m. Invited talk: Applying advanced characterization and simulation methods to understand  
O-IT-04 peculiarities of TiAl alloy and process development  
Florian Pyczak (Geesthacht/DE)

09:30 a.m. Revised phase diagram for the Ti-Al-O ternary system from 35 to 55 at. % aluminum  
O-TA-01 Hirotoyo Nakashima (Tokyo/JP)

09:45 a.m. TiAl embrittlement at high temperatures  
O-TA-02 Camille Thenot (Toulouse/FR)

10:00 a.m. O-phase formation and elastic modulus in the alloy Ti-42Al-8.5Nb  
O-TA-03 Heike Gabrisch (Geesthacht/DE)

10:15 a.m. Kinetics of solid-state phase transformations in ternary Ti–Al–Nb alloys below 1000 °C  
O-TA-04 Benedikt Distl (Düsseldorf/DE)

10:30 a.m.–11:00 a.m. Coffee break

- 11:00 a.m.–12:30 p.m. **Silicides**  
Chair Andreas Leineweber (Freiberg/DE)
- 11:00 a.m. **Invited talk: Off-stoichiometric TiC toughening for Mo- and Mo-Si-B-based alloys**  
O-IT-03 Shuntaro Ida (Sendai/JP)
- 11:30 a.m. **The high temperature behavior of pesting and creep resistant eutectic-eutectoid Mo-Si-Ti alloys**  
O-SI-01 Martin Heilmaier (Karlsruhe/DE)
- 11:45 a.m. **High-energy synchrotron X-ray *in situ* observation of ternary eutectic growth in a directionally solidified Mo-Si-B alloy**  
O-SI-02 Georg Hasemann (Magdeburg/DE)
- 12:00 p.m. **Production and characteristics of spherical MoSiB- and VSiB-powders**  
O-SI-03 Karin Ratschbacher (Nuremberg/DE)
- 12:15 p.m. **Particle strengthening of additively manufactured Me-Si-B (Me = Mo, V) alloys**  
O-SI-04 Janett Schmelzer (Magdeburg/DE)
- .....
- 12:30 p.m.–02:00 p.m. *Lunch*
- .....
- 02:00 p.m.–03:30 p.m. **Physical properties**  
Chair Werner Skrotzki (Dresden/DE)
- 02:00 p.m. **Deformation characteristics of single-phase Nb<sub>2</sub>Co<sub>7</sub> under uniaxial compression test**  
O-PP-04 Toshiaki Horiuchi (Sapporo/JP)
- 02:15 p.m. **Impact of antiphase boundaries on structural, magnetic and vibrational properties of Fe<sub>3</sub>Al**  
O-PP-02 Martin Friak (Brno/CZ)
- 02:30 p.m. **Temperature gradients for characterizing intermetallics**  
O-PP-03 Stephanie Lippmann (Jena/DE)
- 02:45 p.m. **Invited talk: An overview of processing and magnetic properties of L10-structured MnAl**  
O-IT-02 Ian Baker (Hanover, NH/US)
- 03:15 p.m. **Soft magnetic properties of single-phase B2 and B2/BCC multi-principal element alloys**  
O-PP-01 Youxiong Ye (Hanover, NH/US)
- .....
- 03:30 p.m.–03:50 p.m. *Coffee break*
- .....
- 03:50 p.m.–05:05 p.m. **Modelling**  
Chair Yang Yang (Solna/SE)
- 03:50 p.m. **Invited talk: What can EBEF do better?**  
O-IT-05 Nathalie Dupin (Orce/FR)
- 04:20 p.m. **Modelling intermediate phases for the third generation Calphad descriptions – case study of W-C**  
O-MO-01 Zhangting He (Stockholm/SE)



04:35 p.m. O-MO-02	First principles density functional theory prediction of the crystal structure and the elastic properties of $\text{Mo}_2\text{ZrB}_2$ and $\text{Mo}_2\text{HfB}_2$ Rachid Touzani (Magdeburg/DE)
04:50 p.m. O-MO-03	Stability prediction of the $\sigma$ -phase using a supervised machine learning method Jean-Claude Crivello (Thiais/FR)
.....	
05:05 p.m.–05:25 p.m. <i>Coffee break</i>	
.....	
05:25 p.m.–06:40 p.m. Chair	Corrosion Manja Krüger (Magdeburg/DE)
05:25 p.m. O-IT-06	<b>Invited talk:</b> Microstructure related high temperature oxidation behavior of iron aluminides Daniela Zander (Aachen/DE)
05:55 p.m. O-IT-07	<b>Invited talk:</b> Oxidation behavior of a eutectic high temperature alloy Mo-20Si-52.8Ti in dry and wet environments Bronislava Gorr (Eggenstein Leopoldshafen/DE)
06:25 p.m. O-CO-01	Protective aluminum and chromium diffusion coatings for refractory metals at high temperature exposure Anke Silvia Ulrich (Frankfurt/DE)
.....	
07:00 p.m.	Poster session

## 1<sup>st</sup> MSIT | Advanced School

# Diffusion in Materials - Fundamentals and Applications

### The Programme includes

- Diffusion couple technique: a research tool in materials science
- Theory of diffusion
- Simulations using DICTRA with hands-on training
- Evaluation of diffusion couples
- DICTRA in industrial applications

25 – 26 October 2022  
Castle Eberburg, Germany

### Organised by

MSI, Materials Science  
International Services GmbH,  
Stuttgart, Germany

Max-Planck-Institut für  
Eisenforschung GmbH,  
Düsseldorf, Germany

In association with  
Thermo-Calc Software AB,  
Solna, Sweden

Registration starts  
in January 2022

Following the success of the MSIT Winter Schools, MSI and MSIT® are pleased to announce a new series of advanced training events.

The aim of 'The MSIT Advanced Schools' is to give training on one important topic in Materials Science to a much higher level than at our annual Winter School.

The 'MSIT Advanced Schools' are aimed at materials scientists who are already familiar with the subject but are looking for a deeper understanding.



- 09:00 a.m.–10:30 a.m. **TCP phases**  
Chair Stephanie Lippmann (Jena/DE)
- 09:00 a.m. **Invited talk: Machine learning the structural stability of topologically close-packed phases**  
O-IT-08 Thomas Hammerschmidt (Bochum/DE)
- 09:30 a.m. **Invited talk: Design of heat resistant ferritic steels using precipitation of Laves phase**  
O-IT-09 Satoru Kobayashi (Tokyo/JP)
- 10:00 a.m. **Understanding the formation mechanism of  $\sigma$  phase in hyper duplex steels - experiments and computation**  
O-TCP-01 Aurélie Jacob (Vienna/AT)
- 10:15 a.m. **Structural transformation of the  $\sigma$  phase in the Cr–Mn system studied by *in situ* powder neutron diffraction**  
O-TCP-02 Jean-Marc Joubert (Thiais/FR)
- .....
- 10:30 a.m.–11:00 a.m. *Coffee break*
- .....
- 11:00 a.m.–12:30 p.m. **High entropy alloys**  
Chair Martin Heilmaier (Karlsruhe/DE)
- 11:00 a.m. **Invited talk: Design and development of refractory metal (Nb), intermetallic composites, refractory high entropy alloys and refractory complex concentrated alloys**  
O-IT-10 Panos Tsakirooulos (Sheffield/GB)
- 11:30 a.m. **Single-crystal mechanical properties of equiatomic CrMnFeCoNi high entropy alloy and its derivative equiatomic quaternary and ternary medium entropy alloys**  
O-HEA-01 Haruyuki Inui (Kyoto/JP)
- 11:45 a.m. **Study of structural defects in binary and ternary B2 alloys of the AlCoCrFeNi system**  
O-HEA-02 Guy Hillel (Beer Sheva/IL)
- 12:00 p.m. **Effect of Mo and Ta on a duplex bcc+orthorhombic refractory complex concentrated alloy using diffusion couples**  
O-HEA-03 Zhao Huvelin (Chatillon/FR)
- 12:15 p.m. **A novel alloy development approach – biomedical high-entropy alloys**  
O-HEA-04 Maximilian Regenber (Magdeburg/DE)
- .....
- 12:30 p.m.–01:30 p.m. *Lunch*
- .....
- 01:30 p.m. **Excursion and conference dinner**
- 07:00 p.m. **Evening talk: Alloy design for oxidation resistance in the Mo-Si-B system**  
O-IT-14 John Perepezko (Madison, WI/US)



- 09:00 a.m.–10:30 a.m. **Intermetallics**  
Chair Frank Stein (Düsseldorf/DE)
- 09:00 a.m. **Invited talk:** High-entropy Hägg phases – a case study of nitrides and diborides  
O-IT-11 Paul Mayrhofer (Vienna/AT)
- 09:30 a.m. Plastic deformation behavior of metallic-perovskite  $E2_1 M_3AlC_{1-x}$  (M = Ni, Co) observed using  
O-IM-01 nanoindentation measurements  
Yoshisato Kimura (Yokohama/JP)
- 09:45 a.m. Low temperature deformation mechanisms of CoZr and  $Co_{39}Ni_{11}Zr_{50}$  intermetallic  
O-IM-02 compounds  
Werner Skrotzki (Dresden/DE)
- 10:00 a.m. Investigation of the growth of phases in the Cu(Ni)–Sn system  
O-IM-03 Varun Baheti (Roorkee/IN)
- 10:15 a.m. Stable and metastable phase equilibria involving  $Cu_6Sn_5$  – effect of variable composition of  
O-IM-04 an apparently stoichiometric intermetallic  
Andreas Leineweber (Freiberg/DE)
- .....
- 10:30 a.m.–11:00 a.m. *Coffee break*
- .....
- 11:00 a.m.–12:30 p.m. **Iron aluminides**  
Chair Georg Hasemann (Magdeburg/DE)
- 11:00 a.m. **Invited talk:** Iron aluminides – a class of sustainable materials  
O-IT-12 Martin Palm (Düsseldorf/DE)
- 11:30 a.m. Mechanical properties of a cast Fe<sub>3</sub>Al-based iron aluminum alloy at moderate temperatures  
O-IA-01 Eva Kollmannsberger (Landshut/DE)
- 11:45 a.m. Microstructure property correlation of a Mo-Ti-B alloyed iron aluminide  
O-IA-02 Andreas Abel (Berlin/DE)
- 12:00 p.m. Microstructure evolution and phase transformations in Fe-Al-Nb(B) alloys  
O-IA-03 Angelika Gedsun (Düsseldorf/DE)
- 12:15 p.m. The role of Cr on the Al<sub>2</sub>O<sub>3</sub> formation on iron aluminides at intermediate temperatures in air  
O-IA-04 René Daniel Pütz (Aachen/DE)
- .....
- 12:30 p.m.–02:00 p.m. *Lunch*

- 02:00 p.m.–03:30 p.m. **Titanium aluminides II**  
Chair Martin Schloffer (München/DE)
- 02:00 p.m. A study of the deformation mechanisms and fracture behaviour of a TiAl alloy containing ordered  $\beta_0$  phase  
O-TA-05 Alain Couret (Toulouse/FR)
- 02:15 p.m. High temperature deformation behavior of  $\beta$ -solidifying titanium aluminide alloy  
O-TA-06 Manufactured by Electron Beam Powder Bed Fusion (EB-PBF)  
Mirko Teschke (Dortmund/DE)
- 02:30 p.m. Solid solution strengthening of TiAl alloys with zirconium  
O-TA-07 Melissa Allen (Nuremberg/DE)
- 02:45 p.m. Influence of tungsten on the mechanical properties of a  $\gamma$ -TiAl based alloy  
O-TA-08 Benjamin Galy (Toulouse/FR)
- 03:00 p.m. A thermodynamic and properties database for Ti- and TiAl-based alloys  
O-TA-09 Yang Yang (Solna/SE)
- 03:15 p.m. Determination of phase equilibria in the Ti–Al–Si system at 800–1200 °C  
O-TA-10 Zahra Kahrobaee (Düsseldorf/DE)
- 
- 03:30 p.m.–03:50 p.m. *Coffee break*
- 
- 03:50 p.m.–05:05 p.m. **Nickel aluminides and nickel base alloys**  
Chair Florian Pyczak (Geesthacht/DE)
- 03:50 p.m. Diffusion and defects to understand the growth of  $\beta$ -NiAl bond coat on superalloy  
O-NA-01 Esakkiraja Neelamegan (Münster/DE)
- 04:05 p.m. Small scale fracture behavior of nanostructured NiAl-(Cr,Mo) in-situ composites processed  
O-NA-02 by selective electron beam melting  
Andreas Förner (Erlangen/DE)
- 04:20 p.m. Micro-tensile creep testing for NiAl single crystalline miniaturized specimens  
O-NA-03 LiKang Luan (Eggenstein-Leopoldshafen/DE)
- 04:35 p.m. Microstructure evolution of an  $\alpha'/\alpha''$ -strengthened ferritic superalloy  
O-NA-04 Luis Ángel Morales (Erlangen/DE)
- 04:50 p.m. A quantum mechanical study of pressure induced changes of magnetism in austenitic  
O-NA-05 stoichiometric  $\text{Ni}_2\text{MnSn}$   
Martin Friak (Brno/CZ)
- 
- 05:05 p.m.–05:25 p.m. *Coffee break*



05:30 p.m.–06:45 p.m.	Functional intermetallics Chair Paul Mayrhofer (Vienna/AT)
05:30 p.m. O-FI-01	Intermetallic compounds as hydrogenation catalysts – structural and electronic influences Marc Armbrüster (Chemnitz/DE)
05:45 p.m. O-FI-02	The way for elimination of the martensite stabilization effect in NiTi-based alloys Natalia Resnina (Saint Petersburg/RU)
06:00 p.m. O-FI-03	Effect of duration of electropulse treatment on properties of rapidly quenched TiNiCu alloys with high copper content Alexander Shelyakov (Moscow/RU)
06:15 p.m. O-FI-04	TiAl thin films as an alternative metallization for high temperature SAW devices Marietta Seifert (Dresden/DE)
06:30 p.m. O-FI-05	Use of phase equilibria in the Ag-Mg-Sb system for guidance of low temperature thermoelectric applications Silvana Tumminello (Köln/DE)



## Winter School on Materials Chemistry

3-7 April 2022, castle Ebernburg, Germany

### Organised by

MSI, Materials Science International Services GmbH, Germany / Dr. S. Iljenko

Hampton Thermodynamics, UK / Dr. A. Watson

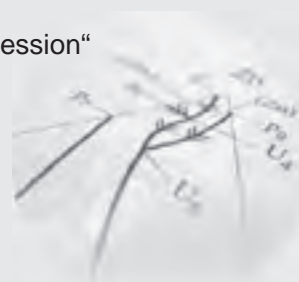
Max-Planck-Institut für Eisenforschung GmbH, Germany / Dr. F. Stein, Dr. M. Palm



Registration starts in September 2021

### The Programme includes

- Principles of Chemical Thermodynamics
- Phase Diagrams and Phase Equilibria (basic and advanced level), with „hands-on session“
- Experimental Determination of Phase Diagrams
- Crystallography with „hands-on session“
- Experimental Methods in Thermodynamics with „hands-on session“
- Application of DFT in the Context of Phase Diagram Modelling
- Computational Materials Thermodynamics
- Calphad Method (with hands-on session)



- 09:00 a.m.–10:30 a.m. **Additive manufacturing of intermetallics**  
Chair Alain Couret (Toulouse/FR)
- 09:00 a.m. **Invited talk: Additive manufacturing of  $\gamma$ -titanium aluminides – challenges, solutions, and future prospects**  
O-IT-13 Christoph Leyens (Dresden/DE)
- 09:30 a.m. **Direct insights into the phase evolution and transformation during a simulated additive manufacturing process**  
O-AM-01 Adriana De Andrade (Geesthacht/DE)
- 09:45 a.m. **Processing of titanium aluminides with high temperature laser beam melting – from the development of a series machine upgrade to typical complex applications**  
O-AM-02 Tobias Maiwald-Immer (Halsbrücke/DE)
- 10:00 a.m. **Thermodynamic analysis of quaternary Al-Mg-Si-Er alloys for applications in additive manufacturing**  
O-AM-03 Mauro Palumbo (Torino/IT)
- 10:15 a.m. **Flexible powder production for additive manufacturing of refractory metal alloys**  
O-AM-04 Frauke Hinrichs (Karlsruhe/DE)
- 
- 10:30 a.m.–11:00 a.m. *Coffee break*
- 
- 11:00 a.m.–12:30 p.m. **Titanium aluminides III**  
Chair Martin Palm (Düsseldorf/DE)
- 11:00 a.m. **Mechanical properties of a 4<sup>th</sup> generation  $\gamma$ -TiAl alloy processed via electron beam powder bed fusion**  
O-TA-11 Marcel Reith (Fürth/DE)
- 11:15 a.m. **Quasi-static and dynamic fracture toughness of a  $\gamma$ -TiAl alloy – measurement techniques, fractography and interpretation**  
O-TA-12 Arthur Lintner (Leoben/AT)
- 11:30 a.m. **Microstructural evolution in gamma TiAl cyclically deformed at room temperature**  
O-TA-13 Tomas Kruml (Brno/CZ)
- 11:45 a.m. **Microstructure and mechanical properties of TNM titanium aluminide alloy after heat treatment and different cooling conditions**  
O-TA-14 Mark Hilleringmann (Aachen/DE)
- 12:00 p.m. **Rapid solidification behavior of an intermetallic  $\gamma$ -TiAl based Ti-48Al-2Cr-2Nb alloy studied by means of in-situ high-energy X-ray diffraction**  
O-TA-15 Gloria Graf (Leoben/AT)
- 12:15 p.m. **Microstructure and mechanical properties of a  $\gamma$ -TiAl alloy with a nano-grained surface layer**  
O-TA-16 Christoph Stangl (Landshut/DE)



- P-01 Structural disorder in a complex Mg rich-Pt phase  
Laura Agnarelli (Dresden/DE)
- P-02 Room temperature plastic deformation of hard and brittle crystals investigated by micropillar compression method  
Hirotaka Suzuki (Kyoto/JP)
- P-03 Fracture toughness of the intermetallic C15 Al<sub>2</sub>Ca Laves phase determined using a micropillar splitting technique  
Uzair Rehman (Düsseldorf/DE)
- P-04 Micropillar compression deformation of single crystal of Fe<sub>3</sub>Ge with the L1<sub>2</sub> structure  
Zhenghao Chen (Kyoto/JP)
- P-05 Distribution of the enantiomorphs in polycrystalline CoSi  
Ulrich Burkhardt (Dresden/DE)
- P-06 Heterogeneous equilibria in the systems Mo-Si-Ti and Mo-Si-Ti-B  
Andreas Czerny (Karlsruhe/DE)
- P-07 Phase-field investigation on multiphase microstructural evolution in Mo-Si-Ti system  
Yuhan Cai (Karlsruhe/DE)
- P-08 Ternary V<sub>55</sub>-V<sub>3</sub>Si-V<sub>5</sub>SiB<sub>2</sub> eutectic reaction in V-Si-B system  
Weiguang Yang (Jülich/DE)
- P-09 New rare-earth palladium intermetallic compound with extended pnictogen ribbons  
Mihai Sturza (Dresden/DE)
- P-10 Shape memory effect during isothermal holding of Ti-Hf-Ni-Cu alloys  
Elena Demidova (Saint Petersburg/RU)
- P-11 Influence of the orientation of columnar grains on the functional properties of the NiTi alloy produced by wire-arc additive manufacturing  
Rashid Bikbaev (Saint Petersburg/RU)
- P-12 Stability of strain variation during isothermal martensitic transformation under cyclic deformation in quenched Ni<sub>51</sub>Ti<sub>49</sub> alloy  
Aleksei Ivanov (Saint Petersburg/RU)
- P-13 Biocompatibility of pure refractory metals and their combination as high entropy alloys  
Janett Schmelzer, Georg Hasemann, Maximilian Regenberg (Magdeburg/DE)
- P-14 Plastic deformation of single crystals of the equiatomic Cr-Co-Ni medium-entropy alloy with the FCC structure  
Le Li (Kyoto/JP)
- P-15 Deformation twinning in single crystals of the equiatomic Cr-Co-Ni medium entropy alloy  
Shogo Kuroiwa (Kyoto/JP)
- P-16 Non-equilibrium grain boundaries in additively manufactured CoCrFeMnNi high-entropy alloy  
Nuri Choi (Münster/DE)
- P-18 TiAl alloy optimization for EBM and usage of selective Al-evaporation for microstructure design  
Martin Schloffer (München/DE)

- P-19 Microstructure and mechanical properties of TiAl4822 alloy built by selective laser melting  
Kazuhiro Mizuta (Hachioji/JP)
- P-20 *In situ* observation of the phase evolution during a physical simulation of the spark plasma sintering process of a  $\gamma$ -TiAl based alloy  
Michael Musi (Leoben/AT)
- P-21 Effect of Zr on the phase equilibria among  $\beta$ -Ti/ $\alpha_2$ -Ti<sub>3</sub>Al/ $\gamma$ -TiAl phases in Ti-Al-Cr system  
Jianhui Yu (Tokyo/JP)
- P-22 On the formation mechanism of banded microstructures in electron beam melted Ti-48Al-2Cr-2Nb  
Reinhold Wartbichler (Leoben/AT)
- P-23 Ti-Al<sub>3</sub>Ti metal-intermetallic composite with a cubic modification of trialuminide stabilized with Ag  
Daria Lazurenko (Novosibirsk/RU)
- P-24 Investigation of the formation processes of intermetallic compounds based on titanium aluminide in the preparation of a composite material reinforced with fibers SiC  
Alexander Lenkovets (Korolev/DE)
- P-25 Screening for O phase in  $\gamma$ -TiAl alloys  
Marcus Willi Rackel (Geesthacht/DE)
- P-26 Oxidation protection of Ni-base superalloys by the F-effect – fundamentals for industrial application  
Hans-Eberhard Zschau (Wurzen/DE)
- P-27 Introduction intermetallics workgroup of Technical University of Liberec  
Pavel Hanus (Liberec/CZ)
- P-28 Formation of intermetallic  $\alpha$ -Al-(Fe,M)-Si and  $\beta$ -Al-(Fe,M)-Si phase in presence of 3d-transition metal elements M in Fe-containing secondary Al-Si casting alloys  
Hanka Becker (Freiberg/DE)
- P-29 Interface layer in Al-steel clad strip prepared by twin-roll casting  
Michaela Šlapáková (Prague/CZ)
- P-30 Production, optimization and investigation of cast FeAlNb parts  
Michael Ghosh (Aachen/DE)
- P-31 Fe-Al-Si-X based intermetallic alloys  
Martin Švec (Liberec/CZ)
- P-32 Grain refinement of FeAl alloys and impact of local solidification time on grain size  
Emir Subašić (Aachen/DE)
- P-33 High temperature oxidation behavior of TiAlCrYSi bond coatings obtained using CHC-PVD method on  $\gamma$ -TiAl  
Radosław Swadźba (Gliwice/PL)



# EXTENDED ABSTRACTS

# Intermetallics 2021

## Oral abstracts

Invited talks (O-IT-01–14) .....	20–45
Session • Physical properties (O-PP-01–04) .....	46–51
Session • Silicides (O-SI-01–04) .....	53–59
Session • Titanium aluminides (O-TA-01–16) .....	61–90
Session • Modelling (O-MO-01–03) .....	92–96
Session • Corrosion (O-CO-01) .....	97
Session • TCP phases (O-TCP-01–02) .....	99–101
Session • High entropy alloys (O-HEA-01–04) .....	103–109
Session • Intermetallics (O-IM-01–04) .....	111–116
Session • Iron aluminides (O-IA-01–04) .....	118–123
Session • Nickel aluminides & Nickel base alloys (O-NA-01–05) .....	125–133
Session • Functional intermetallics (O-FI-01–05) .....	135–142
Session • Additive manufacturing of intermetallics (O-AM-01–04) .....	144–150
<b>Poster abstracts</b>	
Poster session (P-01–33) .....	152–200

**O-IT-01**

**Industrialization of TiAl – Challenges and Surprises**

Volker Güther

GfE Metalle und Materialien GmbH, Nuremberg, Germany, volker.guether@gfe.com

**Introduction**

The aim of this lecture is to give an overview about the industrialization process of the metallurgical production of intermetallic Titanium Aluminide materials including corresponding industrial applications. The period from 1995 to 2020 will be covered.

**Results and Discussion**

Among three competing technologies, VAR processing has been established as the best applicable metallurgical technology of the production of alloyed TiAl based materials against PAM and EBM. Anyhow, there are some remarkable differences between the metallurgical processing of conventional Ti-alloys and TiAl-alloys which have to be mentioned. Specific materials processing related challenges had to be solved in order to prevent the formation of Ti-rich inclusions (incompletely alloyed Ti is a high dense high melting inclusion in the low melting TiAl matrix) or to overcome cracking phenomena which were particularly observed in the production of beta-stabilized TiAl alloy ingots. The technical reasons for such challenges and the corresponding technical solution strategies are being addressed in more detail in the presentation.

Despite of the remarkable progress in VAR processing of TiAl ingots, the most important break-through regarding to materials homogeneity and soundness of small sized semi-finished products was the introduction of skull melting technologies such as VAR Skull Melting and Induction Skull Melting (ISM) with subsequent centrifugal casting in permanent moulds. Currently, almost the entire industrial production of TiAl materials for structural applications is based on skull melting technologies. Furthermore, ISM has successfully demonstrated its capability for multiplicate recycling steps to transfer valuable TiAl revert directly to new products. As a result of recycling, the materials yield (fly-to-buy-ratio) for the production of TiAl LPT blades increased by a factor of almost four resulting in a substantial cost decrease. The state-of-the-art production technology for TiAl LPT blades is being presented. Further efforts on both production technologies and materials development are necessary in order to get Titanium Aluminide products commercially comparable to those of Ni based superalloys.



Fig. 1: Induction Skull Melter after pouring



Fig. 2: Demoulding of a casting wheel

**References**

- [1] V. Güther, M. Allen, J. Klose, H. Clemens, Metallurgical processing of titanium aluminides in industrial scale, *Intermetallics*. **2018**, *103*, 12-22.

**O-IT-02****An overview of processing and magnetic properties of L1<sub>0</sub>-structured MnAl**

Ian Baker and Thomas Keller

Thayer School of Engineering, Dartmouth College, 03755 Hanover, NH, USA, Ian.Baker@Dartmouth.edu,  
Thomas.R.Keller.TH@dartmouth.edu**Introduction**

Demand for high-performance permanent magnets is increasing rapidly for applications such as wind turbine generators and motors in both electric and hybrid cars. This market is served by rare earth (RE) magnets based on Nd<sub>2</sub>Fe<sub>14</sub>B and Sm<sub>2</sub>Co<sub>17</sub>. RE magnets are not without issues; they can chip, suffer thermal shock, and can suffer grain boundary corrosion. However, their biggest problems are: price volatility; that a single country largely controls the RE metals market; and that the extraction of RE metals causes severe environmental degradation. L1<sub>0</sub>-structured  $\tau$ -MnAl, see Figure 1, has been of interest as a permanent magnet since the early 1960s. It has a *theoretical* energy product,  $(BH)_{max}$ , between that of traditional AlNiCo magnets and RE magnets with a value of 96 kJ/m<sup>3</sup> that is comparable to that of *bonded* Nd<sub>2</sub>Fe<sub>14</sub>B magnets and almost two-thirds the value for SmCo magnets on a density-compensated basis. Further, it does not suffer from the technical or societal issues associated with RE magnets, and potentially has the lowest cost per MGOe of any permanent magnet.

**Materials and Methods**

The  $\tau$  phase, which exists over a range of compositions, is metastable and forms from the high temperature  $\epsilon$ -phase by a hybrid massive-martensitic transformation. The martensitic transformation mode dominates at lower temperatures and the diffusion-controlled massive mode dominates at higher temperatures [3,4]. During the transformation from the  $\epsilon$ -phase to the  $\tau$  phase anti-phase boundaries (APBs), twins, stacking faults and dislocations are created, and, depending on the composition and processing conditions, the equilibrium  $\beta$  and  $\gamma_2$  phases can also form, all of which affect the magnetic properties. The grain size can also influence the magnetic properties either directly or by affecting the  $\beta$  and  $\gamma_2$  arrangement and defect formation.

**Results and Discussion**

Although  $\tau$ -MnAl has great potential, the enigma is that the theoretical  $(BH)_{max}$  has never been achieved: mechanically-milled particulates can show high coercivity ( $H_c$ ) but low saturation magnetization ( $M_s$ ) while warm-extruded material can show high  $M_s$  but low  $H_c$ . Since the early studies on hot extrusion of  $\tau$ -MnAl in Japan in 1977 by Ohtani et al. [1] which produced a good magnetic remanence ( $M_r$ ) of 93 emu/g and a  $H_c$  of 215 kA/m in anisotropic magnets, numerous processing routes that have been used to produce MnAl magnets including casting and annealing, hot extrusion, gas atomization, rapid solidification processing, melt spinning, mechanical milling, and equal channel angular extrusion. Mechanical milling of the  $\epsilon$ -phase to produce nanocrystalline grains followed by annealing to produce the  $\tau$ -MnAl with a small amount of the equilibrium  $\beta$  and  $\gamma_2$  phases present has been shown to produce both good  $M_s$  and a  $H_c$  values of 87 emu/g and 382 kA/m, respectively [2], resulting in the highest  $(BH)_{max}$  of isotropic magnets, see Figure 2. Of course, the latter are powders and their consolidation typically leads to a reduction in the amount of the  $\tau$ -MnAl with a corresponding reduction in  $M_s$ .

The fundamental difficulty with improving the magnetic properties of  $\tau$ -MnAl and, thus, achieving the theoretical  $(BH)_{max}$  value is that there is no clear understanding of how the properties depend on the defects (APBs, twins, stacking faults and dislocations) and second phases ( $\beta$  and  $\gamma_2$ ) present. In this presentation, we will provide an overview of the various processing routes that have used to produce  $\tau$ -MnAl and describe how these different processing routes and subsequent heat treatments produce different microstructures and different magnetic behavior.

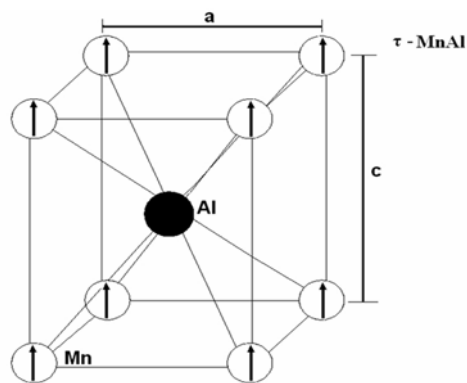


Fig. 1: Crystal structure of  $\tau$ -MnAl. The  $c/a$  ratio is close to unity. The arrows indicate the magnetic dipole directions.

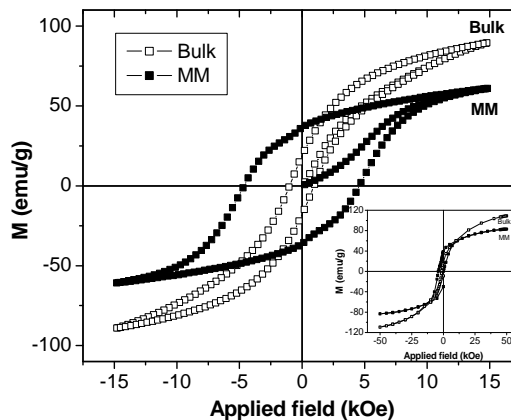


Fig. 2: Magnetic hysteresis loops for bulk  $\tau$ -MnAl and mechanically-milled  $\text{Mn}_{54}\text{Al}_{46}$  powders annealed at 400 °C for 10 mins (inset are the same loops measured at 50 kOe). Note the higher  $M_s$  in the bulk material but higher  $H_c$  in the mechanically-milled powders. From [2].

### References

- [1] T. Ohtani, N. Kato, K. Kojima, Y. Sakamoto, I. Konno, M. Tsukahara, T. Kubo, Magnetic-Properties of Mn-Al-C Permanent-Magnetic Alloys, *IEEE Transactions on Magnetics*. **1977**, *13*, 1328-1330.
- [2] Q. Zeng, I. Baker, Z.C. Yan, Nanostructured MnAl permanent magnets produced by mechanical milling, *Journal of Applied Physics*. **2006**, *99*, E08902-1-3.
- [3] J.M.K. Wiezorek, A.K. Kulovits, C. Yanar, W.A. Soffa, Grain boundary mediated displacive-diffusional formation of  $\tau$ -phase MnAl, *Metallurgical and Materials Transactions A*. **2011**, *42*, 594-604.
- [4] P.-Z. Si, H.-D. Qian, C.-J. Choi, J. Park, S. Han, H.-L. Ge, K.P. Shinde, *In situ* Observation of Phase Transformation in MnAl(C) Magnetic Materials, *Materials*. **2017**, *10*, 1016.

**O-IT-03****Off-stoichiometric TiC toughening for Mo- and Mo-Si-B-based alloys**

Shuntaro Ida, Linye Zhu, Nobuaki Sekido and Kyosuke Yoshimi

Department of Materials Science, Graduate School of Engineering, Tohoku University, 980-8579 Sendai, Japan,  
 shuntaro.ida.e1@tohoku.ac.jp, zhu.linye.r4@dc.tohoku.ac.jp, sekido@material.tohoku.ac.jp,  
 yoshimi@material.tohoku.ac.jp

**Introduction**

Recently, TiC-reinforced Mo-Si-B (MoSiBTiC) alloys, which consist mainly of Mo, Mo<sub>5</sub>SiB<sub>2</sub> (T<sub>2</sub> phase) and TiC phases, have been developed for ultrahigh temperature applications. It has been shown that these alloys possess both excellent high temperature strength and good room temperature fracture toughness [1-5]. Therefore, it is recognized that TiC is a key phase for the design of Mo-Si-B-based alloys.

One of the reasons for the toughness improvement by the TiC addition is through increase in Mo-phase continuity. In the Mo-Si-B ternary system, the Mo phase that forms during solidification is always discontinuous because the eutectic composition is in a relatively Mo-poor region [6]. However, since TiC has a melting point higher than Mo, the eutectic composition associated with Mo and TiC shifts to a more Mo-rich region, thereby changing the matrix to Mo [7]. Accordingly, Mo phase becomes continuous and thus toughness is well improved for MoSiBTiC alloys.

Another point is the toughening of TiC phase. In general, carbide addition is considered to reduce the toughness of alloys because of the low fracture toughness of stoichiometric TiC (only about 3 MPam<sup>1/2</sup>). However, since TiC phase on the fracture surface of the MoSiBTiC alloys shows river patterns similarly to Mo phase, it is suggested that not only Mo but also TiC acts as a fracture-resistant phase. TiC phase equilibrated with Mo and T<sub>2</sub> phases in MoSiBTiC alloys, which should have an off-stoichiometric composition, may have better fracture toughness than the stoichiometric one. The off-stoichiometry probably changes the mechanical properties of TiC, as generally seen in intermetallic compounds.

Therefore, in this study, the elastic property of Mo-Ti-C model alloys is examined, and the effect of the substitution of Mo at the Ti site and structural vacancy formation at the C site on the elastic properties of TiC is investigated.

**Materials and Methods**

The alloy compositions studied were on three kinds of the tie lines of the Mo/TiC two phase region of the Mo-Ti-C ternary system at 1800 °C and on a tie line of the β-Ti/TiC two-phase region of the Ti-C binary system. The compositions are shown in the isothermal section at 1800 °C (Fig. 1). The tie lines are called as tie line 1 to 4 from Mo-rich composition [7]. Alloy ingots were prepared from pure Mo (99.99 wt %), Ti (99.9 wt %), and TiC (99 wt %) in an Ar atmosphere by an arc-melting technique. Hereafter, all compositions are expressed as atomic percentages. Each ingot was melted five times and was turned over each time to avoid segregation. Heat treatment was carried out at 1800 °C for 72 hours for the Mo-Ti-C ternary ingots and at 1500 °C for 72 hours for Ti-C binary ingots in an Ar atmosphere to ensure phase equilibria. The microstructure observation was examined by field-emission (FE) scanning electron microscopy (SEM). Phase identification and the measurement of lattice parameter for constituent phases were conducted by X-ray diffractometry (XRD). Phase compositions were analyzed using a field-emission electron-probe microanalyzer (EPMA) equipped with a wavelength-dispersive X-ray spectroscope (WDX) operated at 10 kV and 5.0 × 10<sup>-8</sup> A. Vickers hardness tests were carried out at room temperature and applied load range was 0.98-4.90 N. Elastic parameters of the alloys after heat treatment were measured using the electromagnetic acoustic resonance (EMAR) method assuming the isotropic elastic medium [8].

**Results and Discussion**

The alloys consisted of solid solution phase (Mo or Ti phase) and TiC phase as shown in the phase diagram (Fig. 1). It was observed that TiC phase had solid-solution-phase precipitates formed during the heat treatment. The lattice parameters of TiC phases were smaller than stoichiometric ones reported so far and all the C contents in TiC phases were less than 50 %, suggesting that structural vacancies were generated at the C site.

The Young's modulus of the bulk alloys on the tie line 1 to 4 is plotted as a function of the volume fraction of the TiC phase ( $V_{TiC}$ ) in Fig. 2. The Young's modulus ( $E$ ), shear modulus ( $G$ ) and bulk modulus ( $K$ ) of the alloys on each tie line vary linearly with increasing  $V_{TiC}$ . The elastic moduli of single-phase TiC at the terminal composition of each tie line were estimated based on the rule of mixture of the Voigt model. The  $K/G$  value used as an indicator of toughness of the TiC phases examined was higher than that of stoichiometric one reported in an early study. Large cracks were generated in bulk stoichiometric TiC by the indentation of 0.98 N. On the other hand, only microcracks were introduced by the indentation of 4.9 N in the TiC phase on the tie line 4 which has the highest  $K/G$  among the TiC phases, and the propagation of microcracks is well suppressed by solid-solution precipitates in the TiC phase. Therefore, increasing  $K/G$  and solid-solution-phase precipitates are effective in improving the toughness of the TiC phase.

It was found that  $K$  is increased by Mo substitution at the Ti site and  $G$  is decreased with the increase of structural vacancies at the C site. They suggest that  $K$  and  $G$  values are affected by the strength of Ti-Ti metallic bond and Ti-C

covalent bond, respectively. Therefore, it is considered that the toughness of the TiC phase is increased by enhancing metallic bonding by substituting element at the Ti site with a higher elastic modulus than Ti and reducing the number of covalent bonds by the formation of structural vacancies at the C site.

Since the TiC phase of the MoSiBTiC alloys has a Mo-rich and C-poor composition, the toughness of the TiC phase should be much higher than that of stoichiometric TiC. Therefore, off-stoichiometric, toughened TiC is useful as a strengthening phase without compromising toughness.

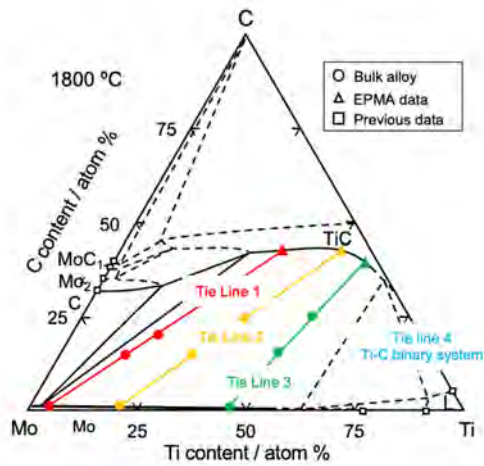


Fig. 1: Isothermal section at 1800 °C of the Mo-Ti-C ternary system.

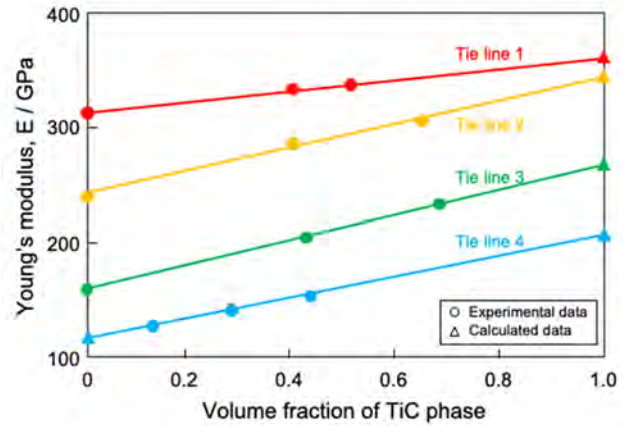


Fig. 2: Change in Young's modulus of alloys on the tie line 1–3 of the Mo-Ti-C ternary system and alloys on the tie line 4 of the Ti-C binary system as a function of the volume fraction of the TiC phase.

#### References

- [1] S. Miyamoto, K. Yoshimi, S.H. Ha, T. Kaneko, J. Nakamura, T. Sato, K. Maruyama, R. Tu, T. Goto, Metall Mater Trans A. **2014**, 45, 1112–1123.
- [2] K. Yoshimi, J. Nakamura, D. Kanekon, S. Yamamoto, K. Maruyama, H. Katsui, T. Goto, JOM. **2014**, 66, 1930–1938.
- [3] S. Yamamoto, K. Yoshimi, J. Kim, K. Yokoyama, J. Jpn. Inst. Met. **2016**, 80, 51–59.
- [4] S.Y. Kamata, D. Kanekon, Y. Lu, N. Sekido, K. Maruyama, G. Eggeler, K. Yoshimi, Sci. Rep. **2018**, 8, 10487.
- [5] T. Moriyama, K. Yoshimi, M. Zhao, T. Masnou, T. Yokoyama, J. Nakamura, H. Katsui, T. Goto, Intermetallics. **2017**, 84, 92–102.
- [6] G. Hasemann, S. Ida, L. Zhu, T. Iizawa, K. Yoshimi, M. Krüger, Materials & Design. **2020**, 185, 108233.
- [7] S. Ida, N. Sekido, K. Yoshimi, High temperature materials and processes. **2020**, 39, 164-170.
- [8] M. Zhao, K. Yoshimi, K. Maruyama, K. Yubuta, Acta Materialia. **2014**, 64, 382-390.



**O-IT-04****Applying advanced characterization and simulation methods to understand peculiarities of TiAl alloy and process development**

Florian Pyczak<sup>1,2</sup>, Heike Gabrisch<sup>1</sup>, Katja Hauschildt<sup>1</sup>, Victoria Kononikhina<sup>1</sup>  
and Marcus W. Rackel<sup>1</sup>

<sup>1</sup>Helmholtz-Zentrum Hereon, 21502 Geesthacht, Germany, florian.pyczak@hereon.de

<sup>2</sup>Brandenburgische Technische Universität Cottbus-Senftenberg, 03046 Cottbus, pyczak@b-tu.de

**Introduction**

Current developments in TiAl alloy and process research are presented and illustrated by examples from the Helmholtz-Zentrum Hereon. TiAl alloys tend to become more complex with respect to composition and phase constitution. By the addition of certain alloying elements, the properties are improved but unexpected side effects can occur. For example Nb and Mo facilitate forging of TiAl alloys by stabilizing the high temperature  $\beta$  phase [1]. However, they also cause the formation of additional phases at lower temperature. In addition, even for the binary Ti-Al system some aspects are still under discussion as for example the stability of the ordered B2 phase. Due to the application of TiAl alloys as aero engine parts since nearly 10 years, the whole live cycle of TiAl parts has come into focus including such aspects as repair and recycling. Processing conditions far away from thermodynamic equilibrium, introduction of additional alloying elements or deviations away from initial alloy composition can further influence the microstructure and thereby the properties of TiAl parts. For a knowledge based further development of TiAl alloys and associated processes it is necessary to employ advanced characterization methods and modelling and simulation. In this contribution, three examples are shown. High energy X-ray diffraction (HEXRD) and electron microscopy are used to investigate the formation of ternary phases in TiAl alloys in the service temperature range. An insight into the disordering of the B2 phase is acquired using neutron and synchrotron diffraction combined with first principles calculations. Transient liquid phase bonding processes are monitored also with HEXRD and the process is optimized based on the obtained results.

**Materials and Methods**

A variety of methods ranging from powder metallurgy to arc melting was used to produce the different TiAl alloys investigated. HEXRD investigations were performed at the high energy materials science beamline operated by Hereon at the Petra III storage ring of the DESY synchrotron in Hamburg while neutron diffraction data stems from the reactor FRM II in Munich. Two modified quenching dilatometers (TA Instruments DIL 805A/D), one adapted for HEXRD and one for neutron diffraction, as well as an induction furnace were used as *in-situ* specimen environments. Temperature measurement was performed with thermo couples in the dilatometers and with a pyrometer in the induction furnace. Electron microscopy investigations were undertaken at a Cs corrected FEI TITAN 80-300 transmission electron microscope at Hereon and at the dedicated aberration-corrected Nion UltraSTEMs (scanning electron microscopes) at Oakridge National Laboratory and at the Laboratoire de Physique de Solides in Orsay. First principle calculations with the software packages ABINIT [2] and VASP [3] used so-called special quasi random structures (SQS) to consider the atomic mixing in the materials. To construct the SQSs the mcsqs routine of the software ATAT [4] was used.

**Results and Discussion**

In the alloy Ti-42Al-8.5Nb the formation of an orthorhombic phase was observed at temperatures below 700 °C by HEXRD. Dissolution and formation of this phase takes place during cycling between 550 and 700 °C. By TEM and STEM investigations with atomic resolution, it became evident that this orthorhombic phase does not form by a nucleation and growth process but by a local distortion of the initial hexagonal lattice of the  $\alpha_2$  phase that assumes the orthorhombic crystal structure. An enrichment of the element Nb in the orthorhombic phase takes place in a subsequent second step [5,6]. This formation of an orthorhombic phase is not restricted to the alloy Ti-42Al-8.5Nb but takes place in a range of TiAl alloy compositions as was found out by a screening study [7].

In binary TiAl alloys in the composition range between 39 and 45 at. % Al no B2 phase was observed, neither by HEXRD at the synchrotron nor by neutron diffraction which is especially sensitive to detect the ordered B2 phase. In literature, statements about the presence or absence of B2 in the binary system are contradictory [8,9]. Considering the energies of formation at 0 K first principles calculations suggest the B2 phase to be more stable than the disordered  $\beta$  phase. But it is easily demonstrated that at elevated temperatures already the contributions from configurational entropy are sufficient to destabilize the B2 phase. While at lower temperatures B2 may be more stable than  $\beta$ , other phases such as  $\gamma$  and  $\alpha_2$  are even more stable so that neither  $\beta$  nor B2 is observed in binary TiAl at those lower temperatures [10].

To find a possibility to repair components of TiAl alloys, transient liquid phase bonding processes were tested using brazing solders based on the Ti-Ni and Ti-Fe system [11]. Initially, neither a good microstructural homogeneity of the braze joint nor acceptable mechanical properties were realized. But an *in-situ* monitoring of the brazing process with HEXRD indicated that too slow equilibration of the chemical composition of the brazing joint as well as excessive grain growth in the joint region were the most serious problems. By optimization of the brazing solder and the process, it was



possible to design processes giving mechanical properties close to those of the substrate material as well as a homogeneous joint microstructure. Figure 1 shows the development of the intensities of the diffraction peaks of different phases with increasing brazing time at 1110 °C for a Ti-24Ni brazing solder (atomic percent) on a TNB-V5 substrate. In Figure 2 the mechanical properties resulting from an optimized process with improved brazing solders is shown. Using an optimized brazing solder with Fe it is possible to achieve nearly the yield strength of the substrate material while the brazed specimen exhibits plastic deformation.

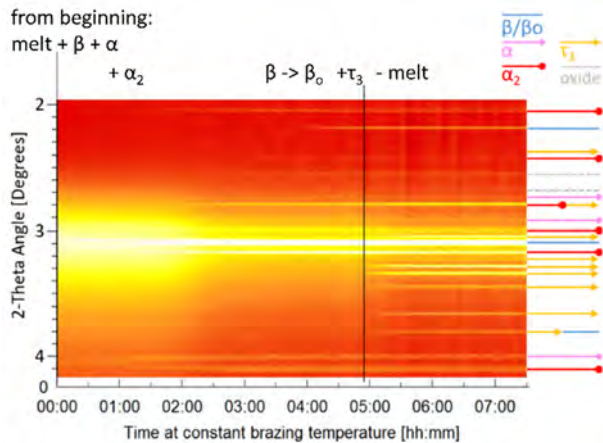


Fig. 1: Development of the diffraction intensities during a transient liquid phase bonding process at 1110 °C using a Ti-24Ni brazing solder

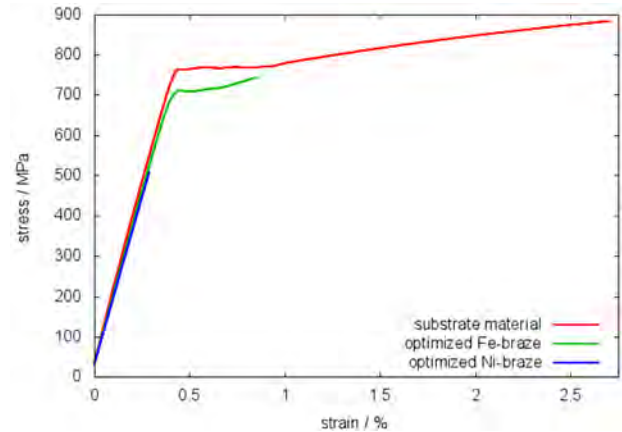


Fig. 2: Room temperature tensile strength of two brazed samples in comparison with substrate material

## References

- [1] S. Mayer, P. Erdely, F.D. Fischer, D. Holec, M. Kasthuber, T. Klein, H. Clemens, Intermetallic  $\beta$ -Solidifying  $\gamma$ -TiAl Based Alloys - From Fundamental Research to Application, *Advanced Engineering Materials*. **2017**, *19(4)*, 1600735.
- [2] X. Gonze, F. Jollet, F. Abreu Araujo, D. Adams, B. Amadon, T. Applencourt et al., Recent developments in the ABINIT software package, *Comput. Phys. Commun.* **2016**, *205*, 106-131.
- [3] G. Kresse, J. Furthmüller, Efficient iterative schemes for ab-initio total energy calculations using a plane-wave basis set, *Phys. Rev.* **1996**, *B 54*, 11169-11186.
- [4] A. van de Walle, Multicomponent multisublattice alloys, nonconfigurational entropy and other additions to the Alloy Theoretic Automated Toolkit, *Calphad*. **2009**, *33*, 266-278.
- [5] M.W. Rackel, A. Stark, H. Gabrisch, N. Schell, A. Schreyer, F. Pyczak, *Acta Materialia*. **2016**, *121*, 343-351.
- [6] H. Gabrisch, U. Lorenz, F. Pyczak, M. Rackel, A. Stark, *Acta Materialia*. **2017**, *135*, 304- 313.
- [7] M.W. Rackel, A. Stark, H. Gabrisch, F. Pyczak, Screening for O phase in advanced  $\gamma$ -TiAl alloys, *Intermetallics*. **2021**, *131*, 107086.
- [8] J.C. Schuster, M. Palm, Reassessment of the Binary Aluminum-Titanium Phase Diagram, *Journal of Phase Equilibria and Diffusion*. **2006**, *27*, 255-277.
- [9] I. Ohnuma, Y. Fujita, H. Mitsui, K. Ishikawa, R. Kainuma, K. Ishida, Phase Equilibria in the Ti-Al Binary System *Acta Materialia*. **2000**, *48*, 3113-3123.
- [10] F. Pyczak, V. Kononikhina, A. Stark, Stability of ordered B2- $\beta_0$  and disordered BCC- $\beta$  phases in TiAl – a first principles study, *Materials Science Forum*. **2021**, *1016*, 1159-1165.
- [11] K. Hauschildt, A. Stark, N. Schell, M. Müller, F. Pyczak, The transient liquid phase bonding process of a  $\gamma$ -TiAl alloy with brazing solders containing Fe or Ni, *Intermetallics*. **2019**, *106*, 48-58.

**O-IT-05****What can EBEF do better?**

Nathalie Dupin<sup>1</sup>, Ursula R. Kattner<sup>2</sup>, Bo Sundman<sup>3</sup>, Mauro Palumbo<sup>4</sup>, Suzana G. Fries<sup>5</sup>,  
Thomas Hammerschmidt<sup>6</sup>, Daniela Ivanova<sup>7</sup> and Sean Griesemer<sup>8</sup>

<sup>1</sup>Calcul Thermodynamique, 63670 Orcet, France, nathdupin@cthermo.fr

<sup>2</sup>National Institute of Standards and Technology, 20899 Gaithersburg, MD, USA, ursula.kattner@nist.gov

<sup>3</sup>OpenCalphad, 91190 Gif-sur-Yvette, France, bo.sundman@gmail.com

<sup>4</sup>Università di Torino, 10125 Torino, Italy, mauro.palumbo@unito.it

<sup>5</sup>Ruhr-University Bochum, 44801 Bochum, Germany, suzana.g.fries@ruhr-uni-bochum.de

<sup>6</sup>Ruhr-University Bochum, 44801 Bochum, Germany, thomas.hammerschmidt@rub.de

<sup>7</sup>Forschungszentrum Jülich GmbH, 52428 Jülich, d.ivanova@fz-juelich.de

<sup>8</sup>Northwestern University, Evanston, IL, USA, seangriesemer2021.3@u.northwestern.edu

**Introduction**

Calphad nowadays allows the calculations of the thermodynamic state of many complex materials of technological interest. These calculations are possible thanks to the existence of multi-component databases based on experimental and theoretical information in low-order systems. Most models currently used for complex phases in these databases are based on the Compound Energy Formalism (CEF). However, this formalism is prone to poor extrapolation behavior in higher order systems, especially when treating phases with complex crystal structures. In this work, the interest of the recently proposed Effective Bond Energy Formalism (EBEF) [1] is studied.

**Method**

CEF and EBEF use the same expression for the configuration entropy and the excess terms. They differ in the expression of the reference term. In the CEF, this term requires the evaluation of the Gibbs energy of all the pure configurations defined by the model of the phase under consideration, while in the EBEF, it is based on bonding energies between elements in different sublattices. The first approximation of the EBEF allows to consider bonding energy only between two elements in two sublattices that can be assessed from binary information.

In a previous study [1], the two formalisms have been compared to describe the extension of the sigma phase in the ternary Mo-Ni-Re system using only binary DFT results [2] in the constituting binary systems.

More systems, different sources for the DFT results and different procedures to derive the bonding energies have been tested since.

**Results and Discussion**

Figure 1 shows the inability of the CEF to extrapolate reasonably the sigma phase stability range in the Mo-Ni-Re system at 1500K using binary DFT results [2] in the constituting binary systems. Figure 2 shows that using the same binary information from DFT, the EBEF allows to better describe this extrapolation. This extension is very close to the one obtained using the binary and ternary information from DFT with the CEF (Fig. 4) even if many of the formation enthalpies for the ternary configurations estimated by the EBEF are not very close to the DFT results (Fig.3).

Different procedures or different DFT sources can modify the resulting phase diagrams. However, the improvement from the CEF is always significant.

The EBEF allows to use as many sublattices in the thermodynamic model as there are Wyckoff sites in the crystallographic structure but with a significant reduction of the total number of model parameters and a clear improvement in the quality of the extrapolation into higher order systems. It is expected to bring better descriptions of complex intermetallic phases in multicomponent materials.

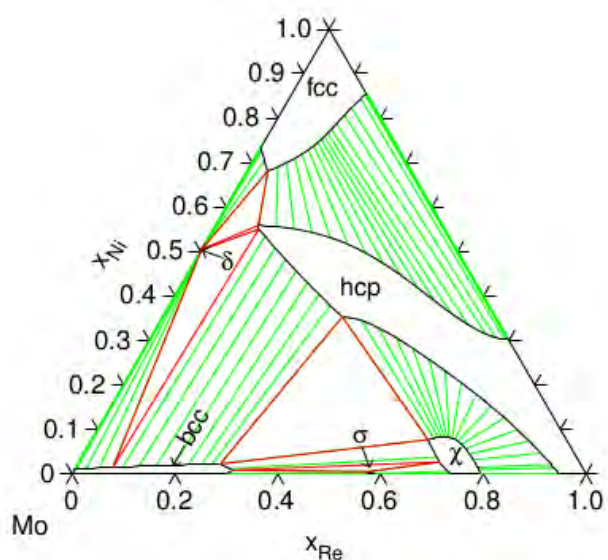


Fig. 1: Mo-Ni-Re 1500 K section calculated with CEF using the DFT binary information [2].

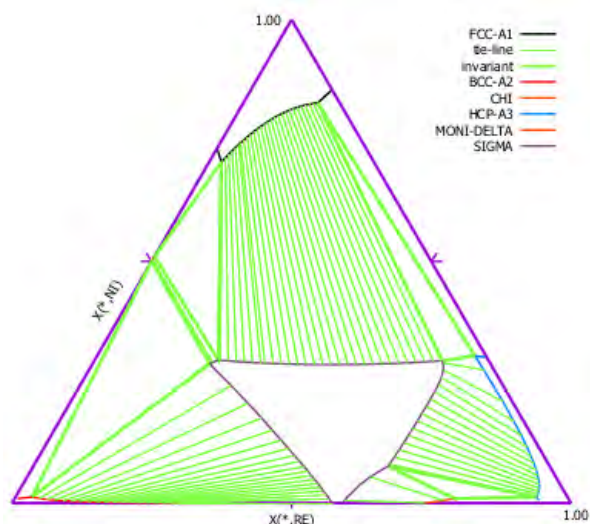


Fig. 2: Mo-Ni-Re 1500 K section calculated with EBEF using the DFT binary information [2].

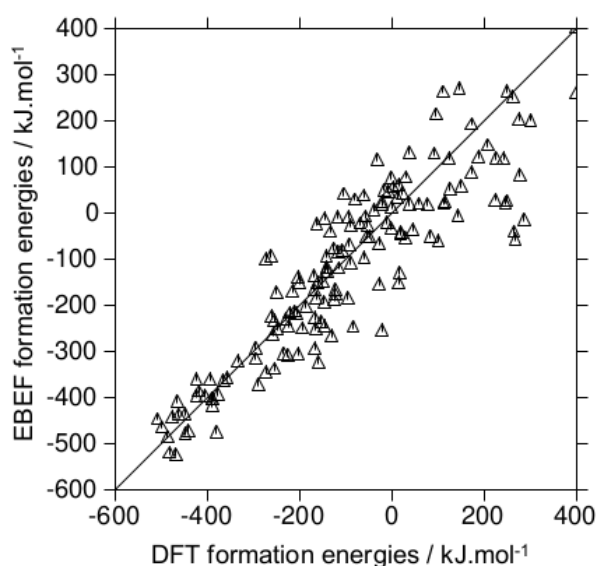


Fig. 3: Comparison of the formation enthalpies of the ternary compounds estimated by EBEF using DFT binary information [2] with the values calculated by DFT [2].

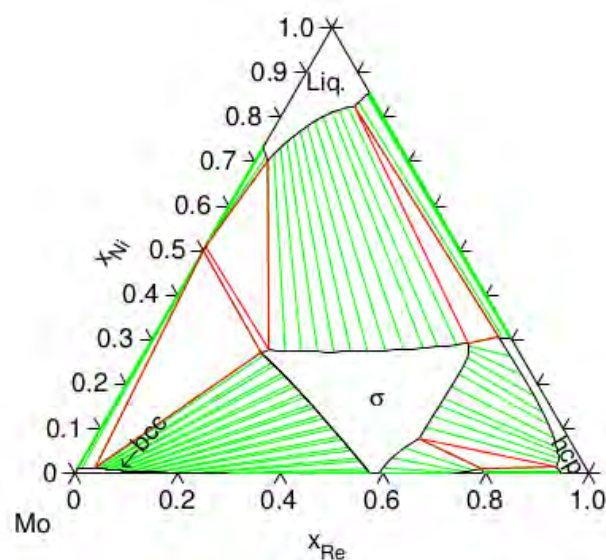


Fig. 4: Mo-Ni-Re 1500 K section calculated with CEF using the DFT binary and ternary information [2].

### References

- [1] N. Dupin, U. R. Kattner, B. Sundman, M. Palumbo, Journal of Research of National Institute of Standards and Technology, **2018**.
- [2] K. Yaqoob, J.-C. Crivello, J.-M. Joubert, Inorganic Chemistry, **2012**, 51(5), 3071–3078.

**O-IT-06****Microstructure related high temperature oxidation behavior of iron aluminides**Daniela Zander and René Daniel PützChair of Corrosion and Corrosion Protection, Foundry Institute, RWTH Aachen University, 52072 Aachen, Germany,  
d.zander@gi.rwth-aachen.de, r.puetz@gi.rwth-aachen.de**Introduction**

Intermetallic iron aluminides are characterized by minor material cost, low density, and notable wear resistance, which make them a potential material for substituting stainless steels and Ni-based alloys in the fields of high temperature applications [1–4].

However, low room temperature ductility and unfavorable creep strength at temperatures above 500 °C have been major drawbacks. Therefore, the design of new iron aluminides, that solve the mentioned detrimental properties, are of special interest. These alloying concepts for improving the creep strength and/or yield strength can include solid solution strengthening and the alloying with e.g. carbides, borides, metastable  $L2_1$  Heusler phase ( $Fe_2XAl$ ) and stable Laves phase forming elements. The improvement of the ductility is also an important research field that includes the design of iron aluminides by amount others adding Cr or B to potentially inhibit the environmental embrittlement, grain refinement, and controlling the formation of precipitates at the Fe-Al grain boundaries to prevent grain coarsening [5]. However, the fast progress of newly invented alloying concepts demands also the consideration of the effects on the high temperature oxidation behavior that can be influenced by the microstructure. In general, the outstanding high temperature oxidation resistance of iron aluminides is related to the formation of a dense and adherent alumina scale [6]. Various polymorphs (e.g.  $\gamma$ -,  $\theta$ -,  $\alpha$ - $Al_2O_3$  etc.) exist that differ in diffusion mechanisms and oxidation rates [6], which can determine the component's life-time. Apart from the formed alumina scale, precipitates like Laves phases, carbides and borides can influence the high temperature oxidation behavior by their selective oxidation which will be discussed.

**Materials and Methods**

The casted iron aluminides were provided by ACCESS e. V., Aachen, Germany. Discontinuous thermogravimetric analysis experiments (TGA) were performed at various temperatures in air. Rectangular specimens were stepwise ground to 1200 grit, ultrasonically cleaned in ethanol, and air dried prior to the oxidation experiments. A hole was drilled below one of the edges to hang the sample in an alumina crucible to ensure that the whole surface was in contact to the atmosphere during oxidation and possible spalling could be collected by the crucible. After several time steps, the samples were removed, cooled to room temperature, and consequently weighed. After the oxidation testing, the specimens were analyzed using a Zeiss Supra 55 VP scanning electron microscope (SEM) with an attached Oxford Ultim® Max energy-dispersive X-ray spectroscope (EDS). Additionally, the crystal structures of the formed oxides were determined by an Empyrean X-ray diffractometer (XRD) using  $Co-K\alpha$  radiation.

**Results and Discussion**

In Figure 1, SEM images of Fe-25Al-5Cr-0.5Zr (at.%) after oxidation in air at 850 °C for 1003 h are depicted. The top view image in Figure 1 a) shows the formation of blade- and whisker-like alumina on the  $Fe_3Al$  matrix, while  $Fe_2O_3$  was locally formed at the interdendritic  $(Fe,Al)_2Zr$  Laves phase. Additionally, the inner oxidation of the Laves phase is shown in the cross-section image in Figure 1 b) that can penetrate several micro-meters deep into the material. The interface between (oxidized) Laves phase and  $Fe_3Al$  matrix may act as transport path for oxygen, which promotes the increase of the oxygen activity at the oxidation front and a proceeding oxidation. It was already reported that the inner oxidation of  $(Fe,Al)_2Zr$  and ZrC can occur at temperature above 900 °C [7,8] but more recent investigations also showed that the inner oxidation of these phases is able to proceed at lower temperatures of 700 °C [9]. The prevention of an interdendritic network of the Laves phase by the addition of TiC can also reduce the depth of inner oxidation and consequently improve the oxidation resistance [9].

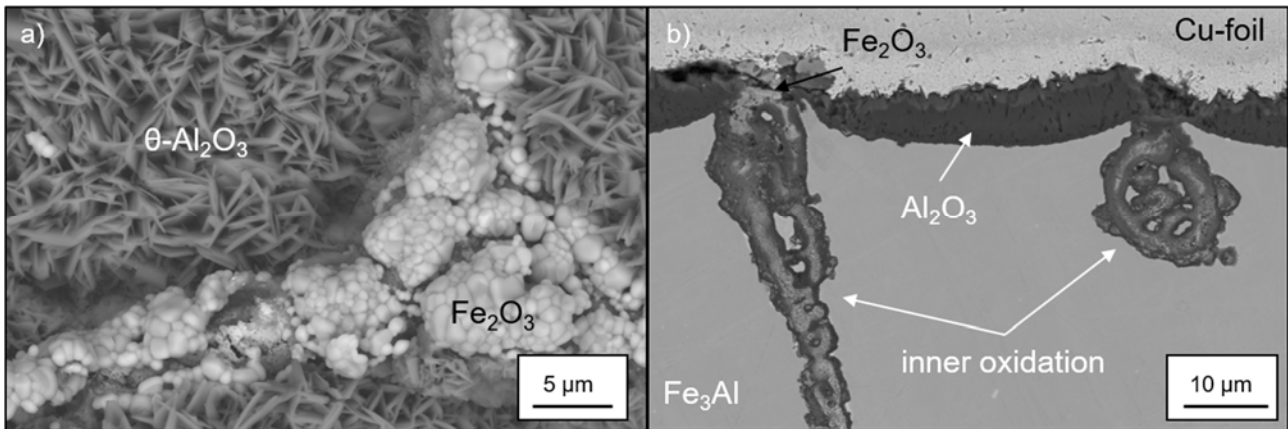


Fig. 1: SEM a) top view and b) cross-section image of Fe-25Al-5Cr-0.5Zr after oxidation in air at 850 °C for 1003 h.

#### Acknowledgment

The financial support from the German Federal Ministry for Economic Affairs and Energy (BMWi) under grant no. 03ET7077B is highly acknowledged.

#### References

- [1] L. Weng, X. Zhang, J. Han, W. Han, C. Hong, *Journal of Alloys and Compounds*. **2009**, *473*, 314-318.
- [1] D.G. Morris, M.A. Muñoz-Morris, *Advanced Engineering Materials*. **2011**, *13*, 43-47.
- [2] P. Hanus, E. Bartsch, M. Palm, R. Krein, K. Bauer-Partenheimer, P. Janschek, *Intermetallics*. **2010**, *18*, 1379-1384.
- [3] N. S. Stoloff, *Materials Science and Engineering: A*. **1998**, *258*, 1-14.
- [4] M. Zamanzade, A. Barnoush, C. Motz, *Crystals*. **2016**, *6*, 1-29.
- [5] M. Palm, F. Stein, G. Dehm, *Annual Review of Materials Research*. **2019**, *49*, 297-326.
- [6] K. Natesan, *Materials Science and Engineering A*. **1998**, *258*, 126-136.
- [7] A. Hotař, M. Palm, P. Kratochvíl, V. Vodičková, S. Daniš, *Corrosion Science*. **2012**, *63*, 71-81.
- [8] A. Hotař, P. Kejzlar, M. Palm, J. Mlnařik, *Corrosion Science*. **2015**, *100*, 147-157.
- [9] D. Zander, R.D. Pütz, *Intermetallics*. **2020**, *126*, 106924.



**O-IT-07****Oxidation behavior of a eutectic high temperature alloy Mo-20Si-52.8Ti in dry and wet environments**

Bronislava Gorr<sup>1</sup>, Matthias Weber<sup>2</sup>, Hans-Jürgen Christ<sup>2</sup>, Susanne Obert<sup>1</sup>, Aditya Srinivasan Tirunilai<sup>1</sup>, Alexander Kauffmann<sup>1</sup> and Martin Heilmaier<sup>1</sup>

<sup>1</sup>Institut für Angewandte Materialien, Karlsruher Institut für Technologie (KIT), Karlsruhe, Germany, bronislava.gorr@kit.edu, susanne.obert@kit.edu, aditya.tirunilai@kit.edu, alexander.kauffmann@kit.edu, martin.heilmaier@kit.edu

<sup>2</sup>Institut für Werkstofftechnik, Universität Siegen, Siegen, Germany, matthias.weber@uni-siegen.de, hans-juergen.christ@uni-siegen.de

**Introduction**

For decades, Mo-based alloys are considered as materials that may replace Ni-based superalloys as the blade material in gas turbines [1,2]. Mo-silicide based alloys with high Ti concentrations represent an attractive and advanced alternative to conventional Mo-Si-B-based alloys. In addition to the high solidus temperature and remarkable mechanical properties [3,4], Mo-Si-Ti alloys exhibit some further crucial benefits: (i) reduced density and (ii) reasonable oxidation resistance in air in a wide temperature range from 800 to 1200 °C [5,6]. The most notable experimental finding is that some Ti-containing Mo-Si alloys do not suffer from pesting and catastrophic oxidation at critical temperatures of around 800 °C [6]. The oxide scales formed on these alloys consist of an outer TiO<sub>2</sub> and an inner duplex TiO<sub>2</sub>-SiO<sub>2</sub> layers. It is well-known that otherwise protective oxides, such as Cr<sub>2</sub>O<sub>3</sub> lose their protective properties in wet environments [7]. The same seems to hold true for SiO<sub>2</sub>-forming alloys. Meschter et al. found that SiO<sub>2</sub> reacts with water vapor to form volatile Si(OH)<sub>4</sub> at high temperatures up to 1300 °C [8]. To understand the effect of water vapor on the oxidation behavior of the novel alloy 27.2Mo-20Si-52.8Ti, this material was oxidized in different atmospheres: (i) air (designated as dry), (ii) Ar-10%N<sub>2</sub>-20%O<sub>2</sub>-10%H<sub>2</sub>O (in vol. %, designated as wet) and (iii) in changing dry to wet and vice versa surroundings. In order to determine the role of the TiO<sub>2</sub> scale which forms as an outer oxide layer in all atmospheres, the thin TiO<sub>2</sub> scale grown in dry air was removed and the corresponding samples were further oxidized under wet conditions. Detailed microstructural analyses using different experimental techniques combined with the oxidation kinetic data contribute to the comprehensive understanding of the oxidation behavior of Mo-Si-Ti alloys in dry and wet atmospheres.

**Materials and Methods**

The details regarding manufacturing and microstructure of the alloy 27.2Mo-20Si-52.8Ti can be found in Ref. [5,6]. The oxidation behavior was studied in a thermogravimetric Rubotherm system under isothermal conditions at 1100 and 1200 °C. The gas flow during the oxidation experiments was set to 6 l/h<sup>-1</sup>. The same setup was utilized during oxidation when samples were exposed to changes alternating between dry and wet atmospheres. In case of samples with removed TiO<sub>2</sub> outer scale, the alloy was first oxidized in dry air for 50h at 1200°C. The higher temperature was chosen to accelerate the scale growth. Subsequently, the outer TiO<sub>2</sub> layer was ground off with SiC grit P4000. Afterwards, oxidation of the sample was continued in the wet atmosphere for the next 25 h at 1200 °C. The crystal structure of corrosion products formed on the samples was analyzed using X-ray diffraction (XRD). To study the oxide morphology and to prepare thin foils for the transmission electron microscopy (TEM), a focused ion beam/scanning electron microscope (FIB/SEM) Dual Beam system (FEI Helios Nanolab 600), which is equipped with a backscatter electron (BSE) detector and an energy dispersive X-ray spectroscopy detector (EDX), was utilized.

**Results and Discussion**

The eutectic alloy Mo-20Si-52.8Ti consists of two phases, a body-centered cubic solid solution and a (Ti,Mo)<sub>5</sub>Si<sub>3</sub> phase (Strukturbericht D8<sub>8</sub>). Both phases are presented in a nearly equal ratio. After oxidation for 50 h at 1100 °C, the values of the mass gain of 3 mg/cm<sup>2</sup> and 4.3 mg/cm<sup>2</sup> were recorded in dry and wet atmospheres, respectively. While the oxidation curve of the experiment conducted in dry air reveals nearly-parabolic characteristics, accelerated linear kinetics was observed during exposure to the wet atmosphere. It should be pointed out that mass loss that is typical of B-containing Mo silicide alloys was not detected in both surroundings at 1100 °C. The experiments with in-situ changing atmospheres additionally reveal that the nature and properties of the oxide scales formed during the initial oxidation stage largely determine the oxidation resistance of the subsequently growing oxides. Figure 1 shows oxidation kinetics of two samples oxidized in dry air for 50 h at 1200 °C. After 50 h oxidation, the outer TiO<sub>2</sub> scales was removed and the two samples were further oxidized in dry and wet atmospheres at 1200 °C. Obviously, the oxidation rate of the samples without the outer TiO<sub>2</sub> exposed to air for the next 25 h does not change notably as compared to the first 50 h oxidation in the same atmosphere and temperature. On the contrary, the sample with the removed TiO<sub>2</sub> layer and subsequently oxidized in the wet atmosphere exhibits an extremely sharp mass gain which is followed by a substantial mass loss which

is apparently attributed to the severe evaporation of  $\text{MoO}_3$ . The weight gains and losses recur several times during 25 h of exposure to the wet gas.

The microstructural analysis of the oxidized samples reveals that both oxide scales, the outer  $\text{TiO}_2$  layer as well as the duplex  $\text{TiO}_2$ - $\text{SiO}_2$  underneath, grow significantly faster in wet than in dry surroundings. Figure 2 representatively demonstrates cross-sections of the samples shown in Fig. 1. The thicknesses of the oxide scales formed on the samples with the removed  $\text{TiO}_2$  and subsequently oxidized in the dry and wet atmospheres yield values of 50  $\mu\text{m}$  and 650  $\mu\text{m}$ , respectively. Considering the oxidation kinetic data as well as the results of the microstructural investigations, it can be concluded that (i) water vapor accelerates the oxidation rate of the alloy Mo-20Si-52.8Ti and (ii) the outer  $\text{TiO}_2$  scale seems to represent a some kind of barrier for the oxygen ingress.

The inferior oxidation resistance in wet environment can primarily be rationalized by the fast diffusion of  $\text{H}_2\text{O}$  through  $\text{SiO}_2$ . It was reported by Roberts et al. [9] that water vapor causes formation of  $\text{SiOH}$  groups which, in turn, lead to additional defects and strains in silica resulting in the increased diffusion of the OH groups in this oxide. It can further be assumed that  $\text{H}_2\text{O}$  increases the concentration of oxygen vacancies in titania accelerating the growth of  $\text{TiO}_2$  and enhancing the oxidation rate [8]. Our future investigations using electron energy loss spectroscopy should shed light on detailed characteristics such as exact stoichiometry of  $\text{TiO}_2$  grown under dry and wet conditions.

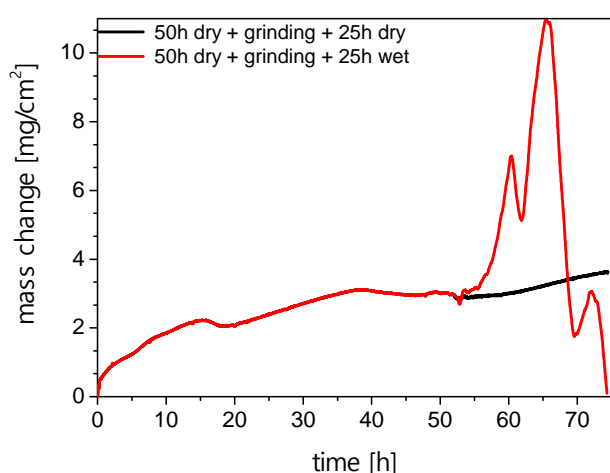


Fig. 1: Oxidation kinetics of the alloy 27.5Mo-20Si-52.8Ti at 1200 °C in dry and wet atmosphere. The outer  $\text{TiO}_2$  scales were removed after exposure to air for 50 h. The samples were further oxidized in dry and wet gases for the next 25 h.

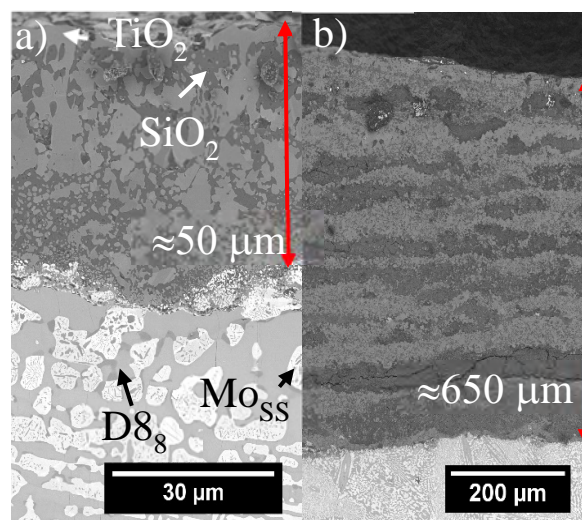


Fig. 2: BSE cross-section images of 27.2Mo-20Si-52.8Ti after 50 h oxidation at 1200 °C in dry atmosphere, removal of the outer  $\text{TiO}_2$  layer and further oxidation for 25 h in a) dry and b) wet atmosphere

#### ACKNOWLEDGEMENTS

THE FINANCIAL SUPPORT BY DEUTSCHE FORSCHUNGSGEMEINSCHAFT (DFG), GRANT NO. GO 2283/3-1, IS GRATEFULLY ACKNOWLEDGED. PART OF THIS WORK WAS PERFORMED AT THE MICRO- AND NANOANALYTICS FACILITY (MNAF) OF THE UNIVERSITY OF SIEGEN.

#### References

- [1] S. Y. Kamata, D. Kanekon, Y. Lu, N. Sekido, K. Maruyama, G. Eggeler, K. Yoshimi, *Scientific Reports*. **2018**, *8*, 10487.
- [2] D. M. Berczik, *US Patent*. **1997**, *No. 5,693,156*.
- [3] D. Schliephake, A. Kauffmann, X. Cong, C. Gombola, M. Azim, B. Gorr, H.-J. Christ, *Intermetallics*. **2019**, *104*, 133-142.
- [4] M. Azim, D. Schliephake, C. Hochmuth, B. Gorr, H.-J. Christ, U. Glatzel, M. Heilmaier, *JOM*. **2015**, *67*, 2621-2628.
- [5] M. Weber, B. Gorr, H.-J. Christ, S. Obert, A. Kauffmann, M. Heilmaier, *Advanced Engineering Materials*. **2020**, *22*, 7.
- [6] S. Obert, A. Kauffmann, M. Heilmaier, *Acta Materialia*. **2020**, *184*, 132-142.
- [7] S. K. Arifin, M. Hamid, A. N. Berahim, M. H. Ani, *IOP Conference Series: Materials Science and Engineering*. **2018**, *290*, 012085.
- [8] P. Meschter, E. Opila, N. Jacobson, *Annual Review of Materials Research*, **2013**, *43*, 559-588.
- [9] G.J. Roberts, J.P. Roberts, *Phys. Chem. Glasses*. **1964**, *26*.



**O-IT-08****Machine learning the structural stability of topologically close-packed phases**

Thomas Hammerschmidt

ICAMS, Ruhr-University Bochum, 44801 Bochum, Germany, thomas.hammerschmidt@rub.de

**Introduction**

One of the most successful approaches to predict the structural stability of materials are quantum-mechanical calculations in the framework of density-functional theory (DFT). The robustness of DFT makes calculations of several hundred atoms a routine task with reliable results for a broad range of physical properties and chemical compositions. The computational cost, however, limits the screening of chemical compositions to only few chemical components or to a small subset of possibly relevant crystal structures. This limitation is a considerable obstacle for the theoretical study of topologically close-packed (TCP) phases. This important class of intermetallic phases is spanned by the possibilities of arranging combinations of the Frank-Kasper polyhedra as building blocks in a periodic way to form a crystal structure. The TCP phases, A15,  $\sigma$ ,  $\chi$ ,  $\mu$ , C14, C15, C36 exhibit up to five Wyckoff sites while the R, M, P,  $\delta$  phase exhibit more than ten Wyckoff sites. The computation of the structural stability of the TCP phases by DFT requires a full sampling of the possible occupations of the Wyckoff sites. E.g., the computation of a  $\sigma$  phase with ternary chemical composition requires DFT calculations for  $3^5=243$  occupancy combinations and is a routine task. However, a five-component  $\sigma$  phase with  $5^5=3125$  occupancy combinations already involves significant computational effort. A ternary R phase with  $3^{11}=177147$  combinations is nearly intractable for DFT calculations within the typically available resources. For this reason, the research on TCP phases by DFT calculations leaves large regions of chemical space and of structural complexity unexplored. A promising route to reach out into this unexplored space is the combination of DFT calculations with modern data-science techniques, particularly with machine learning.

**Materials and Methods**

The prediction of the structural stability of TCP phases by machine-learning (ML) requires the representation of the occupation of the Wyckoff sites in terms of a so-called descriptor. The quality and robustness of the prediction depends critically on the quality of the descriptors. For machine learning the formation energies obtained from DFT calculations, the descriptors are typically based on measures of the atomistic geometry and the distribution of chemical elements. Here, we construct descriptors that additionally include domain knowledge of the interatomic bond from a hierarchy of coarse-grained electronic-structure methods [1]. In particular, we use tight-binding (TB) and analytic bond-order potentials (BOPs) that are derived from a second-order expansion of DFT. Using these descriptors, we train and test ML models with different regression algorithms on DFT data for the TCP phases A15,  $\sigma$ ,  $\chi$ ,  $\mu$ , C14, C15, C36 with different binary and ternary chemical compositions, e.g. Ni-Al-Re, Co-Al-W, Co-Ti-W, Co-Cr-W.

**Results and Discussion**

We demonstrate that our descriptors obtained at the TB/BOP level incorporate domain knowledge of the interatomic interaction in terms of a smooth relation between the local atomic environment and the formation energy. As first level of domain knowledge we employ simple, qualitative TB/BOP models. As second level of domain knowledge we include the bond chemistry in terms of bond-specific interaction Hamiltonians that are obtained from downfolded DFT eigenspectra [2]. As third level of domain knowledge we consider the role of the valence electrons by determining approximate non-selfconsistent bond energies with the bond-specific interaction Hamiltonians. These descriptors of the occupancy of the Wyckoff positions of the TCP phase go beyond purely geometric descriptors that are typically used in ML models of DFT formation energies. In particular, they are scalable in farsightedness within the crystal structure which is key to discriminate the local atomic environments of TCP phases that contain only the small set of Frank-Kasper polyhedra as first nearest-neighbour shell. We demonstrate the application of these descriptors with different levels of domain knowledge to the prediction of the formation energy of TCP phases. As key finding we observe that our descriptors with domain knowledge attain high relative importance in the ML models as compared to other descriptors.

**References**

- [1] J. Jenke, A. Subramanyam, M. Densow, T. Hammerschmidt, D.G. Pettifor, R. Drautz, *Physical Review B*. **2018**, 98, 144102 (1-12)
- [2] J. Jenke, A. Ladines, T. Hammerschmidt, D.G. Pettifor, R. Drautz, *Physical Review Materials*. **2021**, 5, 023801 (1-13)

**O-IT-09****Design of heat resistant ferritic steels using precipitation of Laves phase**

Satoru Kobayashi and Zhetao Yuan

School of Materials and Chemical Technology, Tokyo Institute of Technology, Tokyo, Japan,  
kobayashi.s.be@m.titech.ac.jp, yuan.z.aa@m.titech.ac.jp**Introduction**

High Cr heat resistant ferritic steels are an important class of materials for high temperature components such as pipes and turbines in steam turbine power plants. These steels are designed such that the ferritic matrix, inherited from the martensitic transformation, are strengthened with  $M_{23}C_6$  type carbide and MX type carbonitride particles against dislocation motion, recovery, and recrystallization. The carbide and carbonitride particles are, however, susceptible to particle coarsening and decomposition in the long-term creep deformation and thereby losing their strengthening effects, which is considered to be a main cause of the degradation of long-term creep strength of the steels [1].

Laves phase is an  $A_2B$  type intermetallic phase, which is formed in many Fe based alloy systems [2].  $Fe_2Mo$  and  $Fe_2W$  Laves phase particles are precipitated during creep deformation within the ferritic matrix in conventional high Cr ferritic steels [3]. The Laves phase particles are observed as fine particles along the lath/block boundaries and/or as coarse globular ones, depending on the type of the Laves phase and the content of the Laves phase forming elements. Efforts to improve the creep life of ferritic steels have been made by modification of Laves phase distribution, and positive effects on the creep resistance are reported [3].

One of the present authors [4] recently found that fine Hf-rich particles are precipitated in a form of periodically arrayed rows in Fe-9Cr based alloys containing a low amount of Hf, and explained that the particles are formed through interphase precipitation (IPP) during a phase transformation from the  $\delta$ -ferrite to the  $\gamma$ -austenite, followed by a phase transformation from the  $\gamma$ -austenite to the  $\alpha$ -ferrite. The Hf-rich particles were identified as C14  $Fe_2Hf$  type Laves phase by diffraction pattern analysis [4]. This finding is expected to open a new precipitation route to strengthen heat resistant ferritic steels using IPP of the intermetallic phase. Our recent studies also revealed that  $Fe_2Ta$  type Laves phase is precipitated in the same precipitation route as in the  $Fe_2Hf$  case but with a fibrous morphology and with much slower kinetics than the  $Fe_2Hf$  case. The objective of the present paper is to clarify the criteria to distinguish the precipitation modes and morphology (IPP or fibrous) in the eutectoid-like reaction path in High Cr heat resistant ferritic alloys.

**Materials and Methods**

The alloys studied are a couple of Fe-Cr-0.6Ta ternary eutectoid alloys with different Cr contents from 9.5 to 7.5 %. Hereafter the chemical composition is shown in atomic % unless specified, and the alloys are designated with their Cr content. These alloys were prepared by Argon arc melting as  $\sim 35$  g ingots, cut into cylinders with a diameter of 3mm and a length of 10mm with a hole of 5mm in depth drilled along the longitudinal direction. These specimens were solutionized in the  $\delta$  single phase region, rapidly cooled, isothermally aged in the  $\gamma+Fe_2Ta$  two-phase region for certain periods of time, followed by rapid cooling. In these heat treatments the temperature was tracked using a thermocouple which is inserted in the hole of the specimen.

The microstructures of the heat-treated specimens were characterized on the cross section  $\sim 1$  mm inside of the cylinder base surface with an optical microscope and a field emission scanning electron microscope equipped with a backscattered electron (BSE) detector. The cross section was prepared by grinding, mechanically polishing down to  $1\mu m$   $Al_2O_3$  polishing suspension, and chemical polishing with  $SiO_2$  polishing suspension.

**Results and Discussion**

A change in the precipitation mode was observed from fibrous precipitation to IPP as the Cr content decreases. Figure 1 shows examples of microstructures where  $Fe_2Ta$  Laves phase fibers are seen in a discontinuously precipitated cell in the 9.5Cr alloy (Fig. 1(a)), whereas periodically arrayed rows of Laves phase particles are also seen in the 8.5Cr alloy (Fig. 1(b)). This change in the precipitation mode is associated with an increase in the velocity of  $\delta/\gamma$  interphase boundary migration during isothermal aging in the  $\gamma+Fe_2Ta$  two-phase region. Precipitation of the  $Fe_2Ta$  phase was not recognized in the 7.5Cr alloy where the rate of the interphase boundary migration is even higher.

The competition between fibrous precipitation and IPP can be interpreted such that the former one takes place in case that the Laves phase fibre can grow at the same rate as the velocity of the advancing interphase boundary migration whereas the latter one occurs in case that the Laves phase is not able to grow as fast as the advancing interphase migrates. Absence of interphase precipitation at higher velocity of the  $\delta/\gamma$  interface boundary migration is due to a shortage in time for the nucleation of Laves phase on the interface before the next ledge of the interface is arrived. Semiquantitative interpretation will be shown on the competition between the precipitation mode and the occurrence of the precipitation in the presentation.

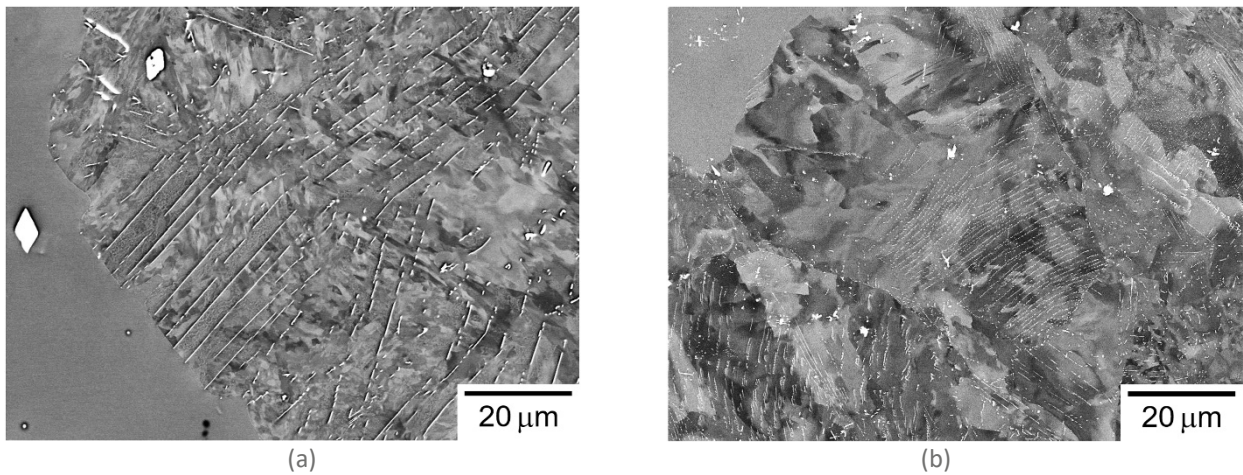


Fig. 1: BSE images of the alloys studied heat-treated: (a) Fe-9.5Cr-0.6Ta alloy isothermally aged at 1050 °C for 1 h, (b) Fe-8.5Cr-0.6Ta alloy isothermally aged at 950 °C for 5 min.

#### References

- [1] F. Masuyama, History of Power Plants and Progress in Heat Resistant Steels. *ISIJ Int.* **2001**, *41*, 612–625.
- [2] H. Okamoto, Phase diagrams of binary iron alloys, Monograph Series on Alloy Phase Diagrams Vol. 9. *ASM Int.* **1993**.
- [3] F. Abe, Effect of fine precipitation and subsequent coarsening of Fe<sub>2</sub>W Laves phase on the creep deformation behavior of tempered martensitic 9Cr-W steels. *Metall. Mater. Trans.* **2005**, *36A*, 321–332.
- [4] S. Kobayashi, K. Kimura, K. Tsuzaki, Interphase precipitation of Fe<sub>2</sub>Hf Laves phase in a Fe-9Cr/Fe-9Cr-Hf diffusion couple. *Intermetallics* **2014**, *46*, 80–84.

**O-IT-10****Design and development of refractory metal (Nb) intermetallic composites, refractory high entropy alloys and refractory complex concentrated alloys**

Panos Tsakirooulos

Department of Materials Science and Engineering, Sir Robert Hadfield Building, The University of Sheffield, S1 3JD Sheffield, UK

**Introduction**

There is need for metallic ultra-high temperature materials (UHTMs) with capabilities beyond those of Ni-based superalloys. The UHTMs must comply with specific property goals about creep, fracture toughness and oxidation. Refractory metal intermetallic composites (RMICs), refractory (metal) high entropy alloys (RHEAs) and refractory (metal) complex concentrated alloys (RCCAs) proffer a paradigm for advanced metallic UHTMs to replace Ni-based superalloys [1–3]. RMICs include Nb-silicide based alloys (RM(Nb)ICs) and Mo-silicide based alloys (RM(Mo)ICs). The latter are not considered in this presentation. Some RM(Nb)ICs are also HEAs, others are also RHEAs or RCCAs [1–6]. Not all RM(Nb)ICs are HEAs, RHEAs or RCCAs.

**Materials and Methods**

RM(Nb)ICs, RHEAs and RCCAs share the same alloying additions, and the parameters  $\delta$ ,  $\Delta\chi$ , VEC,  $\Delta H_{\text{mix}}$ ,  $\Delta S_{\text{mix}}$  and  $\Omega$  ( $=T_m\Delta S_{\text{mix}}/|\Delta H_{\text{mix}}|$ ) describe their alloying behaviour as they do for HEAs [1-3,7,8]. The values of these parameters for bcc solid solutions, metallic UHTMs and HEAs overlap [2,3]. The alloy design methodology NICE [2,3] has made it possible to construct maps based on the above parameters. The maps describe the alloying behaviour of UHTMs and their phases [9-11]. The parameters of alloys and their phases were calculated for those alloys for which reliable chemical analysis (EPMA and EDS with standards) data was available [1–3, 7–11].

**Results and Discussion**

The RM(Nb)ICs are multiphase alloys consisting of intermetallic(s) ( $M_3\text{Si}$  and  $M_5\text{Si}_3$  silicides ( $M=\text{RM}$  and/or transition metal (TM)), C14 Laves phase and A15 compounds) with/without bcc solid solution(s) [1–4], fig.1.

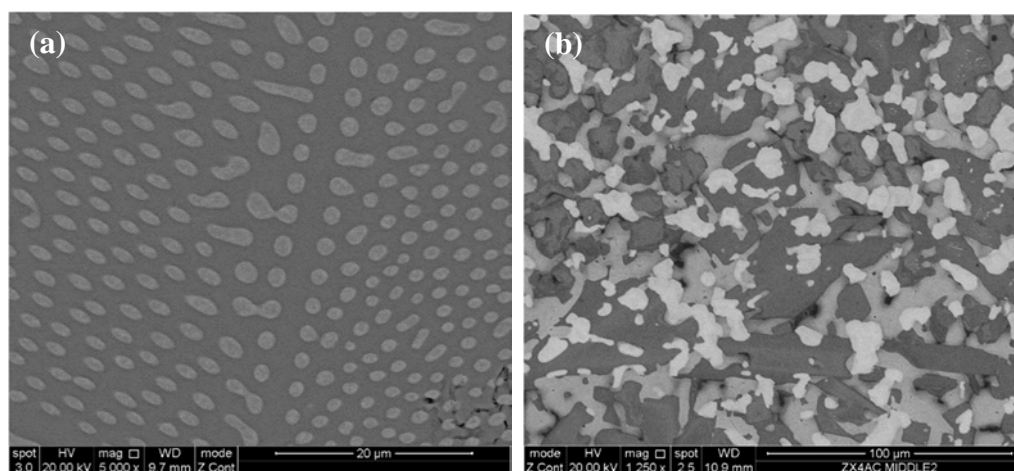


Fig. 1: Microstructures of as cast RM(Nb)ICs. (a) as cast alloy Nb-20.5Si-5.8W-4Hf, DS (OFZ) R=12 mm/h, eutectic of  $\text{Nb}_{55}$  (light phase) and  $\beta\text{Nb}_5\text{Si}_3$  (dark phase), (b) as cast (AM) alloy Nb-24Ti-18Si-5Cr-5Sn, light phase A15- $\text{Nb}_3\text{Sn}$ , slightly darker phase  $\text{Nb}_{55}$ , darker phase  $\beta\text{Nb}_5\text{Si}_3$  and dark phase C14  $\text{NbCr}_2$  Laves.

The RHEAs and RCCAs can be (a) single phase bcc solid solution, (b) two (or more?) solid solutions (of same or different crystal structure), (c) mixture of solid solution(s) and intermetallic(s) (Laves and  $M_5\text{Si}_3$  silicide(s?)) [5,6,12]. The phases of the aforementioned metallic UHTMs can be represented in the same map (fig.2), which is the key map in NICE. The interrelationships of alloys and their phases regarding (i) alloying behaviour (ii) properties and (iii) solute concentrations are captured in the alloy design methodology NICE, the development of which was based on data for RM(Nb)ICs [2] and has been expanded to include data for RM(Nb)ICs that are also HEAs, RHEAs and RCCAs [3]. The database is updated as new data becomes available. NICE is a “goal driven” alloy design approach that leads to the selection of metallic UHTMs worthy of development owing to promising oxidation or creep properties. In NICE the design of an alloy combines constraint(s), say desirable alloying elements and/or phases or RM/TM, or SM/Met ratios in the alloy, with a property goal, say a creep rate ( $\dot{\epsilon}$ ) target or an oxidation weight change ( $\Delta W/A$ ) target.

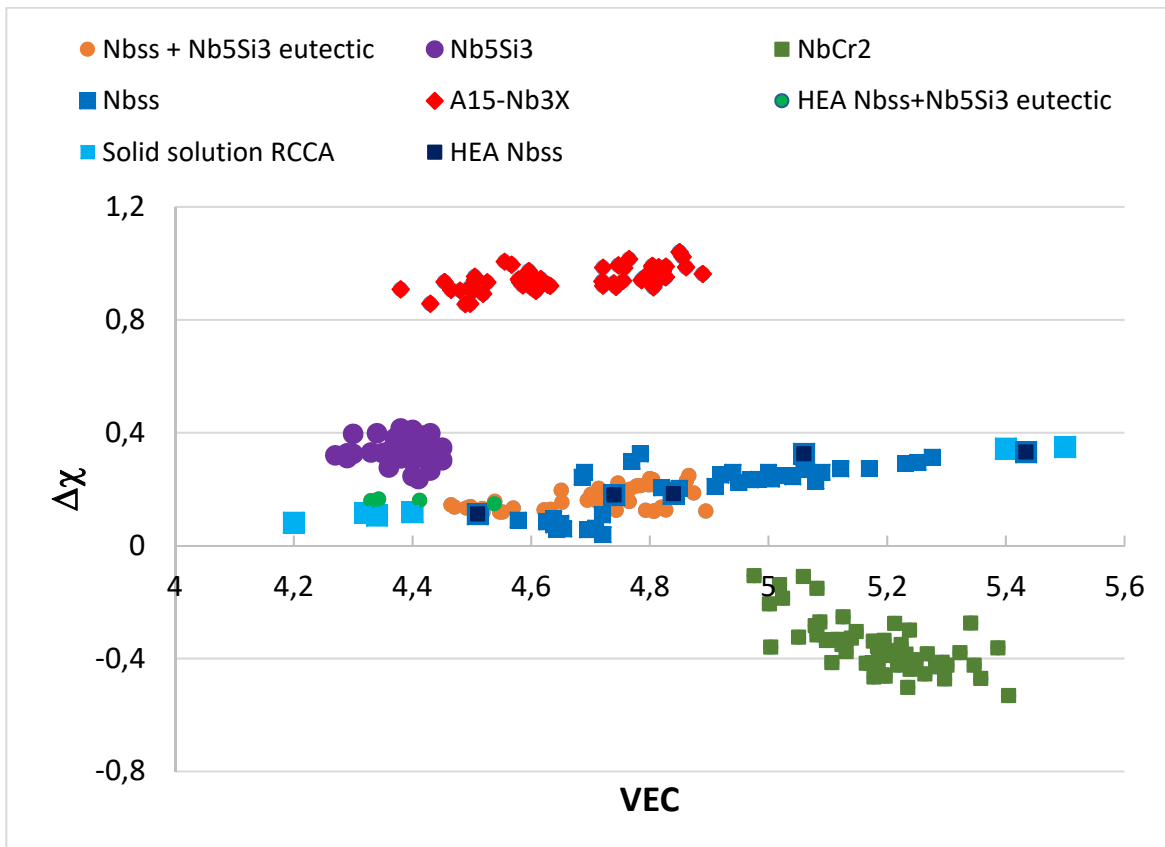


Fig. 2:  $\Delta\chi$  versus VEC map of RM(Nb)ICs with the bcc Nb<sub>ss</sub>, Nb<sub>5</sub>Si<sub>3</sub>, C14-NbCr<sub>2</sub> Laves, eutectics of Nb<sub>ss</sub> and Nb<sub>5</sub>Si<sub>3</sub>, A15-Nb<sub>3</sub>X phases, the bcc solid solution RCCAs studied by Senkov et al. [12] and HEA Nb<sub>ss</sub> and HEA Nb<sub>ss</sub> and Nb<sub>5</sub>Si<sub>3</sub> eutectics in RM(Nb)ICs [1]. The two RCCAs with high VEC values are NbMoTaW and NbMoTaWV, the RCCAs with lower VEC values have Al, Nb and Ti additions with/without Hf.

## References

- [1] P. Tsakiroopoulos, Alloys for application at ultra-high temperatures: Nb-silicide in situ composites. Challenges, breakthroughs and opportunities, *Progress in Materials Science*, **2020**, 100714
- [2] P. Tsakiroopoulos, On Nb silicide based alloys: Alloy design and selection, *Materials* **2018**, 11, 844
- [3] P. Tsakiroopoulos, Refractory Metal (Nb) Intermetallic Composites, High Entropy Alloys, Complex Concentrated Alloys and the alloy design methodology NICE: Mise-en-scène patterns of thought and progress, *Materials* **2021**, 14, 989
- [4] J. Zhao, C. Utton, P. Tsakiroopoulos, On the microstructure and properties of Nb-18Si-6Mo-5Al-5Cr-2.5W-1Hf Nb-silicide based alloys with Ge, Sn and Ti additions (at.%), *Materials* **2020**, 13, 4548
- [5] M. Ghadyani, C. Utton, P. Tsakiroopoulos, Microstructure and isothermal oxidation of the alumina forming Nb<sub>1.7</sub>Si<sub>2.4</sub>Ti<sub>2.4</sub>Al<sub>3</sub>Hf<sub>0.5</sub> and Nb<sub>1.3</sub>Si<sub>2.4</sub>Ti<sub>2.4</sub>Al<sub>3.5</sub>Hf<sub>0.4</sub> alloys, *Materials* **2019**, 12, 222
- [6] M. Ghadyani, C. Utton, P. Tsakiroopoulos, Microstructure and isothermal oxidation of the alumina scale forming Nb<sub>1.45</sub>Si<sub>2.7</sub>Ti<sub>2.25</sub>Al<sub>3.25</sub>Hf<sub>0.35</sub> and Nb<sub>1.35</sub>Si<sub>2.3</sub>Ti<sub>2.3</sub>Al<sub>3.7</sub>Hf<sub>0.35</sub> alloys, *Materials* **2019**, 12, 759
- [7] P. Tsakiroopoulos, On Nb silicide based alloys: Part II, *J. Alloys Compd.* **2018**, 748, 569-576
- [8] P. Tsakiroopoulos, On the Nb silicide based alloys: Part I-The bcc Nb solid solution, *J Alloys Compd.* **2017**, 708, 961-971
- [9] P. Tsakiroopoulos, On the alloying and properties of tetragonal Nb<sub>5</sub>Si<sub>3</sub> in Nb-silicide based alloys, *Materials* **2018**, 11, 69
- [10] P. Tsakiroopoulos, Alloying and properties of C14-NbCr<sub>2</sub> and A15-Nb<sub>3</sub>X (X=Al,Ge,Si,Sn) in Nb-silicide based alloys, *Materials* **2018**, 11, 395
- [11] P. Tsakiroopoulos, Alloying and hardness of eutectics with Nb<sub>ss</sub> and Nb<sub>5</sub>Si<sub>3</sub> in Nb-silicide based alloys, *Materials*, **2018**, 11, 592
- [12] O. N. Senkov, D. B. Miracle, K. J. Chaput, Development and exploration of refractory high entropy Alloys - A review, *J. Mater. Res.* **2018**, 33, 3092-3128



**O-IT-11****High-entropy Hägg phases - a case study of nitrides and diborides**

Paul H. Mayrhofer<sup>1</sup>, Alexander Kirnbauer<sup>1</sup>, Andreas Kretschmer<sup>1</sup>, Peter Polcik<sup>2</sup>, Marcus Hans<sup>3</sup>  
and Jochen M. Schneider<sup>3</sup>

<sup>1</sup>Institute of Materials Science and Technology, TU Wien, 1060 Vienna, Austria, paul.mayrhofer@tuwien.ac.at,  
alexander.kirnbauer@tuwien.ac.at, andreas.kretschmer@tuwien.ac.at

<sup>2</sup>Plansee Composite Materials GmbH, 86983 Lechbruck am See, Germany, peter.policik@plansee.com

<sup>3</sup>Materials Chemistry, RWTH Aachen University, 52074 Aachen, Germany, hans@mch.rwth-aachen.de,  
schneider@mch.rwth-aachen.de

**Introduction**

So called high-entropy materials often outperform their lower-entropy relatives in various aspects, such as thermal stability and mechanical properties. While there are extensive research activities in the field of high-entropy alloys, comparably little is performed for high-entropy ceramics and intermetallics. Here we show, that especially with physical vapor deposition the development of single-phased high-entropy phases is straight-forward. Or, are we just lucky? On the definition-basis for high entropy alloys, the term “high-entropy” is often used also for nitrides, oxides, and borides if at least five corresponding binaries constitute them, and the configurational entropy (per formula unit) amounts to  $S \geq 1.5R$  ( $S$ : entropy and  $R$ : gas constant) [1]. As for such intermetallic phases, basically one sublattice is unchanged and thus the term high-entropy is valid only for the other sublattice (for nitrides, the metal), we suggest to use the more appropriate term of “high-entropy sublattice nitrides”, oxides, borides, etc. [2]. Although, it might be crystal clear that when talking about such high-entropy nitrides, of course only the metal-sublattice is high entropic. Using the sublattice model (Eq. 1) to calculate the entropy of such intermetallic phases [3,4] results in much lower values:

$$S = -k \frac{\sum_i^y a^y \cdot \sum_i^n x_i \cdot \ln x_i}{\sum_i^y a^y} \quad (1)$$

where  $k$  is the Boltzmann constant,  $x_i$  the atomic concentration of element  $i$  on sublattice  $y$ ,  $a^y$  the number of sites on sublattice  $y$  (e.g., for  $\text{TiB}_2$   $a^{\text{Ti}} = 1$  and  $a^{\text{B}} = 2$ ), and  $n$  the number of element species  $i$  at the sublattice  $y$ .

For example, the entropy of a MeN intermetallic phase (of the Hägg type; Me: metal, N: nitrogen), equimolarly comprising 5 different MeN binaries, would amount to 1.61R per formula unit (or at the metal-sublattice per atom), but only to 0.81R per atom. Thus, such nitrides have a high-entropy sublattice (acceptably named also high-entropy nitrides), but they are only low-entropy ( $S < 1R$ ) intermetallics. However, high-entropy materials should never be reduced to their entropy alone, because they offer additional other important exotic effects such as: 1) the “sluggish diffusion”, which proposes kinetic restrictions for transformations due to the increased activation energy for substitutional diffusion and atomistic phenomena that stall diffusion, 2) the “severe lattice distortion”, which suggests that the crystalline structure is extremely deformed, and 3) the “cocktail effect”, which infers that properties are “higher” than the weighted average of the constituents [3]. All high-entropy Hägg phases investigated here, outperform their commonly-used binary or ternary constituents in thermal stability and thermomechanical properties.

**Materials and Methods**

The various nitride [5,6], oxide [7], and diboride [2,8] thin films were deposited by unbalanced magnetron sputtering with a modified Leybold Z400 deposition system. These films are investigated in their as-deposited state as well as after a vacuum annealing treatment up to 1600 °C by scanning and transmission electron microscopy (SEM and TEM), elastic recoil detection analysis (ERDA), atom probe tomography (APT), nanoindentation, and X-ray diffraction (XRD). Additionally, also the oxidation kinetics of selected samples have been investigated upon exposure to ambient air at elevated temperatures. Density functional theory (DFT) calculations employing the Vienna Ab Initio Simulation Package (VASP) was used to calculate energy of formation, elastic constants, and structural parameters of the hexanary compounds as well as their most likely forming lower-entropy products.

## Results and Discussion

The high-entropy sublattice nitrides – sputtered from equimolar powder-metallurgically-prepared  $\text{Hf}_{0.2}\text{Ta}_{0.2}\text{Ti}_{0.2}\text{V}_{0.2}\text{Zr}_{0.2}$ ,  $\text{Al}_{0.2}\text{Ta}_{0.2}\text{Ti}_{0.2}\text{V}_{0.2}\text{Zr}_{0.2}$ , and  $\text{Al}_{0.2}\text{Cr}_{0.2}\text{Nb}_{0.2}\text{Ta}_{0.2}\text{Ti}_{0.2}$  targets – are single-phased fcc-structured. In the as-deposited state their hardness  $H$  values are comparable to those of the constituting binaries, and even slightly below those of some constituting ternaries or quaternaries. But their indentation moduli  $E$  are considerably lower. For example,  $H = 33$  GPa and  $E = 450$  GPa for  $\text{Hf}_{0.23}\text{Ta}_{0.17}\text{Ti}_{0.19}\text{V}_{0.21}\text{Zr}_{0.20}\text{N}$ , while  $H = 36$  GPa and  $E = 520$  GPa for the ternary  $\text{Ti}_{0.69}\text{Zr}_{0.31}\text{N}$ . But even after vacuum-annealing at  $1300$  °C, the  $\text{Hf}_{0.23}\text{Ta}_{0.17}\text{Ti}_{0.19}\text{V}_{0.21}\text{Zr}_{0.20}\text{N}$  still showed 28 GPa of hardness, see Fig. 1. Atom probe tomography of this  $1300$  °C annealed sample indicates a random distribution of the constitutional elements (in agreement with XRD studies), which only could be observed when annealed at  $1500$  °C, see Fig. 2. Interestingly, the  $\text{Al}_{0.20}\text{Cr}_{0.26}\text{Nb}_{0.15}\text{Ta}_{0.16}\text{Ti}_{0.23}\text{N}$  leads to the formation of a single-phase rutile structured high-entropy sublattice oxide upon ambient-air treatments at  $850$  °C. Preparing such oxides directly by sputtering from the equimolar  $\text{Al}_{0.2}\text{Cr}_{0.2}\text{Nb}_{0.2}\text{Ta}_{0.2}\text{Ti}_{0.2}$  target with various  $\text{O}_2$ -to-Ar flow-rate-ratios ( $f_{\text{O}_2}$ , from 0.4 to 4 at a pressure of  $p = 0.4$  Pa) proved their preference to crystallize with the single-phase rutile structure. With increasing  $f_{\text{O}_2}$ , only the deposition rate decreased from 33 to 20 nm/min,  $H$  increased from 22 to 24 GPa, and  $E$  increased from 380 to 410 GPa. Vacuum annealing at  $1200$  °C solely led to a change of their nearly random crystal orientation towards a highly 101-texture.

The hardness of the high-entropy sublattice diborides  $\text{Hf}_{0.19}\text{Ti}_{0.20}\text{Ta}_{0.24}\text{V}_{0.14}\text{Zr}_{0.23}\text{B}_2$  and  $\text{Hf}_{0.15}\text{Ta}_{0.17}\text{V}_{0.19}\text{W}_{0.35}\text{Zr}_{0.15}\text{B}_2$  – non-reactively sputtered from corresponding targets – in their as-deposited state is very high with 47 and 46 GPa, combined with moderate  $E$  values of 550 and 610 GPa. Even after vacuum-annealing at  $1300$  °C, the still single-phased hcp-structured  $\text{Hf}_{0.15}\text{Ta}_{0.17}\text{V}_{0.19}\text{W}_{0.35}\text{Zr}_{0.15}\text{B}_2$  exhibits 45 GPa hardness and nearly no shape-change of its XRD peaks. Contrary, the ternary  $\text{Ti}_{0.39}\text{Zr}_{0.61}\text{B}_2$  already “softened” to 40 GPa upon annealing at  $1100$  °C, see Fig. 1.

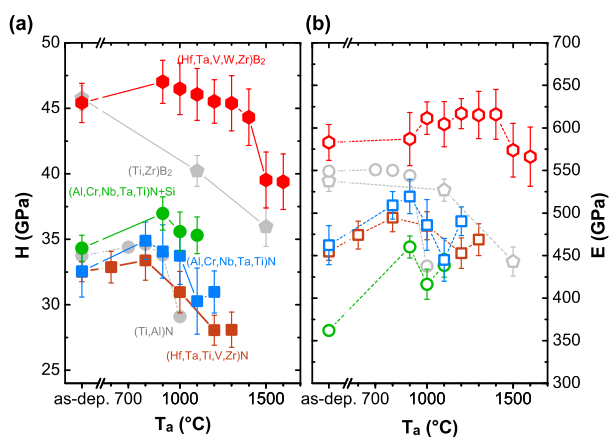


Fig. 1: (a) Hardness  $H$  and (b) indentation modulus  $E$  of the high-entropy sublattice nitrides and borides (grown on sapphire substrates) after vacuum-annealing at temperatures ( $T_a$ ) up to  $1600$  °C. The annealing time at  $T_a$  was 10 min. For comparison also the data for the ternary  $(\text{Ti,Al})\text{N}$  and  $(\text{Ti,Zr})\text{B}_2$  are added.

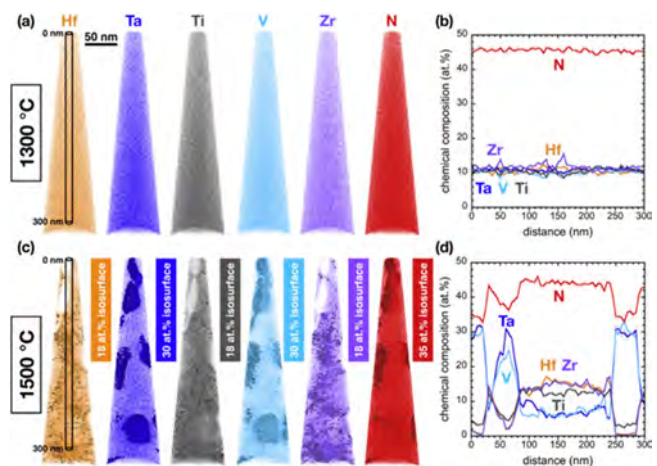


Fig. 2: Local chemical composition of the  $(\text{Hf,Ta,Ti,V,Zr})\text{N}$  prepared with  $f_{\text{N}_2} = 45\%$  at the nanometer scale. (a) Reconstruction of Hf, Ta, Ti, V, Zr, and N atomic positions after vacuum-annealing at  $1300$  °C. (b) Concentration profile of the cylindrical region indicated in (a). (c) Reconstruction of Hf, Ta, Ti, V, Zr, and N atomic positions after vacuum-annealing at  $1500$  °C. (d) Concentration profile of the cylindrical region indicated in (c).

## Conclusions

Based on these results we can conclude that the high-entropy concept is also very beneficial for hard ceramic thin films, especially with respect to the severe lattice distortion and sluggish diffusion, but also in supporting the formation of single-phased crystalline solids. Furthermore, all high-entropy sublattice ceramic thin films studied were relatively insensitive to variations of the deposition parameters – which is good, as their properties are on a high-level.

## Acknowledgments

Financial support by the Austrian COMET Program (project K2 InTribology1, no. 872176) is highly acknowledged.

**References**

- [1] J.-W. Yeh, S.-K. Chen, S.-J. Lin, J.-Y. Gan, T.-S. Chin, T.-T. Shun, C.-H. Tsau, S.-Y. Chang, *Advanced Engineering Materials*, **2004**, 6, 299–303.
- [2] P.H. Mayrhofer, A. Kirnbauer, Ph. Ertelthaler, C.M. Koller, *Scripta Materialia*, **2018**, 149C, 93–97.
- [3] D.B. Miracle, O.N. Senkov, *Acta Materialia*, **2017**, 122, 448–511.
- [4] M. Hillert, *Phase Equilibria, Phase Diagrams and Phase Transformations: Their Thermodynamic Basis*, second ed., Cambridge University Press, Cambridge, UK, **2008**.
- [5] A. Kirnbauer, A. Kretschmer, C.M. Koller, T. Wojcik, V. Paneta, M. Hans, J.M. Schneider, P. Polcik, P.H. Mayrhofer, *Surface and Coatings Technology*, **2020**, 389, 125674, 1–9.
- [6] A. Kretschmer, A. Kirnbauer, V. Moraes, D. Primetzhofer, K. Yalamanchili, H. Rudigier, P.H. Mayrhofer, *Surface and Coatings Technology*, **2021**, 416, 127162, 1–12.
- [7] A. Kirnbauer, Ch. Spadt, C.M. Koller, S. Kolozsvári, P.H. Mayrhofer, *Vacuum*, **2019**, 168, 108850, 1–5.
- [8] A. Kirnbauer, A. Wagner, V. Moraes, D. Primetzhofer, M. Hans, J.M. Schneider, P. Polcik, P.H. Mayrhofer, *Acta Materialia*, **2020**, 200, 559–569.



**O-IT-12****Iron aluminides – a class of sustainable materials**

Martin Palm

Max-Planck-Institut für Eisenforschung GmbH, Düsseldorf, Germany, palm@mpie.de

**Introduction**

To reach the goal of reducing greenhouse emissions and thereby slowing down global warming, the development and usage of more sustainable materials is a key factor. “Sustainable” would not only concern an increased lifetime, but should also apply to the production, efficiency, and recycling of the materials.

Regarding their production, sustainable materials should be resource friendly in that no or little amounts of strategic elements are used and production should be possible by using established production routes, making use of an already existing infrastructure. Sustainable materials should increase the efficiency of existing equipment by enabling lower weights of moving parts and higher operation temperatures, which both result in lower fuel consumption. However, lower density combined with the capability to operate at higher temperatures could also enable re-design or even novel designs, e.g. of combustion engines. If supporting structures are needed, less heavy aggregates also need less extensive support structures, thereby further on saving resources. The increased lifetime of the materials through better corrosion and wear resistance should finally end by completely recycling them.

Efforts on existing materials usually concentrate on improving one property, e.g. enable higher operating temperatures. A novel material that would meet all above aspects would look like a jack of all trades material. However, iron aluminides are capable of addressing all these aspects.

**Resource-friendly iron aluminides**

With 5 wt.% and 8 wt.%, respectively, iron and aluminium are the most abundant metals in the earth’s crust [1] and iron aluminide alloys currently foreseen for structural applications are iron-based alloys with about 26 at. % Al and less than 5 at.% of additional elements. These additional elements are employed for generating specific microstructures for tailoring the properties and sometimes to contribute to an increased strength through solid-solution hardening.

**Iron aluminides with increased strength at high temperatures**

The potential of iron aluminides for developing novel light-weight materials for application at temperatures of 500 – 1000 °C, i.e. replacing highly alloyed steels of even Ni-base superalloys, has been realised since long [2-4]. However, binary Fe-Al alloys become weak at about 500 °C and approaches to increase their strength usually followed concepts established for steels. But, as it proved difficult to impossible to generate microstructures with an even distribution of fine-scaled carbides or intermetallic phases, these efforts came to a halt in the 1990s [4]. And, as often in materials science, the development of alternative strengthening concepts failed due to insufficient knowledge of the respective phase diagrams.

Investigation of iron aluminides and development of iron aluminide-base materials had already been a research topic at the Max-Planck-Institut für Eisenforschung (MPIE) for a long time [5]. Therefore part of the investigations of phase equilibria and phase transformations in relevant Fe–Al–X systems [6] started in the mid-1980s at MPIE, including the binary system and X = C, Cr, Ti, Nb, Ta, Mo, Zr. Based on the then established phase diagrams, new concepts for the strengthening of iron aluminides at high temperatures were successfully developed [7]. These included the generation of coherent microstructures, the suppression of coarsening of the Fe-Al matrix at high temperatures through boride precipitates along the grain boundaries, and generating purposeful distributions of Laves phases by employing their formation from a metastable Heusler phase.

**Production of iron aluminide alloys and parts**

The production and processing of novel materials usually necessitates the employment of advanced or even new ways for their synthesis and their processing can be quite laborious.  $\gamma$ -TiAl base alloys are a current example. In contrast, iron aluminide materials can be produced and processed using standard equipment which is readily available in industries [4].

Production of the alloys at the lab scale usually starts by synthesis from the pure elements, as the aim is to study their basic properties. However, the possibility of their production from commercial steel and aluminium scraps has been demonstrated [8-10]. Industrial partners of MPIE produced melts of several hundred kilos to more than a ton by classical induction melting. Induction melting can even be performed in air, as the dense alumina slags that form on top of the melt produce a gas-tight cover. The possibility of producing parts by standard casting technologies such as precision casting, centrifugal casting or sand casting have been demonstrated [4]. By precipitating borides at the grain boundaries a comparable fine-scaled microstructure is attained and its coarsening during application at high temperatures is avoided.

Thermomechanical processing by rolling and forging on an industrial scale has also been frequently demonstrated. Conditions are usually those otherwise used for Cr-steels and processing was performed in air, as no inert atmosphere

is necessary. Specifically Fe-Al-Ta have been proven well suited for forging, yielding parts of specifically high strength [11]. The various industrial efforts have also shown that thermomechanical processing usually improves ductility compared to the cast counterparts [4].

As addressed in the next chapter, iron aluminides are specifically wear resistant. Therefore, a minimum of tooling is desirable and consequently near-net shape production techniques have been tested to generate a variety of different parts, made out of various iron aluminide alloys. Additive manufacturing by all common laser or electron beam techniques has been performed [12]. Through them, a variety of microstructures can be realised thereby tailoring the properties. Also production of parts by combustion synthesis or spark plasma sintering has been successfully demonstrated [13,14].

#### **Durability of iron aluminides due to excellent corrosion and wear resistance**

Iron aluminum alloys with Al contents exceeding about 18 at.% form dense and adherent  $\alpha$ -Al<sub>2</sub>O<sub>3</sub> (alumina) scales [15] which not only protect them against further quick oxidation, but which yield corrosion resistance in many other media by isolating them from the aggressive surrounding [4]. Iron aluminum alloys also show a high wear resistance [16,17], which, e.g., qualifies them for application as brake discs. For this type of application also friction is an important property. Though less investigated, available information hints also to excellent properties, e.g. a minimum of scuffing compared to reference materials.

Despite their potential, by now only few niche applications have been realised by employing iron aluminium alloys [4,18]. Their limited ductility and insufficient knowledge about fatigue and welding could be reasons for that. As few other materials promise to be as sustainable as iron aluminides, their further development should allow to use them for a wider range of applications.

#### **References**

- [1] B. Mason, Principles of Geochemistry. John Wiley & Sons, New York, **1958**.
- [2] W.J. Lepkowski, J.W. Holladay, The present state of development of iron-aluminum-base alloys. Batelle Meml. Inst., Rep. NP-6509, **1957**, 1-39.
- [3] C.G. McKamey, in: N.S. Stoloff, V.K. Sikka (Eds.): Physical Metallurgy and Processing of Intermetallic Compounds. Chapman & Hall, New York, **1996**, 351-391.
- [4] M. Palm, F. Stein, G. Dehm, Annual Review of Materials Research. **2019**, *49*, 297-326.
- [5] M. Palm, International Journal of Materials Research. **2009**, *100*, 277-287.
- [6] M. Palm, F. Stein (Eds.): Ternary Alloys Vol. 21 - Application-Related Iron-Aluminium Systems, MSI, Stuttgart, **2021**, to be published.
- [7] M. Palm, Intermetallics. **2005**, *13*, 1286-1295.
- [8] P. Kratochvil, Intermetallics. **2008**, *16*, 587-591.
- [9] T. Itoi, Y. Watanabe, Y. Nishikawa, H. Kimura, K. Yoshimi, M. Hirohashi, Intermetallics. **2010**, *18*, 1396-1400.
- [10] D.F.L. Borges, D.C.R. Espinosa, C.G. Schön, Journal of Materials Research and Technology. **2014**, *3*, 101-106.
- [11] P. Janschek, K. Bauer-Partenheimer, R. Krein, P. Hanus, M. Palm, Materials Research Society Symposium Proceedings. **2009**, *1128*, 47-52.
- [12] A. Michalcová, L. Senčerkova, G. Rolink, A. Weisheit, J. Pešička, M. Stobik, M. Palm, Materials Design. **2017**, *116*, 481-494.
- [13] B.H. Rabin, R.N. Wright, Metallurgical Transactions. **1992**, *23A*, 35-40.
- [14] G. Ji, F. Bernard, S. Launois, T. Grosdidier, Material Science and Engineering. **2013**, *559A*, 566-573.
- [15] P. Tomaszewicz, G. Wallwork, Reviews High-Temperature Materials. **1978**, *4*, 75-104.
- [16] M. Johnson, D.E. Mikkola, P.A. March, R.N. Wright, Wear. **1990**, *140*, 279-289.
- [17] A. Magnee, Wear. **1995**, *181-183*, 500-510.
- [18] D.G. Morris, M.A. Muñoz-Morris, Advanced Engineering Materials. **2011**, *13*, 43-47.

**O-IT-13****Additive manufacturing of  $\gamma$ -titanium aluminides - challenges, solutions and future prospects**Christoph Leyens<sup>1,2</sup>, Juliane Moritz<sup>1,2</sup>, Axel Marquardt<sup>1,2</sup>, Mirko Teschke<sup>3</sup> and Frank Walther<sup>3</sup><sup>1</sup>Technische Universität Dresden, Institute of Materials Science (IfWW), 01069 Dresden, Germany, Christoph.Leyens@tu-dresden.de<sup>2</sup>Fraunhofer Institute for Material and Beam Technology IWS, 01277 Dresden, Germany<sup>3</sup>TU Dortmund University, Department of Materials Test Engineering (WPT), 44227 Dortmund, Germany**Introduction**

For more than 30 years, gamma titanium aluminides have been attracting considerable research interest, since their favorable property profile in terms of specific strength and stiffness, oxidation resistance, and creep behavior qualifies them for high-performance applications at elevated operation temperatures. Due to their low density of around 4 g/cm<sup>3</sup>, titanium aluminide alloys are an attractive substitute for the much heavier nickel-base superalloys [1,2]. The introduction of Ti-48Al-2Cr-2Nb low-pressure turbine blades in the GENx jet engine in 2006 allowed a weight saving of about 100 kg per engine. Since then, many other companies in the aviation and automotive industries have been engaged in the serial application of TiAl components [3]. Continuous alloy development has resulted in the TNM-B1 alloy (Ti-43.5Al-4Nb-1Mo-0.1B (in at.%)), which allows even higher maximum service temperatures of up to 750 °C [1]. Nevertheless, conventional processing of titanium aluminide components, e.g. via casting or forging, remains challenging, not least because of the pronounced brittleness of the material. The evolution of additive manufacturing technologies has opened up new possibilities to manufacture complex parts from titanium aluminide [4]. This contribution will give an overview of additive manufacturing approaches for processing TNM-B1, thereby addressing the specific benefits and challenges associated with each technology and taking a look into current and future developments.

**Materials and Methods**

In this contribution, laser metal deposition (LMD), laser powder bed fusion (LPBF), and electron beam powder bed fusion (EB-PBF) for the fabrication of TNM-B1 components will be discussed in detail. Laser metal deposition is a nozzle-based additive manufacturing process which is particularly suited for achieving higher build-up rates or for the extension or repair of existing components. Major challenges during the processing of titanium aluminides may arise from cracking due to the high cooling rates or from oxygen pickup [5]. Secondary energy sources for heat management in the process zone, advanced monitoring systems for process control, and tailored shielding gas concepts can help to overcome these issues. Although laser powder bed fusion is vastly used for additive manufacturing of various materials and alloys, its applicability to titanium aluminides so far has been limited due to cracks originating from high cooling rates and steep thermal gradients. Recently, the development of novel machine technology with the possibility of substrate preheating above the brittle-ductile transition temperature allows the production of crack-free components with high relative densities [6]. Since electron beam powder bed fusion of TNM-B1 is conducted at temperatures around 1000 °C and under vacuum conditions, the aforementioned issues concerning cracking and oxidation can mostly be avoided using this technology. On the other hand, substantial aluminum evaporation and pronounced solidification textures can often be observed [7]. Consequently, a profound understanding of the correlation between process parameters, occurring microstructures, and resulting mechanical properties is crucial for ensuring adequate and reproducible part qualities.

**Results and Discussion**

The capabilities of additive manufacturing can be enhanced further by combining processes in a hybrid approach rather than considering each process individually. Examples for the combination of two additive manufacturing technologies (e. g. EB-PBF and LMD [8]) on the one hand and of additive and conventional technologies (e. g. EB-PBF / LPBF and hot-working [6]) on the other hand will be presented. Last but not least, an outlook on novel and promising alloy concepts in the field of titanium aluminides will be given.

**References**

- [1] H. Clemens, S. Mayer: *Adv. Eng. Mater.* **2013**, *15*, 191.
- [2] H. Clemens, S. Mayer: *Materials at High Temperatures.* **2016**, *33*, 560.
- [3] W. Chen, Z. Li, *Additive Manufacturing for the Aerospace Industry*, Vol. 263, Elsevier. **2019**, 235.
- [4] C. Körner: *International Materials Reviews.* **2016**, *61*, 361.
- [5] S.-K. Rittinghaus, J. Schmelzer, M.W. Rackel, S. Hemes, A. Vogelpoth, U. Hecht, A. Weisheit: *Materials.* **2020**, *13*, 4392.
- [6] I. Sizova, A. Sviridov, M. Bambach, M. Eisentraut, S. Hemes, U. Hecht, A. Marquardt, C. Leyens: *Journal of Materials Processing Technology.* **2021**, *291*, 117024.
- [7] R. Wartbichler, H. Clemens, S. Mayer: *Adv. Eng. Mater.* **2019**, *21*, 1900800.
- [8] A. Seidel, A. Straubel, T. Finaske, T. Maiwald, S. Polenz, M. Albert, J. Näsström, A. Marquardt, M. Riede, E. Lopez, F. Brueckner, E. Beyer, C. Leyens: *Journal of Laser Applications.* **2018**, *30*, 32301.

**O-IT-14****Alloy design for oxidation resistance in the Mo-Si-B system**

John Perepezko, Ranran Su and Longfei Liu

University of Wisconsin-Madison, Department of Materials Science and Engineering, 53706 Madison, WI, USA

**Introduction**

Recently, considerable effort has been devoted to the development of ultra-high temperature structural materials as alternatives to Ni-based superalloys to improve the energy efficiency of gas turbine systems. Among the several potential candidates, Mo-Si-B alloys have drawn much attention due to their high melting point and high temperature strength.

In the Mo-Si-B system, nearly all the research has focused on the Mo-rich corner, especially the  $\text{Mo}_{55}+\text{Mo}_5\text{SiB}_2$  ( $T_2$ ) +  $\text{Mo}_3\text{Si}$  three phase region. Recently, a series of Mo-Si-B alloys in the  $\text{Mo}_{55}+T_2$  ( $\text{Mo}_5\text{SiB}_2$ )+ $\text{Mo}_2\text{B}$  three phase region has been designed to examine the effect of the lower Si solubility limit in the  $\text{Mo}_{55}$  phase on the microstructure, hardness and oxidation behavior. The results showed that the Mo-Si-B alloys in the  $\text{Mo}_{55}+T_2$  ( $\text{Mo}_5\text{SiB}_2$ )+ $\text{Mo}_2\text{B}$  three phase region have higher fracture toughness and the same level oxidation resistance as those in the  $\text{Mo}_{55}+\text{Mo}_5\text{SiB}_2$  ( $T_2$ ) +  $\text{Mo}_3\text{Si}$  three phase region [1].

The Mo-Si-B alloys derive their oxidation protection from the continuous outer layer of borosilica glass that develops upon high temperature exposure [2]. Two separate stages have been identified during isothermal oxidation in dry air above 800 °C. Initially, there are concurrent reactions between the molybdenum and oxygen to form molybdenum trioxide, which starts to sublime above 475 °C, and oxidation of the boron and silicon from the  $T_2$  phase forms a borosilica glass layer.

The addition of Al can be quite beneficial for oxidation resistance due to the formation of  $\text{Al}_2\text{O}_3$  as diffusion barrier. While there is some knowledge of the oxidation of Mo-Si-B-Al alloy, previous work was contradictory and only focused on the alloys in the  $\text{Mo}_{55}+T_2$  ( $\text{Mo}_5\text{SiB}_2$ ) + $\text{Mo}_2\text{B}$  three phase region, so that the Al addition effect on the  $\text{Mo}_{55}+T_2$  ( $\text{Mo}_5\text{SiB}_2$ ) + $\text{Mo}_2\text{B}$  three phase region remains unknown. In the present study, oxidation of Mo-Si-B alloys at different Al addition levels was examined at 800, 1100, 1200, and 1300 °C for both isothermal oxidation and cyclic oxidation. Both the oxidation kinetics and oxide layer morphologies were determined in this work. In addition, to reduce the alloy density further selected substitutions of Ti along with Al was examined.

**Materials and Methods**

The alloy ingots were prepared by repetitive arc-melting of pure Mo (99.95 wt.%), Si (99.99 wt.%), B (99.95 wt.%), Al (99.995 wt.%) and Ti (99.98 wt.%) in a water-cooled Cu mold under a Ti gettered Ar atmosphere. The ingots were re-melted 5 times to achieve a homogeneous element distribution. The base alloy composition is Mo-6Si-12B with a density of 8.9 gm/cm<sup>3</sup> and the Al contents are 1, 2, 4, 8 at.% with a Ti substitution level of 20 at.%.

Heat treatment was carried out at 1800 °C for 50 h in an Ar atmosphere for all samples. Following the termination of the anneal the sample cooled at about 700°C/min. The crystalline phases of all samples were identified by X-ray diffractometry (Bruker D8 Advance). Oxidation exposure of all samples were carried out in a METTLER TOLEDO TGA/DSC 3+ instrument. The oxidation exposure was run for 100 h at 1100~1300 °C in synthetic air (20% O<sub>2</sub> and 80% N<sub>2</sub>) at a flow rate of 50 mL×min<sup>-1</sup>. The microstructures of all samples were observed by scanning electron microscopy (Zeiss Leo-1530 FESEM) with back scattered electron images. The chemical compositions of the constituent phases in the studied alloys were measured using a CAMECA SX50 electron microprobe operated at an accelerating voltage of 6 kV and a current of 6.3 × 10<sup>-9</sup> A. The calibration standards consisted of 99.9% pure Mo, Si, B and Al elements. The B concentration was quantified by separating the intensity of the B K $\alpha$  peak (at 0.182 kV) from the Mo M $\zeta$  peak (at 0.192 kV) using the analysis software Probe for Windows (Advanced Microbeam Inc). A FEI Tecnai F30 field emission gun TEM and a high resolution TEM were used to identify the oxides.

**Results and Discussion**

The homogenization treatment at 1800 °C for 50 hours yielded a partial breakup of the as-cast dendritic structure with a continuous  $\text{Mo}_{55}$  phase and dispersed  $T_2$  phase. At all Al and Ti substitution levels the phase stability was maintained as a  $\text{Mo}_{55}$  and  $T_2$  microstructure with a negligible amount of the  $\text{Mo}_2\text{B}$  phase. The TGA results demonstrated that the Al substitutions do enhance the isothermal oxidation resistance Fig. 1. Moreover, the Al substitutions also suppress the pesting behavior at 800 °C that is a typical issue for Mo alloys. The Ti substitutions do not change in a major way the behavior observed with only the Al substitutions Fig.2. Analysis of the outer oxide scale identified the structure as an aluminoborosilica for the 1 and 2% Al samples, while the 4 % Al sample showed a mixture of aluminoborosilica and mullite and at the 8% Al level the scale was entirely mullite. While the 8% Al alloy exhibited the best isothermal oxidation resistance the crystalline mullite scale degraded the cyclic oxidation resistance so that the 4% Al alloy with a density of 8.7 gm/cm<sup>3</sup> demonstrated the best overall oxidation resistance. For the Mo-6Si-12B-4Al-20Ti alloy with a density of 7.9 gm/cm<sup>3</sup> the oxide scale changed to a mixture of Al doped  $\text{TiO}_2$ ,  $\text{Ti}_{0.25}\text{Al}_{1.75}\text{O}_3$  and amorphous aluminoborosilica and exhibited a shorter transient period before the onset of steady state behavior, Fig. 2. An oxidation kinetics model was developed based upon the independent contributions of the individual phase oxidation rates weighted by their relative phase fractions and sizes that provides a good account of the observed oxidation behavior.

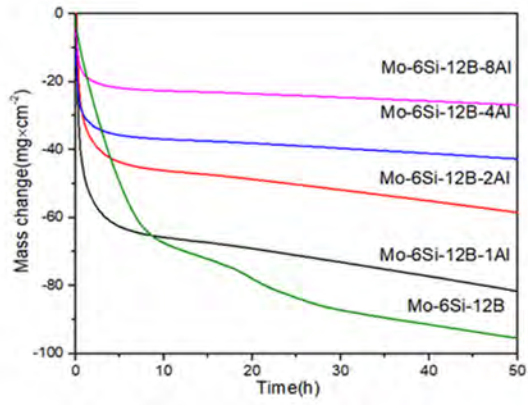


Fig. 1: Isothermal oxidation of Mo-6Si-12B-(0, 1, 2, 4, 8)Al samples at 1300 °C

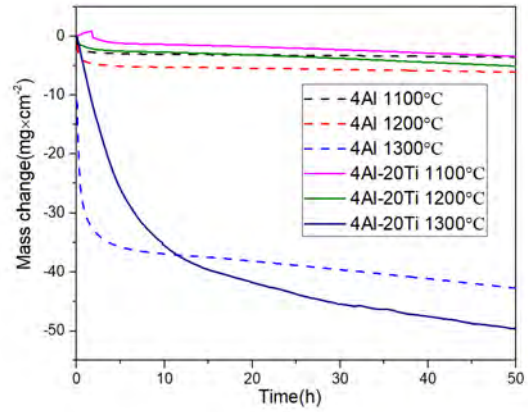


Fig. 2: Isothermal oxidation of Mo-6Si-12B-4Al and Mo-6Si-12B-4Al-20Ti samples at 1100, 1200 and 1300 °C

### References

- [1] L. Liu, C. Shi, C. Zhang, P.M. Voyles, J.H. Fournelle, J.H. Perepezko, *Intermetallics*. **2020**, *116*, 106618.
- [2] F.A. Rioult, S.D. Imhoff, R. Sakidja, J.H. Perepezko, *Acta Materialia*. **2009**, *57*, 4600-4613.

**O-PP-01****Soft magnetic properties of single-phase B2 and B2/BCC multi-principal element alloys**

Youxiong Ye<sup>1</sup>, Ian Baker<sup>1</sup>, Scott D. List<sup>1</sup>, Haixuan Xu<sup>2</sup>, Liubin Xu<sup>2</sup>, Markus W. Wittmann<sup>3</sup>, Si Chen<sup>4</sup>, Eric Woods<sup>5</sup> and Baptiste Gault<sup>5</sup>

<sup>1</sup>Thayer School of Engineering, Dartmouth College, 03755 Hanover, NH, USA, ian.baker@dartmouth.edu, youxiong.ye@dartmouth.edu, scott.d.list@gmail.com

<sup>2</sup>Department of Materials Science and Engineering, The University of Tennessee, 37996 Knoxville, TN, USA, xhx@utk.edu, lxu20@vols.utk.edu

<sup>3</sup>Hypertherm, Inc., South Building, 03766 Lebanon, NH, USA, markus.wittmann@hypertherm.com

<sup>4</sup>Advanced Photon Source, Argonne National Laboratory, 60439 Argonne, IL, USA, sichen@anl.gov

<sup>5</sup>Max-Planck-Institut für Eisenforschung, 40237 Düsseldorf, Germany, e.woods@mpie.de, b.gault@mpie.de

**Introduction**

Soft magnetic materials with high saturation magnetization and low coercivity play a vital role in efficient operation of modern power electronics and electrical machines throughout our world such as generators, transformers, motors etc. [1]. The newly emerging multi-principal element alloys (MPEAs), containing several principal metallic elements with equimolar or nonequimolar mixing (also named high-entropy alloys, HEAs), have drawn extensive research attention due to their excellent mechanical and physical properties [2, 3]. The multi-component concept has also opened up a vast compositional space for designing soft magnetic alloys since desired soft magnetic properties can be achieved via tuning compositions and microstructures [4, 5]. Most of the research for MPEAs is mainly focused on simple solid-solution alloys (FCC or BCC structures) or alloys with intermetallic compound precipitates (L1<sub>2</sub> or B2 phases). Here, we present two unusual design routes for soft magnetic MPEAs, i.e., a single-phase B2 MPEA intermetallic compound and a B2-based MPEA with BCC nanoprecipitates.

**Materials and Methods**

Alloy ingots with nominal atomic compositions of Fe<sub>30</sub>Co<sub>40</sub>Mn<sub>15</sub>Al<sub>15</sub> and Fe<sub>40</sub>Co<sub>30</sub>Mn<sub>15</sub>Al<sub>15</sub> were prepared by arc melting 99.97% Fe, 99.5% Co, 99.9% Mn, and 99.9% Al pieces in a Ti-gettered high-purity argon atmosphere. The ingots were flipped and remelted in a water-cooled copper mold at least three times to ensure the chemical homogeneity. Microstructural characterization of the as-cast samples was performed using a FEI Tecnai F20 transmission electron microscope (TEM) at an accelerating voltage of 200 kV. Samples for TEM observations were either thinned via twin-jet electropolishing in a Struers TenuPol-5 unit with a mixed solution of 30 % nitric acid and 70% methanol at ~20 V at a temperature of -20 °C, or by focused ion beam (FIB) lift-out technique using a Thermo Scientific Helios 5CX Dual Beam instrument. The chemical compositions of the matrix and nanoprecipitates for the two-phase B2/BCC Fe<sub>40</sub>Co<sub>30</sub>Mn<sub>15</sub>Al<sub>15</sub> MPEA were identified using atom probe tomography (APT). Magnetic measurements were performed on both materials using a Lakeshore vibrating sample magnetometer (VSM) with maximum applied field of 10 kOe. At least three tests were performed for each specimen condition to obtain the average magnetization and coercivity.

**Results and Discussion**

Dark-field TEM images of Fe<sub>30</sub>Co<sub>40</sub>Mn<sub>15</sub>Al<sub>15</sub> MPEA show a single-phase structure without any precipitates, see Fig. 1a. The corresponding selected area electron diffraction (SAED) pattern (Fig. 1b) identified a B2-ordered phase. The SAED pattern for Fe<sub>40</sub>Co<sub>30</sub>Mn<sub>15</sub>Al<sub>15</sub> MPEA (Fig. 1d) also indicates a B2 phase, while dark-field TEM images (Fig. 1c) obtained under a  $g = 010$  superlattice reflection clearly reveals an ordered B2 matrix (bright contrast) and disordered BCC precipitates (dark contrast). The BCC precipitates are uniformly distributed with sizes around 10-40 nm. In order to analyze the elemental partitioning between the two B2/BCC phases, APT analysis was executed, see Table 1. Much of the Fe and Mn elements are segregated into the disordered BCC precipitates, whereas Co and Al elements partition to the B2 matrix.

The magnetic properties of both MPEAs were investigated, as shown in Fig. 1e. It is readily seen that both MPEAs can be easily magnetized to the saturated state and exhibit low coercivities when demagnetized. Specifically, the measured saturation magnetization and coercivity for the single-phase B2 MPEA are 162.4 Am<sup>2</sup>/kg and 113.6 A/m, and are very similar at 157.1 Am<sup>2</sup>/kg and 116.2 A/m for the B2/BCC MPEA. The combination of high saturation magnetization and low coercivity for both MPEAs indicates their potential as soft magnetic materials (coercivity < 1000 A/m).



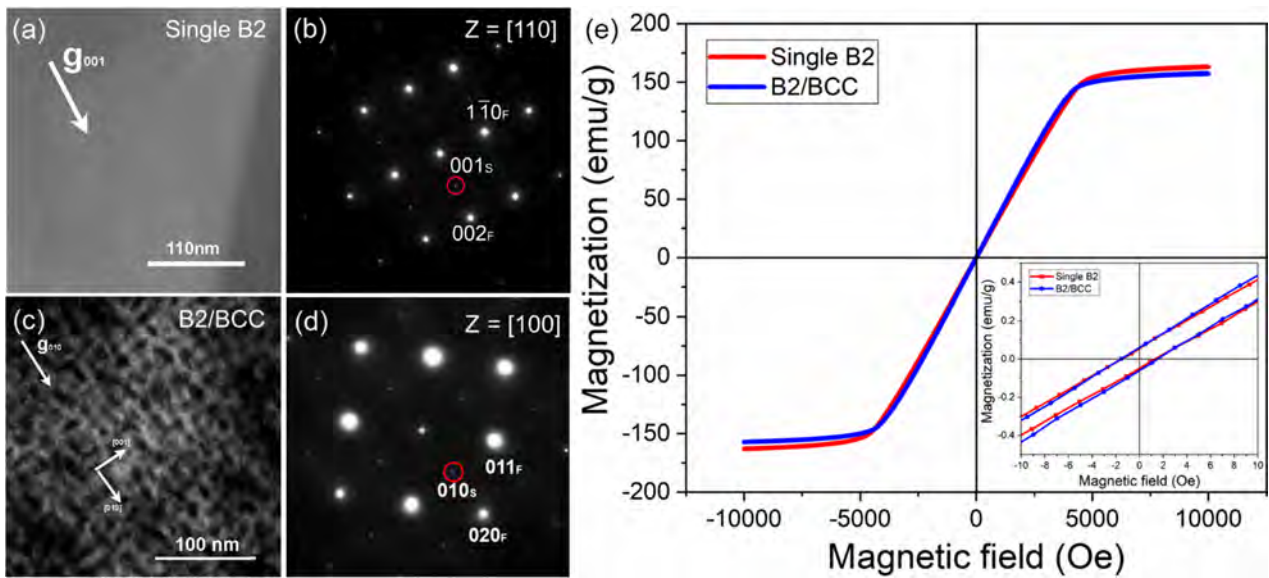


Fig. 1: (a) and (b) Dark-field (DF) TEM image and the corresponding selected area electron diffraction (SAED) pattern for the single-phase B2 MPEA; (c) and (d) DF TEM image and SAED for the B2/BCC MPEA. The zone axes and diffraction vectors  $\mathbf{g}$  used to obtain the images are indicated. (e) Magnetic hysteresis loops for single-phase B2 and B2/BCC FeCoMnAl MPEAs. The inset shows the enlarged view of the loops at low magnetic fields.

	Fe	Co	Mn	Al
Overall	$38.0 \pm 0.1$	$30.4 \pm 0.1$	$14.9 \pm 0.1$	$16.6 \pm 0.1$
B2 matrix	$35.3 \pm 0.1$	$31.6 \pm 0.1$	$13.3 \pm 0.1$	$17.2 \pm 0.1$
BCC precipitates	$50.1 \pm 1.8$	$12.2 \pm 1.8$	$28.9 \pm 2.3$	$8.8 \pm 1.1$

Table 1: Chemical compositions of the B2/BCC MPEA via APT analysis.

## References

- [1] J.M. Silveyra, E. Ferrara, D.L. Huber, T.C. Monson, *Science*. **2018**, 362, eaao0195.
- [2] Y. Zhang, T.T. Zuo, Z. Tang, M.C. Gao, K.A. Dahmen, P.K. Liaw, Z.P. Lu, *Progress in Materials Science*. **2014**, 61, 1-93.
- [3] D.B. Miracle, O.N. Senkov, *Acta Materialia*. **2017**, 122, 448-511.
- [4] Y. Ma, Q. Wang, X. Zhou, J. Hao, B. Gault, Q. Zhang, C. Dong, T.G. Nieh, *Advanced Materials*. **2021**, 33, 2006723.
- [5] T. Zuo, M.C. Gao, L. Ouyang, X. Yang, Y. Cheng, R. Feng, S. Chen, P.K. Liaw, J.A. Hawk, Y. Zhang, *Acta Materialia*. **2017**, 130, 10-18.

**O-PP-02****Impact of Antiphase Boundaries on Structural, Magnetic and Vibrational Properties of Fe<sub>3</sub>Al**Martin Friák<sup>1,2</sup>, Miroslav Černý<sup>1,2,3</sup>, Monika Všíanská<sup>1,2</sup> and Mojmir Šob<sup>1,4,5</sup><sup>1</sup>Institute of Physics of Materials, v.v.i., Czech Academy of Sciences, 616 62 Brno, Czech Republic, friak@ipm.cz, 230038@mail.muni.cz, mojmir@ipm.cz<sup>2</sup>Central European Institute of Technology (CEITEC), Brno University of Technology, 616 69 Brno, Czech Republic, cerny.m@fme.vutbr.cz<sup>3</sup>Faculty of Mechanical Engineering, Brno University of Technology, 616 69 Brno, Czech Republic<sup>4</sup>Department of Chemistry, Faculty of Science, Masaryk University, 611 37 Brno, Czech Republic<sup>5</sup>Central European Institute of Technology, CEITEC MU, Masaryk University, 625 00 Brno, Czech Republic**Introduction**

Antiphase boundaries (APBs) are rather common extended defects appearing in crystals with ordered sublattices. They are formed when one part of a crystal is specifically shifted with respect to the other part. Our computational study focuses on APBs in Fe<sub>3</sub>Al, which belongs to a very promising class of Fe-Al-based materials [1,2]. Regarding APBs in iron aluminides, two types of APBs were experimentally found in the DO<sub>3</sub> superlattice of Fe<sub>3</sub>Al. The first one is characterized by a shift of the interfacing grains in the <100> direction by a half of the lattice parameter defined for a 16-atom cube-shaped DO<sub>3</sub> cell and is associated solely with the DO<sub>3</sub> superlattice (DO<sub>3</sub>-type of APBs). The other type of APBs, that we focus on in the present study, can appear both in the DO<sub>3</sub> superlattice and in the B2 lattice (it is called a B2-type of APBs) and is characterized by a ½<111> shift. We studied the DO<sub>3</sub>-APBs, which are specific to the DO<sub>3</sub> superlattice, in (i) Fe<sub>3</sub>Al with and without Cr additions [3] and (ii) Fe-Al-Ti compounds [4]. In our current research we build upon our expertise with the B2-type of APBs that we theoretically studied in Fe<sub>70</sub>Al<sub>30</sub> alloy [5].

**Materials and Methods**

Our ab initio calculations were performed using the Vienna Ab initio Simulation Package (VASP) [6,7]. We have employed projector augmented wave (PAW) pseudopotentials [8,9]. The exchange and correlation energy was treated within the generalized gradient approximation (GGA) in the parametrization according to Perdew and Wang [10] (PW91) in combination with the Vosko-Wilk-Nusair correction [11] for the exchange and correlation energy. We used 64-atom (shown in Figure 1a), 192-atom and 256-atom supercells built as multiples of the 16-atom cube-shaped cell of Fe<sub>3</sub>Al. The 64-atom supercells are 1x1x4 multiples of the 16-atom cube-shaped cell and 192-atom supercells are 1x1x12 multiples of the 16-atom cell. Finally, the biggest 256-atom supercells were generated by the PHONOPY software [12] as 2x2x1 multiples of the 64-atom supercells (2x2x4 multiples of the 16-atom cell of Fe<sub>3</sub>Al) and were used for phonon calculations. The plane-wave energy cut-off was equal to 400 eV and the product of the number of Monkhorst-Pack k-points and the number of atoms was equal to 27 648 (e. g., 12x12x3 k-point mesh in the case of 64-atom supercells).

**Results and Discussion**

We performed an ab initio study of impact of antiphase boundaries (APBs), which are characterized by a ½<111> shift of atomic planes, on structural, magnetic and vibrational properties of Fe<sub>3</sub>Al. The studied APBs have the {001} crystallographic orientation of their sharp interfaces. There are two types of APB interfaces formed by either two adjacent planes of the twice more abundant Fe<sup>II</sup> atoms or by two adjacent planes containing both Fe<sup>I</sup> and Al atoms (see Fig. 1a). By comparing supercells with the same number of atoms with and without APBs we obtained an averaged APB interface energy equal to 80 mJ/m<sup>2</sup>. We further estimate that the APB interface energy of each of the two types of interfaces (either Fe<sup>II</sup>-Fe<sup>II</sup> or Fe<sup>II</sup>-Al) is within the range of 40-120 mJ/m<sup>2</sup>. The studied APBs significantly affect local magnetic moments of Fe atoms near the defects—they are increased in the case of Fe<sup>II</sup> atoms by as much as 11.8 % and reduced in the case of Fe<sup>I</sup> atoms by up to 4 % (see Fig. 1b). As these changes mutually nearly perfectly compensate, the total magnetic moment increases due to the presence of the studied APBs by less than 1 % (in case of 192-atom supercells with well separated APB interfaces of both types). When comparing phonons in Fe<sub>3</sub>Al with and without APBs within the harmonic approximation (see Fig. 1d,e), we find a clear influence of APBs, such as a significant reduction of the gap in frequencies that separates phonon modes below 7.9 THz and above 9.2 THz in the defect-free Fe<sub>3</sub>Al. An overall impact of APBs-induced changes results in a small increase of the free energy, lower vibrational entropy and a lower harmonic phonon energy (above T = 50 K). For details see our paper [13].



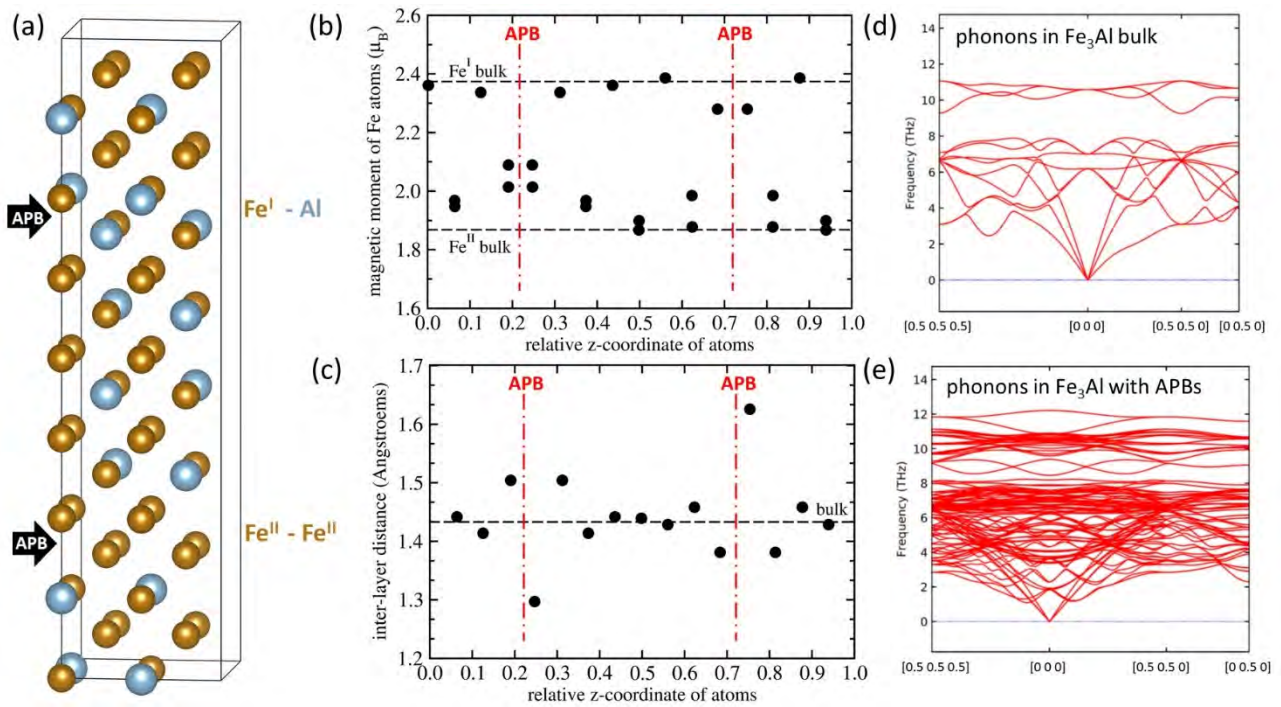


Fig. 1: Visualization of a 64-atom supercell used for modeling APB-containing crystals of  $\text{Fe}_3\text{Al}$  (a). Computed local magnetic moments of Fe atoms (b) and inter-layer distances (c) relative to the bulk values (horizontal dashed lines) with the positions of APBs indicated by vertical dashed-dotted lines. Calculated phonon frequencies (d,e) for the defect-free bulk  $\text{Fe}_3\text{Al}$  (d) and  $\text{Fe}_3\text{Al}$  with the studied APB interfaces (e) that are shown in part (a).

### Funding and Acknowledgments

The authors gratefully acknowledge the Czech Science Foundation for the financial support received under the Project No. 20-08130S (M.F., M.Č. and M.V.). M.F., M. Č. and M.Š. also acknowledge the support from the Institute of Physics of Materials of the Czech Academy of Sciences and from the Ministry of Education, Youth and Sports of the Czech Republic in the range of the Project CEITEC 2020 (Project No. LQ1601). Computational resources were made available by the Ministry of Education, Youth and Sports of the Czech Republic under, in particular, the Project of the IT4Innovations National Supercomputer Center (Project “e-Infrastructure CZ–LM2018140”) within the program Projects of Large Research, Development and Innovations Infrastructures and partly also via the CESNET (Project No. LM2015042) and CERIT-Scientific Cloud (Project No. LM2015085). Figure 1a was produced using the VESTA [14].

### References

- [1] G. Sauthoff, *Intermetallics*; VCH Verlagsgesellschaft: Weinheim, Germany, **1995**.
- [2] M. Zamanzade, A. Barnoush, C. Motz, *A Review on the Properties of Iron Aluminide Intermetallics Crystals*. **2016**, *6*, 10.
- [3] M. Friák, M. Všíanská, M. Šob, *A Quantum-Mechanical Study of Clean and Cr-Segregated Antiphase Boundaries in  $\text{Fe}_3\text{Al}$* . *Materials*. **2019**, *12*, 3954.
- [4] M. Friák, *et al.* *Elasticity of Phases in Fe-Al-Ti Superalloys: Impact of Atomic Order and Anti-Phase Boundaries*. *Crystals*. **2019**, *9*, 299.
- [5] M. Friák, M. Golian, D. Holec, N. Koutná, M. Šob, *An Ab Initio Study of Magnetism in Disordered Fe-Al Alloys with Thermal Antiphase Boundaries*. *Nanomaterials*. **2020**, *10*, 44.
- [6] G. Kresse, J. Hafner, *Ab initio molecular dynamics for liquid metals*, *Phys. Rev. B*. **1993**, *47*, 558-561.
- [7] G. Kresse, J. Furthmüller, *Efficient iterative schemes for ab initio total-energy calculations using a plane-wave basis set*. *Phys. Rev. B*. **1996**, *54*, 11169-11186.
- [8] P. E. Blöchl, *Projector augmented-wave method*. *Phys. Rev. B*. **1994**, *50*, 17953-17979.
- [9] G. Kresse, D. Joubert, *From ultrasoft pseudopotentials to the projector augmented-wave method*. *Phys. Rev. B*. **1999**, *59*, 1758-1775.
- [10] J. P. Perdew, Y. Wang, *Accurate and simple analytic representation of the electron-gas correlation energy*. *Phys. Rev. B*. **1992**, *45*, 13244-13249.
- [11] S. H. Vosko, L. Wilk, M. Nusair, *Accurate spin-dependent electron liquid correlation energies for local spin density calculations: A critical analysis*. *Can. J. Phys.* **1980**, *58*, 1200.
- [12] A. Togo, I. Tanaka, *First principles phonon calculations in materials science*. *Scr. Mater.* **2015**, *108*, 1-5.
- [13] M. Friák, M. Černý, M. Všíanská, M. Šob, *Impact of antiphase boundaries on structural, magnetic and vibrational properties of  $\text{Fe}_3\text{Al}$* . *Materials*. **2020**, *13*, Art. No. 4884.
- [14] K. Momma, F. Izumi, *VESTA 3 for three-dimensional visualization of crystal, volumetric and morphology data*. *J. Appl. Crystallogr.* **2011**, *44*, 1272-1276.

## O-PP-03

## Temperature gradients for characterizing intermetallics

Stephanie Lippmann

Friedrich-Schiller-Universität Jena, Otto Schott Institute of Materials Research, 07743 Jena, Germany,  
stephanie.lippmann@uni-jena.de

The state of a sample in a temperature gradient changes with time. Exceeding the solidus temperature, a two-phase region forms with a high density of solid/liquid interfaces. During holding, local melting and (re-)solidification processes occur that change the phase fractions rapidly. Finally, the solid/liquid region resolidifies completely up to the position of the liquidus temperature. This process allows the synthesis of pure incongruently melting phases and congruently melting phases (also well below their melting temperature if advantageous) enabling further characterization, e.g., measuring heat capacities of intermetallics [1,2]. Fig. 1a shows the first measured heat capacities of  $\text{Al}_3\text{Ni}_2$  (after the phase was synthesized in a temperature gradient) compared to values estimated with Neumann-Kopp rule and predicted with Einstein model. The parameters of the extended Einstein model (EE-model) were fitted based on the experimental data (for details, see ref. [2]).

Below the melting point, the temperature profile along a sample that is exposed to a gradient evolves as a function of the materials' thermal diffusivity during heating and as a function of its heat conductivity in steady state (see e.g. refs. [3-5]). A temporal and spatial high-resolution measurement of temperature profiles allows the determination of thermal properties and, since temperature gradients are employed, also the characterization of their T-dependency with considerably reduced time compared to conventional methods. Fig. 1b shows the T-dependent thermal conductivity of TiAl-TNM, measured in a steady temperature gradient.

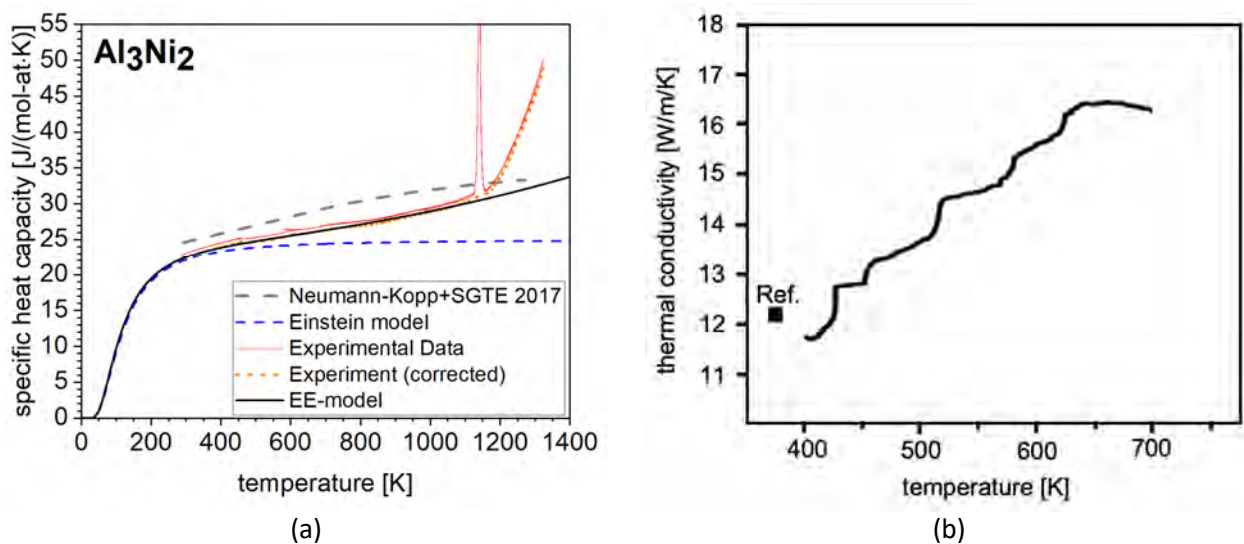


Fig. 1: Exploiting temperature gradients for intermetallics characterization, (a) heat capacity of incongruently melting  $\text{Al}_3\text{Ni}_2$  from 0 K to peritectic temperature, figure from ref. [2] (b) T-dependent thermal conductivity of TiAl-TNM determined using the inverse method described in refs. [3–5]

## References

- [1] S. Lippmann, R. H. Kemsies, M. Schick, B. Milkereit, O. Kessler, M. Rettenmayr, K. Hack: „Synthesis of pure intermetallic phases on the example of the ternary phase  $\tau_1$  in the system Al-Fe-Ni” *Intermetallics*. **2019**, 105, 107-112.
- [2] I. Saenko, H. Engelhardt, P. Hornig, O. Fabrichnaya, S. Lippmann “Specific heat capacity of the intermetallics  $\epsilon$ - $\text{Cu}_3\text{Sn}$ ,  $\eta/\eta'$ - $\text{Cu}_6\text{Sn}_5$ ,  $\text{Al}_3\text{Ni}$  and  $\text{Al}_3\text{Ni}_2$ ”, *Calphad*. **2021**, 74, 102294.
- [3] Q. Zhang, S. Lippmann, A. Grasmann, M. Zhu, M. Rettenmayr „Determination of temperature dependent thermophysical properties using an inverse method and an infrared line camera” *International Journal of Heat and Mass Transfer*. **2016**, 96, 242–248.
- [4] S. Wilhelmy, A. Zimare, R. Rettenmayr, S. Lippmann “Measurement of the Curie temperature based on temperature dependent thermal properties” *International Communications in Heat and Mass Transfer*. **2021**, 124, 105239.
- [5] S. Wilhelmy, A. Zimare, S. Lippmann, M. Rettenmayr: “A temperature gradient evaluation method for determining temperature dependent thermal conductivities” *Measurement Science and Technology*. **2021**.

**O-PP-04****Deformation characteristics of single-phase Nb<sub>2</sub>Co<sub>7</sub> under uniaxial compression test**Toshiaki Horiuchi<sup>1</sup>, Mione Yamaguchi<sup>2</sup>, Konatsu Yamada<sup>2</sup>,Ken-ichi Ikeda<sup>3</sup>, Seiji Miura<sup>3</sup> and Frank Stein<sup>4</sup><sup>1</sup>Laboratory of Advanced Materials for Cold Region, Hokkaido University of Science, 006-8585 Sapporo, Japan, horiuchi@hus.ac.jp<sup>2</sup>Division of Mechanical Engineering, Graduate School of Engineering, Hokkaido University of Science, 006-8585 Sapporo, Japan, 9201102@hus.ac.jp, 9181103@hus.ac.jp<sup>3</sup>Division of Materials Science and Engineering, Faculty of Engineering, Hokkaido University, 060-8628 Sapporo, Japan, ikeda.ken-ichi@eng.hokudai.ac.jp, miura@eng.hokudai.ac.jp<sup>4</sup>Max-Planck-Institut für Eisenforschung GmbH, 40237 Düsseldorf, Germany, f.stein@mpie.de**Introduction**

Recently, materials with “mille-feuille structure” (MFS) have attracted attention because of their unique deformation mechanism by a kink formation process, which is known from long-period stacking ordered (LPSO) phases in Mg alloys (see e. g. [1,2]). The empirical conditions defining MFS material are: (1) alternate stacking of microscopic hard and soft layers, (2) interlamellar distances of submicron or less, (3) operation of slip along with layer interface, and (4) primarily deformed by kink formation without delamination. A crystal structure-based MFS material immediately satisfies the above conditions (1) and (2), and also has the potential of hybrid type MFS material composed of two kinds of lamella materials one of which is a crystal structure-based MFS material. However, such MFS materials have rarely been found. Authors have been investigating the deformation behavior of Nb<sub>2</sub>Co<sub>7</sub> [3,4] as a candidate of a new crystal structure-based MFS material with layered mC18 crystal structure [5], which shows high deformability under compression [6]. However, the details of the deformation characteristics of Nb<sub>2</sub>Co<sub>7</sub> remain unclear. In the present study, in order to confirm whether Nb<sub>2</sub>Co<sub>7</sub> is a new crystal structure-based MFS material, deformation characteristics of single-phase Nb<sub>2</sub>Co<sub>7</sub> under uniaxial compression test were investigated mainly focusing on the kink formation and kink strengthening phenomenon in the Nb<sub>2</sub>Co<sub>7</sub> phase.

**Materials and Methods**

The Co-22.2 at%Nb alloy was cast as an  $\phi$ 20mm cylindrical ingot and was cut into 2×2×4 or 1.25×1.25×2.5 mm<sup>3</sup> square bar samples. The samples were heat-treated at 1000°C for 50h to attain single-phase Nb<sub>2</sub>Co<sub>7</sub>, followed by cooling to room temperature. All the heat treatments were carried out in a differential thermal analyzer (DTA, Shimadzu DTA-50). Uniaxial compression tests were conducted at room temperature for the 2×2×4 and 1.25×1.25×2.5 mm<sup>3</sup> square bar samples with strain rates of 1.99×10<sup>-4</sup> (Orientec RTC-1310A) and 3.75×10<sup>-4</sup> s<sup>-1</sup> (TSL 1500N device), respectively. In-situ observation of the sample surface during the compression test was performed by an optical microscope for the 1.25×1.25×2.5 mm<sup>3</sup> square bar sample. After the compression test, nanoindentation hardness tests with a constant load of 8mN and an indentation rate of 0.4mN/s were conducted using a Berkovich indenter (Hysitron TI 950). Microstructure and crystal structure were observed and analyzed by scanning electron microscopy (SEM) and electron backscatter diffraction (EBSD) pattern analysis.

**Results and Discussion**

Figure 1 shows the resultant load vs. displacement curve of the uniaxial compression test for the 1.25×1.25×2.5 mm<sup>3</sup> square bar sample and the in-situ observed microstructures at the beginning (Fig.1 (b)), at the maximum load (Fig.1 (c)), and after the end of the test (Fig.1 (d)). The plastic strain after the test is only 0.2 % in spite of the relatively high strain applied at the maximum displacement as shown in Fig.1 (c). It implies that the sample exhibits pseudoelastic deformation behavior especially at the lower right part of the sample, while plastic strain inhomogeneously remains mainly at the upper left part of the sample as shown in Fig.1 (d). SEM observation reveals that Nb<sub>2</sub>Co<sub>7</sub> deforms without fracture nor delamination. EBSD analysis also suggests that the plastic deformation of Nb<sub>2</sub>Co<sub>7</sub> is likely attained by the formation of kinks.

For the 2×2×4 mm<sup>3</sup> square bar sample, the final plastic strain after the uniaxial compression test was 3.4 %. Shown in Fig.2 are the results of nanoindentation hardness tests in the vicinity of kinks, which correspond to the microstructure. Some extremely low hardness values might be due to the effect of surface undulation of kinks. As is indicated by the green circles in the figure, the hardness values in the vicinity of kinks are higher on average than those in the rest of the matrix, implying strengthening of Nb<sub>2</sub>Co<sub>7</sub> by kink formation. In addition, detailed SEM observation reveals that the shapes of indentations in the vicinity of kinks become distorted from an equilateral triangle shape, suggesting anisotropic strengthening by kink formation. It is thus concluded that Nb<sub>2</sub>Co<sub>7</sub> might be a promising candidate for a crystal structure-based MFS material.



Fig. 1: Load vs. displacement curve of the uniaxial compression test (a) and the in-situ observed microstructures at the beginning (b), at the maximum load (c), and after the end of the test (d).

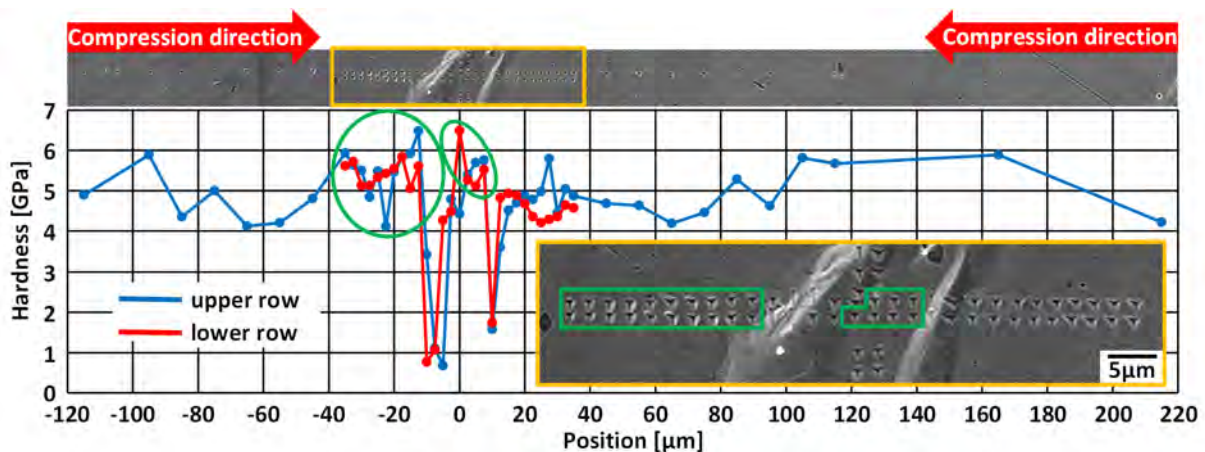


Fig. 2: Nanoindentation hardness in the vicinity of kinks corresponding to the microstructure.

**Acknowledgement**

The authors would like to thank Mr. Kenji Ohkubo at Hokkaido University for his works and valuable comments and suggestions. This work was supported by a grant from JSPS KAKENHI for Scientific Research on Innovative Areas “MFS Materials Science” (Grant Numbers JP18H05482).

**References**

- [1] K. Hagihara, Y. Sugino, Y. Fukusumi, Y. Umakoshi and T. Nakano: Materials Transactions, 52, 6, **2011**, 1096-1103.
- [2] K. Hagihara, M. Yamasaki, M. Honnami, H. Izuno, M. Tane, T. Nakano and Y. Kawamura: Philosophical Magazine, 95, 2, **2015**, 132-157.
- [3] F. Stein, M. Palm, G. Frommeyer, P. Jain, K. S. Kumar, L. Siggelkow, D. Grüner, G. Kreiner, and A. Leineweber: Proc. Materials Research Society Symposium, 1128, **2009**, 457-462.
- [4] T. Horiuchi, K. Yamada, K. Ikeda, S. Miura and F. Stein: Proc. Intermetallics 2019, Bad Staffelstein, Germany, **2019**, 136-137.
- [5] A. Leineweber, G. Kreiner, D. Grüner, R. Dinnebier, F. Stein: Intermetallics, **2012**, 25, 34-41.
- [6] L. Siggelkow, U. Burkhardt, G. Kreiner, M. Palm, F. Stein: Materials Science and Engineering A, **2008**, 497, 174-180.



**O-SI-01****The high temperature behavior of pesting and creep resistant eutectic-eutectoid Mo-Si-Ti alloys**

Martin Heilmaier<sup>1</sup>, Aditya Srinivasan Tirunilai<sup>1</sup>, Susanne Obert<sup>1</sup>, Alexander Kauffmann<sup>1</sup>, Daniel Schliephake<sup>1</sup>, Sandra Kuaffmann-Weiss<sup>2</sup>, Hans Chen<sup>3</sup>, Steven Schellert<sup>4</sup>, Bornislava Gorr<sup>4</sup>, Ronja Anton<sup>5</sup>, Matthias Weber<sup>6</sup> and Hans-Jürgen Christ<sup>6</sup>

<sup>1</sup>Karlsruhe Institute of Technology (KIT), Institute for Applied Materials (IAM-WK), 76131 Karlsruhe, Germany, martin.heilmaier@kit.edu, alexander.kauffmann@kit.edu, susanne.obert@kit.edu, aditya.tirunilai@kit.edu, daniel.schliephake@kit.edu

<sup>2</sup>Karlsruhe Institute of Technology (KIT), Innovation Campus Future Mobility (ICM), 76131 Karlsruhe, Germany, sandra.kauffmann-weiss@kit.edu

<sup>3</sup>Karlsruhe Institute of Technology (KIT), Institute for Technical Physics (ITEP), 76344 Eggenstein-Leopoldshafen, Germany, hans.chen@kit.edu

<sup>4</sup>Karlsruhe Institute of Technology (KIT), Institute for Applied Materials - Applied Materials Physics (IAM-AWP), 76344 Eggenstein-Leopoldshafen, Germany, steven.schellert@kit.edu, bornislava.gorr@kit.edu

<sup>5</sup>German Aerospace Center (DLR), Institute of Materials Research, 51147 Köln, Germany, ronja.anton@dlr.de

<sup>6</sup>University of Siegen, Department of Mechanical Engineering, 57068 Siegen, Germany, matthias.weber@uni-siegen.de, hans-juergen.christ@uni-siegen.de

**Introduction**

In the recent past, it has become necessary to design materials that can cope with the increasing demands of high temperature applications. This is specifically the case for turbine applications where Ni based superalloys are predominantly used. However, since the volume fraction of the  $\gamma'$  phase, critical to creep resistance, is expected to decrease at temperatures above 1100 °C, it may only be employed below this temperature [1]. In order to enhance turbine efficiency, the operating temperature should be increased to higher temperatures [2]. To that end, Mo-Si alloys may be employed as their melting temperatures are in the order of 2000 °C, far in excess of those of Ni based superalloys (closer to 1350 °C [2]). It has previously been observed that Mo-Si-B-Ti alloys exhibit superior oxidation and creep resistance [3, 4]. Here the addition of Ti significantly reduces the density and improves the creep resistance, in comparison to the Mo-Si-B alloy [5]. The reduction in density is linked to the alloying with Ti. The improvement in creep is a result of strengthening of the Mo<sub>SS</sub> phase by solid solution strengthening due to the presence of Ti. This work was extended to investigating Mo-Si-Ti alloys in the eutectic - eutectoid microstructure state. The fine lamellar structure in this case contributes positively to oxidation resistance through quick passivation [6]. The eutectic alloy (Mo<sub>SS</sub> + Ti<sub>5</sub>Si<sub>3</sub>) has been recognized as having high pesting resistance at 800 °C, while the eutectoid alloy (Mo<sub>SS</sub> + Mo<sub>5</sub>Si<sub>3</sub>) reportedly has superior creep resistance [6]. In order to understand the origin for the superior pesting resistance in the former and creep resistance in the latter, multiple alloys of varying Mo-Si-Ti composition were synthesized and investigated. In turn, the creep and oxidation properties were understood to yield an optimal combination in Mo-Si-Ti alloys.

**Materials and Methods**

Alloy development was guided by thermodynamic calculations based on the Calphad method. For this, the PANDAT software package (version 2018) and the commercially available database (PanMo2018a) were used. The alloys were arc-melted from high-purity elements under Ar atmosphere in an AM/0.5 arc melter by Edmund Bühler GmbH. Samples were electrically discharge machined, (i) ground down to SiC grit P2500 for oxidation and creep experiments and, (ii) additionally polished to 1 μm diamond suspension and finished using colloidal suspension (OPS) for metallographic specimens. Microstructural analyses were performed using a LEO EVO 50 scanning electron microscope (SEM) by Zeiss with an integrated energy dispersive X-ray (EDX) spectroscopy system. Images obtained from the SEM were subjected to processing via Corel Photo-Paint and subsequent analyses via ImageJ to distinguish phases and determine their respective area fractions. Grazing incidence X-ray diffraction (GIXRD) analyses were performed using a Rigaku SmartLab diffractometer equipped with a HyPix-3000 detector in OD mode and a CuK $\alpha$  radiation source. The measurements were performed with a parallel beam and a 5° soller slit in the primary beam path at incident angles  $\omega$  varying between 1.2 and 2.5°. Compressive creep tests were performed under vacuum at 1200 °C at varying constant true stresses from 50 to 300 MPa on a universal testing machine by Zwick equipped with a vacuum furnace by Maytec. Cyclic oxidation tests were carried out at 800 °C, 1100 °C and 1200 °C for up to 100 h. The cyclic oxidation tests were conducted under laboratory air in muffle furnaces provided by Gero and Nabertherm.

**Results and Discussion**

Building on the work of Schliephake et al. [6], multiple alloys of the Mo-Si-Ti system were synthesized with varying proportions of Mo to Ti. The range of alloys showed significant pesting resistance at 1100 °C and 1200 °C [7]. However,

the resistance to pesting at 800 °C is lacking in alloys with a more significant eutectoid fraction ( $\text{Mo}_{55} + \text{Mo}_5\text{Si}_3$ ) [7, 8]. Alloys with higher eutectic fractions ( $\text{Mo}_{55} + \text{Ti}_5\text{Si}_3$ ) retain high resistance to pesting at this temperature [8]. It has been seen that the fine scale lamellar microstructure in the eutectic alloy has a minor effect, as a coarse eutectic Mo-Si-Ti alloy is pesting resistant as well [8]. The cause of pesting resistance has been attributed to a minimum Ti solute content in  $\text{Mo}_{55}$  which can quickly form a passivating oxide, as opposed to Mo which forms volatile  $\text{MoO}_3$  [7, 8]. This appears valid regardless of the phase distribution in the alloys and is also seen for alloys with prominent primary solidified  $(\text{Mo,Ti})_5\text{Si}_3$  [9]. Oxide scale characterization in these alloys reveals the presence of an outer  $\text{TiO}_2$  layer with a duplex oxide scale of  $\text{SiO}_2$ - $\text{TiO}_2$  below [7]. At 1200 °C and 1100 °C the volatilization of  $\text{MoO}_3$  is circumnavigated due to accelerated formation of this oxide scale. GIXRD analysis indicate that the titanium oxide in the oxide scale exists as rutile and the silicon oxide was predominantly amorphous in nature, in line with previous findings [10].

Creep characteristics show favorability to the eutectoid microstructure with creep resistance indicated by minimum creep rate evaluated for a range of compressive loads from 50 to 300 MPa at 1200 °C [7]. However, when evaluating the minimum creep rate, accounting for the melting temperatures, it was evident that minimum creep rate scales with homologous temperature [7, 9]. This is the cause for the higher creep resistance seen in eutectoid Mo-21Si-34Ti as opposed to eutectic Mo-20Si-52.8Ti. It may be noted that, assuming power law creep, a stress exponent of  $\sim 3.5$  was determined for all the alloys under investigation indicating dislocation climb controlled creep [7, 9]. In summary the present work is able to characterize the nature of oxidation and creep for a series of Mo-Si-Ti alloys and identify the causes for pesting as well as creep resistance resulting in maximization of both properties. By the optimization process of the original alloy design to primary solidified  $(\text{Mo,Ti})_5\text{Si}_3$ , the resistance against pest oxidation of formerly Ti-rich entirely eutectic alloys were combined with creep resistance of entirely eutectoid alloys.

## References

- [1] T. Grosdidier, A. Hazotte and A. Simon, Precipitation and dissolution processes in  $\gamma/\gamma'$  single crystal nickel-based superalloys, *Materials Science and Engineering A*. **1998**, *256*, 183–196.
- [2] J. H. Perepezko, The Hotter the Engine, the Better, *Science*. **2009**, *326*, no. 5956, 1068 - 1069.
- [3] M. Azim, D. Schliephake, H. C. B. Gorr, H.-J. Christ, U. Glatzel and M. Heilmaier, Creep Resistance and Oxidation Behavior of Novel, *The Journal of The Minerals, Metals & Materials Society*. **2015**, *67*, 2621 - 2628.
- [4] M. Azim, S. Burk, B. Gorr, H.-J. Christ, D. Schliephake, M. Heilmaier, R. Bornemann and P. H. Bolívar, Effect of Ti (Macro-) Alloying on the High-Temperature Oxidation Behavior of Ternary Mo–Si–B Alloys at 820–1,300 °C, *Oxidation of Metals*. **2013**, *80*, 231 - 242.
- [5] J. H. Schneibel, P. F. Tortorelli, R. O. Ritchie and J. J. Kruzic, Optimization of Mo-Si-B intermetallic alloys, *Metallurgical and Materials Transactions A*. **2005**, *36*, 525 - 531.
- [6] D. Schliephake, A. Kauffmann, X. Cong, C. Gombola, C. Azim, B. Gorr, H.-J. Christ and M. Heilmaier, Constitution, oxidation and creep of eutectic and eutectoid Mo-Si-Ti alloys, *Intermetallics*. **2019**, *104*, 133 - 142.
- [7] S. Obert, A. Kauffmann and M. Heilmaier, Characterisation of the oxidation and creep behaviour of novel Mo-Si-Ti alloys, *Acta Materialia*. **2020**, *184*, 132–142.
- [8] S. Obert, A. Kauffmann, S. Seils, S. Schellert, M. Weber, B. Gorr, H.-J. Christ and M. Heilmaier, On the chemical and microstructural requirements for the pesting-resistance of Mo–Si–Ti alloys, *Journal of Materials Research and Technology*. **2020**, *9*, no. 4, 8556 - 8567.
- [9] S. Obert, A. Kauffmann, R. Pretzler, D. Schliephake, F. Hinrichs and M. Heilmaier, The Creep and Oxidation Behaviour of Pesting-Resistant  $(\text{Mo,Ti})_5\text{Si}_3$ -Containing Eutectic-Eutectoid Mo-Si-Ti Alloys, *Metals*. **2021**, *11*, no. 1.
- [10] S. Obert, A. Kauffmann, S. Seils, T. Boll, S. Kauffmann-Weiss, H. Chen, R. Anton and M. Heilmaier, Microstructural and chemical constitution of the oxide scale formed on a pesting-resistant Mo-Si-Ti alloy, *Corrosion Science*. **2021**, *178*.

## O-SI-02

**High-energy synchrotron X-ray *in situ* observation of ternary eutectic growth in a directionally solidified Mo-Si-B alloy**

Georg Hasemann<sup>1</sup>, Linye Zhu<sup>2</sup>, Katja Hauschildt<sup>3</sup>, Malte Blankenburg<sup>4</sup>, Shuntaro Ida<sup>2</sup>, Florian Pyczak<sup>3</sup>, Kyosuke Yoshimi<sup>2</sup> and Manja Krüger<sup>1</sup>

<sup>1</sup>Otto-von-Guericke University Magdeburg, Institute of Materials and Joining Technology, 30106 Magdeburg, Germany, georg1.hasemann@ovgu.de, manja.krueger@ovgu.de

<sup>2</sup>Graduate School of Engineering, Department of Materials Science, Tohoku University, 980-8579 Sendai, Japan, zhu.linye.r4@dc.tohoku.ac.jp, shuntaro.ida.e1@tohoku.ac.jp, yoshimi@material.tohoku.ac.jp

<sup>3</sup>Helmholtz-Zentrum Geesthacht, Institute of Materials Physics, 21502 Geesthacht, Germany, katja.hauschildt@hzg.de, florian.pyczak@hzg.de

<sup>4</sup>Deutsche Elektronen-Synchrotron (DESY), FS-PETRA-D, 22603 Hamburg, Germany, malte.blankenburg@desy.de

**Introduction**

Molybdenum-based alloys such as molybdenum silicides and Mo-Si-B alloys are seen as very promising candidates for the next generation turbine blade material beyond the capability of state-of-the-art Ni-based superalloys and are therefore studied extensively over the last two decades. Mo-Si-B alloys in particular, combine excellent creep properties and acceptable oxidation resistance at high and ultrahigh temperatures. However, the microstructure formation and the materials' properties strongly depend on the processing route of Mo-Si-B alloys. Thus, a holistic approach considering the alloy composition (affecting the phase distribution and volume fraction of phases) and the alloys microstructure has to be pursued to achieve the desired mechanical and oxidation properties to tailor alloys for specific applications.

Directional solidification (DS) offers the possibility to directly control the growth morphology of the microstructure basically by two parameters: the temperature gradient over the solidification front,  $G$ , and the growth rate,  $v$ . In general,  $G$  is determined by the DS system. It depends on technical parameters such as the design and cooling of sample chucks and/or thermal conductivity of the sample material and is therefore difficult to control actively. However,  $v$  can be easily manipulated and adjusted during the DS process.

The present study focuses exclusively on the ternary eutectic growth, microstructure and texture formation during directional solidification of the eutectic alloy Mo-17.5Si-8B. The unique "FlexiDS" sample environment [1] has been used to directly investigate crystal growth of a ternary eutectic Mo-17.5Si-8B alloy. During the *in situ* diffraction experiments at the German synchrotron source at DESY, Hamburg special interest was paid to the liquid-solid transformation and the eutectic decomposition of the liquid phase into the three (eutectic) phases Mo<sub>55</sub>, Mo<sub>3</sub>Si and Mo<sub>5</sub>SiB<sub>2</sub>. The microstructure perpendicular and parallel to the solidification direction was analyzed and the DS textures obtained by *in situ* synchrotron high-energy X-ray diffraction (HEXRD) with a photon energy of 100 keV and SEM-EBSD analysis were compared. The results provide strong evidences for a coupled ternary eutectic growth of the phases Mo<sub>55</sub>, Mo<sub>3</sub>Si and Mo<sub>5</sub>SiB<sub>2</sub>, which could be directly observed during *in situ* experiments for the first time.

**Materials and Methods**

Prior to directional solidification a master alloy of Mo-17.5Si-8B (at.%) was produced using arc-melting and a cold-crucible furnace. Directional solidification was performed using the FlexiDS zone melting device [1], a worldwide unique sample environment that was specially designed to be used for DS *in situ* experiments at the P07 High Energy Materials Science (HEMS) beamline operated by Helmholtz-Zentrum Geesthacht at PETRA III (Deutsches Elektronen-Synchrotron (DESY); Hamburg, Germany). A growth velocity of 60 mm/h and a synchronized rotation speed of 20 rpm for the feed and seed axis was used. For the *in situ* high-energy X-ray diffraction (HEXRD) experiments, a monochromatic beam with a photon energy of 100 keV ( $\lambda = 0.124 \text{ \AA}$ ) and a narrow cross section of  $1 \times 0.5 \text{ mm}^2$  (width and height) was used in transmission mode. A Perkin Elmer XRD 1621 flat panel detector was used to record the Debye-Scherrer diffraction patterns. The software Fit2D was used for azimuthal integration of the recorded 2D-diffraction patterns. For the Rietveld refinement, the upper right quarter of the detector images was used. Thus, the diffraction patterns were integrated from  $0^\circ$  to  $90^\circ$ . Furthermore, the integrated data was normalized to the background intensity. The resulting data files were analyzed by Rietveld and an additional texture analysis refinement using the software MAUD. The DSed microstructures were investigated by SEM (BSE and EBSD) and TEM.

**Results and Discussion**

Fig. 1 shows the determined phase fractions of the melt and of the three eutectic phases during the following states: in the liquid state (red region), during directional solidification (yellow region) and after entire (directed) solidification (blue region). With respect to experimental scatter, the volume fractions of the ternary eutectic are consistent with previous literature findings [2,3]. During the liquid-solid transition via directional solidification, all three solid phases simultaneously form out of the liquid phase. The fraction of the liquid phase is decreasing afterwards. Independently



from the fraction of the liquid phase that is present in the actually observed sample volume, the  $\text{Mo}_{5\text{Si}}$ ,  $\text{Mo}_3\text{Si}$  and  $\text{Mo}_5\text{SiB}_2$  phases grow with an almost constant ratio of their volume fractions relative to each other. This *in situ* observation is a strong experimental evidence for a coupled ternary eutectic growth in the Mo-rich Mo-Si-B system. In addition, the pole figures calculated from the texture analysis of the HEXRD data are shown in Fig. 2. Here it must be noted that, in comparison with the usual methods used to determine texture by HEXRD, only a single image acquired during a  $180^\circ$  sample rotation was analyzed. In addition, only a 1 mm wide sample volume in the center of the rotating bar was analyzed, resulting in a much sharper preferred orientation compared to a "normal" texture measurement. The  $\text{Mo}_{5\text{Si}}$  phase shows a weak  $\langle 001 \rangle$  texture along the growth direction with low intensity. Whereas the texture intensities of  $\text{Mo}_3\text{Si}$  and  $\text{Mo}_5\text{SiB}_2$  were relatively high. The pole figure of the  $\text{Mo}_3\text{Si}$  phase demonstrated a strong preferred orientation of the  $\langle 001 \rangle$  direction along the growth direction. The  $\text{Mo}_5\text{SiB}_2$  phase showed a strong texture formation and grew preferentially in the  $\langle 100 \rangle$  direction with the  $\{001\}$  planes parallel to the growth direction, which is consistent with the microstructure reported by Uemura et al. [4,5]. The eutectic phases had the preferential growth of  $\langle 001 \rangle \text{Mo}_{5\text{Si}} // \langle 001 \rangle \text{Mo}_3\text{Si} // \langle 100 \rangle \text{Mo}_5\text{SiB}_2$  along the temperature gradient and the result agrees with texture recently evaluated [6].

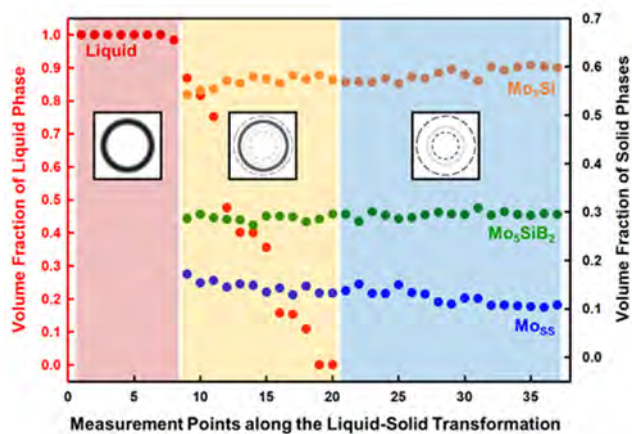


Fig. 1: Fraction of the liquid and solid phases measured along the phase transformation and the eutectic solidification front during DS. Schematic Debye-Scherrer rings as detected during the *in situ* DS measurements are additionally illustrated.

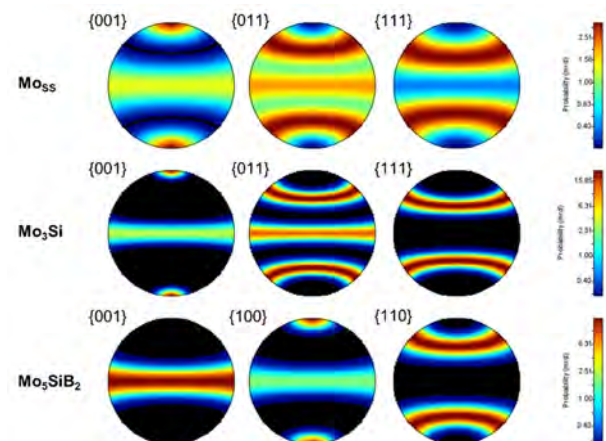


Fig. 2: Pole figures of  $\text{Mo}_{5\text{Si}}$ ,  $\text{Mo}_3\text{Si}$ , and  $\text{Mo}_5\text{SiB}_2$  in a 1 mm sample volume obtained during the *in situ* HEXRD measurements of the directionally solidified alloy Mo-17.5Si-8B.

## Conclusions

The results of the present study can be summarized as follows:

- During the liquid-solid transition, all three eutectic phases simultaneously form out of the solidifying liquid phase.
- Independently from the fraction of the liquid phase that is present in the actually observed sample volume, the  $\text{Mo}_{5\text{Si}}$ ,  $\text{Mo}_3\text{Si}$  and  $\text{Mo}_5\text{SiB}_2$  phases grow with an almost constant ratio of their volume fractions relative to each other.
- The *in situ* observation during DS provides an experimental evidence for a coupled ternary  $\text{Mo}_{5\text{Si}}\text{-Mo}_3\text{Si-Mo}_5\text{SiB}_2$  eutectic growth in the Mo-Si-B system.
- Analyzing the DS texture formation by *in situ* HEXRD diffraction experiments could confirm EBSD texture analysis of the present experiments and recent work [6] showing preferential growth of the ternary eutectic of  $\langle 001 \rangle \text{Mo}_{5\text{Si}} // \langle 001 \rangle \text{Mo}_3\text{Si} // \langle 100 \rangle \text{Mo}_5\text{SiB}_2$  along the solidification direction.

## References

- [1] C. Gombola, G. Hasemann, A. Kauffmann, I. Sprenger, S. Laube, A. Schmitt, F. Gang, V. Bolbut, M. Oehring, M. Blankenburg, et al. *Rev. Sci. Instrum.* **2020**, *91*, 093901.
- [2] G. Hasemann, D. Kaplunenko, I. Bogomol, M. Krüger, *JOM* **2016**, *68*, 2847–2853.
- [3] G. Hasemann, M. Krüger, M. Palm, F. Stein, *Mater. Sci. Forum* **2018**, *941*, 827–832.
- [4] S. Uemura, T. Yamamuro, J.W. Kim, Y. Morizono, S. Tsurekawa, K. Yoshimi, *J. Japan Inst. Met.* **2016**, *80*, 529–538.
- [5] S. Uemura, S.Y. Kamata, K. Yoshimi, S. Tsurekawa, *High Temp. Mater. Process.* **2020**, *39*, 136–145.
- [6] L. Zhu, S. Ida, G. Hasemann, M. Krüger, K. Yoshimi, *Intermetallics* **2021**, *132*, 107131.

## O-SI-03

**Production and Characteristics of spherical MoSiB- and VSiB-Powders**

Karin Ratschbacher and Volker Güther

GfE Metalle und Materialien GmbH, 90431 Nuremberg, Germany, karin.ratschbacher@gfe.com,  
volker.guether@gfe.com**Introduction**

The development of ultra-high temperature alloys has identified MoSiB- and VSiB alloys as promising candidates for future applications. They demonstrate high strength, high melting points and intrinsic protection against oxidation [1–4]. Due to the high melting point and high strength, the materials need to be produced through a powder-metallurgical approach and products built through additive manufacturing. The production of spherical MoSiB and VSiB powders, needed for additive manufacturing, will be introduced in this article. MoSiB and VSiB powders have successfully been processed through additive manufacturing [5–6].

**Materials and Methods**

To produce the feedstock for the Electrode Induction-melting Gas Atomization (EIGA) process, a powder metallurgical route was chosen. Alloying elements were mixed and homogenized, to obtain the following material compositions: [at%] Mo-9Si-8B, V-9Si-13B. The powders were consolidated by hot isostatic pressing (HIPed) at a temperature below the exothermal peak, which was determined beforehand through DSC measurements. The HIPed material was then demoulded from the HIP-container and processed in an EIGA furnace. The dimensions of the feedstock material were 65mm diameter for both materials. Pressure of the atomization gas was between 3 and 5 bar. The resulting raw powder is displayed in Fig.1

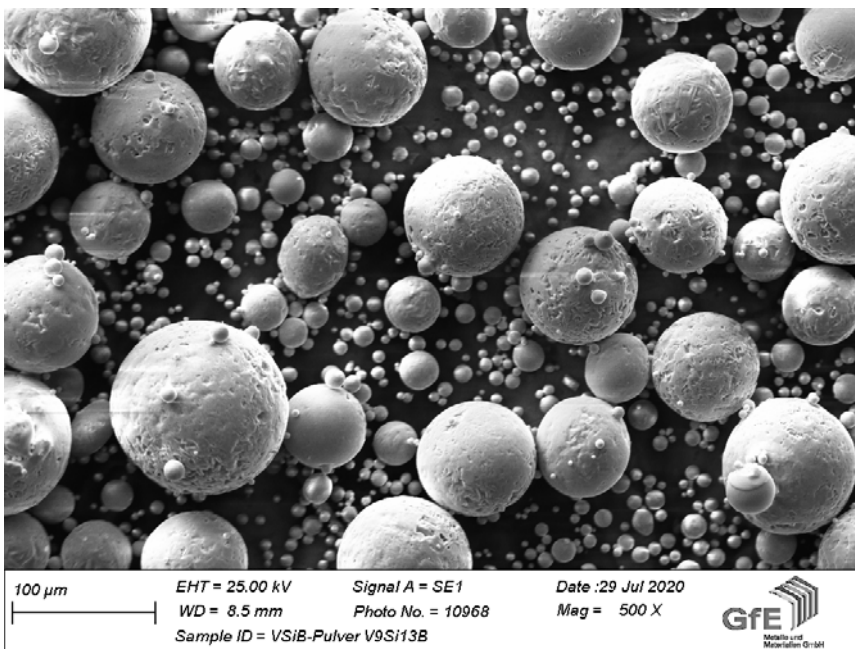


Fig.1: VSiB rawpowder

**Results and Discussion**

Stable process conditions could be obtained and powders with a  $D_{50}$  value of 44  $\mu\text{m}$  were produced. The expected phases could be detected in the MoSiB powder particles, which points to a fully alloyed material, which can be seen in Fig.2. In the VSiB powder the  $V_3\text{Si}$ -Phase could not be detected, as displayed in Fig.3. This is consistent with VSiB alloys with lower Si-content. The obtained powders show good flowability for particles 25–80 $\mu\text{m}$ , which makes them suitable for additive manufacturing.

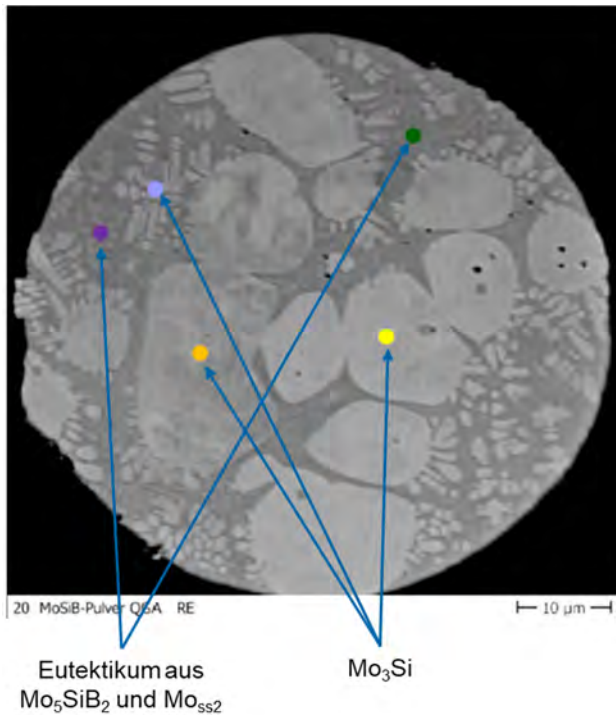


Fig. 2: Phases found in MoSiB powder particles

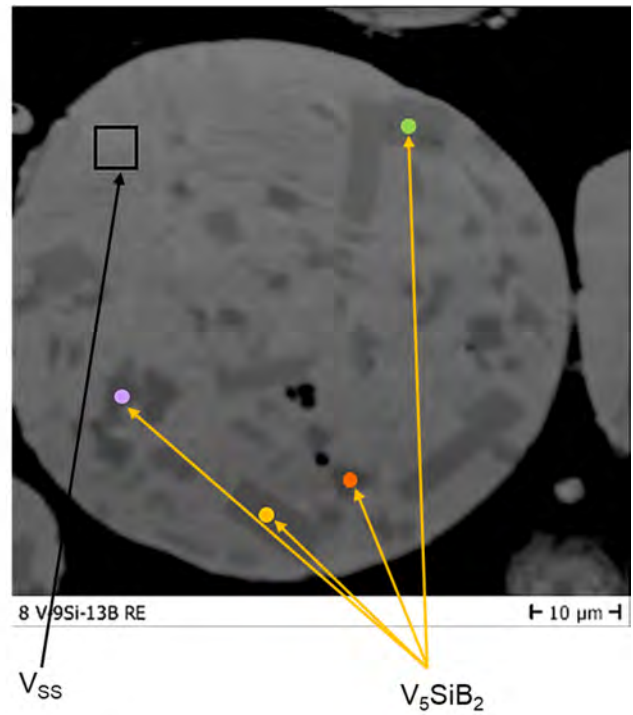


Fig.3: Phases found in VSiB powder particles

### References

- [1] P. Jain, K.S. Kumar, Dissolved Si in Mo and its effects on the properties of Mo–Si–B alloys, *Scripta Materialia*, **2010**, 62, no. 1, 1–4.
- [2] M. Krüger et al., "Correlation between microstructure and properties of fine grained Mo–Mo<sub>3</sub>Si–Mo<sub>5</sub>SiB<sub>2</sub> alloys," *Intermetallics*, **2014**.
- [3] P. Jéhanno, M. Heilmaier, H. Saage, M. Böning, H. Kestler, J. Freudenberger, S. Drawin, Assessment of the high temperature deformation behavior of molybdenum silicide alloys, *Materials Science and Engineering: A*, **2007**, 463, no. 1–2, 216-223.
- [4] G. Hasemann, C. Müller, D. Grüner, E. Wessel, M. Krüger, Room temperature plastic deformability in V-rich V–Si–B alloys, *Acta Materialia*. **2019**, 175, 140-147.
- [5] J. Schmelzer, S.-K. Rittinghaus, A. Weisheit, M. Stobik, J. Paulus, K. Gruber, E. Wessel, C. Heinze, M. Krüger, Printability of gas atomized Mo–Si–B powders by laser metal deposition, *International Journal of Refractory Metals and Hard Materials*. **2019**, 78, 123-126.
- [6] J. Schmelzer, S.-K. Rittinghaus, K. Gruber, P. Veit, A. Weisheit, M. Krüger, Printability and microstructural evolution of a near-eutectic three-phase V-based alloy, *Additive Manufacturing*. **2020**, 34, 101208.

**O-SI-04****Particle strengthening of additively manufactured Me-Si-B (Me = Mo, V) alloys**

Janett Schmelzer<sup>1</sup>, Silja-Katharina Rittinghaus<sup>2</sup>, Markus B. Wilms<sup>2</sup>, Oliver Michael<sup>1</sup>  
and Manja Krüger<sup>1</sup>

<sup>1</sup>Otto-von-Guericke-University Magdeburg, Institute of Materials and Joining Technology, 39106 Magdeburg, Germany, janett.schmelzer@ovgu.de, oliver.michael@ovgu.de, manja.krueger@ovgu.de

<sup>2</sup>Fraunhofer Institute for Laser Technology ILT, 52074 Aachen, Germany, siljakatharina.rittinghaus@ilt.fraunhofer.de, markus.benjamin.wilms@ilt.fraunhofer.de

**Introduction**

Structural materials are faced with enormous requirements concerning strength, wear resistance, but also crack tolerance. In the last decade's refractory metals and their alloys were more and more considered as potential alloys for these requirements.

Besides others, Mo-rich Mo-Si-B alloys are in the focus of research on innovative turbine materials, as they provide high strength at ambient temperatures and satisfactory fracture toughness as well as high thermal resistance and improved creep resistance [1]. Simulations and comparative experimental assessments against Ni-base superalloys already demonstrated the outstanding performance of Mo-Si-B alloys [2,3]. V-Si-B alloys, following a similar alloying concept, was found to offer enormous potential as well, although at a lower temperature regime (up to 1000 °C) in comparison to Mo-Si-B alloys (up to 1300 °C) [4]. Both refractory Me-Si-B (Me = M, V) alloys show up with good ductility and fracture toughness for a microstructure consisting of hard and creep resistant silicide phases surrounded by a more ductile solid solution matrix [5,6]. Conventional processing methods, like powder metallurgy and ingot metallurgy, were already investigated for Me-Si-B alloys [1,4–6] and currently we are working on the establishment of additive manufacturing (AM) for this class of materials [7,8].

However, one limitation on the use of the above-mentioned materials is the notably decreasing creep resistance at higher temperatures. The high strength level at ambient temperatures, which is improved by grain refinement, is not stable at temperatures above  $0.3 \cdot T_m$ . Me-Si-B materials for the use in high temperature application suffer from creep damage, that is mainly observed in the solid solution phase, while the silicide phases provide improved creep resistance. Oxide dispersion strengthening (ODS) is known to increase the high temperature materials strength and creep response of metallic materials. The application of the ODS concept on additively manufactured alloys, like Fe- and Ti-Al-based alloys was already shown [9,10]. The feasibility of the ODS approach in structural Me-Si-B materials produced by additive manufacturing is still unexplored. In this study, a new approach of additive manufacturing of  $Y_2O_3$ -doped Me-Si-B powder is presented. This approach combines the oxide dispersed strengthening (ODS) mechanism and additive processing of innovative intermetallic materials. Homogenously distribution of  $Y_2O_3$  particles in the pre-alloyed Me-Si-B powder material was achieved by means of a short grinding process in a planetary mill. Undoped Me-Si-B powders are used as reference material. Bulk samples were consolidated via direct energy deposition (DED) as a method for AM and examined regarding microstructure, hardness and compression tests.

**Materials and Methods**

*Powder production:* Gas atomized molybdenum and vanadium powder material with the nominal compositions Mo-13.5Si-7.5B (at %) and V-9Si-5B (at %), sized to a fraction of 45–90  $\mu\text{m}$ , was produced by Nanoval GmbH & Co. KG, Germany.  $Y_2O_3$ -particles were provided by abcr GmbH, Germany, with a particle size of approx. 45 nm.

*Milling procedure:* The alloyed powder material was milled together with the  $Y_2O_3$  particles in a planetary ball mill (Pulverisette 4 Classic line, Fritsch GmbH, Germany) equipped with zirconia grinding bowls and yttrium stabilized zirconia (YSZ) grinding balls with a diameter of 5 mm. The milling procedure is characterized by three milling intervals of 20 min (total milling time: 60 min) under protective argon atmosphere to avoid oxidation of the powder material. As a feedstock a manually mixed blend of 99.5 g of Mo-13.5Si-7.5B powder and 0.5 g  $Y_2O_3$  ( $\cong$  7.8 vol. %  $Y_2O_3$ ) as well as 99.5 g V-9Si-5B powder and 0.5 g  $Y_2O_3$  particles ( $\cong$  5.5 vol. %  $Y_2O_3$ ) was used.

*Direct energy deposition:* The DED process was performed in an argon purged inert gas chamber, described in detail in [7,8]. The laser beam source was a fiber coupled diode laser system (LDF2000-30, Laserline GmbH, Germany) with a maximum output of 2 kW.

**Results and Discussion**

$Y_2O_3$  reinforced Mo-13.5Si-7.5B and V-9Si-5B compacts were fabricated by means of directed energy deposition (DED). The powder material used was manufactured via a gas atomization process (Me-Si-B powder) which was followed by a short milling process to achieve a bimodal powder mixture of Me-S-B and homogenously distributed  $Y_2O_3$  particles.



AM of ODS Mo-13.5Si-7.5B and ODS V-9Si-5B pre-alloyed powders was successfully demonstrated in a laboratory scale. The AM builds reveal crack free microstructures as well as a good interlayer bonding. A homogenous distribution of the  $Y_2O_3$  particles within the microstructure for both alloys consolidated was observed (see Figure 1). Furthermore, first mechanical tests indicate an increasing trend in hardness and compressive strength for the  $Y_2O_3$  reinforced alloys at room temperature. High temperature properties will be examined in ongoing investigations and will be presented at the Intermetallics conference.

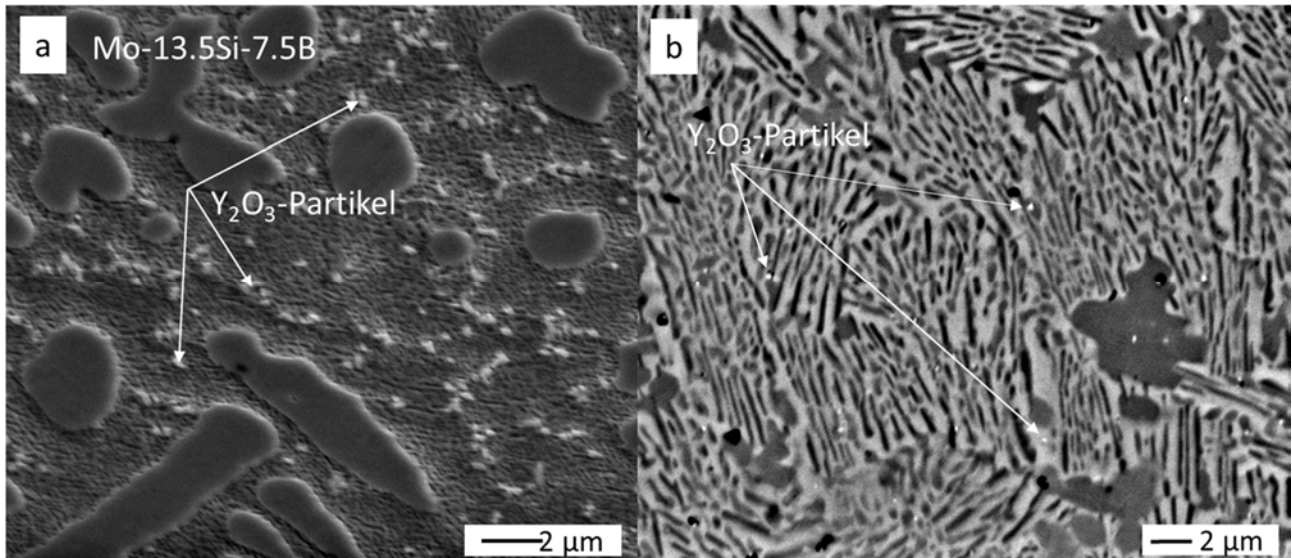


Fig. 1: Homogenously distributed  $Y_2O_3$  particles within the AM manufactured a) Mo-13.5Si-7.5B( $Y_2O_3$ ) and b) V-9Si-5B( $Y_2O_3$ ) alloys.

#### References

- [1] J.H. Perepezko, The hotter the engine, the better, *Science*. **2009**, *326*, 1068–1069.
- [2] K.A. Brindley, M.W. Priddy, R.W. Neu, Integrative Materials Design of Three-Phase Mo-Si-B Alloys, *Integrating Materials and Manufacturing Innovation*. **2019**, *8*, 1–16.
- [3] O. Kauss, H. Tsybenko, K. Naumenko, S. Hütter, M. Krüger, Structural analysis of gas turbine blades made of Mo-Si-B under transient thermo-mechanical loadings, *Computational Materials Science*. **2019**, *165*, 129–136.
- [4] M. Krüger, High temperature compression strength and oxidation of a V-9Si-13B alloy, *Scripta Materialia*. **2016**, *121*, 75–78.
- [5] J.J. Kruzic, J.H. Schneibel, R.O. Ritchie, Ambient- to elevated-temperature fracture and fatigue properties of Mo-Si-B alloys: Role of microstructure, *Metallurgical and Materials Transactions A*. **2005**, *36*, 2393–2402.
- [6] G. Hasemann, C. Müller, D. Grüner, E. Wessel, M. Krüger, Room temperature plastic deformability in V-rich V-Si-B alloys, *Acta Materialia*. **2019**, *175*.
- [7] J. Schmelzer, S.-K. Rittinghaus, A. Weisheit, M. Stobik, J. Paulus, K. Gruber, E. Wessel, C. Heinze, M. Krüger, Printability of gas atomized Mo-Si-B powders by laser metal deposition, *International Journal of Refractory Metals and Hard Materials*. **2019**, *78*, 123–126.
- [8] J. Schmelzer, S.-K. Rittinghaus, K. Gruber, P. Veit, A. Weisheit, M. Krüger, Printability and microstructural evolution of a near-eutectic three-phase V-based alloy, *Additive Manufacturing*. **2020**, *34*, 101208.
- [9] T. Boegelein, S.N. Dryepondt, A. Pandey, K. Dawson, G.J. Tatlock, Mechanical response and deformation mechanisms of ferritic oxide dispersion strengthened steel structures produced by selective laser melting, *Acta Materialia*. **2015**, *87*, 201–215.
- [10] S.-K. Rittinghaus, M.B. Wilms, Oxide dispersion strengthening of gamma -TiAl by laser additive manufacturing, *Journal of Alloys and Compounds*. **2019**, *804*, 457–460.

**O-TA-01****Revised phase diagram for the Ti-Al-O ternary system from 35 to 55 at.% aluminum**Hirotoyo Nakashima and Masao TakeyamaDepartment of Materials Science & Engineering, School of Materials and Chemical Technology,  
Tokyo Institute of Technology, Tokyo, Japan, nakashima.h.aa@m.titech.ac.jp, takeyama@mtl.titech.ac.jp**Introduction**

TiAl alloys are inevitably contaminated with oxygen during manufacturing and service, especially in powder processes or recycling processes. Therefore, the knowledge of the partitioning behavior and solubility of oxygen among phases are critical for alloy design and microstructure control of this alloy. It is qualitatively known that oxygen is enriched into the  $\alpha$  (or  $\alpha_2$ ) phase. However, quantitative reports on the phase equilibria are quite limited, even for the most basic Ti-Al-O ternary system. Menand et al. performed atom probe analysis of Ti-46Al binary alloys without intentional oxygen addition heat-treated at 1273 K and reported that the maximum solubility of oxygen in the  $\gamma$  phase is several hundred at. ppm, while two orders of magnitude higher in the  $\alpha_2$  phase [1]. On the other hand, the isothermal section at 1373 K constructed by Li et al. based on the results of WDS analysis of diffusion couples as well as equilibrated samples shows that the maximum oxygen solubility in the  $\gamma$  phase is about 3 at.% [2], which is two orders of magnitude higher than that reported by Menand et al. although the temperature is 100 K higher. Since the  $\gamma$  phase has higher deformability than the  $\alpha_2$  and  $\beta$  phases and plays an important role in improving the ductility and toughness of TiAl alloys [3], the oxygen content in the  $\gamma$  phase in equilibrium with the other phases and the associated change in phase boundaries are particularly essential information. Therefore, the purpose of this study is to investigate the phase equilibria of the Ti-Al-O ternary system with special attention to the oxygen solubility in the  $\gamma$  phase.

**Materials and Methods**

The alloys studied have nominal compositions of Ti-43Al-xO and Ti-48Al-xO ( $x=0.1, 0.4, 0.6, 1.0$ ) (in at.%). These alloys are arc-melted to 120 g button ingot. The oxygen content in the alloys was adjusted with a TiO<sub>2</sub> powder, and the total amount of oxygen in each ingot was analyzed by inert gas fusion method. All of the alloys were first homogenized at the  $\alpha$  single-phase region and then equilibrated at temperatures from 1273 K to 1573 K for up to 1.2 Ms. The homogenization treatment was conducted by vertical furnace with evacuation system. The sample wrapped with Ta foil were hung in the upper chamber of the furnace, and rolled down to the heat available zone adjusted to a given temperature under backfilled Ar after evacuation down to  $5.0 \times 10^{-3}$  Pa. After holding there for a given time, then it was water quenched by dropping it into water by opening the gate valve. The subsequent equilibration heat treatment was conducted by encapsulating the sample wrapped with Ta foil in silica tube under backfilled Ar after evacuation down to  $1.3 \times 10^{-3}$  Pa. After the heat treatment, sample was water quenched by breaking the capsule. Microstructure and composition analysis were conducted by field-emission electron probe microanalysis (FE-EPMA) equipped with wavelength dispersive X-ray diffraction spectrometer (WDS), energy-dispersive spectrometer (EDS), and soft X-ray emission spectrometer (SXES). The major constituent elements (Ti, Al and Nb) in each phase present in the samples after the equilibration were examined by WDS and also by EDS. The oxygen concentration of the phases present was quantitatively identified by a calibration method obtained using the homogenized  $\alpha$  single-phase samples analyzed by the SXES with the third order reflection of the oxygen-K $\alpha$  emission at around 175 eV. To remove the oxide layer on the sample surface, an Ar-sputtering was performed on the sample before analysis in the sample exchange chamber under vacuum.

**Results and Discussion**

At 1473 K, the oxygen-free Ti-48Al exhibits a microstructure consisting mostly of  $\gamma$ -phase with a small amount of bright-contrast  $\alpha$ -phase at grain boundaries, as shown in Fig. 1 (a). With the addition of 1 at.% oxygen to the alloy, the volume fraction of the  $\alpha$  phase increases to about 25 % (Fig. 1 (b)). The isothermal section at 1473 K drawn based on the composition analysis of each phase is shown in Fig. 2. With increasing oxygen concentration, the  $\alpha$  and  $\gamma$  single-phase regions shrink towards the Ti-rich and Al-rich sides, respectively, resulting in an extension of the  $\alpha+\gamma$  two-phase region. When 1 at.% of oxygen is added to Ti-48Al, the oxygen concentration in the  $\alpha$  phase reaches to 4.35 at.%, while that in the  $\gamma$  phase is 0.21 at.%. In the present study, the  $\alpha+\gamma+\text{Al}_2\text{O}_3$  three-phase coexistence region is not identified, and thus the maximum solubility of oxygen cannot be determined. However, it is strongly suggested that the oxygen content of  $\gamma$  in solution does not exceed 0.5 at.% at this temperature, because the oxygen concentration in the  $\gamma$  phase hardly increases from the base alloy with the oxygen addition, and at the same time, the Al concentration shifts toward the high Al concentration side. It should be noted that the alloy compositions in the figures are those of the as-cast state, and the reason why the tie-lines are located at slightly higher oxygen concentrations side than their alloy compositions is presumably due to the slight increase in oxygen concentration in the alloy during homogenization and subsequent equilibration heat treatment. In the presentation, the temperature dependence of the oxygen solubility in the  $\gamma$  phase will also be discussed.

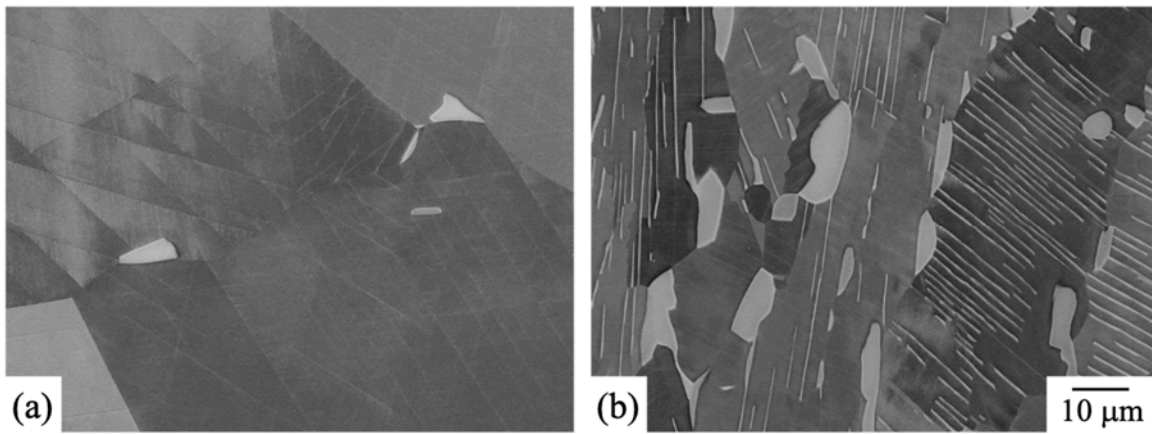


Fig. 1: Backscattered electron images of Ti-48Al (a) without and (b) with 1.0 at.% oxygen equilibrated at 1473 K.

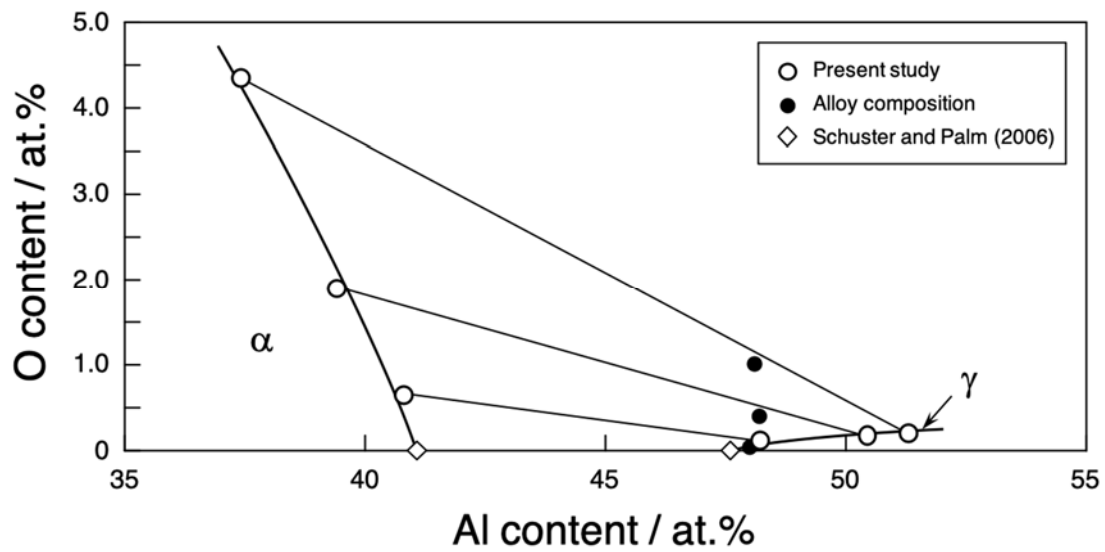


Fig. 2: Partial isothermal section of Ti-Al-O ternary system at 1473 K as obtained from the present data.

References

- [1] A. Huguet, A. Menand, Applied Surface Science. **1994**, 76/77, 191-197.
- [2] X.L. Li, R. Hillel, F. Teyssander, S.K. Choi, F.J.J. Van Loo, Acta Metall. Mater. **1992**, 40, 3149–3157.
- [3] R. Yamagata, Y. Okada, H. Wakabayashi, H. Nakashima, M. Takeyama, MRS Advances. **2019**. 4, 25-26.



## O-TA-02

**TiAl embrittlement at high temperatures**Camille Thenot<sup>1</sup>, Pierre Sallot<sup>4</sup>, Damien Connétable<sup>3</sup> and Jean-Philippe Monchoux<sup>2</sup><sup>1</sup>CEMES-CNRS, UPR 8011, 31055 Toulouse, France, camille.thenot@cemes.fr, monchoux@cemes.fr<sup>3</sup>CIRIMAT, UMR 5085, CNRS INP UPS, ENCIASET 4, 31030 Toulouse Cedex 4, France, damien.connetable@enciaset.fr<sup>4</sup>Safran Tech, 78114 Magny-Les-Hameaux, France, pierre.sallot@safrangroup.com**Introduction**

Titanium-Aluminum alloys (TiAl) are very interesting for applications in turbomachines because of their low density (3,8–4,2 g.cm<sup>-3</sup>) and of their high mechanical strength at high temperatures. However, when exposing TiAl alloys to high temperatures, significant losses of ductility can be observed. Here, we study the role of oxygen in this phenomenon, because this element is known to be very detrimental to the mechanical properties of the TiAl alloys, – whether by penetration from the surface or as a contaminant in solid solution. Because the solubility of O in the  $\gamma$  phase of TiAl is very low ( $\approx 230$  at. ppm [1]), the phenomena accounting for the loss of ductility are difficult to investigate experimentally. Some works have shown that O in solid solution could be at the origin of the anchoring phenomenon of the dislocations by pinning points [2]. These pinning points, whose size is below the detection limit of the transmission electron microscope (TEM), could therefore be structured at the atomic scale. Our first aim is then to determine the atomic structure of the defects formed by O in the TiAl lattice. For this purpose, we have carried out theoretical atomistic calculations by DFT and by a thermodynamic approach, to investigate the structure, at the atomic scale, of the TiAl-oxygen solid solution (diluted O atoms in interstitial sites or forming complex defects). In parallel, we have investigated experimentally the influence of the O concentration on the dislocation mechanisms. For this purpose, we have observed by TEM the microscopic plasticity mechanisms in TiAl materials containing different O concentrations. In addition, *in situ* straining experiments have been carried out, to properly determine the morphology of the dislocations in un-relaxed conditions.

**Materials and Methods**

The embrittlement mechanisms are studied through a double approach. First, the atomic structure of the solid solution and the diffusion mechanisms have been investigated theoretically using first-principles calculations at 0K thanks to the Vienna *ab initio* simulation package (VASP). Then, in order to take the temperature into account in our calculations, a code based on the independent point defect approximation has been used. In parallel, the loss of ductility and the dislocation-oxygen interactions have been characterized and studied experimentally. The alloys used for this purpose were Ti<sub>48</sub>Al<sub>48</sub>W<sub>2</sub>B<sub>0.08</sub> alloys obtained by spark plasma sintering. Tensile tests on these alloys have been carried out on samples exposed in air at 800 °C for 500 h, to characterize the embrittlement phenomenon. Then, to evaluate the influence of oxygen on the bulk mechanical properties, tensile tests on alloys with low and high oxygen concentrations have been performed. The dislocation-oxygen interactions have been studied by characterizations at the microscopic scale using TEM on the two alloys with different oxygen concentrations in solid solution.

**Results and Discussion**

The experimental study has clearly shown a loss of ductility with the increase in oxygen concentration. Indeed, while the average elongation at break of samples with around 835 at. ppm was around 1,1 %, in the case of 3036 at. ppm of oxygen samples, elongation at break was falling to less 0,5 %. Moreover, the presence of pinning points anchoring the dislocations has also been observed (Fig ). Thus, the distance between pinning points has been measured. The measurements reported in Tab thus indicate that when the O concentration increases, the average distance between pinning points decreases. Therefore, this correlation suggests that the pinning points are constituted of O atoms.

Oxygen concentration (at. ppm)	Average distance between pinning points	Standard deviation
834	0.13	0.06
3035	0.08	0.03

Tab 1: Average distance between two pinning points according to the oxygen concentration

Our hypothesis according to which pinning points are made of oxygen has then been studied numerically. DFT results showed the existence of strong interactions between oxygen and lattice defects such as vacancies and anti-sites, as well as strong interactions between oxygen and alloying elements. It has been found that the most probable complex defect was constituted of one oxygen atom in the vicinity of a titanium anti-site, thus forming a *Ti-anti-site + 1 O atom* complex defect (Fig 2). This complex defect is the one having the highest concentration, even compared to the defect *O on stable interstitial sites*.

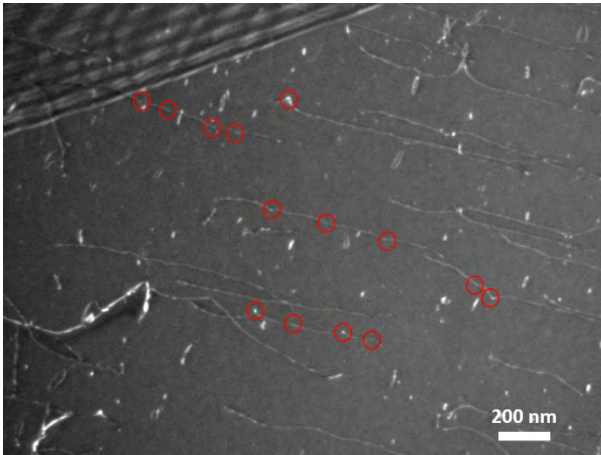


Fig 1: TEM image of pinned ordinary dislocations

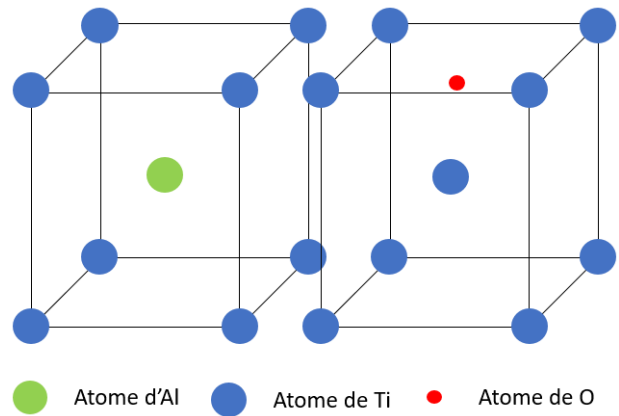


Fig 2 : Representation of the normal TiAl crystal (on the left) and the complex defect 'Ti anti-site + 1 Oxygen atom' (on the right)

Then, the interactions between oxygen and alloying elements have been studied. It has been found that these elements occupy preferably either Ti or Al substitutional sites. Moreover, whatever the alloying element X, the complex defect that has the highest concentration is constituted of  $X \text{ atom} + 1 \text{ O atom}$ . Generally, it has been found that the alloying elements that substitute Ti are not as efficient as the Ti anti-sites for trapping the oxygen atoms. However, if the X alloying element substitute Al atoms, then the number of traps increases because both X and the Ti anti-sites contribute to trap the O atoms, which leads to a slowing down of the diffusion of O in the TiAl system.

In conclusion, the correlation between the pinning points on the dislocations and the X+O complex defects still has to be confirmed. However, recent DFT investigations have shown that the concentration of these complex defects is high enough to exhibit an impact on oxygen diffusivity in TiAl alloys. Indeed, it has been shown that diffusion coefficients calculated taking the complex defects into account, lead to diffusivities two or three orders of magnitude lower than the ideal one calculated in [3]. Therefore, the diffusion mechanisms are now investigated in detail, not only supposing diffusion mechanisms by atomic jumps into interstitial sites, but taking also notably into account the contribution of the complex defects.

#### References

- [1] A. Denquin et al, Scripta Metallurgica et Materialia. **1993**, 28, 1131-1136
- [2] S. Zghal et al, Acta mater. **1998**, 46, 5899-5905.
- [3] Damien Connétable et al, J. Phys.: Condens. Matter, **2020**, 32, 175702

## O-TA-03

**O-phase formation and elastic modulus in the alloy Ti-42Al-8.5Nb**Heike Gabrisch<sup>1</sup>, Michaela Janovska<sup>2</sup>, Marcus.W. Rackel<sup>1</sup>, Florian Pyczak<sup>1</sup> and Andreas Stark<sup>1</sup><sup>1</sup>Helmholtz-Zentrum Hereon, 21502 Geesthacht, Germany, heike.gabrisch@hereon.de, marcus.rackel@hereon.de, florian.pyczak@hereon.de, andreas.stark@hereon.de<sup>2</sup>Institute of Thermomechanics of the Czech Academy of Sciences, 182 00 Prague 8, Czech Republic, janovska@it.cas.cz**Introduction**

In  $\gamma$ -titanium aluminides alloyed with Nb, the orthorhombic O-phase forms in the alloys' microstructure upon annealing in an appropriate temperature range [1–4]. Its stoichiometric composition is  $Ti_2AlNb$ , however the phase exists over a wide composition range [5]. In the past, we studied the formation and morphology of the orthorhombic O-phase in the  $\gamma$ -based alloy Ti-42Al-8.5Nb by High-Energy X-Ray diffraction (HEXRD) and transmission electron microscopy (TEM) [1, 2]. We found, that in the temperature range between 480–680 °C O-phase forms out of the  $\alpha_2$  parent phase by small displacements of atom positions along  $\langle 11\bar{2}0 \rangle$  directions of the hexagonal lattice [2]. The degree of orthorhombic distortion varies with formation temperature and is most pronounced at 550 °C. Above 700 °C, the orthorhombic phase becomes unstable and the lattice reverts to hexagonal symmetry that can be preserved in a metastable state at room temperature by fast cooling.

Single phase O-phase alloys have a lower Young's modulus than single-phase  $\gamma$ -TiAl and  $\alpha_2$ -Ti<sub>3</sub>Al alloys [6]. A lower Young's modulus might be interpreted as weaker interatomic bonding, which in turn might explain improved room temperature ductility [7]. Therefore, the presence of O-phase is thought to improve room temperature ductility in titanium aluminides. However, the measurements made on single-phase alloys, are not necessarily relevant for the behavior of multi-phase alloys, where interphase interfaces and internal stress states influence the mechanical properties.

To address the effect of O-phase formation on mechanical properties in  $\gamma$ -TiAl alloys we subject the alloy Ti-42Al-8.5Nb to long-term annealing experiments at 550 °C and perform in-situ measurements of the elastic constants during this anneal. The results of the in-situ measurements are related to the microstructural features characterized by TEM after different annealing times.

**Materials and Methods**

The alloy Ti-42Al-8.5Nb (at.-%) was prepared by powder metallurgy starting from pure elements as described in [8]. Powder particles with diameters of 45–180  $\mu$ m were filled into titanium cans and were compacted by hot-isostatic pressing (HIP) in argon under 200 MPa at 1250 °C for 2 h.

From the HIPed compacts specimens were cut and heat treated in air at 550 °C for 8 to 672 hours (4 weeks), followed by furnace cooling. HEXRD experiments were performed at the High Energy Materials Science beam line (HEMS) operated by the Helmholtz-Zentrum Hereon at the storage ring PETRA III at the Deutsches Elektronen-Synchrotron (DESY) in Hamburg, Germany. The specimens were investigated at room temperature, in transmission, using high photon energies of 87.1 keV or 100 keV that allow to analyse a large sample volume. During the HEXRD experiments the Debye-Scherrer diffraction rings were recorded on a Perkin Elmer XRD 1621 flat panel detector. The instrumental parameters, the beam centre and the sample-detector-distance were determined using a lanthanum hexaboride (LaB<sub>6</sub>) powder standard.

For Transmission Electron Microscopy, 500  $\mu$ m thick slices were cut from the annealed specimens and discs of 3 mm diameter were drilled out of these slices. The discs were ground manually to about 80–120  $\mu$ m thickness followed by twin jet polishing at -39 °C with a solution of 18 ml perchloric acid in 430 ml methanol and 250 ml 2-buthanol.

Bright-field imaging and HAADF STEM imaging were performed at Hereon with the Cs corrected FEI Titan 80–300 kV operated at 300 kV. Atomic resolution HAADF STEM images were recorded at the Center for Nanophase Materials Sciences, at Oakridge National Laboratory using the Nion UltraSTEM 100 dedicated aberration-corrected STEM at 100 kV and at the Laboratoire de Physique de Solides, Université Paris-Sud using the 200 kV Nion UltraSTEM operated at 100 kV [9].

The elastic constants, C<sub>11</sub> and C<sub>44</sub>, were determined by Resonant Ultrasound Spectroscopy (RUS), assuming isotropic elasticity for the material at the Institute of Thermomechanics in Prague, Czech Republic as described in [submitted to Acta Mat].

**Results and Discussion**

Fig. 1 shows the evolution of the Young's modulus during iso-thermal annealing at 550 °C. for 672 hours. Overall, a small increase from 135.9 to 137.6 GPa is measured, whereby the shape of the E-t-curve shows two distinct regimes. About 80–90 % of the total strengthening takes place during the first 30–40 hours where the E-t-curve exhibits a very steep slope. Thereafter the Young's modulus increases steadily at a much lower rate over the remaining testing time (approximately 640 hours). Fig. 2 shows the microstructure of a specimen annealed for 8 h that belongs to the region of the initial steep increase in E-modulus. The image shows a section of an  $\alpha_2$  lamellae in  $\alpha_2$ -[0001] projection at

atomic resolution. In this viewing direction, Ti and Nb atoms form honey-comb-like hex-rings when the lattice has strict hexagonal symmetry as illustrated in the inset at the bottom left of the image. In the experimental image of the annealed specimen however, the former hex-rings of  $\alpha_2$  phase are distorted along the three  $\langle 11\text{-}20 \rangle$  directions of the hexagonal lattice as indicated by arrows. This initial distortion from  $\alpha_2$  to O-phase takes place without diffusional processes. Investigations of specimens representing the annealing states after 168 and 672 hours show that after these longer annealing times diffusion has set in and Nb is now concentrated in the most strongly distorted regions. These Nb-rich O-phase domains are separated by  $\alpha_2$ -like matrix channels enriched in Al and Ti (168 h) [10]. With prolonged annealing time, after 672 h a splitting mechanism is observed causing a decrease in the size of O-phase domains [11]. Assuming that the microstructural changes are responsible for the observed change in Young's modulus it appears that the initial orthorhombic distortion at constant chemistry is responsible for the largest part of the observed strengthening. The slower increase that follows thereafter is related to the diffusion of Nb and to the formation of smaller O-phase domains.

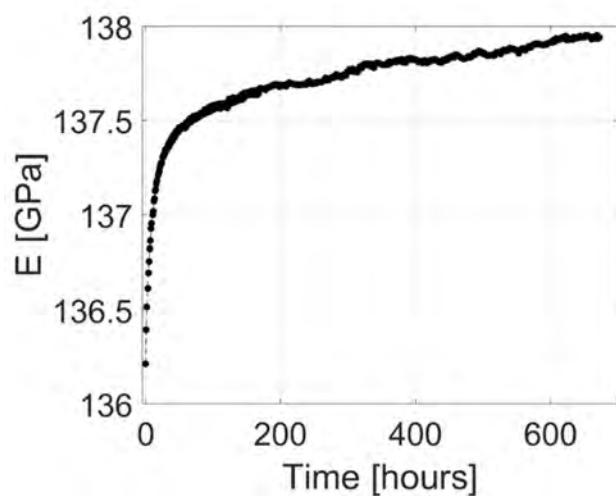


Fig. 1: Development of Young's modulus during iso-thermal anneal at 550 °C.

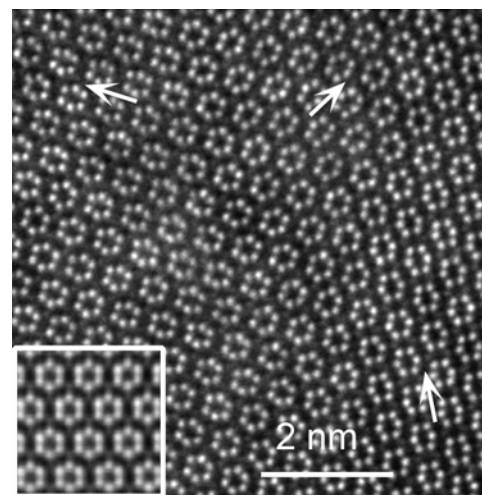


Fig. 2: HAADF-STEM-image of the atomic arrangement in the  $\alpha_2$ -(0001) plane showing the orthorhombic distortion inside  $\alpha_2$  lamella after annealing at 550 °C for 8 h.

#### Acknowledgement

HAADF STEM imaging was conducted under CNMS Proposal ID CNMS2017-R10 at the Center for Nanophase Materials Sciences, which is a DOE Office of Science User Facility.

#### References

- [1] H. Gabrisch, U. Lorenz, F. Pyczak, M. Rackel, A. Stark, *Acta Materialia*. **2017**, *135*, 304- 313.
- [2] M.W. Rackel, A. Stark, H. Gabrisch, N. Schell, A. Schreyer, F. Pyczak, *Acta Materialia*. **2016**, *121*, 343-351.
- [3] G.-d. Ren, J. Sun, *Acta Materialia*. **2018**, *144*, 516- 523.
- [4] G.-d. Ren, C.-r. Dai, W. Mei, J. Sun, S. Lu, L. Vitos, *Acta Materialia*. **2019**, *165*, 215- 227.
- [5] V.T. Witusiewicz, A.A. Bondar, U. Hecht, T.Y. Velikanova, *Journal of Alloys and Compounds*. **2009**, *472(1-2)*, 133-161.
- [6] R.E. Schafrik, *Metallurgical Transactions*. **1977**, A 8A, 1003-1006.
- [7] F. Chu, T.E. Mitchell, B. Majumdar, D. Miracle, T.K. Nandy, D. Banerjee, *Intermetallics*. **1997**, *5*, 147- 156.
- [8] R. Gerling, H. Clemens, F.P. Schimansky, *Advanced Engineering Materials*. **2004**, *6(1-2)*, 23-38.
- [9] ESTEEM, This project has received funding from the European Union's Horizon 2020 research and innovation programme under grant agreement No 823717 – ESTEEM3.
- [10] H. Gabrisch, T. Krekeler, U. Lorenz, M.W. Rackel, M. Ritter, F. Pyczak, A. Stark, in: M.I. R. Shabadi, M. Jeandin, C. Richard and Tara Chandra (Ed.) *THERMEC'2018: 10th International Conference on Processing and Manufacturing of Advanced Materials*, Scientific Net, Paris, France. **2018**, 741- 746.
- [11] H. Gabrisch, T. Krekeler, U. Lorenz, M.W. Rackel, M. Ritter, F. Pyczak, A. Stark, *14<sup>th</sup> World Conference on Titanium*, MATEC Web of Conferences platform, Nantes, France, **2019**.

## O-TA-04

## Kinetics of Solid-State Phase Transformations in Ternary Ti–Al–Nb Alloys below 1000°C

Benedikt Distl and Frank Stein

Max-Planck-Institut für Eisenforschung GmbH, 40237 Düsseldorf, Germany, distl@mpie.de, stein@mpie.de

## Introduction

For a further improvement of the mechanical properties of next generation TiAl-based high-temperature alloys at their application temperatures above 700 °C, it is important to better understand the evolution of microstructure and mechanical properties during application. Therefore, it is necessary to investigate the phase equilibria and kinetics of phase transformations happening in this temperature range. Especially the Ti–Al–Nb system plays an important role as it is the key system for most of the TiAl-based high-temperature alloys currently in use in aviation and automotive industries [1]. In the relevant composition range, there are two ternary intermetallic phases, the so-called O-phase ( $\text{Ti}_2\text{NbAl}$ ,  $oC16$ ,  $Cmcm$ ) [2] and  $\omega_0$ -phase ( $\text{Ti}_4\text{NbAl}_3$ ,  $hP6$ ,  $P6_3/mmc$ ) [3]. Both are important for microstructure stabilization and the mechanical properties at application temperature [4,5]. They form in solid-state reactions from the intermetallic phases ( $\beta\text{Ti}$ )<sub>0</sub> or  $\text{Ti}_3\text{Al}$  ( $\alpha_2$ ) [2,3] depending on microstructure, thermomechanical treatment and composition of the alloy [5]. Although there has been done a lot of research in recent years especially about the formation mechanism of the O-phase [5], there is little known about the kinetics of these transformations. Therefore, this work aims to investigate the kinetics of  $\omega$ - and O-phase formation and to determine equilibrium transition temperatures, transition types, and phase equilibria involved in these transformations.

## Materials and Methods

By utilizing an advanced arc melter with tiltable crucible, a series of ternary Ti–Al–Nb alloys has been produced from high-purity elements Ti (99.995 %), Al (99.999 %) and Nb (99.9 %) for subsequent heat treatments in high-purity Ar-atmosphere. For the heat treatments between 700 and 900 °C, the alloys have been encapsulated in fused silica capsules backfilled with Ti-gettered argon gas. The microstructure is characterized using light optical microscopy (LOM) and scanning electron microscopy (SEM, Zeiss Leo 1550 VP). Phases are characterized by powder X-ray diffraction (P-XRD, Bruker D8 Advanced A25-X1-1) and the phase composition is measured using electron probe microanalysis (EPMA, JEOL JXA-8100). Differential thermal analysis (DTA, Netzsch Pegasus 404C), calibrated with Al, Au and Ni, is used for determination of phase transition temperatures. Different heating rates (1, 2, 5, and 10 K/min) are used to study if the phase transition temperatures are heating-rate dependent. The approach of Zhu et al. [6] is employed, which is an extrapolation method to 0 K/min heating rate that was specially developed to determine the equilibrium transition temperatures of sluggish solid-solid transformations.

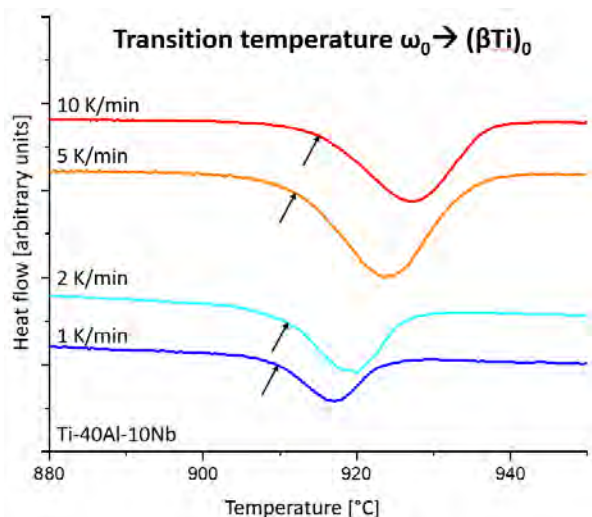


Fig. 1: DTA measurements with different heating rates of alloy Ti-40Al-10Nb (at.%) showing the heating rate dependence of the transition temperature (onset point marked with black arrow) for the transition  $\omega_0 \rightarrow (\beta\text{Ti})_0$

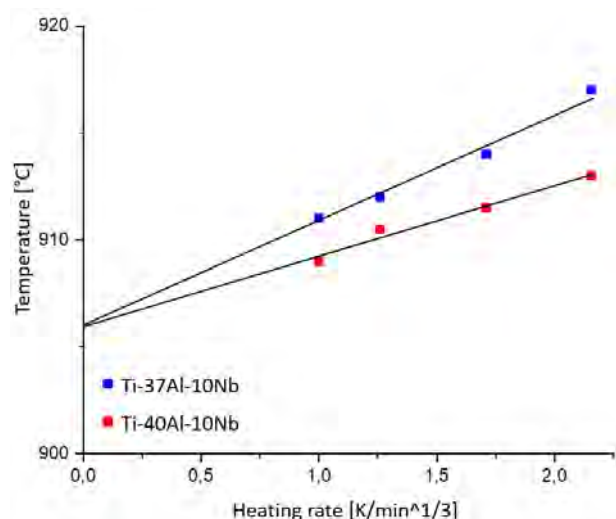


Fig. 2: Equilibrium transition temperatures  $\omega_0 \rightarrow (\beta\text{Ti})_0$  extrapolated to 0 K/min heating rate for different alloys using the approach of Zhu et al. [6]



### Results and Discussion

From the series of produced alloys, a selection was made of those samples that contain large amounts of  $\omega$ - or O-phase. Specimens of these alloys were subjected to DTA heating and cooling cycles with various constant rates.

As can be seen from Fig. 1 the transition temperature of the reversible transition  $\omega_o \rightarrow (\beta\text{Ti})_o$  is heating rate dependent. A plot of the measured transition temperatures as a function of the heating rate shows that there is no simple linear relation and it is not obvious how to extrapolate to 0 K/min heating rate. A possible solution is given by Zhu et al. [6] for sluggish solid-solid reactions where the transition temperature is plotted over the third root of the heating rate. If a respective diagram (see Fig. 2) shows a linear relation, the equilibrium transformation temperature can be determined by extrapolation to 0 K/min heating rate. The fact that the transition temperature is heating rate dependent also indicates that the transformation is most likely a first-order transition, since the transformation steps [2,3] appear to need compositional changes of the phases involved, which require diffusion. This is consistent with the *in situ* high-energy XRD measurements from Stark et al. [7] who showed that the reversible transformation of  $\omega_o \rightarrow (\beta\text{Ti})_o$  consists of two diffusion-controlled steps. This results also agree with the formation mechanism of the O-phase from  $(\beta\text{Ti})_o$  described by Hsiung et al. [8]. They observed that the cubic lattice is distorted and chemical ordering of atoms occurs, which requires a diffusion of atoms to certain lattice sites. This observation is also corroborated by the fact that the O-phase in most cases is reported to have precipitated within a  $\text{Ti}_3\text{Al}$  or  $(\beta\text{Ti})_o$  matrix [5]. In addition, literature shows that temperature plays an important role for the morphology and size of precipitates of these ternary intermetallic phases in the microstructure [5], which is an additional indication for the important role of diffusion in the formation of these phases. Another indicator pointing towards the first-order nature of the transition is the fact that formation and dissolution of the respective phases are not observed at the same temperature in DTA. In case of second-order type reactions as for example order/disorder transformations in the Ti–Al–Nb system, the transition is observed at the same temperature during heating and cooling.

The present work is the first systematic study of the kinetics of phase transformations regarding the low-temperature  $\omega$ - and O-phases of the Ti–Al–Nb system. Both phases play an important role for the mechanical behaviour of TiAl-based alloys. The knowledge about the kinetics of their solid-state phase transformations and the equilibrium transition temperatures together with results from complementing studies on phase equilibria are an essential input for the development of an improved CALPHAD database that aims in designing next-generation TiAl-based alloys to meet the ecological demands of future applications regarding reduced greenhouse gas and noise emissions [9].

This work is part of the ADVANCE project, which has received funding from the Clean Sky 2 Joint Undertaking under the European Union's Horizon 2020 research and innovation programme under grant agreement No. 820647.

### References

- [1] H. Clemens, S. Mayer, *Advanced Engineering Materials*, **2013**, *15*, 191-215
- [2] D. Banerjee, A.K. Gogia, T.K. Nandi, V.A. Joshi, *Acta Metallurgica*, **1988**, *36*, 871-882
- [3] L.A. Bendersky, W.J. Boettinger, B.P. Burton, F.S. Biancaniello, C.B. Shoemaker, *Acta Metallurgica et Materialia*, **1990**, *38*, 931-943
- [4] M. Schloffer, B. Rashkova, T. Schöberl, E. Schwaighöfer, Z. Zhang, H. Clemens, S. Mayer, *Acta Materialia*, **2014**, *64*, 241-252
- [5] H. Zhang, N. Yan, H. Liang, Y. Liu, *Journal of Materials Science & Technology*, **2021**, *80*, 203-216
- [6] Y.T. Zhu, J.H. Devletian, *Metallurgical Transactions A*, **1991**, *22*, 1993-1998
- [7] A. Stark, M. Oehring, F. Pyczak, T. Lippmann, L. Lottermoser, A. Schreyer, *Materials Science Forum*, **2013**, *772*, 85-89
- [8] L.M. Hsiung, W. Cai, H.N.G. Wadley, *Acta Metallurgica et Materialia*, **1992**, *40*, 3035-3049
- [9] ADVANCE: Sophisticated experiments and optimisation to advance an existing CALPHAD database for next generation TiAl alloys, EU-project 820647 within Horizon 2020 / Clean Sky 2\_ (<https://thermocalc.com/about-us/advance/>)



O-TA-05

### A study of the deformation mechanisms and fracture behaviour of a TiAl alloy containing ordered $\beta_0$ phase

Alain Couret<sup>1</sup>, Guy Molénat<sup>1</sup>, Benjamin Galy<sup>1</sup>, Michael Musi<sup>2</sup>, Svea Mayer<sup>2</sup>, Louise Toualbi<sup>3</sup>, Marc Thomas<sup>3</sup>, Helmut Clemens<sup>2</sup> and Jean-Philippe Monchoux<sup>1</sup>

<sup>1</sup>CEMES, Université de Toulouse, CNRS, 31055 Toulouse, France, alain.couret@cemes.fr

<sup>2</sup>Department of Materials Science, Montanuniversität Leoben, 8700 Leoben, Austria

<sup>3</sup>ONERA/DMAS Université Paris Saclay, 92322 Châtillon Cedex, France

#### Introduction

Intermetallic  $\gamma$ -TiAl based alloys of the new generation suitable for high temperature structural applications are commonly containing refractory elements to improve their mechanical properties at elevated temperatures by reducing the dislocation mobility. These elements, e. g. V, Nb, Cr, Mo, Re or W, also promote the formation of the body-centered cubic (bcc) phase, which occurs as disordered  $\beta$  phase (A2 structure) at high temperatures and ordered  $\beta_0$  phase (B2 structure) at lower temperatures. As mentioned in the exhaustive review of Appel and co-workers [1] the role of this phase on mechanical properties is still unclear: "A possible concern for the  $\beta$ -solidifying alloys is the reported reduction in mechanical properties such as room temperature ductility, high-temperature strength and creep resistance associated with the presence of the  $\beta$ /B2 phases". Examining the current literature confirms that the question of the ductility of these  $\beta$ -solidifying TiAl alloys is still unclear. Indeed, on one side, the  $\beta_0$  phase is assumed not to deform plastically [2,3]. Sun *et al.* [4] has found a decrease of the plastic elongation when alloying with elements associated with an increase of the proportion of  $\beta_0$ (B2) phase. On the other side, Morris *et al.* [5] have studied the mechanical properties at room temperature as well as the dislocation microstructure in a Ti-44Al-2Mo alloy (in at.-%) in different metallurgical conditions. Interestingly, the plastic elongation is higher (0.5%) in the as-HIPed alloy which contains the higher proportion of B2 phase (15 vol.-%). These authors have observed two types of dislocations, i.e.  $\langle 100 \rangle$  dislocations and dissociated  $\langle 111 \rangle$  superlattice dislocations, in the  $\beta_0$  grains. They concluded that the limited ductility of this alloy is due to the low mobility of dislocations in the  $\beta_0$  phase and to the lack of slip activity in the  $\alpha_2$  phase.

In this context, the aim of the present work is to investigate the role of this  $\beta_0$  phase on the plasticity and fracture properties of a TNM-TiAl alloy densified by Spark Plasma Sintering (SPS).

#### Materials and Methods

The material was a TNM-TiAl alloy (Ti-43.9Al-4Nb-0.95Mo-0.1B, in at.-% [6,7]) densified by SPS by CEMES (Toulouse, France) [8] using gas-atomized powder.

Tensile tests at room temperature and fracture surfaces studies by scanning electron microscopy (SEM) will be presented. The deformation mechanisms are investigated by *in situ* straining experiments and *post mortem* analyses of deformed samples performed in a transmission electron microscope (TEM).

#### Results and Discussion

Tensile tests have been performed at room temperature on a TNM alloy densified by SPS. The tests have shown a plastic fracture elongation of  $\sim 0.5\%$ , which is not so low since TiAl alloys are well-known to have a moderate ductility. For example, a max. strain of  $\sim 2\%$  is obtained for the best alloys which, however, possess a strength which is significantly lower than that of TNM alloys. Fig. 1a shows a SEM image of the fracture surface of one sample. Cleavage surfaces are of the size of the lamellar colonies. The cleavage is likely to occur at lamellar interfaces. In  $\beta_0$  grains, mainly situated around the lamellar colonies, no particular brittle behaviour is observed.

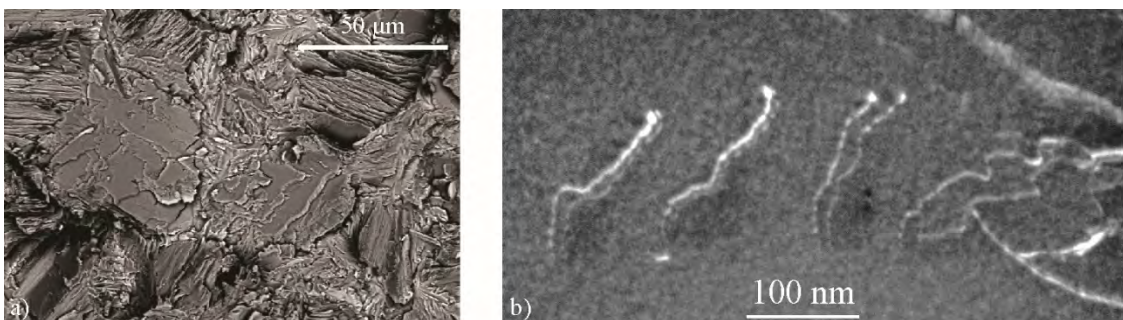


Fig. 1. Microstructural investigations: a) fracture surface (SEM) of a sample deformed at room temperature, b) dislocations (TEM) in the  $\beta_0$  phase.

The deformation microstructure of this alloy, deformed at room temperature, has been investigated by TEM, see Fig. 1b. It consists of  $a\langle 111 \rangle$  superlattice dislocations, which are dissociated into two identical superpartial dislocations bordering an antiphase boundary (APB), consistently with the dissociation scheme:  $a\langle 111 \rangle \rightarrow a/2\langle 111 \rangle + \text{APB} + a/2\langle 111 \rangle$ .

The motion of such  $a\langle 111 \rangle$  superlattice dislocations under stress was studied by performing *in situ* straining experiments in the TEM at room temperature. The main tendency of these dislocations is to move in pile-ups as illustrated in Fig. 2. Here, a few dislocations with a  $a\langle 111 \rangle$  Burgers vector are seen. These dislocations have left slip traces in their wake with a weak contrast on the thin foil surfaces. The determination of the grain orientation through a stereographic analysis has shown that these traces are parallel to the  $\{110\}$  plane containing the Burgers vector. Later on, the dislocations have glided in this plane and plenty of dislocations are present in the pile-up. In Fig. 2b, the pile-up tip is still visible in the observed area and a dislocation loop (arrowed) was formed due to the pinning of one dislocation. Then, numerous dislocations moved in this pile-up during several seconds, as illustrated in Fig. 2c. Each bright dot on the upper trace of the pile-up indicates the presence of one gliding dislocation (Figs. 2b and c). The dynamic sequence allows claiming that several hundreds of dislocations have glided in a few seconds.

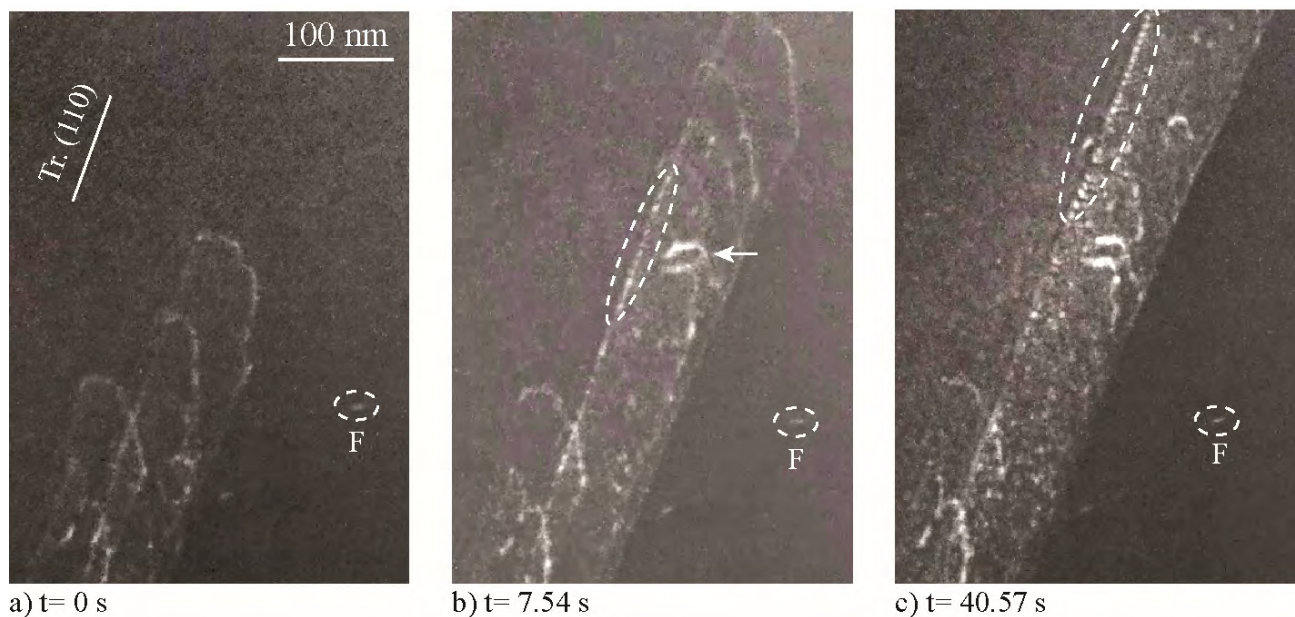


Fig. 2. Images extracted from a TEM *in situ* straining experiment performed at room temperature. The experiment shows the formation of a pile-up of  $a\langle 111 \rangle$  superlattice dislocations. Video sequences will be shown at the conference. F is an affixed point; the dashed ovals on the upper trace mark the end points of gliding dislocations.

All these results indicate a ductile behaviour of the  $\beta_0$  phase. During the presentation, the deformation mechanisms of these  $a\langle 111 \rangle$  superlattice dislocations will be discussed and a scenario to explain the fracture of these  $\beta_0$  containing TiAl alloys will be proposed. Finally, the role of small  $\omega_0$  precipitates on these deformation processes in  $\beta_0$  will be highlighted.

#### Acknowledgements

This study has been conducted in the framework of the cooperative Austrian-French project “Hi-TiAl - 18-CE91-0008-01” co-supported by the French Agence Nationale de la Recherche (ANR) and the Fonds zur Förderung der wissenschaftlichen Forschung (FWF).

#### References

- [1] F. Appel, J. D. H. Paul and M. Oehring, *Gamma Titanium Aluminide Alloys*, Wiley-VCH, Weinheim, Germany, **2011**.
- [2] R. Hoppe and F. Appel, *Acta Mater.* **2014**, 64, 169.
- [3] P. Erdely, P. Staron, E. Maawad, N. Schell, H. Clemens and S. Mayer, *Acta Mater.* **2018**, 158, 193.
- [4] F.S. Sun, C.X. Xiao, S.E. Kim, Y.T. Lee and M.G. Yan, *Met. and Mat. Transactions A.* **2001**, 32A, 1573.
- [5] M.A. Morris and H.G. Li, *Mater. Sci. Eng.* **1995**, 197, 133.
- [6] H. Clemens and S. Mayer, *Adv. Eng. Mater.* **2013**, 15, 191.
- [7] S. Mayer, P. Erdely, F. D. Fischer, D. Holec, M. Kasthuber, T. Klein, and H. Clemens, *Adv. Eng. Mater.* **2017**, 19, 1600735.
- [8] T. Voisin, J.-P. Monchoux, M. Hantcherli, S. Mayer, H. Clemens and A. Couret, *Acta Mater.* **2014**, 73, 107.

**O-TA-06****High temperature deformation behavior of  $\beta$ -solidifying titanium aluminide alloy manufactured by electron beam powder bed fusion (EB-PBF)**Mirko Teschke<sup>1</sup>, Juliane Moritz<sup>2,3</sup>, Axel Marquardt<sup>2,3</sup>, Christoph Leyens<sup>2,3</sup> and Frank Walther<sup>1</sup><sup>1</sup>Department of Materials Test Engineering (WPT), TU Dortmund University, 44227 Dortmund, Germany, mirko.teschke@tu-dortmund.de<sup>2</sup>Technische Universität Dresden, Institute of Materials Science (IfWW), 01069 Dresden, Germany<sup>3</sup>Fraunhofer Institute for Material and Beam Technology IWS, 01277 Dresden, Germany**Introduction**

With the increasing demand for climate-friendly and sustainable solutions in many industries, the reduction of carbon dioxide emissions caused by transport sector is among the most important factors for counteracting climate change. Due to their low density and favorable property profile at elevated temperatures, gamma titanium aluminides may be suitable candidates for replacing the much heavier nickel-base superalloys in aviation and automotive industries [1, 2]. Additive manufacturing via electron beam powder bed fusion (EB-PBF) offers the possibility to manufacture complex near-net-shaped components [3]. The processing in vacuum atmosphere at high temperatures above the brittle-to-ductile transition temperature helps to overcome some of the challenges often encountered in conventional machining of the brittle titanium aluminides [4].

**Materials and Methods**

In this study, the  $\beta$ -solidifying alloy TNM-B1 (Ti-43.5Al-4Nb-1Mo-0.1B, in at.%) is characterized in terms of microstructure and high temperature deformation behavior. The aluminum content of the powder raw material is increased compared to the conventional alloy in order to counteract aluminum evaporation during processing. The specimens are processed by EB-PBF on an Arcam A2X (Arcam AB, Mölndal, Sweden). Cylindrical specimens with a cross-sectional area of 25 mm<sup>2</sup> in the test area are manufactured parallel and vertical to the building direction. In preliminary investigations, the process window of the as-built condition was determined with respect to part density and microstructure. The optimum condition was found for a volumetric energy density of 32.1 J/mm<sup>3</sup>, which has been used for fabricating all specimens investigated in this study. Specimens are analyzed in the as-built condition with no additional heat treatment.

For non-destructive characterization of the specimen material, computed tomographic scans are performed with the  $\mu$ -CT Nikon XT-H 160 (Nikon Metrology, Leuven, Belgium). The  $\mu$ -CT scans are analyzed using VGStudio Max 2.2 software (Volume Graphics, Heidelberg, Germany). A detailed description of the methodology can be found in [5]. To describe the 3D pore morphology, the sphericity  $S$  is used, which is influenced by the defect volume and the pore surface [6].  $S$  can obtain values between 0 and 1, where 1 describes the ideal spherical shape. The initial state is further characterized by scanning electron microscopy at SEM Mira 3 (Tescan, Brno, Czech Republic) including EBSD analyses.

For the mechanical characterization, quasi-static tensile tests according to DIN EN ISO 6892-1 and 2 are performed at room temperature (RT = 23 °C) and elevated test temperatures ( $T = 400, 700, 800, 850$  °C). At least 3 specimens are tested for each temperature and material condition. The influence of the test temperature on the mechanical parameters, such as Young's modulus and tensile strength, is investigated. In addition, the influence of the building direction on the mechanical behavior is investigated by specimens manufactured parallel and vertical to building direction.

The tests are performed on a Instron 8802 servohydraulic fatigue testing system (Instron, Norwood, USA). A Instron CP100635 high-temperature furnace (Instron, Norwood, USA) is used and the strain is detected with a high-temperature extensometer EXH 10-1A (Sandner Messtechnik, Biebesheim, Germany). In addition, continuous temperature increase fatigue tests are performed on the same test system. With a stress ratio of  $R = 0.1$  (range of pulsating stresses), the maximum stress is kept constant and the test temperature is continuously increased. In this way, the entire temperature test range (RT to 850 °C) can be completely examined in one single test, and changes in the cyclic properties, such as the dynamic Young's modulus, can be detected directly. The results are compared with the parameters determined in the tensile test.

**Results and Discussion**

The total analyzed volume in CT investigations is around 140 mm<sup>3</sup> and the relative density is found to be 99.88 %. The pores are randomly distributed inside the material with an average pore diameter of 85  $\mu$ m. The average sphericity is  $S = 0.4$ . As shown in Fig. 1, most of the pores have a sphericity between 0.35 and 0.45, i.e. with a relatively flat shape. At room temperature, the main occurring phases in TNM-B1 are the face-centered tetragonal  $\gamma$ -TiAl phase, the hexagonal  $\alpha_2$ -Ti<sub>3</sub>Al phase, and the body-centered cubic  $\beta_0$ -TiAl phase [1, 7]. The SEM image (Fig. 2) shows lamellar colonies which are composed of alternating  $\gamma$ - and  $\alpha_2$ -laths [8].  $\gamma$ -TiAl grains can be distinguished by their dark color, while the  $\beta_0$ -TiAl phase appears bright [4].

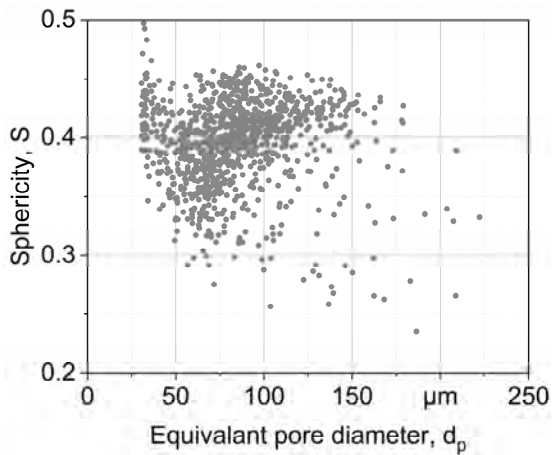


Fig. 1: Sphericity and equivalent diameter of pores

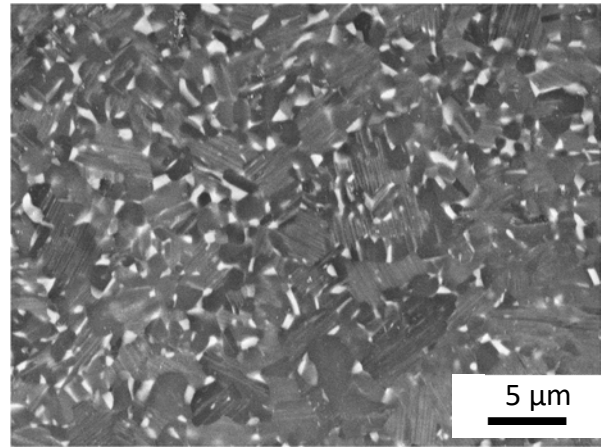


Fig. 2: Scanning electron microscope image of TiAl parallel to building direction

#### Funding

The authors thank the German Research Foundation (Deutsche Forschungsgemeinschaft, DFG) for its financial support within the research project “Microstructure and defect controlled additive manufacturing of gamma titanium aluminides for function-based control of local materials properties” (Project number: 404665753).

#### References

- [1] H. Clemens, S. Mayer, *Advanced Engineering Materials*. **2013**, 4, 191-215.
- [2] R. Wartbichler, H. Clemens, S. Mayer, *Advanced Engineering Materials*. **2019**, 12, 1900800.
- [3] C. Körner, *International Materials Reviews*. **2016**, 5, 361-377.
- [4] S. Mayer, D. Schimbäck, R. Wartbichler, D. Wimler, H. Clemens, H. *Practical Metallography*. **2019**, 9, 567-584.
- [5] M. Awd, F. Stern, A. Kampmann, D. Kotzem, J. Tenkamp, F. Walther, *Metals*. **2018**, 8, 825, 1-14.
- [6] G. Ziólkowski, E. Chlebus, P. Szymczyk, J. Kurzac, *Archives of Civil and Mechanical Engineering*. **2014**, 14, 608-614.
- [7] M. Schloffer, B. Rashkova, T. Schöberl, E. Schwaighofer, Z. Zhang, H. Clemens, S. Mayer, *Acta Materialia*. **2014**, 64, 241-252.
- [8] R. Wartbichler, R. Bürstmayr, H. Clemens, S. Mayer, *Practical Metallography*. **2019**, 4, 220-229.



## O-TA-07

**Solid solution Strengthening of TiAl alloys with Zirconium**Melissa Allen<sup>1</sup>, Volker Güther<sup>1</sup>, Janny Lindemann<sup>2</sup> and Stefan Kardos<sup>3</sup><sup>1</sup>GfE Metalle und Materialien GmbH, Nuremberg, Germany, melissa.allen@gfe.com, volker.guether@gfe.com<sup>2</sup>GfE Fremat GmbH, 09599 Freiberg, Germany, janny.lindemann@gfe.com<sup>3</sup>Montanuniversität Leoben, 8700 Leoben, Austria, stefan.kardos@unileoben.ac.at**Introduction**

The objective of the work is to improve the high temperature mechanical properties of titanium aluminide alloys by using Zirconium for solid solution strengthening. Zr is a rarely used alloying element in titanium aluminides but has a high potential of influencing the high temperature properties positively due to its large atomic radius compared to Ti and/or Al.

**Materials and Methods**

Materials manufacturing is based on single Vacuum Arc Remelting (VAR) using compacted consumable electrodes which consist of Ti sponge, Al granules and master alloys. Resulting VAR ingots are being remelted and homogenized in an Induction Skull Melter and subsequently centrifugally cast in steel molds [1]. In summary 3 different ternary alloys containing 2 at% Zr, 4 at% Zr and 8 at% Zr and 46,5 at% Al each have been manufactured. Cast parts were subject to HIP for closing remaining casting porosity. Different heat treatments (HT) for creating appropriate microstructures have been applied. The favoured microstructure for well-balanced mechanical high temperature properties was defined to be a fully lamellar microstructure [2]. Chemical analyses have been carried out by XRF, ICP and LECO combustion techniques. Phase transition temperatures were determined by DSC measurements. The microstructural analysis was done by metallography and SEM. The tensile tests were done under standard test conditions at room temperature, 300 °C, 700 °C and 850 °C.

**Results and Discussion**

DSC measurements show that the content of Zr within the alloy has a strong influence on the phase transition temperatures as well as on the solidification path. Therefore the microstructures of the different alloys after HIP are not directly comparable and adjusted heat treatments had to be developed for each alloy for generating comparable lamellar microstructures. For the HIP condition an improvement from 0 over 2 and 4 at % Zr could be noted for the high temperature yield strength. For the ternary alloy with 8 at% Zr high temperature properties could not exceed the results of the other alloys because ZrAl phases have formed which lead to an early fail for tensile tests.

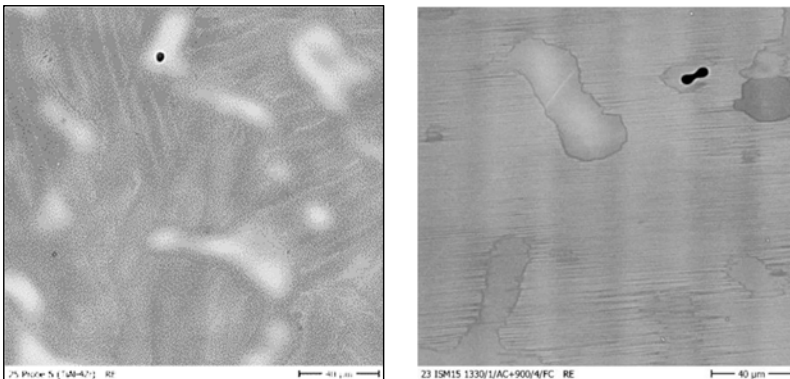


Fig. 1: Microstructure of the Ti-46,5Al-4Zr at% alloy after HIP (left image) and after subsequent heat treatment to a nearly lamellar microstructure (right image). SEM images taken in BSE mode.

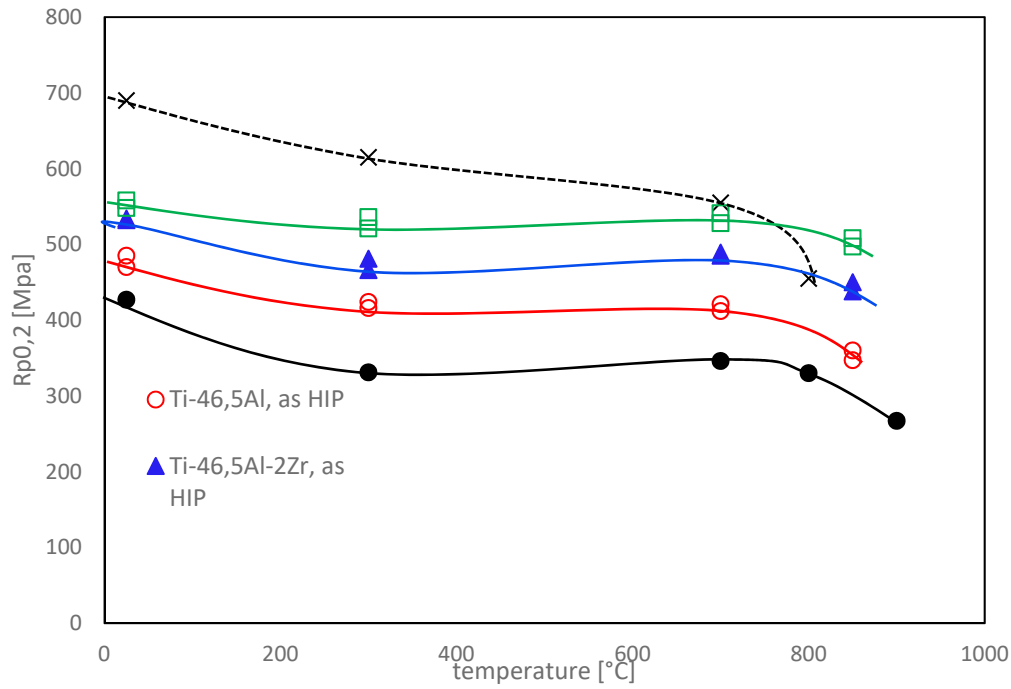


Fig. 2: tensile yield strength at RT, 300 °C, 700 °C and 850 °C of binary and ternary Ti46,5Al-xZr at% alloys compared to TiAl48-2-2 in the as cast + HIP state

The increase of Zr content improves the yield strength in all temperature ranges. The decrease of strength at high temperature above 700°C was determined to be significantly lower compared to State-of-the- industrial TiAl alloys such as TiAl48-2-2 indicating a very effective solid solution strengthening capability of Zr in TiAl alloys.

#### References

- [1] V. Güther, M. Allen, J. Klose, H. Clemens, *Intermetallics*. **2018**, *103*, 12-22.
- [2] M. Beschliesser, A. Chatterjee, A. Lorich, W. Knabl, H. Kestler, G. Dehm, H. Clemens, *Materials Science and Engineering A*. **2002**, *329-331*, 124-129.



## O-TA-08

**Influence of tungsten on the mechanical properties of a  $\gamma$ -TiAl based alloy**

Benjamin Galy<sup>1</sup>, Muriel Hantcherli<sup>1</sup>, Alain Couret<sup>1</sup>, Guy Molénat<sup>1</sup>, Michael Musi<sup>2</sup>, Svea Mayer<sup>2</sup>, Helmut Clemens<sup>2</sup>, Louise Toualbi<sup>3</sup>, Marc Thomas<sup>3</sup> and Jean-Philippe Monchoux<sup>1</sup>

<sup>1</sup>CEMES, Université de Toulouse, CNRS, 31055 Toulouse, France, benjamin.galy@cemes.fr,

muriel.hantcherli@cemes.fr, alain.couret@cemes.fr, guy.molenat@cemes.fr, jean-philippe.monchoux@cemes.fr

<sup>2</sup>Department of Materials Science, Montanuniversität Leoben, 8700 Leoben, Austria, michael.musi@unileoben.ac.at,

svea.mayer@unileoben.ac.at, helmut.clemens@unileoben.ac.at

<sup>3</sup>ONERA/DMAS, Université Paris Saclay, 92322 Châtillon Cedex, France, louise.toualbi@onera.fr,

marc.thomas@onera.fr

**Introduction**

This work deals with the addition of W to  $\gamma$ -TiAl based alloys, which has been found to increase the mechanical strength of these materials up to 800 °C [1]. In fact, this is of interest for their application in creep-exposed parts of aeronautical and automotive engines. The development of TiAl alloys containing W has led in particular to the IRIS alloy, with a composition of Ti-48Al-2W-0.08B [at.%] [2]. This alloy exhibits high strength at elevated temperature and reasonably good ductility at room temperature. This balance in the mechanical properties results from an optimized microstructure, consisting of fine lamellar colonies  $\approx$  40  $\mu$ m in size, which are surrounded by equiaxed  $\gamma$  grains. The observed ductility is attributed to the presence of  $\gamma$  grains at the colony boundaries, while the overall high temperature strength is believed to be the consequence of the lamellar microstructure as well as of the incorporation of W. However, the role of W on the mechanical properties has not been accurately quantified and is, moreover, not well understood. Because the  $\gamma$  phase is the most deformable phase at high temperature, as compared with the lamellar colonies, our objective is to evaluate the influence of W dissolved in this phase, regarding the macroscopic deformation kinetics and the microscopic plasticity mechanisms. For this purpose, model alloys have been processed using a powder metallurgy route, i.e. ingot casting, gas atomization and subsequent powder densification by spark plasma sintering (SPS). A Ti-48Al-2W-0.2B alloy [at.%] and a binary Ti-48Al-0.2B alloy [at.%], which serves as reference material, were produced with nearly  $\gamma$  microstructures. The purpose of the addition of B was to receive a small size of equiaxed  $\gamma$  grains, representative of the  $\gamma$  grains surrounding the lamellar colonies in the IRIS alloy. On these materials, creep tests have been conducted at 800°C. In order to interpret the results, investigations of the microscopic plasticity mechanisms have been carried out, using *post mortem* and *in situ* TEM observations.

**Materials and Methods**

A binary TiAl alloy of composition Ti-48Al-0.2B [at.%] and a TiAl-W alloy of composition Ti-48Al-2W-0.2B [at.%] have been processed by SPS, using prealloyed powders provided by GFE Metalle und Materialien GmbH (Nuremberg, Germany). In both cases, sintering conditions have been employed to adjust a near- $\gamma$  microstructure. These material variants have been submitted to creep tests at 800°C under 36 MPa. For TEM *post-mortem* analysis, some tests were interrupted after 3-5 % of plastic strain. In addition, delicate TEM *in situ* straining experiments at  $\approx$  800 °C have been carried out to investigate the mobility of the dislocations at high temperatures.

**Results and Discussion**

The SPS microstructures of the TiAl and TiAl-W alloys have been investigated by EBSD. It has been verified that the microstructure was mainly constituted of  $\gamma$  phase, in which W was rather homogeneously dissolved in case of the TiAl-W alloy (despite the formation of some W-rich  $\beta_0$  precipitates). In both materials, the average  $\gamma$  grain size was of the order of 1.5–2.5  $\mu$ m. Thus, the initial microstructures of the two alloys were close to each other, the only difference being the presence of W in solid solution in the TiAl-W alloy, the  $\beta_0$  precipitates playing a minor role. The creep tests, conducted at 800 °C under 36 MPa, have shown that the creep rate  $\dot{\epsilon}$  of the TiAl-W alloy ( $\dot{\epsilon} = 1.4 \times 10^{-7} \text{ s}^{-1}$ ) is by a factor of about two lower than for the TiAl alloy ( $\dot{\epsilon} = 3 \times 10^{-7} \text{ s}^{-1}$ ). Therefore, these tests allowed to isolate the effect of W in solid solution concerning the macroscopic creep kinetics.

To account for these observations, the microstructure of materials deformed to 3–5 % in creep has been investigated by TEM *post-mortem* observations. Surprisingly, low dislocation densities and very few sub-boundaries have been observed. Therefore, it seems that mechanisms such as nucleation, multiplication and reorganization of dislocations occur only sparsely. This imposed us to increase the creep stress to 200 MPa, in order to increase the creep rate, thus favoring formation of dislocations. In this case, dislocations could be observed as shown in Fig.1. By indexing their Burgers vectors and their moving planes, using stereographic analysis, clear indications of climb mechanisms were noticed.

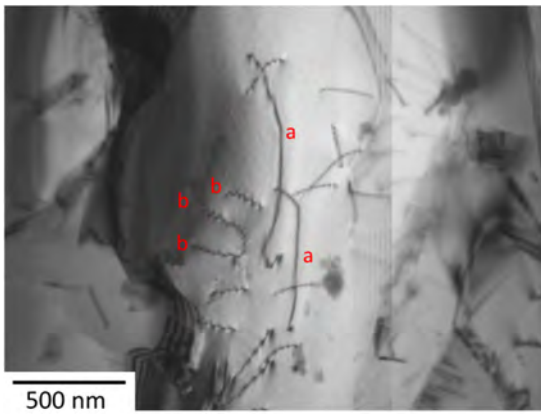


Fig. 1: Dislocations in the TiAl-W sample which was deformed to 3 % strain in a creep experiment at 800 °C. Using stereographic analysis, glide dislocations (a) and climb dislocations (b) have been identified.

Then, delicate TEM *in situ* straining experiments at  $\approx 800$  °C have been carried out. In particular, difficulties due to the fast degradation of the thin zones of the samples in the vacuum at high temperatures had to be overcome. This was achieved either by selecting zones of interest prior to the experiments, or by detecting the onset of plasticity phenomena at lower temperatures. However, it was possible to give evidence of the displacement of edge segments in planes perpendicular or highly inclined to their Burgers vector, which points to the occurrence of mechanisms involving pronounced climb contributions (Fig. 2).

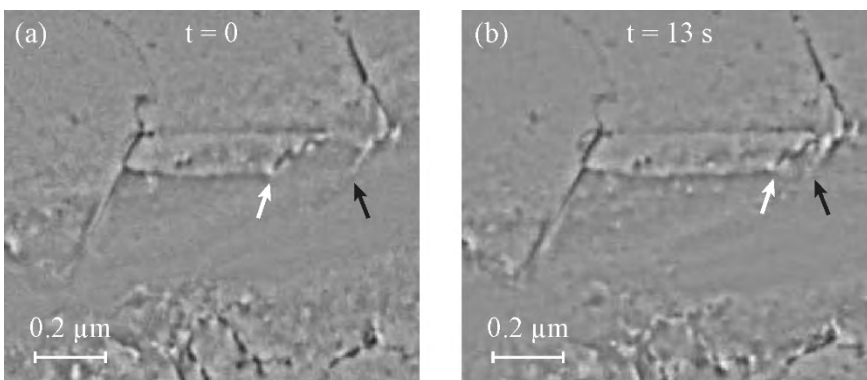


Fig. 2. Images of a TEM *in situ* experiment at  $\approx 800$  °C showing the displacement of an edge dislocation segment (white arrows) in a plane highly inclined to the Burgers vector. The black arrow indicates a fixed dislocation. (a):  $t = 0$ . (b):  $t = 13$  s. Images have been filtered to enhance contrast.

The observed low dislocation density can be interpreted by a Nabarro-Herring (NH) mechanism [3], which is favored by the small size of the grains in the investigated materials (1.5–2.5  $\mu\text{m}$ ). Quantitatively, the experimental creep rates of the TiAl and TiAl-W alloys at 800 °C under 36 MPa are in the range of  $1.5\text{--}3 \times 10^{-7} \text{ s}^{-1}$ . Theoretical values obtained considering a NH mechanism, using an interdiffusion coefficient ( $D$ ) as determined by Sprengel *et al.* [4] ( $D = 1.2 \times 10^{-18} \text{ m}^2/\text{s}$  at 800 °C), lead to  $\dot{\epsilon} = 3 \times 10^{-7} \text{ s}^{-1}$ . Hence, the experimental results and this theoretical evaluation are in quantitative agreement, suggesting that creep is indeed controlled by the NH mechanism. Moreover, the *post mortem* (Fig. 1) and *in situ* (Fig. 2) TEM investigations provide clear indications of dislocation motion by climb. In these two phenomena, NH mechanism and dislocation climb, the underlying elementary mechanism is mass transport by diffusion. Consequently, the creep rate would be controlled by diffusion processes, on which the influence of W remains to be elucidated.

#### Acknowledgements

This study has been conducted in the framework of the cooperative Austrian-French project “Hi-TiAl - 18-CE91-0008-01” co-supported by the French Agence Nationale de la Recherche (ANR) and the Fonds zur Förderung der wissenschaftlichen Forschung (FWF).

#### References

- [1] T. Voisin, J.P. Monchoux, M. Thomas, C. Deshayes and A. Couret, *Metall. Mater. Trans. A*. **2016**, *47*, 6097.
- [2] A. Couret, T. Voisin, M. Thomas and J.P. Monchoux, *JOM*. **2017**, *69*, 2576.
- [3] T.H. Courtney. Mechanical behavior of materials. Waveland Press Inc, Long Grove, Illinois, **2005**.
- [4] W. Sprengel, N. Oikawa and H. Nakajima, *Intermetallics*. **1996**, *4*, 185.

## O-TA-09

## A Thermodynamic and Properties Database for Ti- and TiAl-based alloys

Yang Yang, Qing Chen, Anders Engström and Hai-Lin Chen  
Thermo-Calc Software AB, 169 67 Solna, Sweden, yang@thermocalc.se

## Introduction

Titanium alloys represent a promising class of engineering lightweight structural materials that have been successfully transferred into aerospace applications, *e.g.* as low-pressure turbine blades in jet engines. The development of novel Ti-based alloys needs to be continued in order to further improve properties at elevated temperatures, such as creep strength and corrosion resistance.

CALPHAD is a key enabler to accelerate the understanding and design of multicomponent titanium alloys with a demanding balance of different properties. The major strengths of the CALPHAD method are to obtain reliable self-consistent descriptions of given base systems, and afterwards to be able to combine these systems to obtain predictions in multi-component systems. Particularly, the CALPHAD approach offers a unique and remarkable advantage in accurately obtaining all critical features at the same time for a wide spectrum of compositions.

## Database overview

The reliability of CALPHAD simulations depends on the quality of the database being used. At Thermo-Calc Software we actively develop a thermodynamic database incorporating additional thermophysical property data (such as molar volume with thermal expansion coefficients, viscosity, and surface tension of metallic liquids, electrical resistivity, thermal conductivity) for Ti- and TiAl-based alloys. In this talk, we will present the current state, recent development of the database and calculation examples that are not limited to thermodynamics and phase equilibria in the field of titanium alloys.

## Applications

Volume related properties, such as density, thermal expansivity, as well as lattice parameters for cubic structures, can be readily calculated for different alloys from room temperature into the liquid state with the database. Fig. 1 shows the linear expansion rate for Ti-6Al-4V. A good prediction is made in a wide temperature range, especially in the region close to the beta-transus where the amounts of alpha and beta change rapidly with temperature. The electrical resistivities of the various alloys at room temperature are plotted as a function of alloy composition in Fig. 2. The plot shows that the transition elements which lie close to titanium in the Periodic Table (*i.e.* Zr, Nb) bring about a relatively small increase in the resistivity of alpha-titanium, while the non-transition elements, whether substitutional or interstitial, appear to have a much greater effect. A better understanding of electronic properties of alloys is beneficial to investigate alloying behavior and effects in solid solutions, as well as to facilitate studies on mechanical properties of titanium alloys [4].

More examples related to predictions of various properties for Ti-, TiAl-based alloys will be presented in our talk, including validations against experimental observations in multi-component alloys.

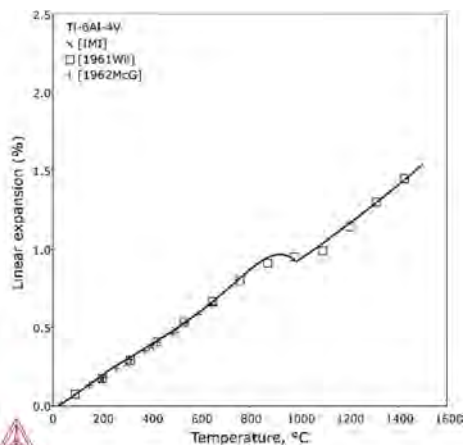


Fig. 1: Linear expansion rate for Ti-6Al-4V.

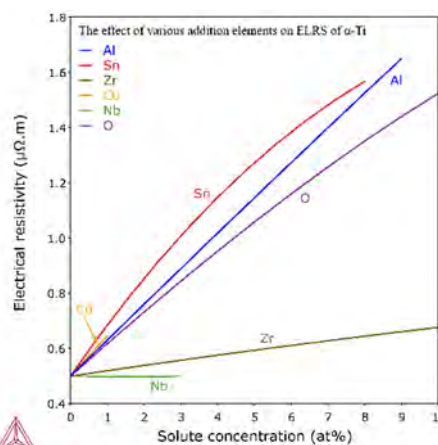


Fig. 2: A comparison of the specific solute resistivities ( $dp/dc$ ) of Ti-based alloys.

## References

- [1] IMI Titanium property data, report MK 140/589.
- [2] D. N. Williams, *Trans. Met. Soc. AIME*, **1961**, 221, 411.
- [3] W. M. McGee, B. R. Matthews, U. S. A. F. Rept. ASD-TDR-62-335 (2A), **1962**.
- [4] R. L. Fleischer, W. R. Hibbard in: *The Relation Between the structure and the Mechanical Properties of Metals*. H. M. Stationary Office, **1963**, 262-297.

**O-TA-10****Determination of Phase Equilibria in the Ti–Al–Si System at 800–1200 °C**Zahra Kahrobaee and Martin Palm

Max-Planck-Institut für Eisenforschung GmbH, 40237 Düsseldorf, Germany, z.kahrobaee@mpie.de

**Introduction**

Advanced  $\gamma$ -TiAl based alloys are nowadays employed in the low-pressure turbine of new aircraft engines, where they have replaced Ni-base superalloys. Due to their lower density, fuel consumption and thereby the amount of emissions could be substantially reduced. However, to increase the engine operation temperature and thus overall efficiency even more, these alloys should be further improved. To reach this goal, the key properties are creep and oxidation resistance, which can be improved through tailoring of the microstructure and alloying [1]. Addition of Si is known to be beneficial in improving the creep resistance through formation of fine-scaled  $\text{Ti}_5\text{Si}_3$  precipitates [2, 3]. Si also substantially improves the oxidation resistance through refining  $\text{TiO}_2$  particles, which results in the formation of a more compact oxide scale and it facilitates Al diffusion in the scale, which restrains further formation of  $\text{TiO}_2$  [4].

Efficient development of  $\gamma$ -TiAl based alloys relies on the knowledge of phase equilibria in dependence of temperature. CALPHAD (CALculation of PHase Diagram) modelling is a widely used method by which phase diagrams and phase transitions can be calculated. CALPHAD modelling crucially depends on the underlying database, which is based on experimental investigations. Available experimental data on phase equilibria in the Ti–Al–Si system, specifically in the Ti-rich part, are at least partially controversial. E.g., for the solid solubility of Si in  $\gamma$ -TiAl at 1000 °C reported data vary between 0 [5] and 3.1 at.% [6]. Also, the solid solubility for Al in  $\text{Ti}_5\text{Si}_3$  in dependence of temperature has not been settled. However, knowledge of the solid solubility of Si in TiAl and Al in  $\text{Ti}_5\text{Si}_3$  in dependence of temperature are essential for the design of more creep resistant  $\gamma$ -TiAl-based alloys, because they yield the volume fraction of  $\text{Ti}_5\text{Si}_3$  at a certain temperature for a given composition.

Within a large-scale collaborative project, the partners Helmholtz-Zentrum Hereon, Germany, Montanuniversität Leoben, Austria, MPIE, and Thermo-Calc Software AB, Sweden are improving thermodynamic data for a number of Ti–Al–X(–Y) systems for the next generation of advanced CALPHAD databases for Ti–Al alloys [7]. As a part of this project, phase equilibria between the Ti–Al-rich phases and  $\text{Ti}_5\text{Si}_3$  between 800–1200 °C are experimentally investigated and specifically the solid solubility of Si in  $\gamma$ -TiAl and Al in  $\text{Ti}_5\text{Si}_3$  were established.

**Materials and Methods**

From high-purity elements, seven alloys have been prepared by crucible-free levitation melting or advanced arc melting. For heat-treatments at 800–1100 °C, slices of the alloys were encapsulated in high-purity quartz tubes back-filled with Ar and annealed for 165–1000 h, followed by quenching in brine. Heat-treatments at 1200 °C were performed using a double-crucible technique [8]. Heat-treatments at 1200 °C were performed for 24 h under flowing dry Ar, subsequently quenching the samples in brine. Compositions of the alloys and impurity contents in the as-cast condition and, for a couple of alloys, after heat treatment were established by wet chemical analysis. Phases were identified by X-ray diffraction (XRD) at room temperature using powder. Compositions of the coexisting phases were established by electron probe microanalysis (EPMA). Phase transformation temperatures were measured on bulk samples by differential thermal analysis (DTA) by heating up to a maximum of about 1400 °C at a heating rate of 10 K/min.

**Results and Discussion**

Fig. 1 (a–e) shows the microstructure of Ti-47.4Al-9.1Si (in at.%) after annealing at 800–1200 °C. Phases were identified by XRD as illustrated in Fig. 2. Observed phases are TiAl +  $\text{TiAl}_2$  +  $\text{Ti}_5\text{Si}_3$  at 800–1100 °C and TiAl +  $\text{Ti}_5\text{Si}_3$  at 1200 °C (Fig. 1).

The enlarged back-scattered electron (BSE) image (Fig. 1 c) shows that  $\text{Ti}_5\text{Si}_3$  appears in two different morphologies, i.e. as large idiomorphic grains and as small spherical particles, which was also observed in most of the other investigated samples. The liquidus projection [6] shows that all alloys which contained large, idiomorphic  $\text{Ti}_5\text{Si}_3$  are located in the field of primary crystallization of  $\text{Ti}_5\text{Si}_3$ . EPMA of these large grains, which formed within the liquid at elevated temperatures, and the small ones, which formed during annealing, showed differences in the Al content of up to 3.5 at.%. Apparently, even annealing for 1000 h at 1000 °C is not sufficient to equilibrate the large, primary  $\text{Ti}_5\text{Si}_3$  grains. Therefore, only small spherical  $\text{Ti}_5\text{Si}_3$  particles were measured, which, in case of the microstructure shown in Fig. 1 c, are in contact with  $\text{TiAl}_2$  and TiAl. Differences between data reported in the literature could be attributed to the aforementioned issue. E.g., the maximum solid solubility of Al in  $\text{Ti}_5\text{Si}_3$  at 1000 °C was found to be 7.4 at.%, compared to 10.9 at.% reported previously [6]. The solid solubility of Si in  $\gamma$ -TiAl is about 0.8 at.% and does not change with increasing temperature.

The established partial isothermal sections in the Ti–Al–Si system will be discussed in detail in the presentation.

### Acknowledgement

This project has received funding from the Clean Sky 2 Joint Undertaking under the European Union's Horizon 2020 research and innovation programme under grant agreement No 820647.

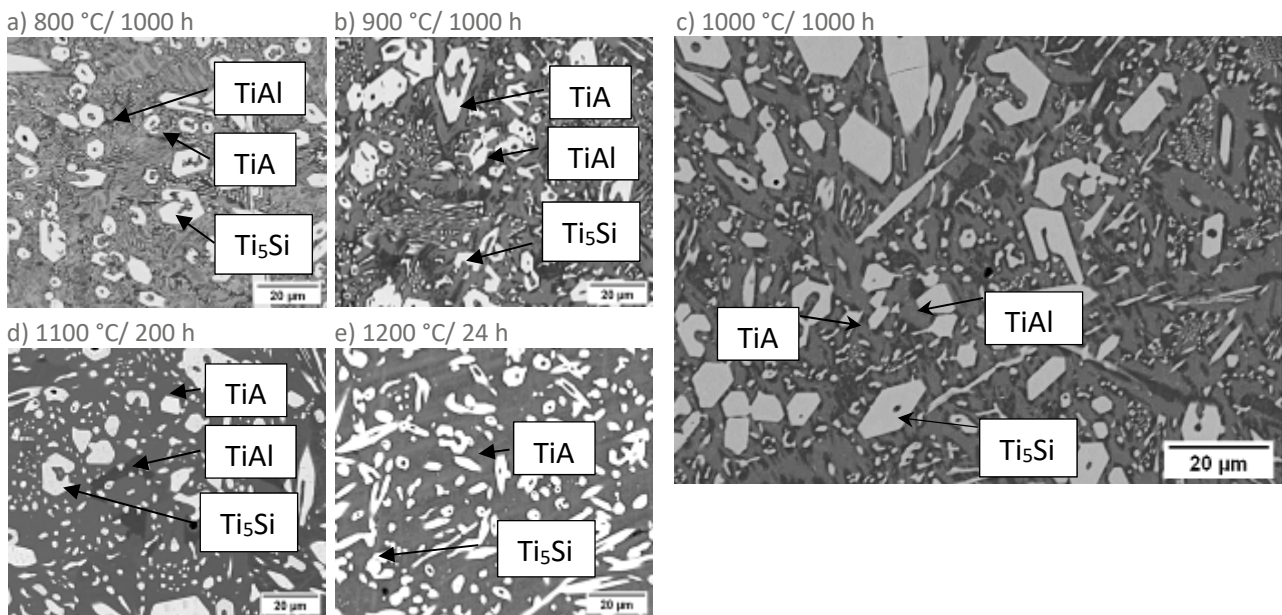


Fig. 1: BSE images of Ti-47.4Al-9.1Si at.% heat-treated at temperatures 800-1200 °C.

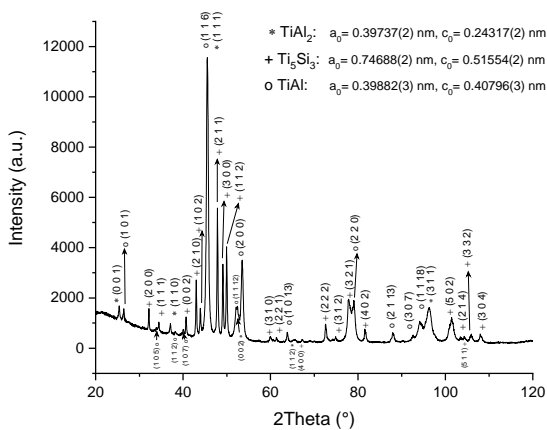


Fig. 2: XRD profile of Ti-47.4Al-9.1Si at.% heat-treated 1000 °C/1000 h.

### References

- [1] H. Clemens, S. Mayer, *Advanced Engineering Materials*. **2013**, 15, 191-215.
- [2] S. Tsuyama, S. Mitao, K.-N. Minakawa, *Materials Science and Engineering: A*. **1992**, 153, 451-456.
- [3] T. Noda, M. Okabe, S. Isobe, M. Sayashi, *Materials Science and Engineering: A*. **1995**, 192, 774-779.
- [4] J. Dai, J. Zhu, C. Chen, F. Weng, *Journal of Alloys and Compounds*. **2016**, 685, 784-798.
- [5] Z. Sun, W. Wu, X. Tian, F. Zhang, C. Ai, X. Zhang, Y. Li, X. Guo, *Intermetallics*. **2020**, 120, 106760.
- [6] S. Liu, F. Weitzer, J.C. Schuster, N. Krendelsberger, Y. Du, *International Journal of Materials Research*. **2008**, 99, 705-711.
- [7] Next Generation TiAl Alloys Advanced by New European Consortium, <https://thermocalc.com/blog/next-generation-tial-alloys-advanced-by-new-european-consortium/>
- [8] R. Kainuma, M. Palm, G. Inden, *Intermetallics*. **1994**, 2, 321-332.



**O-TA-11****Mechanical properties of a 4<sup>th</sup> generation  $\gamma$ -TiAl alloy processed via electron beam powder bed fusion**

Marcel Reith<sup>1</sup>, Mirko Teschke<sup>2</sup>, Martin Franke<sup>1</sup>, Jochen Tenkamp<sup>2</sup>, Frank Walther<sup>2</sup>  
and Carolin Körner<sup>3</sup>

<sup>1</sup>Neue Materialien Fürth GmbH, 90762 Fürth, Germany, marcel.reith@nmfgmbh.de, martin.franke@nmfgmbh.de

<sup>2</sup>Department of Materials Test Engineering, TU Dortmund University, 44227 Dortmund, Germany, mirko.teschke@tu-dortmund.de, jochen.tenkamp@tu-dortmund.de, frank.walther@tu-dortmund.de

<sup>3</sup>Chair of Materials Science and Engineering for Metals, Friedrich-Alexander University Erlangen-Nuremberg, 91058 Erlangen, Germany, carolin.koerner@fau.de

**Introduction**

The good mechanical properties and oxidation resistance at elevated temperatures with a low density of about 4 g/cm<sup>3</sup> make  $\gamma$  titanium aluminides ( $\gamma$ -TiAl) interesting for high temperature applications in the automotive and aerospace industries [1]. These alloys are conventionally produced by isothermal forging or centrifugal casting followed by hot isostatic pressing (HIP) and heat treatment (HT) [1]. However, these processing methods are expensive and time consuming.

Additive manufacturing has been established as an alternative processing route in recent years [2,3]. Especially laser beam powder bed fusion (PBF-LB/M) and electron beam powder bed fusion (PBF-EB/M) of  $\gamma$ -TiAl has been the focus of research [2,3]. PBF-LB/M has several disadvantages compared to PBF-EB/M. For instance,  $\gamma$ -TiAl is prone to cracking, if processed below the brittle to ductile transition temperature (BDTT). Therefore, novel PBF-LB/M machines use a base plate heating to allow the processing of  $\gamma$ -TiAl. However, even with base plate heating of up to 1200°C only the fabrication of small Ti-43.5Al-4Nb-1Mo-0.1B (TNM) cuboids (10 x 10 x 10 mm<sup>3</sup>) is reported [4]. The fabrication of large parts increases the risk of cracking and has not been reported yet. Furthermore, PBF-LB/M leads to higher oxygen contents in the produced parts due to smaller particle size of the powder and no vacuum atmosphere during the build job [4]. In contrast, PBF-EB/M is most suited to build large high quality  $\gamma$ -TiAl parts with low oxygen content due to the inherent vacuum atmosphere and the intensive preheating step.

In order to exploit the full potential of PBF-EB/M, novel alloys tailored to the advantages of additive manufacturing are necessary [5]. The aim of this research is to characterize and compare the static and fatigue properties of a process adapted 4<sup>th</sup> generation  $\gamma$ -TiAl alloy processed via PBF-EB/M.

**Materials and Methods**

The  $\gamma$ -TiAl alloy Ti-47.5Al-5.5Nb-0.5 W (at.%) is processed via electron beam powder bed fusion on an Arcam A2X (Arcam AB, Mölndal, Sweden). In total, 121 cylinders for mechanical characterization are produced. The cylinders for tensile tests have a diameter of 12 mm and a height of 60 mm, while the cylinders for fatigue tests have a diameter of 20 mm and a height of 90 mm. In part, the samples are hot isostatic pressed (HIP) and heat treated (HT). The samples are characterized in regard to defects and microstructure. The cylinders are machined to the final test geometries.

The tensile tests are conducted on a Zwick & Roell Z100 (ZwickRoell, Ulm, Germany) at room temperature, 300 °C, and 850 °C. The strain rate of the tensile test is 0.0001 s<sup>-1</sup>, which is accelerated after a plastic strain of 4% to 0.0003 s<sup>-1</sup> for practical reasons. The tensile specimens and test conditions are according to the limits of DIN EN ISO 6892.

For fatigue investigations, constant amplitude tests, as well as continuous amplitude increase tests, are conducted. For all fatigue tests, a servohydraulic fatigue testing system Instron 8801 with a dynamic extensometer Instron 2620-603 (Instron, Norwood, US) are used. All tests are performed at a stress ratio of R = -1 (fully-reversed loading) at room temperature. The mechanical investigations are complemented with metallographic analysis in form of metallographic sections and fractographic investigations in a scanning electron microscope. The influence of different microstructures on fatigue lifetime in form of S-N (Woehler) curves is investigated. By using the fracture mechanical approach of Murakami [6], the local stress intensity factor of crack-initiating defects for low and high cycle fatigue regimes is determined and correlated with fatigue strength and life [7]. Moreover, the usage of Murakami approach [6] including Noguchi modification [8] for fatigue limit estimation of light metals was evaluated based on hardness, crack-initiating defect size and Young's modulus.

**Results**

The samples show a minimum of defects (misconnections < 0.05 % and gas porosity < 0.3 %) as well as a homogeneous microstructure. The microstructure in as-built condition can be characterized as nearly lamellar  $\gamma$  consisting of small  $\alpha_2/\gamma$  colonies, globular  $\gamma$  and a small amount of  $\beta_0$ -phase. After the heat treatment, a fully lamellar microstructure is observed. Tensile tests are performed at room temperature (see Figure 1), 300 °C and 850 °C for various orientations to demonstrate isotropic properties and high temperature capability.



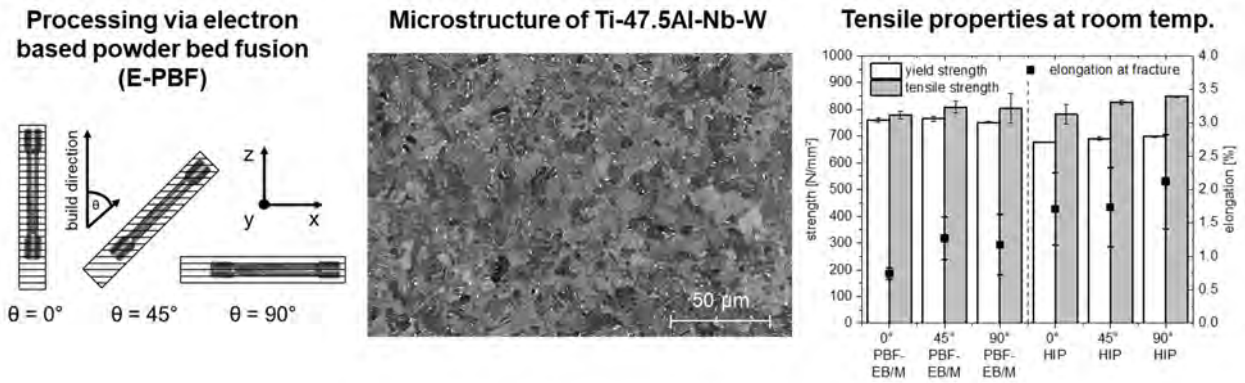


Fig. 1: The samples and results are from a 4<sup>th</sup> generation  $\gamma$ -TiAl alloy processed via PBF-EB/M. Building orientation of tensile and creep samples on the left, the homogeneous microstructure of these samples in the center and the resulting tensile properties at room temperature on the right side [9].

### Funding

The authors thank the German Research Foundation (Deutsche Forschungsgemeinschaft, DFG) for its financial support within the research project “Microstructure and defect controlled additive manufacturing of gamma titanium aluminides for function-based control of local materials properties” (Project number: 404665753).

### References

- [1] B.P. Bewlay, s. Nag, A. Suzuki, M.J. Weimer, *Materials at High Temperatures*. **2016**, *33*, 549-559
- [2] L.E. Murr, S.M. Gaytan, A. Ceylan, E. Martinez, J.L. Martinez, D.H. Hernandez, B.I. Machado, D.A. Ramirez, F. Medina, S. Collins, R.B. Wicker, *Acta Materialia*. **2010**, *58*, 1887-1894
- [3] L. Löber, F.P. Schimansky, U. Kühn, F. Pyczak, J. Eckert, *Journal of Materials Processing Technologie*. **2014**, *214*, 1852- 1860
- [4] D. Schimbäck, J. Braun, G. Leichtfried, H. Clemens, S. Mayer, *Materials and Design*. **2021**, *201*, 109506
- [5] D. Wimler, J. Lindemann, M. Reith, A. Kirchner, M. Allen, W. G. Vargas, M. Franke, B. Klöden, T. Weißgräber, V. Güther, M. Schloffer, H. Clemens, S. Mayer, *Intermetallics*. **2021**, *131*, 107109
- [6] Y. Murakami, Effects of small defects and nonmetallic inclusions on the fatigue strength of metals, *Jsmc Int. J.* **1989**, *32*, 167–180
- [7] J. Tenkamp, M. Awd, S. Siddique, P. Starke, F. Walther, *Metals*. **2020**, *10*, 943
- [8] H. Noguchi; K. Morishige; T. Fujii; T. Kawazoe; S. Hamada, In: *Proc. 56th JSMS Annual Meetings*. **2007**, 137-138
- [9] M. Reith, M. Franke, M. Schloffer, C. Körner, *Materialia*. **2020**, *14*, 100902

## O-TA-12

**Quasi-static and dynamic fracture toughness of a  $\gamma$ -TiAl alloy:  
Measurement techniques, fractography and interpretation**

Arthur Lintner<sup>1</sup>, Reinhard Pippan<sup>2</sup>, Martin Schloffer<sup>3</sup> and Anton Hohenwarter<sup>1</sup>

<sup>1</sup>Montanuniversität Leoben, Department of Materials Science, 8700 Leoben, Austria, arthur.lintner@unileoben.ac.at,  
anton.hohenwarter@unileoben.ac.at

<sup>2</sup>Erich Schmid Institute of Materials Science, 8700 Leoben Austria, reinhard.pippan@oeaw.ac.at

<sup>3</sup>MTU Aero Engines AG, 80995 München, martin.schloffer@mtu.de

### Introduction

Intermetallic titanium aluminide (TiAl) based alloys offer high specific strength, creep- and oxidation resistance together with a high Young's modulus. Due to their low density of about 4 g/cm<sup>3</sup> TiAl-alloys provide potential for weight reduction in several elevated temperature applications [1]. The most critical limitation however, is the low damage tolerance of this material class, caused by insufficient ductility and fracture toughness [2]. For dynamically loaded structural components, crack initiation and propagation occurs under high stress and strain rates and for a proper lifetime estimation, dynamic material parameters would be required. A feasible way to determine the dynamic fracture toughness is, beside the modified Split Hopkinson bar test [3–5], the testing of pre-cracked SENB (Single Edge Notched Bend) specimens using a pendulum [6, 7] or gravity drop hammer. The basic difficulty of such an experiment is that the force being needed for fracture is superimposed by inertial forces, which cannot be easily separated from each other using standard load transducers and data logging systems. The aim of this work is to present a methodology to overcome these problems, identify possible difficulties and determine the fracture toughness of a  $\gamma$ -TiAl alloy over a wide dynamic range.

### Materials and Methods

The material selected for this study is an intermetallic  $\gamma$ -TiAl alloy named TNM, with a chemical composition of Ti-43.5Al-4.0Nb-1.0Mo-0.1B [at. %]. The material was produced by vacuum arc skull remelting followed by centrifugal casting in permanent moulds. After hot isostatic pressing (HIP), the ingots were isothermally forged. The mechanical properties are strongly dependent on the microstructure, which can be adjusted by heat treatments. For balanced properties, a nearly fully lamellar microstructure was chosen. The lamellar colonies consist of fine lamellae of  $\gamma$ -TiAl and  $\alpha_2$ -Ti<sub>3</sub>Al, an ordered hexagonal phase. To conduct quasi-static and dynamic fracture toughness tests, notched and pre-cracked specimens geometrically based on the Charpy standard [8] were used. Sample fabrication was carried out by electro discharge machining (wire EDM) from the forged raw material. The notches were sharpened by polishing with a razor blade and 6  $\mu$ m diamond suspension. A fatigue crack was initiated by cyclic compression loading with a load ratio of  $R = 10$  to achieve  $a_0/W$  ratios between 0.45 and 0.48 with a pre-crack length of about 50 to 100  $\mu$ m. Here,  $a_0$  denotes the depth of the pre-crack and  $W$  the specimen width. The quasi-static experiments were conducted on a Zwick Z100 spindle testing machine, with the specimens loaded in a three-point bending arrangement with a span of 42 mm. In addition, to measure the test load and the crosshead travel, the specimen displacement was recorded with an inductive sensor. Crack propagation under the quasi-static loading conditions was detected using the direct current potential drop (DCPD) technique and the specimens were equipped with a strain gauge near the crack tip to verify the measurement under dynamic loading conditions as explained below. The dynamic experiments were performed on an Instron CEAST 9350 drop tower. The specimens were placed on a support with a span of 42 mm similar to the quasi-static tests. The hardened striking head is shaped like a wedge with a tip radius of 2 mm. Although the striker includes a load sensor for instrumented tests, our measurements are based on a strain gauge, type HBM 1-LY11-0.6/120, applied on each specimen to exclude inertial influences. Since the position of the strain gauge in the elastic near field of the crack tip is crucial, each specimen was calibrated with a quasi-static load of 500 N on the Zwick Z100 testing machine, where also the quasi-static experiments were carried out. The load was chosen to be approx. 40 % of the quasi-static failure load so that crack propagation due to a R-curve behaviour could be neglected. For the dynamic measurements, the dynamic strainmeter TML DC-97A was used, whose analogue signal was tapped from a KRENZ PSO 8160 transient recorder up to a sampling rate of 50 MS/s.

### Results and Discussion

The quasi-static experiments were conducted with a crosshead speed of 0.05 mm/min, resulting in an increase in stress intensity at the crack tip of approximately  $\dot{K} = 0.1$  MPa $\sqrt{m/s}$ . From the results of the direct current potential drop (DCPD) technique, crack resistance curves (R-curves) were plotted. As presented in Fig. 1 up to a crack propagation  $\Delta a$  of nearly 70  $\mu$ m the stress intensity factor  $K_I(a)$  increases, because shielding effects due to microcracks and shear ligaments come into effect with increasing crack length [9, 10]. Up to a  $\Delta a$  of slightly more than 100  $\mu$ m, the stress intensity  $K_I(a)$  then remains almost constant, which implies that the load already decreases until final failure. The mean value of  $K_{I,max}(a)$  was calculated to be 14.5 MPa $\sqrt{m}$ . However, most of the specimens in the presented study

were subjected to fracture toughness tests under dynamic loading conditions on the Instron CEAST 9350 drop tower with different striker velocities varying from 1 to 10 m/s resulting in an increase in stress intensity of  $10^5$  to  $1.3 \cdot 10^6$  MPa $\sqrt{\text{m/s}}$ . A 0.7 mm thick annealed Cu sheet was placed between the specimen and the striker to modulate the impact pulse and reduce specimen vibrations. Fig. 2 exemplarily shows the stress intensity curves determined from the strain gauge measurements in the elastic near-field of the crack tip of experiments performed with a striker velocity of 6 m/s. As in the 10 m/s tests, the striker velocity was only achieved by spring preloading. The curves, which are mostly close together in their rise, can be evaluated according to the principle of the impact response curves [11], whereby experiments that achieve a higher  $K_{I,\text{max}}$  also require a longer time to fracture. The scattered results correspond at least to the quasi-static fracture toughness, but mostly show higher  $K_{I,\text{max}}$  values. The mean value of the dynamic fracture toughness, here assumed by  $K_{I,\text{max}}$ , was found to increase up to a striker velocity of 6 m/s to  $K_{I,\text{max}}(a_0) = 16.8$  MPa $\sqrt{\text{m}}$ . Experiments conducted with a striker velocity of 10 m/s revealed almost the same mean value of  $K_{I,\text{max}}(a_0)$  with a comparable scatter. Even taking into account the possible deviations of the measurement technique observed in quasi-static tests, the results of the dynamic experiments show on average an increase in fracture toughness up to a  $\dot{K}$  of  $10^6$  MPa $\sqrt{\text{m/s}}$ .

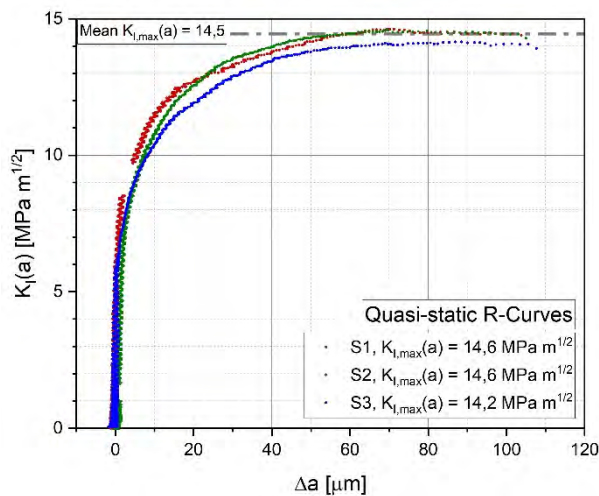


Fig. 1: Crack resistance curves (R-curves) of three quasi-static fracture toughness experiments

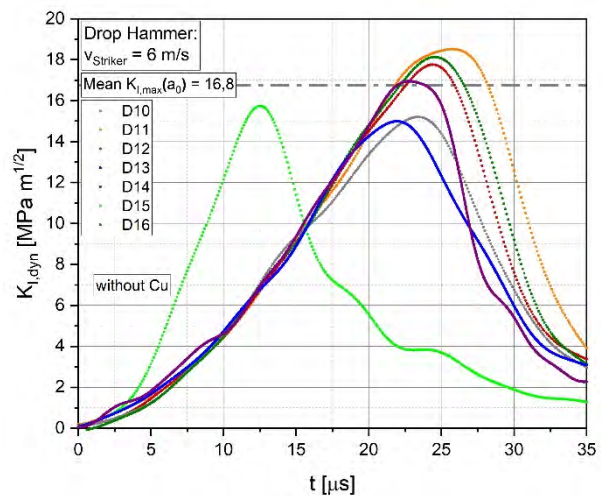


Fig. 2: Stress intensity curves of dynamic fracture toughness experiments conducted with a striker velocity of 6 m/s

## References

- [1] H. Clemens, S. Mayer, Design, Processing, Microstructure, Properties, and Applications of Advanced Intermetallic TiAl Alloys, *Advanced Engineering Materials*. **2013**, 15, no. 4, 191–215.
- [2] K.S. Chan, Understanding Fracture Toughness in Gamma TiAl, *JOM*. **1992**, 44, no. 5, 30–38.
- [3] J.T. Foster, V.K. Luk, W.W. Chen, Dynamic Initiation Fracture Toughness of High Strength Steel Alloys, Livermore, CA (United States), **2008**.
- [4] M. Shazly, V. Prakash, S.L. Draper, Dynamic Fracture Initiation Toughness of a Gamma (Met-PX) Titanium Aluminide at Elevated Temperatures, *Metallurgical and Materials Transactions A*. **2009**, 40, no. 6, 1400–1412.
- [5] M.J. Perez-Martin, B. Erice, F. Galvez, Experimental determination of the dynamic fracture-initiation toughness of high-strength metals, *Engineering Fracture Mechanics*. **2019**, 205, 498–510.
- [6] M. Enoki, T. Kishi, Effect of rate on the fracture mechanism of TiAl, *Materials Science and Engineering A*. **1995**, 192/193, 420–426.
- [7] H. Fukumasu, T. Kobayashi, H. Toda, K. Shibue, Dynamic fracture toughness of a Ti-45Al-1.6Mn alloy at high temperature, *Metallurgical and Materials Transactions A*. **2000**, 31A, no. 3053.
- [8] DIN Deutsche Institut für Normung e.V.: Metallische Werkstoffe - Kerbschlagbiegeversuch nach Charpy: Teil 1: Prüfverfahren, Berlin: Beuth Verlag GmbH, **2017**.
- [9] T. Leitner, M. Schloffer, S. Mayer, J. Eßlinger, H. Clemens, R. Pippan, Fracture and R-curve behavior of an intermetallic  $\beta$ -stabilized TiAl alloy with different nearly lamellar microstructures, *Intermetallics*. **2014**, 53, 1–9.
- [10] M. Schloffer, Gefüge und Eigenschaften der intermetallischen TNM-Legierung, Dissertation, Montanuniversität Leoben, Department Metallkunde und Werkstoffprüfung/Erich Schmid Institut der Österreichischen Akademie der Wissenschaften, **2013**.
- [11] J.F. Kalthoff, S. Winkler, W. Böhme, A novel procedure for measuring the impact fracture toughness  $K_{Id}$  with precracked charpy specimens, *Le Journal de Physique Colloques*. **1985**, 46, C5, 179-186.

## O-TA-13

**Microstructural evolution in gamma TiAl cyclically deformed at room temperature**Tomáš Kruml<sup>1</sup>, Milan Heczko<sup>1</sup>, Veronika Mazánová<sup>1</sup>, Mikhail Linderov<sup>2</sup> and Alexei Vinogradov<sup>3</sup><sup>1</sup>Institute of Physics of Materials, The Czech Academy of Sciences, Brno, Czech Republic, kruml@ipm.cz<sup>2</sup>Institute of Advanced Technologies, Togliatti State University, 445020 Togliatti, Russia<sup>3</sup>Department of Mechanical and Industrial Engineering, Norwegian University of Science and Technology - NTNU, 7491 Trondheim, Norway**Introduction**

The gamma-based titanium aluminides are characteristic for low density, high strength and excellent corrosion resistance at high temperatures [1]. The applications in aircraft and automotive industries appeared during the last decade [2]. However, the lower than expected fatigue and fracture properties at both room and high temperatures and the overall poor ductility and machinability mean that the development of the TiAl alloys is far from being completed [3].

It has been known for a long time that several deformation modes can be activated in monotonic or cyclic loadings of L1<sub>0</sub> gamma TiAl phase: i) slip of ordinary dislocations, ii) slip of superdislocations and iii) mechanical twinning [4,5].

The aim of the study is to investigate in much more details than usual the evolution of the microstructure at the early stages of the fatigue process by various experimental methods. We achieved to propose a quantitative scenario of interplay between dislocation slip, twinning and detwinning within individual cycles.

**Materials and Methods**

The material was an alloy of chemical composition Ti-48Al-2Nb-2Cr-0.82B (at. %) with the near gamma microstructure. The average grain size was about 46 μm. The specimens were cycled in a symmetric strain-controlled regime with constant strain rate at room temperature. Two loading levels were applied with constant strain amplitudes of 0.2 and 0.4%. The methods used for the investigation comprised electron microscopy (TEM, SEM – ECCI/EBSD), in-situ neutron diffraction heating/cooling experiments (see details in [4]), statistical analysis of the hysteresis loop and acoustic emission [6].

**Results and Discussion****Cyclic mechanical properties**

In cyclic tests the material showed cyclic strengthening, which is stronger in the first few (about five) cycles and then attenuates slowly. The low capability of plastic deformation was confirmed by a low number of cycles to failure (312 and 32 cycles for strain amplitudes of 0.2 % and 0.4 %, respectively). The hints for events operating within individual cycles were obtained by analyzing the shape of hysteresis loops within the framework of Polák's statistical theory [7]. The effective stress and distribution of internal stresses in individual microvolumes are measured by this technique.

**Electron microscopy**

Transmission electron microscopy of post-mortem specimens revealed a high density of mechanical twins which were created within the fatigue process (see Fig. 1). Also, an increase in dislocation density as compared to the as-received material.



Fig. 1: Mechanical twins formed during cycling, strain amplitude 0.4%, specimen after failure.

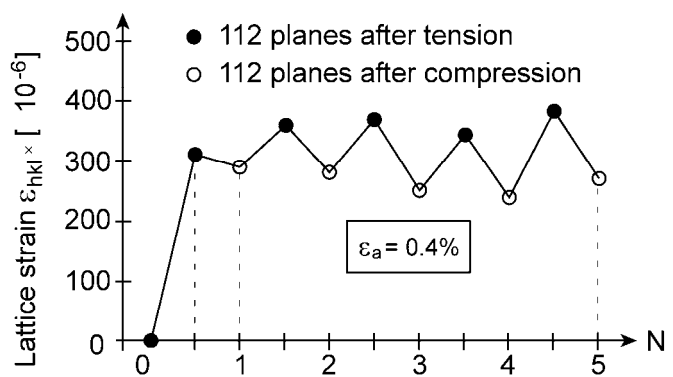


Fig. 2: Lattice strain of {112} planes as a function of cycling.

The twins were observed also by the SEM-ECCI technique which enables observations after a selected number of cycles. It documents a rapid increase of twins within the first cycles.

### **Neutron diffraction**

In-situ neutron diffraction experiments in cyclic testing were performed at Paul Scherrer Institute. As a main result, interplanar distances of selected atomic planes as a function of cycling were obtained. It was found that high lattice strains developed already after the first half-cycle (Fig. 2). The lattice strain corresponds to the volume of created mechanical twins. It decreased by about 20% after a compressive half-cycle, indicating that detwinning of about 20% of twins occurred during cycle reversion.

### **Acoustic emission**

Knowing the rough picture of deformation scenario, acoustic emission analysis has proven to be a very useful tool for deepening the knowledge about the intensity of operating mechanisms with cycles, or even within individual cycles. Both twinning and dislocation slip signals were detected and quantitatively analyzed. It appeared that the twinning is very intense in the first cycles, which corresponds to high cyclic strengthening. The twinning activity increases with the stress, so the highest twin production takes place just before load reversal. When the sense of loading changes, detwinning occurs. The dislocation slip starts earlier and is more homogeneously distributed within one cycle than twinning, as documented by the loop shape analysis and acoustic emission technique. With increasing number of cycles, twinning activity weakens and dislocation slip becomes dominant.

### **Conclusions**

Dislocation slip and twinning operate throughout the entire fatigue test, although their contributions to strain hardening are different. The acoustic emission analysis shows that cyclic plastic deformation commences with ordinary dislocation slip. Twinning appears as a prevailing deformation mode in the first loading cycles. The conclusions are supported by neutron diffraction and electron microscopy.

The whole story in much more details is described in [6].

### **References**

- [1] F. Appel, J.D.H. Paul, M. Oehring, *Gamma titanium aluminide alloys science and technology*. Wiley, Weinheim, **2011**.
- [2] B.P. Bewlay, S. Nag, A. Suzuki, M.J. Weimer, *Materials at High Temperatures*. **2016**, *33*, 549-559.
- [3] T.E.J. Edwards, *Mater. Sci. Technol.* **2018**, *34*, 1919-1939.
- [4] P. Beran, M. Heczko, T. Kruml, T. Panzner, S. van Petegem, *Journal of the Mechanics and Physics of Solids*. **2016**, *95*, 647-662.
- [5] D. Peter, G.B. Viswanathan, A. Dlouhy, G. Eggeler, *Acta Materialia* **2010**, *58*, 6431-6443.
- [6] A. Vinogradov, M. Heczko, V. Mazánová, M. Linderov, T. Kruml, *Acta Materialia* **2021**, accepted.
- [7] J. Polák, *Cyclic Plasticity and Low Cycle Fatigue Life of Metals*, Elsevier, Amsterdam, **1992**.



**O-TA-14****Microstructure and mechanical properties of TNM titanium aluminide alloy after heat treatment and different cooling conditions**

Mark Hilleringmann, Jan Schievenbusch, Pawel Zapala and Matthias Bünck

Access e.V., 52072 Aachen, Germany, m.hilleringmann@access-technology.de,

j.schievenbusch@access-technology.de, p.zapala@access-technology.de, m.buenck@access-technology.de

**Introduction**

The TiAl alloy TNM (Ti-43.5Al-4Nb-1Mo-0.1B, in at.%) was initially developed for the production of low-pressure turbine blades via forging route. Recrystallization during annealing of the forged material leads to a fine microstructure combined with high strength values and creep properties. However, a near net shape casting route would save time and costs in production. Schwaighofer et. al. showed that the mechanical properties of cast and hot isostatic pressed TNM can be fundamentally increased and varied in a wide range exclusively by selected heat treatment steps [1,2]. Annealing temperature and cooling rates determine the resulting microstructure and the final mechanical properties of titanium aluminides [2-5]. In the present study, the fundamental relationship of holding temperature and cooling condition on the resulting microstructure and mechanical properties at room temperature (RT) is qualitatively investigated for industrial scale samples. In addition, combinations of air cooling (AC) and furnace cooling (FC) after heat treatment are performed for the first time and compared with conventional cooling conditions. Based on the results, a novel efficient heat treatment to increase the ductility of  $\beta$ -solidifying  $\gamma$ -titanium aluminide alloys is suggested.

**Materials and Methods**

TNM alloy with nominal composition, produced by GfE Metalle und Materialien GmbH was melted by induction skull melting (ISM) and poured into permanent molds by centrifugal casting process. The casted billets with diameter  $\varnothing 52 \times 182$  mm were subsequently treated by hot isostatic pressing (HIP) at 1200 °C and 200 MPa for 4 h. Finally, the test material was subjected to different heat treatments by varying annealing temperature and cooling rates. Heat treatment cycles were performed at 1250 °C and 1430 °C for 1 h followed by air cooling (AC), furnace cooling (FC) or combination of both cooling conditions (ACFC and FCAC). Combined cooling conditions ACFC and FCAC were carried out starting with 1430 °C annealing temperature, while the change in cooling condition took place at 1250 °C. The material conditions are named 1250-AC, 1430-AC, 1430-FCAC, 1250-FC, 1430-FC and 1430-ACFC, respectively. These annealing temperatures were selected for their relevance to phase transformations and microstructure development. Specimens for tensile tests and metallographic characterization were taken from all named conditions. The mechanical properties were determined in tensile tests at room temperature. Metallographic specimens were prepared to analyze the microstructure by color etching according to Ence and Margolin [6,7]. Light microscopy images were taken to determine the colony sizes as well as the microstructural fractions of lamellar  $\alpha/\gamma$ -colonies,  $\beta$ -phase and globular  $\gamma$ -grains.

**Results and Discussion**

The size of the lamellar  $\alpha/\gamma$ -colonies is significantly determined by the cooling time in the  $(\alpha+\beta)$ -two phase region, cf. fig. 1 b), c), e) and f). Thus, annealing at 1250 °C does not noticeably affect the colony size, cf. Fig. 1 a), d). According to the Hall-Petch relationship, the strength characteristics at RT depend strongly on the colony size, cf. Fig. 2 a). The lamella spacing has only little influence. Consequently, the faster the cooling through the  $(\alpha+\beta)$ -region, the higher the strength values. The proportion of globular  $\gamma$ -grains tends to increase with increasing cooling time through the  $(\alpha+\beta+\gamma)$ -multiphase region, cf. Fig. 2 b). An exception is the 1430-FC state, which has a significantly lower fraction of globular  $\gamma$ -grains than the 1430-ACFC state. This circumstance can be explained by thermodynamics, e.g. by the effect of inner distortion energy on nucleation and growth of new phases while cooling. A higher  $\gamma$ -fraction promotes ductility, cf. Fig. 1. Accordingly, the 1430-ACFC state has the highest ductility, which could be further enhanced by stabilization treatment. Internal studies of this state after annealing at 850 °C for 6 h resulted in a total fracture strain  $A_t$  of 1.12 % at a yield strength of 638 MPa.



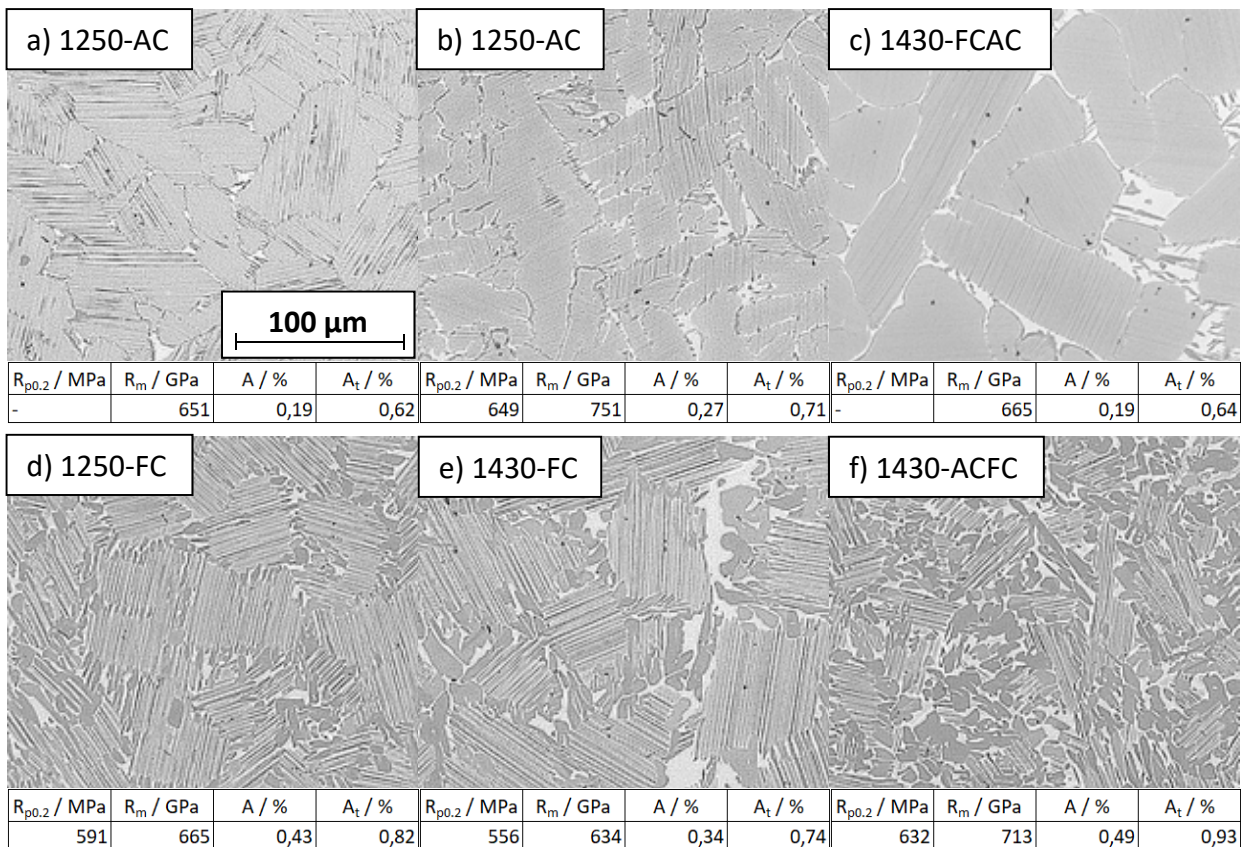


Fig. 1: Microstructure and mechanical properties of TNM after 1 h heat treatment and different cooling conditions.

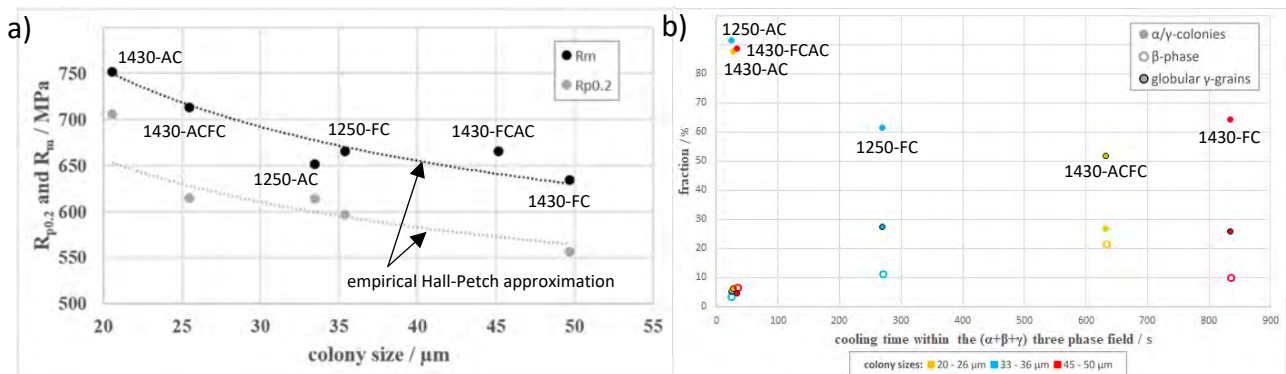


Fig. 2: Correlations of a) colony size and strength values and b) cooling time within the three-phase field and fractions of microstructural constituents.

## References

- [1] E. Schwaighofer, M. Schloffer, T. Schmolzer, S. Mayer, J. Lindemann, V. Guether, J. Klose, H. Clemens, Influence of heat treatments on the microstructure of a multi-phase titanium aluminide alloy, *Praktische Metallographie/Praktische Metallographie*. **2012**, *49*, 124-137.
- [2] E. Schwaighofer et al.: Microstructural design and mechanical properties of a cast and heat-treated intermetallic multi-phase  $\gamma$ -TiAl alloy, *Intermetallics*. **2014**, *44*, 128 – 140.
- [3] V.M. Imayev, R.M. Imayev, T.G. Khismatullin, Mechanical properties of the cast intermetallic alloy Ti-43Al-7(Nb, Mo)-0.2B (at %) after heat treatment, *The Physics of Metals and Metallography*. **2008**, *105*, 484-490.
- [4] M. Thomas, M.P. Bacos, Processing and Characterization of TiAl-based Alloys: Towards an Industrial Scale, *AerospaceLab*. **2011**, *3*, 1-11.
- [5] K. Maruyama, R. Yamamoto, H. Nakakuki, N. Fujitsuna, Effects of lamellar spacing, volume fraction and grain size on creep strength of fully lamellar TiAl alloys, *Mater. Sci. Eng. A*. **1997**, *239–240*:419–428.
- [6] E. Ence and H. Margolin: Phases in titanium alloys identified by cumulative etching. *JOM*. **1954**, *6*, 346–348.
- [7] M. Schloffer, T. Schmolzer, S. Myer, E. Schwaighofer, G. Hawranek, F.-P. Schiansky, F. Pczak, H. Clemens, The Characterisation of a Powder Metallurgically Manufactured TNM Titanium aluminide Alloy Using Complimentary Quantitative Methods, *Praktische Metallographie*. **2011**, *48*, 594-604.

**O-TA-15****Rapid solidification behavior of an intermetallic  $\gamma$ -TiAl based Ti-48Al-2Cr-2Nb alloy studied by means of in-situ high-energy X-ray diffraction**

Gloria Graf<sup>1</sup>, Jan Rosigkeit<sup>2</sup>, Erwin Krohmer<sup>3</sup>, Peter Staron<sup>2</sup>, Helmut Clemens<sup>1</sup>  
and Petra Spoerk-Erdely<sup>1</sup>

<sup>1</sup>Department Materials Science, Montanuniversität Leoben, 8700 Leoben, Austria, gloria.graf@unileoben.ac.at, helmut.clemens@unileoben.ac.at, petra.spoerk-erdely@unileoben.ac.at

<sup>2</sup>Institute of Materials Physics, Helmholtz-Zentrum Hereon, 21502 Geesthacht, Germany, jan.rosigkeit@hereon.de, peter.staron@hereon.de

<sup>3</sup>Institute for Machine Tools and Factory Management, Technische Universität Berlin, 10587 Berlin, Germany, erwin.krohmer@iwf.tu-berlin.de

**Introduction**

Due to their light weight and excellent high-temperature properties  $\gamma$ -TiAl based alloys are ideal candidates for applications in the automotive and aircraft industry [1]. The processing of these alloys via additive manufacturing (AM) brings the advantage of building complex near-net shape components [2]. During AM, however, high cooling rates are applied, leading to out-of-equilibrium conditions. In-situ investigations tracing the phase transformations during rapid solidification would contribute immensely to the understanding of the influence of high cooling rates, especially since  $\gamma$ -TiAl based alloys exhibit several phase transformations upon cooling starting from the liquid phase. Yet only a few in-situ solidification experiments have been conducted so far [3–5]. In this work, an in-situ high-energy X-ray diffraction (HEXRD) investigation is conducted in order to trace the phase transformations during rapid solidification. For this, a thin platelet is laser-melted on its upper edge, while the phase transformations are simultaneously measured.

**Materials and Methods**

The material used was an intermetallic  $\gamma$ -TiAl based Ti-48Al-2Cr-2Nb (in at.%) alloy in as-EBM condition and the production process is described in [6]. The mean chemical composition was measured via X-ray fluorescence spectroscopy and equaled Ti-47.5Al-1.91Cr-2.06Nb-0.01B (in at.%). From the as-EBM material a thin platelet with a cross-section of  $5 \times 5 \text{ mm}^2$  and a thickness of  $400 \mu\text{m}$  was cut with an Accutom-5R from Struers GmbH, Germany. This platelet was used for the in-situ HEXRD experiment conducted at the P07 high-energy materials science (HEMS) beamline operated by Hereon at PETRA III at the Deutsches Elektronen-Synchrotron (DESY) in Hamburg, Germany. The aim of the experiment was to trace the phase transformations during rapid solidification after the laser-melting process. In order to be able to melt the platelet on its upper edge, it was mounted in a sample holder, as can be seen in Fig. 1a. Inside a chamber (described in Ref. [7]), which is not depicted in Fig. 1a, the sample holder and a continuous wave ytterbium fiber laser YLR-400-AC from IPG Laser GmbH, Germany, with a wavelength of  $1070 \text{ nm}$  are located. During the experiment the chamber is flooded with inert Ar gas. For the measurement of the phase transformations during solidification, the synchrotron X-ray beam, with a width of  $400 \mu\text{m}$  and a height of  $100 \mu\text{m}$ , is positioned just below the upper edge of the specimen platelet. The position of the cross-section of the X-ray beam on the platelet is marked in green on the measured platelet depicted in Fig. 1b. In order to melt the platelet, the laser is moved along the upper edge of the specimen, as indicated by the arrow in Fig. 1a. The laser power used was  $100 \text{ W}$  and its velocity equaled  $20 \text{ mm/s}$ . The process is investigated via HEXRD in transmission geometry. The photon energy of the X-ray beam was chosen to be  $100 \text{ keV}$  and the detector frame rate was  $50 \text{ Hz}$ . For the investigation, a PILATUS 3X CdTe 2M area detector from Dectris AG, Switzerland, with a total number of pixels of  $1475 \times 1679$  and a pixel size of  $172 \mu\text{m} \times 172 \mu\text{m}$  was employed. The distance from the specimen to the detector equaled  $1048 \text{ mm}$ . For the evaluation of the experiment, diffraction patterns were obtained by azimuthally integrating the detector images with the aid of the software Fit2D [8].

**Results and Discussion**

Figure 2 shows diffraction patterns that were recorded during the experiment. The starting point at  $0.00 \text{ s}$  is depicted in Fig. 2a. At this point, the laser melted the upper edge of the sample and the material in the measurement volume is completely liquid. This is indicated by the broad amorphous peak visible in the diffraction pattern.

In addition to the broad liquid peak, which is still present in the diffraction pattern in Fig. 2b, the first peaks belonging to solid material have appeared after  $0.02 \text{ s}$ . They correspond to the disordered cubic-room centered  $\beta$ -Ti(Al) phase (A2 structure) and the disordered hexagonal  $\alpha$ -Ti(Al) phase (A3 structure), with the  $\beta$ -Ti(Al) phase as the primary solidification phase [9].

In Fig. 2c the liquid peak has vanished and only solid phase peaks can be seen in the diffraction pattern. This means that solidification of the material in the measurement volume takes place within  $0.04 \text{ s}$ . Furthermore, the  $\beta$ -Ti(Al) phase has completely transformed into  $\alpha$ -Ti(Al) phase.

Figure 2d displays the diffraction pattern and detector image at  $0.92 \text{ s}$  after the starting point in Fig. 2a. It is assumed that the material inside the measurement volume is near room temperature again and that no further phase transformations will take place. After rapid solidification the material mainly consists of ordered hexagonal

$\alpha_2$ -Ti<sub>3</sub>Al phase (D0<sub>19</sub> structure) and a marginal phase fraction of the ordered  $\gamma$ -TiAl phase (L1<sub>0</sub> structure). While in the starting material – which was measured during the in-situ HEXRD experiment, but is not depicted here – the  $\gamma$ -TiAl phase was the major phase, in the rapidly solidified laser-melted material it is the  $\alpha_2$ -Ti<sub>3</sub>Al phase. Thus, the phase transformation to  $\gamma$ -TiAl is strongly suppressed, which can usually be observed for high cooling rates [10, 11].

In summary, phase transformations occurring during rapid solidification of a laser-melted platelet can accurately be measured using this setup. Thus, this setup, which creates conditions similar to AM processes, was proven to be applicable. The primary solidification phase was found to be  $\beta$ -Ti(Al), which transforms to  $\alpha$ -Ti(Al) upon cooling. The subsequent ordering reaction takes place, the formation of  $\gamma$ -TiAl phase is strongly suppressed, though.

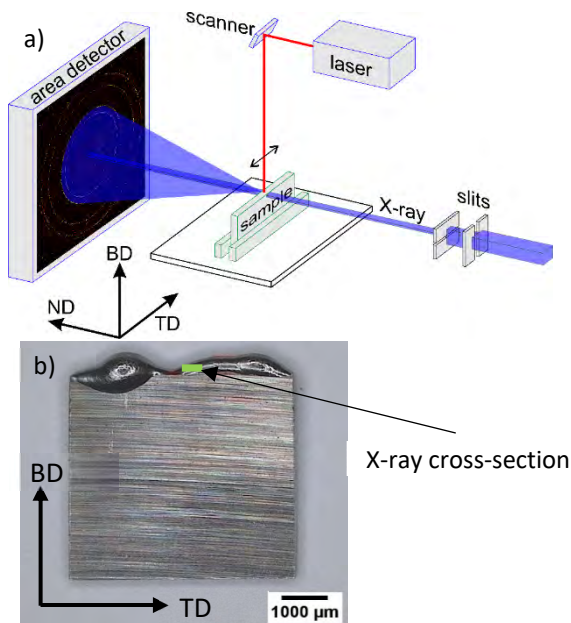


Fig. 1: a) Experimental in-situ HEXRD setup. A laser melts the platelet sample on its upper edge and phase transformations during the melting cycle are measured via HEXRD. The synchrotron X-ray is perpendicular to the sample and the laser. b) Measured sample. The former melt pool is visible on top of the platelet and the X-ray cross-section is marked in green.

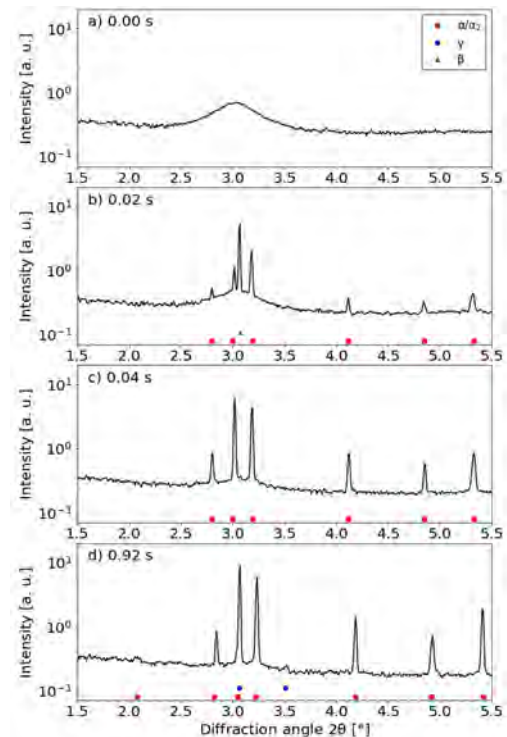


Fig. 2: Diffraction patterns of the in-situ HEXRD solidification experiment. The elapsed time is displayed in the upper left corners.

### Acknowledgements

We acknowledge DESY (Hamburg, Germany), a member of the Helmholtz Association HGF, for the provision of experimental facilities at PETRA III. The beamline P07 (HEMS) is operated by Helmholtz-Zentrum Hereon and we would like to thank Norbert Schell for assistance in using the beamline. Beamtime was allocated for proposal I-20191411. The authors thank Prof. Sara Biamino, Department of Applied Science and Technology (DISAT), Politecnico di Torino, Italy, for providing the starting material and Melissa Allen from GfE Metalle und Materialien GmbH, Nuremberg, Germany for chemical analysis.

### References

- [1] H. Clemens, S. Mayer, *Adv. Eng. Mater.* **2013**, *15*, 191.
- [2] T.C. Dzogbewu, *Manufacturing Rev.* **2020**, *7*, 35.
- [3] C. Kenel, D. Grolimund, J.L. Fife, V.A. Samson, S. van Petegem, H. van Swygenhoven, C. Leinenbach, *Scripta Mater.* **2016**, *114*, 117.
- [4] O. Shuleshova, D. Holland-Moritz, W. Löser, A. Voss, H. Hartmann, U. Hecht, V.T. Witusiewicz, D.M. Herlach, B. Büchner, *Acta Mater.* **2010**, *58*, 2408.
- [5] J. Liu, P. Staron, S. Riekehr, A. Stark, N. Schell, N. Huber, A. Schreyer, M. Müller, N. Kashaev, *Metall. and Mat. Trans. A.* **2016**, *47*, 5761.
- [6] S. Biamino, A. Penna, U. Ackelid, S. Sabbadini, O. Tassa, P. Fino, M. Pavese, P. Gennaro, C. Badini, *Intermetallics.* **2011**, *19*, 776.
- [7] E. Uhlmann, E. Krohmer, F. Schmeiser, N. Schell, W. Reimers, *Rev. Sci. Instrum.* **2020**, *91*, 75104.
- [8] A.P. Hammersley, S.O. Svensson, M. Hanfland, A.N. Fitch, D. Hausermann, *High Pressure Res.* **1996**, *14*, 235.
- [9] N. Saunders, in: Y.-W. Kim, D. M. Dimiduk, M. H. Loretto (Eds.): in *Gamma Titanium Aluminides 1999*. TMS, Warrendale, PA **1999**, 183.
- [10] Z.G. Liu, L.H. Chai, Y.Y. Chen, *J. Alloys Compd.* **2010**, *504*, S491-S495.
- [11] C. Kenel, C. Leinenbach, *J. Alloys and Compd.* **2015**, *637*, 242.

**O-TA-16****Microstructure and mechanical properties of a  $\gamma$ -TiAl alloy with a nano-grained surface layer**Christoph Stangl<sup>1</sup>, Manja Krüger<sup>2</sup> and Holger Saage<sup>1</sup><sup>1</sup>Competence Center for Lightweight Design (LLK), Faculty for Mechanical Engineering, University of Applied Sciences Landshut, Germany, Christoph.Stangl@haw-landshut.de, Holger.Saage@haw-landshut.de<sup>2</sup>Otto-von-Guericke-Universität Magdeburg, Institute of Materials and Joining Technology, Magdeburg, Germany, manja.krueger@ovgu.de**Introduction**

Microstructures with a gradient grain structure are of increasing interest for innovative engineering applications. Such microstructures can be generated by additive manufacturing or appropriate surface manipulation processes. A fine-grained surface layer on a coarse-grained base material can have a supporting effect [1]. In addition, grain refinement in  $\gamma$ -TiAl based alloys leads to a significant increase in ductility [2] beyond that observed in common metallic materials.  $\gamma$ -TiAl alloys are known for their good creep properties, good oxidation resistance and good specific properties due to the low density and are suitable for higher temperature applications [3]. A major disadvantage of these alloys is their low room temperature ductility. In addition, oxidation leads to further embrittlement [4]. It is supposed that interstitially dissolved atoms limit the dislocation movement and lead to increased stress concentrations at the phase boundaries during plastic deformation. Plastic strain is thus reduced by 65 % in a duplex structure leading to premature failure [5]. A fine-grained surface layer on  $\gamma$ -TiAl alloys could have a supporting and protective effect by reducing the stress concentration.

**Materials and Methods**

The  $\beta$ -solidifying alloy from GfE has been used for the experiments. This alloy has a nominal composition of Ti-43.5Al-4Nb-1Mo-0.1B (at. %). The raw material are forging stocks which were processed to tensile specimens. The gauge section of the specimens has a diameter of 4 mm and a length of 20 mm. The surface of the gauge section was remelted at 500 °C under argon using a LASERVORM LV Midi device. The travel direction of the laser was longitudinal in the specimen axis direction. The single tracks have an overlap of 40 %. The specimens were subsequently heat treated at 900 °C for 6 h to obtain approximately the same phase composition of the original forging stocks. Scanning electron microscopy has been used to investigate the microstructure and hardness measurements were made to characterize the layer. In order to determine the mechanical properties, tensile tests and initial fatigue tests were carried out.

**Results and Discussion**

The microstructure of the base material and the remelted area are shown in Figure 1a-d. While the average grain size of the base material is about 5  $\mu\text{m}$ , it is about 0.35  $\mu\text{m}$  in the remelted layer. The layer thickness is in the range of 200  $\mu\text{m}$  and covers approx. 20 % of the sample cross-sectional area. As can be seen in Figure 1b and 1c the phase composition of the fine-grained rim is similar to that of the base material. For example, the  $\beta_0$  content (the white areas in the Figure 1) of the remelted zone is approx. 11 % and that of the base material approx. 14 %. The hardness at the edge is 525 HV and is nearly constant in the fine-grained layer. It then drops gradually towards the base material to 350 HV. Tensile tests at room temperature show a significant supporting effect of the fine-grained surface leading to an increase of the tensile strength by about 14 %.



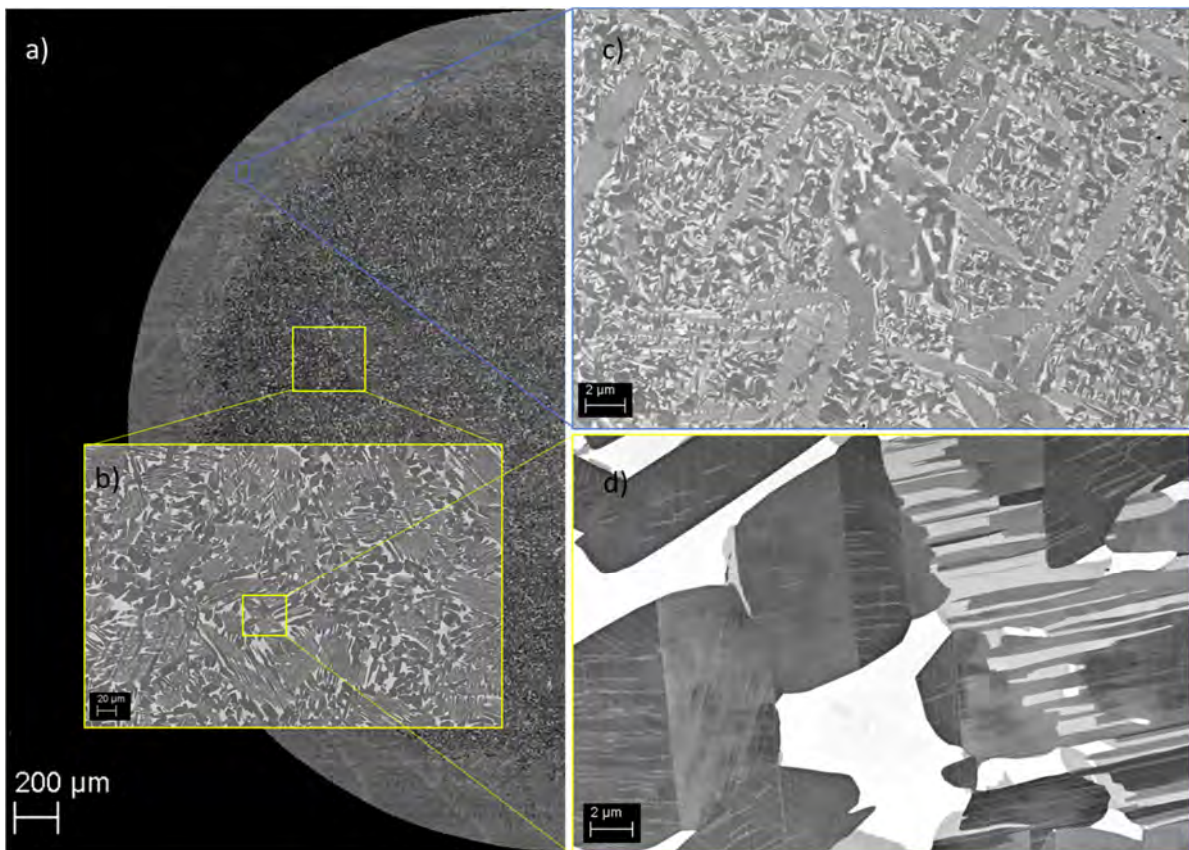


Fig. 1: Microstructure of the specimen cross-section after remelting and heat treatment at 900 °C: Overview (a) enlarged view of an area away from the remelting zone (b and d) and surface region with a refined microstructure (c).

#### References

- [1] T.H. Fang, W.L. Li, N.R. Tao, K. Lu, *Science*. **2011**, 331, 1587-1590.
- [2] J.N. Wang, K. Xie, *Scripta Materialia*. **2000**, 43, 441-446.
- [3] H.Clemens, S.Mayer, *Advanced Engineering Materials*. **2013**, 15/4, 191-215.
- [4] X. Wu, A. Huang, D. Hu, M.H. Loretto, *Intermetallics*. **2009**, 17, 540-552.
- [5] C. Löffl, H. Saage, M. Göken, *International Journal of Fatigue*. **2019**, 124, 138-148.



**O-MO-01****Modelling intermediate phases for the third generation Calphad descriptions - case study of W-C**Zhangting He and Malin Selleby

KTH Royal Institute of Technology, Stockholm, Sweden 10044, zhahe@kth.se

**Introduction**

There have been many attempts to describe the thermodynamic properties of elements and binary systems using physically based model for the third generation of Calphad descriptions. When developing the third generation of Calphad descriptions, it is critical to apply the unary descriptions to higher-order systems. How to model compounds and metastable end-members of solution phases within the framework of compound energy formalism is then of great importance. Since the third generation of Calphad descriptions are valid down to 0 K, the conventional Neumann-Kopp rule cannot be directly applied to describe phases or end-members in order to obey the third law of thermodynamics. Thus, new models are needed to develop the third generation data. A so-called “hybrid” Neumann-Kopp/Einstein model, referred to as the “hybrid” model in the present work, has been successfully used to describe the metastable end-members in the Al-C system [1]. In order to explore modelling the intermediate phases and further examine the validity of this “hybrid” model, the W-C system was chosen to assess based on the third generation unary descriptions since there are multiple intermediate phases in this system, a stoichiometric WC carbide and three solid solution phases with varied carbon solubility, i.e. the fcc and the hcp phases, with  $W_1C_1$ (fcc) and  $W_1C_{0.5}$ (hcp) as the binary stable end-members, and  $W_1C_3$ (bcc) as the metastable binary end-member in the W-C system.

**Materials and Methods**

The W-C system is a critical binary system for cemented carbides. The major tungsten carbide is WC carbide which has an hcp structure. Both W and C atoms form simple hcp sublattice in WC carbide. The higher-carbon solution phase, the fcc phase, has a cubic structure that C atoms can occupy in the octahedral interstitials in the fcc lattice of W atoms. The lower-carbon phase has hcp structure. W atoms form an hcp sublattice in which C atoms randomly distribute in the octahedral sites. As temperature decreases and reaches around 2370 K, an order-disorder transition happens and the disordered hexagonal phase transforms to an ordered orthorhombic symmetry [2].

The heat capacity of the stable WC carbide was experimentally measured by [3]. We took into account the heat capacity data and described WC carbide in a similar way as elements. As W and C atoms have really different harmonic vibrational frequencies [4], following the suggestions in [1], two Einstein temperatures were used to represent the harmonic vibrational frequencies. Accordingly, two Einstein functions were needed to describe the harmonic vibrational contribution to the Gibbs energy. There is no experimental data for the thermochemical properties of the binary end-members of fcc, hcp or bcc. Only the phase equilibria involving these three phases were experimentally determined. Due to the lack of thermochemical data, the “hybrid” model presented in [1] was selected to describe the thermodynamic properties of the end-members of the solid solution phases,  $W_1C_{0.5}$ (hcp),  $W_1C_1$ (fcc) and  $W_1C_3$ (bcc). Besides, the hcp phase was treated as a disordered phase in the present work as the main focus of this work is to examine the models for compounds and end-members.

All the model parameters were optimized using the PARROT module incorporated in Thermo-Calc software package [5]. The selected experimental and theoretical information were used as input data and the optimization was performed iteratively by minimizing the error sum between the calculated values and input data.

**Results and Discussion**

Fig.1 shows the calculated heat capacity of the WC carbide using the Calphad description assessed in the present work. The experimental heat capacity data [3] of the stoichiometric WC carbide were well reproduced using the selected model. It has further confirmed if the atoms in a compound have quite different vibrational frequencies, multiple Einstein temperatures are needed in order to well represent the harmonic vibrational contribution to the Gibbs energy. The calculated phase diagram of the W-C system is presented in Fig.2 in comparison with the selected experimental data [3–6] and the calculated phase diagram using the Calphad description assessed by Gustafson [9] for the second generation of Calphad descriptions. The phase equilibria involving the solid solution hcp, fcc and bcc phases are calculated with satisfactory agreement with the selected experimental phase equilibria data. The thermodynamic properties of hcp, fcc and bcc binary compounds are well described using the “hybrid” model. We can thus conclude that compounds and end-members can be treated as elements if there is enough data for the thermochemical properties. Otherwise, the “hybrid” model can be used to describe their thermodynamic properties.

The hcp phase was treated as a disordered phase for the entire composition range in the present work. However, it has been shown that there exists order-disorder transitions for this phase. For future work on this binary system, the order-disorder transition needs to be considered, and the contribution from the chemical ordering to the Gibbs energy needs to be modelled, which can be a next step of developing the third generation of Calphad descriptions to investigate how to model ordered intermediate phases.

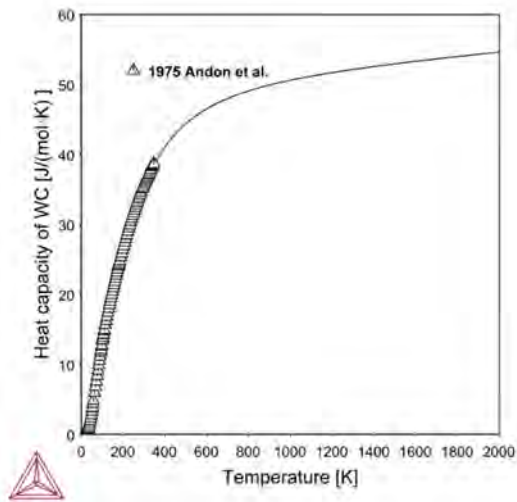


Fig. 1: The calculated heat capacity of the WC carbide

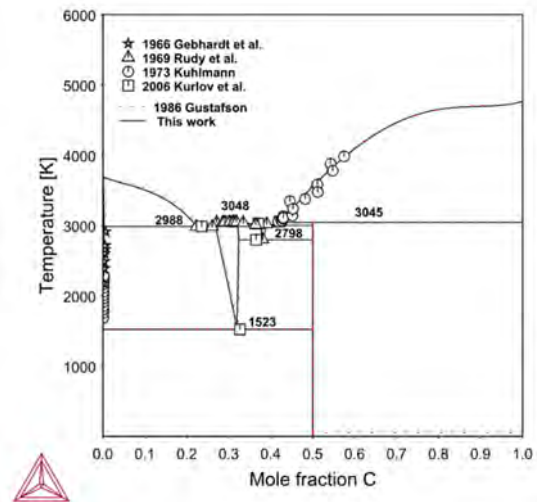


Fig. 2: The calculated phase diagram of the W-C system

### References

- [1] Z. He, B. Kaplan, H. Mao, M. Selleby, *Calphad*, **2021**, 72, 102250.
- [2] A. S. Kurlov, A. I. Gusev, *Inorg. Mater.*, **2006**, 42(2), 121–127.
- [3] R. J. L. Andon, J. F. Martin, K. C. Mills, *J. Chem. Thermodyn.*, **1975**, 7, 1079–1084.
- [4] D. V. Suetin, I. R. Shein, A. L. Ivanovskii, *Phys. B Condens. Matter*, **2009**, 404(14–15), 1887–1891.
- [5] J.-O. Andersson, T. Helander, L. Höglund, P. Shi, B. Sundman, *Calphad*, **2002**, 26(2), 273–312.
- [6] V. E. Gebhardt, E. Fromm, U. Roy, *Z. Metallkd.*, **1966**, 57, 732.
- [7] E. Rudy, Ohio, *Compendium of Phase Diagram Data*, AFML-TR-65-2 (Tech.Rep., Air Force Materials Laboratory, Wright-Patterson, AFB, OH) **1969**, 192-197.
- [8] H. H. Kuhlmann, *Tech. Wiss. Abhand. Osram Ges.*, **1973**, 11, 328–332.
- [9] P. Gustafson, *Mater. Sci. Technol.*, **1986**, 2, 653–658.

**O-MO-02****First principles density functional theory prediction of the crystal structure and the elastic properties of  $\text{Mo}_2\text{ZrB}_2$  and  $\text{Mo}_2\text{HfB}_2$** 

Rachid Stefan Touzani and Manja Krüger

Institute of Materials and Joining Technology, Otto-von-Guericke University Magdeburg, 39016 Magdeburg, Germany, rachid.touzani@ovgu.de, manja.krueger@ovgu.de

**Introduction**

The most challenging goal to develop new high-temperature materials is that they should provide balanced properties in a wide temperature range, i. e., sufficient fracture toughness at low and ambient temperatures, as well as creep strength and appropriate oxidation resistance at ultra-high temperatures. This target could be met by tailored refractory metal alloys, e.g., those based on molybdenum [1–4]. Mostly, the alloying strategy is due to the formation of temperature and oxidation-resistant intermetallic phases in a molybdenum solid solution matrix, like different silicides and borides [5,6]. Recently, systems that incorporate borides as strengthening phases were described in terms of their microstructural evolution and mechanical properties, namely the ternary systems Mo-Hf-B and Mo-Zr-B [7–9]. It could be shown that this class of materials is very attractive in terms of a promising combination of high fracture toughness and outstanding creep resistance. The borides especially, e.g. ZrB, HfB or  $\text{Mo}_2\text{B}$ , and the respective ternary borides that form in Mo-rich alloys, provide excellent creep resistance. However, there is a lack of data on the properties of the ternary phases, especially their thermodynamic stability within the ternary systems Mo-Hf-B and Mo-Zr-B. In our preliminary work so far, we found undescribed ternary phases, which were provisionally named  $\text{Mo}_2\text{HfB}_x$  and  $\text{Mo}_2\text{ZrB}_x$  in previous publications [8, 9]. More precise information on the exact chemical composition of the phases was derived from Atom Probe Tomography (APT) measurements [10]. These results give evidence on the type of phases to be  $\text{Mo}_2\text{MB}_2$  ( $M = \text{Zr, Hf}$ ), but the crystal structure and stability of the phases is still unclear.

The prediction of the crystal structure of new materials or of known crystals at extreme conditions is an ongoing research topic. Diverse methods exist, e.g., Random Sampling [11], Simulated Annealing [12] and Evolutionary Algorithms [13], often in combination with Density Functional Theory (DFT) calculations. One drawback of using these methods, however, can be the high demand of calculation power and/or time. To overcome these drawbacks, a different approach was used to predict the crystal structure of  $\text{Mo}_2\text{MB}_2$  ( $M = \text{Zr, Hf}$ ) by simply using known crystals structures of intermetallics with the 2-1-2 or 3-2 chemical composition within our DFT calculations.

**Materials and Methods**

Based on the measured chemical composition 2-1-2 for Mo, M ( $M = \text{Zr, Hf}$ ) and B, respectively, for the new compounds, we took 50 crystal structures of already known 2-1-2 and 3-2 intermetallics that fulfill the above-mentioned criterion of composition. First-principles calculation were carried out with Quickstep [14], as implemented in CP2K [15] for quick estimation of the total energy. Additionally, the PHONOPY program [16] was used to check for the dynamically most stable structure.

The Density-Of-States calculation and the chemical bonding analysis was done by calculation of the crystal orbital Hamilton population (COHP) [17] and its integrals (ICOHP) of the most stable energy ground-state structure using the tight-binding, linear muffin-tin orbitals with the atomic spheres approximation (TB-LMTO-ASA) [18, 19] as implemented in the TB-LMTO 4.7 program.

For the calculation of the elastic properties, a further structure optimization of the most stable crystal structure was carried out with Quantum ESPRESSO [20, 21]. The elastic properties were determined with thermo\_pw. To calculate the Vickers hardness, Tian et al.'s formula [22] was used.

**Results and Discussion**

The crystal structure of  $\text{Mo}_2\text{ZrB}_2$  and  $\text{Mo}_2\text{HfB}_2$  is predicted to be of the  $\text{AlMn}_2\text{B}_2$  type structure, as it is the most stable in terms of energy (see Fig. 1) and there are no signs of electronic or dynamical instability (see Fig. 2) found in the electronic and phononic density-of-states, respectively. Further the elastic properties of these ternary borides and the isotropic and anisotropic elastic moduli like the bulk, shear and Young's modulus, as well as the Vickers hardness were investigated. It can be shown that the respective values of  $\text{Mo}_2\text{HfB}_2$  are higher than those of  $\text{Mo}_2\text{ZrB}_2$  because of the chemical bonding situation. Also, it is depicted that  $\text{Mo}_2\text{HfB}_2$  is less elastically anisotropic than  $\text{Mo}_2\text{ZrB}_2$ .

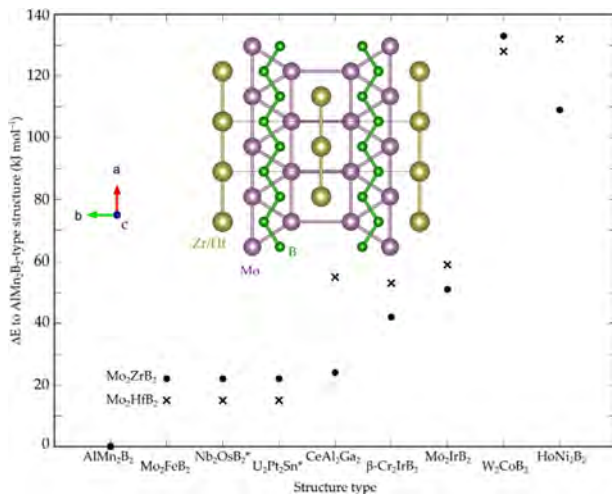


Fig. 1: Crystal structure of the  $\text{AlMn}_2\text{B}_2$  type and energies of nine crystal structure types for  $\text{Mo}_2\text{MB}_2$  ( $M = \text{Zr}, \text{Hf}$ ) relative to the  $\text{AlMn}_2\text{B}_2$  type

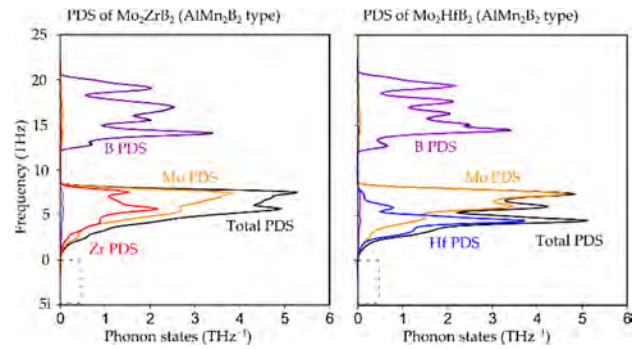


Fig. 2: Phononic density-of-states of  $\text{Mo}_2\text{ZrB}_2$  (left) and  $\text{Mo}_2\text{HfB}_2$  (right)

## References

- [1] J.J. Kruzic, J.H. Schneibel, R.O. Ritchie. *Metall Mater Trans A* **2005**, *36*, 2393–2402.
- [2] X.J. Yu, K.S. Kumar. *Int J. Refract. Hard Met.* **2013**, *41*, 329–338.
- [3] J.H. Perepezko. *Science* **2009**, *326*, 1068–1069.
- [4] F.A. Rioult, S.D. Imhoff, R. Sakidja, J.H. Perepezko. *Acta Materialia* **2009**, *57*, 4600–4613.
- [5] M. Krüger, P. Jain, K.S. Kumar, M. Heilmaier. *Intermetallics* **2014**, *48*, 10–18.
- [6] D. Schliephake, M. Azim, K. von Klinski-Wetzels, B. Gorr, H.J. Christ, H. Bei, E.P. George, M. Heilmaier. *Metall Mater Trans A Phys Metall Mater Sci* **2014**, *45*, 1102–1111.
- [7] V. Bolbut, S. Seils, T. Boll, D. Chassaing, M. Krüger. *Materialia* **2019**, *6*, 100322.
- [8] V. Bolbut, I. Bogomol, P. Loboda, M. Krüger. *J. Alloys Compd.* **2018**, *735*, 2324–2330.
- [9] V. Bolbut, I. Bogomol, C. Bauer, M. Krüger. *Materialwissenschaft und Werkstofftechnik* **2017**, *48*, 1113–1124.
- [10] V. Bolbut, S. Seils, D. Chassaing, T. Boll, M. Krüger. Unpublished work.
- [11] M. U. Schmidt, U. Englert. *J. Chem. Soc. Dalton Trans.* **1996**, *10*, 2077–2082.
- [12] S. Kirkpatrick, C.D. Gelatt Jr, M.P. Vecchi. *Science*, **1983**, *220*, 671–680.
- [13] A.R. Oganov, C.W. Glass. *J. Chem. Phys.* **2006**, *124*, 244704.
- [14] J. VandeVondele, M. Krack, F. Mohamed, M. Parrinello, T. Chassaing, J. Hutter. *Commun. Comput. Phys.* **2005**, *167*, 103–128.
- [15] J. Hutter, M. Ianuzzi, F. Schiffmann, J. VandeVondele. *WIREs Comput. Mol. Sci.* **2014**, *4*, 15–25.
- [16] A. Togo, I. Tanaka. *Scripta Mater.* **2015**, *108*, 1–5.
- [17] R. Dronskowski, P. Blöchl. *J. Phys. Chem.* **1993**, *97*, 8617–8624.
- [18] O.K. Andersen, H.L. Skriver, H. Nohl, B. Johansson. *Pure Appl. Chem.* **1980**, *52*, 93–118.
- [19] O.K. Andersen, O. Jepsen. *Phys. Rev. Lett.* **1984**, *53*, 2571–2574.
- [20] P. Giannozzi, S. Baroni, N. Bonini, M. Calandra, R. Car, C. Cavazzoni, D. Ceresoli, G.L. Chiarotti, M. Cococcioni, I. Dabo, et al. Quantum ESPRESSO: A modular and open-source software project for quantum simulations of materials *J. Phys. Condens. Matter* **2009**, *21*, Art. 395502.
- [21] P. Giannozzi, O. Andreussi, T. Brumme, O. Bunau, M. Buongiorno Nardelli, M. Calandra, R. Car, C. Cavazzoni, D. Ceresoli, M. Cococcioni, et al. *J. Phys. Condens. Matter.* **2017**, *29*, Art. 465901.
- [22] Y. Tian, B. Xu, Z. Zhao. *Int. J. Refract. Met. H.* **2012**, *33*, 93–106.

## O-MO-03

Stability prediction of the  $\sigma$ -phase using a supervised machine learning methodJean-Claude Crivello<sup>1</sup>, Jean-Marc Joubert<sup>1</sup> and Nataliya Sokolovska<sup>2</sup><sup>1</sup>Univ Paris Est Creteil, CNRS, ICMPE, UMR 7182, 94320 Thiais, France, crivello@icmpe.cnrs.fr<sup>2</sup>NutriOmics, INSERM, Sorbonne University Paris, France

## Introduction

Machine learning (ML) is becoming the state-of-the-art method in numerous domains, including material sciences. In this paper, we demonstrate how ML can be used to efficiently predict the heat of formation of a given complex intermetallic phase, here, the  $\sigma$ -phase,  $tP30, D8_b$ .

## Materials and Methods

Based on an independent and unprecedented large first principles dataset containing about 10,000  $\sigma$ -compounds with  $n=14$  different elements, we used a supervised learning approach to predict all the  $\sim 540,000$  possible configurations within a mean absolute error of 23 meV/at ( $\sim 2$  kJ/mol) on the heat of formation and  $\sim 0.06$  Å on the tetragonal cell parameters (Fig. 1).

## Results and Discussion

We show that multi-layer neural network regression results in a significant improvement in the accuracy of the predicted output compared to traditional regression techniques. We also integrated descriptors having physical nature (atomic radius, number of valence electrons), and we observe that they improve the model precision.

We conclude from our numerical experiments that the learning database composed of the binary-compositions only, plays the major role in predicting the higher degree system configurations. Our results open a broad avenue to efficient high-throughput investigations of the combinatorial binary computations for multicomponent prediction of complex intermetallic phases (Fig. 2).

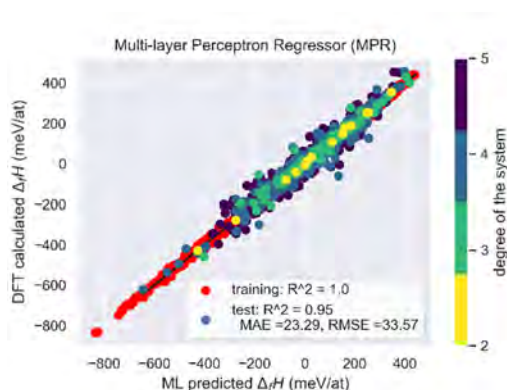


Fig. 1: Prediction of randomized 1001 configurations among the 537,824 ones from the learning of the training database (9974 data in red). The tested 1001 configurations are reported in colors (blue to yellow) corresponding to the degree  $d$  of their system (right side legend). The diagonal line indicates the perfect agreement between DFT calculated and ML predicted values.

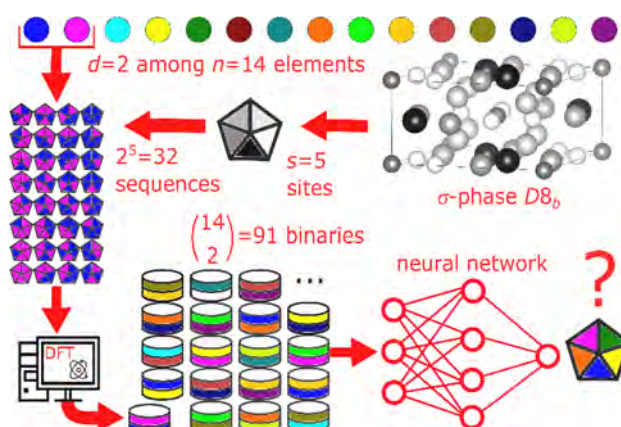


Fig. 2: Chart-flow of the methodology presented in the paper. (i) The crystal structure is summarized as a  $s$  non-equivalent sites figure; (ii) from  $n$  available elements, a given system of system degree  $d$  is selected (e.g.  $d=2$  for binary); (iii) the permutation leads to  $d^s$  unique configurations; (iv) every configuration is calculated by DFT, forming a unit of data; (v) the stack of all all units forms a learning database; then (vi) a supervised machine learning is used to predict multicomponent configurations.

## References

- [1] J.-M. Joubert, Progress in Material Science, **2008**, 53, 528-583  
 [2] J.-C. Crivello, J.-M. Joubert, N. Sokolovska, <https://arxiv.org/abs/2011.10883>



**O-CO-01****Protective aluminum and chromium diffusion coatings for refractory metals at high temperature exposure**

Anke Silvia Ulrich, Katharina Beck and Mathias Christian Galetz

DECHEMA-Forschungsinstitut, 60489 Frankfurt a.M., Germany, silvia.ulrich@dechema.de,

katharina.beck@dechema.de, mathias.galetz@dechema.de

**Introduction**

Attempts to improve the performance and efficiency of internal combustion engines are usually accompanied by an increase in operating temperature. Since the high temperature materials used to date are being employed at their load limits, the demand for new types of material systems is high. Materials of high interest are refractory metals, which are characterized by a particularly high melting point and adequate mechanical properties at high temperatures. Especially alloys based on Molybdenum (Mo), Niobium (Nb), Tantalum (Ta), and Tungsten (W) are of particular interest due to their melting points above 2400 °C [1]. The main drawback for their application is, that these refractory metals show low oxidation resistance at elevated temperatures. Alloying e. g. with Silicon and Boron can counteract detrimental corrosion and simultaneously improve the mechanical properties by intermetallic phase strengthening [2]. However, usually higher concentrations of alloying elements such as Silicon, Chromium or Aluminum are required at the metal surface to ensure the formation of protective slow growing oxide scales. Higher alloying usually counteracts the well-defined mechanical properties; hence, coatings are the best option. Especially Aluminum (Al) and Chromium (Cr) diffusion layers are promising coatings to suppress harmful oxidation at temperatures higher than 1000 °C (Al) and in combustion atmospheres containing also salt deposits (Cr).

This study covers a fundamental investigation on the deposition of such reservoir layers on the pure base metals Ta, Nb, W, and Mo. The growth and the appearance of the oxide scales are investigated. In addition, the positive effect of an additional halogen treatment – commonly known from Ti-Al high temperature alloys [3] – is demonstrated on the formation of the protective oxides over the formation of the refractory oxides.

**Materials and Methods**

The coatings were manufactured using a CVD process, the in-pack cementation. Pure refractory metal samples of Tantalum, Tungsten, Molybdenum, and Niobium (dimensions around 10 mm x 10 mm x 3 mm) were embedded in a powder pack consisting of the diffusant, the respective halide activator, and Al<sub>2</sub>O<sub>3</sub> as an inert filler to prevent pack sintering. For the Al diffusion coatings 1 wt.% Al as diffusant was used and 1 wt.% NH<sub>4</sub>Cl as halide activator. The diffusion process was performed at 1000 °C for 8 h in an Ar – 5 vol.% H<sub>2</sub> atmosphere. For the Cr diffusion coating manufactured on Mo and W 15 wt.% Cr and CrCl<sub>2</sub> (Mo: 2.5 wt.%, W: 1.0 wt.%) and a diffusion step of 8 h at 1100 °C were used. Nb was coated using a powder pack composition containing 30 wt.% Cr and 2.5 wt.% NH<sub>4</sub>Br, a diffusion time of 4 h and a process temperature of 1100 °C. To apply the coating on Ta the pack powder contained 50 wt.% Cr and 2.5 wt.% NH<sub>4</sub>Br and an annealing step of 8 h at 1100 °C was used. To achieve the optimal pack parameters and to enable the prediction of the formed intermetallic phases, the activities of the diffusant halides were investigated using thermodynamic calculations (FactSage).

The protective properties of the formed interdiffusion layers were investigated during oxidation in dry air using thermogravimetry (TGA). The mass change of the sample per unit surface area was measured during oxidation at 700 °C, 900 °C, and 1300 °C up to 100 h and compared to samples without any diffusion coatings. Furthermore, selected coated samples were additionally sprayed with a fluorine containing polymer (PTFE) prior to exposure. In this way, the application of the halogen effect which is known to enhance protective Al<sub>2</sub>O<sub>3</sub> formation over non-protective TiO<sub>2</sub> formation on TiAl-alloys [3] is demonstrated for refractory metal systems.

The formed coatings as well as the reaction products were investigated using optical microscopy, scanning electron microscopy (SEM), qualitative and quantitative Electron Probe Micro Analyzer (EPMA), and X-ray diffraction (XRD) measurements.

**Results and Discussion**

In Fig. 1 examples of Al and Cr coatings deposited on the pure refractory metals are shown. For Al diffusion coatings thicknesses up to 46 µm were obtained consisting of Al rich intermetallic phases. In the case of the Cr coatings thicknesses below 10 µm were obtained. The outer scale formed on the different refractory metals consists of pure Cr in all cases. While Ta and Nb additionally form Laves phases at the scale/substrate interface an additional interdiffusion zone (IDZ) formed on Cr coated Mo. The results are in agreement with the thermodynamic predictions.

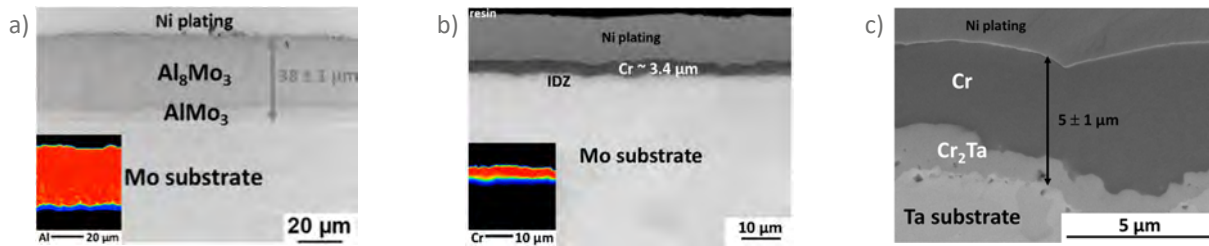


Fig. 1: Examples of a) Al coated Mo after [4], b) Cr coated Mo, and c) Cr coated Ta. The formed metallic and intermetallic phases were labeled based on quantitative EPMA line scans and XRD measurements (not shown here).

Selected results of the oxidation tests of the coated samples can be found in Fig. 2. For Mo it was demonstrated that the detrimental formation of volatile  $\text{MoO}_3$  and thereby the characteristic linear mass loss kinetics can be overcome by Cr as well as Al diffusion coatings shown for oxidation in synthetic air at 700 °C and 1300 °C, respectively.

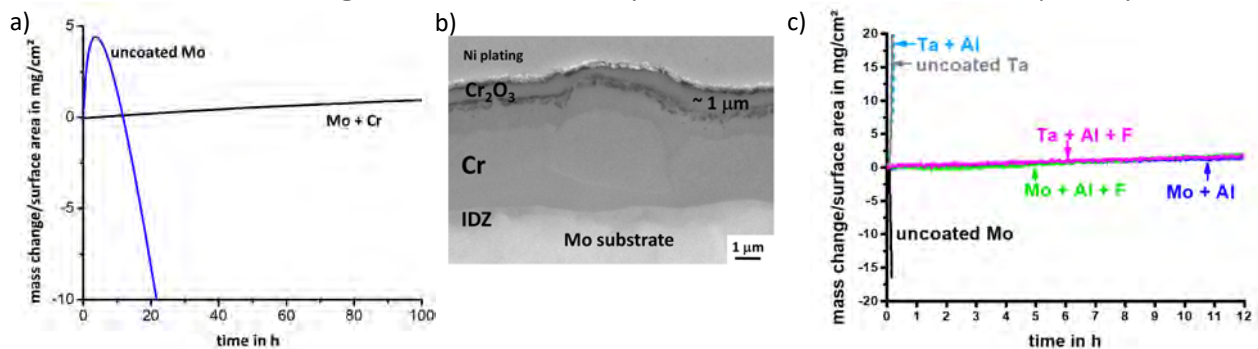


Fig. 2: TGA measurements of coated and uncoated materials are shown in a) for Cr coated Mo oxidized at 700 °C and c) Al coated Mo and Ta oxidized at 1300 °C both in synthetic air. In b) the protective nature of the coatings is shown on the example of the Cr coated Mo substrate from a).

For Al coatings it was found that at oxidation temperatures of 1300 °C the additional application of the fluorine treatment is essential to enable protective oxide scale formation for Nb, Ta, and W (an example is shown in Fig. 2c) for Ta). Thereby, the activity of Al at the substrate surface is enhanced which in turn increases  $\text{Al}_2\text{O}_3$  formation [4]. In the case of Mo the fluorine effect is not required at very high oxidation temperatures as due to the formation of volatile  $\text{MoO}_3$  the Al concentration and thereby its activity at the substrate surface is enhanced intrinsically.

The formation of a continuous and protective  $\text{Cr}_2\text{O}_3$  scale after 100 h oxidation at 700 °C is also shown on the example of Mo in Fig. 2 b). A similar result was obtained for the chromized W at 700 °C which showed an improved oxidation behavior as well. Above 700 °C the substrate materials were attacked before a continuous protective oxide layer could form, hence, the formation of the  $\text{Cr}_2\text{O}_3$  layer is not fast enough over the formation of the refractory metal oxides. Thermodynamic calculations predict a halogen effect for Cr coatings as well which could enhance the formation of a  $\text{Cr}_2\text{O}_3$  scale.

## Conclusion

It was demonstrated that Al and Cr diffusion coatings can be successfully applied on different pure refractory metals. The applied coatings lead to a significant improvement in oxidation resistance during high temperature exposure in synthetic air. Oxidation kinetics and products were characterized demonstrating the formation of protective phases during oxidation.

## Acknowledgement

This work was supported by the Deutsche Forschungsgemeinschaft (DFG) under grant GRK 2561 (Graduate School MatCom-ComMat). The authors would like to thank Ms. S. Rudolphi and Mr. Dr. G. Schmidt for technical and metallographic support. Furthermore, the research is supported by PLANSEE Group by providing the samples.

## References

- [1] J. H. Perepezko, Science. **2009**, 326(5956), 1068-1069.
- [2] M. Heilmaier, M. Krüger, H. Saage, J. Rösler, D. Mukherji, U. Glatzel, R. Völkl, R. Hüttner, G. Eggeler, C. Somsen, T. Depka, The Journal of The Minerals, Metals & Materials Society. **2009**, 61(7), 61-67.
- [3] A. Donchev, M. Schütze, Patent EP 2 428 591, **2008**.
- [4] A. S. Ulrich, M. C. Galetz, Oxidation of Metals. **2016**, 86(5). 511-535.

**O-TCP-01****Understanding the formation mechanism of  $\sigma$  phase in hyper duplex steels - experiments and computation**

Aurélie Jacob, Roman Schuster and Erwin Povoden-Karadeniz

Christian Doppler Laboratory Interfaces and Precipitation Engineering, TU Wien, Getreidemark 9, 1060 Wien, Austria, aurelie.jacob@tuwien.ac.at, roman.schuster@tuwien.ac.at, erwin.povoden-karadeniz@tuwien.ac.at

**Introduction**

Hyper duplex steel possesses good corrosion resistance properties due to the balance of ferrite/austenite close to 50:50. Due to high content of alloying elements such as Cr, Mo and Ni, this steel is prone to formation of secondary phases such as  $\sigma$ . The formation of  $\sigma$  phase in hyper duplex stainless steels (HDSS) is given as eutectoidal in the literature due to the typical microstructural pattern. Nevertheless, our recent investigation of  $\sigma$  phase thermodynamic modeling [1] shows a monovariant reaction of  $\sigma$  phase at high temperatures. In this paper, we show the mechanisms of  $\sigma$  formation in HDSS combining experiments (EPMA, Synchrotron) and thermo-kinetic simulation in order to explain the very fast (few second) formation of  $\sigma$  phase in HDSS.

**Materials and Methods**

The nominal composition of the investigated HDSS is given in Table 1. The steel was melted in an arc furnace under argon condition, and then annealed at 1100°C for solution annealing and subsequently water quenched.

In-situ synchrotron XRD measurements were performed at the beamline P07 at DESY, Hamburg, to track the early stages of  $\sigma$  precipitation during annealing. The set-up allowed us to measure the development of  $\sigma$  formation and the phase fractions of the matrix phases as well as changes in the lattice parameters of  $\sigma$  and the matrix phases with a time resolution of 4 s.

Table 1 – Chemical composition of HDSS (wt. %)

C	Mn	Si	Cr	Ni	Mo	N	Cu	Fe
0.005	2.93	0.19	26.3	6.92	4.61	0.37	0.2	Bal.

In combination, we used thermo-kinetic simulation to evaluate the mechanism of formation of  $\sigma$  phase. Based on the revised thermodynamic modeling of the Fe-Cr-Mn-Mo-Ni system [1], Matcalc [2] as well as Dictra were used to evaluate the early stage precipitation and associated evolution of  $\sigma$  phase fraction.

**Results and Discussion**

Our initial results [3] show a eutectoid like microstructure as mentioned in the literature. Nevertheless, our revision of the thermodynamic modeling [1] of the multicomponent system Fe-Cr-Mo-Mn-Ni demonstrates a non-eutectoid reaction for the formation of the  $\sigma$  phase at high temperatures. Thus, further investigations were carried out in order to understand the mechanism of formation of  $\sigma$  phase in HDSS as well as its fast precipitation behavior.

In-situ measurements at the synchrotron for different annealing temperatures allowed us to get the precipitation kinetic in HDSS in real time scale. It was found that while the ferrite dissolves, austenite forms followed by  $\sigma$ , consuming all the ferrite. One explanation of the fast precipitation of  $\sigma$  phase is enrichment of Mo at the interface between ferrite and austenite, promoting the formation of  $\sigma$  phase, which was confirmed experimentally by EPMA measurements. Also, monovariant reaction was confirmed experimentally [3] forming a  $\sigma$ -rim at  $\gamma/\gamma$  interface.

Comparing the theoretical time-temperature-precipitation (using Matcalc based on mean field approach) for HDSS to experiments prove that using the nominal composition of the steel in the simulation resulted in a too low nose temperature for the computational results (Figure 2 in [2]). Moreover, testing the role of different element enrichment and depletion on precipitation in the simulation showed that also Cr and Ni are important for the precipitation kinetics of  $\sigma$ . Arbitrarily adjusted higher alloying of elements in HDSS in the simulation should indeed be avoided, even though some segregation-like element dynamics is obvious in heat-treated HDSS. In a first step of the implementation of element dynamics in the simulation, segregation as result of casting, representing the first processing step of HDSS, is considered by using Scheil-Gulliver calculations. With the obtained element concentrations, deviating from nominal, we reset the simulation input to a “segregated nominal composition” and simulate the influenced TTP behavior. The results are shown in Figure 1. Indeed, using Scheil-Gulliver segregation simulation does not allow to “picture” all the possible chemical heterogeneities. In order to get in depth of the other causes of Mo enrichment at the interface, Dictra simulation was used to test the role of moving boundary phenomenon. The results show a similar trend as the EPMA measurements, i.e. Mo has high tendency to sit at the interface. It was also found that the dynamics of Mo is really fast which may explain the fast precipitation of the  $\sigma$  phase in HDSS.

Combining synchrotron, EPMA, precipitation thermokinetics and Dictra simulation, we are on the way to a comprehensive understanding of the formation of  $\sigma$  phase in duplex steel grades.

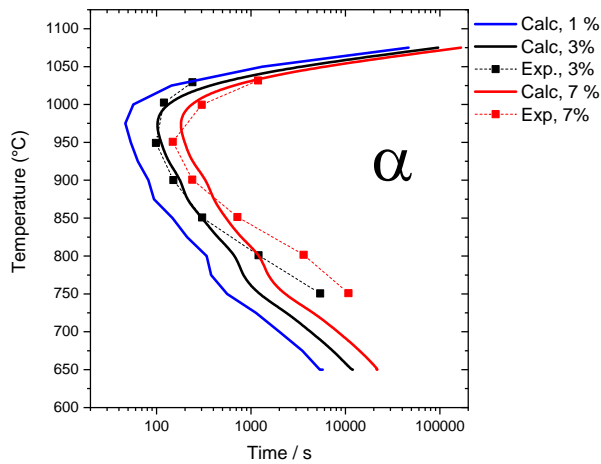


Fig. 1: TTP results of HDSS [2] compared to experiments from Zhang et al. [4] using Scheil-Gulliver results for the segregation of elements.

#### References

- [1] A. Jacob, E. Povoden-Karadeniz, Predictive computations of intermetallic  $\sigma$  phase evolution in duplex steel. I) Thermodynamic modeling of  $\sigma$  phase in the Fe–Cr–Mn–Mo–Ni system, *Calphad Comput. Coupling Phase Diagrams Thermochem.* **2020**, *71*, 101810.
- [2] A. Jacob, E. Povoden-Karadeniz, Predictive computations of intermetallic  $\sigma$  phase evolution in duplex steel. II) Thermo-kinetic simulation in duplex and hyper duplex stainless steels, *Calphad Comput. Coupling Phase Diagrams Thermochem.* **2020**, *71*, 101998.
- [3] S. Kumar, S. Krisam, A. Jacob, F. Kiraly, A. Keplinger, R. Abart, E. Povoden-Karadeniz, Microstructures and element distributions in an aged hyper duplex stainless steel and corresponding hardness variation, *Mater. Des.* **2020**, *194*, 108951.
- [4] B. Zhang, Z. Jiang, H. Li, S. Zhang, H. Feng, H. Li, Precipitation behavior and phase transformation of hyper duplex stainless steel UNS S32707 at nose temperature, *Mater. Charact.* **2017**, *129*, 31–39.

## O-TCP-02

## Structural transformation of the $\sigma$ phase in the Cr–Mn system studied by *in situ* powder neutron diffraction

Jean-Marc Joubert

Univ Paris Est Creteil, CNRS, ICMPE, UMR 7182, 94320 Thiais, France, joubert@icmpe.cnrs.fr

### Introduction

The thermodynamic modeling of the Cr–Mn system by the Calphad method is used for the constitution of thermodynamic databases able to predict the phase amounts and microstructures in multi-component steel systems. In this system, the  $\sigma$  phase deserves a special attention. It is a brittle intermetallic phase that should absolutely be avoided in commercial alloys. The structure of the  $\sigma$  phase is known. It is a Frank-Kasper phase containing 5 sites in the space group  $P4_2/mnm$  [1]. The phase is present in many other transition metal intermetallic systems. It is characterized by a high degree of non-stoichiometry accommodated by atom mixing on the different sites of the structure. As it also exists in Cr–Fe system, its stability in Cr–Mn system and its extension into the ternary Cr–Fe–Mn system should be considered of prime interest in the frame of steel application.

However, its stability in Cr–Mn system is still matter of great uncertainty. There are reports by different experimental techniques (differential thermal analysis, magnetic susceptibility, thermal expansion) of a phase transition as a function of temperature [2]. The transition is represented in the phase diagram of Fig. 1.

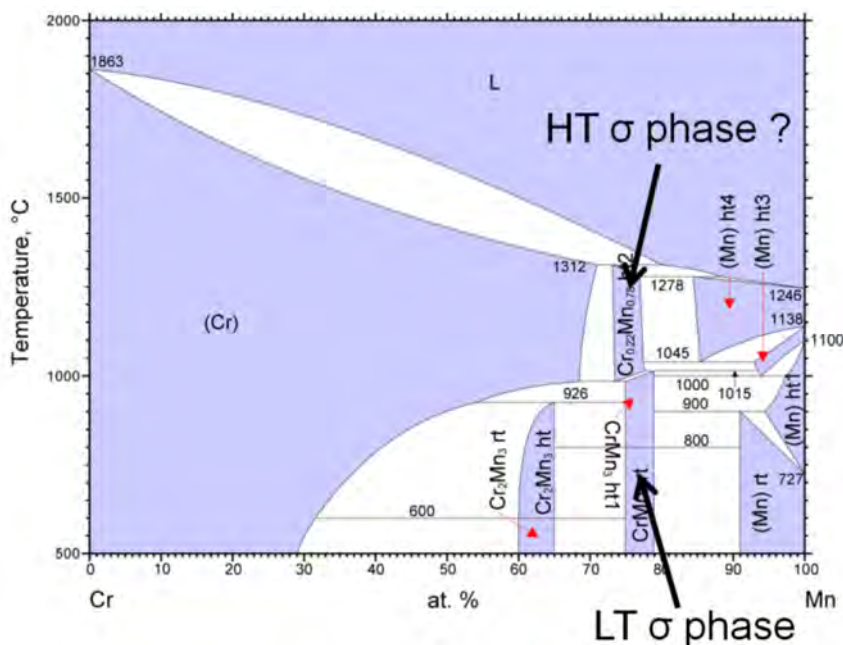


Fig. 1: phase diagram of the Cr–Mn system

The presence of a clear thermal arrest and a huge jump of the thermal expansion at  $\sim 1000^\circ\text{C}$  is in favor of a first-order phase transition. As alloys quenched from the high and low temperature fields both give the same X-ray diffraction pattern of the  $\sigma$  phase, the transformation was thought to be an order-disorder phase transition keeping the average structure of the  $\sigma$  phase. From X-ray diffraction, as Cr and Mn cannot be distinguished, one can neither prove nor disprove the ordering or disordering between the two elements. On the other hand, we had carried out room temperature neutron diffraction measurements of quenched samples from the high and low temperature fields. We observed the same state of order *i.e.* no difference of site occupancies refined by the Rietveld method was detected between the samples [1] in spite of the good diffraction contrast between the two elements.

To summarize, all the techniques used up to now to study the phase transition in the  $\sigma$  phase are indirect techniques. They show a transition at  $\sim 1000^\circ\text{C}$  but do not demonstrate the structural nature of the transition. Our structural *ex situ* neutron diffraction measurement was in contradiction with the existence of a transition. The only possibility to reconcile all the experiments was to suppose that the high temperature phase cannot be retained by quenching. It should therefore be studied by *in situ* diffraction. X-ray cannot be used due to the poor diffraction contrast between the two elements. On the contrary, neutron diffraction is perfectly adapted to the measurement of site occupancies when Cr ( $b=3.6$  fm) and Mn ( $b=3.7$  fm) are mixed. The hypothesis of a phase transition should therefore be clearly seen if it exists.

The present work is therefore reporting new *in situ* neutron diffraction experiments that have been carried out as a function of temperature for two  $\sigma$  phase samples.



### Materials and Methods

The samples have been synthesized by induction melting of the pure melting followed by two annealing treatments: one at high temperature (1100°C, one week) to homogenize the samples, one at low temperature (700 °C, three weeks) to equilibrate the samples in the low temperature phase field. The samples were reduced into powder. The neutron diffraction experiment was performed at the ILL on D1B instrument. The powders were contained in a Nb can, fitted in the high-temperature furnace. Temperature scans were programmed from room temperature up to 1100 °C (heating and cooling) and the diffraction was measured as a function of temperature continuously in different temperature scans. Phases were identified and the neutron diffraction patterns were refined using the Rietveld method. This includes an accurate site occupancy refinement when the  $\sigma$  phase is present.

### Results and Discussion

The main finding of the present work was the identification of the transition occurring around 1000 °C. The results show that it is not an order-disorder transition within the  $\sigma$  phase like previously proposed but rather a phase transition from  $\sigma$  to a *bcc* disordered solid solution. This transformation is similar to what is present in other systems: Cr–Fe, Co–Cr, Mn–V...

The transformation could not be quenched *i.e.* the *bcc* phase transforms back to the  $\sigma$  phase whatever the cooling rate operated during the *in situ* experiment. This explains why this transformation could not be identified in previous work. Site occupancies and lattice parameters were analyzed as a function of temperature. The neighboring phase Cr<sub>2</sub>Mn<sub>3</sub> was also studied in the frame of this investigation.

This study eventually led to an update of the phase diagram.

### References

- [1] J.-M. Joubert, Crystal chemistry and Calphad modelling of the  $\sigma$  phase, *Prog. Mater. Sci.* **2008**, *53*, 528-583.
- [2] E. Wachtel, C. Bartelt, Suszeptibilitätsmessungen im System Chrom-Mangan, *Z. Met.kd.* **1964**, *55* (1), 29-36.

**O-HEA-01****Single-crystal mechanical properties of equiatomic CrMnFeCoNi high-entropy alloy and its derivative equiatomic quaternary and ternary medium-entropy alloys**Haruyuki Inui<sup>1,2</sup><sup>1</sup>Department of Materials Science and Engineering, Kyoto University, 606-8501 Kyoto, Japan<sup>2</sup>Center for Elements Strategy Initiative for Structural Materials (ESISM), Kyoto University, 606-8501 Kyoto, Japan**Introduction**

High-entropy alloys (HEAs) comprise a novel class of scientifically and technologically interesting materials. Among these, the equiatomic CrMnFeCoNi alloy with the face-centered cubic (FCC) structure and some of its derivative equiatomic quaternary and ternary alloys are noteworthy because its ductility and strength increase with decreasing temperature while maintaining outstanding fracture toughness at cryogenic temperatures. However, the origin of these excellent mechanical properties has yet to be understood clearly, because mostly of the lack of studies using their single crystals. In the present study, the plastic deformation behavior of single crystals of the FCC equiatomic CrMnFeCoNi high-entropy alloy and its derivative quaternary (CrFeCoNi) and ternary (CrCoNi) medium-entropy alloys has been investigated in a temperature range of 10–1273 K.

**Results and Discussion**

Deformation occurs via slip of the  $\{111\}\langle 110 \rangle$  system exclusively in the whole temperature range for all alloys investigated. The CRSS values increase with decreasing temperature, especially below room temperature, so that the concept of ‘stress equivalence’ is obeyed for all alloys investigated (Fig. 1). This is a clear indication that the strength of these alloys should be described by a mechanism based on solid-solution hardening. Dislocations are smoothly curved in the slip plane without any preferred line orientation, indicating no significant anisotropy in mobilities of edge and screw segments. Planar  $\frac{1}{2}\langle 110 \rangle\{111\}$  dislocations dissociate widely into Shockley partials for all alloys investigated, indicating their low stacking fault energies. The separation distance for the coupled Shockley partials in the equiatomic CrMnFeCoNi alloy ranges from ~3.5–4.5 nm near the screw orientation to ~5–8 nm near the edge, yielding a stacking fault energy of  $30 \pm 5$  mJ/m<sup>2</sup> [1]. The separation distance for the equiatomic CrCoNi alloy is much larger, yielding the stacking fault energy of  $11 \pm 3$  mJ/m<sup>2</sup>. The observed stacking fault energies of the three alloys investigated seem to be scaled well with the averaged valence electron concentration.

The CRSS values extrapolated to 0 K for polycrystals of equiatomic quinary, quaternary and ternary alloys are reported to be well scaled with the mean-square atomic displacement from the regular FCC lattice points (calculated based on density-functional theory) [2,3]. This seems also the case for the CRSS values at 10 K for single crystals of the present three alloys, although some modifications are definitely needed. Deformation twinning occurs on the conjugate system in the form of the Lüders type deformation in the later stage of deformation at low temperatures in all of the three alloys. While deformation twinning is observed only at low temperatures (typically at 77 K) for CrMnFeCoNi and CrFeCoNi, it is observed even at room temperature for CrCoNi. This is consistent with the observed low stacking fault energy in CrCoNi.

The twinning stress in CrCoNi exhibits a rather steep temperature dependence, in contrast to the previous belief that the twinning stress in FCC alloys does not exhibit significant temperature dependence. On top of that, the twinning stresses at 77 K observed in the three alloys investigated are scaled negatively with the stacking fault energy, whereas the opposite trend is claimed to be true for conventional FCC alloys.

**Conclusions**

- (1) All the three alloys (CrMnFeCoNi, CrFeCoNi & CrCoNi) behaves as a normal FCC solid-solution alloy with reasonable temperature dependence and strain-rate sensitivity of CRSS, although the strength level is far higher than other usual FCC alloys.
- (2) All the three alloys exhibit a low stacking fault energy (12~30 mJ/m<sup>2</sup>) and are therefore susceptible to deformation twinning at low temperatures (77 K), although twinning is observed even at room temperature for CrCoNi with the lowest stacking fault energy.
- (3) Scaling the 0 K strength with MSAD is successful also for single crystals.
- (4) The stacking fault energy is well correlated negatively with the valence electron count.
- (5) The twinning stress is well correlated negatively with the stacking fault energy.

**Acknowledgements**

This work was supported by Grant-in-Aid for Scientific Research on Innovative Areas, ‘High Entropy Alloys – Science of New Class of Materials Based on Elemental Multiplicity and Heterogeneity’ and the Elements Strategy Initiative for Structural Materials (ESISM) from MEXT, Japan.

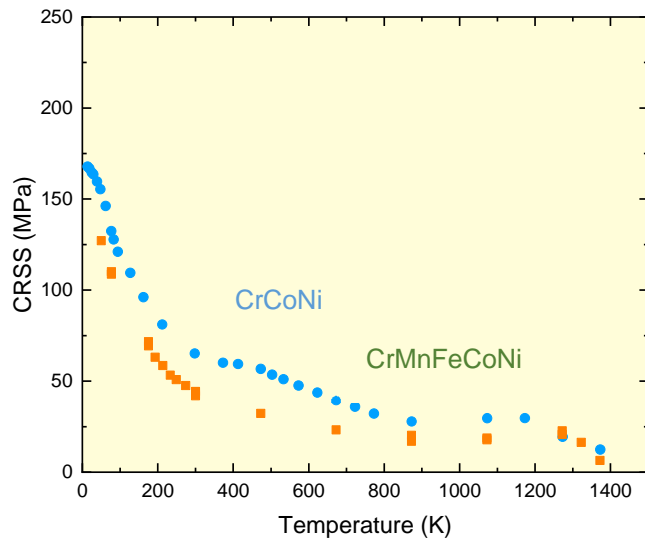


Fig. 1. Temperature dependence of CRSS for CrMnFeCoNi [3] and CrCoNi.

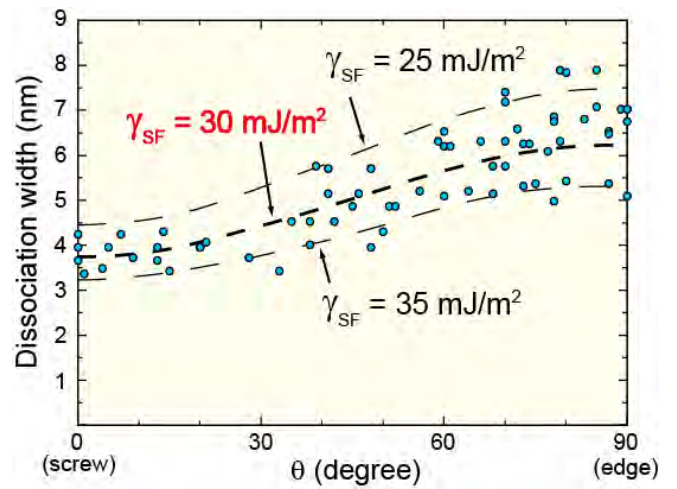


Fig. 2. (a) Dislocation structure and dislocation dissociation in CrMnFeCoNi deformed at room temperature [1].

References

- [1] N.L. Okamoto et al., Scientific Reports. **2016**, *6*, 35863.
- [2] N.L. Okamoto et al., AIP Advances. **2016**, *6*, 125008.
- [3] M. Kawamura et al., Acta Mater. **2021**, *203*, 116454.

**O-HEA-02****Study of structural defects in binary and ternary B2 alloys of the AlCoCrFeNi system**Guy Hillel<sup>1</sup>, Daniel Vidal<sup>1</sup>, Itzhak Edry<sup>2</sup>, Malki Pinkas<sup>2</sup>, David Fuks<sup>1</sup> and Louisa Meshi<sup>1</sup><sup>1</sup>Department of Materials Engineering, Ben-Gurion University of the Negev, 8410501 Beer-Sheva, Israel, guyhill@post.bgu.ac.il, Louisa@bgu.ac.il<sup>2</sup>Nuclear Research Center Negev, 841900 Beer-Sheva, Israel**Introduction**

AlCoCrFeNi high entropy alloy (HEA) shows superior strength at high temperatures as well as good corrosion resistance properties [1]. AlCoCrFeNi equiatomic alloy solidifies in a dendritic manner, where the dendrite (DR) area is enriched in Al-Ni and the inter-dendrite (ID) is Cr-Fe rich; Co has a minor tendency for segregation [2]. Although the DR and ID regions differ in their morphologies, both areas contain Fe-Cr rich disordered BCC (A2) and Al-Ni rich ordered BCC (B2-CsCl) phases as particles (i. e. discontinues phase) or matrix (continues phase).

Despite the obvious potential of the AlCoCrFeNi for engineering applications, its commercialization is hindered, mostly, due to the partial understanding of the alloys` behavior at high temperatures and stability of the constituting phases. The formation of the  $\sigma$  phase at intermediate temperatures ( $\sim 500$ - $750$  °C), which embrittles the alloy, hampers AlCoCrFeNi alloy`s commercialization [3]. It should be noted that several researchers reported that  $\sigma$  phase appears only in the ID region, but not in the DR.

In general, anti-phase boundaries (APB), which appear often in ordered structures, were suggested as having an influence on the magnetic [4], mechanical [5] and plastic [6] properties. Recently [3,7], it was reported that B2 phase, appearing in the AlCoCrFeNi alloy, contains APBs (parallel to  $\{110\}$  planes). In binary B2 structures, dislocations bounding APBs, parallel to  $\{110\}$  planes, were characterized as  $a/2\langle 111 \rangle$  super-partials [8]. In the AlCoCrFeNi HEA, these APBs exhibited different extent of ordering (imposing different strain field in the B2 grains) as a function of region: long range in the DR region and short range in the ID region [3,7]. This fact may provide an explanation for the stress suppressed phase transformation of the  $\sigma$  phase in the DR region.

Current research presents our first attempt to understand these structural defects in order to control their formation in the future. For this purpose, theoretical calculations of stability of APBs in binary B2 phases with and without doping were performed in parallel to experimental characterization of structural defects, namely dislocations and APBs, appearing in these alloys. We have found that out of three B2 binary phases possible in the AlCoCrFeNi system (AlCo, AlNi and AlFe) – AlFe has the lowest energy of formation of APBs. Therefore, this binary system as well as ternaries (doped by Cr and Ni in such way that Cr will substitute Al and Ni – Fe) were used as a starting point for the experimental work.

**Materials and Methods**

AlFe binary alloy was purchased in American Elements (USA). Composition, as measured by Energy Dispersive Spectroscopy (EDS) in Scanning Electron Microscope (SEM), was found to be 48 at.% Al, 52 at.% Fe. Fe(Al<sub>0.6</sub>Cr<sub>0.4</sub>) and Al(Fe<sub>0.6</sub>Ni<sub>0.4</sub>) ternary alloys were produced by arc melting. The purity of the raw metals was above 99.9 %. The ingot was re-melted three times in order to ensure chemical homogeneity. Main tool used in the experimental part of this research was Transmission Electron Microscopy (TEM). Structural characterization was performed on JEOL JEM-2100F (Japan) operating at 200 kV. For this purpose, discs 3 mm in diameter were mechanically grinded on 5 $\mu$ m SiC papers down to a thickness of approximately 100  $\mu$ m and ion milled using Gatan Precision Ion Polishing System - PIPS2 (USA) with 5 keV Ar ions to achieve electron transparency.

In parallel to the experimental path, theoretical calculations were performed using Density Functional Theory (DFT) DFT calculation in the framework of Full Potential Linearized Augmented Plane Waves (FP-LAPW) method were performed [9]. Total supercell energy was obtained from spin-polarized calculations. WIEN2k code (version 17.1) was applied for calculations [9-11].

**Results and Discussion**

DFT calculations show that in the FeAl system, Cr and Ni decrease the magnitude of energy of formation of APB,  $E_{APB}$ . Moreover, doping elements do not show the tendency to segregate to APBs and remain in grains although influence  $E_{APB}$ .

Purchased AlFe binary alloy was found to be B2 single phase with no presence of APBs. Dislocations analysis performed using 2-beam condition method and trace analysis, based on TEM imaging [12], allowed to conclude that the alloy contains two different slip systems –  $\{001\}\langle 100 \rangle$  and  $\{110\}\langle 111 \rangle$ , see Fig. 1a.

Fe(Al<sub>0.6</sub>Cr<sub>0.4</sub>) and Al(Fe<sub>0.6</sub>Ni<sub>0.4</sub>) ternary alloys were also found to be B2 single phase (X-ray diffraction data is not shown here). Cr addition exhibited significant presence of APBs, see Fig. 1b. Addition of Ni in the as cast state has not exhibited APBs defects, but dislocation density as well as variety of vector Burgers types increased.

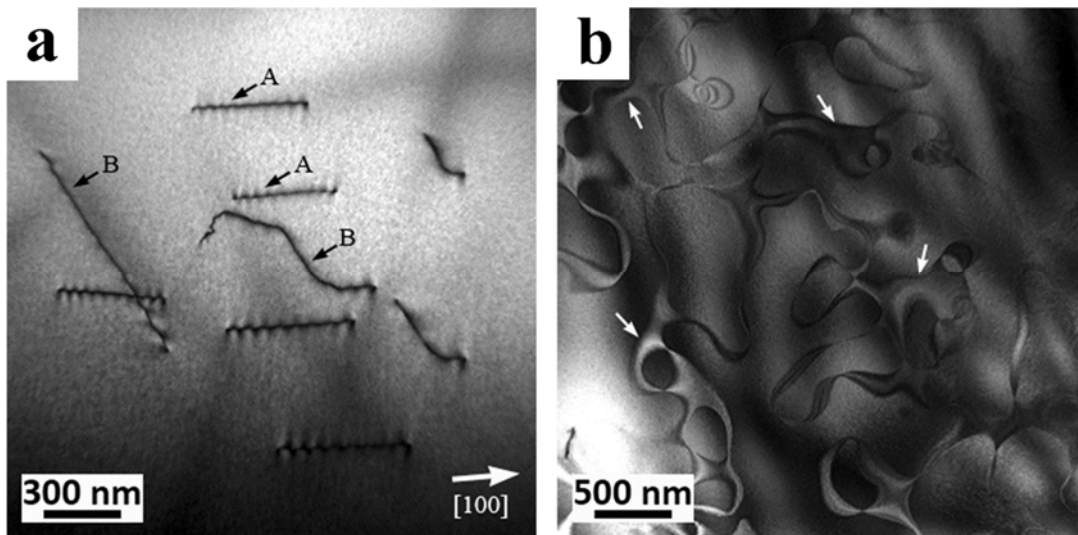


Fig. 1: TEM image of (a) AlFe alloy, exhibiting two different slip systems of dislocations: A  $\{001\}\langle 100\rangle$  and B  $\{110\}\langle 111\rangle$ ; (b) Fe(Al<sub>0.6</sub>Cr<sub>0.4</sub>) alloy. APBs are marked by arrows.

In our presentation, characterization of structural defects appearing in three studied systems will be shown and experimental results will be related to the theoretical calculations.

#### References

- [1] Y. Shi, B. Yang, P.K. Liaw, *Metals*. **2017**, *7*, 43-61.
- [2] Y.P. Wang, B.S. Li, M.X. Ren, C. Yang, H.Z. Fu, *Mater. Sci. Eng. A*. **2008**, *491*, 154–158.
- [3] L. Meshi, Y. Linden, A. Munitz, S. Salhov, M. Pinkas, *Mater. Character.* **2019**, *148*, 171-177.
- [4] C. Mangler, C. Gammer, *Journal of Alloys and Compounds*. **2011**, *509*, 389-392.
- [5] B. Viguier, M. Martinez, J. Lacaze, *Intermetallics*. **2017**, *83*, 64-69.
- [6] Y. Koizumi, S.M. Allen, Y. Minamino, *Acta Materialia*. **2008**, *56*, 5861-5874.
- [7] Y. Linden, M. Pinkas, A. Munitz, L. Meshi, *Scripta Mater.* **2017**, *139*, 49-52.
- [8] P.R. Munroe, I. Baker, *Acta metallurgica et materialia*. **1991**, *39(5)*, 1011-1017.
- [9] K. Schwarz, P. Blaha, G.K.H. Madsen, *Comput. Phys. Commun.* **2002**, *147*, 71-76.
- [10] S. Cottenier, *Density Functional Theory and the Family of (L) APWMethods: A Step-by-Step Introduction*, Instituut Voor Kern-en Stralingsfysica, K.U. Leuven, Belgium, **2002**, ISBN 90-807215-1-4 [http://www/wien2k.at/reg\\_user/textbooks](http://www/wien2k.at/reg_user/textbooks).
- [11] K. Schwarz, G.K.H. Madsen, D. Kvasnicka, J. Luitz, *WIEN2k, An Augmented Plane Wave+Local Orbitals Program for Calculating Crystal Properties*, Techn. Universitat, Wien, Austria, **2017** (ISBN 3-9501031-1-2, revised edition WIEN2k 17.1 (Release 07/03/2017)).
- [12] J.W. Edington, K.T. Russell, *Macmillan International Higher Education*. **1977**, 87-88, 118-128.



**O-HEA-03****Effect of Mo and Ta on a duplex bcc+orthorhombic refractory complex concentrated alloy using diffusion couples**

Zhao Zhao-Huvelin<sup>1</sup>, Antoine Lacour-Gogny-Goubert<sup>2</sup>, Ivan Guillot<sup>3</sup>, Jean-Philippe Couzinie<sup>3</sup>  
and Philippe Vermaut<sup>4</sup>

<sup>1</sup>DMAS, ONERA, Université Paris Saclay, 92320 Châtillon, France, zhao.huvelin@onera.fr

<sup>2</sup>LMS, UMR CNRS 7649, Ecole Polytechnique, 91128 Palaiseau Cedex, France

<sup>3</sup>Université Paris Est Creteil, CNRS, ICMPE, UMR7182, 94320 Thiais, France

<sup>4</sup>PSL Research University, Chimie ParisTech CNRS, Institut de Recherche de Chimie Paris, 75005 Paris, France

**Introduction**

The use of intermetallic alloys remains promising for high temperature applications in aircraft engines. The aerospace industry still requires low density alloys able to work in the range of 800 °C to 1000 °C while keeping high temperature mechanical and environmental properties. To meet such requirements, several trails were explored. The most recent concept has led to the development of high entropy alloys (HEAs) [1-3] and their derivative, so called complex concentrated alloys (CCAs). In the present work, we are interested in the formation of a bcc + orthorhombic (bcc+O) microstructure in the Ti–Nb–Al system. Such development of concentrated multicomponent Ti–Nb–Al-based alloys faces the ongoing challenge of the phase prediction since, previous attempts of designing HEAs alloys by using CALPHAD modelling [4], clearly demonstrated that this approach can provide reliable predictions of number and nature of stable phases but fails to accurately determine transition temperature, phase compositions and phase fractions. Furthermore, none of the previous methods allow to determine precisely the content of alloying element able to retain the bcc+O microstructure with a high-volume fraction of the O phase. Therefore, another approach was chosen in this study, inspired by previous studies that used diffusion couples/multiples to map phase diagrams [5]. In this work, diffusion couples were implemented to investigate the effect of Mo and Ta on a reference quaternary alloy Ti<sub>42</sub>Nb<sub>42</sub>Al<sub>15</sub>Si<sub>1</sub> with an initial bcc+O microstructure. The stability of the O phase was assessed by quantifying the evolution of the orthorhombic phase fraction according to the content of the alloying elements.

**Materials and Methods**

Alloys were designed so that only two elements diffuse in the different diffusion couples. Three alloys, Ti<sub>42</sub>Nb<sub>42</sub>Al<sub>15</sub>Si<sub>1</sub>, Ti<sub>42</sub>(Nb<sub>17</sub>,X<sub>25</sub>)Al<sub>15</sub>Si<sub>1</sub>, with X = Mo or Ta [6,7] were prepared by vacuum arc-melting using raw elements with high purity ( $\geq 99.99$  wt.%) to obtain ingots of 48 × 10 × 17 mm<sup>3</sup>. Diffusion couple assemblies have been described in detail elsewhere [7]. The assembly was then in a furnace at 1300°C/40h under 1 atm of static Ar atmosphere. This assembling step allows to obtain the diffusion gradient. They were then wrapped in tantalum foils and placed in sealed quartz tubes under a vacuum of 10<sup>-4</sup> Pa for precipitation heat treatment at 800 °C and 900 °C for different time periods between 8 and 24 h, followed by furnace cooling. All couples were analyzed by scanning electron microscopy equipped with a backscattered electron (BSE) and an EDS-SAMPLUS energy dispersive spectroscopy (EDS) detector. The concentration profiles were quantitatively measured by coupling EDS-WDS in comparison to the pure Nb, Si, Mo, Ta standards and stoichiometric Ti<sub>3</sub>Al standard. Nb, Ti and Al contents were measured by EDS using IDFIX software and Ta, Si contents by WDS using XMASPLUS software. Phase volume fractions were quantified by image analysis with ImageJ software using ten different micrographs for each couple. More details on the approach used to analyze the diffusion couples have been described in [7].

**Results and Discussion*****After assembling treatment***

Fig. 1(a) shows a SEM-BSE image of the initial interface after assembling of the Mo/Nb couple. Some silicides of (Ti,Nb,X)<sub>5</sub>(Si,Al)<sub>3</sub> composition (X = Mo, Ta) are observed in dark grey in the matrix. EDS profiles in Fig. 1(b) gives the quality of the assembly and the chemical gradient across the interface. Measurements confirm that only two elements have diffused during the treatment. The gradient extends from 25 at.%(Mo) to 0 at.%(Mo) and from 17 at.%(Nb) to 42 at.%(Nb) over approximately 300 μm. A slight evolution of the Al content can also be observed and is due to a difference in the nominal composition of the Ti(Nb,Mo)AlSi end member. However it is very limited if compared to Mo gradient.



Fig. 1 : Mo/Nb Couple after assembling at 1300 °C for 40 h, (a) SEM-BSE showing the EDS dots and (b) the corresponding concentration profiles (at.%).

### After precipitation treatment

After precipitation treatment at 800 °C and 900 °C, the evolution of the microstructure has been characterized by SEM (Fig. 2(a)). The microstructure changes from a single bcc phase area on the left (high Mo content) to a two-phase bcc+O (black needles) area on the right (lower Mo content). The profiles obtained by applying the method of analysis on the Mo/Nb couple after precipitation treatment at 800 °C and 900 °C is given in Fig. 2(a). The phase volume fraction ( $f_v$ ) measured on the Ti42Nb42Al15Si1 at the corresponding temperatures are also reported (open, red circle and purple square) on the graph Fig.2. On both curves, the orthorhombic phase fraction remains constant then decreases suddenly with increasing Mo content. For Mo/Nb couple, at 800 °C and 900 °C, the threshold values are respectively 5.5 at.%(Mo) and 3.5 at.%(Mo). The linear extrapolation of the curves gives an approximation of the end of the bcc+O domain which is around 9 at.%(Mo) and 6.5 at.%(Mo) at 800 °C and 900 °C, respectively. The same method was then applied to the couple of Ta/Nb, and the corresponding profiles showing the evolution of the orthorhombic phase fraction is shown in Fig. 2(b). The orthorhombic volume fraction does not change drastically with Ta content and the duplex microstructure is maintained up to 25at.%(Ta) at both 800°C and 900°C. The O phase fraction remains high and above 30 % at 800°C, on all of the concentration range. At 900 °C it gradually decreases from 38 % of O phase to 12 % between 0 at.%(Ta) and 18 at.%(Ta) and then it steadily increases until it reaches 26 % of O phase at 25 at.%(Ta).

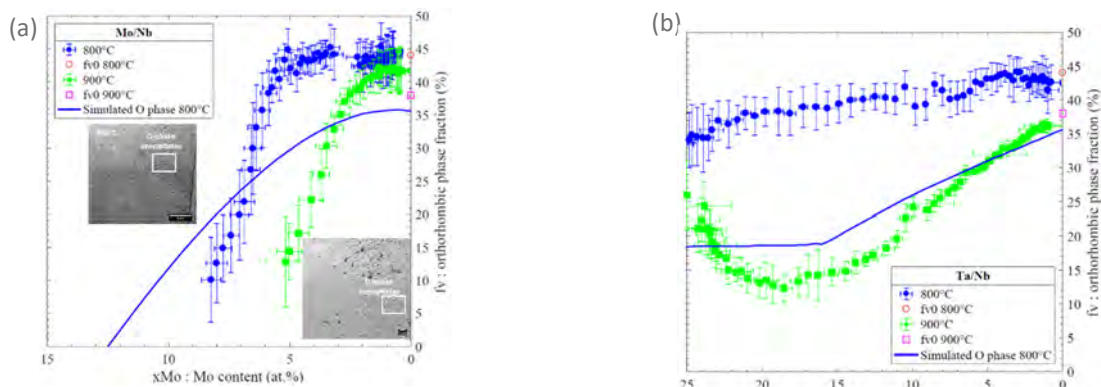


Fig. 2: Experimental and simulated orthorhombic phase fraction (%) evolution according to element content (at.%) for, (a) Mo/Nb, (b) Ta/Nb, couples after precipitation at 800 °C and 900 °C.

Results on both Mo/Nb and Ta/Nb diffusion couples indicate that a heat treatment at 900 °C cause a strong decrease of the O phase fraction and suggest that the systems approach the solvus of the O phase (Fig. 2). The phenomenon can be understood considering that the O phase is stable on a very narrow domain of composition up to 1000 °C [8]. Furthermore the evolution of the O-phase fraction according to the Ta content at 900 °C (Fig. 2b) is explained by the existence of the two different structures of the O-phase of the Ti-Nb-Al system: the O1 phase is expected at high temperature whereas the O2 phase is predicted at low temperatures [9]. Both O1 and O2 own the same space group but only differ from the lattice site occupancies. On that basis three scenarios have been put forward to explain such evolution, and described in detail in [7].

### References

- [1] B. Cantor, I.T.H. Chang, P. Knight, A.J.B. Vincent, *Materials Science of Engineering A*, **2004**, A375, 213–218.
- [2] J.W. Yeh, *et al.*, *Metallurgical and Materials Transactions A*, **2004**, A35 (8), 2533–2536.
- [3] O.N. Senkov, G.B. Wilks, D.B. Miracle, C.P. Chuang, P.K. Liaw, *Intermetallics*, **2010**, 18 (9), 1758–1765.
- [4] O.N. Senkov, J.D. Miller, D.B. Miracle, C. Woodward, *CALPHAD*, **2015**, 50, 32–48.
- [5] J.C. Zhao, *Journal of Materials Research*, **2001**, 16 (6), 1565–1578.
- [6] L. Sikorav, Ph.D. thesis, Université Pierre et Marie Curie, **2017**.
- [7] A. Lacour-Gogny-Goubert, Z. Huvelin, *et al.*, *Intermetallics*, **2020**, 124, 106836.
- [8] V.T. Witusiewicz, A.A. Bondar, U. Hecht, T.Ya. Velikanova, *Journal of Alloys Compd.*, 2009, 472 (1), 133–161.
- [9] K. Muraleedhran, T.K. Nandy, D. Banerjee, *Intermetallics*, **1995**, 3, 187-199.

## O-HEA-04

## A novel alloy development approach - biomedical high-entropy alloys

Maximilian Regenberg, Janett Schmelzer, Georg Hasemann and Manja Krüger

Otto-von-Guericke-University Magdeburg, Institute of Materials and Joining Technology, 39106 Magdeburg, Germany, maximilian.regenberg@ovgu.de

## Introduction

The modern materials class of high-entropy alloys (HEAs) gained tremendous attention in the scientific community over recent years, which can be attributed to two main reasons: Firstly, the new concept of combining several elements (at least 5 principal elements with concentrations between 5 and 35 at.% [1]) in contrast to conventional alloys, mostly containing only two or three major elements. This results in a broad variety of possible combinations thus leading to completely novel alloys with exceptional properties. Secondly, recently developed refractory metal based high-entropy alloys (RHEAs) have shown properties that are superior to the ones of current state-of-the-art alloys, which are attributed to several unique thermodynamic effects [2,3]. However, besides the outstanding mechanical properties, abrasion resistance and thermal resistance, a vast variety of chemical elements used in RHEAs also belongs to the category of biocompatible elements (exemplified in Figure 1), hence leading to potentially new biomedical materials.

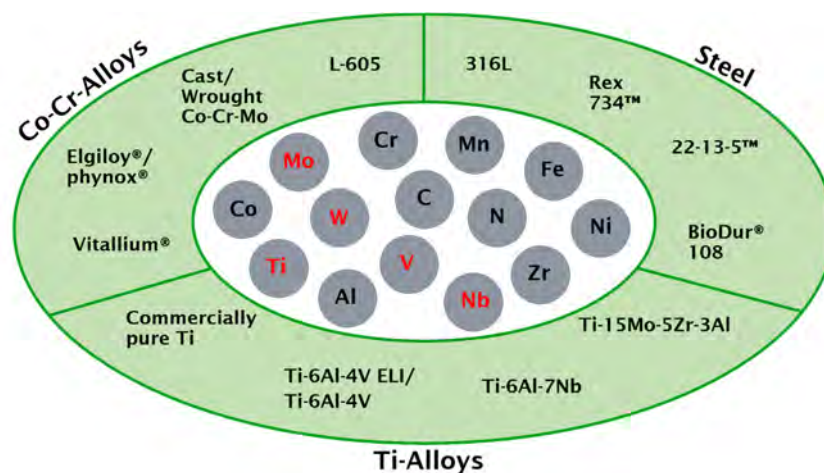


Fig. 3: Schematic representation of state-of-the-art biomaterials and the corresponding chemical elements; Refractory metals of potential interest are highlighted.

To meet the demands for biomedical applications, three main criteria must be fulfilled: Excellent mechanical properties (regarding the force transmission between implant and bone), corrosion resistance (prevention of corrosive damage to the implant) and biocompatibility (no tissue damage by the implant material or by corrosive/ abrasive particles) [4]. Our current research targets these requirements on the basis of previous investigations regarding Mo-Nb-V-W-Ti high-entropy alloys [5], which have confirmed promising mechanical properties. Furthermore, the works from Shi et al. [6] concerning the corrosive capabilities of HEAs are considered to support our theories. However, due to their good biocompatibility [7,8], we have chosen an equiatomic composition of Ta, Nb and Ti as base material for the experiments.

## Materials and Methods

For sample production, high purity elemental chips or flakes of Ta (99.9 %), Nb (99.9 %) and Ti (99.6 %) were used as starting materials and were carefully weighed in. The alloying process was carried out in a conventional arc-melting device under Ar atmosphere. The sample was re-melted five times to ensure sufficient homogeneity of the alloying elements. Afterwards, the produced oblong-shaped (due to the use of an elongated mold) melted product was cut into 2 mm thick slices by means of electric discharge machining (EDM). One slice was used for microstructural analysis and thus metallographically prepared (subsequently grinded with SiC paper under flowing water and polished) afterwards. The remaining slices were cleaned from the EDM-burr and grinded to a defined grit size of 1200 under flowing water. To identify the phases present, X-ray diffraction analysis (XRD) was performed on the samples, using a X'Pert Pro (PANalytical, Almelo, Netherlands). Microstructural observations were carried out by means of scanning electron microscopy (SEM; EVO 15, Zeiss, Oberkochen, Germany), using back-scattered electron (BSE) imaging. To determine the elemental distribution and the chemical composition of the alloy, (Si(Li))-detector Energy-dispersive X-ray spectroscopy (EDS) analysis, equipped with Genesis software (EDAX, Mahwah, NJ, USA) was conducted. Furthermore, to examine and evaluate the biocompatibility of the Ta-Nb-Ti alloy produced, cell cultivation experiments were carried out on the defined surface of the specimens and compared to state-of-the-art biomaterials such as Co-28Cr-6Mo or Ti-6Al-4V, as well as to samples of pure Ta, Nb and Ti.

### Results and Discussion

XRD-analysis revealed that the Ta-Nb-Ti-alloy consists of a single-phase body centered cubical (bcc) crystal structure with an  $Im\bar{3}m$  space group. However, the results of the BSE microstructural analysis (Fig. 4) show a dendritic structure with clearly distinguished interdendritic regions (darker colored regions). EDS-analysis by means of element mappings indicated a higher fraction of high melting Ta in the dendritic crystals, whilst the lower melting Ti was enriched in the interdendritic regions. Nb exhibits an intermediate melting temperature in the alloying composition present, thus being present in the dendrites, as well as predominantly in the interdendritic regions. The observed segregation is attributed to the difference in melting temperatures of the components [5]. However, it is expected that long-term heat treatment will reduce the segregation effects [9]

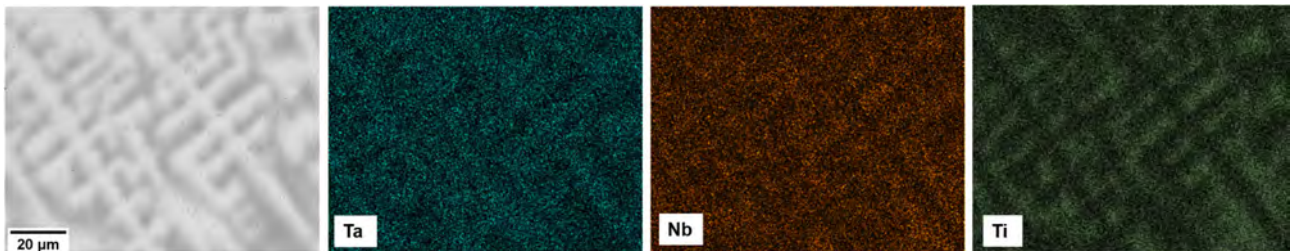


Fig. 4: EDS mappings of the Ta-Nb-Ti alloy.

In ongoing investigations, we use the as-cast alloy for cell cultivation experiments. To determine and evaluate the interaction between the material and the attached tissue (rather than the cells and different surface structures), a comparable surface grade was set on all materials tested. This was achieved by using the same size 1200 grit SiC grinding paper and different grinding times (depending on the hardness, respectively abrasion resistance of the material grinded) for all samples. The surface roughness of the different specimens is validated by using a confocal microscope, as well as a contact angle measuring device. To compare the Ta-Nb-Ti alloy to other biomaterials, osteoblasts and other cultures are then used and cultivated on the materials surfaces. The cell-growth regarding size and numbers is analyzed subsequently and compared to the publications of other working groups (f.e. Nagase et al. [10] with similar approaches to this novel topic of material development). For further investigations, results regarding the different base elements (Ta, Nb and Ti in the present study), as well as various alloying compositions (thus resulting in different microstructures) are to be examined. This helps to generate an understanding for microstructure-growth correlations in terms of f.e. preferred phases and/ or phase combinations (such as intermetallic precipitations or similar).

### References

- [1] M.H. Tsai, J.W. Yeh, High-entropy alloys: A critical review. *Mater. Res. Lett.* **2014**, *2*, 107–123.
- [2] M.C. Gao, P.K. Liaw, J.W. Yeh, Y. Zhang, High-entropy alloys: Fundamentals and applications. **2016**, ISBN 9783319270135.
- [3] E.P. George, W.A. Curtin, C.C. Tasan, High entropy alloys: A focused review of mechanical properties and deformation mechanisms. *Acta Mater.* **2020**, *188*, 435–474.
- [4] S. Houis, U.a. Medizintechnik; E. Wintermantel, S.-W. Ha, Eds.; Springer Berlin Heidelberg: Berlin, Heidelberg, **2009**; ISBN 978-3-540-93935-1.
- [5] M. Regenberg, G. Hasemann, M. Wilke, T. Halle, M. Krüger, Microstructure Evolution and Mechanical Properties of Refractory Mo-Nb-V-W-Ti High-Entropy Alloys. *Metals (Basel)*. **2020**, *10*, 1530.
- [6] Y. Shi, B. Yang, P.K. Liaw, Corrosion-resistant high-entropy alloys: A review. *Metals (Basel)*. **2017**, *7*, 1–18.
- [7] P.J. Andersen, *Metals for use in medicine*, Elsevier Ltd. **2017**, *1*, ISBN 9780081006924.
- [8] L.T. Kuhn, *Biomaterials. Introd. to Biomed. Eng.* **2011**, 219–271.
- [9] O.N. Senkov, D.B. Miracle, K.J. Chaput, J.P. Couzinie, Development and exploration of refractory high entropy alloys - A review. *J. Mater. Res.* **2018**, *33*, 3092–3128.
- [10] T. Ishimoto, R. Ozasa, K. Nakano, M. Weinmann, C. Schnitter, M. Stenzel, A. Matsugaki, T. Nagase, T. Matsuzaka, M. Todai, et al. Development of TiNbTaZrMo bio-high entropy alloy (BioHEA) super-solid solution by selective laser melting, and its improved mechanical property and biocompatibility. *Scr. Mater.* **2021**, *194*, 2–7.



## O-IM-01

**Plastic deformation behavior of metallic-perovskite  $E2_1 M_3AlC_{1-x}$  ( $M = Ni, Co$ )  
observed using nanoindentation measurements**

Yoshisato Kimura<sup>1</sup>, So Murasue<sup>1,2</sup>, Yaw Wang Chai<sup>3</sup>, Manabu Watanabe<sup>1</sup> and Takahito Ohmura<sup>4</sup>

<sup>1</sup>Tokyo Institute of Technology, School of Materials and Chemical Technology, Department of Materials Science and Engineering, 226-8502 Yokohama, Japan, kimura.y.ac@m.titech.ac.jp, watanabe.m.cb@m.titech.ac.jp

<sup>2</sup>Graduate student, *now with*, EBARA Corporation, Japan

<sup>3</sup>Tokyo Institute of Technology, School of Materials and Chemical Technology, 226-8502 Yokohama, Japan, chai.y.aa@m.titech.ac.jp

<sup>4</sup>National Institute for Materials Science (NIMS), Research Center for Structural Materials, 305-0047 Tsukuba, Japan, ohmura.takahito@nims.go.jp

### Introduction

The intermetallic compounds  $E2_1 M_3AlC_{1-x}$  ( $M = Ni, Co$ , and so forth) can be an attractive strengthener of heat resistant alloys, since the  $E2_1$  type ordered crystal structure is similar to that of the  $L1_2$  type  $Ni_3Al$  which is a well-known strengthener of Ni-base superalloys. The ordered structures of  $E2_1$  and  $L1_2$  is differentiated by an interstitial carbon atom whether occupying or not at the cell center of fcc. It can be said that a ternary compound  $E2_1 Co_3AlC_{1-x}$  is stabilized by interstitial carbon atoms, nevertheless  $L1_2 Co_3Al$  does not exist as a stable phase. In the chemical formula of  $Co_3AlC_{1-x}$ ,  $x$  stands for the deficiency of a carbon atom as a vacancy at the carbon-site of the  $E2_1$  ordered structure. Authors' group reported that the extra ordering of C atoms occurs along with the phase transition from  $E2_1 Co_3AlC_{1-x}$  to  $E2_1' Co_3AlC_{0.5}$  at around 1325 K, which results in the existence of C-free (111) planes stacking every other (111) planes. Therefore,  $E2_1' Co_3AlC_{0.5}$  shows excellent ductility and strength using poly- and single-crystal alloys at low temperatures [1,2]. Note that the anti-phase boundary (APB) is formed according to the extra ordering of C atoms. On the other hand, in the case of binary compound  $L1_2 Ni_3Al$ , a C atom behaves like interstitial solute atom but only occupies in the octahedral interstice at the cell center. The objective of the present work is to understand the roles of interstitial C atoms and their effects on mechanical properties in  $E2_1 M_3AlC_{1-x}$  ( $M = Ni, Co$ ) alloys. Mechanical behavior was mainly examined in the atomic-scale using nanoindentation measurements. Additionally,  $E2_1 M_3AlC_{1-x}$  ( $M = Fe, Ti$ ) alloys were also investigated for a comparison.

### Materials and Methods

Single crystals of  $L1_2 Ni_3Al$ ,  $E2_1 Ni_3AlC_{1-x}$ , and  $E2_1' Co_3AlC_{1-x}$  were fabricated by the unidirectional solidification using the optical floating zone melting method (OFZ) under flowing argon gas atmosphere with the positive pressure. Prior to the OFZ, alloy ingots were prepared using arc-melting. The crystal orientation was analyzed by the back reflection Laue method to select planes, [001] and [123], on which nanoindentation and Micro-Vickers hardness measurements were conducted at room temperature. For comparisons, polycrystalline alloys of  $E2_1 Fe_3AlC_{1-x}$  and  $Ti_3AlC_{1-x}$  having coarse grains were also fabricated using arc-melting. Micro-Vickers hardness was measured using the condition; load of 980.7 mN and holding time of 10 s. Nanoindentation measurement was conducted using Berkovich indenter (trigonal pyramid tip) under the condition; the loading rate of 50  $\mu N/s$  and the maximum load of 1000  $\mu N$  (Ni, Fe, Ti-base) and 2000  $\mu N$  (Co-base). Additionally, compression tests were conducted under the initial strain rate of  $10^{-4} s^{-1}$  using specimens of 3 x 3 x 6 mm<sup>3</sup> in dimension.

### Results and Discussion

A load-displacement ( $P-h$ ) curve obtained in nanoindentation is quite informative to consider elastic and plastic mechanical behavior of a material. Typical  $P-h$  curves measured for an  $E2_1 Ni_3AlC_{0.15}$  single crystal are shown in Fig. 1, where the displacement is measured as the penetration depth. So-called pop-in events appear on a  $P-h$  curve of OFZ as-grown specimen (a) as a burst of displacement (or an abrupt jump in displacement). The first pop-in event is thought to be corresponding to the onset of plastic deformation [4,5], for which the generation or/and multiplication of mobile dislocations take place at the critical pop-in load  $P_c$ . Corresponding excursion depth  $\Delta h$  of the pop-in depends on mobile dislocations density and their mobility. On the other hand, the pop-in event is not observed in a specimen (b) which was predeformed about 5 % in compression along the same loading axis with nanoindentation in order to introduce mobile dislocations. This result indicates that the density of introduced mobile dislocations by predeformation is sufficiently high enough to start plastic deformation gradually, and to suppress the possibility of pop-in. We have also found that the pop-in can be reactivated by applying the heat treatment at 337 K for 1 h on the predeformed specimen. Mobile dislocations introduced by predeformation tend to be locked due to the Cottrell type atmosphere formed by the carbon atoms diffusion toward dislocations. Consequently, the pop-in takes place as the locked dislocations are released from locking and solute drag under the sufficiently high applied stress. For instance, this is similar to the well-known Johnston-Gillmann type yielding phenomenon which is governed by the mobile dislocations density and their mobility.



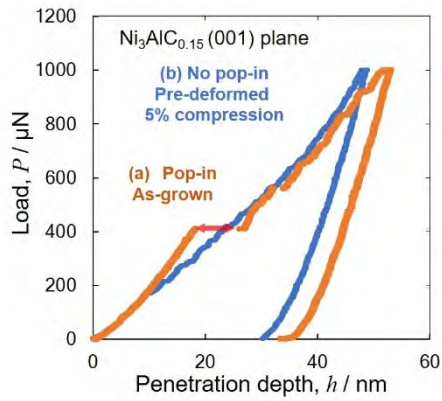


Fig. 1: Typical load-displacement ( $P$ - $h$ ) curves measured for  $E2_1$   $Ni_3AlCo_{0.15}$  single crystals using nanoindentation on (001) plane. Pop-in occurs in as-grown sample (a) while pop-in does not occur in 5% predeformed sample.

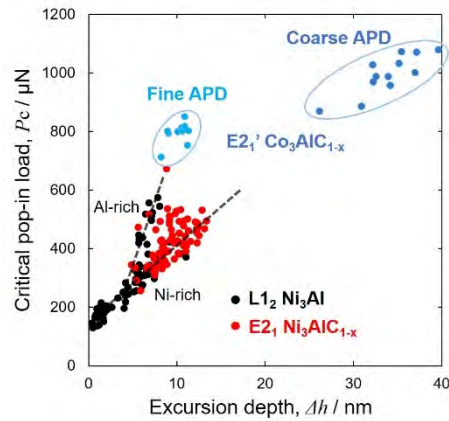


Fig. 2: Relationship between the critical pop-in load  $P_c$  and its corresponding excursion depth  $\Delta h$ . Results were summarized for  $L1_2$   $Ni_3Al$ ,  $E2_1$   $Ni_3AlCo_{1-x}$ , and  $E2_1'$   $Co_3AlCo_{1-x}$  alloys with various chemical compositions.

The relationship between the critical pop-in load  $P_c$  and corresponding excursion depth  $\Delta h$  is shown in Fig. 2. The linear relationship is observed between  $P_c$  and  $\Delta h$  for  $L1_2$   $Ni_3Al$  and  $E2_1$   $Ni_3AlCo_{1-x}$  alloys, showing wide range scatter and distribution from 200 to 600  $\mu N$  in  $P_c$  and from about 1 to 15 nm in  $\Delta h$ . The slope of  $P_c/\Delta h$  qualitatively indicates the tendency of mobile dislocations behavior. Total energy stored and released at a certain  $P_c$  is consumed for generation and/or glide of dislocations, and consequently, total displacement as a result of dislocations glide is given as  $\Delta h$ . The Al-rich specimens show larger  $P_c/\Delta h$  than in the Ni-rich specimens in  $Ni_3Al$  and  $Ni_3AlCo_{1-x}$  alloys, which indicates two interpretations. One is that dislocations require higher  $P_c$  to be generated or multiplied in the Al-rich alloys when compared at the same  $\Delta h$ . The other is that generated mobile dislocations density is higher, or the mobility of dislocations is higher in the Ni-rich alloys when compared at the same  $P_c$ . The relationship between  $P_c$  and  $\Delta h$  is also shown for  $E2_1'$   $Co_3AlCo_{1-x}$  in Fig. 2. It is very surprising that coarse APD specimens show tremendously high  $P_c$  around 1000  $\mu N$  and large  $\Delta h$  about 30 to 40 nm. Even though dislocations require very high stress level to be generated, once high density of dislocations are generated, they can glide rather easily for a distance. Contrary to this, fine APD specimens exhibit high  $P_c$  around 800  $\mu N$  but small  $\Delta h$  about 10 nm, which is interestingly located on the extrapolation of the linear relationship of  $P_c/\Delta h$  for the Al-rich  $Ni_3Al$  and  $Ni_3AlCo_{1-x}$ . The fine APD is supposed to act as the effective resistance to the dislocation glide, however at the same time, the fine APD could act as the effective source of the dislocations generation and multiplication particularly at this extremely high stress level. It is thought that sufficiently high hydrostatic stress to generate dislocations can be achieved locally under the condition of nanoindentation. We are expecting to further understand the mechanism through the detailed observation and analysis using scanning-transmission electron microscopy. It is noteworthy that the fine APD specimen fractures in the elastic region before the onset of plastic deformation in a compression test at room temperature.

#### Acknowledgement

This work was partially supported by the JSPS Grant-in-Aid for Scientific Research, Challenging Research (Exploratory) No.17K18977.

#### References

- [1] Y. Kimura, K. Sakai, Y. Mishima, Phase Equilibria and Diffusion. **2006**, 27, 14-21.
- [2] Y. Kimura, K. Sakai, F.G. Wei, Y. Mishima, Intermetallics. **2006**, 14, 1262-1269.
- [3] Y. Kimura, M. Kawakita, Y. Yuyama and Y.W. Chai, MRS Symp. Proc. **2013**, 1516, 243-248.
- [4] T. Ohmura, L. Zhang, N. Sekido, and K. Tsuzaki, Journal of Materials Research. **2012**, 27, 1742-1749.
- [5] T. L. Li, Y. F. Gao, H. Bei, and E. P. George, Journal of the Mechanics and Physics of Solids. **2011**, 59, 1147-1162.

**O-IM-02****Low temperature deformation mechanisms of CoZr and Co<sub>39</sub>Ni<sub>11</sub>Zr<sub>50</sub> intermetallic compounds**

Werner Skrotzki<sup>1</sup>, Rolf Schaarschuch<sup>1</sup>, Carl-Georg Oertel<sup>1</sup>, Aurimas Pukenas<sup>1</sup>, Guanghui Cao<sup>2</sup>, Jens Freudenberger<sup>3</sup>, Weimin Gan<sup>4</sup>, Ewad Maawad<sup>4</sup> and Robert Chulist<sup>5</sup>

<sup>1</sup>Institute of Solid State and Materials Physics, Technische Universität Dresden, 01062 Dresden, Germany, werner.skrotzki@tu-dresden.de, rolf.schaarschuch@tu-dresden.de, carl-georg.oertel@tu-dresden.de, aurimas.pukenas@tu-dresden.de

<sup>2</sup>Department of Materials Engineering, Shanghai University, 200072 Shanghai, P.R. China, ghcao@shu.edu.cn

<sup>3</sup>Institute for Metallic Materials, Leibniz-Institute for Solid State and Materials Research, 01069 Dresden, Germany, j.freudenberger@ifw-dresden.de

<sup>4</sup>Institute of Materials Physics, Helmholtz-Zentrum Hereon, 21502 Geesthacht, Germany, weimin.gan@hereon.de, ewad.maawad@hereon.de

<sup>5</sup>Institute of Metallurgy and Materials Science, Polish Academy of Sciences, 30-059 Krakow, Poland, r.chulist@imim.pl

**Introduction**

Intermetallic compounds, which in comparison to common metals possess a high degree of covalent and ionic bonding, often have attractive physical, chemical, electrical, magnetic and mechanical properties such as low density, high strength, high stiffness and excellent corrosion resistance. This behavior partially also holds at high temperature. However, because of the general brittle behavior at room temperature (RT) the advantages remain largely unused. The brittleness makes technical applications difficult as intermetallics are already prone to fracture during processing.

Recently, using a sophisticated X-ray diffraction-based technique Ungar et al. [1] in a statistically relevant way showed for CoZr and CoTi tensile deformed at RT to true plastic strains of 12 % and 2 %, respectively, that the hard <110> and <111> slip modes are activated in nearly every grain. However, in contrast to the soft <100> slip mode there was no relation to the Schmid factor. The authors argued that the uniform stress assumption - implicit in Schmid factor analysis - is a poor one for materials which plastically are highly anisotropic at the single crystal level. All arguments for easy activation of hard slip modes as reason for the anomalous ductility of certain intermetallic compounds are summarized in the review of Agnew and Ungar [2].

It is the aim of the present work to contribute to the basic understanding of the increased ductility at low temperatures of the intermetallic compounds CoZr and Co<sub>39</sub>Ni<sub>11</sub>Zr<sub>50</sub> by also studying their deformation behavior at cryogenic temperatures. Thereby, our findings on the ductile rare earth intermetallics YCu [3] and YAg [4] should be extended, respectively put on a broader basis.

**Materials and Methods**

Polycrystalline CoZr and Co<sub>39</sub>Ni<sub>11</sub>Zr<sub>50</sub> were prepared by arc-melting of pure metals in right proportion in a copper mold under argon atmosphere. Cylindrical samples cut from the alloy buttons by electro-erosion were sheathed with stainless steel case. This workpiece was heated for 30 min in air at 1300 K and subsequently rolled in 28 steps with 5 % thickness reduction per pass yielding a rolling degree of 80%. Microstructure and texture of the hot-rolled sheets were determined by electron backscatter and high energy X-ray diffraction, respectively.

Tensile tests from RT down to 4 K combined with stress relaxation tests were carried out on samples cut in rolling direction. The Instron 4502 deformation apparatus used had a He cryostat for temperature adjustment. Phase analysis of the deformed samples was done with diffraction of synchrotron radiation. The dislocation microstructure was analyzed by transmission electron microscopy (TEM).

**Results and Discussion**

The hot-rolled intermetallic compounds are dynamically recrystallized and have a grain size of about 200 μm. Their texture consists of recrystallization components belonging to the α- and γ-fiber of rolled body-centered cubic metals.

Polycrystalline CoZr and Co<sub>39</sub>Ni<sub>11</sub>Zr<sub>50</sub> exhibit a moderate ductility from RT down to 4 K and 125 K, respectively. In contrast to CoZr, Co<sub>39</sub>Ni<sub>11</sub>Zr<sub>50</sub> shows a stress- and thermally-induced phase transformation from B2 to B27. The transition to a brittle behavior takes place when the volume fraction of the harder martensitic phase exceeds a critical value. Compared to other intermetallic compounds, the stronger metallic character of bonding [5] may explain the low Peierls stress estimated for primary <100> slip. It may also be responsible for easier secondary <110> slip, which was proven by TEM. The metallic character may be strengthened by substitution of Co by Ni. Moreover, grain boundary cohesion may be increased leading to a higher fracture stress. These arguments are in line with the moderate ductility at low temperatures of CoZr and its enhancement for Co<sub>39</sub>Ni<sub>11</sub>Zr<sub>50</sub>.

Thermal activation analysis shows that CoZr follows the Cottrell-Stokes law indicating forest dislocation cutting as the rate controlling deformation mechanism, typical for pure fcc metals. The activation parameters determined are compatible with this mechanism. The situation is more complicated for Co<sub>39</sub>Ni<sub>11</sub>Zr<sub>50</sub> because of additional solid solution strengthening and phase transformation.

The results described for CoZr and Co<sub>39</sub>Ni<sub>11</sub>Zr<sub>50</sub> are similar to those of the ductile rare earth intermetallics YAg and YCu, respectively. Therefore, this generalization may help to search for other low temperature ductile systems in the broad class of intermetallic compounds.

**References**

- [1] T. Ungar, G. Ribarik, G. Zilahi, R. Mulay, U. Lienert, L. Balogh, S. Agnew, *Acta Materialia*. **2014**, *71*, 264-282.
- [2] S.R. Agnew, T. Ungar, *IOP Conference Series: Materials Science and Engineering*. **2019**, *580*, 012001.
- [3] C.-G. Oertel, R. Schaarschuch, G. Cao, H.N. Tian, J. Freudenberger, H.-G. Brokmeier, W. Skrotzki, *Scripta Materialia*. **2011**, *65*, 779-782.
- [4] R. Schaarschuch, C.-G. Oertel, G. Cao, J. Freudenberger, H.-G. Brokmeier, W. Skrotzki, *Acta Materialia*. **2018**, *151*, 149-158.
- [5] D. Chattaraj, S.C. Parida, S. Dash, C. Majumder, *International Journal of Hydrogen Energy*. **2012**, *37*, 18952-18958.

**O-IM-03****Investigation of the growth of phases in the Cu(Ni)–Sn system**

Varun A. Baheti<sup>1,3</sup>, Sanjay Kashyap<sup>2,3</sup>, Kamanio Chattopadhyay<sup>3</sup>, Praveen Kumar<sup>3</sup> and Alope Paul<sup>3</sup>

<sup>1</sup>Department of Metallurgical and Materials Engineering, Indian Institute of Technology, 247667 Roorkee, India, varun@mt.iitr.ac.in

<sup>2</sup>School of Physics and Materials Science, Thapar Institute of Engineering & Technology, 147004 Patiala, India

<sup>3</sup>Department of Materials Engineering, Indian Institute of Science, 560012 Bangalore, India

**Introduction**

Understanding the growth of intermetallic phases between under-bump metallization (UBM) and solder is important, as in many cases it controls the electro-mechanical properties of the product. Cu and Ni are the commonly used UBM materials. Cu is used for good bonding because of fast reaction with solder and Ni often acts as a diffusion barrier layer due to its inherently slower reaction kinetics with Sn-based solders. The aim of this work is to conduct experiments in Cu(Ni)–Sn system in the solid–state for estimation of the important diffusion parameters and for understanding the growth mechanism of the phases.

**Materials and Methods**

The experiments are conducted following the diffusion couple technique. The details of experimental work can be found in References [1-3].

**Results and Discussion**

First, the presence of bifurcation of the Kirkendall marker plane, a very special phenomenon discovered recently, is found in a technologically important Cu–Sn system. It was predicted based on estimated diffusion coefficients; however, it could not be detected in the conventional inert marker experiments. As reported in this study, we could detect the locations of these planes based on the microstructural features examined in SEM and TEM. This strengthens the concept of the physico–chemical approach that relates microstructural evolution with the diffusion rates of components and imparts finer understanding of the growth mechanism of phases.

Next, a strong influence of Ni content in Cu on the diffusion–controlled growth of the (Cu,Ni)<sub>3</sub>Sn and (Cu,Ni)<sub>6</sub>Sn<sub>5</sub> phases by coupling different Cu(Ni) alloys with Sn in the solid–state is reported. The diffraction pattern analysis indicates that the presence of Ni does not change the crystal structure of (Cu,Ni)<sub>3</sub>Sn and (Cu,Ni)<sub>6</sub>Sn<sub>5</sub>. However, it strongly affects the microstructural evolution and diffusion rates of components. The growth rate of (Cu,Ni)<sub>3</sub>Sn decreases without changing the diffusion coefficient because of the increase in growth rate of (Cu,Ni)<sub>6</sub>Sn<sub>5</sub>, which grows by consuming (Cu,Ni)<sub>3</sub>Sn at the (Cu,Ni)<sub>3</sub>Sn/(Cu,Ni)<sub>6</sub>Sn<sub>5</sub> interface. With the increase in Ni content, driving forces for the diffusion of components through both the Cu<sub>3</sub>Sn and Cu<sub>6</sub>Sn<sub>5</sub> phases increase for both the components (*i.e.*, Sn and Cu), but at different rates. However, the magnitude of these changes alone is not large enough to explain the high difference in the observed growth rate of the product phases due to Ni addition. For 3 at.% or higher Ni addition in Cu, only the (Cu,Ni)<sub>6</sub>Sn<sub>5</sub> phase grows in the interdiffusion zone. The elongated grains of (Cu,Ni)<sub>6</sub>Sn<sub>5</sub> are found when it is grown from (Cu,Ni)<sub>3</sub>Sn. This indicates that the newly formed intermetallic compound joins with the existing grains of the phase. On the other hand, smaller grains are found when this phase grows directly from Cu in the absence of (Cu,Ni)<sub>3</sub>Sn, indicating the ease of repeated nucleation. Grain size of (Cu,Ni)<sub>6</sub>Sn<sub>5</sub> decreases with further increase in Ni content, which indicates a further reduction of activation barrier for nucleation. The relations for the estimation of relevant diffusion parameters are established, considering the diffusion mechanism in the Cu(Ni)–Sn system, which is otherwise impossible in the phases with narrow homogeneity range in a ternary system. The flux of Sn increases, whereas the flux of Cu decreases drastically with the addition of very small amount of Ni, such as 0.5 at.% Ni, in Cu. Analysis of the atomic mechanism of diffusion indicates the contribution from both lattice and grain boundary for the growth of (Cu,Ni)<sub>6</sub>Sn<sub>5</sub>.

**References**

- [1] V.A. Baheti, S. Kashyap, P. Kumar, K. Chattopadhyay, A. Paul, Bifurcation of the Kirkendall marker plane and the role of Ni and other impurities on the growth of Kirkendall voids in the Cu–Sn system, *Acta Materialia*. **2017**, *131*, 260-270.
- [2] V.A. Baheti, S. Kashyap, P. Kumar, K. Chattopadhyay, A. Paul, Effect of Ni on growth kinetics, microstructural evolution and crystal structure in the Cu(Ni)–Sn system, *Philosophical Magazine*. **2017**, *97(21)*, 1782-1802
- [3] V.A. Baheti, S. Islam, P. Kumar, R. Ravi, R. Narayanan, H. Dong, V. Vuorinen, T. Laurila, A. Paul, Effect of Ni content on the diffusion–controlled growth of the product phases in the Cu(Ni)–Sn system, *Philosophical Magazine*. **2016**, *96(1)*, 15-30.

## O-IM-04

**Stable and metastable phase equilibria involving Cu<sub>6</sub>Sn<sub>5</sub> – effect of variable composition of an apparently stoichiometric intermetallic**

A. Leineweber

Institute of Materials Science, TU Bergakademie Freiberg, 09599 Freiberg, Germany, andreas.leineweber@iww.tu-freiberg.de

**Introduction**

At  $T > 0$  K all phases in multicomponent systems *must* show a finite homogeneity range. This is also true for intermediate, intermetallic phases. In case of many technologically relevant phases there is detailed knowledge of the composition and temperature dependent homogeneity range, as well as possible additional ordered states actually corresponding to distinct phases. In other, nevertheless relevant phases, the knowledge can be very limited, obstructing understanding of phase transformation processes and occurrence of differently ordered states.

Such a situation existed until recently for the Cu<sub>6</sub>Sn<sub>5</sub> *intermetallic*, which quite prominently develops in solder joints of lead-free solders [1]. The crystal structures of the phases belonging to this intermetallic derive from the Ni<sub>2</sub>In/NiAs structure type with a general formula Cu<sub>1+ $\delta$</sub> Sn ( $\delta = 0.2$  for the nominal composition Cu<sub>6</sub>Sn<sub>5</sub>). According to our insight [2-5, submitted], there are a disordered  $\eta$  high-temperature phase as well as two ordered low-temperature phases: stable  $\eta'$  and metastable  $\eta''$ . The resulting phase diagram in the relevant compositional region is shown in Fig. 1.

In the presentation it will be shown how a combination of analysis techniques but also detailed considerations on the crystal chemistry of the differently ordered phases helped elucidating a consistent picture of crystal structures and phase equilibria related to the Cu<sub>6</sub>Sn<sub>5</sub> intermetallic in the Cu–Sn system. Thereby, a partially contradictory collection of views on phase equilibria and crystal structure in the literature could be resolved.

**Materials and Methods**

The investigated Cu–Sn alloys include diffusion couples treated at different temperatures as well as bulk alloys (Cu<sub>57</sub>Sn<sub>43</sub> and Cu<sub>52</sub>Sn<sub>48</sub>) originally molten at 1073 K, rapidly solidified and equilibrated in different two-phase regions of the phase diagram. After heat treatment the alloys were quenched.

Powder X-ray diffraction (PXRD) was performed using CoK $\alpha_1$  radiation at ambient temperature in Bragg-Brentano reflection geometry. In the case of the diffusion couples, residual Sn was leached off prior measurement to get more diffracted intensity from the intermetallic. Lattice parameter determination as well as determination of further structure parameters was done using the Rietveld technique.

Scanning electron microscopy (SEM) on polished cross sections supplemented by electron backscatter diffraction (EBSD) was conducted to identify different phases.

**Results**

Presence and absence of superstructure/satellite reflections in PXRD data allowed determination of the phase state of the intermetallic present ( $\eta$ ,  $\eta'$ ,  $\eta''$ ). The disordered  $\eta$  phase could be quenched by direct contact with water, whereas insufficient quenching could easily lead to broad reflections being indicative for  $\eta'$  and/or  $\eta''$  ordering. The same reflections were, however, narrow, when the heat treatment was conducted with the ordered phase stable at the treatment temperature prior to quenching.

The lattice parameters of the  $\eta$  phase determined at ambient temperature showed some significant variation [3] as a function of alloy composition and heat treatment temperature, the latter implying strongly temperature-dependent phase boundaries of Cu<sub>3</sub>Sn+ $\eta$ / $\eta$  and  $\eta$ / $\eta$ +melt. As described in Ref. [3,4], a function was derived to relate unit-cell volume and composition of the intermetallic in terms the parameter  $\delta$ . Analysis of the unit cell volume revealed that the  $\eta'$  phase appears to be largely stoichiometric Cu<sub>1.20</sub>Sn = Cu<sub>6</sub>Sn<sub>5</sub> if generated in diffusion couples at low temperatures. In contrast the  $\eta$  phase appears to have a maximum compositional range from Cu<sub>1.237</sub>Sn to Cu<sub>1.166</sub>Sn, where the  $\delta$  values from two-phase equilibria lead to the shape of the  $\eta$  field in Fig. 1. As evidenced from diffusion-couple specimens, there is an  $\eta'+\eta$  two-phase region in some temperature range below 473 K (see Fig. 1).

PXRD data also reveal the formation of the ordered  $\eta''$  phase. Its incommensurate ordering was derived to accommodate a variable Cu content with  $\delta > 0.2$  [2,3]. That ordering was approximated in previous works as commensurate  $\eta^8$  [6] or  $\eta^{4+1}$  [7] superstructures. Unrelated reports of these superstructures gave impression of two distinct phases, which most likely do not exist in this way. The  $\eta''$  phase is relatively Cu-rich and is metastable against decomposition into Cu-poorer  $\eta$  or  $\eta'$  and Cu<sub>3</sub>Sn. The  $\eta''$  phase forms upon partitionless ordering of Cu-rich  $\eta$  generated at elevated temperature. This partitionless ordering reveals also that a previously proposed large volume change in the order of 2 % upon ordering [1,8], which has been made responsible for degradation processes of the intermetallic in solder joints, does not exist.

With the knowledge of the phase diagram in Fig. 1 and the common knowledge that composition-change processes require time due for diffusion, also insight into the kinetics and mechanism for compositional change was developed, in



particular by applying time-dependent heat treatments. For example, Cu-rich  $\eta$  generated e.g. at 553 K was further heat treated at 513 K. The latter treatment leads to formation of *new*  $\text{Cu}_3\text{Sn}$  at grain boundaries (see Fig. 2). Taking into account the grain size, also the (volume) interdiffusion coefficient in  $\eta$  was identified based on the kinetics of the composition change of the  $\eta$  phase as monitored by PXRD analysis of a series of quenched specimens treated for different times at 513 K.

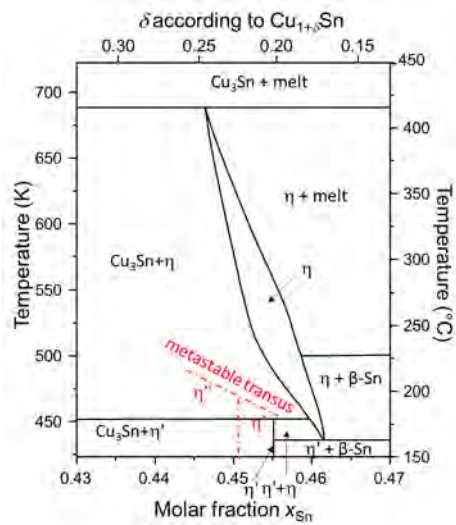


Fig. 1: Part of the phase diagram Cu–Sn in the  $\text{Cu}_6\text{Sn}_5$  region. The red lines depict metastable formation of  $\eta''$  and Cu-rich  $\eta'$ , while the latter is featured under equilibrium conditions as “line compound” at the  $\text{Cu}_6\text{Sn}_5$  composition.

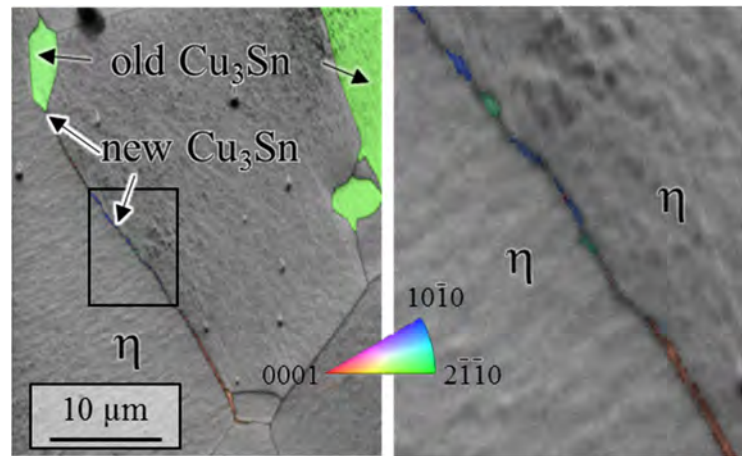


Fig. 2: EBSD image quality maps of  $\text{Cu}_{57}\text{Sn}_{43}$  alloy located in the  $\text{Cu}_3\text{Sn} + \eta$  field superposed by inverse-pole figure coloring for regions identified as  $\text{Cu}_3\text{Sn}$ . The right part corresponds to a magnification of the left part (black rectangle). The alloy was first annealed at 653 K leading to Cu-rich  $\eta$  (see Fig. 1) and to well-rounded  $\text{Cu}_3\text{Sn}$  particles. The shown state is after generating further “new”  $\text{Cu}_3\text{Sn}$  upon annealing at 513 K.

## Conclusion

In-depth reconciliation of crystallographic and phase equilibrium data turned out to be crucial to conclude a new view on the Cu–Sn phase diagram in the  $\text{Cu}_6\text{Sn}_5$  region. That new phase diagram helped to predict and understand occurring phase transformation processes also relevant for the thermal processing of solder joints.

## Acknowledgment

The author thanks Alexander Walsch, Manuel Löffler, and Dr. Stefan Martin (TU Bergakademie Freiberg) as well as Dr. Werner Hügel (Robert Bosch GmbH) and Dr. Christian Wieser (formerly Robert Bosch GmbH) for cooperation on this field and coauthoring the original works.

## References

- [1] D.K. Mu, S.D. McDonald, J. Read, H. Huang, K. Nogita, *Curr. Op. Sol. Stat. Mater. Sci.* **2016**, *20*, 55–76.
- [2] A. Leineweber, C. Wieser, W. Hügel, *Z. Kristallogr.* **2020**, *235*, 445–457.
- [3] A. Leineweber, C. Wieser, W. Hügel, *Scr. Mater.* **2020**, *183*, 66–70.
- [4] C. Wieser, W. Hügel, A. Walsch, A. Leineweber, *J. Electr. Mater.* **2020**, *49*, 245–256.
- [5] C. Wieser, A. Walsch, W. Hügel, A. Leineweber, *J. Alloys Compd.* **2019**, *794*, 491–500.
- [6] A.-K. Larsson, L. Stenberg, S. Lidin, *Z. Kristallogr.* **1995**, *210*, 832–837.
- [7] Y.Q. Wu, J.C. Barry, T. Yamamoto, Q.F. Gu, S.D. McDonald, S. Matsumura, H. Huang, K. Nogita, *Acta Mater.* **2012**, *60*, 6581–6591.
- [8] G. Ghosh, M. Asta, *J. Mater. Res.* **2005**, *20*, 3102–3117.

**O-IA-01****Mechanical properties of a cast Fe<sub>3</sub>Al-based iron aluminum alloy at moderate temperatures**

Eva Kollmannsberger and Holger Saage

Competence Center for Lightweight Design (LLK), Faculty for Mechanical Engineering, University of Applied Sciences Landshut, Germany, Eva.Kollmannsberger@haw-landshut.de, Holger.Saage@haw-landshut.de

**Introduction**

Iron aluminides are considered for use in applications at moderate and high-temperatures, due to their excellent corrosion and oxidation resistance, low costs and good availability of their main components. However, high brittleness at room temperature, a lack of high temperature creep resistance, and environmental embrittlement prevented a widespread use. Ongoing research activities led to improved high temperature creep resistance and ductility at room temperature. Nevertheless, some scientific aspects are still barely understood. For example, fatigue properties have hardly been investigated so far, although they are of great importance for many possible applications [1, 2]. Further, iron aluminides are prone to hydrogen embrittlement in a way that even small variations of the surface roughness may already influence the tensile behaviour [3, 4]. In the presentation, the influence of the surface roughness on tensile strength and strain to failure, their temperature and strain rate dependence as well as the fatigue behaviour are shown.

**Materials and Methods**

The alloy Fe-18.7Al-5.5Cr-0.04Zr-0.36Ti-0.48C (in atom percent) was prepared by sand casting and turned on a lathe into cylindrical specimens. All tests were carried out on mechanically ground and polished specimens. Tensile tests were performed between room temperature and 500 °C with different constant strain rates down to about  $4 \times 10^{-8} \text{ s}^{-1}$ . Surface sensitivity was investigated with tensile tests at room temperature with various surface roughnesses. The surface roughness is quantified by means of the average roughness depth Rz. The fatigue behaviour of the alloy was investigated by strain controlled isothermal low-cycle-fatigue (LCF) experiments at high temperature with a symmetrical tension-compression profile and a constant strain rate of  $10^{-3} \text{ s}^{-1}$ . Changes in microstructure during testing and fracture surfaces were investigated by Scanning-Electron-Microscopy (SEM).

**Results and Discussion**

Surface roughness has a significant influence on the tensile behavior of the used alloy. By reducing the surface roughness from  $R_z = 3 \mu\text{m}$  to  $0.4 \mu\text{m}$ , the strain at failure of the alloy can be increased about by a factor of three in tensile tests at room temperature. Tensile strength increases by about 6 % in case of the sample with the smoother surface. Additionally, the origin of the crack initiation changes from the surface (Fig. 1) to the center of the specimen (Fig. 2) after polishing. The tensile strength increases from about 400 MPa at room temperature to about 570 MPa at 300 °C and decreases again to 340 MPa at 500 °C for a constant strain rate of  $10^{-4} \text{ s}^{-1}$ . Tests with different strain rates have been carried out at 400 °C. A Norton exponent of about 16 has been determined. Within the scope of the presentation, the results of the fatigue tests are presented and compared to those of the established reference steel alloys P91 and P92.

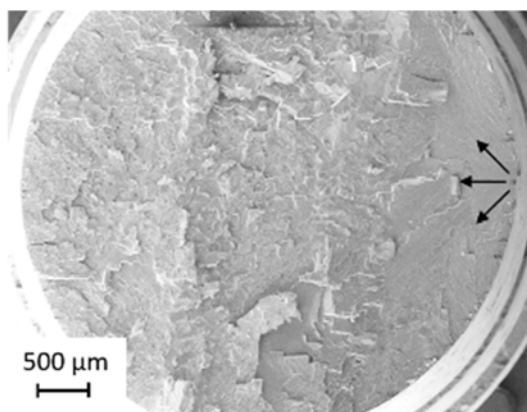


Fig. 1: Fracture surface of Fe-20Al-5Cr-0,05Zr-TiC after tensile test on sample with a surface roughness of  $R_z=3 \mu\text{m}$  showing crack origin at the surface.

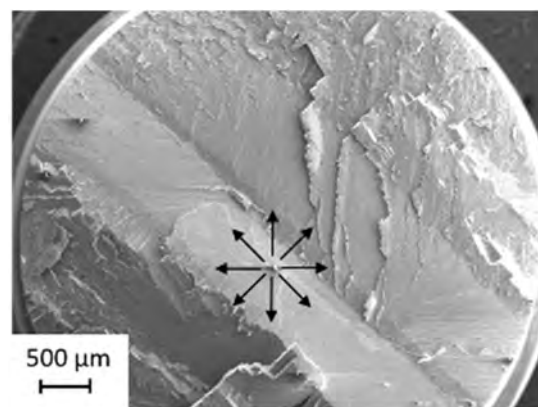


Fig. 2: Fracture surface of Fe-20Al-5Cr-0,05Zr-TiC after tensile test on sample with a surface roughness of  $R_z=0.4 \mu\text{m}$  showing crack origin at the centre of the sample.

**References**

- [1] J.H. Schneibel, H. Rühle, M. Heilmaier, H. Saage, M. Goncharenko, P. Loboda, *Intermetallics*. **2010**, *18*, 1369-1374
- [2] M. Palm, F. Stein, G. Dehm, *Annual Review of Materials Research*. **2019**, *49*, 297-326
- [3] N.S. Stoloff, C.T. Liu, *Intermetallics*. **1994**, *2*, 75–84
- [4] J. Chao, D.G. Morris, M.A. Munoz-Morris, J. L. Gonzalez-Carrasco, *Intermetallics*. **2001**, *9*, 299-308

**O-IA-02****Microstructure property correlation of a Mo-Ti-B alloyed iron aluminide**Andreas Abel<sup>1</sup>, Pawel Zapala<sup>2</sup>, Heiner Michels<sup>2</sup> and Birgit Skrotzki<sup>1</sup><sup>1</sup>Federal Institute for Materials Testing and Research (BAM), Department of Materials Engineering, 12205 Berlin, Germany, andreas.abel@bam.de, birgit.skrotzki@bam.de<sup>2</sup>Access e.V., 52072 Aachen, Germany, p.zapala@access-technology.de, h.michels@access-technology.de**Introduction**

With an increasing demand in more efficient fuel consumption to reduce CO<sub>2</sub> emissions, weight reductions in high-temperature materials at affordable costs gain increasing attention [1]. One potential candidate is the class of intermetallic iron aluminides, combining the advantages in mass savings, high temperature performance and sustainable availability of resources [2]. Continuing interest lies in developing and verifying new alloying concepts to further extend the limits in high temperature strength and room temperature ductility. The addition of Mo, Ti and B was already concluded to show competitive creep properties in comparison to conventional steels while keeping brittleness to a minimum [3]. The AiF research project “WAFEAL – Materials applications for iron aluminides” aims at transferring these findings into a standardized materials dataset and deriving best practices for processing. Among these goals, microstructure plays a key role in understanding the relationship between process characteristics and mechanical properties. Thus, a set of different microstructures adjusted by varying casting methods, wall thicknesses and heat treatments was extensively characterized and correlated with measured hardness. Tensile tests at ambient and high temperatures are planned to allow more conclusions on the microstructure-property relationship.

**Materials and Methods**

The alloy with a target composition of Fe-26Al-4Mo-0.5Ti-1B was made from commercially available high-purity elements (> 99.9 %), which were preprocessed in part to low-melting binary alloys. A total of six step samples with five different wall thicknesses (2.5, 5, 10, 15 and 20 mm) were produced by centrifugal casting with different cooling rates: One part was die-cast (DC) into a permanent copper die, the other part was investment-cast (IC) into a single-use insulated ceramic mold made from Al<sub>2</sub>O<sub>3</sub> and preheated to 1200 °C. Besides the as-cast condition, two more conditions for each casting method were generated by heat treatment in air with furnace cooling: one at 400 °C for 168 h, the other at 1000 °C for 100 h. Phase transitions and melting points were obtained by differential thermal analysis (DTA) on a Setaram TAG24. Present phases were identified by X-ray diffraction (XRD) on bulk samples. Chemical compositions of individual phases were examined by electron probe micro analysis (EPMA) on a JEOL JXA-8900 RL with wavelength-dispersive (WDS) detector. Metallographic sections were cut from the center of each step for microstructural investigations. Phase fractions and grain sizes of macrosections were obtained from light-optical microscopy images of Adler-etched samples. Grain sizes were measured as average grain diameters by Heyn Intercept method. Additional high-magnification images were taken using a ZEISS LEO Gemini 1530 VP Scanning Electron Microscope (SEM). Macrohardness was measured using a KB 30 SR FA Basic hardness tester with a Vickers indenter at 10 kg loading.

**Results and Discussion**

Irrespective of the process variables, the alloy generally exhibits a two-phase mixture of D0<sub>3</sub>-structured Fe<sub>3</sub>Al as matrix and a Mo<sub>2</sub>FeB<sub>2</sub>-type eutectic phase according to DTA, XRD and EPMA. The DC and IC microstructures fundamentally differ from each other in two ways: Firstly, DC microstructures usually showed a microstructural gradient from edge to center with a transition from fine-cellular to columnar to coarse-cellular grains. By contrast, IC microstructures were marked by no directional grain growth with more irregular grain shapes. Secondly, DC average grain sizes at center were on average 59 % smaller than IC grains for equal wall thickness and sample condition. This is partially reflected in macrohardness values which show on average a 6 % higher hardness for DC microstructures in as-cast condition. The difference between DC and IC hardness is even less pronounced after annealing (< 2.5 %). The approximation of hardness values is evoked by a greater influence of heat treatments on the DC as-cast microstructure. Annealing at 400 °C for one week, which dissolves any process-induced vacancies, was especially effective for smaller DC wall thicknesses < 5 mm where hardness decreased significantly. Throughout all DC wall thicknesses, heat treatment at 1000 °C for 100 h exhibited partial restructuring and coarsening of the second phase in microscopical images with an evident decrease in hardness of 5 % compared to the as-cast condition. From these observations, it becomes clear that for the investigated alloy, grain size as microstructural feature is not the only key parameter to mechanical strength. A more profound relationship of different microstructures to mechanical properties shall be established from a series of tensile tests at temperatures up to 650 °C. Specimens will focus on the variation of casting methods and conditions as presented above.

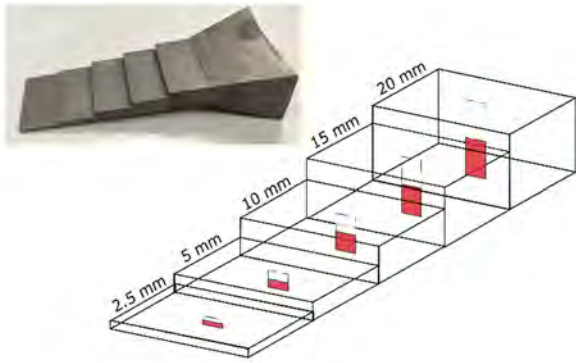


Fig. 1: Scheme and image of cast step samples ranging from 2.5 to 20 mm wall thickness. Highlighted areas indicate the cut sections used for microstructural investigations.

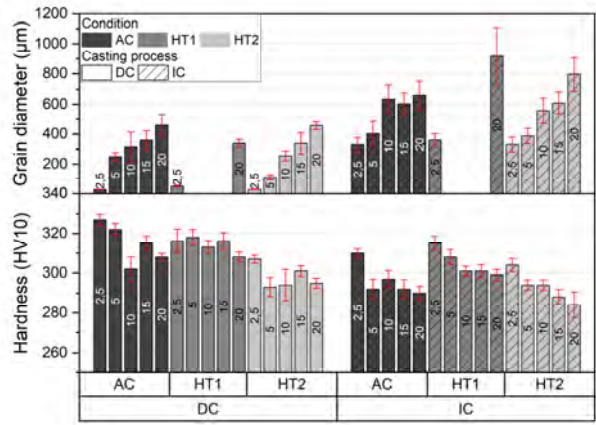


Fig. 2: Comparison of average grain diameter (top) and macrohardness (bottom) for two different casting processes (DC: Die casting (left), IC: Investment casting (right)) and three different conditions (AC: As-cast, HT1: 400 °C for 168 h, HT2: 1000 °C for 100 h). Numbers in columns indicate the respective wall thickness in mm.

**Acknowledgement**

The authors acknowledge the financial support by the German Federal Ministry of Economic Affairs and Energy (BMWi) in the framework of AiF projects (IGF-No.: 20965 N).

**References**

- [1] Clean Sky Joint Undertaking: Clean Sky. EU Horizon 2020 Programme, [www.cleansky.eu](http://www.cleansky.eu), accessed 2021-03-29.
- [2] M. Palm, F. Stein, G. Dehm, Annual Review of Materials Research. **2019**, 49, 297-326
- [3] X. Li, P. Prokopčáková, M. Palm, Materials Science and Engineering A. **2014**, 611, 234-241.

**O-IA-03****Microstructure evolution and phase transformations in Fe-Al-Nb(B) alloys**Angelika Gedsun and Martin Palm

Max-Planck-Institut für Eisenforschung GmbH, Düsseldorf, Germany

a.gedsun@mpie.de, m.palm@mpie.de

**Introduction**

Iron aluminides possess exceptional wear and corrosion resistance alongside to a low density and good mechanical properties and are therefore promising candidates for the development of novel sustainable materials for structural applications at high temperatures [1]. However, creep resistance at high temperature needs to be further enhanced, e. g. through strengthening by coherent or incoherent second phases. In Fe–Al–Nb alloys, different microstructures with fine-scaled, homogeneously distributed C14 Laves phase particles within the matrix and lining the grain boundaries can be obtained through heat treatment, thermo-mechanical processing or boron doping [2].

**Materials and Methods**

To study the microstructural evolution, characterization of phases, and determination of phase transition temperatures, alloys with different compositions containing between 25–34 at.% Al, 2–3 at.% Nb and with or without boron doping were produced by vacuum induction melting and annealed at 700 °C for 1, 10, 100 and 1000 h. The actual compositions of the alloys were established by wet chemical analysis and the compositions of the individual phases in equilibrium were determined by electron probe microanalysis (EPMA). Crystallographic structures of the phases were determined by X-ray diffraction (XRD). Differential thermal analysis (DTA) was performed on selected annealed (700 °C/ 1000 h) samples to determine the phase transition temperatures. Additionally, high temperature XRD (HT-XRD) was performed to characterize the phases upon heating. For the HT-XRD measurements, the annealed (700 °C/1000 h) bulk samples were first heated up from room temperature to 500 °C, annealed for 30 min and then heated up to the measurement temperature under a graphite dome in helium atmosphere. The HT-XRD scans were performed for temperatures 20 K below and above the order-disorder transition temperatures, which were previously determined by DTA. Further measurements were performed prior and post HT-XRD scans at room temperature with and without the graphite dome.

**Results and Discussion**

For the investigated Fe<sub>x</sub>Al<sub>y</sub>Nb alloys, microstructures with homogeneously distributed and fine scaled strengthening Laves phase precipitates in the Fe<sub>x</sub>Al<sub>y</sub> matrix and aligned at grain boundaries could be obtained after heat treatment and boron doping (Fig. 1). It was found that, similar to the Fe<sub>x</sub>Al<sub>y</sub>Ta system [3], the homogeneous distribution of the incoherent stable C14 Laves phase can be achieved when the coherent metastable L21 Heusler phase forms first. No significant effect of boron doping on the microstructure has been observed. More detailed results on the microstructural evolution of selected alloys and their mechanical properties have been reported in [4]. The transition temperatures for the D03-B2 and B2-A2 order-disorder transitions and the solidus and liquidus temperatures in dependence on the Al and Nb content have been determined by DTA (Fig. 2). A comparison with the transition temperatures of binary Fe<sub>x</sub>Al<sub>y</sub> of the same Al content [5] shows that the D03-B2 transition temperature increases by about 35 K, while the B2-A2 transition temperature increases by about 90 K with the addition of Nb. The liquidus temperature decreases by about 30 K and the solidus temperatures by about 80 K with the addition of Nb, thereby increasing the difference between liquidus and solidus temperature. Alloys with 2 at. % Nb, with or without B, exhibit an increase of about 100 K for the B2-A2 transition temperature and about 10 K decrease in the liquidus and solidus temperatures for a higher Al content. The D03-B2 transition temperature does not change with increasing Al content. While B has no effect on the D03-B2 and B2-A2 order-disorder transitions and the liquidus, the solidus is lowered by about 10 K, compared to the un-doped alloys of otherwise same composition. At T < 450 °C an additional peak was observed, which presumably indicates the Curie temperature. In the HT-XRD measurements the D03-B2 transition could be observed by the vanishing (111) superstructure diffraction peak when heating from 560 to 600 °C and the B2-A2 transitions by the vanishing of the (100) diffraction peak when heating from 650 to 890 °C (Fig.3). Further, the coefficient of thermal expansion (CTE) was calculated from the lattice parameters. For all alloys the tendency towards an increasing CTE with higher temperatures was observed. The calculated CTE values are about 20 \*10<sup>-6</sup> K<sup>-1</sup> and in good agreement with reported literature data [6].



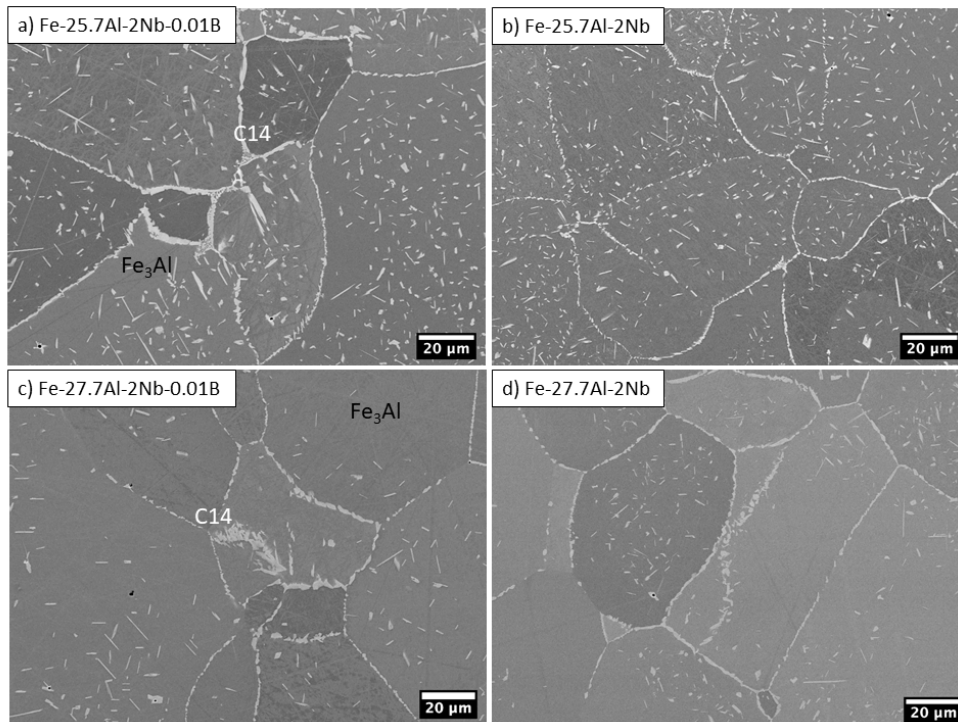


Fig. 1: Back-scattered-electron (BSE) micrographs of alloys with different Al content, with and without boron doping, annealed at 700 °C for 1000 h. The matrix phase was determined as Fe<sub>3</sub>Al and the bright precipitates as C14 Laves phase.

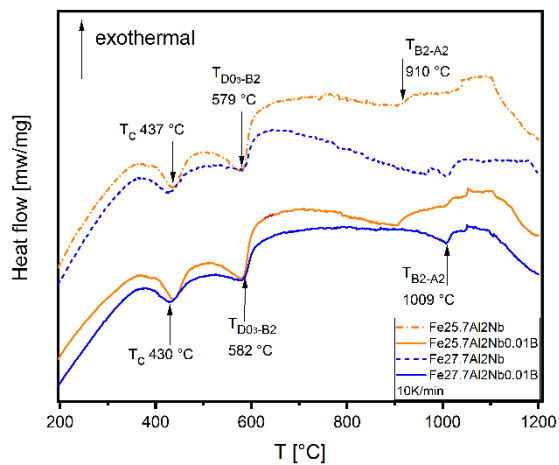


Fig. 2: DTA heating curves (10 K/min) of the alloys with different Al content.

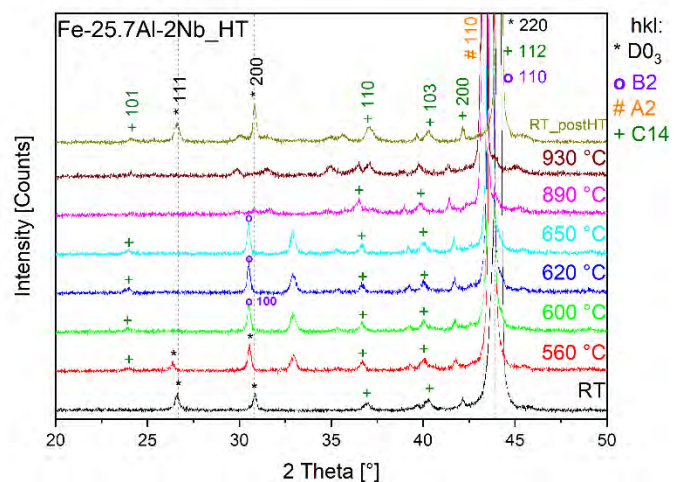


Fig. 3: HT-XRD scans at different temperatures for the alloy Fe<sub>25.7</sub>Al-2Nb (10 K/min, 0.75 °/min).

### Acknowledgements

Financial support by the Federal Ministry for Economic Affairs and Energy through grant 0324317C is gratefully acknowledged. The authors would like to thank Mr. Kulse for the alloy preparation, Mr. Christiansen for the DTA, Ms. Wossack for the EPMA analysis and Mr. Benjamin Breitbach for the HT-XRD measurements.

### References

- [1] C. G. McKamey, Iron Aluminides, in: *Physical Metallurgy and Processing of Intermetallic Compounds*. N.S. Stoloff and V.K. Sikka. Chapman Hall, New York, **1996**, 351-391.
- [2] R. Krein and M. Palm. *Acta Materialia*. **2008**, 56(10), 2400-2405.
- [3] P. Prokopčáková, M. Švec and M. Palm, *International Journal of Materials Research*. **2016**, 107(5), 396-405.
- [4] A. Gedsun, F. Stein, M. Palm, *MRS Advances*. **2021**, 6, 176-182.
- [5] F. Stein and M. Palm, *International Journal of Materials Research*. **2007**, 98(7), 580-588.
- [6] M. Švec, *Defect and Diffusion Forum*, **2016**, 368, 41-44.

**O-IA-04****The role of Cr on the Al<sub>2</sub>O<sub>3</sub> formation on iron aluminides at intermediate temperatures in air**

René Daniel Pütz and Daniela Zander

Chair of Corrosion and Corrosion Protection, Foundry Institute, RWTH Aachen University, 52072 Aachen, Germany,  
r.puetz@gi.rwth-aachen.de, d.zander@gi.rwth-aachen.de

**Introduction**

Iron aluminides are considered as a potential material to substitute stainless steels and Ni-based alloys for high temperature applications at intermediate temperatures [1,2]. Commonly known advantages include the excellent oxidation behavior, good wear resistance, relatively low density, and low costs due to the easily available elements Fe and Al [1-4]. However, the low room temperature ductility and the declining strength at higher temperatures have been major drawbacks of iron aluminides. Therefore, several alloying concepts have been investigated in recent years to solve e.g. the lack of ductility. Apart from reported beneficial effects of added borides or the refining of the microstructure, alloying with Cr might improve the ductility due to reduced hydrogen induced embrittlement [5].

In the literature, opposing results were reported with respect to the influence of Cr on the oxidation behavior of Fe-Al alloys. Cr promotes the third-element effect (TEE) by decreasing the critical threshold of Al that is needed to form a dense and adherent alumina scale, which consequently hinders the growth of Fe-based oxides [6]. On the contrary, an increase in the oxidation rate especially in the early stage of oxidation has been reported in the literature for Fe-Al containing Cr either due to the formation of Cr<sub>2</sub>O<sub>3</sub> in the early stage or due to a doping effect by the incorporation of Cr ions within the alumina lattice [7,8]. The crystal structure of Al<sub>2</sub>O<sub>3</sub> can also influence the oxidation kinetics of alumina forming alloy systems. At intermediate temperatures (700 - 1000 °C), transitional/metastable alumina polymorphs like θ-, δ-, and/or γ-Al<sub>2</sub>O<sub>3</sub> were reported to be formed [9]. These modifications exhibit higher corrosion kinetics due to an increased number of defects compared to stable α-Al<sub>2</sub>O<sub>3</sub> (corundum). The metastable alumina polymorphs can transform to stable α-Al<sub>2</sub>O<sub>3</sub> depending on e.g. temperature and time. Stable α-Al<sub>2</sub>O<sub>3</sub> is usually present at temperatures above 900 - 1000 °C, whereas different alloying elements like Zr are mentioned to promote the establishment of α-Al<sub>2</sub>O<sub>3</sub> instead of metastable alumina polymorphs [10]. For binary iron aluminide, α-Al<sub>2</sub>O<sub>3</sub> was found even at the intermediate temperature of 700 °C in the early stage due to a nucleation effect of α-Al<sub>2</sub>O<sub>3</sub> at hexagonal Fe<sub>2</sub>O<sub>3</sub> rather than a transformation from metastable alumina polymorphs [11]. On the contrary, the metastable alumina polymorphs θ- and γ-Al<sub>2</sub>O<sub>3</sub> were determined after short time and long-term oxidation experiments of iron aluminides at 700 °C containing Cr [12,13]. Due to the presence of further alloying elements like Zr in the mentioned studies, the growth of metastable alumina polymorphs could not be clearly associated to the alloying element Cr.

Therefore, in order to understand the influence of Cr on the Al<sub>2</sub>O<sub>3</sub> modification for DO<sub>3</sub>-based iron aluminides, two alloy systems Fe-26Al and Fe-25Al-5Cr (both in at.%) were oxidized at 700 and 800 °C in air for 178 h. The formed oxides were investigated using x-ray diffraction (XRD), scanning electron microscopy (SEM), and energy dispersive X-ray spectroscopy (EDS).

**Materials and Methods**

The iron aluminides Fe-26Al and Fe-25Al-5Cr (both in at.%) utilized for this study were provided by the Max-Planck-Institut für Eisenforschung in Düsseldorf, Germany, as vacuum induction melted cylindrical ingots with a diameter of approximately 32 mm.

Discontinuous thermogravimetric analysis (TGA) was performed in a Nabertherm chamber furnace at 700 and 800 °C in air for 178 h. Specimens (approximately 15 mm x 13 mm x 3 mm) were stepwise ground to 1200 grit, ultrasonically cleaned in ethanol, and air dried prior to the oxidation experiments. A hole was drilled 1 mm below one of the 13 mm edges to hang the sample in an alumina crucible to ensure that the whole surface was in contact to the atmosphere during oxidation and possible spalling could be collected by the crucible. The samples were inserted in the furnace at the designated temperature. After several time steps, the samples were removed, cooled at room temperature, and consequently weighed using a Sartorius micro balance (10<sup>-6</sup> g). After the oxidation testing, the specimens were analyzed using a Zeiss Supra 55 VP scanning electron microscope (SEM) with an attached Oxford Ultim<sup>®</sup> Max energy-dispersive X-ray spectroscope (EDS). Additionally, the crystal structures of the formed oxides were determined by an Empyrean X-ray diffractometer (XRD) using Co-K<sub>α</sub> radiation.

**Results and Discussion**

The TGA results revealed an increased mass gain of Fe-25Al-5Cr compared to the binary iron aluminide Fe-26Al at 700 °C as well as 800 °C in air for 178 h. These findings showed a detrimental influence of Cr on the oxidation kinetics at intermediate temperatures of iron aluminides. Additionally, SEM cross-section images confirmed thicker oxide layers on Fe-25Al-5Cr compared to Fe-26Al at both investigated temperatures. SEM top view images after 178 h in air at both temperatures revealed a blade- and whisker-like oxide morphology for Fe-25Al-5Cr. The blade- and whisker-like oxide

at Fe-25Al-5Cr after 178 h at 800 °C in air is depicted in Figure 1 a). The blade- and whisker-like alumina morphology was described to be related to the metastable  $\theta$ -Al<sub>2</sub>O<sub>3</sub> modification due to the growth by the outward diffusion of Al<sup>3+</sup> [14]. The XRD measurements also indicated the presence of  $\theta$ -Al<sub>2</sub>O<sub>3</sub> for Fe-25Al-5Cr at 800 °C after 178 h, while at 700 °C the alumina modification was difficult to distinguish by XRD due to the small oxide layer thickness. Therefore, TEM investigations are considered for clarification. On the contrary, SEM top view images for binary Fe-26Al after 178 h in air at both temperatures revealed an equiaxed oxide morphology, which is most likely related to the formation of  $\alpha$ -Al<sub>2</sub>O<sub>3</sub>. The equiaxed oxide at Fe-26Al after 178 h at 800 °C in air is depicted in Figure 1 b). XRD measurements also indicated the presence of  $\alpha$ -Al<sub>2</sub>O<sub>3</sub> at 800 °C. The formation of  $\alpha$ -Al<sub>2</sub>O<sub>3</sub> for binary iron aluminides was described at 700 °C in the early stage due to the nucleation of  $\alpha$ -Al<sub>2</sub>O<sub>3</sub> at hematite because of the similar crystal structure of both oxides [11]. Therefore, the presence of Cr seemed to prevent or hamper either the nucleation of  $\alpha$ -Al<sub>2</sub>O<sub>3</sub> or the transformation from  $\theta$ -Al<sub>2</sub>O<sub>3</sub> to  $\alpha$ -Al<sub>2</sub>O<sub>3</sub>. In order to analyze the growth of potential oxides in the early stage in more detail, X-ray reflectometry (XRR) and X-ray photoelectron spectroscopy (XPS) investigations are underway.

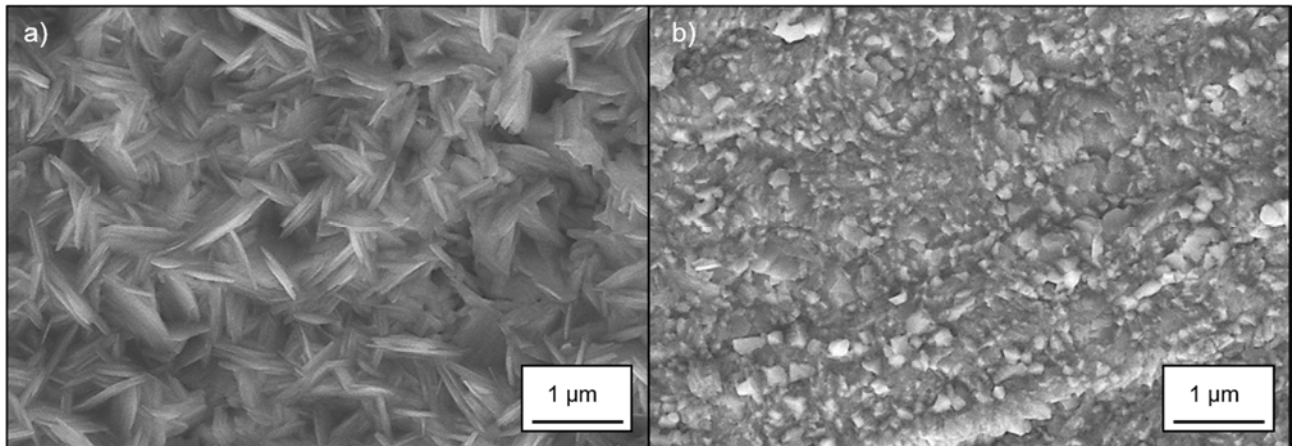


Fig. 1: SEM top view images after oxidation at 800 °C in air for 178 h of a) Fe-25Al-5Cr and b) Fe-26Al.

#### Acknowledgment

Dr. Martin Palm (Max-Planck-Institut für Eisenforschung, Düsseldorf, Germany) is highly acknowledged for providing the material.

#### References

- [1] M. Zamanzade, A. Barnoush, C. Motz, *Crystals*. **2016**, *6*, 1-29.
- [2] D.G. Morris, M.A. Muñoz-Morris, *Advanced Engineering Materials*. **2011**, *13*, 43-47.
- [3] D.G. Morris, M.A. Muñoz-Morris, *Materials Science and Engineering A*. **2007**, *462*, 45-52.
- [4] M. Palm, *International Journal of Materials Research (formerly Z. Metallkd.)*. **2009**, *100*, 277-287.
- [5] M. Palm, F. Stein, G. Dehm, *Annual Review of Materials Research*. **2019**, *49*, 297-326.
- [6] Z. G. Zhang, F. Gesmundo, P. Y. Hou, Y. Niu, *Corrosion Science*. **2006**, *48*, 741-765.
- [7] D. B. Lee, G. Y. Kim, J. G. Kim, *Materials Science and Engineering: A*. **2003**, *339*, 109-114.
- [8] N. Babu, R. Balasubramaniam, A. Ghosh, *Corrosion Science*. **2001**, *43*, 239-2254.
- [9] K. Natesan, *Materials Science and Engineering A*. **1998**, *258*, 126-136.
- [10] S. Chevalier, P. Juzon, G. Borchardt, A. Galerie, K. Przybylski, J.P. Larpin, *Oxidation of Metals*. **2010**, *73*, 43-64.
- [11] P. Brito, H. Pinto, A. Kostka, *Corrosion Science*. **2016**, *105*, 100-108.
- [12] K. Nowak, M. Kupka, *Materials Chemistry and Physics*. **2012**, *132*, 902-908.
- [13] D. Zander, R.D. Pütz, *Intermetallics*. **2020**, *126*, 106924.
- [14] B.A. Pint, J.R. Martin, L.W. Hobbs, *Solid State Ionics*. **1995**, *78*, 99-107.



## O-NA-01

Diffusion and defects to understand the growth of  $\beta$ -NiAl bond coat on superalloyE. Neelamegan<sup>1,3</sup>, A. Gupta<sup>2</sup>, V. Jayaram<sup>1</sup>, T. Hickel<sup>2</sup>, S. Divinski<sup>3</sup> and Alope Paul<sup>1</sup><sup>1</sup>Department of Materials Engineering, Indian Institute of Science, 560012 Bangalore, India, eneelame@uni-muenster.de, qjayaram@iisc.ac.in, aloke@iisc.ac.in<sup>2</sup>Max-Planck-Institut für Eisenforschung GmbH, 40237 Düsseldorf, Germany, hickel@mpie.de<sup>3</sup>Institute of Materials Physics, University of Münster, 48149 Münster, Germany, divin@uni-muenster.de

## Introduction

Platinized  $\beta$ -NiAl bond coat increases the cyclic oxidation resistance and coating life by reducing sulfur segregation between the bond coat and thermally grown oxide (TGO) layer. However, it enhances Ni and Al's interdiffusion rates, too, leading to an increase in the thickness of the interdiffusion zone (IDZ) developed between the bond coat and superalloy[1]. This results in an unwanted loss of Al from the bond coat, leading to a decrease in the turbine blade's service life. Hence, it is essential to understand the diffusion-controlled growth and microstructural evolution of IDZ at elevated temperature based on quantitative diffusion analysis[1,2].

## Materials and Methods

Composition dependent diffusion coefficients are estimated in B2-Ni(Co,Pt)Al quaternary system by utilizing the pseudo-binary (PB)[3] and pseudo-ternary (PT) diffusion couple methods [4,5], which was not possible earlier by the conventional method. The estimated diffusion coefficients are correlated with ab-initio calculated defect concentration to explain the diffusion mechanism. The diffusion couple technique is followed to understand the growth of IDZ between the bond coat and superalloy, which mimics the aircraft engine application's actual structure. IDZ's are investigated further by elemental X-ray mapping of Electron Probe Microanalyser (EPMA), and the Phases were identified by indexing Selected Area Electron Diffraction (SAED) patterns of Transmission Electron Microscopy (TEM).

## Results and Discussion

In the PB method, only two-component develop the diffusion profile keeping the others remains constant such that one can estimate the composition dependent interdiffusion coefficients in multicomponent system. In our B2-Ni(Co,Pt)Al quaternary system, Ni and Al were allowed to develop the diffusion profiles to estimate the Pt and Co effect on Ni and Al's interdiffusion. The Pt-addition increases the interdiffusion coefficient, but Co-addition decreases. Figure 1 indicates the interdiffusion coefficients and the thermodynamic driving force follows an opposite trend. Defects play a significant role in the diffusion mechanism in this system[6]. Defect concentrations calculated with ab-initio explain that the addition of Pt increases the concentration of vacancies on the Ni sublattice, facilitating diffusion. According to the triple defect diffusion mechanism, a distinct impact of Pt-alloying on the diffusion barriers is predicted, whereas Co-alloying keeps the diffusion barriers almost unaffected.

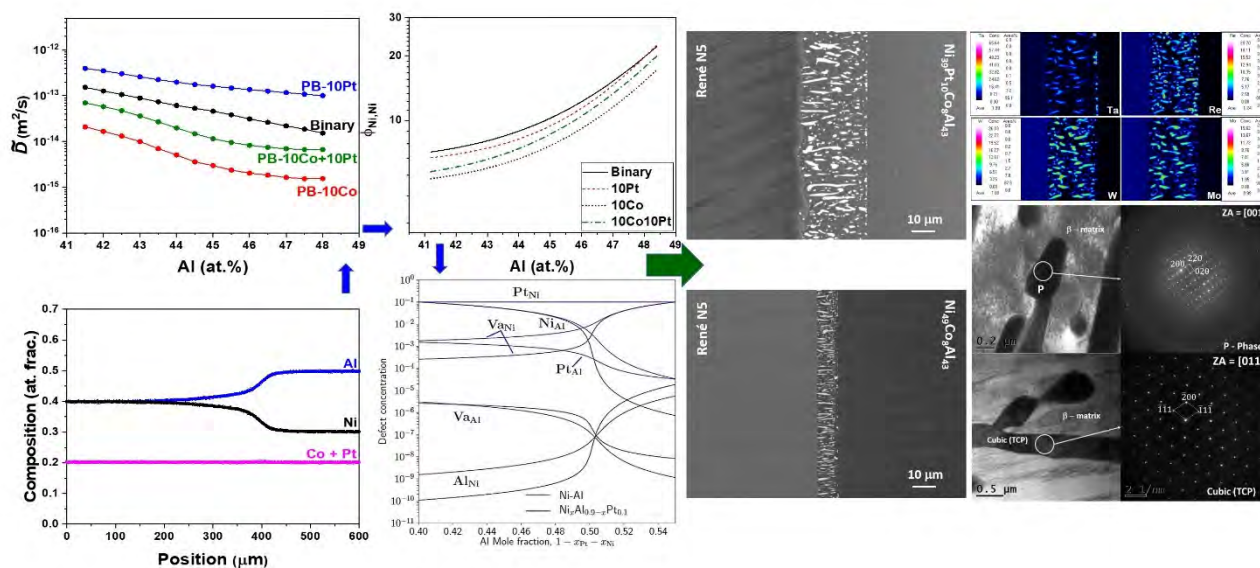


Fig.1. Schematic flow diagram to understand the growth of interdiffusion zone between the superalloy and bond coat

In the PT Method, Ni, Co, and Al develop the diffusion profiles, which indicates the main interdiffusion coefficients increase significantly in the presence of Pt, but the cross interdiffusion coefficients change marginally, causing a minor change in these components' diffusional interactions. The estimated diffusion coefficients are utilized to explain the increase in the thickness of the IDZ between the B2-Ni(Co,Pt)Al bond coat and single crystal superalloy René N5. Quantitative EPMA reveals that the IDZ consists of TCP precipitates, which are rich in refractory elements. These precipitates were identified as cubic Laves phase and Orthorhombic P-phase. Pt-addition does not change the nature of these precipitates formed on the IDZ.

### Conclusions

Pseudo-binary interdiffusion coefficients of Ni-Al are found to increase in the presence of Pt but decrease in the presence of Co. In the pseudo-ternary diffusion couples, Ni, Co, and Al develop diffusion profiles keeping Pt concentration constant. Quaternary PT-interdiffusion coefficients in the presence of Pt are compared with those for the ternary Ni-Co-Al system. The main interdiffusion coefficients of Ni and Co increase, whereas the cross interdiffusion coefficients change marginally. The observed trends are opposite to the changes of the relevant thermodynamic factors and the ab-initio calculated defect concentrations are used to rationalize the diffusion behaviour. The vacancy concentration on the Ni-sublattice is found to increase in the presence of Pt. The diffusion barriers predicted according to the triple defect mechanism support the experimentally-observed influence of Pt and Co additions on diffusion. An increase in the interdiffusion rates of Ni and Al in the presence of Pt enlightens the role of Pt in the growth of the interdiffusion zone between the bond coat and a superalloy. EPMA and TEM analyses indicate that the nature of the precipitates is unaltered by addition of Pt.

### References

- [1] P. Kiruthika, S.K. Makineni, C. Srivastava, K. Chattopadhyay, A. Paul, Growth mechanism of the interdiffusion zone between platinum modified bond coats and single crystal superalloys, *Acta Mater.* **2016**, *105*, 438–448.
- [2] N. Esakkiraja, A. Gupta, V. Jayaram, T. Hickel, S. V. Divinski, A. Paul, Diffusion, defects and understanding the growth of a multicomponent interdiffusion zone between Pt-modified B2 NiAl bond coat and single crystal superalloy, *Acta Mater.* **2020**, *195*, 35–49.
- [3] A. Paul, A pseudobinary approach to study interdiffusion and the Kirkendall effect in multicomponent systems, *Philos. Mag.* **2013**, *93*.
- [4] N. Esakkiraja, K. Pandey, A. Dash, A. Paul, Pseudo-binary and pseudo-ternary diffusion couple methods for estimation of the diffusion coefficients in multicomponent systems and high entropy alloys, *Philos. Mag.* **2019**, *99*, 2236–2264.
- [5] N. Esakkiraja, A. Paul, A novel concept of pseudo ternary diffusion couple for the estimation of diffusion coefficients in multicomponent systems, *Scr. Mater.* **2018**, *147*.
- [6] S. Divinski, Chapter 10 - Defects and Diffusion in Ordered Compounds, in: A. Paul, S.B.T.-H. of S.S.D. Divinski Volume 1 (Eds.), Elsevier. **2017**, 449–517.



**O-NA-02****Small scale fracture behavior of nanostructured NiAl-(Cr,Mo) *in-situ* composites processed by selective electron beam melting**

Andreas Förner<sup>1</sup>, Jakob Bandorf<sup>1</sup>, Abdullah Jamjoom<sup>2</sup>, Steffen Neumeier<sup>1</sup>,  
Carolin Körner<sup>2</sup> and Mathias Göken<sup>1</sup>

<sup>1</sup>Friedrich-Alexander-Universität Erlangen, Materials and Engineering Institute I, Erlangen, Germany,  
andreas.foerner@fau.de

<sup>2</sup>Friedrich-Alexander-Universität Erlangen, Materials and Engineering for Metals, Erlangen, Germany

**Introduction**

NiAl-Cr and NiAl-(Cr,Mo) eutectic *in-situ* composites are promising high temperature materials due to a high melting point, excellent oxidation behavior and their low density [1,2]. The B2 intermetallic NiAl is reinforced by a refractory Cr phase to combine the beneficial properties of both phases. Mo can be added to the eutectic alloy to change the morphology from Cr rods to Cr plates when exceeding a threshold of 0.6 at.% Mo. Using directional solidification, the coarse reinforcing phase (Cr,Mo) solidifies well aligned embedded in a brittle NiAl Matrix [3]. Despite their promising characteristics, the application in the realm of aerospace and energy conversion is limited due to a poor room temperature fracture toughness and insufficient high temperature strength [1]. In this study, selective electron beam melting (SEBM) is used to process nanostructured eutectic materials. High cooling rates are beneficial to obtain fine cellular-lamellar structures with extremely fine phases in the regime of 5 to 400 nm [4]. Higher hardness and higher strength than their as-cast counterpart promises enhanced mechanical properties. Like the coarse as-cast microstructure, also the nanostructured, alternating phases show crack hindering mechanisms which can enhance the fracture resistance [4]. The aim of this research is to characterize the microstructure, mechanical properties with emphasis on fracture behavior of a NiAl-28Cr-6Mo eutectic *in-situ* composite processed additively by selective electron beam melting.

**Materials and Methods**

The eutectic *in-situ* composite NiAl-28Cr-6Mo is processed by selective electron beam melting. An Arcam A2X (GE Additive) is used to build 15 x 15 x 20 mm<sup>3</sup> cubes in subsequent layers with a standard hatch pattern. Various process parameters are used to create columnar and equiaxed cell morphologies with rod or lamellar microstructures by using very fast cooling rates. The cross section of the samples are analyzed using SEM and FIB (Crossbeam XB540, Zeiss GmbH) as well as APT technique (LEAP 4000x HR, Cameca Inc.) for microstructural characterization. The room temperature fracture toughness was determined using micro-cantilevers prepared by Ga FIB milling as described in [5] and tested with an *in-situ* Indenter (FemtoTools AG) displacement controlled. With a size of B x W x L = 3 x 3 x 12 μm<sup>3</sup> and a fibbed sharp notch with a crack to height ratio of a/W = 1/3 the fracture toughness  $K_{I0.1}$  is determined according to ASTM E399 and E1820 [6,7]. Different fracture mechanisms and deformation mechanisms are visualized using SEM *in-situ* video observation, STEM and TEM (CM200, Philips). Furthermore, compression tests and compression creep tests were performed at different loads starting at room temperature up to 1300 K.

**Results and Discussion**

The SEBM specimens consist of a cellular structure. Depending on the SEBM process parameters, in particular the area energy and the beam offset, columnar or equiaxed cells can be found. With respect to the solidification speed, a three dimensional cross-linked (Cr,Mo) network can be found for high cooling rates, whereas lamellar (Cr,Mo) strengthening phases are present at lower cooling rates (see Fig.1b). The morphology of the cells and phases is determined by the solidification and cannot be transformed via heat treatments. The phase distance of the NiAl and the (Cr,Mo) phases within the cells is in the regime of 5 to 400 nm. Depending on the building height, there is coarsening due to the *in-situ* heat treatment introduced by the electron beam during layer-wise additive manufacturing. This coarsening is the reason for a decreasing hardness with increasing building height. This highly flexible approach allows fine-tuning of the microstructure to get all desired morphologies and phase distances within one specimen. The mechanical properties therefore need to be tailored on a micro-mechanical scale in dependence of the local cell shape and phase distance. Compression tests show a significant higher yielding stress over the entire temperature range than the cast composite. Depending on the process parameters, the yield stress with 1043 to 1344 MPa is more than twice the stress than it is for polycrystalline NiAl with 424 MPa at 900K [1]. According to the Hall-Petch strengthening of fine phases, also the hardness is increased by more than 50 % compared to the as-cast *in-situ* composite. Creep tests at 900 °C with 100 to 300 MPa compressive load show a creep performance similar to TiAl alloys currently used in aerospace applications. Compression tests perform best for larger, columnar cells exhibiting a cross-linked (Cr,Mo) network. Fracture toughness was measured with micro cantilever bending tests (see Fig.1a). They provide a suitable approach to test local features of nanostructured materials. Cross-linked rods, lamellar phases and coarse phases at cell boundaries are tested on a small scale and best morphologies with the highest fracture resistances are identified. In case of a cross-linked (Cr,Mo)

network, the fracture toughness increases with rising phase thickness up to  $10 \text{ MPam}^{0.5}$  for 150nm. This increase is in good agreement with enhanced dislocation activity and therefore plastic deformation in larger phases. At first, the crack interacts with the (Cr,Mo) network and is not able to propagate very far in the brittle NiAl matrix. Therefore, specimens fracture abruptly with instable crack growth at the maximum load applied (Fig.1c). If phases are thicker than 30 nm, both the (Cr,Mo) and the NiAl phase show plastic deformation induced by the interface dislocation network. For coarse phases at the cell boundaries, stable crack growth is present. For phase distances larger than 100 nm also stable crack growth and crack hindering mechanism can be observed in the cross-linked network structure. For the three dimensional cross-linked network, the fracture is isotropic. In contrast, a lamellar (Cr,Mo) morphology is able to deflect, renucleate and bridge the propagating crack more easily. This leads to high fracture toughness of  $10 \text{ MPam}^{0.5}$  for cantilevers with (Cr,Mo) phases in crack arrester orientation but only  $3 \text{ MPam}^{0.5}$  for the detrimental crack divider orientation. Depending on the local (Cr,Mo) lamellar orientation, both stable and instable crack growth are visible. Crack propagation can be measured via contact stiffness during testing. This can be correlated with SEM live in-situ videos showing stable and unstable crack growth with high precision on the nanoscale. Lamellar phases show a low initiation toughness, whereas their work of fracture and their critical fracture toughness is quiet high. This study presents nanostructured in-situ composites processed by additive manufacturing with prominent crack hindering mechanisms despite their small phases and the brittle character of B2 NiAl. Crack hindering is enhanced by the higher amount of interfaces per volume in contrast to directional solidified materials.

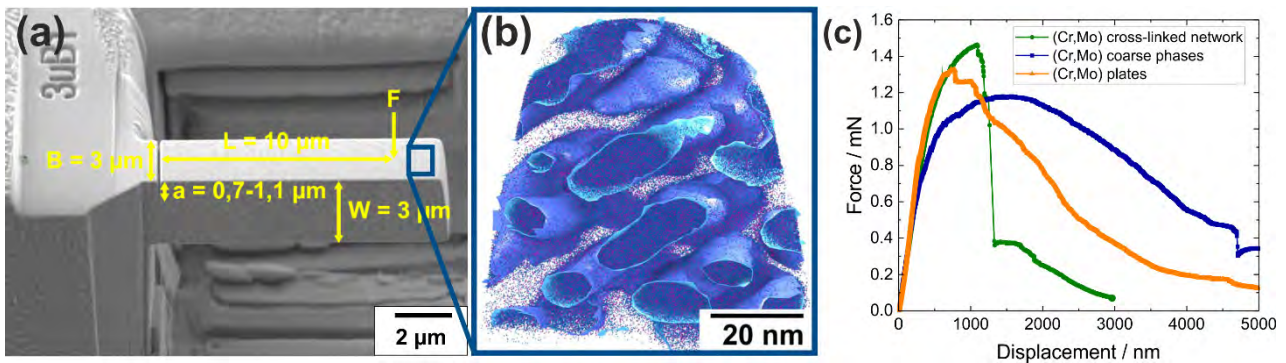


Fig. 1: SEM micrograph of the dimensions of a micro bending cantilever processed by Ga-FIB milling in additively manufactured NiAl-28Cr-6Mo (a). It consists of nanostructured NiAl and (Cr,Mo) phases that are displayed via the 40 at.-% Cr isosurface in the Atom Probe Tomography (b). Depending on the microstructure, three different fracture behaviours and crack propagations can be identified in the Force-Displacement diagram of the micro bending cantilevers (c).

## References

- [1] D. R. Johnson et al., *Intermetallics*. **1995**, 3, 99-113
- [2] S. V. Raj et al., *Metallurgical and Materials Transactions*. **2002**, 33A, 597-612.
- [3] H.E. Cline and J.L. Walter, *Metallurgical Transactions*. **1970**, 1.10, 2907-2917.
- [4] A.Förner et al., *Scientific Reports*. **2020**, 10(1), 1-9.
- [5] D. DiMaio et al., *Journal of Materials Research*. **2005**, 5, 299-302.
- [6] ASTM International: ASTM E399–90 Standard Test Method for Plane-strain Fracture Toughness of Metallic Materials, Vol. 03.01 (ASTM International, West Conshohocken). **1991**, 1–34.
- [7] ASTM International: ASTM E1820–13 Standard Test Method for Measurement of Fracture Toughness, Vol. 03.01 (ASTM International, West Conshohocken). **2014**, 1–54.

**O-NA-03****Micro-tensile creep testing for NiAl single crystalline miniaturized specimens**LiKang Luan<sup>1</sup>, Heinz Riesch-Oppermann<sup>2</sup> and Martin Heilmaier<sup>3</sup><sup>1</sup>Dantec Dynamics, 89077 Ulm Germany, lln@dantecdynamics.com<sup>2</sup>Karlsruhe Institute of Technology, Institute for Applied Materials (IAM), 76344 Eggenstein-Leopoldshafen, Germany, heinz.riesch-oppermann@kit.edu<sup>3</sup>Karlsruhe Institute of Technology, Institute for Applied Materials (IAM), 76131 Karlsruhe, Germany, martin.heilmaier@kit.edu**Introduction**

Tensile creep test of Dog-bone shaped NiAl single crystalline miniaturized specimens in size of sub-mm scale were carried out with [110] soft and [100] hard orientations up to 1000 °C. A contactless strain measurement based on Digital Image Correlation (DIC) was used in a customized setup, which provides a strain accuracy better than  $10^{-4}$  at 1000 °C and simultaneously enables the analysis of strain distribution of the miniaturized specimens. The creep behavior of the miniaturized specimens in both orientations showed an influence of the specimen geometry that decreasing steady state/min creep strain rates were observed in specimens with larger ratios of length to the square of thickness ( $L/h^2$  ratios). Misorientation and GND density analysis by using EBSD were carried out for further study of the influence of specimen geometry on creep behavior.

**Materials and Methods**

Miniaturized specimens were manufactured with different gauge lengths (700  $\mu\text{m}$  and 1400  $\mu\text{m}$ ), widths and thicknesses (200, 300 and 400  $\mu\text{m}$ ) in [110] soft and [100] hard orientations. A customized setup for tensile creep test up to 1000 °C was designed by using a load cell for load control and DIC for strain measurement. A closed-loop feedback of the load and strain signal was used to maintain a constant stress during the tensile creep test. Strain distribution analysis with DIC was used to study the strain evaluation and localization on the miniaturized specimens during the tensile creep test. EBSD measurements of the miniaturized specimens interrupted at different creep stages were carried out, and the corresponding Geometrically Necessary Dislocation (GND) density based on Kernel Average Misorientation (KAM) were determined to study its influence on creep behavior of the miniaturized specimens.

**Results and Discussion**

The creep behavior of specimens with the smallest  $L/h^2$  ratios showed a good agreement to the conventional-sized specimens [1]. However, a reducing steady-state/min creep strain rates of miniaturized specimen with increasing  $L/h^2$  ratios were observed in both [110] soft and [100] hard orientations (see Figure 1). Strain distribution analysis with DIC showed that an increasing shear strain localization was observed in specimens with larger  $L/h^2$  ratios, where increasing misorientation and GND density were determined (see Figure 2).

The influence of GNDs on the creep behavior showed a dependence on the crystal orientation: For specimens in [110] soft orientation, the GNDs obstruct the  $\langle 100 \rangle$  dislocation glide resulting in decreased creep strain rates. Meanwhile, for specimens in [100] hard orientation, the  $\langle 110 \rangle$  dislocations decompose into two  $\langle 100 \rangle$  dislocations [2]. The edge part of these dislocations is effectively sessile and can move only via  $\langle 100 \rangle$  dislocation climb. Therefore, a weaker influence of the GNDs on the creep behavior of the specimens in [100] hard orientation was detected compared to the specimens tested in [110] soft orientation.

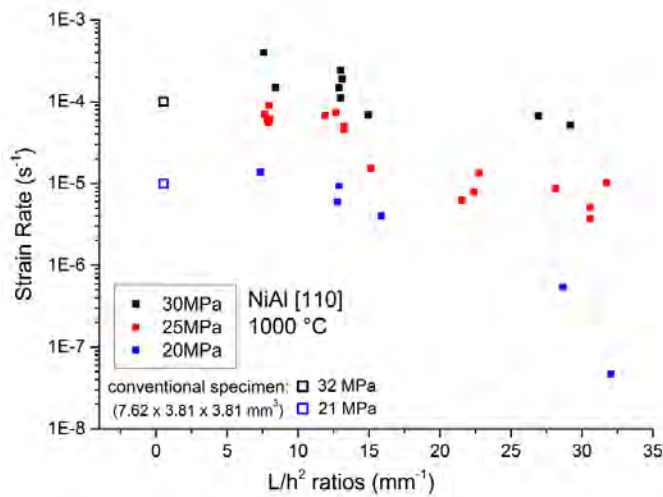


Fig. 1: Diagram of steady-state/min creep strain rates vs. the ratio of gauge length to the square of thickness ( $L/h^2$  ratios) of the miniaturized specimens and the conventional specimens in size of  $7.62 \times 3.81 \times 3.81 \text{ mm}^3$  in [110] soft orientation [1].

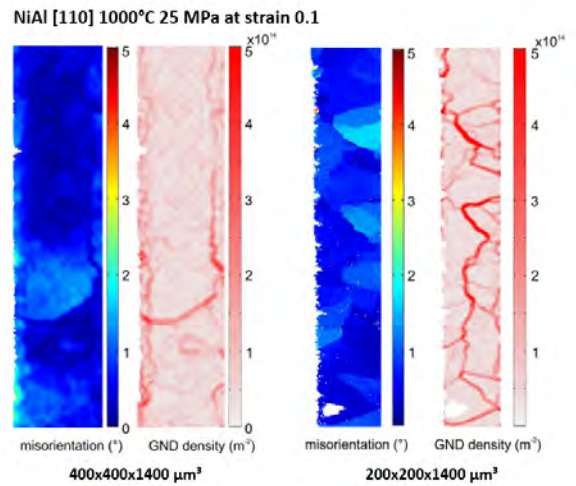


Fig. 2: Misorientation and GND distribution of two specimens with same gauge length of  $1400 \mu\text{m}$  and different width and thickness of  $200 \mu\text{m}$  tested at  $1000^\circ\text{C}$  and  $25 \text{ MPa}$  interrupted at a strain of  $0.1$ . Increased misorientation and GND density was observed in specimen with a larger  $L/h^2$  ratio.

**References**

- [1] K. R. Forbes, U. Glatzel, R. Darolia, and W. D. Nix, High-temperature deformation properties of NiAl single crystals, *Metallurgical and Materials Transactions A*. **1996**, 27, no. 5, 1229–1240.
- [2] M. Mills, J. Angelo, M. Daw, J. Weinburg, and D. Miracle, Fine structure of a  $\langle 011 \rangle$  dislocations and the mechanical properties of NiAl in the hard orientation, *Materials Science and Engineering: A*. **1995**, 192, 134–141.

## O-NA-04

**Microstructure evolution of an  $\alpha'/\alpha''$ -strengthened ferritic superalloy**

Luis Ángel Morales<sup>1</sup>, Andreas Bezold<sup>2</sup>, Andreas Förner<sup>2</sup>, Steffen Neumeier<sup>2</sup>,  
 Carolin Körner<sup>1</sup> and Christopher Zenk<sup>1</sup>

<sup>1</sup>Chair of Materials Science and Engineering for Metals (WTM), Friedrich-Alexander-Universität Erlangen-Nuremberg, Germany, Luis.Morales@fau.de

<sup>2</sup>Institute of General Material properties (WW1), Friedrich-Alexander-Universität Erlangen-Nuremberg, Germany

**Introduction**

Ferritic superalloys based on the Fe-Al-Ni system are promising materials for high-temperature applications, due to their combination of reasonable ductility and creep resistance[1,2]. The microstructure of these materials consists of an A2 ( $\alpha$ -Fe solid solution) matrix with B2-ordered ( $\alpha'$ , based on NiAl) precipitates[2,3]. By alloying beyond the ternary system, the properties of both phases and the final performance of the alloy are enhanced[4]. A way to improve their creep resistance is the partial transformation of  $\alpha'$  into  $L2_1$  (based on  $Ni_2AlTi$ ,  $\alpha''$ ) by adding Ti [5]. This transformation facilitates an  $\alpha/\alpha'/\alpha''$  microstructure; this type of material has previously been referred to as *Hierarchical Precipitate Strengthened Ferritic Alloy* (HPSFA) [6], due to the fact that smaller precipitates form within larger ones. In this work, we report the development of a novel hierarchical  $\alpha/\alpha'/\alpha''$  ferritic superalloy with Co and Cu additions. Co was added as solid solution strengthener, whereas Cu serves as  $L2_1$  phase stabilizer and also induces the formation of Cu-rich BCC nano-precipitates [7]. The main goal of the study is the analysis and evolution of its microstructure with the aim to design a suitable heat-treatment that optimize the alloy's mechanical performance.

**Materials and Methods**

The investigated alloy Fe-18Al-10Ni-5Co-10Cr-1.87Mo-2.5Ti-1.5Cu at.% has been arc-melted from 99.99 % pure elements under a protective argon atmosphere. The determination of the actual chemical composition of the alloys has been performed by EDS. DSC measurements were conducted on as-cast specimens at 10 °C/min heating and cooling rates. Samples for microstructure analysis were solution treated at 1200 °C for 1h and air-cooled followed by aging between 800 °C and 1100 °C for 1 h to 150 h. For volume fraction and particle size characterization, scanning electron microscopy (SEM) images of nearly oriented  $\langle 100 \rangle$  grains were analyzed. Transmission electron microscopy (TEM) diffraction-contrast imaging was conducted to reveal the finer details of the hierarchical microstructure. Atom-probe tomography (APT) has been performed to additionally obtain information on the elemental partitioning behavior and interesting microstructural features that have been identified in TEM.

**Results and Discussion**

Alloying with 10 at. % Cr, 1.87 at. % Mo, 2.5 at. % Ti, and 1.5 at. % Cu in the quaternary Fe-Al-Ni-Co system has resulted in an  $\alpha/\alpha'/\alpha''$  hierarchical alloy (HPSFA2 +Co+Cu), with promising coarsening-resistance up to 900 °C. Co and Cu partition to the  $\alpha'/\alpha''$  precipitates. Strongly depending on the heat treatment, this alloy forms a variety of drastically different microstructures, some of which look very promising. After the solid solution and aging heat treatments, its microstructure consists of a coherent network of separated cubic precipitates that coarsen to plates oriented in the elastically soft  $\langle 001 \rangle$  directions. Microstructural analysis of the mean radius evolution in the range of 800 °C to 950 °C revealed that the precipitates exhibit at 800 °C a lower coarsening exponent than the  $t^{1/3}$  predicted by the Lifshitz-Slyozov-Wagner (LSW) theory for multicomponent alloys. This phenomenon has been attributed to the hierarchical nature of its precipitates. Furthermore, after furnace cooling above 950°C, a strong reprecipitation phenomenon was found to take place not just in the matrix but inside of the primary precipitates. According to the aging temperature and size of the primary precipitates, these re-precipitated particles can take up a high volume fraction and their plate-like morphology suggests that they are elastically constrained. TEM dark-field microscopy using the  $\alpha'$  and  $\alpha''$  superlattice reflections confirmed the presence of a hierarchical  $\alpha/\alpha'/\alpha''$  microstructure and provide crystallographic information of the nanosize reprecipitation. Fig. 1 illustrates these results for a sample solution treated and aged at 900 °C /5 h. Fig. 1(a) shows the SAED pattern in the  $\langle 101 \rangle$  zone axis, confirming the presence of the superlattice reflections  $\alpha'$  and  $\alpha''$ . The BF micrograph presented in Fig. 1(b) expose the presence of secondary  $\alpha'$  precipitates in the matrix, and a complex hierarchical network of nanosized A2 and B2 precipitates within the primary  $\alpha'/\alpha''$  precipitates. Complementary APT measurements have allowed relating the phase crystallographic distribution observed by TEM, with the measured phase compositions. Furthermore, APT analysis confirmed the formation of Cu-rich clusters and disclosed anti-phase domains which must have formed during the  $\alpha' \rightarrow \alpha''$  ordering reaction. Fig. 2 displays an APT reconstruction of the same specimen as before. All mentioned phases can be resolved: the  $\alpha$  matrix (rich in Fe, Cr, and Mo), the primary  $\alpha'$  precipitates (rich in Al, Ni, Co, and Fe) partially transformed into  $\alpha''$  (correspondent to Ti rich domains) and inside them, the reprecipitation of  $\alpha$ . Additionally, the presence of Cu-rich BCC nanoparticles could be confirmed both in the primary  $\alpha'/\alpha''$  precipitates and the  $\alpha$  matrix, where they often adjoined secondary  $\alpha'$  precipitates.



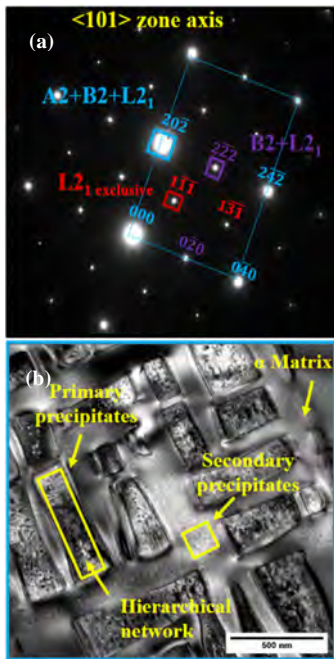


Fig. 1: HPSFA2 +Co+Cu ST and aged at 900 °C /5h (a) SAED in the <101> zone axis (b) BF micrograph

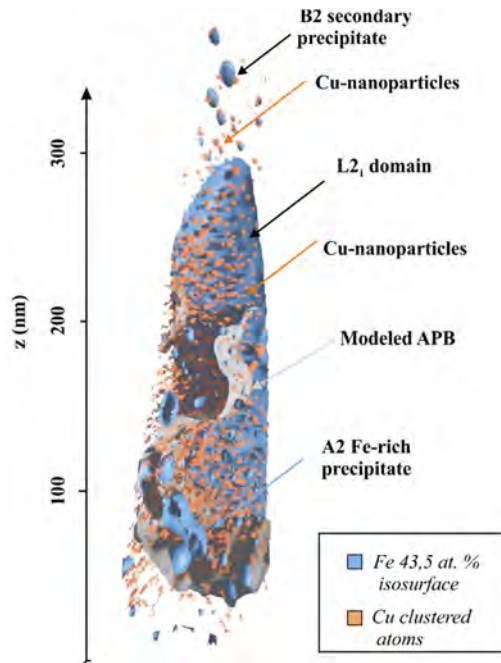


Fig. 2: APT reconstruction showing Cu-nanoparticles formation in the parent precipitate

References

[1] O. Ikeda, I. Ohnuma, R. Kainuma, K. Ishida, *Intermetallics*. **2001**, *9*, 755–761.  
 [2] I. Jung, G. Sauthoff, *Creep Fract. Eng. Mater. Struct.* **1987**, 257–270.  
 [3] A.J. Bradley, *J. Iron Steel Inst.* **1951**, *168*, 233.  
 [4] Z.K. Teng, C.T. Liu, M.K. Miller, G. Ghosh, E.A. Kenik, S. Huang, P.K. Liaw, *Mater. Sci. Eng. A*. **2012**, *541*, 22–27.  
 [5] C.H. Liebscher, V. Radmilovic, U. Dahmen, M. Asta, G. Ghosh, *J. Mater. Sci.* **2013**, *48*, 2067–2075.  
 [6] G. Song, Z. Sun, L. Li, X. Xu, M. Rawlings, C.H. Liebscher, B. Clausen, J. Poplawsky, D.N. Leonard, S. Huang, Z. Teng, C.T. Liu, M.D. Asta, Y. Gao, D.C. Dunand, G. Ghosh, M. Chen, M.E. Fine, P.K. Liaw, *Sci. Rep.* **2015**, *5*, 16327.  
 [7] Z.B. Jiao, J.H. Luan, M.K. Miller, Y.W. Chung, C.T. Liu, *Mater. Today*. **2017**, *20*, 142–154.

O-NA-05

### A quantum mechanical study of pressure induced changes of magnetism in austenitic stoichiometric Ni<sub>2</sub>MnSn

Martin Friák<sup>1</sup>, Martina Mazalová<sup>1,2</sup>, Ilja Turek<sup>1</sup>, Adéla Zemanová<sup>1</sup>, Jiří Kaštil<sup>3</sup>, Jiří Kamarád<sup>3</sup>, Martin Míšek<sup>3</sup>, Zdeněk Arnold<sup>3</sup>, Oldřich Schneeweiss<sup>1</sup>, Monika Všianská<sup>2,1</sup>, Martin Zelený<sup>4,5</sup>, Aleš Kroupa<sup>1</sup>, Jana Pavlů<sup>2</sup> and Mojmír Šob<sup>1,2,6</sup>

<sup>1</sup>Institute of Physics of Materials, v.v.i., Czech Academy of Sciences, 616 62 Brno, Czech Republic, friak@ipm.cz, 394206@mail.muni.cz, turek@ipm.cz, zemanova@ipm.cz, schneew@ipm.cz, 230038@mail.muni.cz, kroupa@ipm.cz, mojmir@ipm.cz

<sup>2</sup>Department of Chemistry, Faculty of Science, Masaryk University, 611 37 Brno, Czech Republic, houserova@chemi.muni.cz

<sup>3</sup>Institute of Physics, v.v.i., Czech Academy of Sciences, 182 21 Prague 8, Czech Republic, kastil@fzu.cz, kamarad@fzu.cz, misek@fzu.cz, arnold@fzu.cz

<sup>4</sup>Faculty of Mathematics and Physics, Charles University, 121 16 Prague 2, Czech Republic, zeleny@ipm.cz

<sup>5</sup>Faculty of Mechanical Engineering, Institute of Materials Science and Engineering, Brno University of Technology, 616 69 Brno, Czech Republic

<sup>6</sup>Central European Institute of Technology, CEITEC MU, Masaryk University, 625 00 Brno, Czech Republic

#### Introduction

The Heusler alloys are one of the most prominent family of compounds currently studied due the presence of an extraordinary magneto-structural transition in their phase diagrams because this non-diffusive martensitic transition is accompanied nearly always by very pronounced changes of physical properties of the alloys (see, e.g., Ref. [1]). The stoichiometric austenite Ni<sub>2</sub>Mn-based alloys crystallize in the cubic Fm-3m structure (L<sub>21</sub>, full Heusler) and exhibit a long range ferromagnetic arrangement of moments below the Curie temperature, see, e.g., Ref. [2] and references therein. Our research was motivated by the fact that quantum-mechanical studies of pressure-induced changes in different magnetic states of stoichiometric Ni<sub>2</sub>MnSn with point defects, in particular swaps, are quite rare and, therefore, we aimed at filling this gap in common knowledge. We also have our own experimental data [2] and we hope that our theoretical results can shed a new light on very intriguing pressure-induced changes in Ni-Mn-Sn compounds.

#### Materials and Methods

Our ab initio calculations were performed using the Vienna Ab initio Simulation Package (VASP) [3,4]. We have employed projector augmented wave (PAW) pseudopotentials [5,6]. The exchange and correlation energy was treated within the generalized gradient approximation (GGA) [7]. We have used 16-atom supercells with the L<sub>21</sub> austenitic phase of stoichiometric Ni<sub>2</sub>MnSn (see Figure 1b) and its substitutional variants for swap-containing states. The plane-wave energy cut-off was equal to 700 eV and the product of the number of Monkhorst-Pack k-points and the number of atoms was equal to 8192, i.e., 8x8x8 k-point mesh with its origin shifted to (1/2, 1/2, 1/2) in the case of 16-atom supercells. The Methfessel-Paxton order 1 smearing was applied with the smearing parameter equal to 0.23.

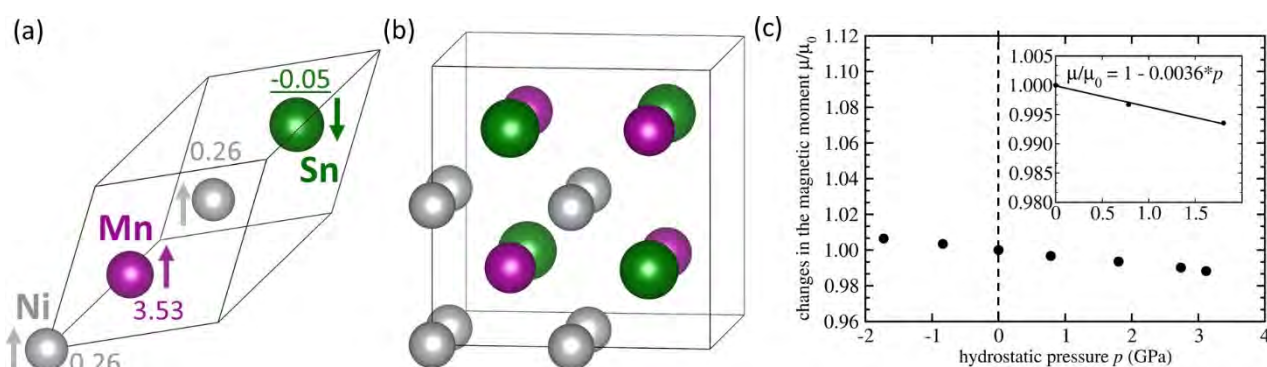


Fig. 1: Schematic visualizations of 4-atom rhombohedral primitive unit cell (a) and 16-atom computational supercell (b) of the stoichiometric Ni<sub>2</sub>MnSn with the austenitic structure (L<sub>21</sub>, full Heusler structure). Arrows in part (a) indicate the orientation of local magnetic moments and numbers accompanying them are their magnitudes in Bohr magnetons with negative underlined values indicating an antiparallel orientation. Computed pressure-induced changes of the total magnetic moment  $\mu$  relative to its zero-pressure value  $\mu_0$  is shown in part (c) where the inset contains a linear fit through the values in the lower-pressure region.

### Results and Discussion

We have performed an ab initio study of a series of stoichiometric Ni<sub>2</sub>MnSn states with austenitic (full Heusler type) structure using 16-atom computational supercells. In particular, we have focused on pressure-induced changes in their magnetic state as we have our own experimental data for austenitic Ni<sub>2</sub>MnSn [2]. Motivated by the facts that our calculations (i) give the total magnetic moment of the defect-free stoichiometric Ni<sub>2</sub>MnSn higher than the experimental value by 12.8 % and (ii) predict it to be more sensitive to hydrostatic pressures, our study was focused on the role of point defects in this material. We have studied the effect of Mn-Ni, Mn-Sn and Ni-Sn swaps in the stoichiometric Ni<sub>2</sub>MnSn and we also compared states with both ferromagnetic (FM) and anti-ferromagnetic (AFM) coupling between (i) the swapped Mn atoms and (ii) the Mn atoms on the Mn sublattice for most of these atomic configurations (for some atomic configurations we were not able to stabilize them in our calculations). By analyzing the magnetic moments of states with swaps we show their complexity and significant influence on materials properties. In particular, they can lead to total magnetic moments twice smaller than those in the defect-free Ni<sub>2</sub>MnSn and pressure-induced changes in the total magnetic moment can be nearly three times larger but also smaller depending on the type of defects and the coupling of Mn atoms. Importantly, we find both qualitative and quantitative differences also in the pressure-induced changes of magnetic moments of individual atoms even for the same global magnetic state. Lastly, the FM-coupled and AFM-coupled states with very different magnetic properties have sometimes formation energies different only by a few meV per atom. It then seems that a few mechanisms acting at once contribute into the above mentioned theory-experiment discrepancy. The complexity of the Ni-Mn-Sn system make it on one hand quite challenging to study but, on the other hand, possibly allows for a flexible fine-tuning of functional properties of these materials within a theory-guided materials design based on utilizing properties of various types of defects. For details see our recent paper [8].

### Funding

The authors acknowledge the Czech Science Foundation for the financial support received under the Project No. 20-16130S entitled “Multifunctional properties of powdered Ni-Mn-Sn intermetallics”.

### Acknowledgments

We also acknowledge financial support by the Ministry of Education, Youth and Sports of the Czech Republic in the range of the Project CEITEC 2020 (Project No. LQ1601), Project CZ.02.1.01/0.0/0.0/15\_003/0000487-MATFÚN, and, regarding the experimental part, the experiments were performed in MGML (mgml.eu), which is supported within the program of Czech Research Infrastructures (project no. LM2018096). Computational resources were made available by the Ministry of Education, Youth and Sports of the Czech Republic under the Project of the IT4Innovations National Supercomputer Center (project “e-Infrastructure CZ-LM2018140”) within the program Projects of Large Research, Development and Innovations Infrastructures and via the CESNET (Project No. LM2015042) and CERIT-Scientific Cloud (Project No. LM2015085). Parts of Figure 1 were visualized using the VESTA software [9] (version 3, National Museum of Nature and Science, 4-1-1, Amakubo, Tsukuba-shi, Ibaraki 305-0005, Japan).

### References

- [1] T. Graf, C. Felser, S. S. Parkin, Simple rules for the understanding of Heusler compounds, *Prog. Solid State Chem.* **2011**, *39*, 1-50.
- [2] J. Kaštil, J. Kamarád, O. Isnard, Y. Skourski, M. Míšek, Z. Arnold, Effect of pressure and high magnetic field on phase transitions and magnetic properties of Ni<sub>1.92</sub>Mn<sub>1.56</sub>Sn<sub>0.52</sub> and Ni<sub>2</sub>MnSn Heusler compounds, *J. Alloys Compd.* **2015**, *650*, 248-255.
- [3] G. Kresse, J. Hafner, Ab initio molecular dynamics for liquid metals, *Phys. Rev. B.* **1993**, *47*, 558-561.
- [4] G. Kresse, J. Furthmüller, Efficient iterative schemes for ab initio total-energy calculations using a plane-wave basis set. *Phys. Rev. B.* **1996**, *54*, 11169-11186.
- [5] P. E. Blöchl, Projector augmented-wave method. *Phys. Rev. B.* **1994**, *50*, 17953-17979.
- [6] G. Kresse, D. Joubert, From ultrasoft pseudopotentials to the projector augmented-wave method. *Phys. Rev. B.* **1999**, *59*, 1758-1775.
- [7] J. P. Perdew, K. Burke, M. Ernzerhof, Generalized gradient approximation made simple. *Phys. Rev. Lett.* **1996**, *77*, 3865-3868.
- [8] M. Friák, M. Mazalová, I. Turek, A. Zemanová, J. Kaštil, J. Kamarád, M. Míšek, Z. Arnold, O. Schneeweiss, M. Všianská, M. Zelený, A. Kroupa, J. Pavlů, M. Šob, An ab initio study of pressure-induced changes of magnetism in austenitic stoichiometric Ni<sub>2</sub>MnSn, *Materials.* **2021**, *14*, Art. No. 523.
- [9] K. Momma, F. Izumi, VESTA 3 for three-dimensional visualization of crystal, volumetric and morphology data. *J. Appl. Crystallogr.* **2011**, *44*, 1272-1276.

**O-FI-01****Intermetallic compounds as hydrogenation catalysts – structural and electronic influences**

Marc Armbrüster<sup>1</sup> and Yuri Grin<sup>2</sup>

<sup>1</sup>Faculty of Natural Sciences, Institute of Chemistry, Materials for Innovative Energy Concepts, Chemnitz University of Technology, 09107 Chemnitz, Germany, marc.armbruester@chemie.tu-chemnitz.de

<sup>2</sup>Max-Planck-Institut für Chemische Physik fester Stoffe, 01087 Dresden, Germany, Juri.Grin@cpfs.mpg.de

**Introduction**

Intermetallic compounds offer a peculiar combination of crystal and electronic structure, which is very much different to the elements and substitutional alloys. This leads to new catalytic functionality in heterogeneous gas-phase catalysis [1] as well as electro catalysis [2-4] and has been explored intensively in the past years. While many studies are concerned with identifying the catalytic properties in various reactions, intermetallic compounds can also be deployed as platform materials to investigate and understand structural and electronic influences on the catalytic properties in specific reactions. This deep understanding allows then to develop innovative catalytic materials, e.g. noble-metal free hydrogenation catalysts [5,6].

Selective hydrogenation is of outmost importance for many catalytic processes in industry. The semi-hydrogenation of acetylene to ethylene (Eq. 1) is such a reaction, being applied to provide a clean ethylene feed for the production of polyethylene (70 million tons per year [7]) and ethylene oxide (26 million tons per year [8]). Over-hydrogenation to ethane (Eq. 2) as well as carbonaceous deposits by dehydrogenation (Eq. 3) have to be avoided to reduce loss of product.



In this study, electronic influences as well as the effect of the local structure on the catalytic properties is explored by the recently [9] uncovered isostructural series (Ga,Sn)Pd<sub>2</sub> (Co<sub>2</sub>Si type of crystal structure) and variation of the crystal structure, respectively.

**Materials and Methods**

Intermetallic compounds were synthesized from high-purity elements using arc-melting in an argon-filled glovebox (O<sub>2</sub> and H<sub>2</sub>O below 0.1 ppm). Samples were subsequently annealed in evacuated quartz-glass ampoules to reach thermodynamic equilibrium. All materials were thoroughly characterized by powder X-ray diffraction, metallography and X-ray photoelectron spectroscopy (XPS) before being subjected to catalytic testing. Catalytic tests were conducted under industrially relevant acetylene-to-ethylene ratios of 1:100 at 200 °C. Catalytic reactor studies at ambient pressure were corroborated by *operando* near-ambient pressure XPS at BESSY to study the segregation behavior under catalytic conditions as well as the stability of the compounds.

**Results and Discussion**

The different crystal structures of the many intermetallic compounds in the system Ga-Pd allows testing different local structural motifs in catalysis. Small and isolated active sites limit the number of different adsorption modes of acetylene, thus the possibilities for the side reactions (Eq. 1 and Eq. 2). Thus, selectivity towards ethylene should increase with decreasing number of Pd-Pd contacts in the crystal structures. Having established the integrity of the compounds GaPd<sub>2</sub>, GaPd as well as Ga<sub>7</sub>Pd<sub>3</sub> by *operando* near-ambient pressure XPS measurements the observed catalytic properties can directly be assigned to the intermetallic compounds [10]. The results show clearly the benefit of the isolated active sites (65-75 % selectivity to ethylene) compared to only 20 and 30 % ethylene selectivity for elemental palladium and the alloy Ga<sub>5</sub>Pd<sub>95</sub>, respectively.

Out of the three intermetallic compounds GaPd<sub>2</sub> possesses the highest activity. Thus, this compound was chosen to address electronic influences in the reaction. The isostructural series (Ga,Sn)Pd<sub>2</sub> allows to vary the valence electron concentration in minute steps by the ratio of gallium to tin. Since the substitution is coming along with only minor changes in distances and no variation in the number of palladium atoms surrounding a palladium atom, the change in catalytic properties can directly be assigned to changes in the electronic structure. Also here, the *operando* stability was investigated by near-ambient pressure XPS, resulting in high stability and a preference of gallium segregation over tin. Variation of the catalytic properties with composition is shown in Fig. 2. The activity varies strongly over the different materials, revealing an ideal composition of the material at x = 0.28 which is around three times more active than GaPd<sub>2</sub>. Very interesting is the behavior of the selectivity with changing valence electron concentration – it is not changing, staying at excellent values of more than 80 % over the whole range. This is a rare case of complete decoupling of the effects of electronic and structural influences. While the electronic properties solely act on the activity, the structural motif of the palladium coordination dictates solely the selectivity.

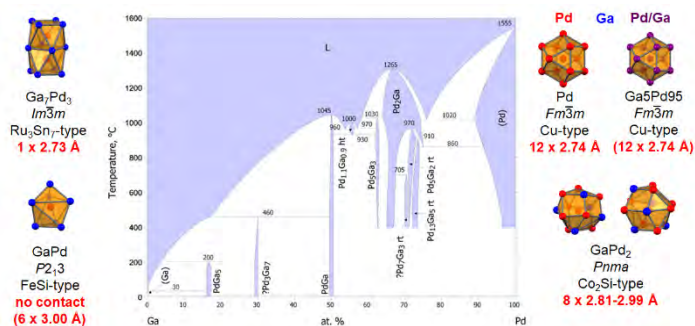


Fig. 1: Ga-Pd phase diagram [11] and coordination of the Pd atoms in the intermetallic compounds  $\text{GaPd}_2$ ,  $\text{GaPd}$  and  $\text{Ga}_7\text{Pd}_3$  with number of Pd-Pd contacts and closest Pd-Pd distances. Elemental Pd and the substitutional alloy  $\text{Ga}_5\text{Pd}_{95}$  are given for comparison.

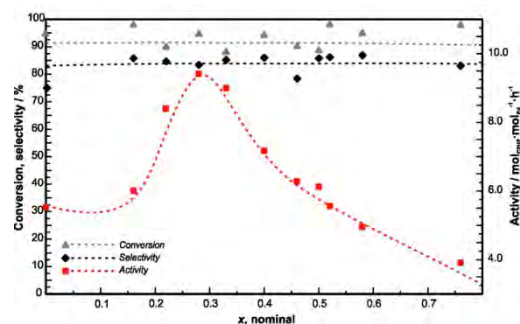


Fig. 2: Composition-dependent catalytic properties of the isostructural series  $(\text{Ga}_{1-x}\text{Sn}_x)\text{Pd}_2$ . The electronic effect is only affecting the activity, while the excellent selectivity is maintained.

### Acknowledgements

Part of the results were obtained within the framework of the project “Exploring Electronic Effects in Selective Hydrogenation by  $(\text{Ga},\text{Sn})\text{Pd}_2$ ” funded by the Deutsche Forschungsgemeinschaft (DFG, AR 617/14-1, GR 1793/19-1) and are based upon a very fruitful cooperation with R. Schlögl (Fritz Haber Institute of the Max Planck Society, Berlin) and P. Gille (Ludwig Maximilians University, Munich). Exchange and discussion within the European Integrated Center for the Development of New Metallic Alloys & Compounds ([www.ecmetac.eu](http://www.ecmetac.eu)) are thankfully acknowledged.

### References

- [1] M. Armbrüster, Yu. Grin, *Science and Technology of Advanced Materials* **2020**, *21*, 767.
- [2] L. Röbner, M. Armbrüster, *ACS Catalysis* **2019**, *9*, 2018-2062.
- [3] I. Antonyshyn, A. M. Barrios Jiménez, O. Sichevych, U. Burkhardt, M. Schmidt, I. Veremchuk, A. Ormeci, I. Spanos, A. Tarasov, D. Teschner, G. Algara-Siller, R. Schlögl, Yu. Grin, *Angewandte Chemie International Edition* **2020**, *59*, 16770 – 16776.
- [4] A. M. Barrios Jiménez, U. Burkhardt, R. Cardoso Gil, K. Höfer, S. G. Altendorf, R. Schlögl, Yu. Grin, I. Antonyshyn, *ACS Advanced Energy Materials* **2020**, *3*, 11042-11052.
- [5] M. Armbrüster, K. Kovnir, M. Friedrich, D. Teschner, G. Wowsnick, M. Hahne, P. Gille, L. Szentmiklósi, M. Feuerbacher, M. Heggen, F. Girgsdies, D. Rosenthal, R. Schlögl, Yu. Grin, *Nature Materials* **2012**, *11*, 690-693.
- [6] K.L. Hodge, J.E. Goldberger, *Journal of the American Chemical Society* **2019**, *141*, 19969-19972.
- [7] T.E. Nowlin, *Global Polyethylene Business Overview*, in *Business, and Technology of the Global Polyethylene Industry*, John Wiley & Sons, Inc.: Hoboken, **2014**, 1–45.
- [8] *Global Ethylene Oxide (EO) Industry Outlook to 2023 – Capacity and Capital Expenditure Forecasts with Details of All Active and Planned Plants*, Report Code: GDCH0060ICR, GlobalData UK Ltd, **2019**.
- [9] O. Matselko, Yu. Grin, R. Gladyshevskii, U. Burkhardt, *Materials Characterization* **2019**, *147*, 443-452.
- [10] M. Armbrüster, *Science and Technology of Advanced Materials* **2020**, *21*, 303-322.
- [11] MatNavi, National Institute for Materials Science (NIMS).



**O-FI-02****The way for elimination of the martensite stabilization effect in NiTi-based alloys**Natalia Resnina and Sergey Belyaev

Saint-Petersburg State University, 198504 Saint-Petersburg, Russia, resnat@mail.ru

**Introduction**

NiTi-based shape memory alloys are widely used as sensors, actuators, heat engines, thermal coupling due to their unique ability for strain recovery and stress generation. Such functional behaviour is caused by the thermal elastic martensitic transformations. However, the martensite stabilization effect is observed in the samples after preliminary deformation. This effect is revealed as the shift in the temperatures of the reverse transformation during the first heating just after the deformation. The larger the preliminary strain the larger the shift in the transformation temperatures. The realization of this effect is negative for the NiTi shape memory alloys application because it does not allow to predict the temperatures at which the strain recovery occurs. Thus, it is necessary to find the way for the elimination of this effect in the NiTi alloys.

Previously, it was shown that the martensite stabilization effect took place after all types of the preliminary deformation of the NiTi alloys such as active deformation in the martensite state; cooling under a stress and stress induce martensite transformation. It was assumed that the nature of this phenomenon was the damage of the intermartensite boundaries during the interaction of the martensite plates. In this case, the larger driving force should be provided to move the damaged boundary during the reverse transformation that increased the transformation temperatures. Thus, to eliminate the martensite stabilization effect, it is necessary to provide the preliminary deformation at which the interaction between the martensite plates is absent or small. Such way of the deformation can not be realized during the martensite reorientation because the whole alloy volume is in the martensite crystals. However, it can be attained when the preliminary deformation occurs by cooling under a stress or stress-induce martensitic transformation because in these ways the oriented martensite crystals appear in the austenite phase. The aim of the present study is to verify this assumption.

**Materials and Methods**

The Ni<sub>50</sub>Ti<sub>50</sub> and Ni<sub>51</sub>Ti<sub>49</sub> alloys were used in the study. Samples were water quenched from 900 °C (10 min). After such heat treatment, the samples underwent the martensite transformation from the cubic B2 phase ordered as CsCl (austenite phase) to monoclinic B19' phase (martensite phase) on cooling and B19' → B2 reverse transformation takes place on subsequent heating.

The samples were subjected to two different ways of the preliminary deformation: cooling under a stress or deformation in the austenite state by the stress-induced martensitic transformation. To realize the formation of the oriented martensite without interaction between the plates, the different fraction of the forward transformation was realized on cooling under a stress or on active deformation. After preliminary deformation, the samples were unloaded and subjected to heating through the temperature range of the reverse transformation to study the shape memory effect and to determine the temperatures of the reverse transformation during the first heating. After that, the samples were cooled and heated to study the strain variation during the two-way shape memory effect and to determine the temperatures of the reverse transformation during the second heating.

All tests were carried out in the Lloyd 30k Plus or Shimadzu AG-50kN testing machines equipped with thermal chamber. The stress was measured by standard sensor whereas, the strain was measured by the videoextensometer that registered the difference in the length between two white marks shown on the sample gauge length.

**Results and Discussion**

The results of the study shows that if the incomplete stress induced martensitic transformation was realized during the active deformation in the austenite state, the martensite stabilization effect was not found. In this case, the strain recovery took place at temperatures close to the temperatures of the reverse transformation in non-deformed sample. An increase in the volume fraction of the oriented martensite led to the observation of the martensite stabilization effect. If the preliminary deformation was realized on cooling under a stress in non-complete temperature range of the forward transformation, the martensite stabilization effect was not observed. The larger the temperature range of the forward transformation was realized on cooling under a stress, the larger the value of the martensite stabilization effect. Thus, the results of the study confirm the assumption that the martensite stabilization effect can be eliminated if during the preliminary deformation the oriented martensite plates do not interact.

**Acknowledgments**

This work was supported by Russian Science Foundation (grant number 18-19-00226).

## O-FI-03

### Effect of duration of electropulse treatment on properties of rapidly quenched TiNiCu alloys with high copper content

Alexander Shelyakov<sup>1</sup>, Nikolay Sitnikov<sup>1,2</sup>, Kirill Borodako<sup>1</sup> and Irina Zaletova<sup>1,2</sup>

<sup>1</sup>Department of Solid State Physics and Nanosystems, National Research Nuclear University MEPhI (Moscow Engineering Physics Institute), 115409 Moscow, Russian Federation, alex-shel@mail.ru

<sup>2</sup>Federal State Unitary Enterprise “Keldysh Research Center”, 125438 Moscow, Russian Federation, sitnikov\_nikolay@mail.ru

#### Introduction

The rapidly quenched quasi-binary TiNi–TiCu alloys with high copper content (more than 25 at.%) are of great interest as shape memory materials due to the possibility of significantly decreasing the magnitude of temperature and deformation hysteresis in comparison with the binary TiNi alloy. This encourages the use of these alloys to create high-speed micro-mechanical devices for Micro Electro-Mechanical Systems (MEMS) [1-3]. We recently developed a series of microtweezers – a micromechanical tool for gripping and holding of micro- and nanoscale objects for their further spatial manipulation and preparation -and experimentally demonstrated the operation of the devices and their compatibility with most of the existing micro- and nanopositioning systems [4-6]. However these alloys can form brittle Ti-Cu phases upon crystallization from amorphous state by isothermal heat treatment and therefore do not exhibit SME. Recently it was shown that electropulse annealing with pulse duration of 10 ms fundamentally changed the microstructure of the alloys which proved to have extraordinary physical and mechanical properties, in particular, the alloys containing 36 and 38 at.% Cu exhibited clear shape memory behavior [7]. In this work, we studied the influence of the duration of electropulse treatment on the structure and martensitic transformation (MT) of TiNiCu alloy with high copper content.

#### Materials and Methods

The test material was the quasi-binary TiNi–TiCu alloy with 30 at.% copper content produced by melt spinning technique at a cooling rate of about  $10^6$  K/s in the form of amorphous ribbons with a thickness of around 40  $\mu\text{m}$  [8,9]. In order to crystallize from the amorphous state, alloy specimens were exposed to electric pulse with duration in the range from 1000 to 1 ms and amplitude ensuring the Joule heating of the alloy to the crystallization temperature.

#### Results and Discussion

X-ray diffraction studies have shown that at room temperature all samples are completely in the martensitic state, which is confirmed by the presence of reflections of the B19 orthorhombic phase in the diffraction patterns and the absence of pronounced peaks of other phases (Fig. 1). When the alloy is heated to a temperature of 75 °C, the peaks of the B19 phase disappear, and only reflections of the B2 austenite phase are present, that is, the alloy passes into a completely austenitic state as a result of the B19  $\leftrightarrow$  B2 MT. A decrease in the duration of the electropulse treatment from 1000 ms to 1 ms does not lead to a change in the phase composition of the alloys, although the intensity of the peaks of the B19 phase for shorter crystallization times is somewhat lower.

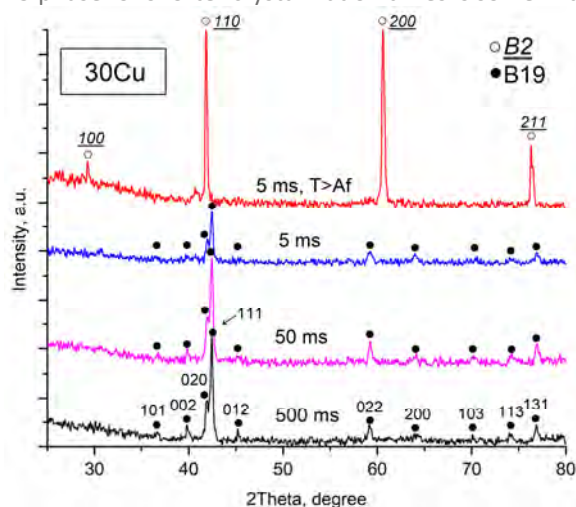


Fig. 1: X-ray diffraction patterns of the rapidly quenched TiNi–TiCu alloy with 30 at.% Cu alloy after electropulse crystallization by a single pulse of different duration: 5 ms, 50 ms, and 500 ms.

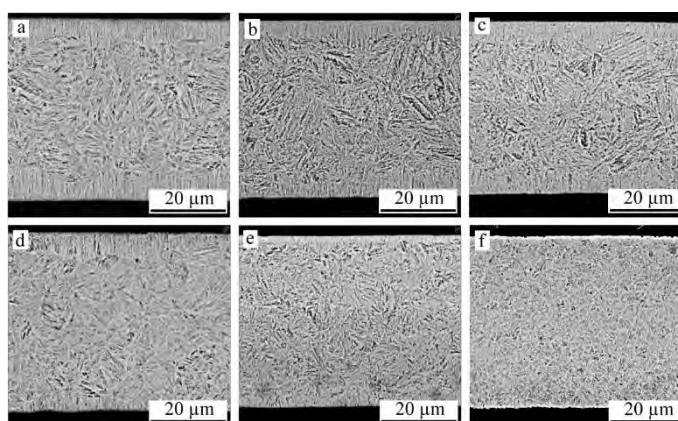


Fig. 2: SEM images of cross-section of rapidly quenched 30Cu alloy ribbons after electropulse crystallization by a single pulse of 1 ms (a), 5 ms (b), 50 ms (c), 100 ms (d), 500 ms (e), and 1000 ms (f)

Investigation of the cross-section of the ribbons in a scanning electron microscope (SEM) revealed an uneven distribution of crystals over the ribbon thickness (Fig. 2): near the ribbon surfaces, a columnar crystal structure is formed, while in the ribbon volume there are single or grouped large grains with characteristic sizes from 3 up to 12 microns. The transverse dimensions of the columnar crystals are from 0.5 to 2  $\mu\text{m}$ , and their height is in the range from 2 to 5  $\mu\text{m}$ . An increase in the pulse duration from 1 ms to 100 ms does not lead to any noticeable changes in the microstructure of the alloys; however, with a further increase in the exposure duration to 1000 ms, both the average grain size and the height of the columnar crystals significantly decrease.

At the same time, using differential scanning calorimeter (DSC), it was found that an increase in the duration of the electropulse treatment causes a decrease in the MT temperatures, while the MT enthalpy remains practically unchanged. In addition, the exposure time has a significant effect on the shape of the DSC curves, which is manifested in the bifurcation of the peaks of heat release and absorption during MT with a decrease in the exposure time less than 500 ms. Obviously, this is due to the bimodal structure of the alloys (Fig. 2), which can have different MT temperatures and lead to superposition of peaks from each structure and bifurcation of the common peak.

### Acknowledgments

The study is supported by Russian Science Foundation (project No. 19-12-00327).

### References

- [1] I. Stachiv, E. Alarcon, M. Lamac, *Metals*. **2021**, *11*, 415.
- [2] M. Kohl, H. Ossmer, M. Gueltig, C. Megnin, *Shape Mem. Superelasticity*. **2018**, *4*, 127-142.
- [3] J.M. Jani, M. Leary, A. Subic, M.A. Gibson, *Mater. Design*. **2014**, *56*, 1078-1113.
- [4] A. Shelyakov, N. Sitnikov, K. Borodako, V. Koledov, I. Khabibullina, S. von Gratowski, *J Micro-Bio Robot*. **2020**, *16*, 43-51.
- [5] A. Shelyakov, N. Sitnikov, A. Menushenkov, V. Fominski, *Acta Physica Polonica*. **2018**, *134(3)*, 708-713.
- [6] A. Irzhak, D. Zakharov, V. Koledov V et al. *J. Alloys Compd*. **2014**, *586*, 464-468.
- [7] A. Shelyakov, N. Sitnikov, I. Khabibullina, N. Tabachkova, V. Fominski, N. Andreev, *Mater. Lett*. **2019**, *248*, 48-51.
- [8] A.V. Shelyakov, O.N. Sevryukov, N.N. Sitnikov, K.A. Borodako, I.A. Khabibullina, *J. Phys.: Conf. Ser.* **2020**, *1686*, 012056.
- [9] A.V. Shelyakov, N.N. Sitnikov, A.P. Menushenkov, A.A. Korneev, R.N. Rizakhanov, N.A. Sokolova, *J. Alloys Compd*. **2013**, *577*, 251-254.

**O-FI-04****TiAl Thin Films as an Alternative Metallization for High-Temperature SAW Devices**

Marietta Seifert, Eric Lattner, Siegfried Menzel, Steffen Oswald and Thomas Gemming

Leibniz IFW Dresden, Helmholtzstr. 20, 01069 Dresden, Germany, marietta.seifert@ifw-dresden.de, e.lattner@ifw-dresden.de, s.menzel@ifw-dresden.de, s.oswald@ifw-dresden.de, t.gemming@ifw-dresden.de

**Introduction**

Besides its application as bulk material in aerospace structural components or in gas turbines, the TiAl alloy is a promising material for the realization of electrodes in high-temperature sensor devices. Despite TiAl's higher tendency to oxidation, its use as an electrode material in high-temperature Surface Acoustic Wave (SAW) devices is beneficial. Compared to noble metals like Pt, TiAl has low costs and a lower density, which leads to lower mechanical losses. The behavior of TiAl thin films with a total thickness of 200 nm deposited on high-temperature stable piezoelectric  $\text{Ca}_3\text{TaGa}_3\text{SiO}_{14}$  (CTGS) and on thermally oxidized Si ( $\text{SiO}_2/\text{Si}$ ) substrates was investigated after heat treatments up to 800 °C for 10 h.

**Materials and Methods**

Ti/Al multilayer samples were prepared by magnetron sputtering or e-beam evaporation from elemental targets resulting in a thickness of the individual layers of 10 or 20 nm and a total thickness of 200 nm on  $\text{SiO}_2/\text{Si}$  and CTGS substrates. The layer stacks started with Ti and the uppermost layer was Al. For comparison, TiAl alloy films deposited by co-sputtering were analyzed. To prevent a chemical reaction between the TiAl film and the substrate and to protect the films from oxidation during the annealing, for some of the samples  $\text{SiO}_2$  (Fig. 1a) or AlNO barrier and cover layers with a thickness of 20 nm deposited by magnetron sputtering were used. To realize the  $\gamma$ -TiAl phase formation and to investigate the high-temperature stability, the films were annealed up to 800 °C and analyzed regarding their phase formation by X-ray diffraction (XRD) and their film morphology by cross section imaging, transmission electron microscopy (TEM) with energy dispersive X-ray analysis (EDX) as well as Auger electron spectroscopy (AES) and X-ray photoelectron spectroscopy (XPS).

**Results and Discussion**

The analyses showed that for the co-sputtered samples deposited on  $\text{SiO}_2/\text{Si}$  no TiAl phase formation was realized at all. Without a cover layer, these films started to oxidize already during annealing at 400 °C in high vacuum (HV) and were strongly oxidized at 600 °C in HV [1].

In contrast to this, a 20 nm thick  $\text{SiO}_2$  cover layer protected the sputtered TiAl films deposited on  $\text{SiO}_2/\text{Si}$  substrates from oxidation during annealing in high vacuum up to 600 °C (Fig. 1b). However, the results also revealed that already at this temperature, a chemical reaction between Ti and the  $\text{SiO}_2/\text{Si}$  substrate took place for the multilayer samples. The formation of  $\text{Ti}_5\text{Si}_3$  at the interface between the film and the substrate was proven by EDX in the TEM and by XRD. After annealing at 800 °C in HV, the samples were completely destroyed and consisted of  $\text{Al}_2\text{O}_3$  and Ti silicide (Fig. 1c) [1].

In contrast to the films with the  $\text{SiO}_2$  cover layer, the sputtered TiAl films on  $\text{SiO}_2/\text{Si}$  substrates with an AlNO barrier and cover layer were stable up to 800 °C in HV and 600 °C in air. Also on CTGS, the films were not oxidized up to 600 °C in HV and in air and only showed a slight degradation after annealing at 800 °C in HV [2]. However, at 800 °C, a slight degradation of upper region of the CTGS was observed.

Electron energy loss spectroscopy in the TEM revealed that there was a chemical reaction between the AlNO barrier and the Ti already after annealing at 600 °C, leading to the formation of Ti-N phases.

XPS depth profiles and local EDX analysis in the TEM of such a sample with AlNO barrier and cover layers annealed at 800 °C in HV proved the formation of  $\text{Al}_2\text{O}_3$  at local positions on top of the sample and the reaction between the Ti and AlNO barrier layer leading to a Ti-rich layer which also contained TiN (Fig. 2).

To investigate the influence of the deposition method on the behavior of the films, TiAl multilayers prepared by e-beam evaporation using AlNO barrier and cover layers were deposited on  $\text{SiO}_2/\text{Si}$  and CTGS substrates as well. For these samples, AlNO cover and barrier layers with less oxygen (8 at-% instead of 16 at-%) were used.

The analyses of these samples showed that the TiAl phase formation was reduced as compared to the sputtered samples. These films were also less temperature stable than the sputtered films with the AlNO layers with higher O content. Already after annealing at 600 °C in HV and in air a slight degradation (formation of  $\text{Al}_2\text{O}_3$ ) was observed. After annealing at 800 °C in HV, the samples were completely oxidized. Besides  $\text{Al}_2\text{O}_3$  in the former central region of the film,  $\text{TiO}_2$  was formed on top of the films. For the samples on  $\text{SiO}_2/\text{Si}$  substrates, again Ti silicide was formed at the interface [2].

The sputtered and evaporated films differ in the energy of the deposited particles. In case of sputtering, the energy is a few eV, so that the particles have a high mobility on the surface of the growing film. This leads to a high density of the grown film and supports a crystallographic ordering. In contrast to this, the evaporated particles possess an energy in the order of 0.1 eV, which results in a lower density, more defects and a reduced crystallographic ordering. The stronger oxidation of the evaporated samples might be explained with the reduced TiAl phase formation and

therefore higher affinity of Ti and Al to O and with the less protective behavior of the AlNO barrier layers with the lower O content [2].

In summary, the results showed that the sputtered TiAl multilayer films with AlNO cover and barrier layers with an O content of 16 at-% are suited as a cost-efficient alternative material to the expensive Pt for electrodes in high-temperature SAW sensors with an application temperature of up to 600 °C [2].

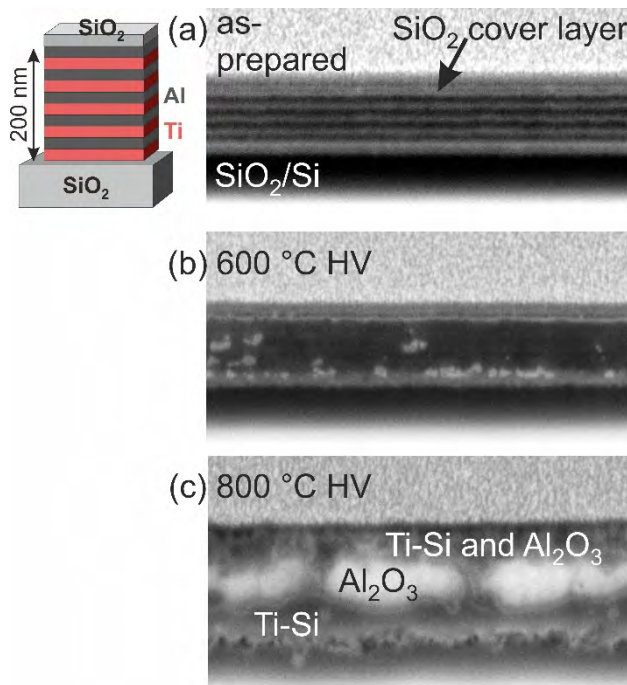


Fig. 1: Cross section images of a Ti/Al multilayer sample with 20 nm individual layer thickness on SiO<sub>2</sub>/Si substrates with 20 nm SiO<sub>2</sub> cover layer in the as-prepared state and after annealing at 600 °C and 800 °C in HV for 10 h [1].

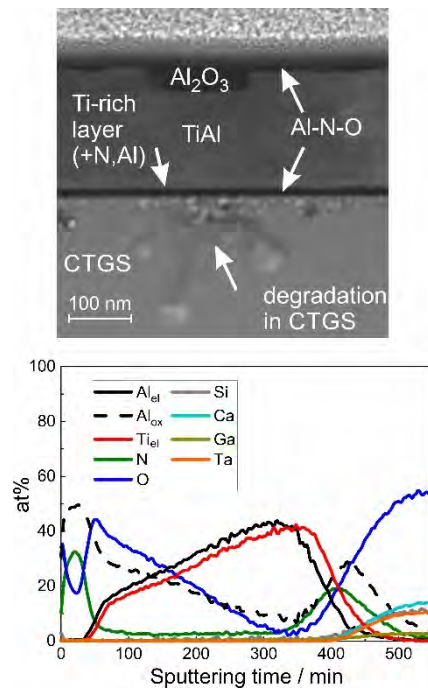


Fig. 2: STEM image (predominant elemental contrast) of a sputtered Ti/Al multilayer sample (individual layer thickness: 10 nm) with AlNO barrier and cover layer on CTGS after annealing at 800 °C in HV for 10 h [2].

#### Funding information

The work was supported by German BMBF under grant InnoProfile-Transfer 03IPT610Y and BMWI under grant 03ET1589 A.

#### References

- [1] M. Seifert, E. Lattner, S.B. Menzel, S. Oswald, T. Gemming, *Materials*. **2020**, *13*(9), 2039.
- [2] M. Seifert, E. Lattner, S.B. Menzel, S. Oswald, T. Gemming, Study of TiAl thin films on piezoelectric CTGS substrates as an alternative metallization system for high-temperature SAW devices, *Journal of Materials Research and Technology*, accepted **2021**.



**O-FI-05****Use of phase equilibria in the Ag-Mg-Sb system for guidance of low temperature thermoelectric applications**

Silvana Tumminello<sup>1</sup>, Léo Millerand<sup>1</sup>, Julia Camut<sup>1</sup>, Suzana G. Fries<sup>2</sup>, Johannes de Boor<sup>1,3</sup>  
and Eckhard Müller<sup>1,4</sup>

<sup>1</sup>Institute of Materials Research, German Aerospace Center, 51170 Cologne, Germany, silvana.tumminello@dlr.de

<sup>2</sup>ZGH - Materials Research Department, Ruhr-University Bochum, 44801 Bochum, Germany

<sup>3</sup>Institute of Technology for Nanostructures, University of Duisburg-Essen, 47057 Duisburg, Germany

<sup>4</sup>Institute of Inorganic and Analytical Chemistry, Justus Liebig University Giessen, 35392 Giessen, Germany

**Introduction**

AgMgSb-based thermoelectric (TE) materials are potential candidates for near-room temperature applications in thermoelectric generators [1]. The ternary compound  $\alpha$ -AgMgSb exhibits two polymorphic transformations at high temperature resulting in structures with poor TE properties; thus, limiting the functional temperature range to the  $\alpha$ -AgMgSb phase. The low temperature polymorph,  $\alpha$ , with a tetragonal crystal lattice ( $I-4c2$ ) is stable up to 327 °C where the transformation  $\alpha$  to tetragonal  $\beta$ -AgMgSb occurs; and  $\beta$  to cubic  $\gamma$ -AgMgSb transformation takes place at 427 °C [2]. The efficiency of a thermoelectric material for energy conversion is given by its figure of merit ( $zT$ ) as a function of temperature:

$$zT = \sigma S^2 T / \kappa \quad (1)$$

where  $\sigma$  is the electrical conductivity,  $S$  the Seebeck coefficient,  $T$  the absolute temperature and  $\kappa$  the thermal conductivity of the material. In practice,  $zT$  is calculated from TE properties measured in polycrystalline and multiphase materials accounting for the contribution of all phases the final microstructure. In the case of the ternary stoichiometric phase  $\alpha$ -AgMgSb, multiphase equilibrium becomes particularly relevant due to the significant challenge of synthesizing a single phase material.

Equilibrium thermodynamics is essential knowledge that can be used as guidance for the characterization of the obtained microstructures allowing the identification of stable and metastable phases, to derive information on the possible phase transformations occurring during synthesis, and to outline possible diffusion-paths in the temperature-composition space. Computational thermodynamics complements early experimental investigation of phase diagrams of a few isothermal sections by allowing access to the phase equilibria in the whole temperature-composition range. In this way phase stability during synthesis and service of functional materials can be better identified and optimized.

The phase equilibrium of the system Ag-Mg-Sb has been experimentally studied in the Ag-rich corner and two isotherms where determined, at 450 °C and 550 °C [3]. To the best of our knowledge, no thermodynamic assessment of this ternary is available in the literature until now. Therefore, in this work we optimize a set of Gibbs energies for the Ag-Mg-Sb system based on the most suitable description for the binaries available in the literature [4, 5, 6], to subsequently calculate thermodynamic quantities with a twofold aim: first, to facilitate the phase identification in any stage of the synthesis process and, second, to bring support in the determination of a synthesis route leading to the desired microstructure based on the ternary phase  $\alpha$ -AgMgSb.

**Materials and Methods**

Pellets of TE material were synthesized by mechanical alloying of the elemental powders. Initial milling and consolidation was done to form the AgMg compound as precursor and afterwards elemental Sb was added for ball-milling to form AgMgSb. Subsequently, the alloyed powder was consolidated in a current assisted sinter press at 300 °C during 8 min under 85 MPa. The pellets surface was prepared for imaging by a typical metallographic procedure and the resulting microstructures were inspected by electron microscopy equipped with backscattered-electron (SEM-BSE) and spectroscopy detector (SEM-EDS). The crystal structure investigation was done on the bulk pellets by conventional X-ray diffraction, XRD. The TE properties were measured using in-house developed equipment (HT-S- $\sigma$ ).

For the thermodynamic modeling we use the Calphad methodology [7] and the Thermo-Calc software v2021a [8, 9] for the thermodynamic assessment.

**Results and Discussion**

Initial results are summarized in Fig. 1, two SEM-BSE micrographs of typical microstructures of TE pellets synthesized with different Sb content are shown linked to their overall composition in the equilibrium isotherm. The matrix is the  $\alpha$ -AgMgSb phase in both cases, however, the nature of the secondary phases is different, and consequently, their TE figure of merit shows significant differences. The  $zT$  values calculated from measured TE properties as a function of temperature are shown in the figure, in black the  $zT$  corresponding to the microstructure on the left with (Ag) fcc terminal solid solution and  $Mg_3Sb_2$  as secondary phases. In red color, the  $zT$  corresponding to the microstructure on

the right, where the identified secondary phases were elemental Sb and  $Mg_3Sb_2$ . From the comparison of the TE figure of merit we observe, in relation to the secondary phases, that (Ag) can have a more detrimental effect than elemental Sb on the zT values.

Finally, Fig. 1 also shows the isothermal section at 450 °C adapted from [3] limited to the Ag-rich corner thus, showing the need of thermodynamic models for further investigations on multiphase stability and thermodynamic properties of the AgMgSb compound. In this work we provide understanding on the phase equilibrium and transformations of the synthesized  $\alpha$ -AgMgSb-based material.

During this presentation a step-by-step of the equilibrium calculation guidance will be shown in order to prove and validate the concept.

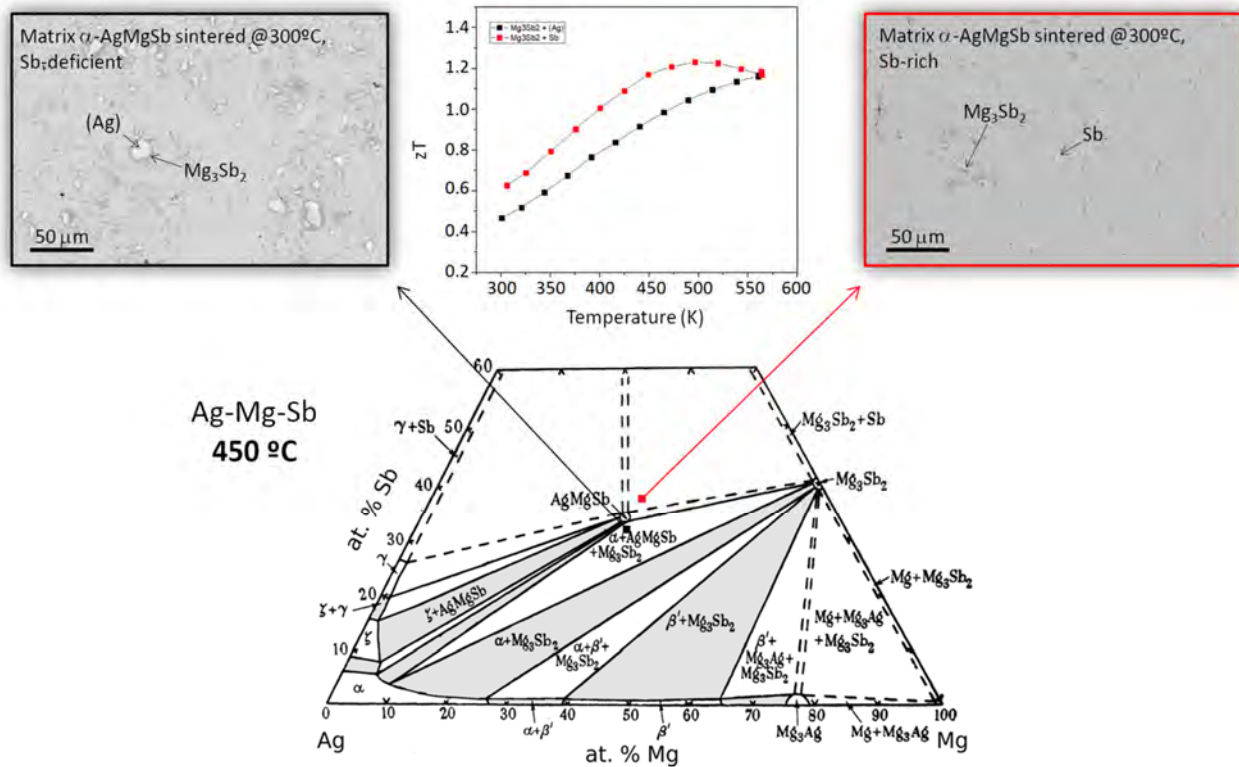


Fig. 1: Isothermal section of the Ag-Mg-Sb system adapted from [3] and SEM-BS micrographs of two typical microstructures of the  $\alpha$ -AgMgSb matrix phase and different secondary phases. The functionality of the  $\alpha$ -AgMgSb-based material can be observed in the calculated zT figure of merit in the range from room temperature up to 300 °C.

## References

- [1] J. Camut et al., *Materials* (Basel). **2019**, *12*, 1857.
- [2] J. L. Mi et al., *Chem. Mater.* **2017**, *29*, 6378-6388.
- [3] B. R. T. Frost and G. V. Raynor, *Proc. R. Soc. A Math. Phys. Eng. Sci.* **1950**, *203*, 132–147.
- [4] M. Lim, J.E. Tibballs, P.L. Rossiter, *Z. Metallk.* **1997**, *88*, 162–168.
- [5] T. Balakumar and M. Medraj, *Calphad.* **2005**, *29*, 24–36.
- [6] C. S. Oh, J. H. Shim, B. J. Lee, D. N. Lee, *J. Alloys Compounds.* **1996**, *238*, 155-166.
- [7] H. Lukas, S. G. Fries, and B. Sundman, *Computational Thermodynamics. The Calphad Method.* Cambridge University Press, **2007**.
- [8] J.O. Andersson, T. Helander, L. Höglund, P.F. Shi, B. Sundman, *Calphad.* **2002**, *26*, 273-312.
- [9] Thermo-Calc Software. <https://thermocalc.com/>

**O-AM-01****Direct insights into the phase evolution and transformation during a simulated additive manufacturing process**

Adriana De Andrade, Andreas Stark, Peter Staron, Florian Pyczak and Marcus W. Rackel

Helmholtz-Zentrum Hereon, 21502 Geesthacht, Germany, Adriana.Andrade@hereon.de, Andreas.Stark@hereon.de, Peter.Staron@hereon.de, Florian.Pyczak@hereon.de, Marcus.Rackel@hereon.de

**Introduction**

In modern jet engines,  $\gamma$ -TiAl alloys are used to replace classical nickel-based super alloys as structural material for low-pressure turbine blades. Up to now, there are two  $\gamma$ -TiAl alloys in service. The so-called TNM<sup>®</sup> alloy with a nominal composition of Ti-43.5Al-4Nb-1Mo-0.1B and the Ti-48Al-2Nb-2Cr (Ti4822) alloy (all compositions in at. %). Currently, two manufacturing processes are used depending on the alloy composition. A complex multistep-forging route produced the low-pressure turbine blades made out of the TNM<sup>®</sup> alloy and a cast route is performed for the Ti4822 alloy. In the future, powder bed-based additive manufacturing (AM) processes are expected to become an established alternative [1]. Usually, processes are used which selectively melt a powder bed by means of an electron or laser beam and generate the workpiece layer by layer. Due to the temporarily high and concentrated energy input, extremely high cooling rates occur. This is not only true for the melted material but also for layers below the actually melted surface. For multiphase systems like TiAl alloys the process and property control during the building process requires understanding of the phase and microstructure formation under such dynamic conditions given by the rapid heating and cooling cycles. In situ high-energy X-ray diffraction (HEXRD) experiments enable a direct observation of the phase evolution during thermal cycling by the use of a heating and quenching dilatometer. An unambiguous reconstruction of this high temperature situation is not possible subsequently in the cooled specimen, as they are masked by phase transformations at lower temperatures and the associated changes of microstructure. In this study, we present first results of a simulated AM process using a range of cycling heating and cooling HEXRD experiments to gain direct insights into the phase evolution.

**Materials and Methods**

The investigated powder metallurgical Ti-48Al-2Nb-2Cr alloy was produced by Electron Induction Gas atomization process at the Helmholtz-Zentrum Hereon. The powder with a particle size of 90–180  $\mu\text{m}$  was filled into cylindrical titanium capsules and compacted by hot isostatic pressing (HIP) at Quintus technologies Application Centre in Västerås, Sweden. An optimised HIP cycle was performed at 1300 °C/1.5 h/200 MPa/fast cooling followed by an aging heat treatment in the same facility at 800 °C/1.5 h/120 MPa. The in situ high-energy X-ray cycling experiments were performed at the High Energy Materials Science beamline (HEMS) operated by Helmholtz-Zentrum Hereon at PETRA III at the Deutsches Elektronen-Synchrotron (DESY), Hamburg, Germany. The in situ measurements were performed in a TA Instruments DIL 805A/D dilatometer using a beam size of 0.5 mm by 0.5 mm and a photon energy of 100 keV ( $\lambda = 0.12398 \text{ \AA}$ ) [2]. During the HEXRD, experiments the Debye-Scherrer diffraction rings were recorded on a Perkin Elmer XRD 1621 flat panel detector (pixel size 200 by 200  $\mu\text{m}$ ). An exposure time of 0.1 s was used. The analysis was performed using the programs Fit2D [3] and MAUD[4]. The performed heating and cooling cycles are shown in Figure 1.

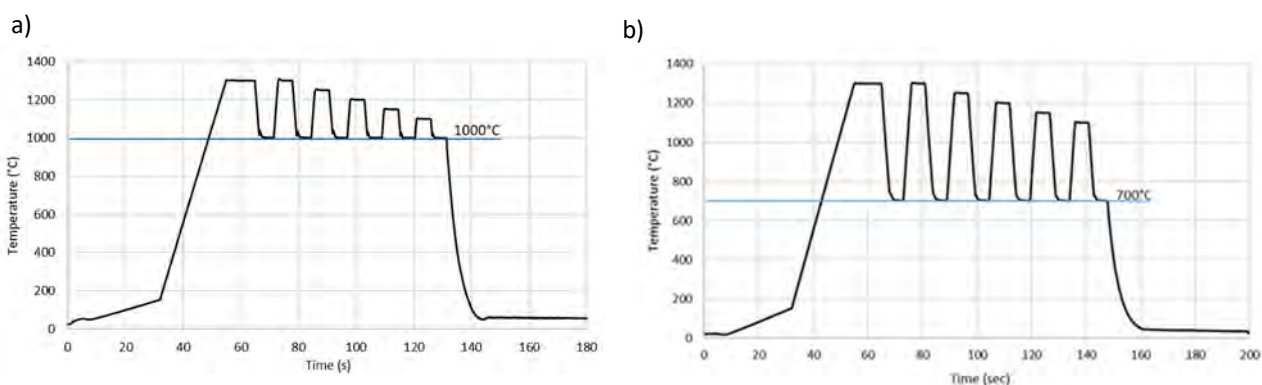


Fig. 1: Time-temperature curve of the performed in situ experiments. The start temperature was 1300 °C. Holding time was 10 s, followed by five heating and cooling cycles with holding temperatures decreasing by 50 °C. The heating rate was 186 °C/s and the cooling rate was 185 °C/s. The simulated powder bed temperature was a) 1000 °C and b) 700 °C.

## Results and Discussion

The microstructure of the investigated samples consists of a duplex structure with a very high proportion of grains with lamellar structures (see Figure 2a). The lamellar grains consist of  $\alpha_2$  and  $\gamma$  phase, whereas the globular grains consist of  $\gamma$  phase [5]. Additionally, a very small volume fraction ( $< 1\%$ ) of ordered  $\beta_0$  phase was also present and identified by HEXRD. After the experiment, no significant change in the microstructure can be seen (Figure 2b). Figure 2c presents an overview of the results obtained by HEXRD experiments. The unrolled Debye-Scherrer diffraction patterns are correlated with the time-temperature curve of the performed experiment. The maximum temperature of 1300 °C was chosen due to technical reasons. The lower holding temperature should simulate a pre-heated powder bed with a temperature of 1000 °C. The cycling temperature profile is intended to simulate a regular energy input during the additive manufacturing process. By a constantly decreasing maximum temperature, the associated temperature gradient from the first building layer to the current, underlying building layer is modelled.

From the results, it can be stated for the present phases ( $\alpha/\alpha_2$ ,  $\gamma$ ) that, due to the high cooling rates, there is no chemically and structurally homogeneous state during the whole experiment. This is indicated in particular by the very low c/a ratio in the  $\gamma$  phase close to 1 and the constantly changing site occupation at the 2d and 6h positions in the  $\alpha/\alpha_2$  phase. Depending on the existing maximum holding temperature and the subsequent cooling, different metastable phase states arise, which will be discussed in detail. The development of the lattice parameters, volume fractions, and order parameters as a function of the process parameters could be determined for all phases present.

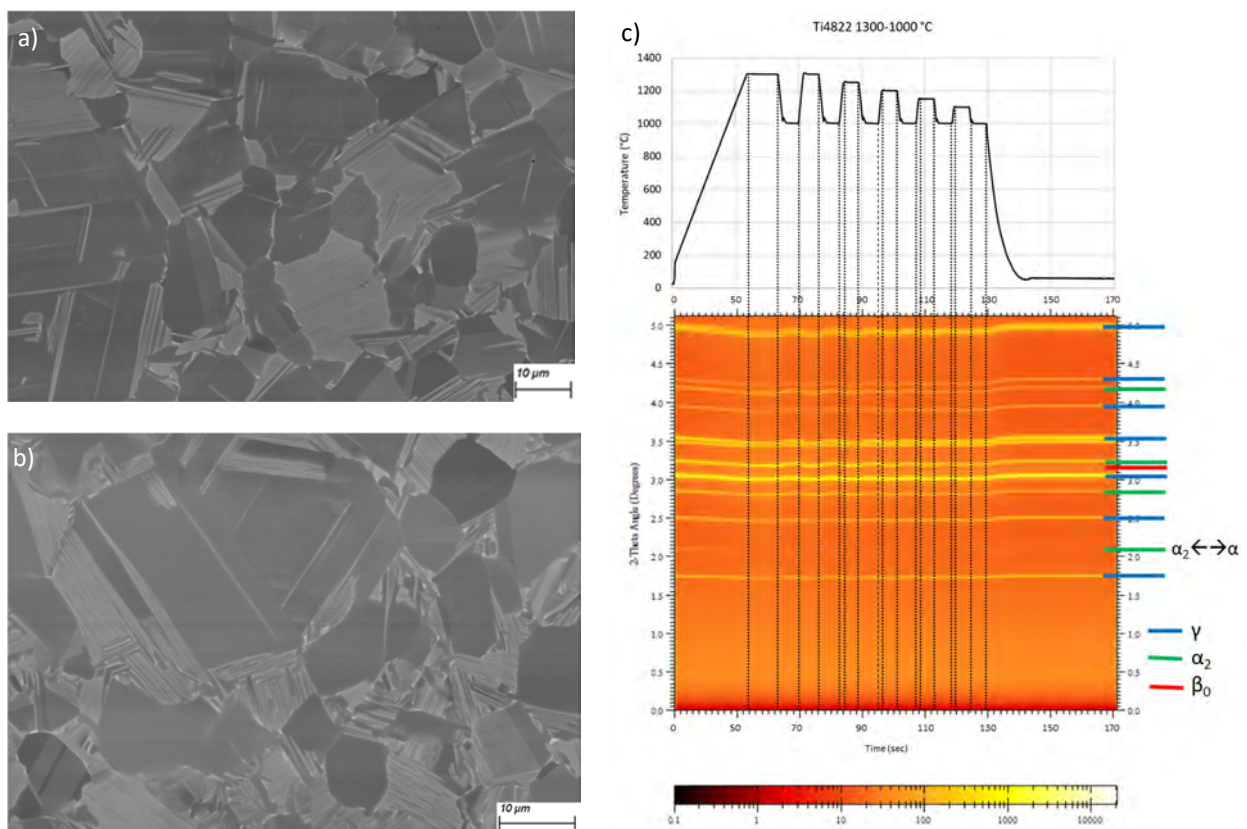


Fig. 2: Microstructural evolution and corresponding diffraction pattern of the HEXRD experiment. a) Reference microstructure b) Microstructure after cycling experiment c) Unrolled Debye-Scherrer diffraction rings of the Ti-48Al-2Nb-2Cr alloy correlated with time-temperature curve.

## References

- [1] W. Chen and Z. Li, "11 - Additive manufacturing of titanium aluminides," in *Additive Manufacturing for the Aerospace Industry*, F. Froes and R. Boyer, Eds.: Elsevier, **2019**, 235-263.
- [2] M. W. Rackel, A. Stark, H. Gabrisch, and F. Pyczak, "Screening for O phase in advanced gamma-TiAl alloys," (in English), *Intermetallics*. **2021**, 131.
- [3] A. P. Hammersley, "FIT2D: An Introduction and Overview," ESRF Internal Report, **1997**.
- [4] L. Lutterotti, "Total pattern fitting for the combined size-strain-stress-texture determination in thin film diffraction," (in English), *Nucl Instrum Meth B*. **2010**, 268, no. 3-4, 334-340.
- [5] P. V. Cobbinah and W. R. Matizamhuka, "Solid-State Processing Route, Mechanical Behaviour, and Oxidation Resistance of TiAl Alloys," (in English), *Adv Mater Sci Eng*. **2019**, 2019.



**O-AM-02****Processing of titanium aluminides with high temperature laser beam melting - from the development of a series machine upgrade to typical complex applications**

Tobias Maiwald-Immer<sup>1</sup>, Michael Härtel<sup>1</sup>, Reinhold Wartbichler<sup>2</sup>, Helmut Clemens<sup>2</sup>  
and Svea Mayer<sup>2</sup>

<sup>1</sup>AM Metals GmbH, 09633 Halsbrücke, Germany, tobias.maiwald-immer@am-metals.de,  
michael.haertel@am-metals.de

<sup>2</sup>Department of Materials Science, Montanuniversität Leoben, 8700 Leoben, Austria,  
reinhold.wartbichler@unileoben.ac.at, helmut.clemens@unileoben.ac.at, svea.mayer@unileoben.ac.at

**Introduction**

AM Metals GmbH belongs to the EOS Group and is responsible for customer-related process, material and application-specific development of commonly known and totally new technologies in 3D printing [1]. In the course of this work, AM Metals GmbH demonstrates the processability of high-performance intermetallic TNM-based alloys with the Laser Beam Melting (LBM) process. The LBM process offers a huge potential, due to its good material quality of high densification and great freedom of design, to manufacture geometrically complex structures with a high resolution and surface quality as well as the possibility of hybrid manufacturing. Together with the specific strength and specific stiffness of the material, high temperature applications between 400 °C and 800 °C can be implemented.

**Materials and Methods**

In order to process hardly weldable materials, like TiAl, a prototype system was developed by AM Metals GmbH based on an upgraded series machine of the standard EOS-M290 system. This new EOS-M290HT system is equipped with a high temperature (HT) modification kit including cooling of the process chamber and an inert gas purification system as well as an additional process monitoring and data logging. The outstanding feature of the EOS-M290HT is the heating and monitoring system for the uppermost powder bed layer – the process zone – up to 1200 °C, which is independent from the building height of the part. The separate base plate heating up to 900 °C enables the control of the temperature field in the part.

With this machine prototype EOS-M290HT a process development for the TNM and TNM<sup>+</sup> alloy was done. Therefore, powders with the nominal TNM and TNM<sup>+</sup> composition and an optimized particle size distribution for the HT LBM process were processed. The relative density, defect size, chemistry and resulting phases as well as the effect of post-processing heat treatments are characterized by using high resolution analysis methods under variation of the powder composition, process conditions and building height. The mechanical properties of different heat-treated conditions were characterized by tensile, creep and high-cycle fatigue (HCF) tests. At this point it should be noted that the process can also be transferred to other engineering TiAl alloys.

An important target of this research was to realize typical applications for TiAl with this machine prototype in a reproducible quality beside the needed cubes and tensile bars. In addition, some surface finishing methods were tested for different applications.

**Results and Discussion**

The LBM EOS-M290HT machine has a cylindrical build chamber with a diameter of 120 mm and a build height of 230 mm. The machine is running at a temperature level between 600 °C and 1200 °C for different R&D topics since 3 years very stable and without damaging the process chamber, scanner, laser, filter system, etc.

It is possible with these two heating units to adjust and control the temperature distribution in the whole part during the build job. Especially, the temperature level of the uppermost powder bed layer can be set to the needed target temperature within seconds. Furthermore, it is possible to homogeneously heat up each new powder layer during the recoating process without an additional pre- and post-heating step. The temperature distribution and level are almost constant during the whole scanning process of the layer. The EOS-M290HT has the same productivity and build rates like a standard machine without pre-heating. Using the gas purification system, it is possible to run the whole job at an oxygen level below 200 ppm. All measured data, especially the measured temperature distribution in the uppermost powder bed layer by an infrared (IR) camera, are recorded and can be analyzed after the build job.

After developing the scan parameters, the control parameter of the separate heating system and adjusting the pre-heating temperature, crack-free TiAl samples with a relative density of above 99.95 % and a very small defect size could be produced. The transfer from small reference samples to larger vertical tensile bars and even real complex applications, like valves, turbocharger turbine wheels and aero engine blades was realized in typical LBM quality. The process conditions of pre-heating and the oxygen level were constant even during long build jobs, which allow a crack-free manufacturing of large and complex parts. Figure 1 shows the pre-heated process zone as well as reference geometry and realized applications. A huge benefit of the HT LBM process is that there are only minimal sinter effects in the powder. The powder can be easily removed after the build job. This gives the user the chance to realize cavities,



internal structures and cooling channels within the applications. Furthermore, the potential of hybrid manufacturing, for e.g. the shaft and a wheel of a turbocharger, was demonstrated.

Aging effects of the powder were analyzed, and first recycling concepts were discussed. Concerning the chemistry in the as-built condition an aluminum loss of 0.5 wt% to 0.9 wt% and an O<sub>2</sub> level between 800 ppm and 1000 ppm was measured.

Starting from the as-built condition, calorimetric analyses were done to measure the phase transition temperatures as a reference for further heat treatment steps. In the case of TiAl, the microstructure, phase contents and phase morphologies can be adapted to different TiAl-specific applications depending on the required mechanical properties. That is why various heat treatment strategies were tested in combination with hot isostatic pressing (HIP) to generate a near gamma (NG), a nearly lamellar gamma (NL  $\gamma$ ) and a nearly lamellar beta (NL  $\beta$ ) microstructure. Figure 2 shows the results of the different heat treatments on the microstructure. In the as-built condition and also after some standard heat treatments, some inhomogeneities in the microstructure were documented because of the Al loss and the aging effect during the build job. In case of the NL  $\beta$  microstructure and the NG microstructure, first steps towards an optimized heat treatment to achieve a homogeneous microstructure and thus optimal creep or tensile properties were conducted.

Tensile tests were performed at different temperatures between 20 °C and 800 °C on horizontally and vertically built samples exhibiting NL  $\gamma$ , NG and NL  $\beta$  microstructures.

Creep tests were performed at 750 °C and 780 °C with 150 MPa and 200 MPa for the NL  $\beta$  and the optimized NL  $\beta$  condition (see Fig. 2(5)). Good results were generated for both alloys as well as for all temperatures and loads, heat treatments and for the horizontal and vertical build direction. For the optimized NL  $\beta$  microstructure an excellent minimal creep rate of  $1.9 \cdot 10^{-9}$  1/s was measured at 750 °C and 150 MPa.

Rotating bending tests were performed in the NL  $\beta$  condition for both alloys. A fatigue limit between 350 MPa to 450 MPa was measured. In all cases, inhomogeneities in the microstructure and not defects were the reason of the failure. A much higher fatigue limit is expected for the optimized NL  $\beta$  and NG microstructure because of the improved microstructural homogeneity as it will be reported in a forthcoming publication [2].

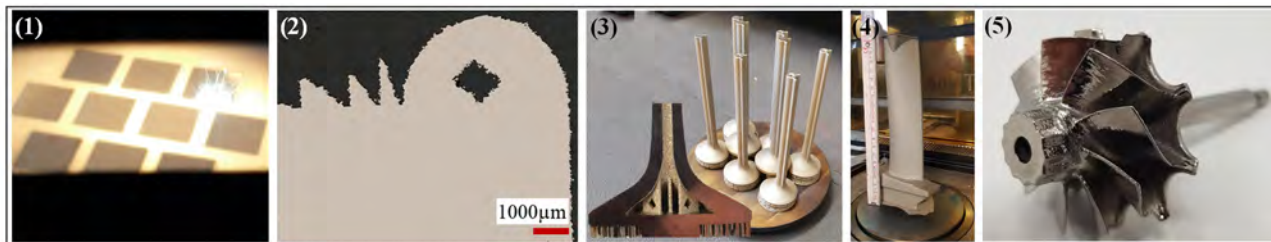


Fig. 1: (1) Hot process zone (up to 1200 °C possible) of the EOS-M290HT; (2) cross-section of a TiAl-TNM reference sample with a density of >99.97 % and which is free of cracks; (3) TiAl-TNM build job of 8 inlet valves with inner structures; (4) TiAl-TNM aero engine blade with a height of 23 cm; (5) TiAl-TNM hybrid manufacturing of a turbocharger wheel and shaft with surface finishing. All components are shown with the permission of the respective customers of AM Metals.

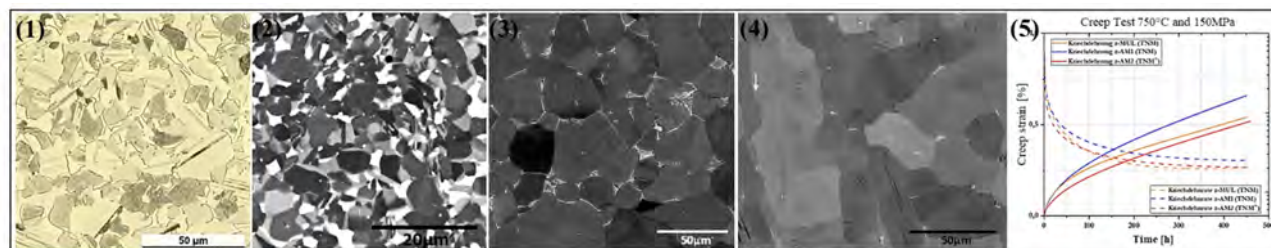


Fig. 2: Different types of microstructures adjusted via heat treatments in TNM samples which were manufactured via LBM: (1) NL  $\gamma$  (2) NG; (3) NL  $\beta$ ; (4) NL  $\beta$  using an optimized heat treatment; (5) creep strain and creep rate at 750 °C and 150 MPa of TiAl-TNM with NL  $\beta$  microstructure (blue), TiAl-TNM<sup>+</sup> with NL  $\beta$  microstructure (red) and TiAl-TNM with optimized NL  $\beta$  microstructure (orange).

## References

- [1] AM Metals GmbH, <https://am-metals.de>, 2021.
- [2] R. Wartbichler, F. Pürstl, T. Maiwald-Immer, H. Clemens, S. Mayer, in preparation. 2021.

**O-AM-03****Thermodynamic analysis of quaternary Al-Mg-Si-Er alloys for applications in additive manufacturing**Mauro Palumbo, Matteo Vergnano and Marcello Baricco

Dip. di Chimica, Università di Torino, 10125 Torino, Italy, mauro.palumbo@unito.it

**Introduction**

Ternary Al-Mg-Si alloys are well known as traditional casting Al-base light alloys. More recently, these alloys have been used in newly developed processing methods such as additive manufacturing (AM), where the repeated melting/solidification cycles make it extremely important to have raw materials with suitable properties. For example, alloys with a low “solidification window”, i.e. the difference between the liquidus and solidus temperatures, will reduce possible segregations and inhomogeneities in the microstructure obtained after solidification. The addition of inoculants to these alloys can further enhance their solidification behavior. For example, the addition of Scandium to ternary Al-Mg-Si alloys (Scalmalloys) [1] has led to fine-grained crack-free microstructure with fine particles of  $Al_3Sc$  which show higher tensile and fatigue strengths. Other rare-earths such as Erbium are expected to behave similarly and possibly even better. In this work, we have carried out a thermodynamic analysis of the quaternary Al-Mg-Si-Er system using the CALPHAD approach augmented by using Density Functional Theory (DFT) calculations to obtain thermodynamic properties of ternary compounds. A quaternary thermodynamic database has been developed and subsequently used to investigate properties of quaternary alloys, including the solidification behavior. A comparison with available thermodynamic data measured in our laboratory [2] has also been carried out to validate the calculated results.

**Materials and Methods**

In the present work, thermodynamic calculations have been carried out using the CALPHAD method as implemented in the ThermoCalc software v. 2021a [3]. DFT calculations were carried out using the VASP code v. 5.4 [4]. All DFT parameters in the calculations were set to obtain a numerical precision below 2 meV/at ( $\sim 0.2$  kJ/mol).

**Results and Discussion**

In order to create the quaternary database, available assessments in the literature were used for the subsystems [5,6]. A reassessment of the binary Er-Si system has been performed despite the fact that an assessment was already available in the literature [7]. This was necessary to adopt a model (Redlich-Kister) for the liquid phase which is compatible with the other subsystems. A full assessment of the ternary Al-Si-Er system was carried out based on the available experimental data and the DFT calculations performed in this work for all ternary compounds. As for the ternary Mg-Si-Er system, no ternary compounds have been reported and we have extrapolated its properties from the binary subsystems.

Based on the quaternary database, several alloys have been investigated. In particular, their solidification behavior was analyzed using Scheil-Gulliver simulations as shown in Fig. 1. The calculated results were compared with microstructural data obtained by electronic microscopy. Thermodynamic data such as liquidus and solidus temperatures and enthalpies of melting were also calculated using the quaternary database and compared with experimental data. The solidification window of quaternary alloys was calculated at different compositions as shown in Fig. 2. Finally, the nucleation of  $Al_3Er$  particles and the competition with other phases was investigated by calculating their thermodynamic driving force for nucleation.

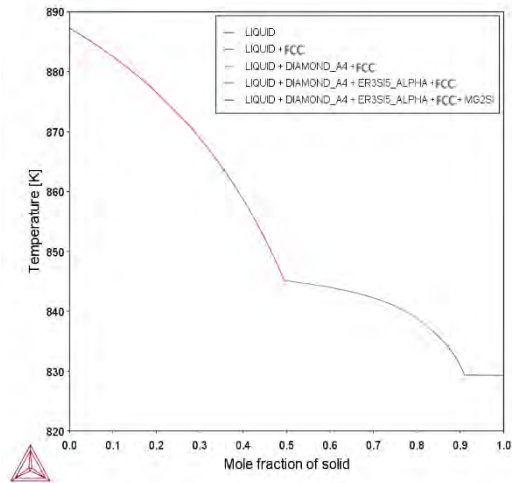


Fig. 1: Scheil-Gulliver solidification for Al-7Si-0.6Mg-0.4Er

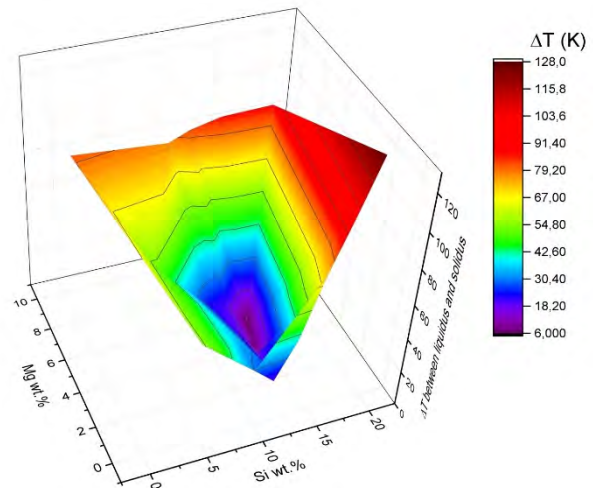


Fig. 2: Solidification window for Al-Mg-Si-Er quaternary alloys with fixed  $X(\text{Er})=0.03$  as a function of Mg and Si compositions

### References

- [1] M. Awd, J. Tenkamp, M. Hirtler, S. Siddique, M. Bambach and F. Walther, *Materials*. **2017**, 1-17.
- [2] S. Marola, PhD thesis, Università di Torino, Italy.
- [3] <http://www.thermocalc.se>
- [4] <http://www.vasp.at>
- [5] I. Ansara, A. T. Dinsdale and M. H. Rand, COST507 database.
- [6] G. Cacciamani, A. Saccone, R. Ferro, *Journal of Phase Equilibria*. **2002**, 23, 38-50
- [7] J. Kim, I.-H. Jung, *J. Chem. Thermodynamics*. **2015**, 81, 253-272

**O-AM-04****Flexible powder production for additive manufacturing of refractory metal alloys**

Frauke Hinrichs<sup>1</sup>, Daniel Schliephake<sup>1</sup>, Sascha Seils<sup>1</sup>, Susanne Obert<sup>1</sup>, Alexander Kauffmann<sup>1</sup>, Karin Ratschbacher<sup>2</sup>, Melissa Allen<sup>2</sup> and Martin Heilmaier<sup>1</sup>

<sup>1</sup> Karlsruhe Institute of Technology (KIT), Institute for Applied Materials (IAM-WK), 76131 Karlsruhe, Germany, martin.heilmaier@kit.edu, alexander.kauffmann@kit.edu, frauke.hinrichs@kit.edu, daniel.schliephake@kit.edu, sascha.seils@kit.edu, susanne.obert@kit.edu

<sup>2</sup>GfE Metalle und Materialien GmbH, 90431 Nuremberg, Germany, Karin.Ratschbacher@gfe.com, Melissa.Allen@gfe.com

**Introduction**

For additive manufacturing (AM) of metallic and intermetallic materials as well as for various powder metallurgical process routes, the quality and properties of elemental and alloy powders are essential. The most important characteristics of powders for AM include interrelating size distribution, particle shape and morphology, flowability, energy absorption and reflection, humidity, thermal conductivity, the reactivity with oxygen and the resulting formation of oxide layers [1]. Currently, most industrial powders for AM are manufactured by gas atomization (GA), where a jet of melt falls through a nozzle in an inert atmosphere and is atomized by a high impact gas stream. However, the production of refractory metal alloy powders remains challenging, not only due to their high liquidus temperatures of more than 2000 °C and the reactivity of the constituting elements but also due to the formation of brittle intermetallic phases. The brittle nature of these alloys restricts application of commonly available GA techniques, e.g. the casting of consumable electrodes for processes like electrode induction GA (EIGA) or plasma rotating electrode process (PREP) becomes difficult.

A novel ultrasonic atomization (UA) process was used to produce powders of a pesting resistant Mo-Si-Ti alloy in laboratory scale, whereas a modified EIGA process was used to produce powders of the same composition in industrial quantity. The powders were analyzed and compared with regards to their suitability for AM. Furthermore the process stability of UA for the production of reactive and refractory alloy powders was evaluated through material analysis pre- and post-atomization. For the trials a refractory metal alloy on Mo-Si-Ti basis was chosen. The recently developed alloy shows exceptional oxidation resistance at intermediate temperatures of about 800 °C [2], which is rarely observed for high-Mo containing alloys [3].

**Materials and Methods**

Three ingots of the alloy Mo-20Si-52.8Ti (at. %) were arc melted in an Ar atmosphere by using an Edmund Bühler GmbH AM/0,5 arc melter. The ingots were then cast into rods with a diameter of 10 mm. The rods were atomized in an ATOLab+ (3DLab Ltd.). Fig. 1 a shows the principle of UA with the ATOLab+. A plasma arc is ignited between the electrode and the crucible in an evacuated and then Ar (99,998 % purity) filled process chamber. The crucible is attached onto a sonotrode. The input rod is gradually melted to create a melt pool on the vibrating crucible. The ultrasonic vibration of the sonotrode causes droplets to separate from the melt pool. The droplets are carried by flowing Ar and rapidly solidify to powder particles. The powders from each rod were kept separately in order to assess process stability and reproducibility.

EIGA powder was produced by GfE Metalle und Materialien GmbH. Due to the brittle nature of the alloy, the EIGA electrode was manufactured through a powder metallurgical process. Elemental Mo and Ti as well as SiTi-prealloyed powders were mixed to achieve a homogeneous powder mixture. The mixture was enclosed in a Ti-capsule and consolidated into rod shape through hot isostatic pressing (HIP). The rods were machined to achieve the required shape for EIGA. Alloy formation to the target composition was achieved in-situ during induction melting of the electrode tip. All powder batches were sieved in an Ar filled glove box with -100 µm mesh size prior to further analysis. Consolidation of the powders into cylindrical pellets with diameters of 20 mm was carried out at maximum temperatures of 1200 °C and 1300 °C, both with temperature ramps of 100 K/min and for dwell times of 5 min by field assisted sintering technique (FAST) with a Typ HP D device (FCT Systeme GmbH).

For microstructure analysis, scanning electron microscope (SEM, EVO 50, Carl Zeiss AG) micrographs in backscattered electron (BSE) contrast were obtained from cross sections of the as cast material, powder particles (UA and EIGA powders, cf Fig. 1 b and c) and the consolidated samples. For particle analysis, BSE micrographs of the particle morphology were taken, after placing some powder on an adhesive C pad. The BSE micrographs were binarized using the software ImageJ and individual particle shapes were approximated by ellipsoids. Energy dispersive X-ray spectroscopy (EDX) was performed on all metallographically prepared samples using an Auriga cross beam SEM (Carl Zeiss AG) to track changes in alloy composition throughout the processing steps. To determine the phases present, X-ray diffraction (XRD) analyses were carried out using a D2 phaser system (Bruker). Interstitial O and N content was tracked by means of hot gas carrier extraction on a Leco TC600 device.

## Results and Discussion

The powder particles produced with UA had a size distribution of 90 % of the particle diameters being in between 40 and 80  $\mu\text{m}$  with satisfactory reproducibility. The aspect ratio (AR) of the approximated ellipsoid diameters showed that  $AR_{90} \leq 1.2$  which indicates a shape close to spherical. A narrow size distribution suggests that the droplet formation was largely determined by the capillary model as described in Ref. [4]. On a vibrating surface wetted with a liquid, excitation of standing surface waves occurs. With increasing intensity of the vibration, the maxima of the standing waves pile up into thin columns until they become hydrodynamically unstable and uniform droplets detach at the tip [5]. The decisive parameters for efficient atomization of the liquid phase are a sufficiently large excitation amplitude and a sufficiently low viscosity of the melt [6]. Microstructure analysis also suggests a fast solidification of the droplets. The eutectic microstructure obtained is ultra-fine and the formation of primary  $\text{Ti}_5\text{Si}_3$  that can often be found in arc melted samples [2] is suppressed. The EIGA powder, however, showed a microstructure that was less fine structured, and the formation of eutectic colonies and the visibility of primary  $\text{Ti}_5\text{Si}_3$  suggests a lower cooling rate compared to the UA powder, cf. Fig. 1 c with Fig. 1 b, respectively. Furthermore, the EIGA powder has a wider particle size distribution, compared with the UA powder. The particle diameters of the EIGA powder appear to be rather bimodal with peaks at about 10 and 40  $\mu\text{m}$  and a slightly higher value for  $AR_{90}$  of 1.5. XRD analysis showed no changes in present phases through UA, and elemental analysis confirmed that there is neither a substantial change in alloy composition through the process. Oxygen levels in the order of 1000 wt. ppm were at satisfactory level for the development state of the processes but could yet be improved for future applications in additive manufacturing.

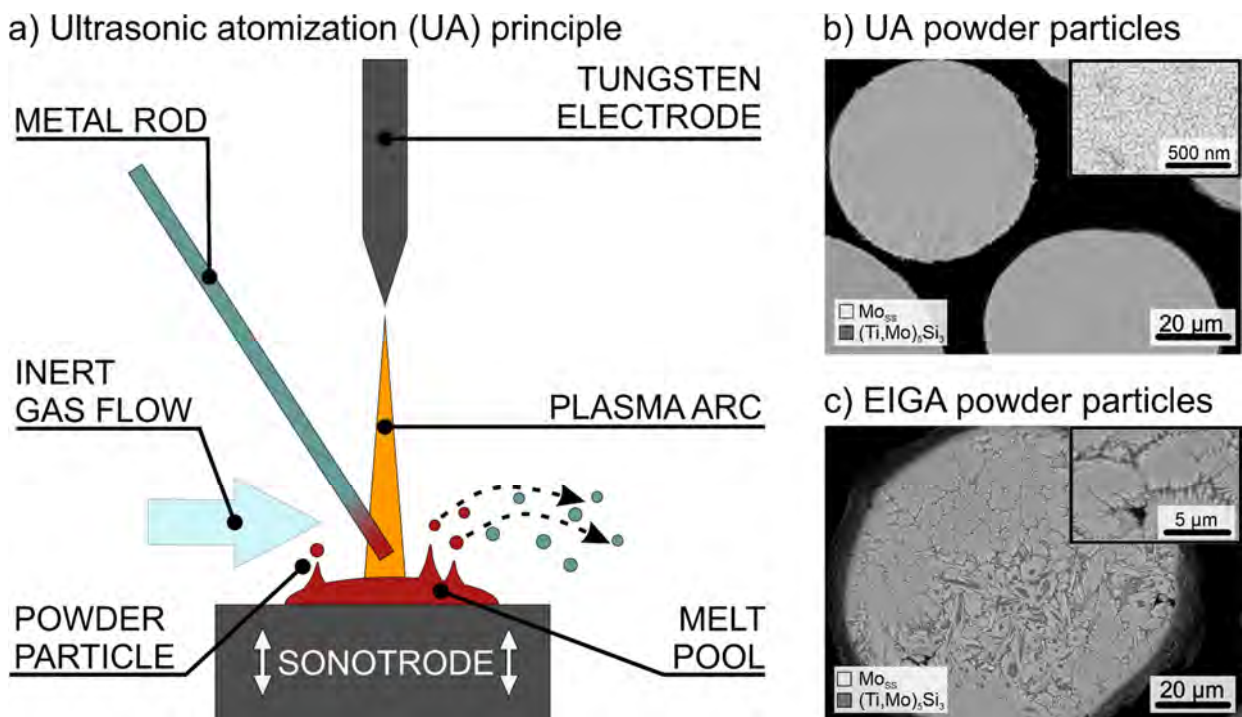


Fig. 5 Principle of the ultrasonic atomization process (a), BSE micrographs of powder particles produced by UA (b) and EIGA (c)

## References

- [1] S. Dietrich, M. Wunderer, A. Hüssel, and M. F. Zaeh, A New Approach for a Flexible Powder Production for Additive Manufacturing, *Procedia Manuf.* **2016**, *6*, 88–95.
- [2] D. Schliephake *et al.*, Constitution, oxidation and creep of eutectic and eutectoid Mo-Si-Ti alloys, *Intermetallics*. **2019**, *104*, no. October 2018, pp. 133–142.
- [3] J. H. Perepezko, M. Krüger, and M. Heilmaier, Mo-Silicide Alloys for High-Temperature Structural Applications, *Mater. Perform. Charact.* **2021**, *10*.
- [4] W. Eisenmenger, Dynamic properties of the surface tension of water and aqueous solutions of surface active agents with standing surface waves in the frequency range from 10kHz to 1.5MHz, *Acoustics*. **1959**, *9*, no. 4, 327–340.
- [5] U. Reimann and R. Pohlman, Optimierung Der Vernebelung Von Flüssigkeiten Mit Ultraschall Unter Berücksichtigung Der Probleme Bei Höheren Frequenzen, *Forsch. im Ingenieurwesen/Engineering Res.* **1976**, *42*, no. 1, 1–7.
- [6] E. G. Lierke and G. Griebhammer, The formation of metal powders by ultrasonic atomization of molten metals, *Ultrasonics*. **1967**, no. October, 713–718.



P-01

### Structural disorder in a complex Mg rich-Pt phase

Laura Agnarelli, Andreas Leithe-Jasper, Yurii Prots and Juri Grin

Max-Planck -Institut für Chemische Physik fester Stoffe, Dresden, Germany, laura.agnarelli@cpfs.mpg, Andreas.Leithe-Jasper@cpfs.mpg.de, Yurii.Prots@cpfs.mpg.de, grin@cpfs.mpg.de

#### Introduction

After the discovery of the semiconducting behavior of the intermetallic  $\text{Be}_5\text{Pt}$  phase [1] our interest has turned to finding other intermetallic compounds which could show similar physical properties, with particular attention to a possible Mg-rich phase in the Mg-Pt system. No Mg-Pt phase diagram is reported in literature and only few phases are already known [2,3,4,5]; in particular R. Ferro [6], after a metallographic analysis of a Mg rich Mg-Pt sample, reported that a phase with composition around  $\text{Mg}_6\text{Pt}$  could exist. However, a complete solution and refinement of its crystal structure is still missing.

#### Materials and Methods

The sample was synthesized by annealing Mg granules and Pt powder at 600 °C for 2 weeks. A single crystal was taken from the crushed annealed sample, it was glued to thin glass fibers and was analyzed at room temperature using a Rigaku AFC7 diffraction system equipped with a Saturn 724 + CCD detector using Mo-K $\alpha$  radiation. Absorption correction was performed by a multi-scan procedure. The structure was solved and refined in the non-centrosymmetric space group  $F-43m$  with  $a=20.1273$  (1) Å. The chemical composition of the sample was determined to be  $\text{Mg}_{87.67}\text{Pt}_{12.33}$  from WDXS performed with a Microprobe Cameca SX100, Scanning Electron Microscope (SEM) Jeol JSM7800F using  $\text{Mg}_2\text{Si}$  as standard for Mg and Pt as standard of Pt. The composition obtained from metallography analysis is in good agreement with the data obtained from single crystal solution.

#### Results and Discussion

The structural motif of  $\text{Mg}_{28.87}\text{Pt}_{4.06}$  can be described as made up by interpenetrating Mackay clusters [7] where the empty spaces left by these in the unit cell are filled by tetrahedral units of four  $\text{PtMg}_9$  tricapped trigonal prisms and Pearce clusters [8] made of tetrahedral units of face sharing  $\text{PtMg}_{12}$  icosahedra (Figure 1). In this way the 347 Mg atoms (comprising 9 independent positions) and the 49 Pt atoms (comprising 3 independent positions) build up the complex crystal structure. The structure can be also described as an arrangement of sets of nested polyhedra units or “clusters” sitting in high symmetry points of the unit cell (Figure 2). Three of the fifteen atomic sites (M1a, M1b and Mg8 sites) of the phase show disorder which influence both the second shell of the Mackay clusters and one of the nested polyhedral units.

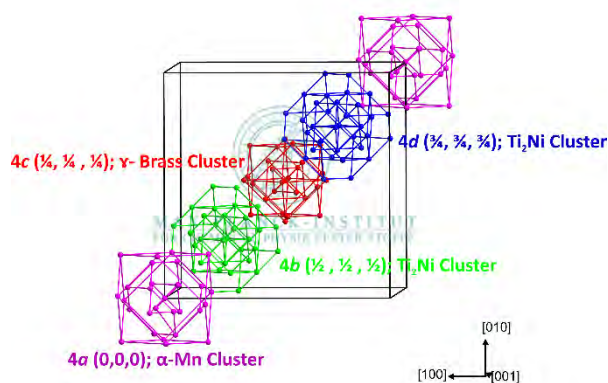
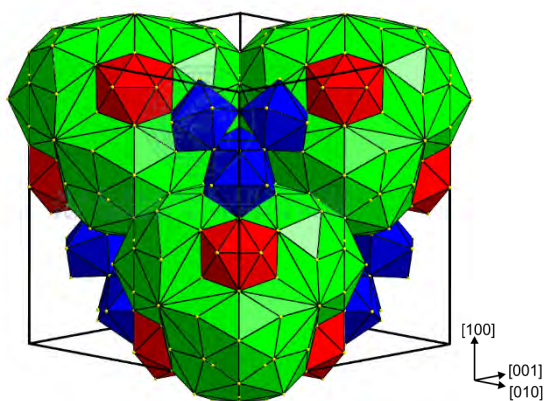


Fig. 1: Space filling arrangement of Mackay clusters (green), tetrahedral units of four  $\text{PtMg}_9$  tricapped trigonal prisms (blue) and the Pearce clusters (red).

Fig. 2: Arrangement of the nested polyhedral units in high symmetry point of the unit cell.

#### References

- [1] A.Amon, E. Svanidze, A. Ormeci, M. König, D. Kasinathan, D. Takegami, Y. Prots, Y. Liao, K.Tsuei, L.Tjeng, A. Leithe Jasper, Y. Grin, *Angewandte Chemie International Edition*. **2019**, *58*, 15928 – 15933
- [2] H. H. Stadelmaier, W.K. Hardy, *Zeitschrift für Metallkunde*. **1961**, *52*, 391-396
- [3] R. Schmitt, J. Glaser, H.-J. Meyer, *Zeitschrift für Anorganische und Allgemeine Chemie*. **2006**, *632*, 2198-2200
- [4] W. Bronger, W. Klemm, *Zeitschrift für Anorganische und Allgemeine Chemie*. **1962**, *319*, 58-81
- [5] K.-J. Range, P. Hafner, *Journal of Alloys and Compounds*. **1992**, *183*, 430-437
- [6] R. Ferro, G. Rambaldi, *Journal of the Less Common Metals*. **1960**, *2*, 383-391
- [7] A.L. Mackay, *Acta Crystallographica*. **1962**, *15*, 916
- [8] E.A. Lord, S. Ranganathan, *Eur. Phys. J.D.* **2001**, *15*, 335-343

P-02

**Room temperature plastic deformation of hard and brittle crystals investigated by micropillar compression method**Hiroataka Suzuki<sup>1</sup>, Masaomi Okutani<sup>1</sup>, Kyosuke Kishida<sup>2</sup> and Haruyuki Inui<sup>2</sup><sup>1</sup>Department of Materials Science and Engineering, Kyoto University, 606-8501 Kyoto, Japan, suzuki.hiroataka.87s@st.kyoto-u.ac.jp, okutani.masaomi.g14@kyoto-u.jp<sup>2</sup>Department of Materials Science and Engineering, Kyoto University, 606-8501 Kyoto, Japan  
Center of Elements Strategy Initiative for Structural Materials (ESISM), Kyoto University, 606-8501 Kyoto, Japan  
kishida.kyosuke.6w@kyoto-u.ac.jp, inui.haruyuki.3z@kyoto-u.ac.jp**Introduction**

Hard and brittle materials including intermetallic compounds and ceramics, have been widely used as strengthening phases in various metallic alloys mostly because of their extremely high strength, which is closely related to their complex crystal structures. In general, these hard materials exhibit quite brittle behavior at low temperature in bulk-scale mechanical tests, while they can be plastically deformed only at very high temperature above 1000 °C. These characteristics of plastic deformation of these hard and brittle materials cause serious difficulty in identifying operative deformation modes. Recently, micropillar compression tests of single crystalline materials have been found to be useful for studying deformation behavior of brittle materials such as Si, GaAs at temperatures far below their ductile to brittle transition temperatures observed for bulk-scale specimens [1,2]. In our research group, we have systematically applied the micropillar compression method to various hard materials including transition-metal silicides, Laves phase, SiC, borides and carbides, and have successfully confirmed that most of them are plastically deformable at room temperature [3-6]. In this study, we investigated room temperature deformation behavior of sigma-FeCr and alpha-Mn, both of which have very complicated crystal structures of the tetragonal D8<sub>b</sub>-type (*tP30*, space group: *P42/mnm*, *c/a* ~0.52, Fig. 1) and cubic A12-type (*cI58*, space group: *I43m*, *a* = 0.8905nm, Fig. 2) structures, respectively, focusing on the similarity in their crystal structures composed of atomic layers with the Kagome-type atomic arrangement.

**Materials and Methods**

Ingots with a nominal composition of Fe-50 at%Cr were prepared by arc-melting. The arc-melted ingots were cut into small blocks, cold-rolled and then heat-treated to obtain polycrystalline specimens of Fe-Cr sigma phase. Rectangular parallelepiped micropillar specimens of sigma-FeCr and alpha-Mn single crystals with various loading axis orientations were fabricated on single crystal regions of polycrystalline sigma Fe-Cr and electrolytic alpha-Mn with 99.999 % purity using focused-ion beam (FIB) technique. Compression tests were performed on a nanoindenter equipped with a flat punch diamond tip. All micropillars were tested under a constant displacement rate (initial strain rate:  $1 \times 10^{-4} \text{s}^{-1}$ ) condition at room temperature in air. Deformation microstructures of the deformed micropillars were investigated by scanning electron microscopy (SEM), transmission electron microscopy (TEM) and scanning transmission electron microscopy (STEM). Specimens for TEM/STEM observations were prepared by the FIB-SEM lift-out technique.

**Results and Discussion**

Plastic flow was observed at room temperature for all tested micropillars of both sigma-FeCr and alpha-Mn mostly exhibiting a smooth transition from elastic to plastic deformation similar to those observed for ductile materials. Four and three different slip systems were identified to be operative in sigma-FeCr and alpha-Mn, respectively, depending on the loading axis orientation. It is thus confirmed that there are sufficient numbers of independent slip systems to satisfy the von-Mises criterion. The values of critical resolved shear stress (CRSS) for the identified three slip systems are extremely high about 1.9 - 2.5 GPa. The CRSS value for each slip system increases with decreasing specimen size, following an inverse power-law relationship with a very low power-law exponent (< 0.1), which is much smaller than those reported for FCC (0.5 - 1) and BCC (0.3 - 0.5) metals. Details of the identified slip systems including their dislocation structures will be presented

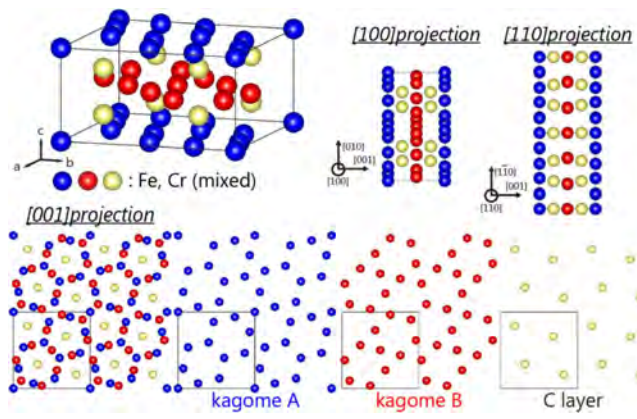


Fig. 1: Crystal structure of sigma-FeCr.

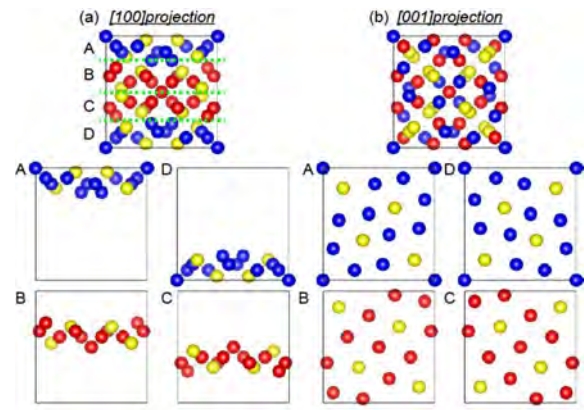


Fig. 2: Crystal structure of alpha-Mn.

### References

- [1] J. Michler, K. Wasmer, S. Meler, F. Östlund, K. Leifer, Applied Physics Letters. **2007**, *90*, 043123.
- [2] S. Korte-Kerzel, MRS Communications. **2017**, *7*, 109-120.
- [3] K. Kishida, T. Maruyama, H. Matsunoshita, T. Fukuyama, H. Inui, Acta Materialia. **2018**, *159*, 416-428
- [4] K. Kishida, Y. Shinkai, H. Inui, Acta Materialia. **2020**, *187*, 19-28.
- [5] K. Kishida, T. Fukuyama, T. Maruyama, H. Inui, Scientific Reports. **2020**, *10*, 17983.
- [6] K. Kishida, T. Maruyama, T. Fukuyama, H. Inui, Science and Technology of Advanced Materials. **2020**, *21*, 805-816.

**P-03****Fracture toughness of the intermetallic C15 Al<sub>2</sub>Ca Laves phase determined using a micropillar splitting technique**

Uzair Rehman, Chunhua Tian, Frank Stein, James P. Best and Gerhard Dehm

Max-Planck-Institut für Eisenforschung GmbH (MPIE), 40237 Düsseldorf, Germany,  
u.rehman@mpie.de, c.tian@mpie.de, stein@mpie.de, j.best@mpie.de, dehmm@mpie.de

**Introduction**

The cubic C15 Laves Al<sub>2</sub>Ca phase is prevalent in several alloy systems, most notably in a selection of magnesium alloys, where previous research has shown that an increase in Al<sub>2</sub>Ca can lead to grain refinement in AZ31 alloys [1]. The impact of the Al<sub>2</sub>Ca phase on the mechanical properties of magnesium alloys has also been a focus of previous research: Al<sub>2</sub>Ca precipitates in a magnesium matrix are reported to serve as obstacles against non-basal slip of the <a> type dislocation during creep deformation [2], while the phase is also reported to improve the grain-boundary strength in magnesium alloys [3]. However, Al<sub>2</sub>Ca has also been found to catalyze hot cracking in Mg-Al-Ca alloys due to the difference in thermal expansion coefficient between Al<sub>2</sub>Ca and the Mg matrix [3]. As such, the fracture toughness of the intermetallic Al<sub>2</sub>Ca phase is of significant importance for understanding the mechanical response of a series of technologically-important Mg-alloys.

**Materials and Methods**

Samples were cast with 66.7 at. % aluminum and 33.3 at. % calcium target compositions, followed by annealing at 600°C for 24 hrs to improve homogeneity, reduce internal stresses and promote equilibrium phase formation. The annealed sample was mechanically ground and then polished to a 0.04 µm surface finish with an OP-U colloidal silica suspension. Scanning electron microscopy (SEM) using a Zeiss Auriga was performed to image the microstructure, followed by electron backscatter diffraction (EBSD) for phase confirmation. To determine the hardness and elastic modulus for fracture toughness calculations, 15 indents were made approximately 10 µm apart, at a constant strain rate of 0.05/s and a maximum displacement of 500 nm. A diamond Berkovich tip geometry (Synton-MDP) was used, with a KLA-Tencor G200 nanoindentation device. Micropillars of ca. 5 µm diameter were then fabricated into single grain regions using a gallium focused ion beam (FIB) SEM workstation at 30 keV to a minimum polishing current of 240 pA (Zeiss Auriga). Finally, the fracture toughness of the Al<sub>2</sub>Ca was determined at room temperature using pillar splitting tests performed on the pillars with a diamond cube corner geometry (Synton-MDP) using an ASMEC UNAT-II in-situ nanoindentation system with the SEM (Zeiss Gemini).

**Results and Discussion**

Fig. 1(a) shows the sample microstructure, containing an Al<sub>2</sub>Ca matrix and an Al<sub>4</sub>Ca skeleton phase. EBSD analysis confirmed the matrix phase as the Al<sub>2</sub>Ca, and also revealed a grain size in excess of 100 µm, which was beneficial for milling several pillars in the same grain to reduce any impact of orientation on the fracture toughness results. Berkovich indentation was then performed and provided an average elastic modulus of 110 ± 2 GPa and hardness of 5.8 ± 0.1 GPa. Micropillar indentation splitting was used in-situ inside the SEM to determine the toughness, where FIB-milled pillars with an aspect ratio of 1 to 2 are fractured using a sharp indenter allowing for measurement of the critical load to form a fracture instability under the sharp tip [4]. This method is relatively simple, and does not require post-mortem measurement of the crack length or geometry. The relationship between fracture toughness ( $K_c$ ) is determined from the critical load at failure ( $P_c$ ), pillar radius ( $R$ ) and gamma ( $\gamma$ ), which is a dimensionless quantity dependent on the ratio of elastic modulus and hardness ( $E/H$ ), as shown in Eq. 1:

$$K_c = \gamma \frac{P_c}{R^{3/2}} \quad (1)$$

The measured  $E/H$  ratio of 19 from nanoindentation testing was then used to determine the corresponding value of gamma using a published data set [5]. Fig. 2(a) shows a post-mortem image of one of the pillars, where it is observed that a three-way crack propagates from the indentation point towards the edges of the pillar. Load-displacement curves obtained from the pillar splitting are shown in Fig. 2(b); the maximum load on the curves depicts the critical failure load of each pillar. Finally, Eq. 1 was used to determine the fracture toughness of each pillar using the pillar radius measured using the imaging software, leading to a calculated average fracture toughness for the Al<sub>2</sub>Ca micropillars of 1.20 ± 0.17 MPa√m. As this is an ongoing project, more pillars will be tested to improve the statistical accuracy and precision of the toughness data, while extending the toughness measurements to elevated temperatures is also planned.



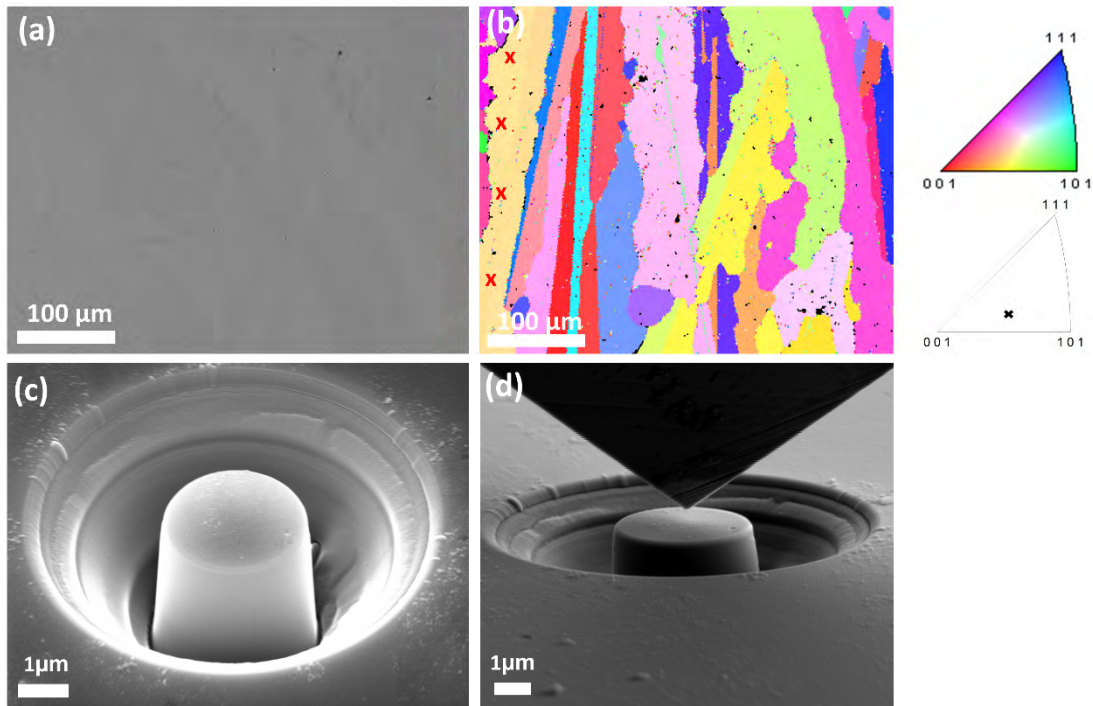


Fig. 1: (a) Backscattered electron (BSE) image of the polished sample surface, (b) EBSD of the region of interest and associated inverse pole figure (IPF) maps showing  $\text{Al}_2\text{Ca}$  grain orientations and red crosses showing pillar locations, (c) SEM image of FIB-milled pillar, (d) pillar before the splitting test imaged within the SEM.

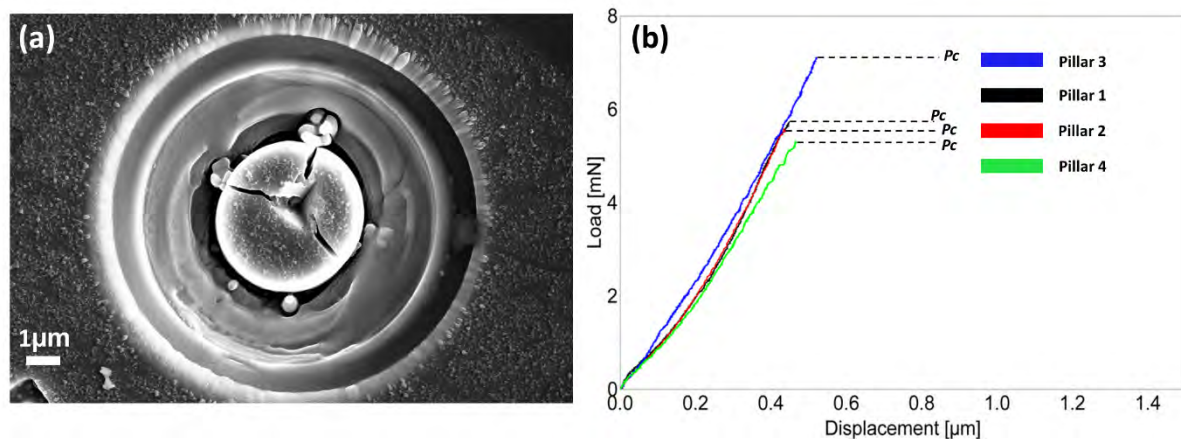


Fig. 2: (a) Post-mortem image after the pillar splitting test, (b) load-displacement curves obtained from pillar splitting

**Acknowledgments**

The authors acknowledge financial support by the Deutsche Forschungsgemeinschaft (DFG) through project B06 of the SFB1394 Structural and Chemical Atomic Complexity–From Defect Phase Diagrams to Material Properties, project ID 409476157. The authors would also like to thank Dr. Hauke Springer for providing the samples, as well as Dr. Martin Palm, Irina Wossack, Leon Christiansen, Jing Rao and Mohammed Kamran Bhat for their support during this research.

**References**

[1] Z.T. Jiang, B. Jiang, J.Y. Zhang, J.H. Dai, Q.S. Yang, Y.A. Qin, F.S. Pan, Transactions of Nonferrous Metals Society of China. **2016**, 26, 1284-93.  
 [2] A. Suzuki, N.D. Saddock, J.R. TerBush, B.R. Powell, J.W. Jones, T.M. Pollock, Metallurgical and Materials Transactions. **2008**, 39, 696.  
 [3] H. Zhang, & S. Wang, Journal of Materials Research. **2012**, 27, 1631.  
 [4] M. Sebastiani, K.E. Johanns, E.G. Herbert, F. Carassiti & G.M. Pharr, Philosophical Magazine. **2015**, 95, 1928-44.  
 [5] S. Bruns, L. Petho, C. Minnert, J. Michler, K. Durst, Materials & Design. **2020**, 186, 108311.



P-04

**Micropillar compression deformation of single crystal of Fe<sub>3</sub>Ge with the L1<sub>2</sub> structure**Zhenghao Chen<sup>1</sup> and Haruyuki Inui<sup>2</sup><sup>1</sup>Center for Elements Strategy Initiative for Structural Materials (ESISM), Kyoto University, Kyoto, Japan,  
chen.zhenghao.6e@kyoto-u.ac.jp<sup>2</sup>Department of Material Science and Engineering, Kyoto University, Kyoto, Japan  
inui.haruyuki.3z@kyoto-u.ac.jp**Introduction**

Many intermetallic compounds with the L1<sub>2</sub> structure such as Ni<sub>3</sub>Al have been known to exhibit the 'yield stress anomaly' (YSA), in which the yield stress increases with the increase in temperature. There is a general agreement that the yield stress anomaly occurs as a result of thermally-activated cross-slip of the superlattice dislocation with *b* (Burgers vector)=[10 $\bar{1}$ ] dissociated into the APB (anti-phase boundary)-scheme (shown below as (Eq. 1)) from (111) octahedral to (010) cube slip planes [1, 2].



However, all L1<sub>2</sub> compounds do not necessarily behave similarly to exhibit YSA. The L1<sub>2</sub>-Fe<sub>3</sub>Ge is frequently counted as a typical exception for this [3, 4]. The reason for this has usually been described to be instability of the APB fault on (111) that owing to the unstable or of very high energy of the APB fault on (111), the APB dissociation scheme of the superlattice dislocation with *b*=[10 $\bar{1}$ ] according to Eq.1 cannot occur. Instead, another dissociation scheme called the SISF (superlattice intrinsic stacking fault) scheme (shown below as (Eq. 2)) is believed to occur on (111) for this L1<sub>2</sub> compound.



However, due to the practical impossibility of the single crystal preparation for Fe<sub>3</sub>Ge, knowledge on the deformation mechanism of this L1<sub>2</sub> compound is very limited. All previous studies on Fe<sub>3</sub>Ge are based on polycrystals and found that slip occurs on (001) exhibiting a normal temperature dependence of yield stress [5-7].

In the present study, we investigate the room-temperature deformation behavior of single crystals of Fe<sub>3</sub>Ge with the L1<sub>2</sub> structure at room temperature as a function of crystal orientation with the use of small-scale specimens in the micropillar form cut out from polycrystals by FIB machining, in order to see if slip on {111} occurs in Fe<sub>3</sub>Ge. We then discuss factors controlling the occurrence of either slip on {111} or slip {010} as well as the expected mechanical properties carried by slip on {111} in Fe<sub>3</sub>Ge.

**Materials and Methods**

Ingots with a nominal composition of Fe-25 at.% Ge were prepared by arc-melting high-purity Fe and Ge in a proper ratio under an Ar gas flow. The ingots were annealed at 1273 K for 1 week for homogenization, then at 873 K for 2 months for the L1<sub>2</sub>-phase formation, followed by water quenching. Micropillar specimens with a square cross section having an edge length *L* ranging from 1 to 10 μm and an aspect ratio of about 1:2.5 were cut from the oriented specimens. Three compression-axis orientations,  $[\bar{1}, 1, 15]$ ,  $[\bar{1}13]$  and  $[\bar{5}68]$  were selected. The Schmid factors for possible (111)[10 $\bar{1}$ ] and (010)[10 $\bar{1}$ ] slip systems are listed in Tables 1 for each loading axis orientation, together with the *N* value (the Schmid factor ratio for these two slip systems). The propensity for the occurrence of (111)[10 $\bar{1}$ ] slip is expected to increase with the decrease in the *N* value. Micropillar specimens were deformed in compression at room temperature with nominal strain rate of 1 × 10<sup>-4</sup> /s. Deformation microstructures developed in the deformed micropillars were investigated by transmission electron microscopy (TEM). Specimens for TEM observations were prepared by FIB-SEM in-situ lift-out technique. Thin foil specimens for TEM analysis were cut out parallel to the observed slip plane (either (111) or (010)) as much as possible.

**Results and Discussion**

In addition to slip on (010), slip on (111) is observed to occur in Fe<sub>3</sub>Ge for the first time. The CRSS (critical resolved shear stress) for (111)[10 $\bar{1}$ ] slip, estimated by extrapolating the size-dependent strength variation to the 'bulk' size, is ~240 MPa, which is almost 6 times that (~40 MPa) for (010)[10 $\bar{1}$ ] slip similarly estimated, as shown in Fig. 1. The dissociation scheme for the superlattice dislocation with *b*=[10 $\bar{1}$ ] is confirmed to be of the APB (anti-phase boundary)-type both on (010) and on (111), in contrast to the previous prediction for the SISF (superlattice intrinsic stacking fault) scheme on (111) because of the expected APB instability. While superlattice dislocations do not have any preferential directions to align when gliding on (010) (indicative of low frictional stress at room temperature), the alignment of superlattice dislocations along their screw orientation is observed when gliding on (111), see the dark-field weak-beam image of (111) slip dislocations (Fig. 2). This is proved to be due to thermally-activated cross-slip to form Kear-Wilsdorf locks, indicative of the occurrence of yield stress anomaly that is observed in many other L1<sub>2</sub> compounds such as Ni<sub>3</sub>Al.

Hence, the CRSS for (010) slip is expected to show no temperature or orientation dependence owing to the curved dislocation configuration. The reported normal temperature dependence of yield stress in (010) polycrystal deformation is believed to be attributed to the effect of solid solution hardening due to the off-stoichiometry of the compound. On the other hand, a strong yield stress temperature dependence is predicted in (111) slip of Fe<sub>3</sub>Ge, according to the typical K-W lock configuration of (111) deformed dislocation structure, as shown in Fig 2. The APB energies on (111) and (010) are estimated from the corresponding dislocation dissociation width to be 99±9 and 91±12 mJ/m<sup>2</sup>, respectively. When judge from the elastic and energetic anisotropy of APB on (010) and (111), the yield stress anomaly for slip on (111) is expected to occur in this L<sub>12</sub>-Fe<sub>3</sub>Ge.

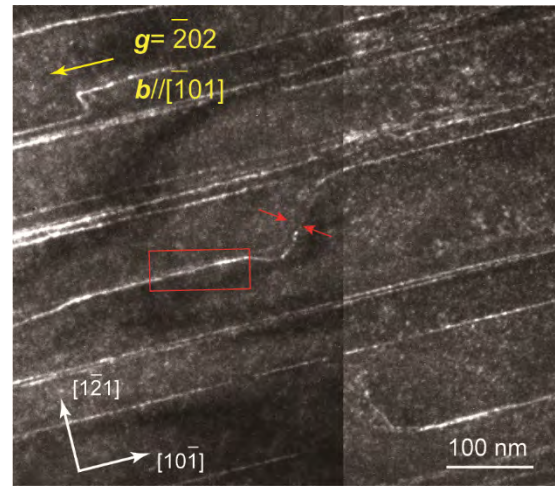
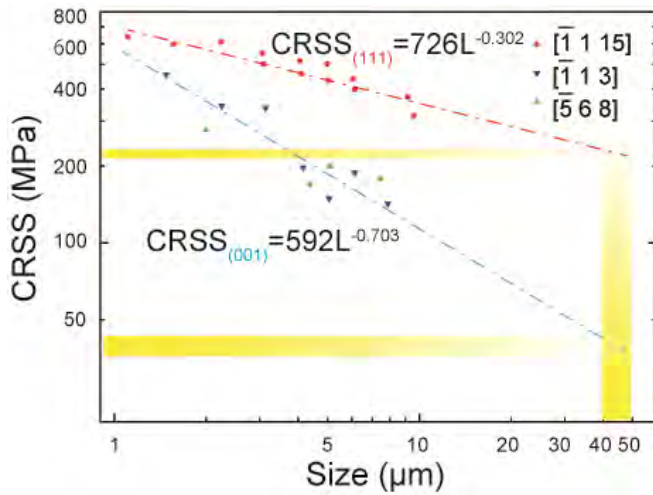


Fig. 1: Specimen size dependence of CRSS for slip on (010) ( $[\bar{1}13]$ - and  $[\bar{5}68]$ -orientated crystals) and (111) ( $[\bar{1},1,15]$ -orientated crystals).

Fig. 2: Weak-beam dark-filed TEM image of a typical deformation microstructure carried by slip on (111) in a  $[\bar{1},1,15]$ -orientated crystal. The thin foil was cut parallel to the (111) slip plane.

Loading-axis orientation		$[\bar{1}115]$	$[\bar{1}13]$	$[\bar{5}68]$
Schmid factor	(111) $[10\bar{1}]$	0.433	0.447	0.383
	(010) $[10\bar{1}]$	0.093	0.386	0.499
N-factor: (010) $[10\bar{1}]$ / (111) $[10\bar{1}]$		0.216	0.865	1.301

Table 1: Schmid factors for slip on (111) and (010) and N-factors for each loading-axis orientation.

References

- [1] G. Saada, P. Veyssiere, Dislocations in Solids. **1996**, *10*, 253-441.
- [2] D.P. Pope, V. Vittek, J. L. Bassani, dislocations in solids. **1996**, *10*, 135-185.
- [3] A.H.W. Ngan, I.P. Jones, R.E. Smallman, The stability of antiphase boundaries on {111} planes in the L<sub>12</sub> compound Fe<sub>3</sub>Ge and its relation to the abnormal negative temperature dependence of yield strength, Philosophical Magazine. **1992**, *A 66(1)*, 55-72.
- [4] O.N. Mryasov, Y.N. Gornostyrev, M.v. Schilfgarde, A.J. Freeman, Superdislocation core structure in L<sub>12</sub> Ni<sub>3</sub>Al, Ni<sub>3</sub>Ge and Fe<sub>3</sub>Ge: Peierls–Nabarro analysis starting from ab-initio GSF energetics calculations, Acta Materialia. **2002**, *50*, 4545-4554.
- [5] T.J. Balk, M. Kumar, K.J. Hemker, Influence of Fe substitutions on the deformation behavior and fault energies of Ni<sub>3</sub>Ge-Fe<sub>3</sub>Ge L<sub>12</sub> intermetallic alloys, Acta Materialia. **2001**, *49*, 1725-1736.
- [6] A.H.W. Ngan, I.P. Jones, R.E. Smallman, On the abnormal negative temperature dependence of yield strength in the L<sub>12</sub> compound Fe<sub>3</sub>Ge, Philosophical Magazine. **1992**, *A 65(4)*, 1003-1020.
- [7] A.H.W. Ngan, I.P. Jones, R.E. Smallman, the negative temperature dependence of yield strength in the L<sub>12</sub> compound Fe<sub>3</sub>Ge, materials Science and Engineering. **1992**, *A 153*, 387-391.

P-05

## Distribution of the enantiomorphs in polycrystalline CoSi

Ulrich Burkhardt

Max-Planck-Institut für Chemische Physik fester Stoffe, 01187 Dresden, Germany, Ulrich.burkhardt@cpfs.mpg.de

### Introduction

Many interesting material properties such as non-linear optical behavior are related to the absence of an inversion centre in the crystal structure. Phases with a chiral crystal structure have recently attracted particular attention, as the occurrence of superconductivity or the formation of helically ordered magnetic states in these phases suggest unusual interactions in solids. However, the determination of handedness is not always trivial, since the two enantiomorphic variants of a chiral phase can weaken or even cancel each other out. The fraction and distribution of the enantiomorphic structural variants may therefore play an important role in polycrystalline materials. Local crystallographic properties are often determined with the electron backscatter diffraction (EBSD) method. Due to the spatial resolution, both individual grain boundaries and parameters such as texture and average grain size of a polycrystalline material can be determined. However, common evaluation methods do not take the handedness into account. Investigations on  $\alpha$ -quartz have shown that Kikuchi patterns of left- and right-handed  $\alpha$ -quartz differ [1]. In simulations, experimental Kikuchi pattern are reproduced in a good approximation. In particular, the consideration of dynamic electron multiple scattering processes leads to handedness-dependent differences. Therefore, an assignment of handedness can be made by the better fit of an experimental Kikuchi pattern with one of the two simulated Kikuchi patterns. The quantitative comparison between experimental and simulated Kikuchi pattern with the cross-correlation method [2] are the basis for enantiomorph distribution maps. These EBSD based maps show the distribution of the two enantiomorph variants in a polycrystalline material. In our previous studies on the chiral phase CoSi (FeSi structure type  $P2_13$ ), we have shown that the EBSD-based determination of the two enantiomorphs – e.g. CoSi with A-form according to [3] and CoSi with the B-form - agrees with the result of single-crystal X-ray diffraction [4]. Both enantiomorphs of CoSi show the same symmetry (space group  $P2_13$ ). The studies on CoSi presented here reveal that the preparation method has a significant influence on the occurrence and distribution of the two variants with different handedness.

### Materials and Methods

Preparation method 1: CoSi phase have been crystallized from the liquid phase by slow cooling from 1600°C to 1200°C with cooling rate of 0.2 K/min. The cross-section showed several grains with notable different grain orientation according to EBSD measurements.

Preparation method 2: CoSi was synthesized by isothermal reaction of the elements cobalt (powder) and silicon (powder) in the presence of iodine at 700 °C in evacuated fused silica tubes during 120 h.

Preparation method 3: After preparation method 2 several CoSi crystals were recrystallized during 3 weeks by a chemical transport reaction in a temperature gradient from 700 °C (source) to 800 °C (sink), and a transport agent concentration of 0.5 mg/cm<sup>3</sup> iodine. Preparation method 2 and 3 resulted well faceted crystals with typical dimensions of 1 mm that were frequently agglomerated.

The experimental backscattered Kikuchi diffraction patterns were acquired using an EBSD system (Bruker Nano, Germany) attached to a scanning electron microscope JEOL JSM7800 F. The EBSD measurements have been performed on mounted and metallographically prepared materials. A best-fit pattern matching approach was used to find the orientation and the chirality corresponding to each experimental Kikuchi pattern. The normalized cross-correlation coefficient  $r$  ( $0 \leq r \leq 1$ ) between the experimental and the simulated Kikuchi pattern of the reference structure was optimized according to [2], with an additional test against the inverted structure to discriminate between the enantiomorphs. For each experimental pattern, two optimized correlation coefficients  $r_{+E}$  and  $r_{-E}$  were obtained from the fit to the simulated Kikuchi pattern of the CoSi A-form, and the CoSi B-form, respectively. For the final assignment, the difference of the correlation coefficients  $\Delta r = r_{+E} - r_{-E}$ , in relation to their average value  $r_m = (r_{+E} + r_{-E})/2$  is used. A large average value  $r_m$  indicate a good fit to the simulated data, while a simultaneous large difference  $|\Delta r|$  indicates a reliable discrimination of the enantiomorph.

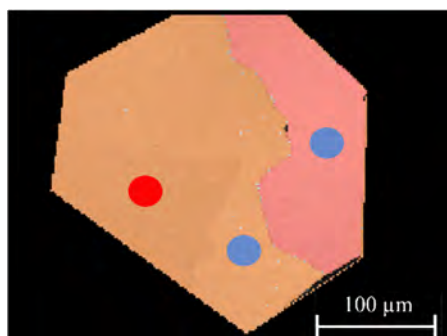
The pattern evaluation yielded  $r_m \geq 0.65$  and  $|\Delta r| \geq 0.01$ . These values are similar to our previous studies on CoSi [4] and allowed a clear assignment of the enantiomorphs for all evaluated Kikuchi patterns.

### Results and Discussion

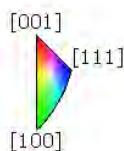
The Kikuchi pattern evaluation by the cross-correlation method revealed only the B- form of CoSi phase crystallized from the liquid phase (preparation method 1). The cross-section showed different grains with different orientation of the unit cell but without any change of the handedness of the CoSi crystal structure (no micrograph given in this abstract). The preparation of CoSi crystals by isothermal reaction of cobalt and silicon powders (preparation method 2) resulted well faceted crystallites. The crystallites are built up by several domains with different orientation of the unit cell and frequently changes of the handedness of the CoSi phase (Fig. 1) are observed. The change of handedness is not always related to the change in the orientation of the unit cell. In these crystals we find boundaries which are formed by

domains of different handedness and almost the same orientation of the unit cell of the CoSi phase (Fig.1). Crystals prepared by chemical transport reaction (preparation method 3) are well faceted. These crystals show the same habit as the crystallites prepared by method 2. All crystals prepared by method 3 are single crystals and agglomerated crystals show almost always the same handedness.

The EBSD based determination of the distribution of the enantiomorphs in polycrystalline materials opens new possibilities for the systematic investigations of the relation between handedness and material properties. In addition to observations on the influence of the preparation process on the enantiomorph distribution, first results on the characterization of boundaries will be presented, taking into account the handedness of the domains involved.



### CoSi



Enantiomorph assignment  
 ● A-form  
 ● B-form



Fig. 1: Crystallite prepared by isothermal reaction of the elements cobalt and silicon (preparation method 2).

Domains: Color gives the orientation of the CoSi unit cell parallel to the sample surface (s. color code above)  
Dots: color is related to the handedness.

Fig. 2: Agglomerated crystals prepared by chemical transport reaction (preparation method 3)

### References

- [1] A. Winkelmann, G. Nolze, Ultramicroscopy. **2015**, 149, 58-63.
- [2] G. Nolze, G., R. Hielscher, A. Winkelmann, Crystal Research and Technology **2016**, 52, 1600252.
- [3] C. H. Spence, J. M. Zuo, M. O’Keeffe, K. Marthinsen, R. Hoier, Acta Cryst. A **1994**, 50, 647 – 650.
- [4] U. Burkhardt H. Borrmann, P. Moll, M. Schmidt, Y. Grin, A. Winkelmann, Sci Rep **2020**, 10, 4065 (2020).

P-06

### Heterogeneous equilibria in the systems Mo-Si-Ti and Mo-Si-Ti-B

Andreas K. Czerny, Magnus Rohde, Clemens Hausner and Hans J. Seifert

Karlsruhe Institute of Technology, Institute for Applied Materials (IAM-AWP), 76344 Eggenstein-Leopoldshafen, Germany, andreas.czerny@kit.edu, magnus.rohde@kit.edu, clemens.hausner@kit.edu, hans.seifert@kit.edu

#### Introduction

Contemporary superalloys for gas turbines already perform at 90% of their solidus temperature, limiting the potential for further increase of the operating temperatures. This necessitates the development of novel materials with a comparable set of characteristics, but a capability to withstand higher temperatures, if the requirements of modern gas turbines, like increasing efficiency and load flexibility, are to be met. Promising possibilities are alloys located in the system Mo-Si-Ti(-B), which have been under investigation for several years and show viable properties in terms of high-temperature mechanical parameters and corrosion resistance.

The group of Chang [1] developed a thermodynamic database for the system Mo-Si-Ti-B, which is widely used for CALPHAD-type analyses to guide the materials development. Based on new results, some areas of the phase diagram warrant further investigation. This contribution aims to refine the thermodynamic phase modelling in the metal-rich area of the Mo-Si-Ti diagram, which is important for future applications. Additionally, several Mo-Si-Ti-B alloys were investigated, to verify, if the results of the ternary system can be extended into the quaternary system.

#### Materials and Methods

Several alloys with varying compositions were produced by vacuum arc melting from high-purity raw materials. The purities of the materials were as follows: Mo 99.95%, Si 99.9985%, B 95-97%, Ti 99.6%. The arc melter was located in a glove box with a controlled Argon atmosphere; oxygen and water contaminations within the box were in the order of 1 ppm. All samples were prepared as 1500 mg buttons and remelted five times. Subsequently, the samples were annealed at 1425 °C for 330 h in a flowing Argon atmosphere and were furnace cooled. In selected cases, samples were additionally heat treated at the same temperature for 24 h and quenched in water, to investigate if the relatively slow cooling in the furnace leads to the precipitation of additional phases. To prepare the samples for analysis, the buttons were bisected and the cut surface was ground and polished to a roughness of 0.04 µm.

The samples were characterized via SEM, EDX, WDX and XRD to analyze the microstructure and phases present. ICP-OES was used to verify the actual composition of the samples after arc melting matches the nominal compositions.

#### Results and Discussion

While significant areas of the Mo-Si-Ti phase diagram could be verified, the technologically relevant three-phase regions  $\beta(\text{Mo,Ti})-(\text{Mo,Ti})_3\text{Si}-(\text{Mo,Ti})_5\text{Si}_3$  as well as  $\beta(\text{Mo,Ti})-(\text{Mo,Ti})_5\text{Si}_3-(\text{Ti,Mo})_5\text{Si}_3$  could not be reconfirmed in comparison to [1]. Instead, samples analyzed exhibited the three-phase regions  $\beta(\text{Mo,Ti})-(\text{Mo,Ti})_3\text{Si}-(\text{Ti,Mo})_5\text{Si}_3$  and  $(\text{Mo,Ti})_3\text{Si}-(\text{Mo,Ti})_5\text{Si}_3-(\text{Ti,Mo})_5\text{Si}_3$ , respectively, with a small two-phase field of  $(\text{Mo,Ti})_3\text{Si}-(\text{Ti,Mo})_5\text{Si}_3$  between them. The results support a publication by Schliephake et al. [2], who also found indications for the three-phase equilibrium  $\beta(\text{Mo,Ti})-(\text{Mo,Ti})_3\text{Si}-(\text{Mo,Ti})_5\text{Si}_3$ . Fig. 1 shows the metal-rich area of the Mo-Si-Ti phase diagram as obtained by Yang et al., superimposed with the three-phase equilibria obtained in this work, shown in red and blue, respectively. Quaternary alloys, with the admixture of Boron, confirm the existence of the proposed three-phase equilibria and their extension into quaternary space.

Additionally, the results show strong indications for the existence of an invariant transition reaction

$\text{Mo}_3\text{Si} + \text{Ti}_5\text{Si}_3 \rightleftharpoons \beta(\text{Mo,Ti}) + \text{Mo}_5\text{Si}_3$  in the vicinity of the chosen annealing temperature of 1425 °C. This value is far lower than the previously calculated temperature of 1870.2 °C [3], which is based on the results obtained by Yang et al. [1], but not directly observed by them experimentally.

The results reported suggest that the thermodynamic database should be refined further, as the area under investigation in this work has direct consequences for the application of the material.



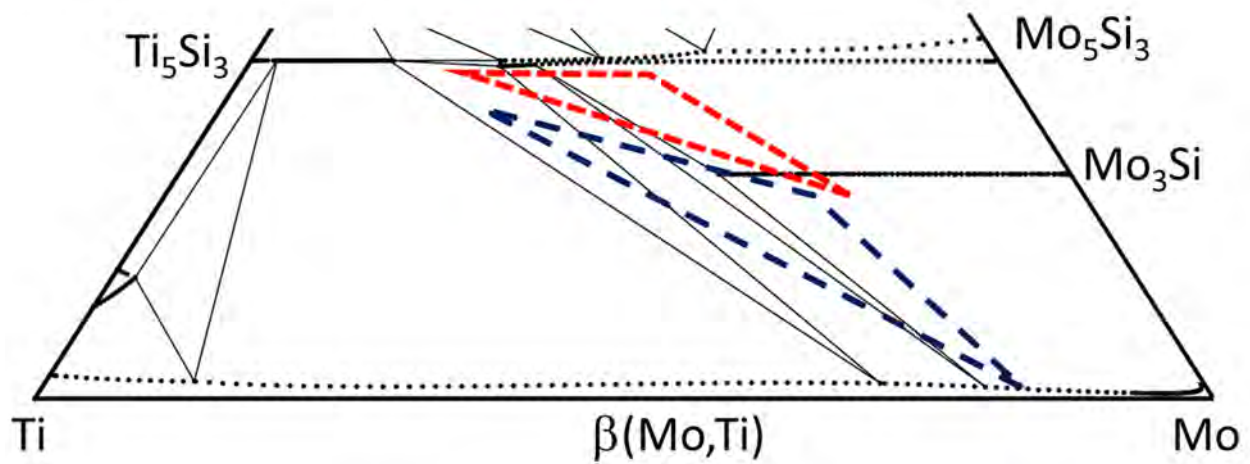


Fig. 1: The schematic Mo-Si-Ti phase diagram at 1425 °C according to the work of Yang [1]. Superimposed in dashed lines are the three-phase equilibria found in this work:  
 Top (red):  $Ti_5Si_3$ - $Mo_5Si_3$ - $Mo_3Si$   
 Bottom (blue):  $\beta(Mo,Ti)$ - $Mo_3Si$ - $Ti_5Si_3$ .

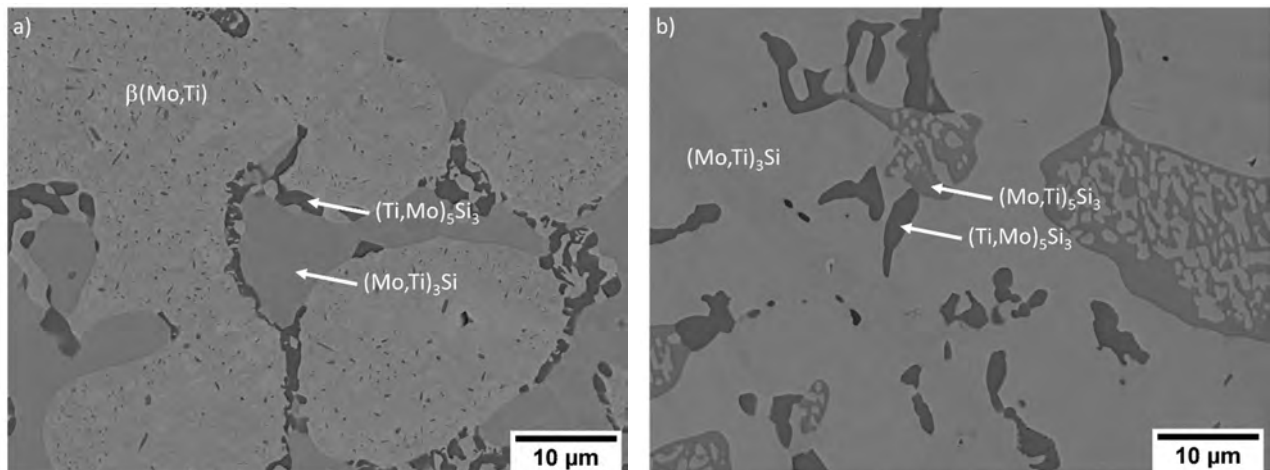


Fig. 2: Micrographs showing the three-phase equilibria found in this work. The samples were heat treated at 1425 °C for 330 h in Argon flow and furnace-cooled.

- a)  $\beta(Mo,Ti)$ - $(Mo,Ti)_3Si$ - $(Ti,Mo)_5Si_3$
- b)  $(Mo,Ti)_3Si$ - $(Mo,Ti)_5Si_3$ - $(Ti,Mo)_5Si_3$

**References**

- [1] Y. Yang, Y. A. Chang, L. Tan, Y. Du, *Materials Science and Engineering*. **2003**, *A361*, 281-293.
- [2] D. Schliephake, M. Azim, K. von Klinski-Wetzel, B. Gorr, H.-J. Christ, H. Bei, E. P. George, M. Heilmeier, *Metallurgical and materials transactions*. **2014**, *A 45.3*, 1102-1111.
- [3] A. Bondar, H. L. Lukas, *Landolt-Börnstein New Series*. **2004**, *IV/11A4*, 385-405.

P-07

## Phase-field investigation on multiphase microstructural evolution in Mo-Si-Ti system

Yuhan Cai<sup>1</sup>, Fei Wang<sup>1</sup> and Britta Nestler<sup>1,2</sup>

<sup>1</sup>Institute of Applied Materials, Karlsruhe Institute of Technology (KIT), 76131 Karlsruhe, Germany,  
yuhan.cai2@kit.edu, fei.wang@kit.edu, britta.nestler@kit.edu

<sup>2</sup>Institute of Digital Materials Science, Karlsruhe University of Applied Sciences, 76133 Karlsruhe, Germany,  
britta.nestler@kit.edu

### Introduction

In recent decades, Mo-Si based alloys have become an excellent alternative to Ni-based superalloys for high-temperature applications. To meet the requirement of modern industrial applications, many attempts of improving the solidification microstructure have been made to enhance the performance of this alloy. The manufactured Mo-Si-Ti alloy with eutectic ( $L \rightarrow \text{Ti}(\text{Mo})_5\text{Si}_3 + \beta(\text{Mo,Si,Ti})$ ) and eutectoid ( $\text{Mo}(\text{Ti})_3\text{Si} \rightarrow \text{Ti}(\text{Mo})_5\text{Si}_3 + \beta(\text{Mo,Si,Ti})$ ) structures, for instance, shows both an outstanding oxidation behavior as well as a reasonable creep resistance [1]. Based on the experimental observation, the occurrence of the phase transitions between the four simultaneously existing phases may have a significant influence on the microstructural evolution. In the present study, we use a phase-field model to explore the microstructural evolution in the Mo-Si-Ti ternary system. We conduct simulations for the eutectic reaction and investigate the development of the lamellar structure. The relationship between the growth velocity  $v$ , the lamellar spacing  $\lambda$ , and the driving force  $\Delta c$  has been clarified and is in accordance with the classic Jackson-Hunt theory. For the four-phase reaction, the influence of the  $\text{Mo}(\text{Ti})_3\text{Si}$  (MS) phase on the growth of the lamellar structure is scrutinized.

### Materials and Methods

In the present study, we use a phase-field model with the grand-potential formulation [2] to investigate the microstructural evolution in the Mo-Si-Ti system. The temporal phase-field evolution equation is derived by the variational approach to describe the movement of interface and writes as following:

$$\tau \epsilon \frac{\partial \varphi_\alpha}{\partial t} = 2\sigma_{\alpha\beta} \epsilon \nabla^2 \varphi_\alpha - \frac{1}{\epsilon} \frac{\partial w(\varphi)}{\partial \varphi_\alpha} - [\Psi^\alpha(\boldsymbol{\mu}) - \Psi^\beta(\boldsymbol{\mu})] h'(\varphi_\alpha) - \lambda \quad (1)$$

$$\alpha = 1, \dots, N, \beta \neq \alpha$$

Furthermore, the total amount of solute in the system is conserved. Therefore, we introduce a diffusion equation based on Fick's law. The evolution equation for the concentration fields can be derived as

$$\frac{\partial c_i}{\partial t} = \nabla \cdot \left( \sum_{j=1}^K M_{ij}(\boldsymbol{\varphi}, \boldsymbol{\mu}) \nabla \mu_j \right). \quad (2)$$

Here,  $M_{ij}(\boldsymbol{\varphi}, \boldsymbol{\mu}) = \sum_{\alpha=1}^N M_{ij}^\alpha(\boldsymbol{\varphi}, \boldsymbol{\mu}) h(\varphi_\alpha)$  is the mobility.

We focus on the phase transitions between liquid phase,  $\text{Ti}(\text{Mo})_5\text{Si}_3$ ,  $\text{Mo}(\text{Ti})_3\text{Si}$ , and  $\beta(\text{Mo,Si,Ti})$  phases.

### Results and Discussion

For a eutectic phase transition, we investigate the growth of the lamellar structure, which consists of  $\text{Ti}(\text{Mo})_5\text{Si}_3$  (TS) and  $\beta(\text{Mo,Si,Ti})$  phases. The initial setup for the simulations is illustrated in Fig. 1. In order to eliminate the influence of the boundaries perpendicular to the solidification front, we use an infinite domain that is modeled by periodic boundary conditions. At the boundary far from the solidification front in the liquid, a constant flux of melt into the domain is realized by the Dirichlet boundary condition. Fig. 1(a) depicts the time evolution of the lamellae pair corresponding to the case of a simultaneous nucleation of two solids (TS and  $\beta$ ). Fig. 1(b) illustrates the relationship between the growth velocity  $v$  and the lamellar spacing  $\lambda$  for the evolution with a different driving force. In all simulations, the liquid concentration deviates from the equilibrium concentration, which provides the driving force for the growth of lamellae pair. The corresponding initial concentration of the liquid phase is set as  $\mathbf{c}^l = (0.4265, 0.3635, 0.21)$ ,  $(0.3795, 0.4105, 0.21)$ , and  $(0.4265, 0.3635, 0.21)$ , respectively. It is noteworthy that the initial concentration of silicon in the liquid phase is constant in all three cases. Hence there is only one independent component in the present study and the concentration deviation is defined as:

$$\Delta c = \mathbf{c}^l - \mathbf{c}_e^l, \quad (3)$$

where  $c$  represents the concentration of molybdenum,  $\mathbf{c}^l$  is the initial liquid concentration, and  $\mathbf{c}_e^l$  denotes the eutectic composition. The yellow, blue, and violet lines represent the growth of the lamellar structure with  $\Delta c = 0.2175, 0.1705, \text{ and } 0.1235$ , respectively. In all three cases, the growth velocity increases with the extending  $\lambda$  at the beginning and then decreases. This result is in accordance with the Jackson-Hunt theory. For a stable growth, the  $\lambda$  should be restricted in a reasonable range. Otherwise, one phase will be overgrown by the other.

In addition, based on the experimental observation by Yang et al. [3], the TS phase has the possibility to nucleate at the surface of primarily solidified  $\beta$  particle. Therefore, we explore the second case, as shown in Fig. 2 (a). In this case, there is a new influence factor: the width of the TS phase  $d$ . For a fixed  $\lambda$ ,  $d$  should be limited in a specific interval, so as to ensure a steady growth, as demonstrated in Fig. 2(b).

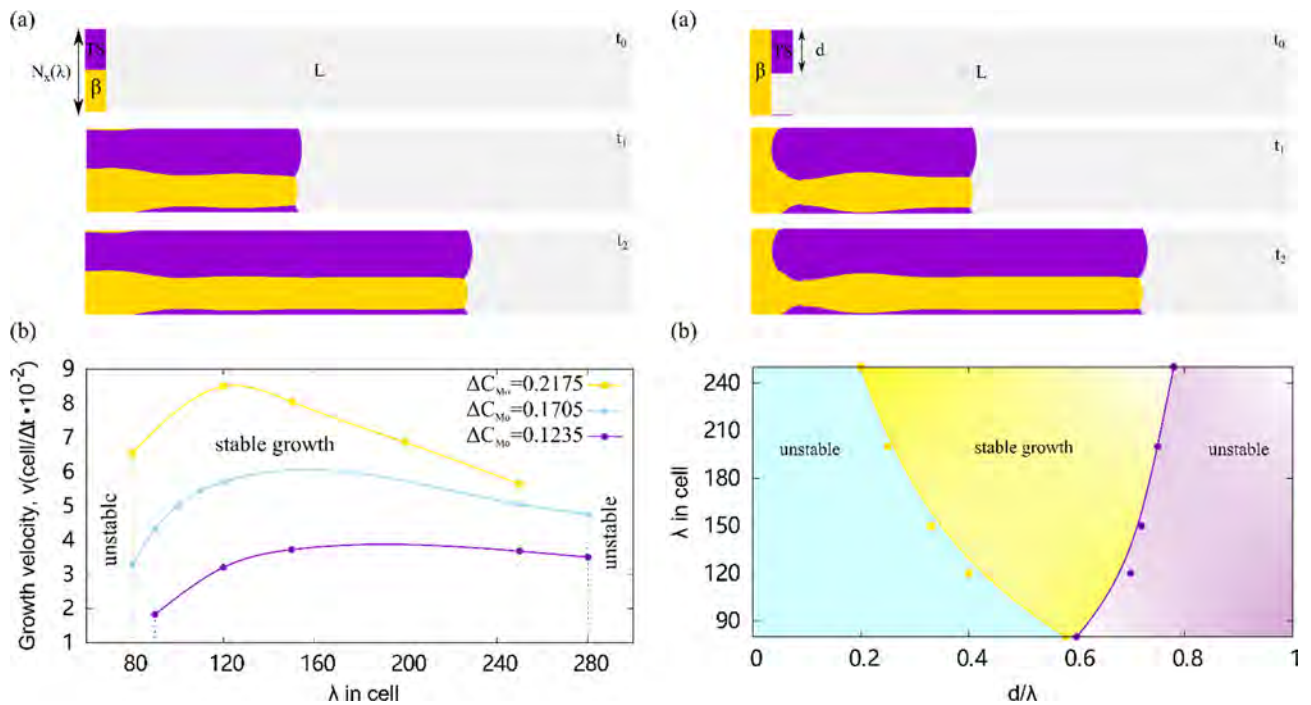


Fig. 1: (a) The evolution of the lamellae pair from  $t_0$  to  $t_2$ . Violet represents the TS phase and the  $\beta$  phase is colored in gold. The remaining gray domain is filled with melt. (b) The relationship between the growth velocity  $v$  and the lamellar spacing  $\lambda$  for the evolution with different driving force  $\Delta c$ . The yellow, blue, and violet lines represent the growth of the lamellar structure with  $\Delta c = 0.2175$ ,  $0.1705$ , and  $0.1235$ , respectively.

Fig. 2: (a) The evolution of the lamellae pair for the case of the nucleation of the TS phase on the surface of the  $\beta$  phase from  $t_0$  to  $t_2$ . (b) The relationship between the lamellar spacing  $\lambda$  and the width of the TS phase  $d$ . The yellow squares denote the minimum width  $d_{min}$  while the violet points represent the maximum width  $d_{max}$  for the stable growth. The stable growth region is colored in yellow. The blue and violet regions show that one phase is overgrown by the other.

References

[1] Schliephake, D., Kauffmann, A., Cong, X., Gombola, C., Azim, M., Gorr, B., ... & Heilmaier, M. *Intermetallics*, **2019**, *104*, 133-142.  
 [2] Choudhury, Abhik, and Britta Nestler. *Physical Review E*, **2012**, *85.2*: 021602.  
 [3] Yang, Y., Chang, Y. A., Tan, L., & Du, Y. *Materials Science and Engineering: A*, **2003**, *361(1-2)*, 281-293.

P-08

**Ternary  $V_{ss}$ - $V_3Si$ - $V_5SiB_2$  eutectic reaction in V-Si-B system**

Weiguang Yang<sup>1</sup>, Georg Hasemann<sup>2</sup>, Mustafa Yazlak<sup>3</sup>, Bronislava Gorr<sup>4</sup>, Ruth Schwaiger<sup>1</sup>  
and Manja Krüger<sup>2</sup>

<sup>1</sup>Forschungszentrum Jülich GmbH, Institute of Energy and Climate Research, Microstructure and Properties of Materials (IEK-2), 52425, Jülich, Germany, w.yang@fz-juelich.de, r.schwaiger@fz-juelich.de

<sup>2</sup>Otto-von-Guericke University Magdeburg, Institute of Materials and Joining Technology, 39106, Magdeburg, Germany, georg1.hasemann@ovgu.de, manja.krueger@ovgu.de

<sup>3</sup>University Siegen, Institute of Materials Technology, 57076, Siegen, Germany, Mustafa.Yazlak@uni-siegen.de

<sup>4</sup>Karlsruhe Institute of Technology, Institute for Applied Materials - Applied Materials Physics (IAM-AMP), 76344 Eggenstein-Leopoldshafen, Germany, bronislava.gorr@kit.edu

**Introduction**

Due to the high melting temperature, which is positively related to most high-temperature properties, vanadium-based alloys are promising candidates for high-temperature structural applications. One of the most attractive vanadium-based systems is V-Cr-Ti, where mainly single-phase vanadium solid solution ( $V_{ss}$ ) alloys were developed for tritium breeding blanket in fusion reactors [1,2]. Nevertheless, the V-Cr-Ti alloys have poor oxidation resistance, although the addition of Cr and Ti can increase the oxidation resistance of vanadium [3]. Si and B can be added to further improve the oxidation resistance by forming intermetallic phases such as  $V_3Si$ ,  $V_5Si_3$  and  $V_5SiB_2$  [4,5]. Furthermore, the intermetallic phases  $V_3Si$  and  $V_5SiB_2$  can also improve the high-temperature strength and creep resistance according to the recent work on the powder metallurgical (PM) processed V-9Si-13B alloy (the unit of at.% is always used in the present work) [5–8]. The compositional choice of this PM V-9Si-13B alloy was based on the isothermal section of the V-Si-B system at 1600 °C presented by Nunes et al. [9] and the consideration on the phase fraction to form a solid solution matrix with fine distributed and embedded intermetallic phases. However, in order to produce the three-phase  $V_{ss}$ - $V_3Si$ - $V_5SiB_2$  alloys via a casting process, the liquidus projection in the three-phase field would be helpful for the choice of alloy compositions. A systematic investigation of the liquidus projection in the vanadium-rich region of the V-Si-B system was carried out recently via arc-melting [10] to reevaluate the thermodynamically calculated liquidus projection by Pinto da Silva et al. [11]. A ternary eutectic was found, but until now the eutectic alloy composition has not been reported. Thus, the aim of the present work is to determine the ternary eutectic reaction via arc-melting and to modify the liquidus projection.

**Materials and Methods**

Different V-Si-B alloys, nominal compositions are shown in Fig. 1, were produced by conventionally arc-melting under argon atmosphere. The raw materials for arc-melting were carefully weight in form high-purity elemental turnings of V (99.7 wt.%) and granules of Si (99.99 wt.%) and B (99.0 wt.%) to produce a 15 g sample for each alloy investigated. Each button was remelted and flipped five times in order to ensure a homogenous compositional distribution of all elements. A weight loss < 1% indicates that the compositions after arc-melting can be identical with the nominal composition. The chemical compositions were checked by inductively coupled plasma optical emission spectroscopy (ICP-OES). After metallographic preparation, a Zeiss Merlin and Zeiss Supra 50 VP scanning electron microscope (SEM) were used to observe the microstructures using the secondary electron (SE) and the backscatter electron (BSE) mode. Energy-dispersive X-ray (EDS) was performed to check the composition of each phase. Further, electron backscatter diffraction (EBSD, Oxford Instruments) with a scanning step size smaller than 0.25  $\mu\text{m}$  was used to identify the phases and obtain the phase maps. Further, the polished bulk samples were directly used to perform X-ray diffraction (XRD) to identify the crystal structure of phases. The lattice parameters of phases were determined using the software GSAS-II [12] by the Pawley refinement [13], where the intensities of reflection peaks are variable.

**Results and Discussion**

The observed primary phases or the observed first eutectic microstructures for each alloy investigated in the present work are indicated by the filled symbols in Fig. 1, while the alloys investigated in the work of Hasemann [10] are marked with the open symbols. According to the observed microstructures, the liquidus projection obtained by Hasemann [10] can be slightly modified. Firstly, the ternary invariant eutectic reaction  $L \leftrightarrow V_{ss} + V_3Si + V_5SiB_2$  is moved toward the composition of alloy V-9Si-6.5B (#3) because almost the entire sample is composed of the three-phase  $V_{ss}$ - $V_3Si$ - $V_5SiB_2$  eutectic microstructures as shown in Fig. 2. Thus, the ternary eutectic alloy composition V-9Si-6.5B is identified. Secondly, the invariant peritectic reaction  $L + V_3B_2 \leftrightarrow V_{ss} + V_5SiB_2$  might be slightly shifted to lower Si- and higher B-concentrations, quite close to the composition of alloy V-8Si-6.5B (#5). The alloy solidifies within the  $V_{ss}$  primary area but seemingly very close to the two-phase  $V_{ss}$ - $V_5SiB_2$  eutectic valley, which indicates its position being located right of the peritectic reaction. Finally, both monovariant  $V_{ss}$ - $V_5SiB_2$  and  $V_3Si$ - $V_5SiB_2$  reaction lines near the ternary eutectic reaction seem to be relatively parallel to a B concentration of around 6.5 at.%. The microstructure of the alloys V-8.5Si-6.5B (#6), V-9.5Si-6.5B (#7) and V-10Si-6.5B (#8) provide the experimental evidence for this assumption.

Alloy V-8.5Si-6.5B (#6) is considered as being located very close to the monovariant  $V_{55}\text{-}V_5\text{SiB}_2$  reaction line, while alloy V-9.5Si-6.5B (#7) and V-10Si-6.5B (#8) are very close to the monovariant  $V_3\text{Si-V}_5\text{SiB}_2$  reaction line. It should be noted that the present results are influenced by the high cooling rates in the arc-melting furnace and are expected to be slightly different as compared to the theoretical liquidus projection obtained under equilibrium conditions. The modified liquidus projection can be used to design as-cast V-Si-B alloys with different microstructures close to the ternary eutectic reaction. Some of them having representative microstructures, e.g. two-phase  $V_{55}\text{-}V_5\text{SiB}_2$  and three-phase  $V_{55}\text{-}V_3\text{Si-V}_5\text{SiB}_2$  eutectic microstructures, will be mechanically tested and investigated in the future.

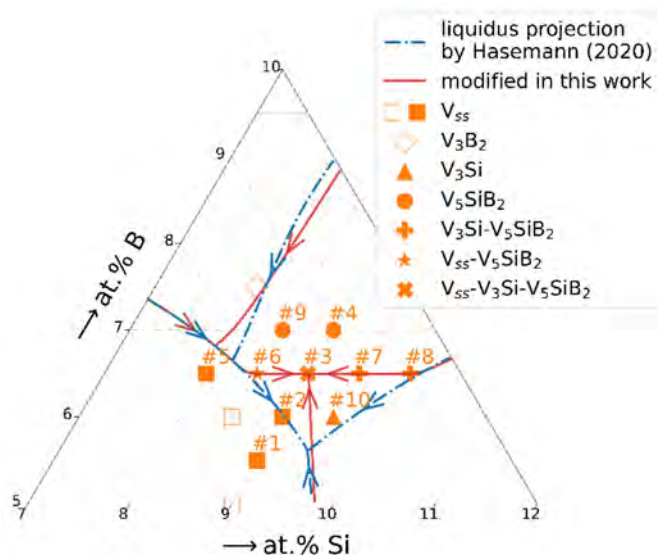


Fig. 1: modified liquidus projection.

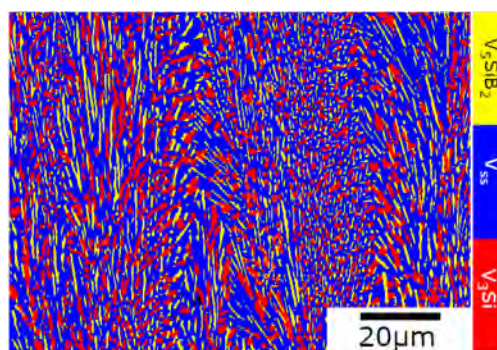


Fig. 2: EBSD phase map of alloy V-9Si-6.5B (#3).

References

- [1] D.L. Smith, B.A. Loomis, D.R. Diercks, *Journal of Nuclear Materials*. **1985**, *135*, 125–139.
- [2] S.J. Zinkle, H. Matsui, D.L. Smith, A.F. Rowcliffe, E. van Osch, K. Abe, V.A. Kazakov, *Journal of Nuclear Materials*. **1998**, 258–263, 205–214.
- [3] K. Natesan, M. Uz, *Fusion Engineering and Design*. **2000**, *51–52*, 145–152.
- [4] J. Williams, M. Akinc, *Intermetallics*. **1998**, *6*, 269–275.
- [5] M. Krüger, *Scripta Materialia*. **2016**, *121*, 75–78.
- [6] M. Krüger, J. Schmelzer, M. Helmecke, *Metals*. **2016**, *6*, 241.
- [7] M. Krüger, V. Bolbut, F. Gang, G. Hasemann, *JOM*. **2016**, *68*, 2811–2816.
- [8] M. Krüger, B. Köppe-Grabow, *Practical Metallography*. **2017**, *54*, 293–307.
- [9] C.A. Nunes, B.B. de Lima, G.C. Coelho, P.A. Suzuki, *Journal of Phase Equilibria and Diffusion*. **2009**, *30*, 345–350.
- [10] G. Hasemann, *Journal of Alloys and Compounds*. **2020**, *824*, 153843.
- [11] A.A.A. Pinto da Silva, N. Chaia, F. Ferreira, G. Carvalho Coelho, J.-M. Fiorani, N. David, M. Vilasi, C.A. Nunes, *Calphad*. **2017**, *59*, 199–206.
- [12] B.H. Toby, R.B. Von Dreele, *Journal of Applied Crystallography*. **2013**, *46*, 544–549.
- [13] G.S. Pawley, *Journal of Applied Crystallography*. **1981**, *14*, 357–361.



P-09

## New Rare-earth Palladium Intermetallic Compound with Extended Pnictogen Ribbons

Mihai I. Sturza<sup>1</sup>, M. Lourdes Amigó<sup>1</sup>, Jorge I. Facio<sup>1</sup>, Federico Cagliaris<sup>1</sup>,  
Sabine Wurmehl<sup>1</sup> and Bernd Büchner<sup>2</sup>

<sup>1</sup>Leibniz Institute for Solid State and Materials Research, IFW Dresden, 01069 Dresden, Germany,  
m.i.sturza@ifw-dresden.de, m.l.amigo@ifw-dresden.de, j.facio@ifw-dresden.de, f.cagliaris@ifw-dresden.de,  
s.wurmehl@ifw-dresden.de

<sup>2</sup>Institute of Solid State and Materials Physics, TU Dresden, 01062 Dresden, Germany, B.Buechner@ifw-dresden.de

### Introduction

Strongly correlated electron materials can show interesting physical properties such as special forms of magnetism [1,2] and unconventional superconductivity [3,4] driven by thermal and quantum fluctuations. As one candidate class of materials, intermetallic compounds exhibiting strong electron–electron or electron–lattice interactions [5,6] may host such fascinating and unusual phenomena.

With regard to our interest on the exploratory synthesis of layered compounds with homoatomic square lattices (namely Sb nets) co-existing with and without magnetic slabs, we began our investigation in an effort to re-examine the crystal growth of LaPdSb<sub>3</sub>. To the best of our knowledge there is only one report in the literature about this palladium layered intermetallic compound [7]. From the efforts to grow larger crystals of LaPdSb<sub>3</sub> for physical properties measurements by using Sb as flux, we have discovered a new ternary antimonide, La<sub>6</sub>Pd<sub>2+x</sub>Sb<sub>15</sub> (x = 0.28), with p-type metallic behavior as discussed in the work at hand. In a nutshell, we report the synthesis, structure, and properties of this ternary rare-earth palladium intermetallic phase, which can be considered a stuffed variant of the orthorhombic La<sub>6</sub>MnSb<sub>15</sub> structure type, in which square pyramidal and tetrahedral sites are partially occupied by Pd atoms.

### Materials and Methods

**Crystal Growth of La<sub>6</sub>Pd<sub>2+x</sub>Sb<sub>15</sub> (x = 0.28).** The reaction mixtures consisted of rare-earth element La (0.4197g, 3.02 mmol), Pd (0.2411g, 2.26 mmol), and Sb (~2g, ~16.4 mmol) were loaded into 2 mL Canfield Crucible Set (CCS – frit-disc alumina crucibles set) [8]. Next, the alumina crucibles were placed in fused-silica tubes and flame-sealed under a vacuum of < 10<sup>-5</sup> mbar. In a Nabertherm programmable chamber furnace, the tubes were heated to 1125°C in 14 h, held at 1125°C for 12 h, cooled to 700°C with rate of 3°C/h. After dwelling at 700 °C for a few hours, the tubes were quickly centrifuged to filter the crystals formed from excess liquid Sb metal. Remaining Sb flux was tried to be removed from the sample by dissolution in a 1:1:1 mixture of HCl, HNO<sub>3</sub>, and H<sub>2</sub>O or in a dilute solution of HCl, followed by gravity filtration and rinsing with H<sub>2</sub>O and acetone to isolate the crystals of La<sub>6</sub>Pd<sub>2+x</sub>Sb<sub>15</sub> (x = 0.28).

**Scanning Electron Microscopy.** Microstructure and composition were analyzed by scanning electron microscopy on cleaned single crystals on a Zeiss EVOMA15 with AzTec software equipped with an electron microprobe analyzer for semi-quantitative elemental analysis using the energy dispersive x-ray (EDX) mode.

**Single Crystal X-ray Diffraction.** A single crystal of La<sub>6</sub>Pd<sub>2+x</sub>Sb<sub>15</sub> was selected and mounted on the tip of quartz fiber for X-ray diffraction. Intensity data were collected at 298 K using  $\omega$  scans on a STOE IPDS-II imaging plate diffraction system using graphite-monochromatized Mo K $\alpha$  radiation ( $\lambda = 0.71073$  Å) operating at 50 kV and 40 mA with a 34 cm diameter imaging plate.

**Band Structure Calculations.** We performed fully relativistic calculations based on Density Functional Theory using the Perdew-Burke-Ernzerhof implementation of the Generalized Gradient Approximation, as implemented in the FPLO code.

**Magnetization measurements.** For the magnetization measurements, we used a Vibrating Sample Magnetometer (VSM) from Quantum Design. Measurements were carried out as a function of temperature or magnetic field in the temperature range 1.8 K to 300 K and up to 7 T.

**Charge Transport.** Resistivity, magnetoresistivity and Hall resistivity measurements were performed on single crystals. The resistivity as a function of temperature was measured in a dip-stick sample holder immersed in a Dewar with liquid He while the magnetoresistivity and the Hall resistivity measurements were carried out in an OXFORD cryostat with a superconducting magnet under magnetic fields up to  $\mu_0 H = 15$  T.

### Results and Discussion

From single-crystal XRD data, we have determined that the La<sub>6</sub>Pd<sub>2.28</sub>Sb<sub>15</sub> compound crystallizes in the orthorhombic La<sub>6</sub>MnSb<sub>15</sub> – structure type (space group *I*mmm; *a* = 4.3082(9) Å, *b* = 15.399(3) Å, *c* = 19.689(4) Å; *Z* = 2). The structure of La<sub>6</sub>Pd<sub>2.28</sub>Sb<sub>15</sub> is isostructural with La<sub>6</sub>MSb<sub>15</sub> (M = Mn, Zn) [9,10] and Pr<sub>6</sub>InSb<sub>15</sub> [11], they exhibit the same substructures of Sb and the same coordination environment for the rare earth elements. The crystal structure is a three-dimensional framework (Fig. 1) composed of various squares and ribbons that extend along the *a* axis, including complex Sb–Sb bonding. Three types of antimonide substructures are present in La<sub>6</sub>Pd<sub>2.28</sub>Sb<sub>15</sub>: four-atom-wide ribbon, linked to similar ribbons by Sb(6)–Sb(6) pairs, three-atom-wide ribbon, and single Sb(3) atoms centered within La<sub>6</sub> trigonal prisms. The

Pd atoms partially fill two type of interstitial sites with either square pyramidal or tetrahedral geometry. The palladium is partially occupied on certain positions as observed in single crystal XRD.

Magnetization measurements (Fig. 2) indicate that the intrinsic magnetic behavior of  $\text{La}_6\text{Pd}_{2+x}\text{Sb}_{15}$  ( $x = 0.28$ ) is diamagnetic, which we associate with Landau diamagnetism slightly larger than Pauli paramagnetism in this compound. The Pauli paramagnetism can be estimated from the band structure calculation as  $\chi_P = \mu_B^2 g(\epsilon_F)$ , where  $g(\epsilon_F)$  is the density of states at the Fermi energy. We obtain  $\chi_P = 3.2 \times 10^{-4} \text{emu.mol}^{-1}$ , a value an order of magnitude larger than the measured diamagnetic response at, e.g., 160K. This suggests that the band-structure contributes with the same order of magnitude to the Pauli paramagnetism and to the Landau diamagnetism in this material.

The resistivity ( $\rho$ ) decreases when lowering the temperature, indicating metallic behavior, and at low temperatures  $\rho$  depends quadratically on  $T$ . Interestingly, both the Hall resistivity and magnetoresistance present a nonlinear dependence on the applied magnetic field, suggesting a multiband behavior. This is supported by density-functional electronic structure calculations which show a complex Fermi surface originated in the antimonide substructures and containing both electron and hole pockets as well as open sheets. Particularly interesting is the large magnetoresistivity (up to 200 % at low temperature). The  $\text{La}_6\text{Pd}_{2.28}\text{Sb}_{15}$  [12] is a new example of the compounds where atoms with  $d^{10}$  configuration can be inserted into the interstitial sites within the Sb-anionic framework, as  $\text{Pr}_6\text{InSb}_{15}$  and  $\text{La}_6\text{MnSb}_{15}$ .

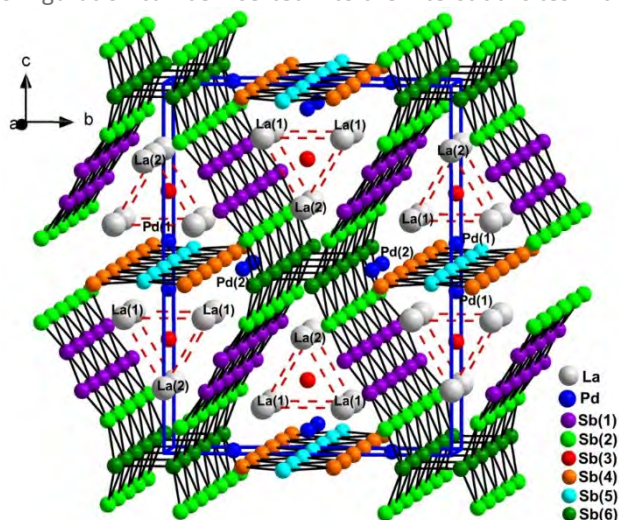


Fig. 1: Ball-and-stick representations of three-dimensional structure of  $\text{La}_6\text{Pd}_{2.28}\text{Sb}_{15}$  viewed down the crystallographic  $a$ -axis. The red dashed lines outline the La trigonal prisms.

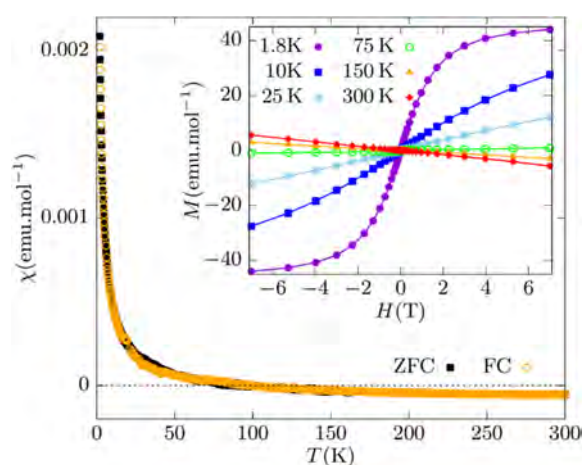


Fig. 2: Temperature dependence of the susceptibility for zero field cooling (ZFC) and field cooling (FC) procedures. Inset: Field dependence of the magnetization for several temperatures.

## References

- [1] M. C. Francisco, C. D. Malliakas, R. T. Macaluso, J. Prestigiacomo, N. Haldolaarachchige, P. W. Adams, D. P. Young, Y. Jia, H. Claus, K. E. Gray, M. G. Kanatzidis, *J. Am. Chem. Soc.* **2012**, *134*, 12998-13009.
- [2] S. J. Crerar, L. Deakin, A. Mar, *Chem. Mat.* **2005**, *17*, 2780-2784.
- [3] S. Guo, D. P. Young, P. W. Adams, X. S. Wu, J. Y. Chan, G. T. McCandless, J. F. DiTusa, *Phys. Rev. B* **2011**, *83*, 174520.
- [4] M. Sturza, F. Han, C. D. Malliakas, D. Y. Chung, H. Claus, M. G. Kanatzidis, *Phys. Rev. B* **2014**, *89*, 054512.
- [5] Q. Lin, G. J. Miller, *Acc. Chem. Res.* **2018**, *51*, 49-58.
- [6] H. Hegger, C. Petrovic, E. G. Moshopoulou, M. F. Hundley, J. L. Sarrao, Z. Fisk, J. D. Thompson, *Phys. Rev. Lett.* **2000**, *84*, 4986-4989.
- [7] E. L. Thomas, D. P. Gautreaux, J. Y. Chan, *Acta Cryst. E* **2006**, *62*, i96-i98.
- [8] C. Petrovic, P. C. Canfield, J. Y. Mellen, *Philos Mag* **2012**, *92*, 2448-2457.
- [9] A. Benavides Katherine, T. McCandless Gregory, Y. Chan Julia, Z. Kristallogr. – Cryst. Mater., **2017**; Vol. 232, p 583.
- [10] O. Sologub, M. Vybornov, P. Rogl, K. Hiebl, G. Cordier, P. Woll, *J. Solid State Chem.* **1996**, *122*, 266-272.
- [11] A. V. Tkachuk, T. Tam, A. Mar, *Chem. Met. Alloys* **2008**, *1*, 76 - 83.
- [12] M. I. Sturza, M. L. Amigó, J. I. Facio et al., *Journal of Solid State Chemistry* **2020**, *291*, 121578:

P-10

**Shape memory effect during isothermal holding of Ti-Hf-Ni-Cu alloys**Elena Demidova<sup>1</sup>, Sergey Belyaev<sup>1</sup>, Natalia Resnina<sup>1</sup>, Pavel Pchelnykov<sup>1</sup>  
and Alexander Shelyakov<sup>2</sup><sup>1</sup>Saint-Petersburg State University, 199034 Saint-Petersburg, Russia, lena-demi@yandex.ru, spbelyaev@mail.ru, resnat@mail.ru, st073586@student.spbu.ru<sup>2</sup>National Research Nuclear University MEPhI (Moscow Engineering Physics Institute), 115409 Moscow, Russia, alex-shel@mail.ru**Introduction**

It has been found, that some NiTi-based shape memory alloys may undergo the forward martensite transformation during isothermal holding at temperatures close to start temperature of the forward transition  $M_s$  [1-3]. Moreover, in [4-5] it was shown, that realization of such transformation under a constant stress was accompanied by reversible strain variation. During isothermal holding of  $Ti_{40.7}Hf_{9.5}Ni_{44.8}Cu_5$  strain rose up to saturation, which value depended on holding parameters (stress and temperature) in non-monotonic way with the maximum of 3,5 %, that was found at  $M_s^\sigma - 6$  °C ( $M_s^\sigma$  – start temperature of the forward transformation under a stress) under 160 MPa. Such isothermal strain variation may be very useful for applications: usually to use shape memory alloys it is necessary to cool and heat the element in complete temperature range of martensite transformations, which may be quite wide and inconvenient in practice.

It should be noted, that isothermal martensite formation was found only in alloys with high density of substitutional defects, for instance in Ti-Hf-Ni-Cu alloys, where Hf and Cu atoms partially substituted atoms in Ti and Ni sub-lattices respectively. So, Hf and Cu atoms played roles of substitutional defects in this alloy system. Previously, it was found that the variation in the Cu/Ni ratio influenced the kinetics of the isothermal martensitic transformation. As the martensitic transformation is the reason for the strain variation, hence one may assume that the Ni/Cu ratio may affect the isothermal strain variation and the dependencies of the isothermal strain on the stress and holding temperature. Therefore, the aim of the present work was to study the isothermal strain variation caused by oriented martensite formation in Ti-Hf-Ni-Cu shape memory alloys with different Cu and Ni ratio.

**Materials and Methods**

The isothermal strain variation was studied in thin ribbons of  $Ti_{40.7}Hf_{9.5}Ni_{49.8-x}Cu_x$  alloys where X = 5, 8, 10, 15 at.%. The ribbons have the amorphous structure and were crystallized before the study of the functional properties. After crystallization, all alloys except  $Ti_{40.7}Hf_{9.5}Ni_{34.8}Cu_{15}$ , underwent the forward B2  $\rightarrow$  B19' transformation on cooling and the reverse B19'  $\rightarrow$  B2 transition on heating. No thermoelastic martensite transformations were found on cooling and heating of the  $Ti_{40.7}Hf_{9.5}Ni_{34.8}Cu_{15}$  alloy under stress free state. However, this alloy is used for the study of the isothermal strain variation because it is known that cooling under a stress may shift the transformation temperatures and induce the phase transformation. To study strain variation during isothermal holding sample under a constant stress was cooled down to holding temperature, held for 60 minutes and heated. The strain, which rose during holding, was called isothermal strain. The applied stress was varied from 160 MPa to 400 MPa and holding temperature belonged to the temperature range of the forward transformation.

**Results and Discussion**

It was found, that during isothermal holding under a stress in all studied alloys except  $Ti_{40.7}Hf_{9.5}Ni_{34.8}Cu_{15}$  alloy, an additional rise in reversible strain was observed due to oriented martensite formation. Influence of holding parameters on isothermal strain in alloys with different Cu/Ni ratio was similar to the one that was previously found for  $Ti_{40.7}Hf_{9.5}Ni_{44.8}Cu_5$  in [4]. The maximum isothermal strain was found at temperature  $M_s^\sigma - 6$  °C however, the stress at which the maximum isothermal strain was observed depended on the Cu/Ni ratio. An increase in copper concentration led to a decrease in maximum isothermal strain. In  $Ti_{40.7}Hf_{9.5}Ni_{34.8}Cu_{15}$  alloy, the strain variation was not observed neither on cooling under a stress nor on isothermal holding under a stress. So, it can be concluded, that an increase in Cu concentration caused the degradation of isothermal effects in Ti-Hf-Ni-Cu alloys, that may be due to the fact, that the larger Cu concentration, the less alloy volume fraction undergoing the isothermal martensite transformation.

This work was supported by Russian Scientific Foundation (grant number 18-19-00226)

**References**

- [1] S. Kustov, D. Salas, E. Cesari, R. Santamarta, J. Van Humbeeck, *Acta Materialia*. **2012**, *60*, 2578-2592.
- [2] Y. Ji, D. Wang, X. Ding, K. Otsuka, X. Ren, *Physical Review Letters*. **2015**, *114*, 055701.
- [3] H. Akamine, Y. Soejima, T. Nakamura, F. Sahar, T. Fukuda, T. Kakeshita, M. Nishida, *Material Transactions*. **2020**, *61(1)*, 37-41.
- [4] E. Demidova, S. Belyaev, N. Resnina, A. Shelyakov, *Material Letters*. **2019**, *254*, 266-268.
- [5] A. Ivanov, S. Belyaev, N. Resnina, V. Andreev, *Sensors and Actuators A*. **2019**, *297*, 111543.

**P-11**

**Influence of the orientation of columnar grains on the functional properties of the NiTi alloy produced by wire-arc additive manufacturing**

Rashid Bikbaev<sup>1</sup>, I. A. Palani<sup>2</sup>, Natalia Resnina<sup>1</sup>, S.S. Mani Prabu<sup>2</sup>, Sergey Belyaev<sup>1</sup>,  
M. Manikandan<sup>2</sup>, S. Jayachandran<sup>2</sup> and Anshu Sahu<sup>2</sup>

<sup>1</sup>St. Petersburg State University, Saint Petersburg, Russia, BikbaevRM@yandex.ru

<sup>2</sup>Indian Institute of Technology Indore, Indore, India

**Introduction**

Feature of the samples produced by additive technologies is the formation of columnar grains, which are formed during the solidification of the melt. The formation of such a structure leads to the appearance of a texture due to grains growing along [001] direction. Since the functional properties of NiTi-based alloys depend on the texture, it can be expected that the functional properties of NiTi alloy samples fabricated by additive technologies will differ from the properties of alloys manufactured by conventional technologies. Therefore, the aim of this work was to study the influence of the orientation of the columnar grains on functional properties of the NiTi alloy sample produced by wire-arc additive manufacturing.

**Materials and Methods**

A 5-layered «wall» sample was deposited on a titanium substrate by wire-arc additive manufacturing (WAAM) using the Ni50.9Ti49.1 wire. The dog-bone samples which included the 3<sup>rd</sup> and 4<sup>th</sup> layers in the gauge length were cut from a cross-section of the «wall». A 3-layered massive sample of the TiNi alloy was deposited on a titanium substrate by WAAM using the same NiTi wire. Each layer consisted of 5 rows in one plane. The bulk sample was cut into plates with a thickness of 0.9 mm, which were used to cut the dog-bone samples for tension tests with working width and length of 1 mm and 6 mm. Three types of samples were cut out at angles of 0, 45, and 90° compared to the direction of layer growth.

All samples were annealed at 450 °C for 10 hours. After such heat treatment, martensitic transformations occur in the layers at different temperatures due to various Ni and Ti concentrations in the NiTi phase. The martensitic transformations were measured by differential scanning calorimetry (DSC). The results of the study showed that in the samples cut from the massive sample and in the fourth layer of the "wall" sample, the B2→R→B19' transformation occurred on cooling. In the third layer of «wall» sample, the B2→B19' transformation took place. On heating in all samples and in all layers the B19' → B2 transformation was observed. For the study of functional properties the samples were deformed by tension at a temperature of 22 °C, unloaded, heated through a reverse transition temperature range to study the shape memory effect, and subjected to a thermal cycle to study the two-way shape memory effect.

**Results and Discussion**

The results showed that in a sample cut along the build-up of layers, the maximum reversible strain and strain to failure is higher than in samples that were cut at 45 and 90 degrees. A comparison of the maximum reversible strain in a sample cut from a massive sample at an angle of 0 degree and in a sample cut from a «wall» sample showed that in the first case, the reversible strain was 1.5 times larger. This may be due to the fact that in a massive sample, columnar grains do not have a preferable orientation along [001], since in the presence of rows in the same plane, the heat transfer can occur in different directions. In a «wall» sample, the heat is transferred only by the substrate, so the preferable orientation of the columnar grains takes place and a texture effects the functional properties more intensive.

**Acknowledgement**

The study was carried out within joint DST-RSF project (RSF #19-49-02014, DST #DST/INT/RUS/RSF/P-36).

P-12

### Stability of strain variation during isothermal martensitic transformation under cyclic deformation in quenched Ni<sub>51</sub>Ti<sub>49</sub> alloy

Aleksei Ivanov<sup>1</sup>, Artur Gabrielian<sup>1</sup>, Sergey Belyaev<sup>1</sup>, Natalia Resnina<sup>1</sup> and Vladimir Andreev<sup>2,3</sup>

<sup>1</sup>Saint-Petersburg State University, 199034 Saint-Petersburg, Russian Federation, ileavenovasky@gmail.com

<sup>2</sup>MATEK-SMA Ltd., 117449 Moscow, Russian Federation

<sup>3</sup>Baikov Institute of Metallurgy and Materials Science, RAS, 119991 Moscow, Russian Federation

#### Introduction

It was found that martensitic transformation during isothermal holding of quenched Ni<sub>51</sub>Ti<sub>49</sub> alloy under a stress was accompanied by a strain variation [1]. Due to this fact, the isothermal transformation may be attractive for using in some applications to decrease working temperature or stress range. However, it is well known, that quenched NiTi alloys have poor stability of functional properties under cyclic deformation [2]. Therefore, it is necessary to study the stability of the isothermal strain variation in quenched Ni<sub>51</sub>Ti<sub>49</sub> alloy under cyclic loading with intermediate holding.

#### Materials and Methods

The Ni<sub>51</sub>Ti<sub>49</sub> alloy (MATEK-SMA Ltd., Moscow, Russia) wire samples with a diameter of 1.5 mm and a length of 100 mm were water quenched from 850 °C for 15 min and subjected to 100 thermal cycles through a temperature range of martensitic transformation to stabilize the transition temperatures. After heat treatment, the B2 ↔ B19' martensitic transformation occurred in the alloy on cooling and heating at temperatures of  $M_s = -43$  °C,  $M_f = -63$  °C,  $A_s = -24$  °C,  $A_f = -9$  °C. In [3] it was shown that this alloy underwent the isothermal B2 → B19' transformation and holding of the sample at  $M_s$  temperature led to the formation of 45 % martensite phase.

To study the stability of strain variation during mechanical cycling with isothermal holding, the samples were cooled under zero stress to the holding temperature and held for 40 minutes to stabilize the sample temperature. After that, the samples were subjected to mechanical cycling in the following scheme: loading to some stress, held for 20 minutes under constant stress and unloaded. Additionally, the mechanical cycling without holding was performed. The applied stress was varied from 100 to 300 MPa and the holding temperature was chosen within or outside the temperature range of martensitic transformation under stress. If the residual strain was measured after unloading, the sample was heated through the temperature range of the reverse transformation after each mechanical cycle. All mechanical tests were performed using "Shimadzu – AG-50" testing machine equipped with the thermal chamber. The strain of the sample was measured by videoextensometer.

#### Results and Discussion

It was found that quenched Ni<sub>51</sub>Ti<sub>49</sub> alloy exhibited the good stability of functional properties in cyclic tests without holding. Total strain obtained on loading to the same stress remained constant with cycles. An irreversible strain and a critical stress for stress-induced martensite formation decreased with an increase in cycle number.

During the holding of the sample under a stress after the first loading, the strain additionally increased and completely recovered on subsequent unloading. In the second cycle, a critical stress for martensite formation decreased that increased the strain variation on loading however, the strain variation during the holding decreased. Starting the third cycle, the strain variation on holding was not observed. Maximum isothermal strain of 5 % was found on holding under 280 MPa at the  $M_s$  temperature in the first cycle. An increase in cycle number led to a decrease in irreversible strain and starting from third cycle this strain was equal to zero.

Therefore, the results obtained showed that the strain variation associated with the isothermal transformation on holding of the quenched Ni<sub>51</sub>Ti<sub>49</sub> alloy was observed in the first and the second cycles. The holding of the sample under a stress was not accompanied by the strain variation in the further cycles. This showed that an increase in the cycle number suppressed the isothermal martensitic transformation on holding that might be caused by an increase in the defect density that changed the kinetics of the transformation.

#### Acknowledgement

This work was supported by Russian Science Foundation (grant number 18-19-00226).

#### References

- [1] A. Ivanov, S. Belyaev, N. Resnina, V. Andreev, Sensors and Actuators A: Physical. **2019**, 297, 111543
- [2] C. Maletta, E. Sgambitterra, F. Furguele, R. Casati, A. Tuissi, International Journal of Fatigue. **2014**, 66, 78-85
- [3] N. Resnina, S. Belyaev, E. Demidova, A. Ivanov, V. Andreev, Materials Letters. **2018**, 228, 348-350



**P-13**

**Biocompatibility of pure refractory metals and their combination as high entropy alloys**

Janett Schmelzer<sup>1</sup>, Georg Hasemann<sup>1</sup>, Maximilian Regenber<sup>1</sup>, Ulf Betke<sup>1</sup>, Manja Krüger<sup>1</sup>, Heike Walles<sup>2</sup> and Michael Scheffler<sup>1</sup>

<sup>1</sup>Otto-von-Guericke-University Magdeburg, Institute of Materials and Joining Technology, 39106 Magdeburg, Germany, janett.schmelzer@ovgu.de

<sup>2</sup>Otto-von-Guericke-University Magdeburg, Institute for Chemistry - Core Facility Tissue Engineering, 39106 Magdeburg, Germany

**Introduction**

Artificial prostheses can be successfully implanted in the human body for many years and improve mobility, vitality and the quality of life of many patients. A large variety of different metallic and ceramic implant materials, such as alumina toughened zirconia (ATZ) [1], Ti-Al-V [2,3], Ti-Mo-Zr-Al [4], Co-Cr-Mo [5,6] are herefore in clinical use. However, there is an ongoing demand and scientific interest to improve performance and longevity of implants in terms of tribological performance, wear resistance, corrosion and especially in bio- and tissue compatibility to prevent, i.e., inflammation reactions.

The innovative material class of refractory metal based medium (MEAs)- and high-entropy alloys (HEAs) represents a unique alloy design strategy for developing new biomedical materials. Next to attractive mechanical properties and superior wear, respectively, corrosion resistance, MEAs/HEAs are very promising materials regarding the context of biocompatibility. This is based on the fact that a large number of potential chemical elements needed to achieve the above-mentioned properties belong to the category of biocompatible materials, such as Ta, Ti, Nb, Mo, V, Zr, W etc. Newly-developed bio-HEAs like Ti-Zr-Hf-Cr-Mo and Ti-Zr-Hf-Co-Cr-Mo overcome the limitation of classical metallic biomaterials by an improvement of mechanical hardness and biocompatibility all together, as reported in [7]. In order to gain a deeper understanding concerning the biocompatibility of the alloying elements mentioned above, systematic investigations of pure Ta and Nb as well as Ti-6Al-4V were carried out. Furthermore, an alloying approach emphasized by Nagase et al. [7], regarding the biocompatibility and thus foreign body induced inflammation reactions of an equiatomic Ta-Nb-Ti alloy is taken into account for our experiments. The results serve as a careful analysis for a subsequent MEA/HEA alloy design with superior biocompatibility and strength in comparison to conventional implant materials.

**Materials and Methods**

As a first step, to prove the influence of different composites, 15 x 15 mm glass cover slips (272-KKA2.1, Carl Roth) were sputter coated (Q150T ES; Quorum Technologies Ltd., Laughton, UK) with Ti and Ta, sterilized and either used for cell cultivation experiments or modified with collagen I or fibronectin, which are important components of the extracellular matrix (ECM), subsequently.

Secondly, bulk metallic Ta and Nb samples (supplied by H.C. Starck Hermsdorf GmbH, Germany) were compared to Ti-6Al-4V (HERMIT GmbH, Munich, Germany) and an as-cast Ta-Nb-Ti sample for biocompatibility and cell culture investigations. The arc-melted equiatomic alloy Ta-Nb-Ta was produced using high purity elemental chips or flakes of Ta (99.9 %), Nb (99.9 %) and Ti (99.6 %). The sample was re-melted five times to ensure sufficient homogeneity of the alloying elements.

For cell cultivation experiments, the samples were cut into 2 mm thick slices und grinded to a grit size of 1200 using SiC paper, to have a relative comparison of the metals' surfaces. However, slight limitation in the surface roughness due to different hardness values are considered for this first preliminary study. The roughness and the wetting behavior of the investigated surfaces is determined by means of measuring the surface contact angle and are part of ongoing investigations. Microstructural observations of the arc-melted alloy Ta-Nb-Ti were carried out using scanning electron microscopy (SEM; EVO 15, Zeiss, Oberkochen, Germany) in the back-scattered electron (BSE) mode. To determine the elemental distribution and the chemical composition of the alloy, (Si(Li))-detector Energy-dispersive X-ray spectroscopy (EDS) analysis, equipped with Genesis software (EDAX, Mahwah, NJ, USA) was conducted.

To evaluate the cell- and biocompatibility, cell cultivation experiments were carried out on the defined surfaces of the specimens. In this study fibroblasts (FBs) and mesenchymal stromal cells (MSCs) were used. The fibroblasts were isolated from fascia biopsies of donors with different ages. The MSCs were provided by an established cell bank at the University of Wuerzburg [8]. Cell proliferation behavior on the metallic surfaces was monitored by modifying the cells with nontoxic fluorescent colors, using CellTracker fluorescent probes (Green CMFDA (C7025) or RED CMTPIX (C34552), Invitrogen). Additionally, actin filaments of the cells were stained with CytoPainter Phalloidin-iFluor 647 reagent (ab176759, Abcam) and the nuclei of the cells were blue counterstained with blue 4',6-diamidino-2-phenylindole (DAPI) (D1306, ThermoFischer). If necessary, cells were fixed on the surface by an incubation in 30 ml 4 % formalin (256462, Applichem) for 12 hours at 4 °C.

The sputtered glass cover slips and the bulk metallic samples were incubated at 37 °C for 24 hours in a 0.5 mg/ml ECM-protein solution. Thereafter they were transferred in a 12 well plate and immediately seeded with the specific cell type in the cell type specific density.

### Results and Discussion

The Ta and Ti metallized 15 x 15 mm glass cover slips were cultivated with fibroblasts and MSCs. The experimental procedure allows to study the cell vitality on plain 2D metalized surfaces. Cell colonization with primary human fibroblasts (FB) and human MSCs was first cultured for one week on Ti and Ta sputtered planar surfaces. All surfaces revealed dense, about 100 nm thick metallic layers [9].

The cells grow either in direct contact to the metallic surfaces or on additionally modified ECM components with collagen I or fibronectin coated surfaces. Fig. 1 a) depicts the proliferation rate over time in dependence from the surface concept. As a result, vitality of both cell types after one week of cultivation was observed independent from the surface and is shown in Fig. 1 b) and c). It is noticeable that the metals Ti and Ta have been colonized very well by the stem cells without a coating of ECM components, whereas the fibroblasts preferred the surface components of the ECM. All over the FBs reveal a nearly equivalent proliferation rate on Ti and Ta substrate material, whereas the stem cells have a significantly higher proliferation on Ti surfaces. This study allows first insights in an evaluation process for ideal surface conditions, regarding cell proliferation over time for Ti and Ta metallized supports as a base for the development of innovative biocompatible MEAs/HEAs.

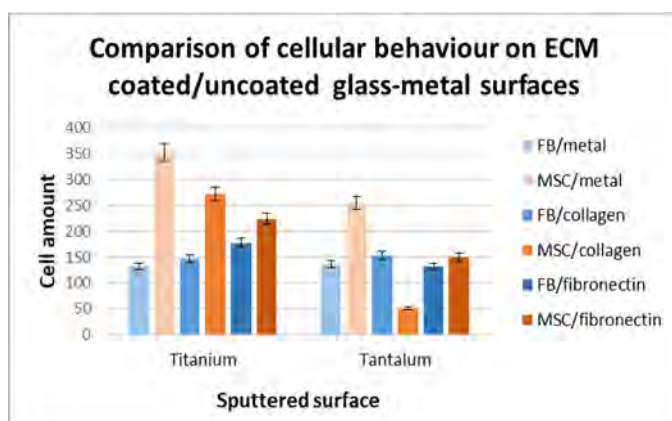


Fig. 1: Comparison of cellular behavior on different glass-metal surfaces cells (GFP labeled)

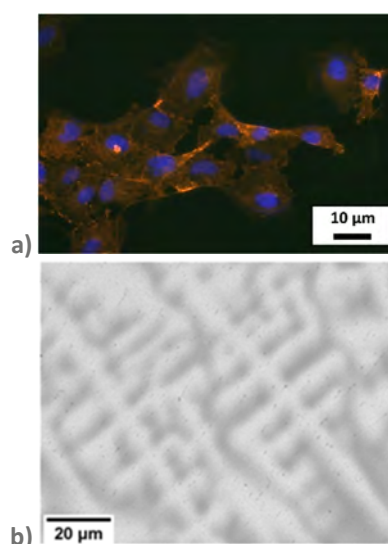


Fig. 2: a) blue stained (Dapi) nuclei on formalin fixed samples and b) microstructure of as-cast Ta-Ti-Nb

### References

- [1] J. Bertrand, D. Delfosse, V. Mai, F. Awiszus, K. Harnisch, C.H. Lohmann, *Bone Joint J.* **2018**, *100-B*, 882–890.
- [2] D. Kuroda, M. Niinomi, M. Morinaga, Y. Kato, T. Yashiro, *Mater. Sci. Eng. A.* **1998**, *243*, 244–249.
- [3] A. Sidambe, *Materials (Basel)*. **2014**, *7*, 8168–8188.
- [4] H.-M. Kim, H. Takadama, T. Kokubo, S. Nishiguchi, T. Nakamura, *Biomaterials*. **2000**, *21*, 353–358.
- [5] M. Crackau, N. Märtens, K. Harnisch, A. Berth, J. Döring, C.H. Lohmann, T. Halle, J. Bertrand, *J. Biomed. Mater. Res. Part B Appl. Biomater.* **2020**, *108*, 1764–1778.
- [6] J. Döring, M. Crackau, C. Nestler, F. Welzel, J. Bertrand, C.H. Lohmann, *J. Mech. Behav. Biomed. Mater.* **2019**, *97*, 212–221.
- [7] T. Nagase, Y. Iijimab, A. Matsugakib, K. Ameyamac, T. Nakanob, *Mater. Sci Eng. C.* **2020**, *107*, 110322.
- [8] D. Confalonieri, Ph.D. Thesis, Julius-Maximilians-University Würzburg, **2017**.
- [9] G. Hasemann, U. Betke, M. Krüger, H. Walles, M. Scheffler, article submitted to *Materials (MDPI)*.

**P-14****Plastic Deformation of Single Crystals of the Equiatomic Cr-Co-Ni Medium-Entropy Alloy with the FCC Structure**

Le Li, Zhenghao Chen, Shogo Kuroiwa, Kyosuke Kishida and Haruyuki Inui  
 Department of Materials Science and Engineering, Kyoto University, 606-8501 Kyoto, Japan,  
 li.le.52c@st.kyoto-u.ac.jp, chen.zhenghao.6e@kyoto-u.ac.jp, kuroiwa.shougo.78a@st.kyoto-u.ac.jp,  
 kishida.kyosuke.6w@kyoto-u.ac.jp, inui.haruyuki.3z@kyoto-u.ac.jp

**Introduction**

The equiatomic Cr-Mn-Fe-Co-Ni and its derivatives high-entropy alloys (HEAs), have been recognized as a new class of promising structural materials due to their exceptional strength-ductility combinations at ambient and cryogenic temperatures [1,2]. In single phase HEAs with FCC structures, the high yield strengths are mainly attributed to significant solid-solution hardening. Systematic work has revealed that the equiatomic Cr-Co-Ni exhibits remarkably higher strength and ductility than the Cr-Mn-Fe-Co-Ni and other subsets [3]. The improved strengths have motivated intensive detailed research to explore their micro-scale origins via experimental approaches and theoretical calculations. These results have implied that the type and bonding of atoms, instead of number of elements, are more important for solid solution hardening in HEAs. The high strength is believed to be related to the severe and ubiquitous crystal lattice distortion, such as the mean-square atomic distortion (MSAD) model [4]. The excellent tensile ductility of the Cr-Co-Ni MEA is generally attributed to the high propensity of deformation twinning resulting from its low stacking fault energy [5]. Of interest to note is that thin layers of the hexagonal close packed (HCP) structure are formed in association with deformation twins in the Cr-Co-Ni MEA [6,7]. This indicates that not only TWIP (twinning induced plasticity) but also TRIP (transformation induced plasticity) are responsible for the excellent tensile ductility of the Cr-Co-Ni MEA as in the case of high-Mn steels. However, it is well known that in polycrystals grain size and boundaries induce scattered results of mechanical response. Therefore, single crystals are of prime important to investigate the yield stress, critical resolved shear stress (CRSS) and twinning shear stress. There are only three attempts on the mechanical response of Cr-Co-Ni single crystals but the twinning shear stress is much lower than that of polycrystals and theoretical calculation [8-10]. In the present study, we investigate the plastic deformation behavior of bulk single crystals of the equiatomic Cr-Co-Ni in a wide temperature range of 14~1373 K, in order to experimentally deduce materials parameters (such as CRSS for slip, twinning shear stress as well as stacking fault energy).

**Materials and Methods**

The equiatomic Cr-Co-Ni ingots were prepared by arc melting and the single crystal rods were grown by the floating zone method. The single crystals were annealed at 1473 K for 1 week followed by water quenching.  $[\bar{1}23]$  oriented specimens were cut down for universal tests in compression (size  $2 \times 2 \times 5 \text{ mm}^3$ ) and tension (gage section  $2 \times 2 \times 5 \text{ mm}^3$ ). The specimens were finally electro-polished. Compression tests were conducted from 10K to 1373 K with the strain rate in the range of  $1 \times 10^{-5} - 1 \times 10^{-2} \text{ s}^{-1}$ , while tensile tests were carried out at room temperature and 77 K at the strain rate of  $1 \times 10^{-4} \text{ s}^{-1}$ . Deformation markings on the specimen surface were examined by optical microscopy and scanning electron microscopy (SEM) equipped with an electron back-scatter diffraction (EBSD) apparatus and an energy-dispersive spectroscopy (EDS) detector. Deformation fine microstructures were examined by transmission electron microscopy (TEM) and scanning transmission electron microscopy (STEM). Thin foils for TEM/STEM observations were prepared by electro-polishing with a solution of nitric acid, ethylene glycol and methanol (2:5:20 by volume).

**Results and Discussion**

The CRSS for the  $\{111\} \langle 110 \rangle$  slip system at room temperature and 77 K does not depend on the sense of load (either in tension or in compression). The CRSS increases with decreasing temperature and a dulling of the temperature dependence of CRSS due to the inertia effects is clearly observed to occur below 50 K. The extrapolated CRSS at 0 K is calculated to be 225 MPa, which is in agreement with the polycrystalline result (215 MPa) divided by Taylor factor. This value is considerably higher than that (168 MPa) similarly obtained for the Cr-Mn-Fe-Ni-Co quinary equiatomic HEA [11]. The CRSS results of Cr-Co-Ni are in good agreement with the stress equivalence of solid solution strengthening, as the Cr-Mn-Fe-Ni-Co alloy is. Overall, the temperature dependence behaviors of the Cr-Co-Ni MEAs are quiet similar to that of conventional binary fcc alloys, except for much higher CRSS and steeper temperature dependence of CRSS at cryogenic temperatures. It indicates that solid solution strengthening is indeed the dominant strengthening mechanism in the Cr-Co-Ni alloys as the case in conventional fcc alloys. The stacking fault energy deduced from the dislocation separation distance is  $14 \text{ mJm}^{-2}$ , low enough to account for deformation twinning both at 77 K and room temperature. Twinning at 77K occurs on conjugate  $(\bar{1}\bar{1}1)$  planes in the form of Lüders deformation after primary slip with the onset twinning shear stress of 470 MPa, while at room temperature, it occurs on primarily (111) planes uniformly after primary and subsequent conjugate slip with the onset twinning shear stress of 402 MPa. HCP layer formation is observed in association with twinning both at 77 K and room temperature.

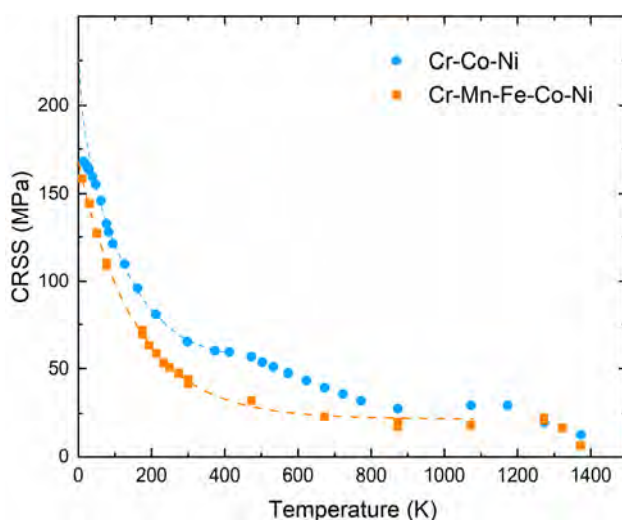


Fig. 1: The temperature dependence of CRSS

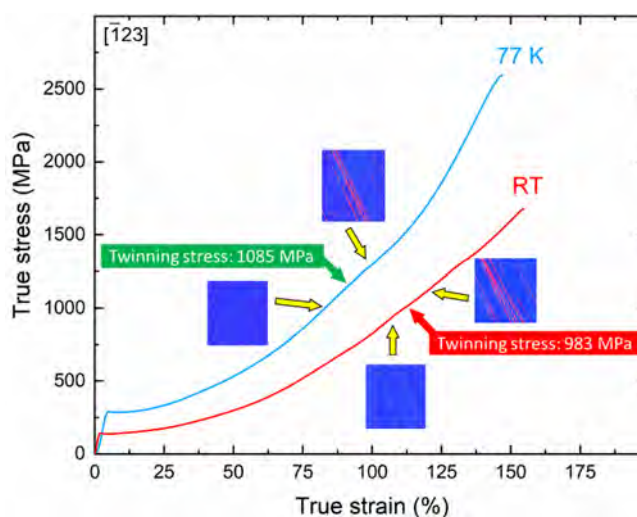


Fig. 2: Tensile true stress-true strain curves

### References

- [1] B. Gludovatz, A. Hohenwarter, D. Catoor, E. H. Chang, E. P. George, R. O. Ritchie, A fracture-resistant high-entropy alloy for cryogenic applications, *Science*. **2014**, *345*, 1153-1158
- [2] B. Gludovatz, A. Hohenwarter, K. V. Thurston, H. Bei, Z. Wu, E. P. George, R. O. Ritchie, Exceptional damage-tolerance of a medium-entropy alloy CrCoNi at cryogenic temperatures, *Nature Communication*. **2016**, *7*, 10602.
- [3] Z. Wu, H. Bei, G. M. Pharr, E. P. George, Temperature dependence of the mechanical properties of equiatomic solid solution alloys with face-centered cubic crystal structures, *Acta Materialia*. **2014**, *81*, 428-441
- [4] N. L. Okamoto, K. Yuge, K. Tanaka, H. Inui, E. P. George, Atomic displacement in the CrMnFeCoNi high-entropy alloy—A scaling factor to predict solid solution strengthening, *AIP Advance*. **2016**, *6*, 125008.
- [5] G. Laplanche, A. Kostka, C. Reinhart, J. Hunfeld, G. Eggeler, E. P. George, Reasons for the superior mechanical properties of medium-entropy CrCoNi compared to high-entropy CrMnFeCoNi, *Acta Materialia*. **2017**, *128*, 292-303.
- [6] J. Miao, C. E. Slone, T. M. Smith, C. Niu, H. Bei, M. Ghazisaeidi, G. M. Pharr, M. J. Mills, The evolution of the deformation substructure in a Ni-Co-Cr equiatomic solid solution alloy, *Acta Materialia*. **2017**, *132*, 35-48.
- [7] C. Niu, C. R. LaRosa, J. Miao, M. J. Mills, M. Ghazisaeidi, Magnetically-driven phase transformation strengthening in high entropy alloys, *Nature Communication*. **2018**, *9*, 1363.
- [8] B. Uzer, S. Picak, J. Liu, T. Jozaghi, D. Canadinc, I. Karaman, Y. I. Chumlyakov, I. Kireeva, On the mechanical response and microstructure evolution of NiCoCr single crystalline medium entropy alloys, *Materials Research Letters*. **2018**, *6*, 442-449.
- [9] W. Abuzaid, L. Patriarca, A study on slip activation for a coarse-grained and single crystalline CoCrNi medium entropy alloy, *Intermetallics*. **2020**, *117*, 106682.
- [10] G. Laplanche, M. Schneider, F. Scholz, J. Frenzel, G. Eggeler, J. Schreuer, Processing of a single-crystalline CrCoNi medium-entropy alloy and evolution of its thermal expansion and elastic stiffness coefficients with temperature. *Scripta Materialia*, **2020**, *177*, 44-48.
- [11] M. Kawamura, M. Asakura, N. L. Okamoto, K. Kishida, H. Inui, E. P. George, Plastic deformation of single crystals of the equiatomic Cr–Mn–Fe–Co–Ni high-entropy alloy in tension and compression from 10 K to 1273 K. *Acta Materialia*, **2021**, *203*, 116454.

## P-15

**Deformation twinning in single crystals of the equiatomic Cr-Co-Ni medium entropy alloy**Shogo Kuroiwa<sup>1</sup>, Li Le<sup>1</sup>, Kyosuke Kishida<sup>2</sup> and Haruyuki Inui<sup>2</sup><sup>1</sup>Department of Materials Science and Engineering, Kyoto University, 606-8501 Kyoto, Japan, kuroiwa.shougo.78a@st.kyoto-u.ac.jp, li.le.52c@st.kyoto-u.ac.jp<sup>2</sup>Department of Materials Science and Engineering, Kyoto University, 606-8501 Kyoto, Japan, Center of Elements Strategy Initiative for Structural Materials (ESISM), Kyoto University, 606-8501 Kyoto, Japan, kishida.kyosuke.6w@kyoto-u.ac.jp, inui.haruyuki.3z@kyoto-u.ac.jp**Introduction**

High-entropy and medium-entropy alloys that contain almost equal amounts of three or more constituent elements often form single-phase solid solutions because the entropy of the configuration contributes significantly to the phase stability. Since many of these HEA/MEA single-phase solid solution alloys have been found to exhibit various attractive mechanical properties, they have been extensively studied as candidates for new structural materials in recent years [1-6]. Among various single-phase HEA/MEA discovered so far, the ternary equiatomic Cr-Co-Ni MEA with the face-centered cubic (FCC) structure has attracted considerable attention because it has been reported to exhibit both the highest strength and highest low-temperature ductility among the equiatomic Cr-Mn-Fe-Co-Ni HEA and its derivative quaternary and ternary MEAs [7,8]. Previous studies on the deformation behavior of the FCC-type HEA/MEAs have suggested that deformation twinning plays an important role for their high tensile ductility. However, details of deformation twinning have not been fully clarified yet. It is thus quite important to investigate the twinning behavior of these FCC-type HEA/MEAs. In the present study, we systematically investigated the details of twinning behavior of the equiatomic Cr-Co-Ni MEA single crystals by tensile tests as a function of the loading axis orientation and temperature.

**Materials and Methods**

Single crystals of the equiatomic Cr-Co-Ni solid solution alloy were prepared by directional solidification using an optical floating zone furnace in Argon atmosphere. Specimens for tensile tests with various loading axis orientations were cut from the single crystals by electrical discharge machining. Tensile tests were conducted on an Instron-type testing machine at room temperature and 77K at a strain rate of  $1 \times 10^{-4}$ /s. Deformation microstructures at various stages of tensile test were investigated by optical microscopy, scanning electron microscopy (SEM), electron backscattered diffraction (EBSD) in SEM, transmission electron microscopy (TEM) and scanning transmission electron microscopy (STEM).

**Results and Discussion**

Stress-strain curves obtained for the  $[\bar{1}23]$ -oriented single crystals tested at room temperature and 77K exhibit stage I (easy glide region, very low work-hardening) followed by stage II (linear hardening region, very high work-hardening), which is common to single crystals of many conventional FCC metals with single-slip orientations. Both critical resolved shear stress (CRSS) for the primary slip system and work-hardening rate in stage II are confirmed to increase with decreasing temperature. In stage II, a sudden decrease in the work-hardening rate is observed at both tested temperature. Detailed microstructure observations together with orientation analysis by EBSD confirm that the sudden change in the work-hardening rate in stage II is associated with the onset of deformation twinning. The occurrence of deformation twinning at room temperature is in marked contrast to the case of the equiatomic Cr-Mn-Fe-Co-Ni HEA single crystals for which deformation twinning is activated only at lower temperatures [9]. The onset shear stress for the deformation twinning is found to increase with decreasing temperature. These characteristics of deformation twinning are consistent well with those observed in some conventional FCC metals with relatively low stacking fault energy [10]. Details of the deformation twinning, including temperature and orientation dependence of operative twinning modes will be presented.

**References**

- [1] J.W. Yeh, S.K. Chen, S.J. Lin, J.Y. Gan, T.S. Chin, T.T. Shun, C.H. Tsau, S.Y. Chang, *Advanced Engineering Materials*. **2004**, *6*, 299-303.
- [2] B. Cantor, L.T.H. Chang, P. Knight, A.J.B. Vincent, *Materials Science and Engineering*. **2004**, *A375*, 213-218.
- [3] B. Gludovatz, A. Hohenwarter, D. Catoor, E.H. Chang, E.P. George, R.O. Ritchie, *Science*. **2014**, *345*, 1153-1158
- [4] D.B. Miracle, O.N. Senkov, *Acta Materialia*. **2016**, *122*, 448-511.
- [5] N.L. Okamoto, S. Fujimot, Y. Kambara, M. Kawamura, Z.M.T. Chen, K. Tanaka, H. Inui, E.P. George, *Scientific Reports*. **2016**, *6*, 35863.
- [6] E.P. George, W.A. Curtin, C.C. Tasan, *Acta Materialia*. **2020**, *188*, 435-474.
- [7] G. Laplanche, A. Kostka, C. Reinhart, J. Hunfeld, G. Eggeler, E.P. George, *Acta Materialia*. **2017**, *128*, 292-303.
- [8] Z. Wu, H. Bei, G.M. Pharr, E.P. George, *Acta Materialia*. **2014**, *81*, 428-441.
- [9] M. Kawamura, M. Asakura, N.L. Okamoto, K. Kishida, H. Inui, E.P. George, *Acta Materialia*. **2021**, *203*, 116454.
- [10] T. Mori, H. Fujita, *Transactions of the Japan Institute of Metals*. **1977**, *18*, 17-24.



P-16

**Non-equilibrium grain boundaries in additively manufactured CoCrFeMnNi high-entropy alloy**

Nuri Choi<sup>1,2</sup>, Vladislav Kulitckii<sup>1</sup>, Josua Kottke<sup>1</sup>, Bengü Tas<sup>1</sup>, Jungho Choe<sup>3</sup>, Ji Hun Yu<sup>3</sup>, Sangsun Yang<sup>3</sup>, Joo Hyun Park<sup>2</sup>, Jai Sung Lee<sup>2</sup>, Gerhard Wilde<sup>1</sup> and Sergiy V. Divinski<sup>1</sup>

<sup>1</sup>Institute of Material Physics, University of Münster, 48143 Münster, Germany, choin@uni-muenster.de, gwilde@uni-muenster.de

<sup>2</sup>Department of Materials Science and Chemical Engineering, Hanyang University, 15588 Ansan, Republic of Korea, jslee@hanyang.ac.kr

<sup>3</sup>Center for 3D Printing Materials Research, Korea Institute of Materials Science, 51508 Changwon, Republic of Korea

**Introduction**

Additive manufacturing (AM) is one of the newest manufacturing processes with remarkable advantages. It allows a direct production of complex-shaped metals with less restrictions for a wide range of compositions using the laser or electron beams as an energy source. The repetitive melting/solidification cycles during the laser scanning process is known to induce the microscopic defects such as porosity, dislocation pile-ups and residual internal stress [1]. Those defects are generally unfavorable as they degrade the properties of AM metals and alloys and are in a focus of intensive research. Furthermore, intensive defect production may generate metastable states of the alloys which could be probed by dedicated diffusion measurements.

It is well known that the mechanical stress, i. e. severe plastic deformation drifts high-angle grain boundaries (at least a fraction of them) towards a “non-equilibrium” or deformation-modified state as it was demonstrated by observations of the enhanced grain boundary diffusion rates [2,3]. Similarly, the thermal stresses applied to AM alloys during manufacturing may cause the “non-equilibrium” state of grain boundaries, too. Hence, the authors focused on the correlative investigation of the microstructure evolution and grain boundary diffusion in AM alloys. As the grain boundaries contribute to the various fundamental material properties, the knowledge of grain boundary diffusion would provide the guidelines to predict long-term functioning properties under service or aging conditions.

**Materials and Methods**

A homogenized master piece of CoCrFeMnNi high-entropy alloy (HEA) was used for producing a high-purity HEA powder via a gas-atomization process. The powder of the size ranges from 10 to 45  $\mu\text{m}$  was classified and used for selective laser melting to manufacture the final specimens. Three different scanning strategies were chosen to obtain designed microstructures with respect to the laser scanning and building directions as portrayed in Fig. 1, namely the A, B and C routes. The average relative density of the specimens was  $99.4 \pm 1.7\%$ . A contribution of the residual porosity to atomic diffusion was measured by dedicated experiments and it can safely be excluded. The analysis of microstructures was carried out by electron back-scatter diffraction (EBSD) and TSL OIM Analysis 5 software. The specific analyzing parameters are described in Ref. [4]. The  $^{63}\text{Ni}$  radioisotope was used to probe the kinetic properties of grain boundaries in the AM produced alloy [4].

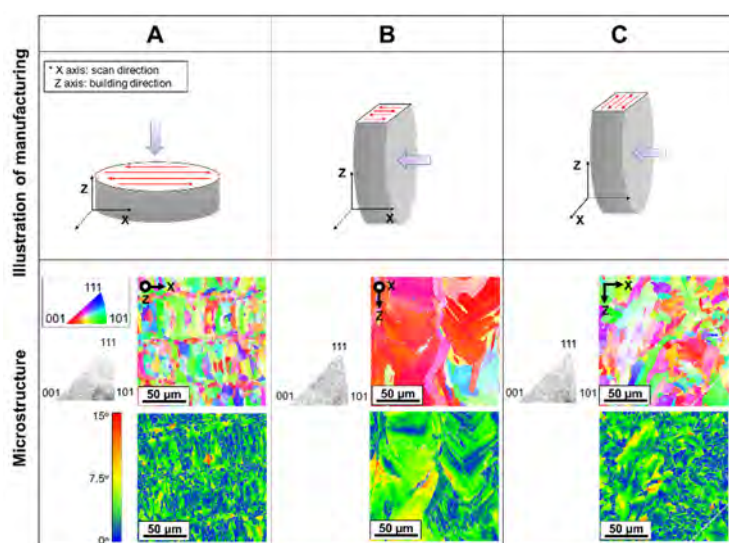


Fig. 6: Scheme of manufacturing strategy and microstructure with different scan and build directions.

**Results and Discussion**

As shown in Fig. 1, the microstructure of an AM produced material is dominantly influenced by the laser scan and build directions. A hierarchical microstructure with the interchanging layers of equiaxed and columnar grains is found. The equiaxed fine grains are generated in overlapped scanning areas which represent re-melted zones. The <001> oriented and coarse columnar grains are parallel to the build direction, built due to epitaxial solidification under heat flux from  $N$ th to the  $(N+1)$ th layer [5]. The re-melted layers during repeated unidirectional melting reveal a significant level of residual stress due to imposed thermal gradients. The residual strains are characterized by an increased density of geometrically necessary dislocations (GNDs), presented by the Kernel averaged misorientation (KAM) distribution maps in Fig. 1. The KAM values for the fully recrystallized and homogenized matrix is close to zero. It is obvious that AM CoCrFeMnNi HEA has considerable internal strains and especially the re-melted areas are under higher stresses.

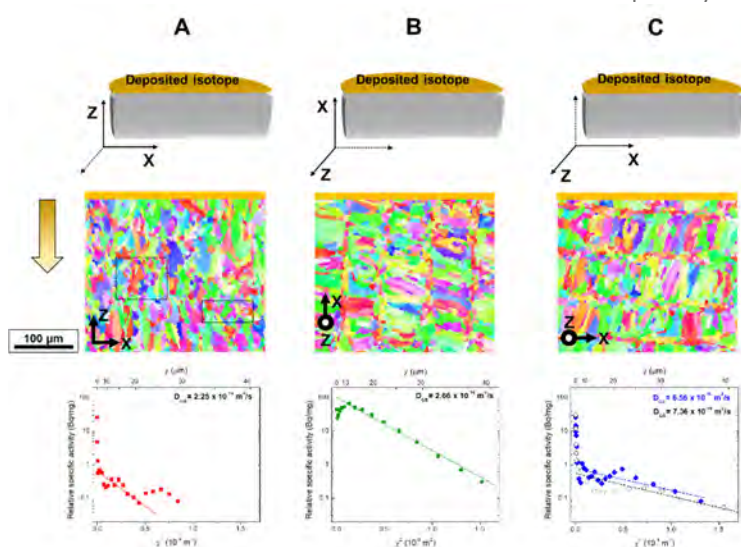


Fig. 7: Cross-sectional microstructure and experimental diffusion profile for specimen A, B and C.

According to Harrison’s classification of grain boundary diffusion regimes [6], the condition of the diffusion experiments (at 500K for 72 hours) corresponded to the C-type kinetics, when volume diffusion of the tracer is frozen. Under these conditions, the penetration depths via volume and grain boundary (relaxed high-angle interfaces) diffusion paths for Ni in polycrystalline CoCrFeMnNi HEA are estimated to be  $10^{-6}$  nm [7] and 1 nm [8]. Nevertheless, a deep penetration of Ni tracer in as-produced AM CoCrFeMnNi HEA is found, about 20 to 40  $\mu$ m (Fig.2). The deep tracer penetration is removed when the sample is pre-annealed at 773K for 1 hr, the annealing treatment which does not induce any significant change of the microstructure.

These facts substantiate a different state of grain boundaries in the AM material. The experimental diffusion coefficients,  $D_{gb}$ , in AM HEA are of the order of  $10^{-16}$  m<sup>2</sup>/s while the expected  $D_{gb}$  values for well-annealed polycrystalline HEA are of the order of  $10^{-24}$  m<sup>2</sup>/s [8]. This enhanced diffusivity implies that AM HEA possesses at least a fraction of non-equilibrium grain boundaries and this state is removed by low-temperature annealing.

How far does the non-equilibrium state of grain boundaries in AM alloy resemble that after severe plastic deformation? This fundamental question is a subject of current research.

**References**

[1] Y. Wang, J. Shi, *Procedia Manufacturing*. **2018**, 26, 941-951.  
 [2] S.V. Divinski, *Diffusion Foundation*. **2015**, 5, 57-73.  
 [3] G. Wilde, S.V. Divinski, *Materials Transactions*. **2019**, 60, 1302-1315.  
 [4] N. Choi, V. Kulitckii, J. Kottke, B. Tas, J. Choe, J.H. Yu, S. Yang, J.H. Park, J.S. Lee, G. Wilde, S.V. Divinski, *Journal of Alloys and Compounds*. **2020**, 844, 155757.  
 [5] R.R. Dehoff, M.M. Kirka, W.J. Sames, H. Bilhuex, A.S. Tremsin, L.E. Lowe, S.S. Babu, *Materials Science and Technology*. **2015**, 31, 931-938  
 [6] L. Harrison, *Transactions of the Faraday Society*. **1961**, 57, 1191-1199.  
 [7] M. Vaidya, S. Trubel, B.S. Murty, G. Wilde, S.V. Divinski, *Journal of Alloys and Compounds*. **2016**, 688, 994-1001,  
 [8] M. Vaidya, K. Pradeep, B. Murty, G. Wilde, S.V. Divinski, *Scientific Reports*. **2017**, 7, 12293,

**P-18****TiAl alloy optimization for EBM and usage of selective Al-evaporation for microstructure design**Martin Schloffer<sup>1</sup>, Martin Franke<sup>2</sup> and Carolin Körner<sup>3</sup><sup>1</sup>MTU Aero Engines AG, 80995 Munich, Germany, martin.schloffer@mtu.de<sup>2</sup>Neue Materialien Fürth GmbH, 90762 Fürth, Germany, martin.franke@nmfgmbh.de<sup>3</sup>Chair of Materials Science and Engineering for Metals, Friedrich-Alexander-Universität Erlangen-Nuremberg, Erlangen, Germany, carolin.koerner@fau.de**Introduction**

Additive manufacturing (AM) offers interesting possibilities for part and microstructure design in the future. To understand the influence of the electron beam melting (EBM) process on microstructure and mechanical properties the conventional TNM TiAl alloy was processed via EBM and compared with results generated via forging.

**Materials and Methodes**

The TNM alloy, primary developed and optimized for the forging process, has some advantages and disadvantages when produced via EBM. The diversity is caused by the different process parameters where cyclical heating, high temperature gradients and fast solidification offers new possibilities via the EBM process. Specimens were additively manufactured with different EBM process parameters for mechanical testing to understand their influence on material properties.

**Results and Discussion**

The beta solidifying TNM alloy offers strong anisotropy of mechanical properties caused by a beta solidification texture during EBM melting [1]. To avoid anisotropy a few new TiAl alloy compositions which offers very fine grained, isotropic microstructures in as build state were developed [2,3]. The new alloys combine high ductility with high strength or high creep resistance in via HIP (hot isostatic pressing) heat treated condition. Further scanning strategies were developed to control the Aluminum loss during EBM very carefully. In detail, the EBM process can provide a certain Aluminum loss up to a few at.% to customize the microstructure at each position in the part as required and as needed [4]. Heat treatment and hot isostatic pressing were adjusted to the new TiAl's alloy in order to maintain different types of microstructure while eliminating defects like misconnections. For the first time, additively manufactured parts with two different microstructures and well-defined transition zone, see Figure 1, were characterized in detail [4]. This AM specific new feature of selective Al-evaporation is a big advantage of additive manufacturing. This feature opens the potential to tune the required properties very specific at different positions and have as example different creep and ductility properties in different areas of turbine blades.

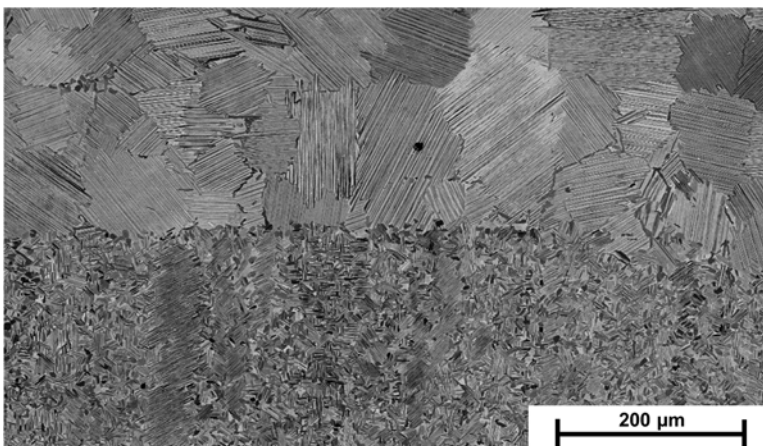


Fig. 1: The usage of adopted EBM Parameters allows to adjust different microstructures and a well-defined transition zone between in one part. Top of the part consists of a homogeneous coarse Fully Lamellar (FL) microstructure, the bottom consists of a fine grained Nearly Lamellar Gamma (NLg) microstructure.

**References**

- [1] R. Wartbichler, Electron Beam Melting of a  $\beta$ -Solidifying Intermetallic Titanium Aluminide Alloy, *Adv. Eng. Mater.* **2019**, *21*, 1900800
- [2] D. Wimler et al., Designing advanced intermetallic titanium aluminide alloys for additive manufacturing, *Intermetallics*. **2021**, *131*, 107109
- [3] M. Reith et al., Processing 4th generation titanium aluminides via electron beam based additive manufacturing – characterization of microstructure and mechanical properties, *Materialia*. **2020**, *14*, 100902
- [4] MTU Patent, Method for producing a component from graded TiAl alloy and component produced therefrom, DE102018202723, US2019299288

**P-19**

**Microstructure and mechanical properties of TiAl4822 alloy built by selective laser melting**

Kazuhiro Mizuta, Yuta Hijikata, Tatsuya Fujii, Kazuhiro Gokan and Koji Kakehi

Department of System Design, Tokyo Metropolitan University, 192-0397 Tokyo, Japan, mizuta-kazuhiro@ed.tmu.ac.jp

**Introduction**

Application of additive manufacturing (AM) has been widely studied. Super lightweight alloys such as Ti-48Al-2Cr-2Nb (TiAl4822) is one of the interests in aerospace and automotive fields. In this study, selective laser melting (SLM) with a new heating system and an inert gas control unit was applied to Ti-48Al-2Cr-2Nb. Microstructure of additively manufactured TiAl4822 by SLM was analyzed and its relationship to the mechanical properties was evaluated. The results were also compared with electron beam melting (EBM) which has been a standardized AM process for TiAl4822.

**Materials and Methods**

An M290 (EOS GmbH Electro Optical Systems) with a high-temperature modification unit that features a cooling of the process chamber and an inert gas purification system was used to build the sample. The TiAl4822 powder was prepared and used for SLM. Microstructure was analyzed by scanning electron microscope (SEM) (HITACHI High-Tech, S3700N). Electron back-scatter diffraction (EBSD) (TSL Solutions, OIM) was applied to observe details of the microstructure, such as grain size and phase condition. Tensile test was performed by a universal testing machine (SHIMAZU AG-10TE) at 750 °C at a strain rate of  $4.2 \times 10^{-4} \text{ s}^{-1}$ . A machined specimen with a length of 19.6 mm, width of 2.8 mm, and thickness of 3.0 mm in the parallel part was used. The tensile load was applied in the same direction as build direction.

**Results and Discussion**

The microstructure of the SLM specimen was relatively homogeneous, while that of the EBM specimen showed a layered structure consisting of  $\gamma$  phase and duplex region. The average grain size in the SLM specimen was  $6.9 \mu\text{m}$  which was 63 % smaller than that of the EBM. Following Hall-Petch Law [1], the microstructure of the SLM specimen reflected the longer elongation and higher tensile strength than the as-built EBM specimen. Homogeneous structure in the SLM also could avoid the delamination between the different layers identified in the EBM specimen. Especially, the elongation of the SLM specimen was 5.75% and 8.3 times that of the as-built EBM specimen. Further investigation such as anisotropy of the AM parts by the SLM and other mechanical properties such as fatigue and creep need to be carried out in the future

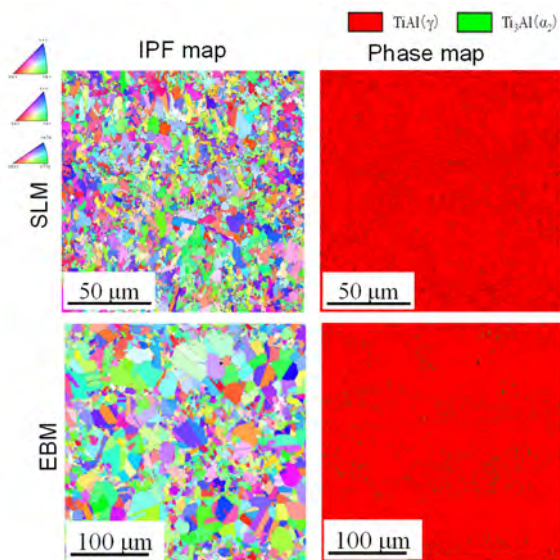


Fig. 1: Inverse pole figures (IPF) and phase map of the SLM specimen and the EBM specimen. SLM specimen showed homogeneous small  $\gamma$ , while the EBM specimen shows a heterogeneous structure with coarse  $\gamma$  and duplex.

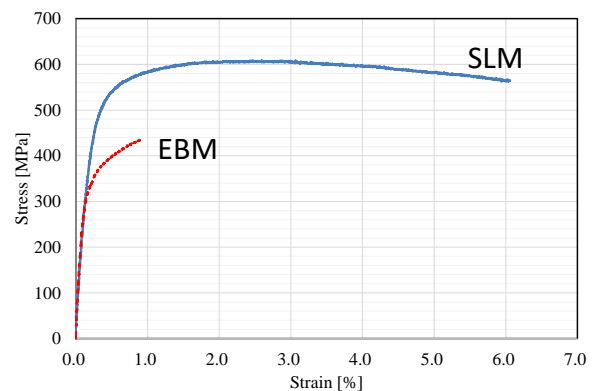


Fig. 2: Tensile stress-strain curves at 750°C. The yield stress, tensile stress, and elongation of the SLM specimen were greater than that of the EBM specimen.

**Acknowledgments**

The authors thank Dr. Tobias Maiwald-Immer of AM Metals GmbH for supporting the experiments using the new SLM system. This study was supported by the Ministry of Economy, Trade, and Industry (METI), Japan.

**References**

[1] C. Mercer, W.O. Soboyejo, Scripta Materialia. 1996, 35 1, 17-22.



P-20

### ***In situ* observation of the phase evolution during a physical simulation of the spark plasma sintering process of a $\gamma$ -TiAl based alloy**

Michael Musi<sup>1</sup>, Benjamin Galy<sup>2</sup>, Jean-Philippe Monchoux<sup>2</sup>, Alain Couret<sup>2</sup>, Helmut Clemens<sup>1</sup>  
and Svea Mayer<sup>1</sup>

<sup>1</sup>Chair of Physical Metallurgy and Metallic Materials, Department of Materials Science, Montanuniversität Leoben, 8700 Leoben, Austria, michael.musi@unileoben.ac.at, helmut.clemens@unileoben.ac.at, svea.mayer@unileoben.ac.at

<sup>2</sup>CEMES, Université de Toulouse, CNRS, 31055 Toulouse, France, benjamin.galy@cemes.fr, monchoux@cemes.fr, alain.couret@cemes.fr

#### **Introduction**

The excellent material-specific properties of intermetallic  $\gamma$ -TiAl based alloys make them excellent candidates for the high-temperature applications in the automotive and aerospace industry. Due to the combination of the outstanding creep resistance and the high yield strength with their low density of about  $4 \text{ gcm}^{-3}$ , these alloys are considered as suitable replacement for the twice as heavy Ni-based alloys in the case of turbine blades in advanced aircraft engines [1,2]. Generally, two different phases can be present in the microstructure at room temperature, the ordered tetragonal face-centered  $\gamma$ -TiAl phase and the ordered hexagonal  $\alpha_2$ -Ti<sub>3</sub>Al phase. At high temperatures, the disordered body-centered cubic  $\beta$ -Ti(Al) and the disordered counterpart of the  $\alpha_2$  phase, the hexagonal  $\alpha$ -Ti(Al) phase, exist. Depending on the alloying concept, the  $\beta$  phase or, respectively, the ordered body-centered cubic  $\beta_0$ -TiAl phase can be stabilized at room temperature by sufficient additions of  $\beta$ -stabilizing elements, e.g. Mo, Nb and W [1]. A powder metallurgical technique of particular interest for the processing of  $\gamma$ -TiAl based alloys is spark plasma sintering (SPS), as it has been demonstrated for various alloys, for example the IRIS alloy [3] and the TNM alloy [3,4]. In contrast to additive manufacturing, such as electron-beam melting and selective laser melting, in which powders are re-melted, SPS completely relies on solid-state processes. A full densification of the powder is achieved by the simultaneous application of a pulsed electric current and uniaxial pressure. Consequently, the duration of a typical SPS cycle is only about 30 min, including heating and cooling times [5]. A major advantage of SPS of  $\gamma$ -TiAl based alloys is the ability to control the microstructure of the material and, thus, its mechanical properties. By adjusting the dwell temperature with respect to the corresponding phase diagram, a variety of different microstructures can be obtained, which, consequently, renders further heat treatments unnecessary in most cases [3]. Due to the short dwelling times at high temperatures, the kinetics of the occurring phase transformations have a particular impact on the final microstructure. The aim of the present study is, therefore, to monitor the phase evolution of a  $\gamma$ -TiAl based alloy during a physical simulation of the SPS process for the first time by *in situ* high-energy X-ray diffraction (HEXRD).

#### **Materials and Methods**

The  $\gamma$ -TiAl based alloy investigated in the presented study had the chemical composition Ti-46.3Al-2.2W-0.2B (in at.%). Prealloyed powder was produced by electrode induction melting inert gas atomization (EIGA) and sieved in a particle size range of 25–50  $\mu\text{m}$ . To monitor the phase evolution, an *in situ* HEXRD experiment was conducted at the beamline P07 at the Deutsches Elektronen Synchrotron (DESY), Germany, using a synchrotron radiation with a mean photon energy of 73.6 keV. The physical simulation of the SPS process during the *in situ* HEXRD measurement was realized with a self-designed sample holder made of Mo along with a modified 805A/D dilatometer from Bähr, Germany, for the temperature control [6,7]. The powder was exposed to a temperature profile representing the one of a conventional SPS cycle. A dwell temperature of 1325 °C and a dwell time of 3 min have been chosen and heating and cooling rates of 100 K/min were applied. From the obtained diffraction data captured with a Perkin Elmer XRD 1621 area detector, information regarding the evolution of the volume fractions and the lattice parameters of the individual phases were extracted by means of Rietveld analysis. The microstructure of the *in situ* HEXRD specimen was characterized with a scanning electron microscope (SEM) in backscattered-electron mode and an acceleration voltage of 20 kV.

#### **Results and Discussion**

Rietveld analysis of the diffraction data allows the monitoring of the phase evolution during the physical simulation of the SPS process. The resulting volume fractions of the  $\alpha/\alpha_2$  phase, the  $\beta/\beta_0$  phase, and the  $\gamma$  phase as a function of time are presented in Fig. 1. A high amount of  $\alpha/\alpha_2$  phase is present at the beginning of the experiment in the material due to the high cooling rates during the EIGA atomization, which results in a material condition far from thermodynamic equilibrium. During the first part of the heating segment, the phase fractions stay constant due to lack of thermal activation. However, once a temperature of about 700 °C is exceeded, the amount of  $\gamma$  phase significantly increases, while the volume fractions of  $\alpha/\alpha_2$  and  $\beta/\beta_0$  decreases, in order to approach a condition closer to thermodynamic equilibrium. Generally, a high  $\gamma$  phase fraction is expected for an alloy with an Al content of 46.3 at.%, which is reflected in this first major phase transformation [6]. Further heating results in the dissolution of the  $\gamma$  phase, the second important phase transformation, and, thus, in an increase of the  $\alpha/\alpha_2$  phase fraction. During the dwelling segment at



1325 °C, both  $\alpha$  and  $\beta$  phase are present. The subsequent cooling segment is characterized by the formation of  $\gamma$  phase at the expense of the  $\alpha/\alpha_2$  phase [6]. After the *in situ* HEXRD experiment, the material consists of approximately 90 vol.% of  $\gamma$  phase, 7 vol.% of  $\alpha/\alpha_2$  phase, and 3 vol.% of  $\beta/\beta_0$  phase.

The microstructure of the *in situ* HEXRD specimen was investigated by SEM. It should be noted that although some densification of the powder has occurred during the *in situ* HEXRD experiment, a high porosity is still present inside the material because no pressure was applied during the experiment itself. A micrograph of the microstructure is shown in Fig. 2. The microstructure consists of lamellar  $\alpha_2/\gamma$  colonies, which are surrounded by  $\beta_0/\gamma$  phases. Such a microstructure is in accordance with the phases observed during the dwelling segment, i.e. the  $\alpha$  phase and the  $\beta$  phase. During the cooling segment the  $\gamma$  lamellae form inside the present  $\alpha$  grains, which, ultimately, undergo an ordering reaction into  $\alpha_2$ . The  $\gamma$  phase precipitates also to some extent inside the  $\beta$  phase, which, combined with the ordering of  $\beta$  into  $\beta_0$ , results in the formation of the observed  $\beta_0/\gamma$  phases at borders [6,8]. A comparison of the microstructure of the *in situ* HEXRD specimen with the microstructure of a SPS material densified at the same dwell temperature revealed a very good accordance between these two. This proves that the physical simulation of the SPS process was indeed successful and that the obtained phase evolution is trustworthy.

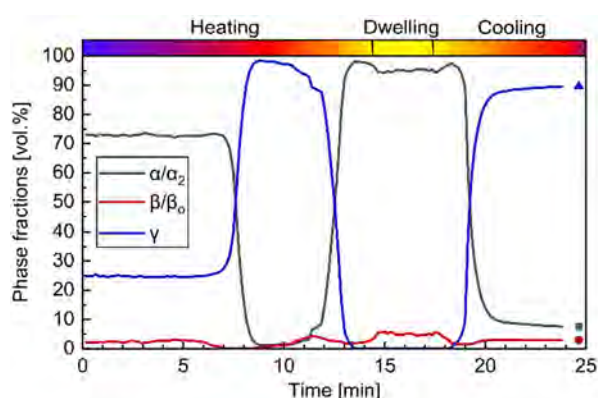


Fig. 1: Evolution of the volume fractions of the  $\alpha/\alpha_2$  phase (gray), the  $\beta/\beta_0$  phase (red), and the  $\gamma$  phase (blue) during the *in situ* HEXRD experiment. Several different phase transformations are observed during the physical simulation of the SPS process (see text) [6].

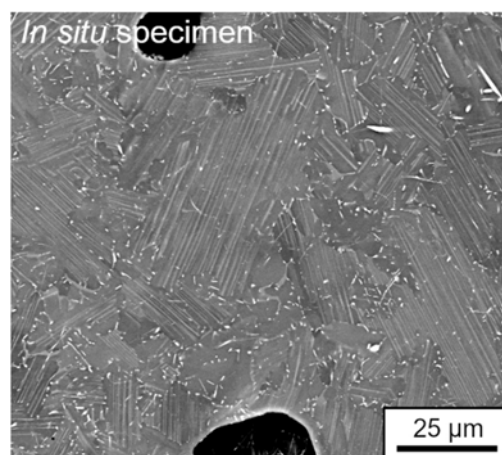


Fig. 2: SEM micrograph of the microstructure of the *in situ* HEXRD specimen using backscattered-electron contrast. Lamellar  $\alpha_2/\gamma$  colonies as well as  $\beta_0/\gamma$  phases at their borders are visible. The  $\gamma$  phase exhibits a dark gray contrast, while the  $\alpha_2$  phase appears in gray and the  $\beta_0$  phase in light gray. Additionally, two large pores can be seen in the micrograph [6].

### Acknowledgements

With regard to the *in situ* diffraction experiments, the support of the DESY management and user office is gratefully acknowledged. We appreciate the commitment of the Helmholtz-Zentrum Hereon beamline staff who contributed greatly to the success of the experiments performed. This research has been conducted in the framework of the cooperative Austrian-French project “Hi-TiAl” co-supported by the Austrian Science Fund (FWF) (Project Number I 3932-N36) and the French Agence Nationale de la Recherche (ANR).

### References

- [1] S. Mayer, P. Erdely, F. D. Fischer, D. Holec, M. Kasthuber, T. Klein, H. Clemens, *Advanced Engineering Materials*. **2017**, *4*, 1600735.
- [2] B. P. Bewlay, S. Nag, A. Suzuki, M. J. Weimer, *Materials at High Temperatures*. **2016**, *4-5*, 549–559.
- [3] A. Couret, T. Voisin, M. Thomas, J.-P. Monchoux, *Journal of The Minerals, Metals & Materials Society*. **2017**, *69*, 2576–2582.
- [4] T. Voisin, J.-P. Monchoux, M. Hantcherli, S. Mayer, H. Clemens, A. Couret, *Acta Materialia*. **2014**, *73*, 107–115.
- [5] T. Voisin, L. Durand, N. Karnatak, S. Le Gallet, M. Thomas, Y. Le Berre, J.-F. Castagné, A. Couret, *J. Mater. Process. Technol.* **2013**, *213*, 269–278.
- [6] M. Musi, B. Galy, J.-P. Monchoux, A. Couret, H. Clemens, S. Mayer, in preparation. **2021**.
- [7] P. Staron, T. Fischer, T. Lippmann, A. Stark, S. Daneshpour, D. Schnubel, E. Uhlmann, R. Gerstenberger, B. Camin, W. Reimers, E. Eidenberger, H. Clemens, N. Huber, A. Schreyer, *Advanced Engineering Materials*. **2011**, *8*, 658–663.
- [8] T. Voisin, J.-P. Monchoux, M. Perrut, A. Couret, *Intermetallics*. **2016**, *71*, 88–97.

P-21

**Effect of Zr on the phase equilibria among  $\beta$ -Ti/ $\alpha_2$ -Ti<sub>3</sub>Al/ $\gamma$ -TiAl phases in Ti-Al-Cr system**

Jianhui Yu, Hirotoyo Nakashima and Masao Takeyama

School of Materials and Chemical Technology, Tokyo Institute of Technology,

2-12-1-S8-8 Tokyo, Japan, yu.j.al@m.titech.ac.jp, nakashima.h.aa@m.titech.ac.jp, takeyama@mtl.titech.ac.jp

**Introduction**

$\gamma$ -TiAl based alloys, with excellent low density and high creep resistance, have attracted much attention as a substitute for nickel-based superalloys at elevated temperatures up to 1073 K. However, the application of this class of material to low-pressure turbine blades in jet engines is limited. Attempting to improve the mechanical properties of TiAl alloys at high temperatures, a new microstructure design principle with the transformation pathway of  $\beta+\alpha\text{-Ti}\rightarrow\alpha\rightarrow\alpha+\gamma\rightarrow\beta+\alpha+\gamma$  was established [1,2], which is available in multi-component systems containing  $\beta$  stabilizing elements, M (e.g. V, Nb, Cr, Mo). Based on our previous phase diagram studies, we found that the  $\beta+\alpha+\gamma$  three-phase coexistence region appears, and it shifts toward lower Al and M concentrations with decreasing temperature in the Ti-Al-M ternary systems, as represented by Cr [3]. Therefore, it is possible to optimize the volume fraction and morphology of the hard  $\beta$ -phase and ductile  $\gamma$ -phase in the microstructure, based on the phase diagrams. In the present study, we focus on Zr as an alloying element, and aim to clarify the phase equilibria among  $\beta/\alpha_2/\gamma$  phases in the Ti-Al-Cr-Zr quaternary system as well as the Ti-Al-Zr ternary. As with the previously investigated M elements, it has been reported that the three-phase coexistence region appears in the Ti-Al-Zr ternary system. Meanwhile, Zr has a different character compared to M-elements as it is partitioned into the  $\gamma$  phase with respect to the  $\beta$  and  $\alpha_2$  phase [4]. Therefore, thermodynamic features different from those of the Ti-Al-M are expected.

**Materials and Methods**

In order to verify the effect of Cr-Zr addition on the phase equilibria in Ti-Al alloys, the alloys with nominal compositions of Ti-(41-44)Al-(2-3)Cr-(3-5)Zr (all in at. %) were investigated in this study. All the alloys were arc-melted five times into button ingots of about 25 g under argon atmosphere. High purity titanium, aluminum, chromium and zirconium (>99.9 %) were used as raw materials for fabrication. The loss of mass for each alloy was lower than 1 %. Then, the ingots were cut into several pieces with at least 6 mm for each side by EDM. For the heat-treatments, specimens were firstly homogenized at 1673 K for 30 min ( $\beta$  single phase) or at 1573 K for 24 h ( $\alpha$  single phase) by a vertical furnace which can be filled with argon after evacuation. At the end of homogenization heat-treatments, the samples were water-quenched by dropping them into the water under the gate valve. Then all the samples were equilibrated at temperatures from 1273 K to 1473 K for up to two months in quartz capsules which were evacuated and filled with Ar. Water quench was also performed to the samples after equilibration heat-treatment. Microstructures were observed by scanning electron microscopy (SEM). Composition analyses of each present phase in the equilibrated alloys were performed by electron-probe microanalysis (EPMA) equipped with wavelength-dispersive X-ray spectroscopy (WDS), under the condition of 20 kV accelerated voltage and 20 nA probe current. The homogenized samples were selected as the standard. The phase diagram calculations were performed using Pandat software and compared with experimental results obtained in this study.

**Results and Discussion**

The results of composition analyses for each phase respectively in studied alloys are summarized and shown in Fig. 1. With the replacement of Cr with Zr, the three-phase co-existence region shifts to the high M content side. The change in the terminal composition of each phase is large for  $\beta>\gamma>\alpha_2$  in that order. The partition coefficient of total M elements between  $\alpha_2$  and  $\gamma$  phase ( $k^{\alpha_2/\gamma}$ ) decreases with the increasing Zr/M ratio in the alloys, which means that the Zr addition has an effect to enhance the solid solubility of M in the  $\gamma$  phase more than in the  $\alpha_2$  phase. As a  $\beta$  phase stabilizing element, the addition of Zr seems to have a weaker effect than Cr due to the higher terminal composition of the  $\beta$  phase in the three-phase co-existence region compared to that in the Ti-Al-Cr ternary system. However, it is noted that the terminal composition of the  $\beta$  phase in the system of combined addition is even higher than both two ternary systems, which demonstrates a special interaction between these two elements in the formation of  $\beta$  phase. In order to clarify this effect, the relationship between critical M contents for the formation of  $\beta$  phase and Zr/M ratio is plotted in Fig. 2. It is interesting to find that the critical contents in the alloys with 0.5 Zr/M ratio deviates from the straight line connecting the ternary systems in the direction that  $x_M$  increases, which implies that there is a positive interaction to destabilize the  $\beta$  phase against the  $\alpha_2$  and  $\gamma$  phase. In the further study, alloys with different Zr/M ratio will be studied to examine this interaction between Cr and Zr and the temperature dependance on the phase equilibria will be discussed.

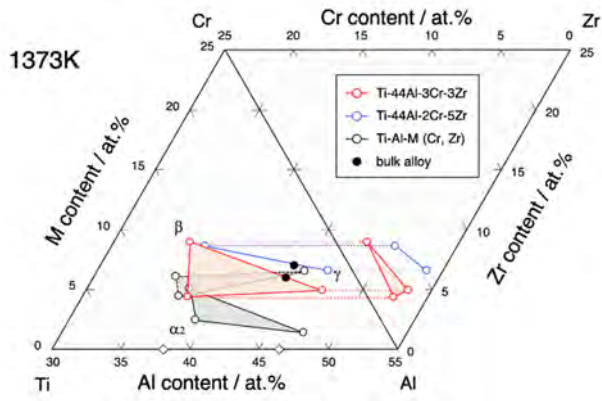


Fig. 1: The parallel projection showing analyzed terminal compositions of the phases present in the Ti-Al-Cr-Zr quaternary alloys at 1373 K together with that of Ti-Al-Cr and Ti-Al-Zr ternary systems.

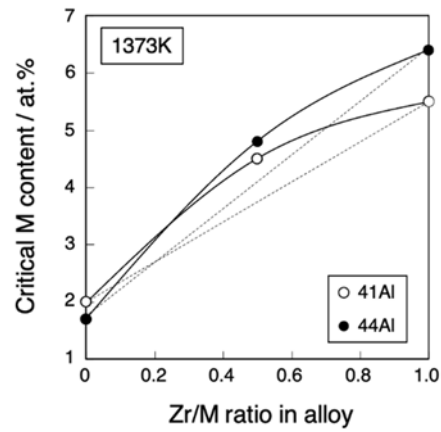


Fig. 2: Critical M contents for the formation of  $\beta$  phase with different Zr/M ratio.

References

- [1] R. Yamagata, Y. Okada, H. Wakabayashi, H. Nakashima, M. Takeyama, Microstructure Design for Enhancement of Room-temperature Ductility in Multi-component TiAl Alloys. *MRS Advances*, **2019**, 4.25-26: 1523-1529.
- [2] H. Wakabayashi, L. J. Signori, A. Shaaban, R. Yamagata, H. Nakashima, M. Takeyama, Design Approaches and Achievements of Novel Wrought TiAl Alloys for Jet Engine Applications. *MRS Advances*, **2019**, 4.25-26: 1465-1470.
- [3] H. Nakashima, Phase Equilibria in the Quaternary TiAl Alloys with the Combined Addition of Substitutional Elements — Phase Stability of High and Low-temperature  $\beta$ -Ti Phase—, PhD dissertation, Tokyo Institute of Technology, **2015**.
- [4] R. Kainuma, Y. Fujita, H. Mitsui, I. Ohnuma, K. Ishida, Phase equilibria among  $\alpha$  (hcp),  $\beta$  (bcc) and  $\gamma$  (L10) phases in Ti-Al base ternary alloys. *Intermetallics*, **2000**, 8.8: 855-867.

P-22

**On the formation mechanism of banded microstructures in electron beam melted Ti-48Al-2Cr-2Nb**

Reinhold Wartbichler<sup>1</sup>, Helmut Clemens<sup>1</sup>, Svea Mayer<sup>1</sup>, Cristian Ghibaudo<sup>2,4</sup>, Giovanni Rizza<sup>3</sup>,  
Manuela Galati<sup>3,4</sup>, Luca Iuliano<sup>3,4</sup>, Sara Biamino<sup>2,4</sup> and Daniele Ugues<sup>2,4</sup>

<sup>1</sup>Department of Materials Science, Montanuniversität Leoben, Austria, reinhold.wartbichler@unileoben.ac.at

<sup>2</sup>Department of Applied Science and Technology, Integrated Additive Manufacturing (IAM) Centre, Politecnico di Torino, Italy

<sup>3</sup>Department of Management and Production Engineering, Integrated Additive Manufacturing (IAM) Centre, Politecnico di Torino, Italy

<sup>4</sup>Consorzio Interuniversitario Nazionale per la Scienza e Tecnologia dei Materiali (INSTM), Italy

**Introduction**

Intermetallic  $\gamma$ -TiAl based alloys offer outstanding creep properties, high specific strength and sufficient oxidation resistance at application temperature in the range from 600 to 800 °C [1]. These properties make them prosperous candidates to substitute heavy Ni-based alloys offering weight savings up to 50% [2,3]. Drawbacks include their inherent brittleness as well as reactive melts, which complicate processing and drive costs [4]. In this regard, electron beam melting (EBM), a powder bed additive manufacturing technology, offers low impurity pickup due to the vacuum environment and elevated processing temperature, enabling the manufacturing of TiAl components with increased geometrical complexity [5]. Still, microstructures of electron beam melted titanium aluminides often show a banded character and suffer from Al loss due to process related evaporation decreasing room temperature ductility [6-8]. As the formation mechanism of banded microstructures in electron beam melted Ti-48Al-2Cr-2Nb (in at. % unless stated otherwise) is not yet fully understood, a scientific explanation is presented in this work.

**Materials and Methods**

Against this background, several samples of a Ti-48Al-2Cr-2Nb alloy were manufactured by EBM with a specific set of different processing parameters. Microstructures, phase composition as well as chemical distribution were investigated by scanning electron microscopy, X-ray diffraction and electron backscatter diffraction. In addition, electron probe micro-analysis was used to investigate the chemical distribution of aluminum. Location-dependent mechanical properties with regard to their processing history were studied by micro-hardness testing. Finally, all results were compared to a vertical section of the Ti-Al-Cr-Nb alloy system obtained by thermodynamic equilibrium calculations where the phase transformation temperatures were verified by thermo-mechanical analysis.

**Results and Discussion**

All samples revealed near- $\gamma$  microstructures of  $\gamma$ -TiAl,  $\alpha_2$ -Ti<sub>3</sub>Al and  $\beta_0$ -TiAl due to the intrinsic long-term annealing during the EBM process. With increasing energy input the microstructures received a banded nature with alternating layers of coarse  $\gamma$  grains and fine grained zones of  $\gamma$  and  $\alpha_2$  with traces of  $\beta_0$  due to the loss and inhomogeneous distribution of Al. These characteristics are also reflected in the local hardness, where fine grained zones of  $\gamma$  and  $\alpha_2$  reveal higher values. Due to Al loss, the overall chemistry made a shift towards the Ti-rich side of the phase diagram. This effect is reflected by a change in equilibrium phase composition and a drop of the  $T_{\alpha\text{Transus}}$  phase transformation temperature. As a consequence of the inhomogeneous Al distribution  $\alpha_2$  does preferably dissolve in Al-rich zones during the long-term annealing under formation of the near- $\gamma$  microstructure. Subsequently, secondary recrystallization, a grain coarsening effect appearing in one part of the microstructure while the other, fine-grained part is stabilized by second phase particles, takes place in Al-rich zones leading to bimodal microstructures with large  $\gamma$ -grain bands.

**References**

- [1] D.M. Dimiduk, *Materials Science and Engineering: A*. **1999**, *263*, 281–288.
- [2] A. Lasalmonie, *Intermetallics*. **2006**, *14*, 1123–1129.
- [3] Y.-W. Kim, D.M. Dimiduk, *JOM*. **1991**, *43*, 40–47.
- [4] X. Wu, *Intermetallics*. **2006**, *14*, 1114–1122.
- [5] S. Biamino, A. Penna, U. Ackelid, S. Sabbadini, O. Tassa, P. Fino, M. Pavese, P. Gennaro, C. Badini, *Intermetallics*. **2011**, *19*, 776–781.
- [6] M. Todai, T. Nakano, T. Liu, H.Y. Yasuda, K. Hagihara, K. Cho, M. Ueda, M. Takeyama, *Additive Manufacturing*. **2017**, *13*, 61–70.
- [7] A. Klassen, V.E. Forster, V. Juechter, C. Körner, *Intermetallics*. **2014**, *49*, 29–35.

P-23

**Ti-Al<sub>3</sub>Ti metal-intermetallic composite with a cubic modification of trialuminide stabilized with Ag**Daria Lazurenko<sup>1</sup>, Ivan Petrov<sup>1</sup>, Vyacheslav Mali<sup>2</sup> and Andreas Stark<sup>3</sup><sup>1</sup>Novosibirsk State Technical University, 630073 Novosibirsk, Russia, pavlyukova\_87@mail.ru, petrov.2017@stud.nstu.ru<sup>2</sup>Lavrentiev Institute of Hydrodynamics, 630090 Novosibirsk, Russia, vmali@mail.ru<sup>3</sup>Helmholtz-Zentrum Hereon, 21502 Geesthacht, Germany, andreas.stark@hzg.de**Introduction**

In recent decades, Ti-Al<sub>3</sub>Ti multilayer metal-intermetallic composites attract attention due to the unique combination of their properties [1]. For example, the specific stiffness of such materials is almost twice that of steel, the specific strength is similar or higher than that of almost all metal alloys, and the specific hardness is at the level of many ceramic materials. Also, this type of material is able to effectively resist high-speed shock loads. However, their wide application is limited by low plasticity and fracture toughness due to the extremely high brittleness of titanium trialuminide.

One of the ways to increase the fracture toughness of Al<sub>3</sub>Ti consists in alloying with transition metals intending to modify the tetragonal lattice of Al<sub>3</sub>Ti to a cubic L1<sub>2</sub> structure [2-4]. The cubic lattice has a larger number of slip systems compared to the tetragonal D0<sub>22</sub> structure, which in turn improves plasticity.

This approach was applied to modify the structure of the cast Al<sub>3</sub>Ti-based alloys and improve their plasticity [5-7]. In our previous study, we modified the structure of Al<sub>3</sub>Ti with Cu, which was part of the metal-intermetallic composite [8]. Choice of the alloying element was realized on the basis of thorough in situ X-ray synchrotron diffraction analysis which allowed to establish the reaction routes when heating together pure metallic components to 830 °C and find the elements able to stabilize the L1<sub>2</sub> structure of titanium trialuminide without formation of additional phases in the composite [9]. Apart from Cu, Ag also was found to be an element that promotes the formation of Ti-Ti(Al<sub>1-x</sub>Ag<sub>x</sub>)<sub>3</sub> at the particular heating stages.

The aim of this study was to find the appropriate sintering regimes of the Ti-Al-Ag sample. For this purpose, in situ X-ray synchrotron diffraction analysis of the Ti-Al-Ag sample heated to the temperature of 1250 °C was carried out. The temperature corresponding to the maximum fraction of the Ti(Al<sub>1-x</sub>Ag<sub>x</sub>)<sub>3</sub> solid solution in the structure of the samples can be considered as the efficient sintering temperature and can be chosen for the further fabrication of the multilayer metal-intermetallic composite by spark plasma sintering.

**Materials and Methods**

For in situ X-ray synchrotron diffraction analysis, thoroughly mixed Al, Ti, and Ag powders were prepared. The nominal composition of the mixture was Ti46-Al48.2-Ag5.8 (at. %). This ratio provided the excess of Ti in the same proportion as in the structure of multilayer Ti-Al<sub>3</sub>Ti composites. Heating was provided by the induction furnace of a modified DIL805A/D dilatometer. The samples were heated at a rate of 10 K/min up to the temperature of 1250 °C and held at this temperature for 5 minutes followed by cooling. The experiment was carried out in a high-purity argon atmosphere at a pressure of 0.8 mbar.

Diffraction patterns were obtained at Petra III synchrotron radiation source of the German Electron Synchrotron (Deutsches Elektronen-Synchrotron – DESY) in the High Energy Materials Science Beamline (P07) operated by Helmholtz-Zentrum Geesthacht. The radiation energy was 100 keV which corresponds to a wavelength of 0.124 Å. The spot size was 1×1 mm. Diffraction rings were recorded using a Perkin Elmer XRD1621 2D detector with a resolution of 2048×2048 pixels and a pixel size of 200×200 μm in transmission mode. The sample-to-detector distance was equal to 1809 mm. The Debye-Scherrer diffraction rings were continuously recorded during heating, holding, and cooling with a frequency of 0.1 Hz. The total exposition time was 4 seconds and was provided by summation of 40 frames exposed for 0.1 seconds each. Two-dimensional diffraction rings were azimuthally integrated and analyzed as typical Intensity - 2θ powder diffraction patterns.

Multilayer composites were produced by spark plasma sintering (SPS) in Lavrentiev Hydrodynamic Institute (SB RAS, Novosibirsk) using a LABOX-1575 SPS machine. Commercially pure titanium and aluminum foils were alternately stacked and interspersed by homogeneous layers of silver powder between them, and then placed in a titanium shell with an inner diameter of 26 mm. Such a set was covered with a cap with an outer diameter of 30 mm. This setup allowed performing the reactive sintering at temperatures exceeding the aluminum melting point [10]. The thickness of metallic foils was 50 μm. Sintering was performed at 930 °C under a pressure of 40 MPa for 10 minutes. The reference sample consisted of alternately stacked Ti and Al foils and was produced in the same way. However, the sintering temperature was lower (830 °C).

The microstructure of fabricated material was investigated by scanning electron microscopy (SEM) in the secondary electron mode using a Carl Zeiss EVO 50XVP microscope equipped with an X-ACT (Oxford Instruments) energy



dispersive X-ray (EDX) spectrometer. Phases formed in the MIL composite were investigated by X-ray diffraction (XRD) analysis. Diffraction patterns were recorded using an ARL X'TRA diffractometer with Cu K $\alpha$  radiation. The fracture toughness was estimated based on Vickers micro indentation tests using a Wolpert Group 402 MVD tester and during a 3-point bending test.

### Results and Discussion

Analysis of the data obtained by in situ by synchrotron X-ray radiation diffraction analysis revealed the following sequence of the reactions proceeding at the heating of the Ti-Al-Ag sample to 1250 °C. Up to a temperature of about 625 °C, phase transformations do not occur in the system. After 625 °C, the reflections corresponding to silver and aluminum disappeared simultaneously with the appearance of Al<sub>3</sub>Ti reflections. The maximum intensity of the Al<sub>3</sub>Ti reflections corresponded to the temperature of 700 °C. At further heating, the intensity of the Al<sub>3</sub>Ti reflections decreased, which was accompanied by the appearance of peaks of the L1<sub>2</sub> solid solution. Al<sub>3</sub>Ti reflections completely disappeared at 980 °C. The L1<sub>2</sub> Ti(Al<sub>1-x</sub>Ag<sub>x</sub>)<sub>3</sub> phase existed in the sample up to 1150 °C. At higher temperatures, primary phases were fully transformed to TiAl and Ti<sub>3</sub>Al with Ag dissolved in them.

Thus, the above analysis has shown that the L1<sub>2</sub> solid solution was stable in the ternary system in the temperature range from 700 to 1150 °C. However, the maximum intensity of its peaks corresponded to the temperature of 930 °C. At the same time, the intensity of the reflections of tetragonal titanium trialuminide was close to a minimum at 930 °C. Consequently, one can conclude that this temperature is the most rational for the formation of a multilayer Ti-Ti(Al<sub>1-x</sub>Ag<sub>x</sub>)<sub>3</sub> composite with the minimum fraction of additional phases.

Spark plasma sintering of the multilayer composite at 930 °C allowed to obtain a sample that consisted of Ti and Ti(Al<sub>1-x</sub>Ag<sub>x</sub>)<sub>3</sub> layers with Ag-rich inclusions at the grain boundaries (Fig. 1). XRD analysis revealed that these inclusions corresponded to the Ag<sub>2</sub>Al compound. The excess of Ag in the intermetallic layers resulted from the squeezing of Al from the reaction zone when sintered at such a high temperature. However, in spite of the formation of an additional intermetallic phase, the fracture toughness of the sample, alloyed with Ag increased compared to the reference sample.

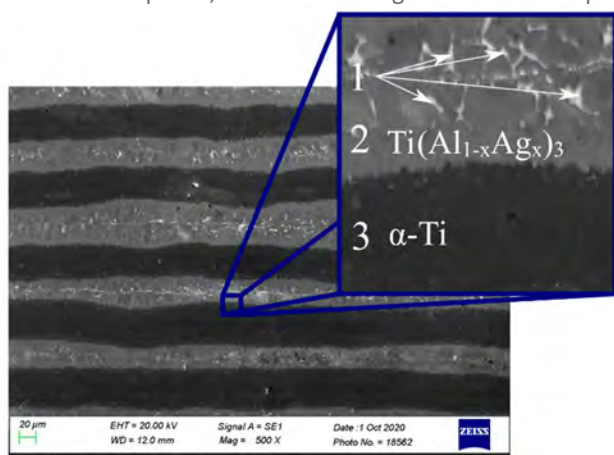


Fig. 1: The structure of the Ti-Ti(Al<sub>1-x</sub>Ag<sub>x</sub>)<sub>3</sub> composite obtained by spark plasma sintering

### References

- [1] K.S. Vecchio, JOM. **2005**, 57 (3), 25-31.
- [2] D.E. Mikkola, J.P. Nic, S. Zhang, W.W. Milligan, ISIJ International. **1991**, 31 (10), 1076-1079.
- [3] M. Kogachi, S. Minamigawa, K. Nakahigashi, Scripta Metallurgica et Materialia. **1992**, 27(4), 407-412.
- [4] J.P. Nic, S. Zhang, D.E. Mikkola, Scripta Metallurgica et Materialia. **1990**, 24(6), 1099-1104.
- [5] M.B. Winnicka, R.A. Varin, Scripta Metallurgica et Materialia. **1990**, 24, 611-615.
- [6] M.B. Winnicka, R.A. Varin, Scripta Metallurgica et Materialia. **1989**, 23, 1199-1202.
- [7] R. Lerf, D.G. Morris, Acta Metallurgica et Materialia. **1991**, 39, 2419-2430.
- [8] D.V. Lazurenko et. al, Materials & Design. **2018**, 151, 8-16.
- [9] D.V. Lazurenko et. al, Journal of Alloys and Compounds, in press.
- [10] D.V. Lazurenko et. al, Metallurgical and Materials Transaction A. **2015**, 46, 4326-4334.

**P-24**

**Investigation of the formation processes of intermetallic compounds based on titanium aluminide in the preparation of a composite material reinforced with fibers SiC**

Alexander S. Lenkovets, A.Yu. Oleshko, G.D. Skosirskaya, R.E. Khvostov  
and A.P. Galantsev

JSC «Kompozit», 141076 Korolev, Russian Federation, info@kompozit-mv.ru

**Introduction**

Intermetallic compounds based on aluminum titanium are actively used in aerospace engineering. One of the promising materials is the use of intermetallic compounds for strengthening the matrix material in metal composite materials reinforced with fibers SiC.

**Materials and Methods**

Aluminum alloy AD1 (99.9% Al) and titanium alloy VT1-0 (99.9% Ti) were used as the matrix material. For hardening, silicon carbide monofilaments produced by JSC " GNIICHTEOS" with a strength of at least 3000 MPa were used. The measurement of the lattice parameter and the phase analysis of titanium aluminide were carried out on a DRON-4 diffractometer using CoK $\alpha$  radiation. The study of the microstructure and chemical composition was carried out using a scanning electron microscope.

**Results and Discussion**

According to the standard technology used in [4], samples of a composite material matrix were obtained, which consists of layers of titanium and aluminum containing silicon carbide fibers. Metallographic studies of the obtained samples of the composite material showed the presence of an intermetallic Ti<sub>3</sub>Al interlayer formed as a result of hot pressing, which contributes to the limit of tensile strength. Data on the mechanical properties of the composite material are presented in Table 1.

Thus, on the basis of the studies carried out, it can be concluded that the use of intermetallic compounds based on titanium aluminides for use in composite metal materials reinforced with silicon carbide fibers can be drawn.

Name MKM component	Volumetric content of a component in MCM,V, %	Component material strength, MPa	Calculated value of tensile strength, MPa	Experimental value of MCM ultimate strength, MPa
Metal composite BT1-0 – AD1 – SiC				
Matrix alloy VT1-0	40	500	892*	~934
Matrix alloy AB1	25	100		
Fibers SiC	35	3000		

\* taking into account the coefficient of loss of strength K = 0,7

Table 1: Mechanical properties of composite material depending on the volume fraction of components.

**References**

- [1] J. Liu, M. Dahmen, V. Ventzke, N. Kashaev, R. Poprawe, The effect of heat treatment on crack control and grain refinement in laser beam welded betasolidifying TiAl-based alloy. *Intermetallics*. **2013**, *40*, 65-70.
- [2] S. Simoes, F. Viana, M. Kocak, A.S. Ramos, M.T. Vieira, M.F. Vieira, Microstructure of reaction zone formed during diffusion bonding of TiAl with Ni/Al multilayer. *J. Mater. Eng. Perform.* **2012**, *21*, 678-682.
- [3] Pat. US 8,784,065 B2, United States, Friction welding of titanium aluminide turbine to titanium alloy shaft / Yang et al.; Caterpillar Inc., Filed: May 24, **2011**. Prior pub. Nov. 29, 2012.
- [4] S. Kyle-Henney, S. Flitcroft, R. Shatwell, D. Gibbon, G. Voss, P. Harkness, carbide monofilament reinforced titanium composites for space structures a new material option. Proc. '12<sup>th</sup> European Conference on Space Structures, Material & Environmental Testing' Noordwijk, The Netherlands, 20-23 March 2012 (ESA SP-691, Juli **2012**).

P-25

### Screening for O phase in $\gamma$ -TiAl alloys

Marcus W. Rackel, Andreas Stark, Heike Gabrisch and Florian Pyczak  
Helmholtz-Zentrum Hereon, 21502 Geesthacht, Germany, marcus.rackel@hereon.de

#### Introduction

In  $\gamma$ -based TiAl alloys alloying is performed to improve the mechanical properties, oxidation resistance and process ability. In particular,  $\beta$ -stabilising elements such as niobium, molybdenum or vanadium and minor alloying (interstitial) elements such as carbon, silicon or boron are used to improve the aforementioned alloy properties. Alloying has the consequence that the alloy's properties, as well as the phase constitution, chemistry and transition temperatures of the major phases change significantly. It is also possible that new phases form. Recently, the formation of an orthorhombic phase, namely the O phase, was observed using high-energy X-ray diffraction (HEXRD) experiments in a Ti-42Al-8.5Nb alloy [1, 2]. The present O phase has a Cmc<sub>2</sub>m structure and is known to have a stoichiometric composition of Ti<sub>2</sub>AlNb. In the investigated Ti-42Al-8.5Nb alloy, the chemical composition differs from the ideal stoichiometric one. The O phase forms out of the parent  $\alpha_2$  phase at temperatures below 700 °C by small displacements of atom positions along  $\langle 11-20 \rangle$  directions of the hexagonal lattice plane.

The alloy composition Ti-42Al-8.5Nb is not far away from  $\beta$ -stabilized TiAl alloys that are actually in service as for example TNM<sup>®</sup>. In addition, 700 °C is well within the range of typical operation temperatures of parts made from those alloys. Insofar it is interesting for applications whether such an orthorhombic phase does also form in other  $\gamma$ -based TiAl alloys. In the present study a series of  $\gamma$ -TiAl alloys is screened by HEXRD for signs of O phase. The emergence of the O phase is clearly evident in HEXRD measurements by the splitting of former  $\alpha_2$  20-20 and  $\alpha_2$  20-21 peaks. In order to investigate the causes and circumstances of the orthorhombic phase formation, 13 alloy compositions were chosen that are either close to compositions of commercial alloys or that allow to identify the effects of different single alloying elements on the orthorhombic phase formation.

#### Materials and Methods

The 13 investigated alloys in the composition range of Ti-(42-48) Al-(0.1-10) X (X = one or more elements of Nb, Mo, Mn, V, Ta, Cr, C, B, Si) were produced by either powder metallurgy, casting or casting or hot extrusion. For further details the reader is referred to [1].

The material was annealed in a high-temperature furnace in air. All specimens (two specimens for each composition) were held at 700 °C for 5 hours and subsequently air cooled (named reference state). After the first heat treatment a second heat treatment was performed with the respective second samples at 550 °C for 20 hours followed by subsequent furnace cooling. The samples were measured with HEXRD in both heat treatment conditions at the High Energy Materials Science beamline (HEMS) operated by Helmholtz Center Hereon at PETRA III at the Deutsches Elektronen-Synchrotron (DESY), Hamburg, Germany. The measurements were performed at room temperature, in transmission using a beam size of 0.5 mm by 0.5 mm and a photon energy of 87.1 keV ( $\lambda = 0.14235 \text{ \AA}$ ). During the HEXRD, experiments the Debye-Scherrer diffraction rings were recorded on a Perkin Elmer XRD 1621 flat panel detector (pixel size 200 by 200  $\mu\text{m}$ ). An exposure time of 0.2 s was used and 20 images were collected and summed up for each specimen to increase the dynamic range of the detector. The analysis was performed using the program Fit2D [3] and MAUD[4].

#### Results and Discussion

In the majority of the investigated  $\gamma$ -TiAl alloys an orthorhombic phase with Cmc<sub>2</sub>m structure does form after aging heat treatment at 550 °C for 20 h. Alloying with Nb, Mo, Ta, V, shows that either a minimum amount of a single element or a combination of alloying elements above a specific threshold can cause an orthorhombic phase formation in TiAl alloys. Niobium is one of the most commonly used alloying elements in  $\gamma$ -based TiAl alloys. For niobium the threshold lies between 5 and 7.5 at.%. The finding that the O phase can form in vanadium containing alloys (Ti-45Al-8V) is new.

Aluminium is the alloying element with the most significant influence on the phase constitution and solidification path of TiAl alloys. For aluminium an upper limit was also found, below which the orthorhombic O phase is formed when a sufficiently high amount of  $\beta$ -stabilising elements is present. This limit lies between 46 and 47 at.%. However, it must also be mentioned that with increasing aluminium content, the phase fraction of the parent  $\alpha_2$  phase ( $\approx 2 \text{ vol.-%}$ ) is significantly reduced. Moreover,  $\alpha_2$  is the parent phase from which the O phase forms. Based on the current observations, it cannot yet be clearly determined whether the precipitation kinetics decrease at higher Al-content or whether the stability limit of the O phase with respect to Al content has been exceeded.

Furthermore, it was observed that micro alloying by (interstitial) elements such as carbon (C) or boron (B) has no effect on O phase formation [1]. This is surprising, as for example carbon is known as a strong  $\alpha$  and  $\alpha_2$  stabilising element that shows a strong influence on the phase constitution. By comparing an alloy with carbon (Ti-42Al-8.5Nb-0.2C) with an alloy without

carbon (Ti-42Al-8.5Nb) we find that equivalent proportions of O phase have formed from  $\alpha_2$  phase after temperature exposure at 550 °C for 20 h.

a) Ti-48Al-45Nb-4Ta alloy, no O phase formation.

b) Ti-45Al-7.5Nb alloy, O phase formation.

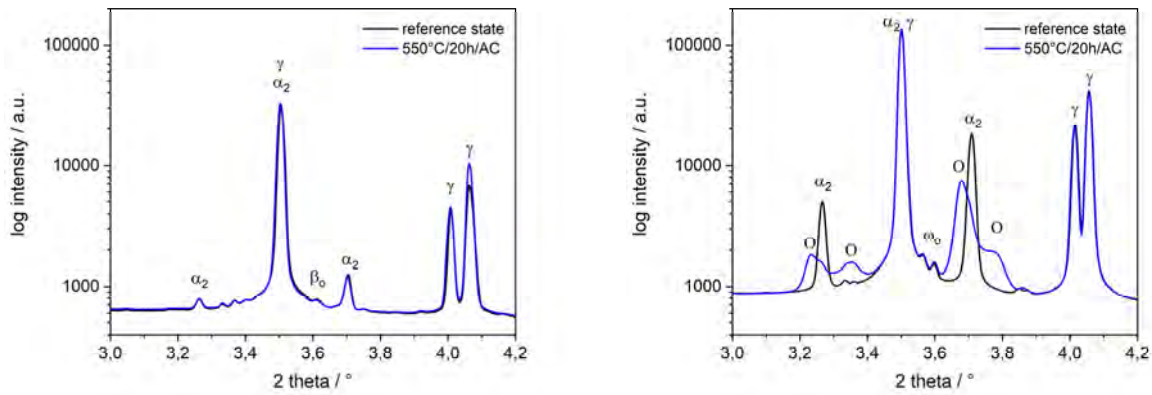


Fig. 1: Diffraction pattern derived from HEXRD measurements. Black curve reference state, blue curve after temperature exposure at 550 °C for 20 h.

**References**

[1] M. W. Rackel et al., Screening for O phase in advanced  $\gamma$ -TiAl alloys. *Intermetallics*. **2021**, *131*, 107086.  
 [2] M.W. Rackel et al., Orthorhombic phase formation in a Nb-rich  $\gamma$ -TiAl based alloy – An *in situ* synchrotron radiation investigation. *Acta Mater*. **2016**, *121*, 343-351.  
 [3] A. P. Hammersley, FIT2D: An Introduction and Overview. ESRF Internal Report. **1997**.  
 [4] L. Lutterotti, Total pattern fitting for the combined size-strain-stress-texture determination in thin film diffraction. *Nuclear Instruments and Methods in Physics Research, Section B: Beam Interactions with Materials and Atoms*. **2010**, *268(3-4)*, 334-340.

P-26

## Oxidation protection of Ni-base superalloys by the F-effect – fundamentals for industrial application

Hans-Eberhard Zschau<sup>1</sup>, Alexander Donchev<sup>2</sup>, Mathias C. Galetz<sup>2</sup>

<sup>1</sup>Werkstoffprüfung und -forschung, 04808 Wurzen, Germany, dr.zschau@hotmail.com

<sup>2</sup>DECHEMA-Forschungsinstitut, 60486 Frankfurt, Germany, alexander.donchev@dechema.de, mathias.galetz@dechema.de

### Introduction

Ni-base superalloys with Al-amounts between 2-5 wt.% possess good mechanical properties as materials for high temperature technology, whereas Al-rich coatings must be applied to overcome the insufficient oxidation resistance at temperatures above 950 °C. Recently an alternative way based on the halogen (fluorine) effect was proposed [1] allowing the formation and growth of a dense protective alumina scale by using the relatively low Al-content of the alloy as reservoir. A thermodynamic model was developed explaining this fluorine effect for Ni-base alloys. Beam line ion implantation was used for screening of the F amount to verify the conditions predicted by the thermodynamic model and to investigate the long-term behavior of the oxidation protection under isothermal and cyclic conditions. In this paper the results obtained with ion implantation are summarized. The results serve as a benchmark to determine the optimized parameters for alternative fluorination methods. A comparison with the F-effect for TiAl-alloys is discussed.

### Change of the Oxidation Mechanism for Ni-base alloys via the F – Effect

Oxidation of Ni-base alloys does not lead to the formation of a protective continuous pure alumina scale on the surface, but rather a complex layered structure of spinel phases and a significant amount of internal oxidation is formed (fig. 1, top). The change in alumina formation from a discontinuous internal to a continuous dense protective external oxide scale can be achieved by an “artificial” increase of the Al-activity on the surface. This can be realized by using the fluorine effect. Thermodynamic calculations showed the existence of a region for a positive fluorine effect for the Ni-based alloy IN 738 at temperatures between 900-1200 °C [2]. These results had to be transformed into fluorine concentrations by a screening using ion implantation. Samples of IN 738 with dimensions (10 x 10 x 2) mm<sup>3</sup> were polished down to 4000 grit SiC. F-fluences were implanted between 10<sup>16</sup> and 4 x 10<sup>17</sup> F/cm<sup>2</sup>. The chosen ion energy of 38 keV corresponds to a projected range of ca. 35 nm depth. Prior to implantation the F-depth profiles were calculated by using the Monte Carlo code T-DYN [3]. The implanted F-depth profiles can be measured by using non-destructive Proton Induced Gamma-ray Emission analysis (PIGE). After oxidation at 1050 °C for 24 – 60 hours in air, post oxidation studies were performed. The prepared metallographic cross-sections reveal the oxide structures. The untreated sample shows a non-protective internal growing alumina scale (fig 1, top). For some implanted samples, the oxidation mechanism was changed into the formation of a dense protective external alumina scale (fig. 1, bottom). This occurred within an interval of fluences between 5 x 10<sup>16</sup> and 1 x 10<sup>17</sup> F/cm<sup>2</sup> (fig. 2) or – in terms of concentration – for maximal F-amounts between 10 – 15 at.%.

The long term behavior of the oxidation protection was confirmed for oxidation times up to 1000 h at 1050 °C in air for isothermal and cyclic conditions.

### Comparison with the F-effect for γ-TiAl-alloys

The F-effect also works for TiAl-alloys with Al-contents between 40 - 50 at.% Al. The optimal value for the maximal F-amount is about 40 at.% F in a depth of ca. 35 nm. This corresponds to a fluence of 2 x 10<sup>17</sup> F/cm<sup>2</sup> for F-ions implanted with energy of 20 keV [2]. After oxidation at 900 °C for 12 – 24 hours in air a dense protective alumina scale is established on the surface.

### Conclusions for alternative fluorination methods of Ni-base alloys

Any other process of fluorination (e. g. via liquid or gas phase) should realize a fluorine enrichment as illustrated in fig. 2. Of course, a diffusion F-profile will be expected in contrast to the implanted profiles, as shown for TiAl-alloys [4]. However, the key parameters are a maximal F-concentration of ca. 10...17 at.% F and an integral F-dose between values of 5 x 10<sup>16</sup> and 1 x 10<sup>17</sup> F/cm<sup>2</sup>.



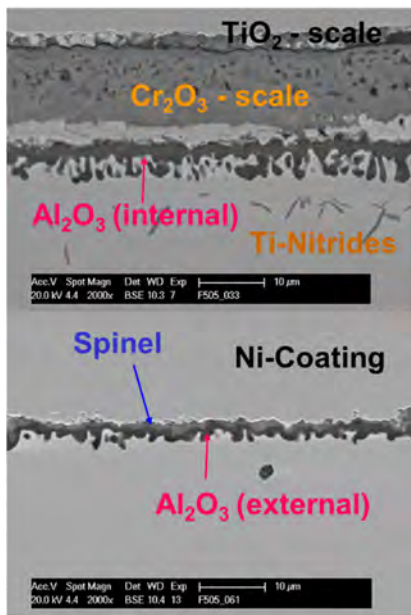


Fig.1: Oxide scale on IN738.  
 Top: Untreated after oxidation (48h/1050°C/air),  
 Bottom: F-Implanted ( $10^{17}$  F/cm<sup>2</sup>) after oxidation (60h/1050°C/air).

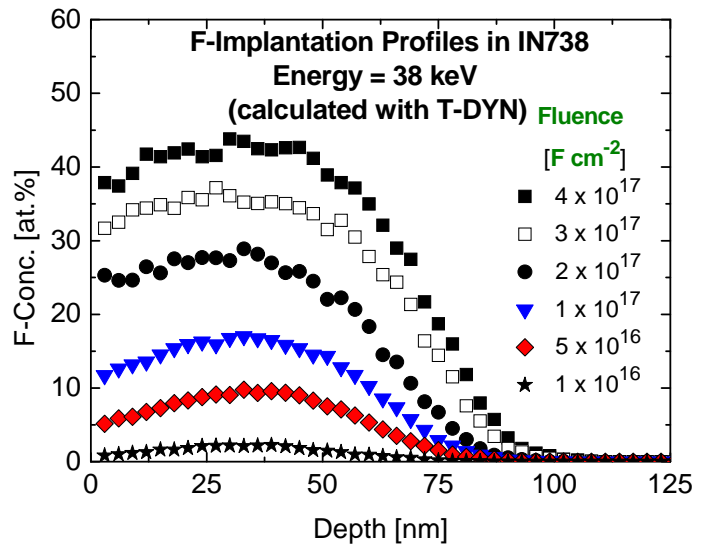


Fig. 2: F-depth profiles within IN 738 calculated with Monte Carlo code T-DYN [3]. A positive fluorine effect was found for fluences between  $5 \times 10^{16}$  and  $1 \times 10^{17}$  F/cm<sup>2</sup>.

**References**

- [1] H.-E. Zschau, D. Renusch, P. Masse, M. Schütze, *Materials at High Temperatures*. **2009**, *26*, 85-89.
- [2] H.-E. Zschau and M. Schütze, in: Mark S. Goorsky (Ed.): *Ion Implantation*. InTech, Rijeka, **2012**, 409-436.
- [3] J. Biersack, *Nucl. Instr. & Meth. in Phys. Res.* **1999**, *B 153*, 398-409.
- [4] H.-E. Zschau, B. Möller, D. Emig, D. Hipper, A. Donchev, M.C. Galetz, *Proceedings Intermetallics 2019*; Eds. M. Heilmaier, M. Krüger, S. Mayer, M. Palm, F. Stein; Conventus Congressmanagement & Marketing GmbH, Jena, Germany (2019) ISBN 978-3-948023-07-2, 90-91.

P-28

## Formation of intermetallic $\alpha_c$ -Al-(Fe,M)-Si and $\beta$ -Al-(Fe,M)-Si phase in presence of 3d-transition metal elements $M$ in Fe-containing secondary Al-Si casting alloys

Hanka Becker, Lukas Richter and Andreas Leineweber

Institute of Materials Science, TU Bergakademie Freiberg, 09599 Freiberg, Germany, hanka.becker@iww.tu-freiberg, lukas.richter2@student.tu-freiberg.de, andreas.leineweber@iww.tu-freiberg.de

### Introduction

Fe is regarded as the most harmful metallic impurity element in secondary, i. e. recycled, Al-Si-casting alloys. This is attributed to the formation of intermetallic phases in presence of Fe. Especially plate-shaped  $\beta$ -Al-(Fe,M)-Si phase particles have harmful effects on the mechanical and casting properties [1]. The  $\alpha_c$ -Al-(Fe,M)-Si can solidify in various morphologies from coarse polyhedral to fine dendritic or irregular, often called Chinese-script, shaped particles [2] depending on the presence of transition metal elements  $M$  and solidification conditions. Thereby, removal of large compact Fe-containing  $\alpha_c$ -particles can efficiently reduce the Fe-content in the secondary Al-Si-casting alloys while the fine  $\alpha_c$ -particles have less detrimental effect on the mechanical properties. As small amounts of transition metal elements such as 0.3 at% Mn and 0.03 at% Cr are known to promote the formation of the  $\alpha_c$  phase at the expense of the  $\beta$  phase [3]. High cooling rates can enhance the effect. Thereby, the  $\alpha_c$  phase is a ternary phase of the Al-Si-Mn system with a large homogeneity range towards Fe and a quaternary phase of the Al-Si-Cr-Fe system [4].

Most technical relevant Al-Si-casting alloys contain further transition metal elements as alloying or impurity elements. In literature it is unclear if or to which extent their presence affects the formation of the  $\alpha_c$  and  $\beta$  phase. Thermodynamic calculations cannot simulate these effects as especially the  $\alpha_c$ -Al-(Fe,M)-Si is, due to the lacking knowledge, not or inaccurately implemented in the currently existing data bases. In the present study, the effect of 3d-transition metal elements on the formation or suppression of  $\alpha_c$ - and  $\beta$ -phase is approached by investigation of the quaternary Al-Si alloys with Fe and  $M$ . Thus, this understanding contributes to the targeted production of Fe-containing secondary Al-Si alloys with unproblematic intermetallic particles.

### Material and Methods

In the present study, the intermetallic phase formation in AlSi7.1at%(1.5at%-x)FexM alloys with  $x = 0, 0.3, 0.375, 0.6, 0.75$  at% and  $M = V, Cr, Mn, Co, Ni, Cu$  and  $Zn$  was investigated. The alloys were produced by arc melting from the pure elements and then remolten at 850°C in Ar atmosphere in Al<sub>2</sub>O<sub>3</sub> crucibles. Subsequently, cooling rates of 0.05, 1.4, 11.4 K/s and melt conditioning, i. e. furnace cooling to 620°C and holding for 1 h followed by quenching, were applied. The microstructures with focus on the intermetallic phases of all samples was scrutinized using scanning electron microscopy including energy dispersive X-ray spectroscopy and electron backscatter diffraction (EBSD).

### Results and Discussion

The microstructures contain three main types of intermetallic particles in view of the general morphology: plate-shaped, coarse polyhedral and Chinese-script particles. Plate-shaped  $\beta$ -Al-(Fe,M)-Si particles have formed in presence of all tested alloying elements and slow cooling rates (Tab. 1). However, its formation can be suppressed in presence of sufficient amounts of  $M$  and application of high cooling rates in favor of the formation of the  $\alpha_c$  phase with  $M = Mn, Cr$  and  $V$  and the  $\tau_1$ -(Al,Si)-(Fe,M) phase with  $M = Co$  and  $Ni$  (Fig. 1).  $Cu$  and  $Zn$  do not suppress the  $\beta$  phase. The content of other transition alloy elements than Fe is generally low in the  $\beta$  phase. Thus, efficiently  $\beta$  phase-suppressing transition metal elements must lead to the formation of suitable other Fe- and  $M$ -containing intermetallic phases during solidification. Due to the comparably higher solubility of  $Cu$  and  $Zn$  in the Al-solid solution, these elements do not suppress the  $\beta$  phase formation during solidification although subsequent heat treatment might transform the  $\beta$  phase into other phases [5].

In the investigated compositional range of Al-Si-casting alloys, next to Fe, presence of  $V, Cr$  or  $Mn$  is necessary to form the  $\alpha_c$  phase. Thereby, the  $\alpha_c$  phase is identified as a truly quaternary phase occurring in the Al-Si-Fe-V and Al-Si-Fe-Cr systems. According to the measured chemical composition, the transition metal elements can substitute for each other in a wide range. Additionally, variation of the Si content with  $V, Cr$  or  $Mn$  content hints at electron-contributions on the phase stability. A first model for the description of the homogeneity range of the  $\alpha_c$  phase is suggested. Prospectively, this will be used for implementation of the  $\alpha_c$  phase in thermodynamic data bases.

The morphology of the  $\alpha_c$  phase varied from coarse polyhedral particles to particles with Chinese-script morphology (Fig. 1 (a-c)). It must be pointed out that these morphologies can easily lead to misidentification of the  $\alpha_c$  phase in other systems e. g. with  $Co$  and  $Ni$  in which similar morphologies can be observed (Fig. 1 (d)). Due to the wide homogeneity range of the  $\alpha_c$ -phase also chemical compositions can be misleading. Therefore, it is recommended to use complementary methods such as EBSD for phase identification.

Finally, the systematic knowledge on the effect of the 3d-transition metal elements on the intermetallic phase formation with focus on the  $\alpha_c$ - and  $\beta$ -phase contributes to dealing with Fe-impurities in technical Fe-containing secondary Al-Si alloys.

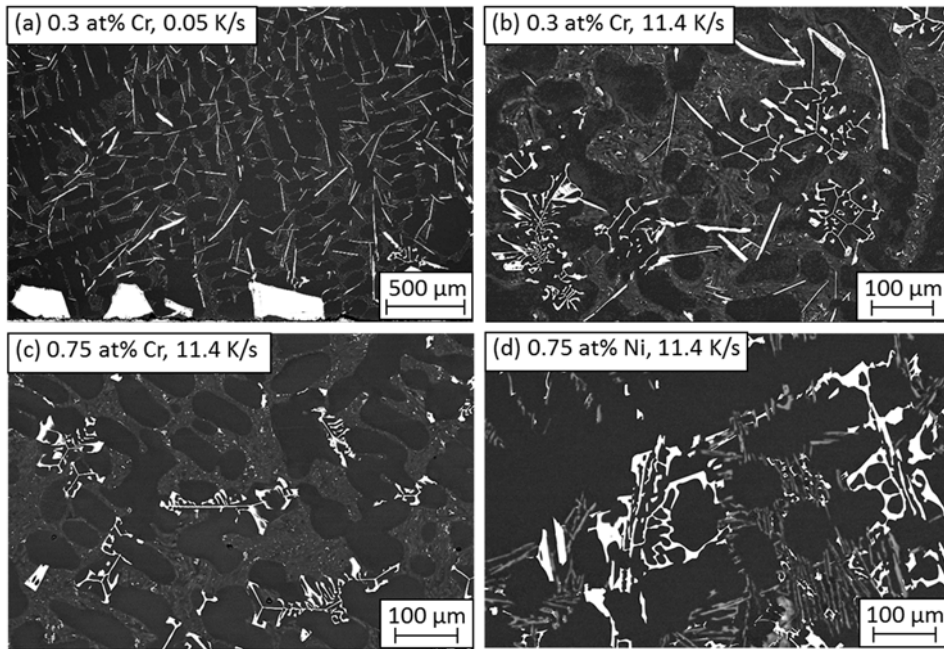


Fig 1: Exemplary microstructures of AlSi7.1at%(1.5at%-x)FexM alloys with (a-c)  $M = \text{Cr}$  and (d)  $M = \text{Ni}$ . The microstructures in (a-c) show plate-shaped  $\beta$  particles and  $\alpha_c$  particles in (a) coarse polyhedral morphology and in (b), (c) Chinese-script morphology. In (d) particles in Chinese-script morphology are illustrated which are identified as  $\tau_1$ -(Al,Si)-(Fe,M) phase.

AlSi7.1at%(1.5at%-x)FexM	$M =$						
	V	Cr	Mn	Co	Ni	Cu	Zn
$\beta$ phase	✓	✓	✓	✓	✓	✓	✓
$\alpha_c$ phase	✓	✓	✓	-	-	-	-

Table 1: Occurrence of  $\alpha_c$  and  $\beta$  phase in Fe-containing Al-Si alloys with 3d-transition metal elements  $M$ . Note that besides the  $\alpha_c$  and  $\beta$  phase presence of other intermetallic phases is not indicated.

**References**

[1] T. O. Mbuya, B.O. Odera, S. P. Ng'ang'a, International Journal of Cast Metals Research. **2003**, 16, 451–465.  
 [2] H. Becker, D. Irmer, A. Leineweber, O-IA-05 p. 132, In: Proceedings Intermetallics. **2019**, Eds. M. Heilmaier, M. Krüger, S. Mayer, M. Palm, F. Stein; Conventus Congressmanagement & Marketing GmbH, Jena, Germany (2019) ISBN 978-3-948023-07-2.  
 [3] L. Zhang, J. Gao, L.N.W. Damoah, and D.G. Robertson: Mineral Processing and Extractive Metallurgical Review. **2012**, 33, 99–157.  
 [4] H. Becker, A. Thum, B. Distl, M. J. Kriegel, A. Leineweber, Metallurgical and Materials Transactions A. **2018**, 49, 6375–6389.  
 [5] C. B. Basak, N. Hari, Scientific Reports. **2017**, 7, 5779, 1–10.

P-29

## Interface layer in Al-steel clad strip prepared by twin-roll casting

Michaela Šlapáková<sup>1</sup>, Barbora Křivská<sup>1</sup> and Olexandr Grydin<sup>2</sup>

<sup>1</sup>Charles University, Faculty of Mathematics and Physics, Department of Physics of Materials, 121 16 Prague 2, Czech Republic, slapakova@karlov.mff.cuni.cz

<sup>2</sup>Paderborn University, Chair of Materials Science, 33098 Paderborn, Germany

### Introduction

Joining of aluminum and steel sheets enables to obtain material combining low weight with high strength, which are very attractive properties for structural applications in many branches of industry [1,2]. An alternative way to produce clad sheet materials is twin-roll casting (TRC). An advantage of this type of fabrication is based on a direct preparation of the clad sheet from a melt of one metal and a solid strip of the other one which are fed simultaneously between cooled rolls of a twin-roll caster. Number of steps of the surface preparation is partially reduced compared to roll bonding [3].

When the clad material is subjected to a thermal exposure during manufacturing of a final product, diffusion between the metals is enhanced and undesirable formation of a brittle Al-Fe rich intermetallic layer (IMC) can be initiated, resulting in deterioration of mechanical properties of the composite [4,5].

### Materials and Methods

The aluminum–steel clad sheet was twin–roll cast in laboratory conditions. A melt of a technical pure aluminum EN AW-1070 was fed simultaneously with strip of solid austenitic steel type 1.4301/304 L into the caster, creating 2.5 mm thick strip with Al:Fe ratio 4:1. The clad material was subjected to isochronal annealing up to 600 °C. The microstructure development was monitored by scanning (SEM) and transmission electron microscopy (TEM) and by X-ray computed tomography (XCT). The mechanical properties were evaluated by the means of tensile tests and resistivity measurements.

### Results and Discussion

After casting, no intermetallic layer was observed in the material. Its formation was documented during isochronal annealing. The growth of the layer was unhomogeneous, which was documented by both in-situ annealing in TEM (Fig. 1) and X-ray computed tomography, which allows 3-dimensional observation of the layer. The in-situ annealing in TEM has also shown, that the IMC layer grows parabolically into the steel side, which is in contradiction with the observation in SEM, which indicate growth into the aluminum side. The main constituents of the IMC layer formed on the interface were identified as  $\text{Al}_5\text{Fe}_2$  and  $\text{Al}_{13}\text{Fe}_4$ . The isochronal annealing did not influence the tensile properties of the material, only slight decrease of the ductility with increasing the annealing temperature was observed. According to measurement of electrical resistivity [6], the most resilient bond between the Al and steel layer should be present the material heat treated up to 350 °C, where the bond was enhanced by diffusion, but no detrimental layer was formed on the interface.

### Acknowledgments

The financial support of projects GAČR 20-00355Y, SVV-260582 and DFG SCHA 1484/21-1 is highly acknowledged.

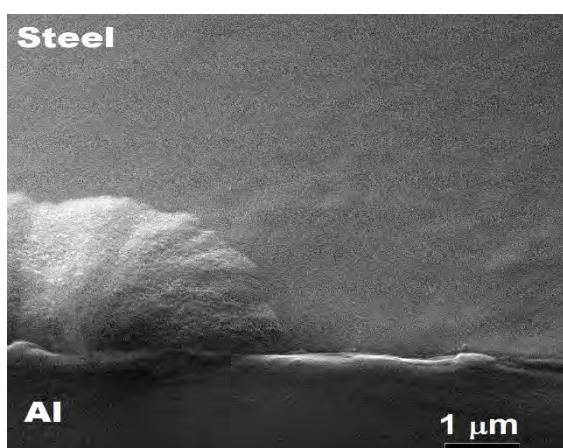


Fig. 1: Al-Fe interface after in-situ annealing in TEM to 420 °C with forming intermetallic layer

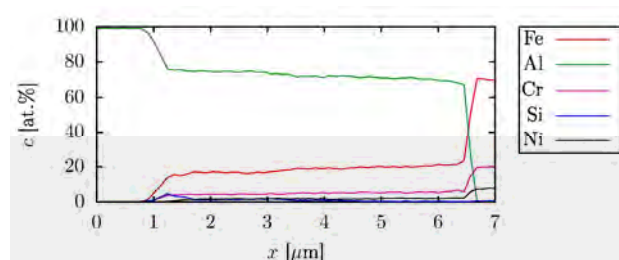


Fig. 2: EDX line chemical analysis of Al-Fe interface

### References

- [1] P. Groche, S. Wohletz, M. Brenneis, C. Pabst and F. Resch, *J. Mater. Process. Technol.* **2014**, *214*, 1972–1994
- [2] O. Grydin, G. Gerstein, F. Nürnberger, M. Schaper and V. Danchenko, *J. Manuf. Process.* **2013**, *15*, 501–507
- [3] K. Khaledi, S. Rezaei, S. Wulfinghoff and S. Reese, *Int. J. Solids Struct.* **2018**, *160*, 68–79
- [4] A. K. Prasada Rao, K. H. Kim, J. H. Bae, G. T. Bae, D. H. Shin and N. J. Kim, *Mater. Sci. Forum.* **2009**, 618–619 467–471
- [5] J. H. Bae, A. K. Prasada Rao, K. H. Kim and N. J. Kim, *Scr. Mater.* **2011**, *64*, 836–839
- [6] H. Manesh, *Materials Science and Technology.* **2006**, *22*, 634–640.

P-30

**Production, optimization and investigation of cast FeAlNb parts**Michael Ghosh and Heiner Michels

Access e.V., 52072 Aachen, Germany, m.ghosh@access-technology.de, h.michels@access-technology.de

**Introduction**

The further development and characterization of components from several Fe-Al alloys by different production routes is the main topic in 'Pro-FeAl' [1,2], a German government funded research project with 4 industrial and 3 scientific partners. Results of the activities carried out in the project at Access e.V. during the last 2 years for producing, optimizing and characterizing of FeAlNb-castings are presented. The castings are intended for further processing/completion by forging and in the long term their use in conventional power plants is envisaged. Both the production by gravity casting in permanent moulds under normal pressure and the investigations of the casting-parts are addressed here. For the comparison and analysis of the manufacturing process, the temperature course in the crucible before and in the casting part after casting is utilised. In addition, the simulation supported optimization of the casting process is presented. The experimental focus of the work is based on a bundle of investigations carried out at the cast parts:

- Computer Tomography (CT): porosity, contraction cavity, cracks, inclusions
- Light microscopy: grain structure
- Scanning electron microscopy (including EDX): grain structure, phases, inclusions, alloy composition and trace elements
- Chemical analysis: alloy composition and chemical impurities
- 3D-Scanner: dimensions of casting components

These investigations do not only characterize the quality, but also create the possibility to investigate causal relationships between process parameters and properties of the casting parts. Their behaviour in the forging process and the properties of the forged parts produced from them are examined by other project partners, so that the main results are only briefly listed here.

**Materials and Methods**

The production of FeAlNb casting samples with a composition ratio of 73.0 : 25.0 : 2.0 (at.-%) was mainly done in an induction-powered, continuously argon-rinsed roll-over oven (manufacturer: Inductotherm Europe Ltd.), in which the alloy components are molten stepwise in an Al<sub>2</sub>O<sub>3</sub>-crucible: First, iron (purity 99.9 %) is liquefied, then Al<sub>2</sub>ONb80 (wt.-%) (purity 99.9 %) or alternatively niobium (purity: 99.9 %) is dissolved in the iron-melt and finally aluminium (purity 99.98 %) is added. After a runner-mould-combination is fixed on the oven table directly above the crucible and when the melt reaches a specified temperature (around 1500°C), the table is rotated by 180 ° using a previously simulation-optimized tilting program so that the melt flows smoothly through the runner into the mould. Two different moulds are used:

- Double mould for simultaneously producing two pre-contoured forging blanks of identical shape as starting components for a combined casting-forging route (initial weight mostly around 5.5kg)
- Mould for the production of a cylindrical casting as a starting component of the monolithic forging route (initial weight around 3.5kg)

In order to enable a rapid cooling and thusly producing a fine grain structure, both moulds are made of copper, providing high thermal conductivity. Both runners are made of cast iron to keep temperature loss minimal while the melt passes through the runner. In the course of the project, the following measurements were established for process monitoring and characterization: With a thermocouple attached to the inner crucible wall the temperature at the bottom of the crucible during heating and melting is measured, and with a thermocouple that grows into the feeder of the cast part, its temperature course is recorded locally during the solidification and cooling process. The MAGMA5 simulation software was used to optimize individual process phases with respect to different requirements:

- Tilting: Smooth form filling
- Solidification: Directional solidification with low porosity in the component part of the casting
- Cool down: Uniform cooling to reduce thermal stresses

To characterize the cast parts, CT and 3D scans are carried out. Investigations by means of light and scanning electron microscopy are carried out on stepwise polished slices, which are prepared from the feeder of the cast parts by water jet.

**Results and Discussion**

The cast parts produced generally have a smooth surface with only non-critical irregularities (small sink marks and only in exceptional cases hairline cracks in the component area). 3D scans of the components produced by removing the feeder show only a slight deviation in dimensional accuracy from the CAD model of the component (1 to 2 mm surface difference). By CT, in the cast parts porous areas and cavities of different size become visible (Fig. 1): per forging blank between 100 and 2500 features with a median size between 0.01 and 0.02 mm<sup>3</sup> and a maximum value from 5 to 80 mm<sup>3</sup> are detected. In the case of



centerline porosity, simulations suggest that the cause is insufficient melt supply during solidification. In some cast parts, centimetre long hairline cracks are also visible in the CT examinations. Nevertheless hairline cracks, porous areas and cavities did not cause any negative consequences in the later forging process at project partner Leistritz Turbinentechnik GmbH and thus can be seen as an indicator for good workability of the casted FeAlNb-material.

The grain structure was made visible by macro-etching a polished sample from the feeder area. Among other things, the grain structure depends sensitively on the temperature of the melt at the time of tilting. Since the pouring temperature can vary from part to part, not always the same grain structure is observed. Even for the two pre-contoured forging blanks from the same casting the grain structure at a comparable position is sometimes different. This could possibly be caused by the different paths of the melt as it flows into the two halves of the mould.

The examination of the microstructure shows for all castings that a finely distributed Laves phase has formed in the FeAlNb matrix. The Laves phase occurs both inside the grains and at grain boundaries (Fig. 2). Typical for all samples is that the Laves phase is locally inhomogeneously distributed. Its average area share ranges from 2 % to 5 % in the various casts. Since niobium is enriched in the Laves phase, its content in foreign phase-free FeAlNb areas (=matrix) is reduced up to 0.5 at.-% (values from EDX measurements) compared to the niobium concentration averaged over several sample positions per casting. In addition, in all samples studied, two further phases occur much less frequently than the Laves phase: AlN and NbC. Their exact stoichiometric compositions have not been determined yet. AlN sometimes even accumulates locally and is often associated with the Laves phase and/or with NbC to a conglomerate.

The occurrence of the Laves phase in the casting parts is not undesirable, as it can ideally be used to improve the mechanical properties (e.g. increase creep resistance) [3]. This has also been observed in terms of increasing the yield stress for casted FeAlTa [4]. For certain composition ratios of FeAlTa, a microstructure comparable to that observed here for FeAlNb with Laves phase in grains and at grain boundaries is known [4]. However, for the FeAlTa with the same composition ratio as here for FeAlNb (73:25:2 at-%), the Laves phase only takes a portion of 0.5 vol% [4]. It was therefore initially feared that there was no longer enough niobium in the FeAlNb matrix to form additional, strength-promoting (e.g. on grain boundaries) Laves phase during the forging process. In addition, the already existing Laves phase was considered less effective due to its uneven distribution in the samples and its partly relatively large shape. However, the pre-contoured forging blanks were well-forgeable at Leistritz Turbinentechnik GmbH and investigations by the project partner Karlsruher Institut für Technologie show that the share of the Laves phase is greatly increased and the grain structure refined by the forging process.

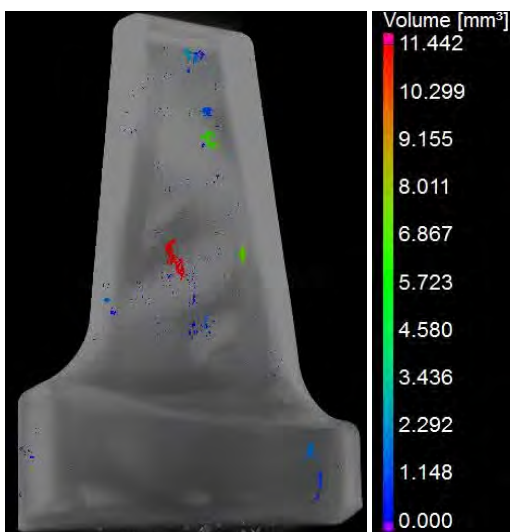


Fig. 1: Porosity in a pre-contoured forging blank.

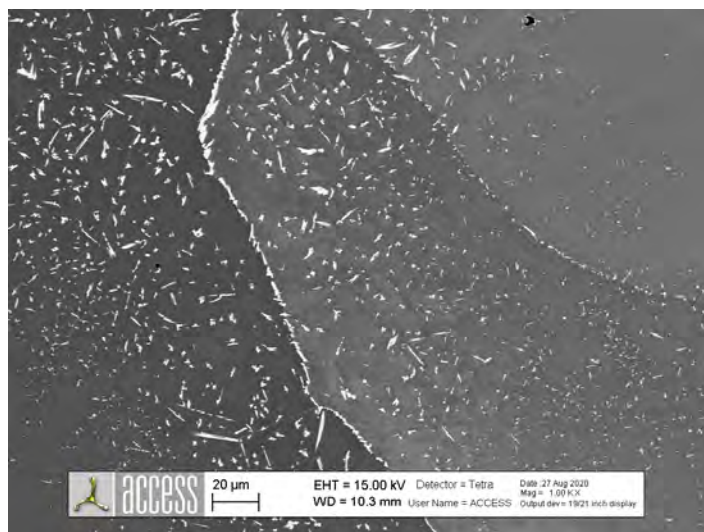


Fig. 2: Laves Phase in grains and at grain boundary.

### Acknowledgement

The authors acknowledge the financial support by the German Federal Ministry of Economic Affairs and Energy (BMWi) in the framework of Pro-FeAl (project number 0324317D).

### References

- [1] Pro-FeAl: Prozessentwicklung für wirtschaftliche, effiziente Turbinenkomponenten aus Eisenaluminiden (BMWi-Kennzeichen 020E-41V7889)
- [2] M. Ghosh, H. Michels, M. Bünck in: M. Heilmaier, M. Krüger, S. Mayer, M. Palm, F. Stein (Eds.): Proceedings Intermetallics 2019. Conventus Congressmanagement & Marketing GmbH, Jena, Germany, **2019**, 206-207.
- [3] M. Palm, F. Stein, G. Dehm, Annual Review of Materials Research. **2019**, *49*, 297-26
- [4] D.D. Risanti, G. Sauthoff, Intermetallics. **2005**, *13*, 1313-1321

**P-32****Grain refinement of FeAl alloys and impact of local solidification time on grain size**Emir Subašić<sup>1</sup>, Jan Freihammer<sup>2</sup> and Heiner Michels<sup>1</sup><sup>1</sup>Access e.V., 52072 Aachen, Germany, e.subasic@access-technology.de, h.michels@access-technology.de<sup>2</sup>Otto Junker GmbH, 52152 Simmerath, Germany, jan.freihammer@otto-junker.com**Introduction**

While Fe-Al intermetallics show low ductility at room temperature, improving this key material property could trigger a broader employment of this class of materials in production of components, e.g. for energy sector applications such as steam turbine parts, or large cast parts under static load, like housings.

Reducing the grain size is an approach to improve ductility for a variety of cast metals as well as Fe-Al intermetallics [1]. In the frame of the FeAl-GuD project, a comprehensive investigation of the effects of various grain refining additives and techniques on the resulting Fe-Al intermetallics microstructure was carried out. A segment of this work coping with the grain refinement of Fe-25Al-1.5Ta (at. %) was already reported elsewhere [2]. The present contribution is devoted to the gravity sand casting and grain refinement of Fe-20Al-5Cr-0.5Zr (at. %) treated with TiC. A relation between columnar grains width and local solidification time is established and recommended here as an equation suitable for further numerical simulation modelling purposes.

**Materials and Methods**

Fe-Al Fe-20Al-5Cr-0.5Zr (at. %) was melted under inert gas (Argon) in a 0.8 t induction furnace lined with an Al<sub>2</sub>O<sub>3</sub>-MgO based refractory ramming mix. Shortly before the end of the melting process 0.75 wt.-% TiC was added to act as grain refiner. The melt was then cast into a sand mold, simultaneously producing the three samples of differing diameters to be investigated. The raw materials used were Fe 99.8, Al 99.5, Cr 99.9, FeZr and Titanium Carbide (TiC) powder which would be representative of those used in the small-midscale industrial production of this material.

Due to the nature of the start material and the industrial melting procedure, small amounts of impurities were present (~0.06 wt.-% Si ~0.06 wt.-% Mn, ~0.6 wt.-% Ni).

During the microstructure characterization, the samples were etched using a color-etching procedure based on [3]. Color contrasts were produced under bright-field illumination and polarized light. A Zeiss Axio imager M optical light microscope was used for imaging of the samples under polarized light. An XY-table was used for the acquisition of MosaiX images, which enabled grain analysis over the cross-section of the metallographic specimens. The circular intercept procedure, as described in [4], was applied in order to determine columnar grain width.

Numerical simulation of mold filling and solidification is done by use of software MAGMA5. Material data for the simulated Fe-Al intermetallic alloy Fe-20Al-5Cr-0.5Zr (at. %) were calculated by Thermo-Calc and imported into the MAGMA data base. CAD data of cylindrical specimens as well as elements of gating and feeding system were designed with CAD-modeler of star-ccm+, imported in MAGMA preprocessor and enmeshed afterwards. Evaluation of simulation results was done in MAGMA postprocessor.

Exponential regression modelling was done in Excel. Fitting estimation was done by calculation of the coefficient of determination (R<sup>2</sup>).

**Results and Discussion**

Circular intercept length was measured for circles with radii of 5 mm and 6.25 mm. The investigated cylindrical specimens possessed diameters of 22 mm, 38 mm and 62 mm. After conducting circular intercept evaluation, the obtained circular intercept lengths (columnar grain widths) were as follows:

- For circle radius 5 mm: 341 μm, 683 μm, 806 μm (respective specimen diameters: 22 mm, 38 mm, 62 mm)

- For circle radius 6,25 mm: 364 μm, 644 μm, 785 μm (respective specimen diameters: 22 mm, 38 mm, 62 mm)

Average values of circular intercept lengths are: 352.5 μm, 663.5 μm, 795 μm (for 22 mm, 38 mm, 62 mm diameters respectively) – these values were used for establishing Eq. 1.

The grain size characterization by use of the circular intercept procedure is shown in Fig. 1. The micrograph represents the etched Fe-20Al-5Cr-0.5Zr (at.%) sample, treated with TiC grain refiner, with a diameter of 22 mm. Applying a circle of radius (R) 6.25 mm led to 108 interceptions (n) in total. Finally, an average circular intercept length (columnar grain width) thusly obtained is 364 μm.

Local solidification time values obtained from the mold filling and solidification calculation in cylindrical specimens with diameter of 15 mm, 30 mm and 60 mm were 36 s, 120s and 340 s, respectively. An example of the local solidification time distribution in the cutting plane of a cylindrical specimen with diameter 60 mm is shown In Fig. 2.

Relations between secondary dendrite arm spacing and local solidification time are already known as a reliable criterion for connecting processing parameter with resulting microstructure and their subsequent evaluation. An example of such equation for alloy A356 is given in [5]. Such relations are usually given in form of an exponential equation, which was determined based on the results obtained for the analyzed Fe-Al samples. It was found, that the

ripening exponent values vary from 0.33 toward 0.5 [6]. The actual dependence of the columnar grain width  $w_{\text{columnar}}$  from the local solidification time  $t_{\text{local}}$  is given by Eq. 1:

$$w_{\text{columnar}} = 100.75 (t_{\text{local}})^{0.37} \quad (1)$$

Coefficient of determination is the square of Pearson's correlation coefficient  $R$ . Both of these statistical indices are used for evaluation how well the regression predictions approximate the real data points. For continuous random variables  $X$  and  $Y$  (here  $w_{\text{columnar}}$  and  $t_{\text{local}}$ ), Pearson's correlation coefficient is calculated as a quotient of the covariance  $\sigma_{XY}$  and the product of standard deviations  $\sigma_X$  and  $\sigma_Y$  [7]. Values of  $0.9 \leq |R| < 1$  indicate a very strong correlation. Coefficient of determination for Eq. 1 is  $R^2 = 0.93$  and Pearson's correlation coefficient is  $R = 0.96$ , indicating a very strong correlation for here developed model.

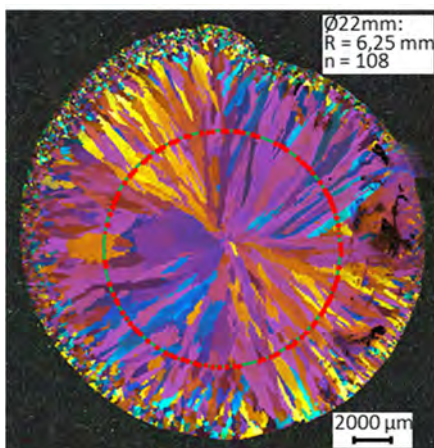


Fig. 1: The grain size characterization by use of the circular intercept procedure; The micrograph of etched specimen made of Fe-20Al-5Cr-0.5Zr (at.%) and treated with TiC grain refiner; Specimen has a diameter of 22 mm; Circle of 6,25 mm radius (R) led to 108 interceptions (n) in total; An average intercept length thus obtained is 364  $\mu\text{m}$ .

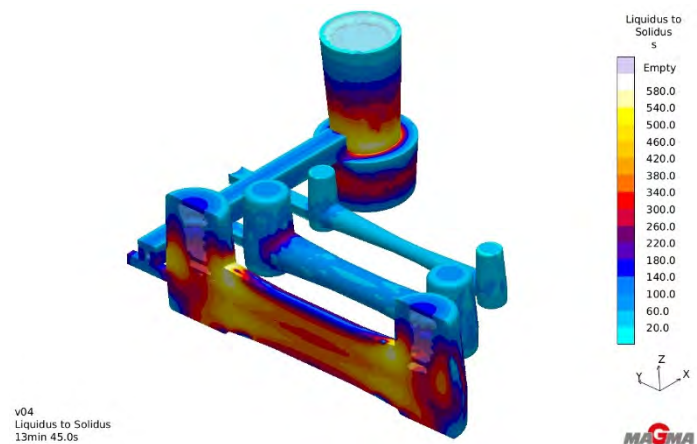


Fig. 2: Calculated local solidification time ('Liquidus to Solidus'-criterion) at the end of solidification for casting trials with three cylindrical specimens of various diameters; A central perpendicular cut-view through the cylindrical specimen with a diameter of 60 mm and accompanied side feeders; Distribution of the local solidification time in the cutting plane can be easily tracked by the calculated values.

### Outlook

In cooperation with project partners from the Centre of Excellence for Lightweight Design at Landshut University of Applied Sciences and Chair of Corrosion and Corrosion Protection at RWTH Aachen University, a comprehensive data set including thermomechanical properties and corrosion resistance of FeAl-based alloys will be completed. To increase the prediction accuracy of the suggested model (Eq. 1), further instrumented experiments to calibrate simulation settings are planned as well as a final verification based on a complex shaped demonstrator part.

### Acknowledgements

The authors gratefully acknowledge financial support by the BMWi German Federal Ministry of Economics and Energy through grants No. 03ET7077A and 03ET7077D.

### References

- [1] D.G. Morris, M.A. Morris-Muñoz, *Intermetallics*. **1999**, 7, 1121-1129.
- [2] E. Subašić, A. Gußfeld, H. Michels, in: M. Heilmaier, M. Krüger, S. Mayer, M. Palm, F. Stein (Eds.): *Proceedings Intermetallics 2019*. Conventus Congressmanagement & Marketing GmbH, Jena, Germany, **2019**, 202-203.
- [3] E. Schaberger-Zimmermann, R.D. Pütz, E. Subašić, D. Zander, *Practical Metallography*. **2021**, 58, 120-128.
- [4] T.N. Kutz, D. Zander, *Corrosion*. **2017**, 73, 648-654.
- [5] M. Shabani, A. Mazahery, *Archives of Metallurgy and Materials*. **2011**, 56, 671-675.
- [6] S. Steinbach, L. Ratke, *International Journal of Cast Metals Research*. **2007**, 20, 140-144.
- [7] T. Subašić, *Probability and mathematical statistics*. University of Zenica, Zenica, Bosnia and Herzegovina, **2008**.

**P-33****High temperature oxidation behavior of TiAlCrYSi bond coatings obtained using CHC-PVD method on  $\gamma$ -TiAl**

Radosław Swadźba<sup>1</sup>, Bogusław Mendala<sup>2</sup>, Lucjan Swadźba<sup>2</sup>, Uwe Schulz<sup>3</sup>, Nadine Laska<sup>3</sup>  
and Peter-Philipp Bauer<sup>3</sup>

<sup>1</sup>Łukasiewicz Research Network - Institute for Ferrous Metallurgy, Gliwice, Poland, rswadzba@imz.pl

<sup>2</sup>Silesian University of Technology, Katowice, Poland

<sup>3</sup>German Aerospace Center (DLR), Institute of Materials Research, Linder Hoehe, 51147 Cologne, Germany

**Introduction**

$\gamma$ -TiAl intermetallics have recently been successfully applied on low pressure turbine blades of modern aircraft engines due to their low density, high specific strength and creep resistance, all of which make them excellent alternatives for Ni-based superalloys. The next milestone achieved in the field of these materials was the application of additive manufacturing technology for production of turbine blades<sup>1,2</sup>. However, the application of TiAl intermetallics is limited to maximum temperature between 750 – 850 °C due to their low high temperature oxidation resistance<sup>3,4</sup>. This is the motivation for development of novel protective coatings that will allow for increasing the operational temperature of TiAl intermetallics.

**Materials and Methods**

This work concerns the application of Closed Hollow Cathode - Physical Vapor Deposition (CHC-PVD) method for the deposition of TiAlCrYSi bond coatings for Thermal Barrier Coatings (TBCs) on  $\gamma$ -TiAl 48-2-2 alloy for high temperature oxidation protection. In the CHC-PVD process, the samples were placed within the hollow cathode with diameter of 80 mm and length of 160 mm and nominal composition Ti-54Al-14Cr-0.5Si-0.5Y (at. %). Prior to coating deposition the samples were subjected to argon ion bombardment using 150 V bias voltage in order to remove contamination from their surfaces. The coating deposition power was 500 W and the argon pressure was maintained at 0.5 mbar Ar for 4 hours. After deposition of the bond coating the samples were pre-oxidized at 900 °C for 2 hours in pure O<sub>2</sub> atmosphere and coated with 7YSZ using EB-PVD method. The coated samples were subjected to the cyclic oxidation test at 900 °C in 1 hour cycles based on which mass change curves as a function of time were prepared. The study involved the detailed analysis of the coating's growth mechanism, initial microstructure as well as phase transformations using high resolution Transmission and Scanning Transmission Electron Microscopy (HRTEM and STEM) as well as Scanning Electron Microscopy (SEM) and high temperature X-ray diffraction (HT-XRD).

**Results and Discussion**

In the as-deposited state the obtained CHC-PVD TiAlCrYSi bond coating was found to be characterized by a columnar („Type T”) microstructure that contained both amorphous and crystalline regions. It has been found using HRTEM that the latter were composed of a strongly textured, hexagonal C14 Ti(Al,Cr)<sub>2</sub> Laves phase. The coated alloy was subjected to the cyclic oxidation test at 900 °C with 1 hour cycles and the lifetime of 1000 cycles was achieved without any spallation of the YSZ top coating. The microstructure of the coating was investigated after 100, 500 and 1000 cycles. It was found that the initially amorphous bond coating transforms to a mixture of  $\gamma$ -TiAl and C14 Ti(Al,Cr)<sub>2</sub> Laves phase during pre-oxidation and YSZ deposition (Fig. 1a). Due to depletion in Al during the high temperature oxidation the bond coating transformed to a continuous layer of the Laves phase. Detailed microstructural investigations using STEM allowed to characterize the thermally grown oxide (TGO) scale (Fig. 1b), which was found to be composed of nanometric layers of titania, equiaxed (Al,Cr)<sub>2</sub>O<sub>3</sub> and columnar  $\alpha$ -alumina. These investigations provided microstructural evidence for the Cr effect on the formation of Al<sub>2</sub>O<sub>3</sub> during pre-oxidation treatment. Yttrium was found to segregate to the grain boundaries of alumina oxide scale during high temperature oxidation, indicating the occurrence of the reactive element (RE) effect. Upon further high temperature oxidation the TGO grew in the form of columnar  $\alpha$ -Al<sub>2</sub>O<sub>3</sub> and maintained excellent adhesion between the ceramic top coating and the TiAlCrYSi bond coating.

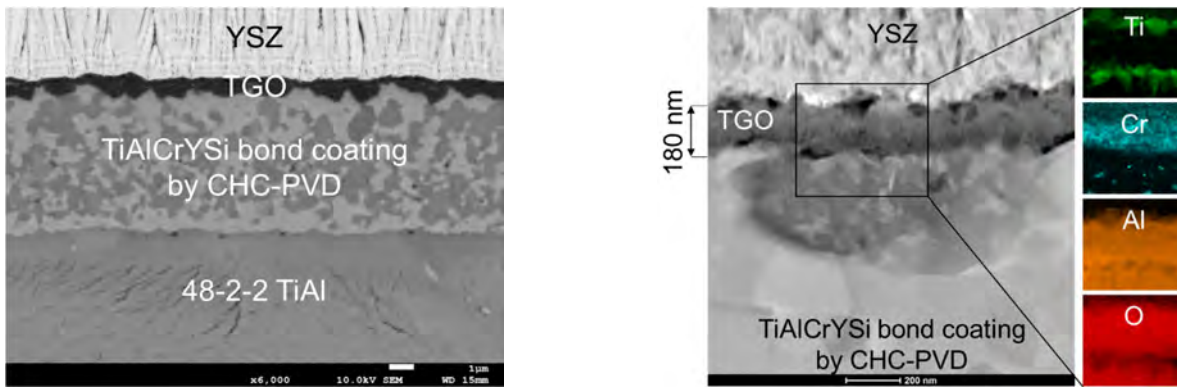


Fig. 1: Microstructure of the TiAlCrYSi bond coating deposited on 48-2-2 TiAl by CHC-PVD method (a) and (b) STEM-HAADF image and EDS mapping of the Thermally Grown Oxide (TGO) in the as-deposited condition.

### References

- [1] Y.W. Kim, S.L. Kim, *JOM*. **2018**, *70*, 553–560.
- [2] B.P. Bewlay, S. Nag, A. Suzuki, M.J. Weimer, *Materials at High Temperatures*. **2016**, *33*, 549–559.
- [3] M. Schütze, *JOM*. **2017**, *69*, 2602–2609.
- [4] R. Pflumm, S. Friedle, M. Schütze, *Intermetallics*. **2015**, *56*, 1–14.



<b>A</b>		<b>D</b>		<b>H</b>	
Abel, A.	13, 119	De Andrade, A.	16, 144	Hammerschmidt, T.	12, 27, 33
Agnarelli, L.	17, 152	de Boor, J.	142	Hans, M.	38
Allen, M.	14, 73, 150	Dehm, G.	155	Hantcherli, M.	75
Amigó, M. L.	167	Demidova, E.	17, 169	Hanus, P.	18
Andreev, V.	171	Distl, B.	9, 67	Härtel, M.	146
Anton, R.	53	Divinski, S.	125, 177	Hasemann, G.	10, 13, 17, 55, 109
Armbrüster, M.	15, 135	Donchev, A.	191		165, 172
		Dupin, N.	10, 27	Hauschildt, K.	25, 55
<b>B</b>				Hausner, C.	161
Baheti, V.	13, 115	<b>E</b>		He, Z.	10, 92
Baker, I.	10, 21, 46	Edry, I.	105	Heczko, M.	84
Bandorf, J.	127	Engström, A.	77	Heilmaier, M.	10, 12, 31, 53
Baricco, M.	148				129, 150
Beck, K.	97	<b>F</b>		Hickel, T.	125
Becker, H.	18, 193	Facio, J. I.	167	Hijikata, Y.	180
Belyaev, S.	127, 169, 170, 171	Förner, A.	14, 127, 131	Hillel, G.	12, 105
Best, J. P.	155	Franke, M.	80, 179	Hilleringmann, M.	16, 86
Betke, U.	172	Freihammer, J.	198	Hinrichs, F.	16, 150
Bezold, A.	131	Freudenberger, J.	113	Hohenwarter, A.	82
Biamino, S.	185	Friak, M.	10, 14, 48, 133	Horiuchi, T.	10, 51
Bikbaev, R.	17, 170	Fries, S. G.	27, 142	Huvelin, Z.	12, 107
Blankenburg, M.	55	Fujii, T.	180		
Borodako, K.	138	Fuks, D.	105	<b>I</b>	
Büchner, B.	167			Ida, S.	10, 23, 55
Bünck, M.	86	<b>G</b>		Ikeda, K.	51
Burkhardt, U.	17, 159	Gabrielian, A.	171	Inui, H.	12, 103, 153, 157, 174, 176
		Gabrisch, H.	9, 25, 65, 189	Iuliano, L.	185
<b>C</b>		Galati, M.	185	Ivanov, A.	17, 171
Cagliaris, F.	167	Galetz, M. C.	97		
Cai, Y.	17, 163	Galy, B.	14, 69, 75, 181	<b>J</b>	
Camut, J.	142	Gan, W.	113	Jacob, A.	12, 99
Cao, G.	113	Gault, B.	46	Jamjoom, A.	127
Chai, Y. W.	111	Gedsun, A.	13, 121	Janovska, M.	65
Chen, Z.	17, 157, 174	Gemming, T.	140	Jayachandran, S.	170
Chen, Q.	77	Ghibaud, C.	185	Jayaram, V.	125
Chen, H.-L.	77	Ghosh, M.	18, 196	Joubert, J.-M.	12, 96, 101
Chen, S.	46	Gokan, K.	180		
Chen, H.	53	Göken, M.	127	<b>K</b>	
Choe, J.	177	Gorr, B.	11, 31, 165	Kahrobaee, Z.	14, 78
Choi, N.	17, 177	Graf, G.	16, 88	Takehi, K.	180
Christ, H.-J.	31, 53	Grin, J.	135, 152	Kardos, S.	73
Chulist, R.	113	Grydin, O.	195	Kauffmann, A.	31, 53, 150
Clemens, H.	69, 75, 88, 146, 181, 185	Guillot, I.	107	Keller, T.	21
Connétable, D.	63	Gupta, A.	125	Kimura, Y.	13, 111
Couret, A.	14, 16, 69, 75, 181	Güther, V.	9, 20, 57, 73	Kirnbauer, A.	38
Couzinie, J.-P.	107			Kishida, K.	153, 174, 176
Crivello, J.-C.	11, 96			Kobayashi, S.	12, 34
Czerny, A.	17, 161			Kollmannsberger, E.	13, 118
				Kononikhina, V.	25
				Körner, C.	80, 127, 131, 179



Kottke, J.	177	Müller, E.	142	<b>S</b>	
Kretschmer, A.	38	Murasue, S.	111	Saage, H.	90, 118
Křivská, B.	195	Musi, M.	18, 69, 75, 181	Sahu, A.	170
Krohmer, E.	88			Sallot, P.	63
Krüger, M.	9, 11, 55, 59, 90	<b>N</b>		Schaarschuch, R.	113
	94, 109, 165, 172	Nakashima, H.	9, 61, 183	Scheffler, M.	172
Kruml, T.	16, 84	Neelamegan, E.	14, 125	Schellert, S.	53
Kuaffmann-Weiss, S.	53	Nestler, B.	163	Schievenbusch, J.	86
Kulitckii, V.	177	Neumeier, S.	127, 131	Schliephake, D.	53, 150
Kuroiwa, S.	17, 174, 176			Schloffer, M.	14, 17, 82, 179
		<b>O</b>		Schmelzer, J.	10, 17, 59, 109, 172
<b>L</b>		Obert, S.	31, 53, 150	Schneider, J.	38
Lacour-Gogny-Goubert, A.	107	Oertel, C.-G.	113	Schuster, R.	99
Lattner, E.	140	Ohmura, T.	111	Schwaiger, R.	165
Lazurenko, D.	18, 186	Okutani, M.	153	Seifert, M.	15, 140
Le, L.	176	Oswald, S.	140	Seifert, H. J.	161
Lee, J. S.	177			Seils, S.	150
Leineweber, A.	10, 13, 116, 193	<b>P</b>		Sekido, N.	23
Leithe-Jasper, A.	152	Palani, I. A.	170	Selleby, M.	92
Lenkovets, A.	18, 188	Palm, M.	13, 16, 41, 78, 121	Shelyakov, A.	15, 138, 169
Leyens, C.	16, 43, 71	Palumbo, M.	16, 27, 148	Sitnikov, N.	138
Li, L.	17, 174	Park, J. H.	177	Skrotzki, W.	10, 13, 113
Lindemann, J.	73	Paul, A.	115, 125	Skrotzki, B.	119
Linderov, M.	84	Pchelnikov, P.	169	Šlapáková, M.	18, 195
Lintner, A.	16, 82	Perepezko, J.	12, 44	Sokolovska, N.	96
Lippmann, S.	10, 12, 50	Petrov, I.	186	Spoerk-Erdely, P.	88
List, S.	46	Pinkas, M.	105	Srinivasan Tirunilai, A.	31, 53
Liu, L.	44	Pippan, R.	82	Stangl, C.	16, 90
Luan, L.	14, 129	Polcik, P.	38	Stark, A.	65, 144, 186, 189
		Povoden-Karadeniz, E.	99	Staron, P.	88, 144
<b>M</b>		Prots, Y.	152	Stein, F.	13, 51, 67, 155
Maawad, E.	113	Pukenas, A.	113	Sturza, M.	17, 167
Maiwald-Immer, T.	16, 146	Pütz, R. D.	13, 29, 123	Su, R.	44
Mali, V.	186	Pyczak, F.	8, 9, 14, 25, 55	Subašić, E.	18, 198
Mani Prabu, S. S.	170		65, 144, 189	Suzuki, H.	17, 153
Manikandan, M.	170			Švec, M.	18
Marquardt, A.	43, 71	<b>R</b>			
Mayer, S.	69, 75, 146, 181, 185	Rackel, M. W.	18, 25, 65	<b>T</b>	
Mayrhofer, P.	13, 15, 38		144, 189	Takeyama, M.	61, 183
Mazánová, V.	84	Ratschbacher, K.	10, 57, 150	Tas, B.	177
Menzel, S.	140	Regenberg, M.	12, 17, 109, 172	Tenkamp, J.	80
Meshi, L.	105	Rehman, U.	17, 155	Teschke, M.	14, 43, 71, 80
Michael, O.	59	Reith, M.	16, 80	Thenot, C.	9, 63
Michels, H.	119, 196, 198	Resnina, N.	15, 137, 169	Thomas, M.	69, 75
Millerand, L.	142		170, 171	Tian, C.	155
Miura, S.	51	Richter, L.	193	Tirunilai, A. S.	31, 53
Mizuta, K.	18, 180	Riesch-Oppermann, H.	129	Toualbi, L.	69, 75
Molénat, G.	69, 75	Rittinghaus, S.-K.	59	Touzani, R.	11, 94
Monchoux, J.-P.	63, 69, 75, 181	Rizza, G.	185	Tsakiropoulos, P.	12, 36
Morales, L. Á.	14, 131	Rohde, M.	161	Tumminello, S.	15, 142
Moritz, J.	43, 71	Rosigkeit, J.	88		

**U**

Ugues, D. 185  
Ulrich, A. S. 11, 97

**V**

Vergnano, M. 148  
Vermaut, P. 107  
Vidal, D. 105  
Vinogradov, A. 84

**W**

Wallis, H. 172  
Walther, F. 43, 71, 80  
Wang, F. 163  
Wartbichler, R. 18, 146, 185  
Watanabe, M. 111  
Weber, M. 31, 53  
Wilde, G. 177  
Wilms, M. B. 59  
Wittmann, M. 46  
Woods, E. 46  
Wurmehl, S. 167

**X**

Xu, H. 46  
Xu, L. 46

**Y**

Yamada, K. 51  
Yamaguchi, M. 51  
Yang, W. 17, 165  
Yang, Y. 10, 14, 77  
Yang, S. 177  
Yazlak, M. 165  
Ye, Y. 10, 46  
Yoshimi, K. 23, 55  
Yu, J. 18, 183  
Yu, J. H. 177

**Z**

Zaletova, I. 138  
Zander, D. 11, 29, 123  
Zapala, P. 86, 119  
Zenk, C. 131  
Zhu, L. 23, 55  
Zschau, H.-E. 18, 191









## OUR CORE COMPETENCIES IN THE USE OF TITANIUM ALUMINIDES:

- Production of Titanium Aluminide Ingots
- Manufacturing of TiAl semi-finished products with excellent homogeneity
- Dimensions according to customer requirements
- Production of TiAl powder for additive manufacturing
- Manufacturing of rolled TiAl sheets



Learn more about our materials on: [www.gfe.com](http://www.gfe.com)

GfE Metalle und Materialien GmbH

# Powerful collaboration



Be it in a digital, hybrid or present form – all solutions  
for your conference from a single source

**conventus**  
CONGRESSMANAGEMENT  
[www.conventus.de](http://www.conventus.de)

